RGNZ/MGPB

Rudarsko-geološko-naftni zbornik

The Mining-Geological-Petroleum Engineering Bulletin



Godište XXXVIII, broj 78 / *Anno XXXVIII, number 78*



Korito rijeke Save kod Podsuseda, 12. 8. 2022.
Fotografirala prof. dr. sc. Jelena Parlov.

The riverbed of the Sava River near Podsused, Zagreb, 12 August 2022.
Photograph taken by Prof. Jelena Parlov.

RGNZ/MGPB

Rudarsko-geološko-naftni zbornik

The Mining-Geological-Petroleum Engineering Bulletin

Hrvatski znanstveni časopis / *Croatian scientific journal*

Godište XXXVIII, broj 78 (vol. 41, sv. 2) / *Anno XXXVIII, number 78 (vol. 41, issue 2)*

Referira se u / *Indexed and abstracted in:*
Chemical Abstracts, Emerging Sources Citation Index (Thomson Reuters, WoS, Core Collection), Compendex + Geo Abstracts (Geobase) + Scopus (Elsevier), GeoRef, Geotechnical abstracts, Google Scholar (via PDFs on http://hrcak.srce.hr/rgn-zbornik), Petroleum Abstracts, Norwegian register for scientific journals, series and publishers.

Akademske baze i pretraživači (otvorena pristupa) / *Academic databases and search engines (open access)*:
DOAJ (received DOAJ Seal), DOI (CrossRef), Geoscience e-journal, Electronic Journals Library, Hrčak, JournalSeek.

Komercijalne baze i pretraživači / *Commercial databases and search engines*:
EBSCO Publishing Services, ProQuest (SciTech, Natural Science, Environmental Science, Earth Science, Technology Collection, Materials Science collections).

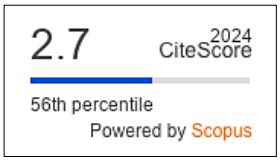
Uvjeti uporabe otvorenoga pristupa časopisu i njegovim arhivama dani su na / *Open access license and archiving is available*:
http://www.sherpa.ac.uk/romeo/search.php?id=2374&format=full&fIDnum=%7c.

UDK/*UDC* 62:66:51-56
Mrežna inačica / *Online:* ISSN 1849-0409
Tiskana inačica / *Print:* ISSN 0353-4529
DOI Prefix: doi.org/10.17794/rgn

Izdavač
Sveučilište u Zagrebu Rudarsko-geološko-naftni fakultet, Pierottijeva 6, HR-10000 Zagreb

Publisher
University of Zagreb Faculty of Mining, Geology and Petroleum Engineering, Pierottijeva 6, 10000 Zagreb, Croatia





2026.





Izjava o recenzentskom postupku/*Peer Review Statement:*

Svi predani rukopisi prolaze jednostruko anonimni postupak recenziranja
koji provode najmanje dva neovisna recenzenta.
Uredništvo donosi konačnu odluku na temelju ocjena recenzenata i općih uredničkih standarda.

All submitted manuscripts undergo a single blind peer review process conducted by at least two independent reviewers.
The editorial board makes the final decision based on reviewers' evaluations and overall editorial standards.

Etika objavljivanja/*Publication Ethics:*

Časopis poštuje najviše standarde akademskog integriteta i etičkog objavljivanja.

The journal upholds the highest standards of academic integrity and ethical publishing.
https://ojs.srce.hr/index.php/rgn/about

Izjava o otvorenom pristupu/*Open Access Statement*:

Svi su članci dostupni u otvorenom pristupu pod licencom CC BY 4.0.
Autorima i čitateljima ne naplaćuju se nikakve naknade.

All articles are open access under a CC BY 4.0 license.
No fees are charged to authors or readers.

Odricanje od odgovornosti/*Disclaimer*:

Stavovi izneseni u člancima objavljenim u časopisu Rudarsko-geološko-naftni zbornik
isključivo su stavovi autora.
Časopisom upravlja neovisni urednički odbor i slijedi međunarodno priznate
najbolje prakse u znanstvenom izdavaštvu.

The views expressed in the articles published in the Mining-Geological-Petroleum Engineering Bulletin are solely those of the authors.
The journal is governed by an independent editorial board and follows internationally recognized best practices in scholarly publishing.

Glavni i odgovorni urednik: Tomislav Korman, Sveučilište u Zagrebu Rudarsko-geološko-naftni fakultet
Zamjenik glavnog i odgovornog urednika: Zoran Kovač, Sveučilište u Zagrebu Rudarsko-geološko-naftni fakultet

Urednici polja:
Lidia Hrnčević (naftno rudarstvo i energetika), Sveučilište u Zagrebu Rudarsko-geološko-naftni fakultet
Zlatko Briševac (rudarstvo), Sveučilište u Zagrebu Rudarsko-geološko-naftni fakultet
Duje Smirčić (geologija), Sveučilište u Zagrebu Rudarsko-geološko-naftni fakultet
Krešimir Pavlić (matematika, fizika, znanosti o svemiru), Sveučilište u Zagrebu Rudarsko-geološko-naftni fakultet

Tehnički urednik: Dubravko Domitrović, Sveučilište u Zagrebu Rudarsko-geološko-naftni fakultet
Zamjenica tehničkog urednika: Josipa Kapuralić, Sveučilište u Zagrebu Rudarsko-geološko-naftni fakultet

Uredнички odbor:
Članovi sa Sveučilišta u Zagrebu Rudarsko-geološko-naftnog fakulteta:
Sanja Bernat Gazibara
Marija Macenić
Šime Bilić
Mario Klanfar

Vanjski članovi:
Moshood Onifade, Federation University, Australija
Manoj Khandelwal, Federation University, Australija
Satria Bijaksana, Institut Teknologi Bandung, Bandung, Indonezija
Maria Alzira Pimenta Dinis, UFP Energy, Environment and Health Research Unit (FP-ENAS), University Fernando Pessoa, Porto, Portugal
Vasyl Hryhorovych Lozynskyi, Dnipro University of Technology, Ukraine, Dnipro, Ukraina
Josip Ivšinović, Vodnikova 17, Zagreb, Hrvatska
Sara Kasmaeeyazdi, University of Bologna, Bologna, Italija
Aleksandar Mezga, Sveučilište u Zagrebu Prirodoslovno-matematički fakultet, Geološki odsjek, Zagreb, Hrvatska
Ivica Skokić, Sveučilište u Zagrebu Geodetski fakultet, Opservatorij Hvar, Croatia
Francesco Tinti, University of Bologna, Department of Civil, Chemical, Environmental and Materials Engineering, Italija
Mojtaba Yari, Isfahan University of Technology Department of Mining Engineering, Isfahan, Iran

Lektura engleskih tekstova:
Dubravka Pleše, Sveučilište u Zagrebu Rudarsko-geološko-naftni fakultet

Lektura hrvatskih tekstova:
Ivana Matas Ivanković, Institut za hrvatski jezik i jezikoslovlje

Izdavački savjet: Fakultetsko vijeće

Za izdavački savjet: Vladislav Brkić, dekan

Adresa na Hrčkovom OJS-u: https://hrcak.srce.hr/ojs/index.php/rgn/index

Adresa na Hrčku (arhiva): https://hrcak.srce.hr/rgn-zbornik

E-pošta glavnoga urednika: tomislav.korman@rgn.unizg.hr

Prijelom
Gredice, Horvaćanska 67, HR-10000 Zagreb

Naklada
elektroničko izdanje, pet brojeva godišnje

Editor-in-Chief:
Tomislav Korman, University of Zagreb Faculty of Mining, Geology and Petroleum Engineering, Croatia

Deputy Editor-in-Chief:
Zoran Kovač, University of Zagreb Faculty of Mining, Geology and Petroleum Engineering, Croatia

***Editors of scientific fields**:*
Lidia Hrnčević (Petroleum Engineering and Energetics),
University of Zagreb Faculty of Mining, Geology and Petroleum Engineering, Croatia
Zlatko Briševac (Mining),
University of Zagreb Faculty of Mining, Geology and Petroleum Engineering, Croatia
Duje Smirčić (Geology),
University of Zagreb Faculty of Mining, Geology and Petroleum Engineering, Croatia
Krešimir Pavlić (Mathematics, Physics, Space Sciences),
University of Zagreb Faculty of Mining, Geology and Petroleum Engineering, Croatia

***Tehnical editor**:*
Dubravko Domitrović, University of Zagreb Faculty of Mining, Geology and Petroleum Engineering, Croatia

***Assistant Technical Editor**:*
Josipa Kapuralić, University of Zagreb Faculty of Mining, Geology and Petroleum Engineering, Croatia

Editorial board:

Members from the University of Zagreb Faculty of Mining, Geology and Petroleum Engineering, Croatia:
Sanja Bernat Gazibara
Marija Macenić
Šime Bilić
Mario Klanfar

Non-Faculty Members of the Editorial Board:
Moshood Onifade,
Federation University, Australia
Manoj Khandelwal,
Federation University, Australia
Satria Bijaksana,
Institut Teknologi Bandung, Bandung, Indonesia
Maria Alzira Pimenta Dinis,
UFP Energy, Environment and Health Research Unit (FP-ENAS), University Fernando Pessoa, Porto, Portugal
Vasyl Hryhorovych Lozynskyi,
Dnipro University of Technology, Ukraine, Dnipro, Ukraine
Josip Ivšinović,
Vodnikova 17, Zagreb, Croatia
Sara Kasmaeeyazdi,
University of Bologna, Bologna, Italy
Aleksandar Mezga,
University of Zagreb Faculty of Science, Geological Department, Croatia
Ivica Skokić,
University of Zagreb Faculty of Geodesy, Observatory Hvar, Croatia
Francesco Tinti,
University of Bologna, Department of Civil, Chemical, Environmental and Materials Engineering, Italy
Mojtaba Yari,
Isfahan University of Technology Department of Mining Engineering, Isfahan, Iran

English proofreading:
Dubravka Pleše,
University of Zagreb Faculty of Mining, Geology and Petroleum Engineering, Croatia

Croatian proofreading:
Ivana Matas Ivanković,
Institute of Croatian Language and Linguistics, Croatia

Publishing council*: Faculty Council*

Chairman of Council*: Vladislav Brkić, Dean*

The Open Journal System web site: *https://hrcak.srce.hr/ojs/index.php/rgn/index*

The Croatian scientific and professional journals archive (Hrčak): *https://hrcak.srce.hr/rgn-zbornik*

E-mail of the Editor-in-Chief: *tomislav.korman@rgn.unizg.hr*

Layout
Gredice, Horvaćanska 67, HR-10 000 Zagreb

Edition
e-publication, five issues per year

Sadržaj/*Contents*

Radovi/*Papers*

1.	Geomechanical Analysis to Determine The Maximum Limit of Water Injection in the Keutapangan Formation, "ZA" Field, North Sumatra Basin *(Zahra Adinda Billqish, Andika Wicaksono, Sismanto Sismanto)*	1-14
2.	Study of the bactericidal-inhibitor properties of new reagents *(Guseyn Gurbanov, Aysel Gasimzade)*	15-30
3.	Optimization of Stope Dimensions in a Geotechnically Complex Mine Using Automated Stability Analysis *(Mohammad Army, Tri Karian, Takashi Sasaoka, Akihiro Hamanaka, Firly Rachmaditya Baskoro, Budi Sulistianto, Hideki Shimada)*	31-46
4.	Feasibility analysis of granitic rocks for use in the dimension stone industry *(Ekin Köken)*	47-57
5.	Facies Architecture and Sedimentary Provenance of the Miocene Ombilin Formation: Interplay of Tectonics and Eustasy in a Neogene Intermontane Basin, Central Sumatra, Indonesia *(Aurio Erdi, Syahreza S. Angkasa, Eko Suwarno, Aswan)*	59-84
6.	The Effect of Calcium and Magnesium Ions on a Crude Oil-Brine-Carbonate Rock System for Enhanced Oil Recovery by Sophorolipid Solution *(Indah Widiyaningsih, Ivan Kurnia, Harry Budiharjo Sulistyarso, Tutuka Ariadji, Taufan Marhaendrajana)*	85-95
7.	Geodynamic and Paragenetic Evolution of the Jbel Houanite Mineralization (Sb-Au; Pb-Zn) Eastern High Atlas of Morocco *(Jaouad Choukrad, Abdelkhiar Ait ali, Mohammed Charroud, Nacir El moutaouakkil, Boubker Boukili, Amine talih)*	97-112
8.	Unveiling Shale Gas Reservoir Structures with Seismic and MT Data: WALDIM-Based Study from East Kalimantan Indonesia *(Suharsono, Yustisio Dianwiyono, Edy Wijanarko, Wahyu Hidayat, Muhammad Fachrul Rozi Kurniawan, Yudha Agung Pratama)*	113-128
9.	Predicting Peak Particle Velocity Induced by Mining Blasting Using Optimized Deep Learning with Coronavirus Herd Immunity Algorithm *(Davood Mohammadi Sargini, Mohammad Ataei, Reza Mikaeil, Akbar Esmaeilzadeh)*	129-146
10.	Hydraulic Connectivity Between the Sava River and Lake Jarun During Drought: A High-Resolution Monitoring and Time Series Approach *(Jelena Parlov, Filip Šegović, Kristijan Posavec, Zoran Kovač)*	147-161
11.	The Effect of Kaolinite on Calcium Carbonate Water-Based Drilling Fluid *(Mohammed Abdalraheem, Basfar S, Elkatatny S)*	163-174
12.	Management of Frame-Anchor Fastening Parameters for Preparatory Excavations in Monorail-Based Heavy Cargo Delivery *(Andrii Herasymenko, Leonid Shyrin, Rostyslav Yegorchenko, Ivan Iniutkin, Yuliya Pazynich)*	175-188
13.	Improving the efficiency of in-situ uranium leaching via oxygen-enriched lixiviant injection *(Khalidilla Yussupov, Erbolat Aben, Gulfarizada Abdissattar, Saifilmalik Myrzakhmetov, Dalelkhan Akhmetkanov)*	189-196
14.	Hydrogeochemical properties of thermal springs for natural therapeutic uses in medical geology at the Ciwidey area, West Java, Indonesia *(Rizka Maria, Heri Nurohman, Hilda Lestiana, Riostantieka Mayandari Shoedarto, Eki Naidania Dida, Jakah Jakah, Ernowo Ernowo, Yudi Rahayudin)*	197-211
15.	The Integrated Analysis of Basement Faults in North Bangka Island, Indonesia, Using Surface Lineament Density and Gravity Anomaly Enhancement *(Harnanti Yogaputri Hutami, Edy Sunardi, Iyan Haryanto, Sonny Winardhi, Nugroho Prasetyo, Nur Ayu Anas, Erlangga Ibrahim Fattah)*	213-228

RGNZ/MGPB

Geomechanical Analysis to Determine The Maximum Limit of Water Injection in the Keutapangan Formation, "ZA" Field, North Sumatra Basin

Rudarsko-geološko-naftni zbornik
(The Mining-Geology-Petroleum Engineering Bulletin)
DOI: 10.17794/rgn.2026.2.1

Original scientific paper

Zahra Adinda Billqish[1], Andika Wicaksono[2], Sismanto Sismanto[1]*

[1] *Geophysics Laboratory, Department of Physics, Faculty of Mathematics and Natural Sciences, Universitas Gadjah Mada, Jl. Geografi, Yogyakarta, 55281, Indonesia.*

[2] *Pertamina Hulu Rokan, Jl. Prof. DR. Satrio no. 30, Jakarta, Indonesia.*

Abstract

The "ZA" Field is located in the North Sumatra Basin and is predominantly affected by geopressure issues. As such, geomechanical analysis is crucial during drilling operations to mitigate potential hazards. The geomechanical analysis conducted in this study utilizes a 1D Mechanical Earth Model (MEM), which includes the following components: overburden stress, pore pressure, rock strength, rock elastic properties, and minimum horizontal stress. The data used in this analysis were obtained from the following sources: wireline logging for all geomechanical calculations, pressure tests to validate pore pressure values, fracture gradient data to validate the minimum horizontal stress curve, step-rate tests to determine the injection pressure limit, and well reports. The "ZA" Field exhibits a complex geopressure regime, ranging from underpressure to overpressure, with transitional zones that combine both conditions. Overpressure is primarily attributed to loading mechanisms, while underpressure results from historical fluid extraction during previous drilling activities. Lithological analysis indicates that the reservoir consists of shaly sand and fine-grained formations. Due to the shallow burial depth, these rocks remain poorly consolidated, resulting in a narrow safe injection window above the pore pressure. This constraint is exemplified by one well, where the maximum allowable injection pressure was 7.63 MPa, with only a 2 MPa margin above the pore pressure.

Keywords:
1D MEM, pore pressure, rock strengths, rock elastic properties, minimum horizontal stress

1. Introduction

Geomechanics plays a crucial role in minimizing hazards during drilling operations. It is used to analyze fault seal potential, predict pore pressure, assess wellbore stability, and evaluate various stimulation methods (**Lanin, 2021**). With current technological advancements, various methods have been applied in geomechanical data processing, one of which is machine learning-based approaches such as real-time LWD analysis. This technology enables the rapid and accurate estimation of geomechanical parameters, thereby supporting more effective, safe, and efficient decision-making during drilling operations and reservoir management (**Liu et al., 2025**). Neglecting geomechanical considerations has led to numerous incidents, including the Lapindo mudflow disaster. This disaster was triggered by subsurface overpressure, where the drilling mud weight was insufficient to counteract the formation pressure. As a result, the high-pressure mud erupted to the surface (**Nuraini, 2023**). This incident underscores the importance of geomechanical applications, particularly developing a Mechanical Earth Model (MEM), to mitigate subsurface risks.

The Mechanical Earth Model (MEM) is a comprehensive representation of rock mechanical properties, fracture behaviour, and subsurface stresses, pressures, and temperatures at depth. Geoscientists use MEM to predict rock deformation and failure during drilling. MEM integrates geological, geophysical, and field measurement data, including core tests, well logs, drilling records, and production data (**Zain et al., 2020**). Additionally, MEM helps estimate the maximum allowable fluid injection pressure, which must be carefully calibrated based on reservoir pore pressure and in-situ stress conditions. Excessive injection pressure can fracture cap rocks, leading to fluid leakage into unintended formations (**Rozamuri et al., 2022**). Mechanical Earth Models (MEMs) can be categorized into one-dimensional (1D) and three-dimensional (3D) models. The 1D MEMs demonstrate significant potential in addressing various challenges associated with reservoir planning and management. Furthermore, they also serve as a foundational step toward the development of 3D MEMs. This pro-

* Corresponding author: Sismanto
e-mail address: sismanto@ugm.ac.id
Received: 5 May 2025. Accepted: 20 September 2025.
Available online: 13 March 2026

gression can enhance the understanding of reservoir behaviour and improve predictive capabilities in geologically complex environments (**Verma et al., 2021**).

Previous geomechanical studies on the Keutapang Formation were conducted by **Aziz & Bolt (1984)** and **Yosandian et al. (2014)**. **Aziz & Bolt (1984)** attributed overpressure in the formation to high sedimentation rates and recommended a mud weight of 16.5 ppg for safe drilling. Similarly, **Yosandian et al. (2014)** confirmed overpressure in the Keutapang Formation, with density-sonic transit time cross-plots showing no evidence of mineral transformation. Another geomechanical study was conducted in southwest Iran, which used 1D MEMs to predict pressure and deformation changes, also assess the risk of fault reactivation and caprock stability. This approach can recognize the risk management of injection in old reservoirs. Although the processing is easier, if the data is incomplete, it can make the model less accurate and the risk of failure increases due to extreme conditions that cannot always be predicted (**Saadatnia et al., 2023**). This study aims to further investigate subsurface conditions through geomechanical analysis and determine the maximum safe injection pressure limit Keutapangan Formation, "ZA" Field, North Sumatra Basin.

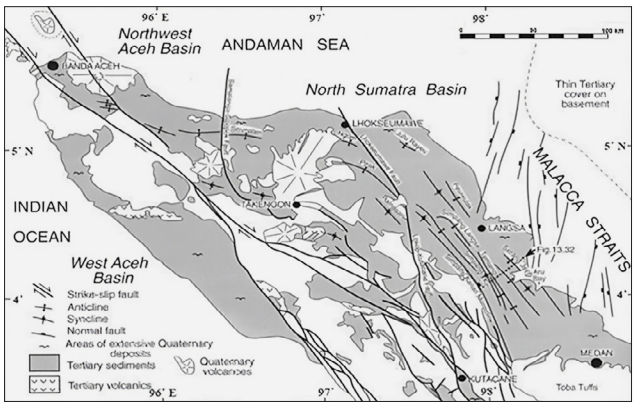


Figure 1. North Sumatra Basin (**Wardhana et al., 2021**)

2. Geological Setting

The North Sumatra Basin is one of Sumatra's three back-arc basins, situated along the western margin of Sundaland and spanning approximately 60,000 km², covering both onshore and offshore areas (**Tampubolon et al., 2017**). It is bounded by (see **Figure 1**); The Barisan Mountains to the southwest (SW), the Asahan Arch to the southeast (SE), the Andaman Sea to the northwest (NW), and the Malacca Platform to the northeast (NE).

The basin's dominant structural trends align in NW-SE and NE-SW directions. As shown in **Figure 1**, the North Sumatra Basin lies within a tectonically active zone on the western edge of the Sibumasu Block, where multiple tectonic events have significantly influenced its geological evolution. The basin's complex structural framework results from rotational and translational movements of major tectonic plates (**Wardhana et al., 2021**). The basin's tectonic model is primarily governed

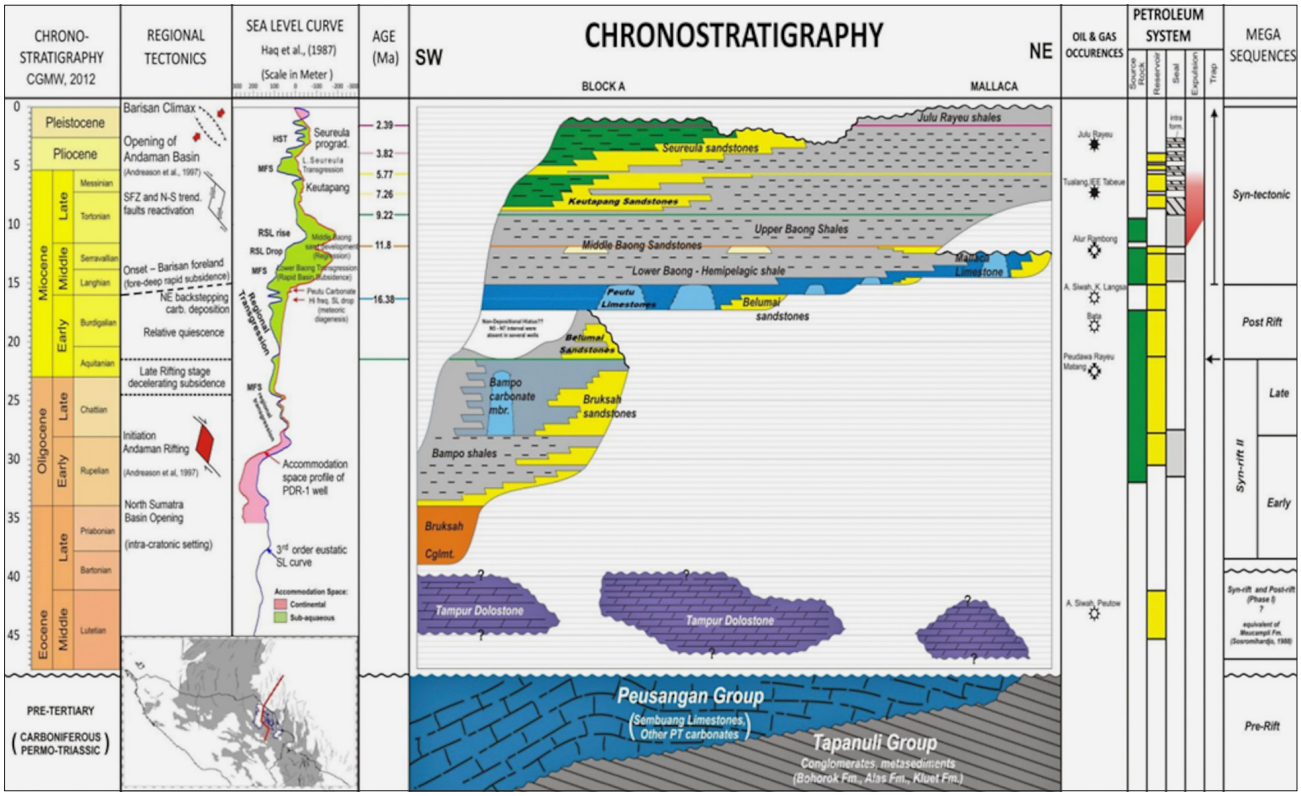


Figure 2. Basin stratigraphy (**Syarifuddin et al., 2018**)

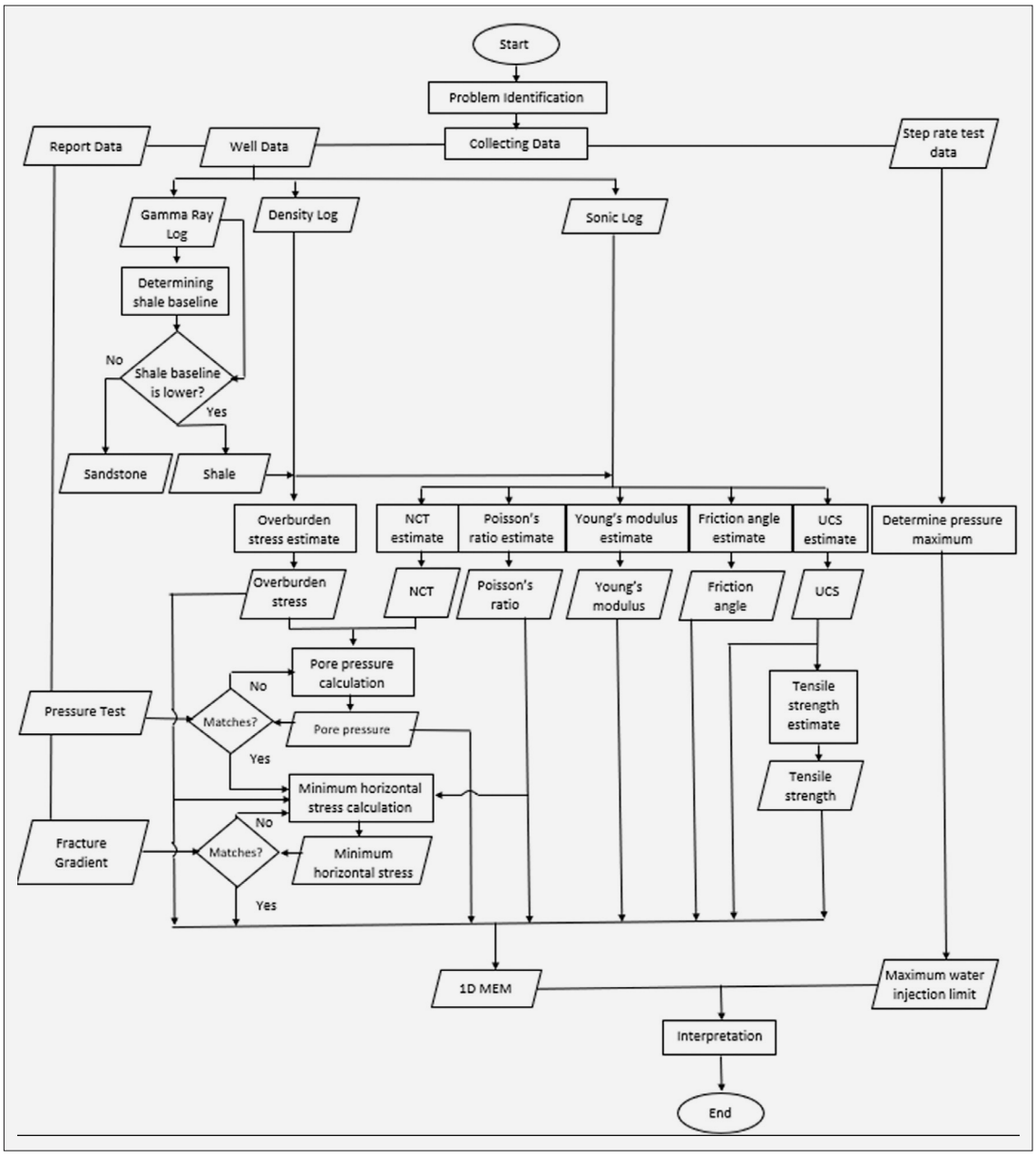


Figure 3. Flowchart

by a dextral strike-slip fault system (**Wardhana et al., 2021**).

Based on the stratigraphic column of the North Sumatra Basin (see **Figure 2**), nine formations have been identified:

1. Tampur-Meucampli Formation: composed of carbonate and dolomite sediments with chert nodules, deposited in sublittoral to marine environments. It is located on the eastern high of the basin near the Asahan Arch.
2. Meucampli Formation: consists of clastic sediments exposed in northwest Aceh
3. Parapat/Bruksah Formation: dominated by conglomerates and sandstones, with sandstone derived from local horst block contributions.
4. Bampo Formation: characterized by poorly laminated, pyritic carbonate shale with low carbonate content (**Muchlis & Elder, 2020**)
5. Peutu-Belumai Formation: consists of claystone and siltstone, moderately to highly calcareous, often fossil-rich, and slightly glauconitic (**Soepardji, 1983**). Belumai Formation: Comprises fine-to medium-grained sandstones, located in the eastern shelf area of the basin
6. Baong Formation: composed of shale, sandstone, and mudstone (**Wardhana et al., 2021**).
7. Keutapang Formation: features fine sandstone and clay with interbedded shale and thin limestone layers (**Prasetyo et al., 2021**).

8. Seurula Formation: consists of sandstone, shale, and clay
9. Julu Rayeu Formation: comprised of fine- to coarse-grained sandstone and claystone (**Astawa et al., 2012**).

3. Materials and Methods

This research involves 26 wells across the North Sumatra Basin. The data used includes wireline logging, pressure test, fracturing report, and well reports. The wireline logging data used comprises gamma ray logs, sonic logs, and density logs, all of which are available for every well. Pressure test data only available for one well (Well-23) and fracturing report data, includes step rate test data and fracture gradient, is available for only one well (Well-7). All geomechanical data calculations were performed in Microsoft Excel, where the processing flow can be seen in **Figure 3**.

The data limitations and applications are that the limited availability of pressure test data (only one well) limits its direct comparisons across the field and prevents extrapolation to other wells, single-well step rate test is applied conservatively and locally without generalization to field-wide operations, and fracture gradient data serves as key validation for stress field modelling. The integration of these datasets enables robust pore pressure prediction through Eaton's method with empirical validation, accurate determination of injection pressure limits for reservoir management, and comprehensive stress field characterization for wellbore stability analysis

All data processing and interpretations follow standard petroleum engineering protocols, with quality control measures applied to ensure data reliability. Where data is limited (pressure tests, step rate tests), conservative engineering approaches are employed to mitigate uncertainty. While this study does not include direct validation using numerical simulations, core-based MEMs, or machine learning approaches, the mechanical parameters and equations adopted in the 1D MEM construction are consistent with widely accepted geomechanical modelling practices as demonstrated in numerous previous studies, such as **Zain et al. (2020)**, **Shen et al. (2024)**, and **Larsen et al. (2000)**.

Overburden stress is caused by the weight of the overlying formation layers. Density logs are typically used to determine the overburden stress. The value of the overburden stress can be obtained using the equation (**Knoll, 2016**),

$$\sigma_v = \int_0^z \rho(z) g dz \quad (1)$$

Where:

σ_v – overburden stress (Pa),
$\rho(z)$ – bulk density (kg/m^3),
z – depth (m),
g – gravity constant (m/s^2).

Hydrostatic pressure is caused by static or non-moving fluid at a certain depth (**Wicaksono, 2021**). Hydrostatic pressure is defined by

$$P = \rho_w g z \quad (2)$$

Where:

P – hydrostatic pressure (Pa),
ρ_w – water density (kg/m^3),
g – gravity constant (m/s^2),
z – depth (m).

The Normal Compaction Trend (NCT) represents a linear relationship derived from optimally compacted intervals in low-permeability formations. This fundamental geomechanical parameter serves two critical functions, i.e. baseline reference for normal pressure conditions, and a diagnostic tool for identifying geopressure zones where pore pressure exceeds hydrostatic pressure (see **Figure 4**).

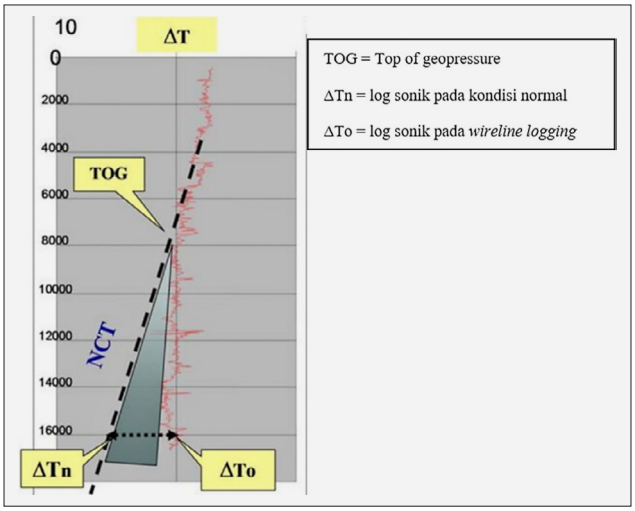


Figure 4. Pore pressure prediction based on NCT (**Shaker, 2007**)

Key characteristics of NCT exhibit an exponential decrease with depth, it requires Δt_mudline (sonic transit time at mud-line) as the input parameter, typical range of 185-200 μs/ft (**Zhang, 2013**), and formation-specific variations may occur based on lithology.

In pore pressure prediction, the primary reference for Eaton's method calculations and critical for identifying transition zones between pressure regimes, enables the detection of under-compaction anomalies (**Shaker, 2007**). The NCT curve's reliability depends on the quality of sonic log data, proper selection of reference shales, and accounting for regional geological variations. This methodology provides the foundation for accurate pore pressure prediction, essential for well planning and drilling hazard mitigation.

$$\Delta t_n = \Delta t_m + (\Delta t_{ml} - \Delta t_m) e^{-cz} \quad (3)$$

Where:

Δt_n – transit time value in Normal Compaction Trend (μs/ft),

Δt_m – transit time value in wireline logging (μs/ft),
Δt_{ml} – transit time value of mudline (μs/ft),
c – constant,
z – depth (m).

Pore pressure refers to the fluid pressure within rock pore spaces. Under normal hydrostatic conditions, it equals the pressure exerted by a vertical column of formation water. Direct measurement techniques include Repeat Formation Tester (RFT), and Modular Dynamic Tester (MDT**) (Wicaksono, 2021**). Wireline log-based pore pressure calculations achieve greater accuracy in shale intervals than in sandstone due to fundamental differences in compaction behaviour:

Especially in Shale Characteristics: extremely low permeability inhibits fluid escape, mechanical compaction under overburden stress leads to fluid retention and pressure buildup, and diagenetic processes can further enhance overpressure conditions. While for Sandstone behaviour, higher permeability enables fluid redistribution, and rapid pressure equalization occurs despite diagenetic effects (**Osborne, 1997**).

The Eaton method was developed for the Gulf of Mexico's undercompacted, overpressured shales. This widely used technique derives from the principle of effective stress. The method can be identified the specifically designed for shale formations; incorporates sonic, resistivity, or density log data; relies on normal compaction trend analysis; and is particularly effective in young, Tertiary basins.

This equation to approach remains fundamental in modern pore pressure prediction workflows, though it requires careful calibration with direct pressure measurements in each basin.

$$\sigma_{eff} = \sigma_v - P_p \tag{4}$$

Where:

σ_{eff} – effective stress (Pa),
σ_v – overburden stress (Pa),
P_p – pore pressure (Pa).

Terzaghi's principle states that when a rock experiences vertical stress, that stress is countered by the pore fluid pressure within the rock, which consists of pore pressure and effective stress. Effective stress can be correlated with log data such as resistivity, wave velocity, or transit time to establish the Eaton relationship in (**Knoll, 2016**)

$$P_p = \sigma_v - (\sigma_v - P)\left(\frac{\Delta t_m}{\Delta t_n}\right)^n \tag{5}$$

Where:

σ_v – overburden stress (Pa),
P – hydrostatic pressure,
Δt_m – transit time value in wireline logging (μs/ft),
Δt_n – transit time value in Normal Compaction Trend (μs/ft),
n – constant that is used for calibration.

The elastic properties of rocks can be classified into static and dynamic elastic properties. Static elastic properties are obtained through core analysis to determine Young's modulus and Poisson's ratio, with depth-specific information limited to the locations where core samples are taken. In contrast, dynamic elastic properties are derived from sonic log measurements (**Knoll, 2016**). Based on laboratory testing, static and dynamic elastic properties are not identical due to differences in strain magnitude. The measured modulus is not purely elastic, as it includes additional irreversible deformation caused by friction. This indicates that static strain is always greater than dynamic strain, resulting in static elastic modulus values that are consistently lower than dynamic elastic modulus values (**Knoll, 2016**). The equation for static Young's modulus is presented in (**Amin et al, 2022**);

$$E_s = \left(0.076 \times \left(\frac{304.8}{\Delta t_p}\right)^{3.23}\right) \tag{6}$$

Where:

E_s – static young modulus (GPa),
Δt_p – slowness of compression wave (μs/ft).

Poisson's ratio is defined as the (negative) ratio of lateral strain to axial strain under uniaxial stress conditions (**Tandirerung, 2023**). The equation for Poisson's ratio is presented in **Christaras et al. (1994)**;

$$\nu_{sta} = 0.71\nu_{dyn} + 0.063 \tag{7}$$

Where:

ν_{sta} – static Poisson ratio and ν_{dyn} – dynamic Poisson ratio.

Rock strength is the ability of a rock to resist external deformation when subjected to external stress (**Gunawan et al., 2017**). Rock strength can be represented by unconfined compressive strength (UCS), tensile strength, and friction angle. An empirical approach is commonly applied using various correlation methods. One such technique involves relating uniaxial compressive strength (UCS) to the compressional wave transit time interval, as shown in Equation 8 (**Amin et al., 2022**). Rock strength based on UCS is classified into four categories, as presented in **Table 1** (**Attewell & Farmer, 1976**).

Rock strength refers to a formation's capacity to withstand external stresses without permanent deformation (**Gunawan et al., 2017**). This fundamental geomechanical property is typically quantified through three key parameters;

1. Strength Parameters (Unconfined Compressive Strength (UCS), Tensile Strength, and Internal Friction Angle).
2. Empirical Determination Methods (The most common approach utilizes established correlations, including UCS derivation from compressional wave (P-wave) transit time (Δt) (**Amin et al., 2022**), and other log-derived relationships (sonic, density, or resistivity-based).

Table 1: Rock strength classification based on UCS (**Attewell & Farmer, 1976**)

Strength Classification	Strength Range (MPa)	Typical Rock Types
Very weak	10-20	Weathered and weakly compacted sedimentary rocks
Weak	20-40	Weakly-cemented sedimentary rocks, schist
Medium	40-80	Competent sedimentary rocks, some low-density coarse-grained igneous rocks
Strong	80-160	Competent igneous rocks, some metamorphic rocks, and fine-grained sandstones

3. UCS Classification System: Attewell and Farmer's (1976) classification, as referenced in **Wilson et al. (2022)**, categorizes rock strength into four distinct classes based on UCS magnitude (see **Table 1**)

This classification system provides essential guidance for Wellbore stability analysis, Hydraulic fracturing design, Sand production prediction, and Drilling parameter optimization

The empirical correlations remain particularly valuable when core data is unavailable, though they require regional calibration for optimal accuracy in different geological settings (**Moos et al., 1999** in **Knoll. 2016**).

$$UCS = 42.1 \exp\left(1.9 \times 10^{-11} \rho {V_p}^2\right) \quad (8)$$

Where:

UCS – unconfined compressive strength (MPa),

ρ – density log (g/cm^3),

V_p – compressional wave velocity (m/s).

Tensile strength is defined as the maximum amount of tensile stress that a material can withstand before failure occurs. In the context of rock mechanics, tensile strength is crucial as it affects the stability and integrity of rock structures (**Perras & Diederichs, 2014**). According to **Perras & Diederichs (2014)**, an empirical equation for tensile strength is presented in;

$$T = \frac{1}{10} \times UCS \quad (9)$$

Where:

T – tensile strength (MPa),

UCS – unconfined compressive strength (MPa).

The tensile strength can be classified for various rock types based on **Lockner (1995)**, as shown in **Figure 5**.

The friction angle is a measure of a rock's ability to resist shear stress. It represents the ratio between the normal force and the resultant force during failure caused by shear stress. The friction angle, along with UCS, is essential for many commonly used failure criteria to estimate rock strength at depth. An empirical equation to calculate the friction angle is presented in **Zain et al. (2020)**;

$$\varphi = 26.5 - 37.4\left(1 - \phi - V_{clay}\right) + \\ + 62.1\left(1 - \phi - V_{clay}\right)^2 \quad (10)$$

Where:

φ – friction angle (°),

ϕ – porosity,

V_{clay} – volume of clay.

Based on **Linh et al. (2021)**, the friction angle is categorized into three groups, as shown in **Table 2.**

Minimum horizontal stress represents the threshold at which rock begins to fracture, indicating the rock's strength limit (**Wicaksono, 2021**). This stress can be measured using extended leak-off tests (XLOT) or mini-frac tests. In these methods, fluid is injected into the wellbore to pressurize the exposed rock interval until fracturing occurs. As pumping continues at a constant rate, the fracture propagates away from the wellbore.

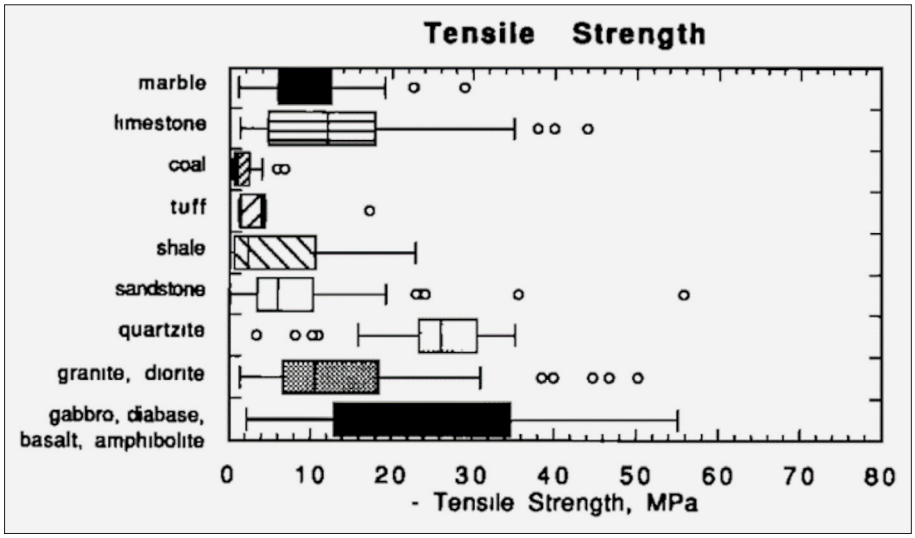


Figure 5. Classification of tensile strength (**Lockner, 1995**)

Table 2. Classification of friction angle (**Linh et al., 2021**)

Classification	Friction angle (degree)	Type of rock
Low	20-27	Schist (mica), clay, marl
Medium	27-34	Sandstone, siltstone, chalk, gneiss, slate
High	34-40	Basalt, granite, limestone, and conglomerate

The fracture grows in a direction perpendicular to the least principal stress, as this orientation requires the least energy for propagation. Consequently, the pressure required to propagate the fracture is equal to or greater than the minimum horizontal stress (**Knoll, 2016**).

Fracture propagation will cease when the rate of fluid leakage from the fracture and wellbore into the formation exceeds the rate of fluid injection. If pumping is stopped, fluid continues to leak from the fracture walls until the fracture closes and becomes disconnected from the wellbore. The fracture closes once the pressure falls below the normal stress acting on it, which corresponds to the minimum horizontal stress, and the value of the minimum horizontal stress can be calculated using an equation (**Knoll, 2016**),

$$S_{hmin} = \frac{\nu}{1-\nu}\left(\sigma_v - P_p\right) + P_p \qquad (11)$$

Where:

S_{hmin} – minimum horizontal stress (Pa),

ν – poisson ratio,

σ_v – overburden stress (Pa),

P_p – pore pressure (Pa).

The injection pressure window refers to the pressure range used to inject fluid into the reservoir, where the pressure must be high enough to induce shear failure and enhance permeability, yet low enough to avoid damaging the formation. Elevated injection pressures can trigger shear failure, thereby improving permeability. An effective degree of shear failure can be achieved by maintaining injection pressures within this optimal window (**Collins, 2002**).

Determining the appropriate injection pressure window requires an understanding of both the pore pressure and the minimum horizontal stress. Pore pressure represents the fluid pressure within the formation, while the minimum horizontal stress defines the lower bound beyond which rock fracturing will occur.

Underpressure is defined as a pressure that is lower than hydrostatic pressure. It typically occurs when fluids are extracted from a reservoir, leading to a reduction in fluid volume and, consequently, a decrease in pore pressure. This phenomenon is commonly observed in depleted fields – reservoirs that have already produced oil and gas.

In addition to production-related causes, underpressure can also occur naturally. Naturally occurring underpressure can be classified into gravity-driven and geologically driven processes. Gravity-driven underpressure arises from changes in elevation, flow rates, or the selected reference for the hydrostatic gradient. In contrast, geologically induced underpressure results from geological changes that alter the intrinsic properties of rocks or the pressure–volume–temperature (PVT) conditions of fluids, preventing the fluid pressure from equilibrating with its surroundings (**Birchall et al., 2022**).

Overpressure can be categorized into two main mechanisms: loading and unloading. The loading mechanism (see **Figure 6a**) is typically caused by rapid sedimentation in a basin, during which the fluids within the rock pores are unable to escape – a process known as disequilibrium compaction. This mechanism generally produces consistent patterns in sonic and density logs, reflecting the imbalance between fluid retention and the rate of pore compaction. As sediment accumulates, vertical stress – or gravitational loading – increases, potentially generating excess pressure due to uneven compaction (**Buntoro et al., 2022**).

The unloading mechanism (see **Figure 6b**), on the other hand, contributes to overpressure through processes that transfer the load from grain-to-grain contact within the rock to the fluids occupying the pores (**Buntoro et al, 2022**). This can occur when pore fluids are introduced or when part of the solid matrix spontaneously transforms into fluid, increasing pore pressure – assuming the fluid cannot escape. In such cases, a portion of the stress previously supported by the rock

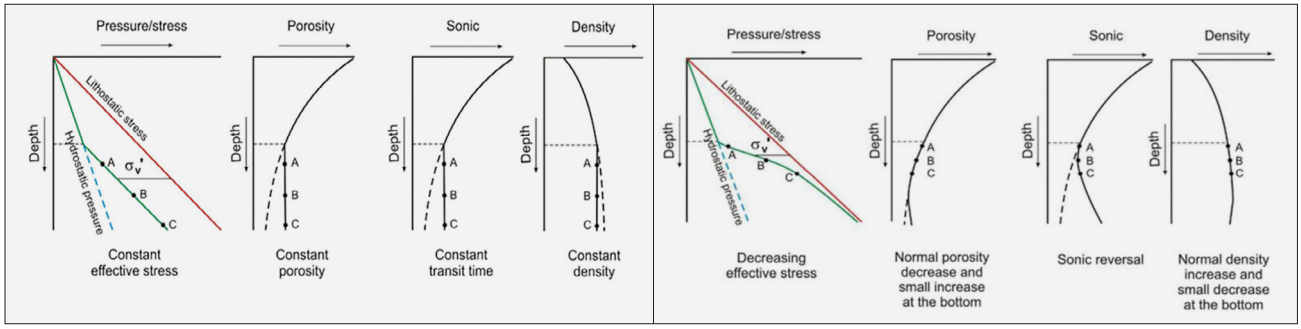


Figure 6. Overpressure mechanism a) Loading mechanism b) Unloading mechanism

framework is transferred to the pore fluid, resulting in elevated pore pressure due to load redistribution (**Buntoro et al., 2022**).

4. Results and Discussion

4.1. Analysis of 1D Mechanical Earth Model

This study presents a one-dimensional geomechanical model analysis conducted on 26 wells within the Keutapang Formation of the 'ZA' Field, located in the North Sumatra Basin. The analysis encompasses pore pressure, elastic properties, rock strength, the injection pressure window, and injection pressure limits.

The pore pressure anomalies identified in this study are classified into three categories: underpressure, overpressure, and a combination of overpressure and underpressure. Each well exhibits distinct pore pressure behaviour at various depths, as summarized in **Table 3**.

Table 3. Depth of overpressure-underpressure in each well

Wells	Pore Pressure Problem	Depth of Pore Pressure (m)
ZA-3	*Underpressure*	440-640
ZA-5	*Underpressure*	500-680
ZA-21	*Underpressure*	410-540
ZA-22	*Underpressure*	425-580
ZA-26	*Underpressure*	340-710
ZA-1	*Overpressure*	550-630
ZA-6	*Overpressure*	320-430
ZA-7	*Overpressure*	630-750
ZA-8	*Overpressure*	350-590
ZA-11	*Overpressure*	470-510
ZA-13	*Overpressure*	340-600
ZA-16	*Overpressure*	250-310 & 420-540
ZA-20	*Overpressure*	300-390
ZA-2	*Overpressure-Underpressure*	530-570 ; 590-830
ZA-4	*Overpressure-Underpressure*	490-560 ; 655-835
ZA-9	*Overpressure-Underpressure*	500-560 ; 660-750
ZA-10	*Overpressure-Underpressure*	520-570 ; 600-660
ZA-12	*Overpressure-Underpressure*	490-560 ; 560-720
ZA-14	*Overpressure-Underpressure*	490-540 ; 590-735
ZA-15	*Overpressure-Underpressure*	470-520 ; 590-750
ZA-17	*Overpressure-Underpressure*	480-530 ; 620-680
ZA-18	*Overpressure-Underpressure*	465-510 ; 560-710
ZA-19	*Overpressure-Underpressure*	470-520 ; 720-790
ZA-23	*Overpressure-Underpressure*	540-560 ; 590-710
ZA-24	*Overpressure-Underpressure*	550-595 ; 595-720
ZA-25	*Overpressure-Underpressure*	490-530 ; 560-730

Out of the 26 wells analyzed, three representative wells are selected to illustrate each type of pore pressure condition. **Figure 7** presents an example of a one-dimensional Mechanical Earth Model (MEM) curve displaying an underpressure condition. Underpressure occurs when the pore pressure is lower than the hydrostatic pressure. As shown in **Figure 7**, the pore pressure (green curve) lies to the left of the hydrostatic pressure (red curve).

The underpressure mechanism observed in the study area is attributed to fluid extraction from the reservoir during past production activities. This condition commonly arises in depleted fields, where reduced fluid volume within the rock leads to a drop in pore pressure. As the amount of fluid in the pore spaces becomes insufficient to support the overburden pressure, underpressure conditions are developed.

Figure 8 presents a sample of one-dimensional Mechanical Earth Model (MEM) curves illustrating an overpressure condition. Overpressure occurs when the pore pressure exceeds the hydrostatic pressure. As shown in **Figure 8**, the pore pressure (green curve) is positioned to the right of the hydrostatic pressure (red curve).

The overpressure mechanism observed in the study area is attributed to a sedimentation rate that outpaces the rate at which fluids can escape from the rock pores, a process referred to as the loading mechanism. This typically occurs at relatively shallow formation depths. In such cases, fluids become trapped within the rock matrix rather than being expelled, resulting in a buildup of pore pressure and the development of overpressure.

Figure 9 presents a sample of one-dimensional Mechanical Earth Model (MEM) curves illustrating a combined overpressure–underpressure condition. Overpressure occurs when the pore pressure exceeds the hydrostatic pressure, while underpressure occurs when the pore pressure falls below the hydrostatic pressure. As shown in **Figure 9**, the pore pressure (green curve) lies both to the right and left of the hydrostatic pressure (red curve). The overpressure observed in the study area is attributed to a sedimentation rate that exceeds the rate of fluid expulsion from the rock pores, a process commonly referred to as the loading mechanism. In contrast, the underpressure condition is linked to fluid extraction from the reservoir during past production activities. The presence of both overpressure and underpressure within a single well may result from rapid sedimentation overlying an underpressured formation.

4.2. Analysis of Rock Elastic Properties and Rock Strengths

The wells in this field exhibit a relatively consistent range of elastic properties and rock strength. Young's modulus values range from 0.5 to 2 GPa, while Poisson's ratio is approximately 0.2. These values suggest that the rocks are relatively deformable and susceptible to fracturing.

In terms of rock strength, the wells display unconfined compressive strength (UCS) values in 42 MPa,

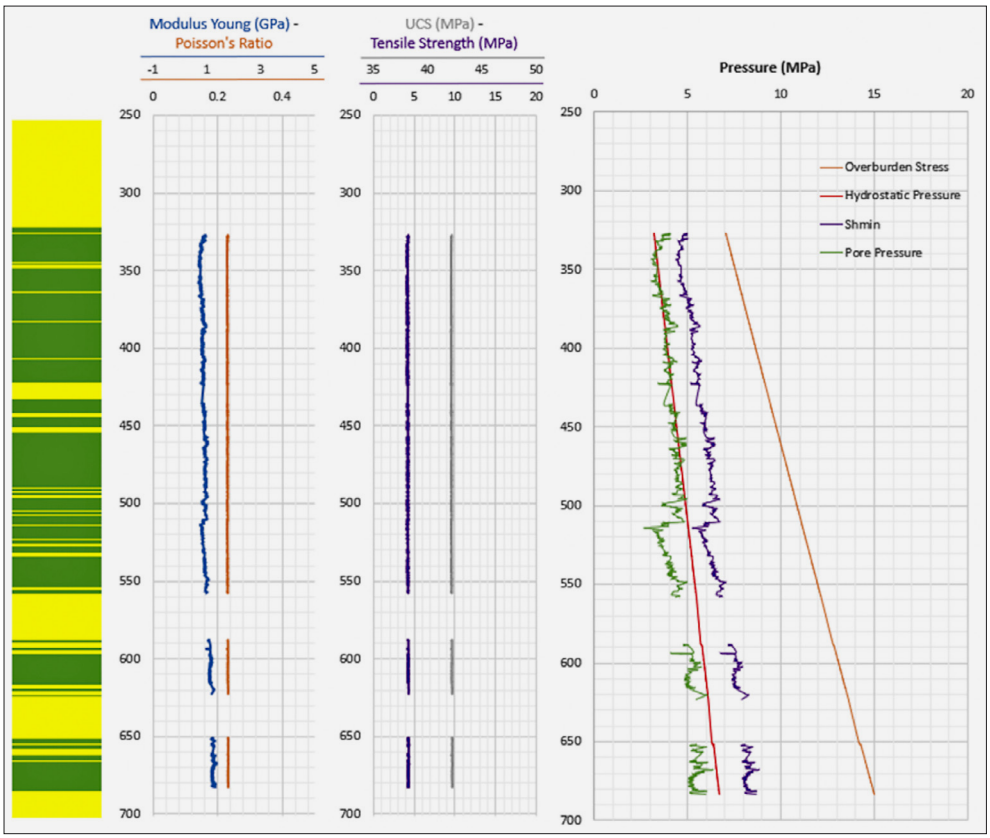


Figure 7. 1D MEM of ZA-5 well

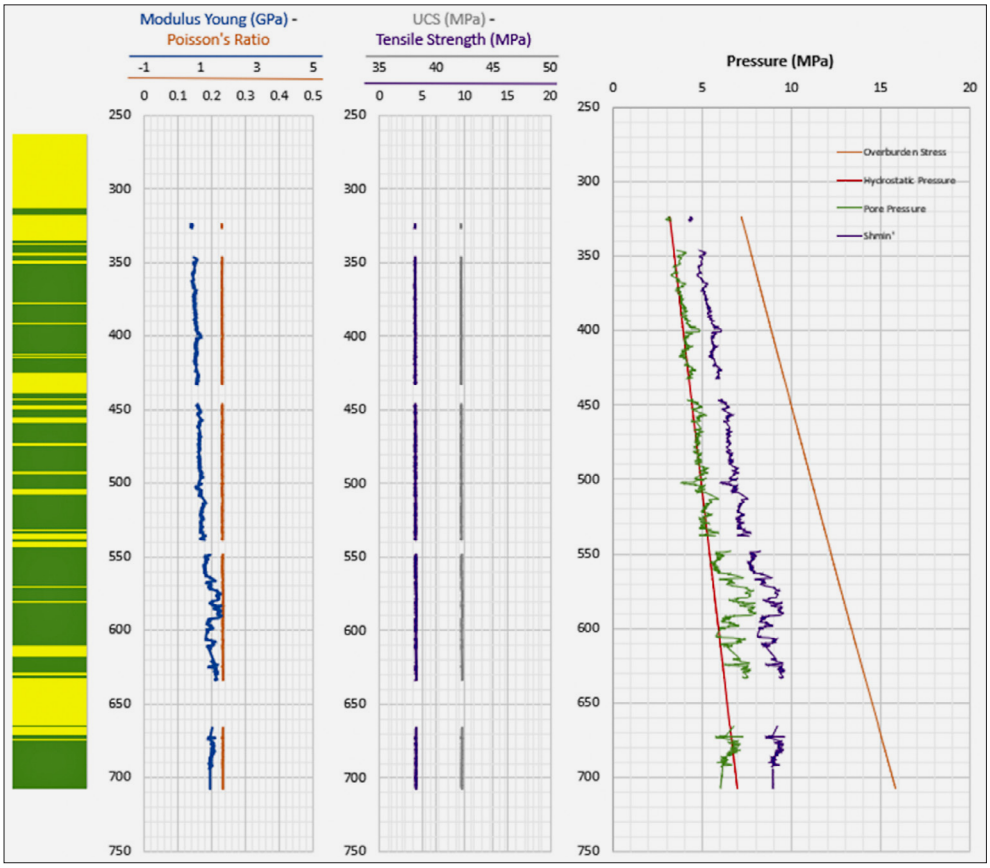


Figure 8. 1D MEM of ZA-1 well

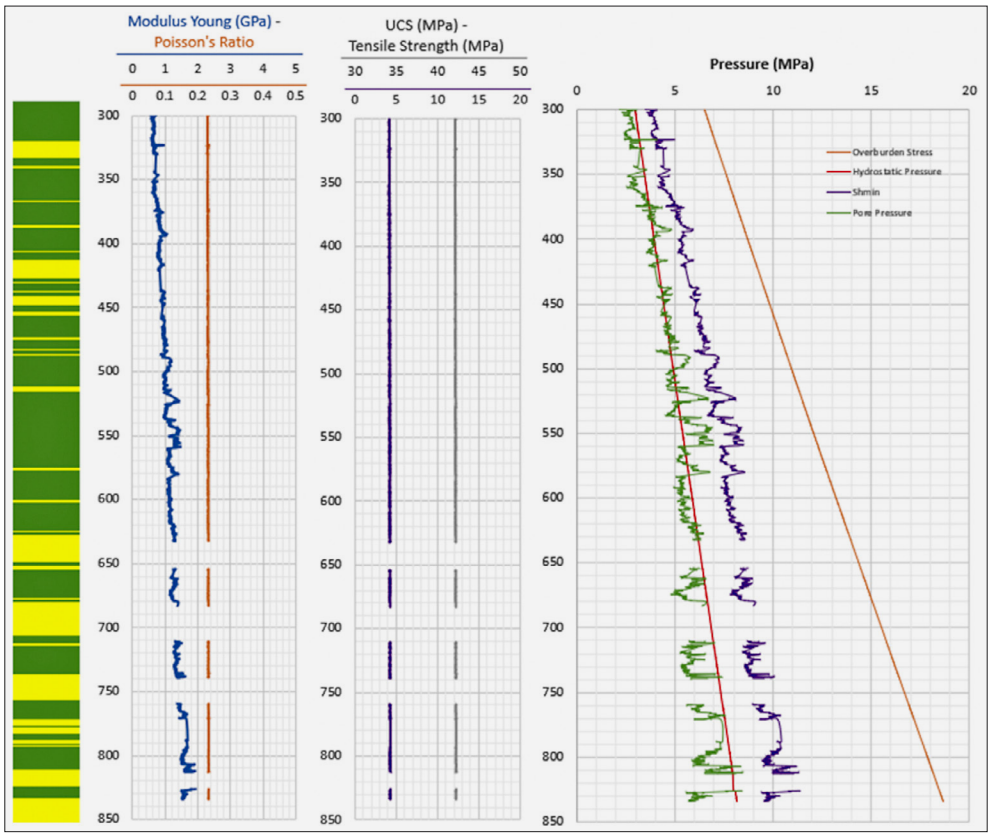


Figure 9. 1D MEM of ZA-4 well

Table 4. Rock strength for each well

Sumur	UCS (MPa)	*Tensile strength (MPa)*	*Friction angle (°)*
ZA-3	42	4	22-29
ZA-5	42	4	22-26
ZA-21	42	4	20-32
ZA-22	42	4	20-30
ZA-26	42	4	20-27
ZA-1	42	4	21-30
ZA-6	42	4	21-26
ZA-7	42	4	20-35
ZA-8	42	4	22-26
ZA-11	42	4	22-30
ZA-13	42	4	21-29
ZA-16	42	4	21-25
ZA-20	42	4	20-25
ZA-2	42	4	21-31
ZA-4	42	4	20-23
ZA-9	42	4	20-29
ZA-10	42	4	21-26
ZA-12	42	4	21-26
ZA-14	42	4	21-31
ZA-15	42	4	21-25
ZA-17	42	4	21-25
ZA-18	42	4	22-28
ZA-19	42	4	21-27
ZA-23	42	4	20-28
ZA-24	42	4	20-29
ZA-25	42	4	20-24

tensile strength in 4 MPa, and friction angles ranging from 20° to 31°. Detailed rock strength values for each well are provided in **Table 4**.

These data indicate that the formations are composed of weak sedimentary rocks with a shaly sand lithology. This lithology, characterized by fine grain size, tends to be more resistant to deformation if the rocks are well-compacted. However, in these wells, the rocks are not yet fully compacted, as evidenced by the relatively low friction angles. A low friction angle implies that the rock grains can be easily displaced under shear stress.

4.3. Analysis of Injection Window and Limit

The injection window is defined by the pressure range between the pore pressure (formation pressure) and the minimum horizontal stress, or fracture gradient. The minimum horizontal stress tends to approximate the overburden pressure at greater depths and the hydrostatic pressure at shallower depths. In this field, the injection window is relatively wide, encompassing both overpressure (1–2 MPa) and underpressure (1.5–5 MPa). The injection window for each well is detailed in **Table 5**.

Based on these values, the formations in this field are considered to be relatively shallow, as the pressures are closer to hydrostatic pressure than to overburden pressure. In addition to the injection window, this study also identifies the maximum injection limit. This limit is determined from the maximum pressure step-rate test, which is avail-

Table 5. Injection window for each well

Wells	Injection Window (MPa)	Pore Pressure	Depth of Pore Pressure (m)
ZA-3	2.5	underpressure	440-640
ZA-5	2	underpressure	500-680
ZA-21	3	underpressure	410-540
ZA-22	5	underpressure	425-580
ZA-26	2.5	underpressure	340-710
ZA-1	1	overpressure	550-630
ZA-6	1	overpressure	320-430
ZA-7	2	overpressure	630-750
ZA-8	1.5	overpressure	350-590
ZA-11	1	overpressure	470-510
ZA-13	1	overpressure	340-600
ZA-16	1	overpressure	250-310 & 420-540
ZA-20	1	overpressure	300-390
ZA-2	2 & 2	overpressure & underpressure	530-570 ; 590-830
ZA-4	2 & 3	overpressure & underpressure	490-560 ; 655-835
ZA-9	1 & 2	overpressure & underpressure	500-560 ; 660-750
ZA-10	2 & 3	overpressure & underpressure	520-570 ; 600-660
ZA-12	2 & 4	overpressure & underpressure	490-560 ; 560-720
ZA-14	1.5 & 2.5	overpressure & underpressure	490-540 ; 590-735
ZA-15	1.5 & 3	overpressure & underpressure	470-520 ; 590-750
ZA-17	1.5 & 2.5	overpressure & underpressure	480-530 ; 620-680
ZA-18	2 & 4	overpressure & underpressure	465-510 ; 560-710
ZA-19	1 & 3	overpressure & underpressure	470-520 ; 720-790
ZA-23	1.5 & 2.5	overpressure & underpressure	540-560 ; 590-710
ZA-24	2 & 2	overpressure & underpressure	550-595 ; 595-720
ZA-25	1 & 2	overpressure & underpressure	490-530 ; 560-730

able in the fracturing report data. However, this data is only available for well ZA-7, with a value of approximately 1106 psi or 7.63 MPa. Consequently, the other wells do not have defined maximum injection limits based on step-rate tests. This pressure represents the threshold at which the formation begins to fracture; therefore, to prevent formation damage or fluid leakage, injection pressures exceeding 1106 psi or 7.63 MPa are not allowed.

4.4. Water Injection Evaluation on Z-600 Layer

This study also includes an injection evaluation in the "ZA" Field, specifically targeting the Z-600 marker. The

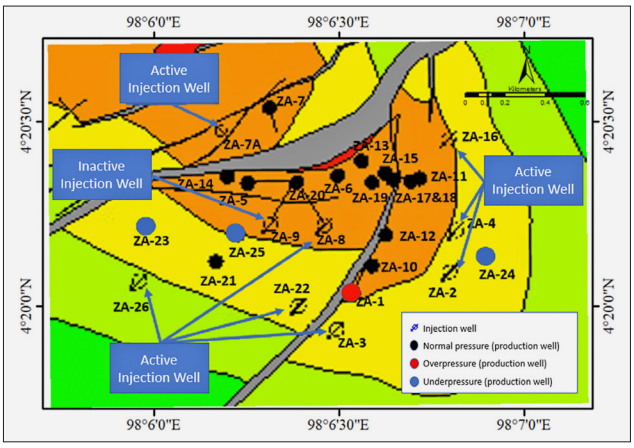


Figure 10. Pore pressure condition after water injection in Z-600 reservoir layer

Z-600 marker refers to a stratigraphic horizon identified from well log responses, and its lateral continuity is limited to log-based correlation across the study wells. It is situated at a depth of approximately 600 meters, with a thickness ranging from 30 to 40 meters. Although the depth varies due to local geological structures, the correlation of this marker does not imply regional geological homogeneity. Wells marked with black circles indicate normal pressure, red circles indicate overpressure, and blue circles indicate underpressure.

Figure 10 shows that, among the production wells, only one well – ZA-1 – experiences overpressure in the Z-600 layer. This overpressure condition is due to the continuous injection of fluid from injection well ZA-3, which causes the pore pressure of ZA-1 to exceed the hydrostatic pressure. This occurs because injection well ZA-3 not only supports production well ZA-1, but also injects fluid into wells ZA-10 and ZA-12 until their pressures return to normal.

Figure 10 also shows production wells that experience underpressure in the Z-600 layer, including wells ZA-24, ZA-23, and ZA-25. Well ZA-23 experiences underpressure despite its proximity to injection wells ZA-2 and ZA-4, which is attributed to its low permeability. The low permeability hinders the flow of injected fluid into the production well. Meanwhile, wells ZA-23 and ZA-25, despite having relatively high permeability, also experience underpressure. This is due to the distance between injection well ZA-22 and production well ZA-23, as well as the fact that injection well ZA-26 is located in a different structural contour than ZA-23. Additionally, well ZA-25 receives injection only from ZA-8, as an injection well ZA-9 has not yet been put into operation. It is assumed that injection well ZA-8 prioritizes injection into production wells within the same structural contour.

Based on this evaluation, it is concluded that the production wells in the "ZA" Field contribute to enhanced oil recovery, although three production wells are still experiencing under-pressure.

5. Conclusions

This study developed a one-dimensional Mechanical Earth Model (1D MEM) that includes elastic properties (Young's modulus and Poisson's ratio), rock strength parameters (UCS, tensile strength, and friction angle), overburden pressure, pore pressure, and minimum horizontal stress. Based on the 1D MEM for each well in the "ZA" Field, several pore pressure anomalies were identified, including over-pressure, under-pressure, and combined overpressure-under-pressure conditions. Underpressure is primarily attributed to fluid depletion from previous production activities, while overpressure results from loading mechanisms.

Each well in the field exhibits UCS values is 42 MPa, tensile strength is 4 MPa, and friction angles ranging from 20° to 31°. These values suggest that the rocks in this field are mechanically weak, likely due to their fine-grained texture. The wells are characterized by shaly sand lithology, which is associated with relatively low friction angles. This is likely due to the unconsolidated nature of the formation, making the rock grains more susceptible to shear under friction. This observation is further supported by reports of sand production events in the "ZA" Field. Additionally, the injection pressure window in each well is relatively wide, both in terms of overpressure (1–2 MPa) and underpressure (1.5–5 MPa). The maximum injection pressure value is currently available only for well ZA-7, recorded at approximately 1106 psi or 7.63 MPa. Therefore, step-rate tests are still required for the remaining wells to determine their actual maximum injection limits.

The results of the geomechanical analysis, particularly through the development of a Mechanical Earth Model (MEM), provide a strong technical basis for defining the safe upper limit of injection pressure. This information directly supports operational decision-making, including injection rate optimization, formation damage risk mitigation, and well planning – ultimately enhancing both safety and field operation efficiency.

Acknowledgement

The authors gratefully acknowledge Pertamina Hulu Rokan for providing the data essential to this research. Sincere appreciation is also extended to any reviewer for their invaluable guidance and supervision throughout the preparation of this manuscript.

6. References

Amin, T., Baroek, M., Santana, S., Sapiie, B. & Gunawan I. (2022). 1D Geomechanical Modeling and Critically-Stressed Fractures Analysis In Naturally Fractured Reservoir, Muara Laboh Geothermal Field, West Sumatra, Indonesia. *Bulletin Of Geology*, *6(1),* 851-865. https://buletingeologi.com/index.php/buletin-geologi/issue/view/15

Astawa, I., Silalahi, I., & Rahardiawan, R. (2012). Geologi Bawah Permukaan Laut Perairan Lembar Peta 0421, Daerah Istimewa Aceh. *Jurnal Geologi Kelautan*, 10(2), 101-115. https://media.neliti.com/media/publications/230393-geologi-bawah-permukaan-dasar-lautperair-f3fb3ce1.pdf.

Attewell P. B. & Farmer I.. W. (1976). Principles of engineering geology. Chapman and Hall, London.

Aziz, A. & Bolt, L.H. (1984). Occurrence and detection of abnormal pressures from geological and drilling data, North Sumatra Basin. *Proc. Indon. Petrol. Assoc*., 13, 194-220.

Birchall, T., Senger, K., & Swarbrick, R. (2022). Naturally Ocuuring Underpressure – A Global Review. *Petroleum Geoscience*, 28. https://doi.org/10.1144/petgeo2021-051?ref=pdf&rel=cite-as&jav=VoR.

Buntoro, A., Rahmad, B., Asmorowati, D., Lukmana, A., Fattah, A. & Anuraga, E. (2022). Overpressure mechanism prediction based on well log and mineralogy analysis from drill cuttings of well NSE-001 in the North Sumatra Basin area, Indonesia. *Journal of Petroleum Exploration and Production Technolog,*. 12, 2801-2815. https://doi.org/10.1007/s13202-022-01482-5.

Collins, P. (2002). Injection Pressures for Geomechanical Enhancement of Recovery Processes in The Athabasca Oil Sands. SPE/Petroleum Society of CIM/CHOA 79028. http://dx.doi.org/10.2118/79028-MS.

Christaras, B., Auger, F., & Mosse, E. (1994). Determination of the moduli of elasticity of rocks. Comparison of the ultrasonic velocity and mechanical resonance frequency methods with direct static methods. *Materials and Structures, 27(4), 222-228*.

Gunawan, A., Sapiie, B., & Wibowo, B. (2017). Analisis Geomekanika Pada Batuan Dasar, Di Area Js-1 Ridge Bagian Selatan, Cekungan Jawa Timur Utara. *Bulletin of Geology*, 1 (1), 1-18. http://dx.doi.org/10.5614/bull.geol.2017.1.1.1.

Knoll, L. (2016). The Process of Building a Mechanical Earth Model Using Well Data.Thesis. Department Petroleum Engineering. Montan University.

Lanin, E. (2021). Rock Mechanical Properties of Indonesian Organic-Rich Shales and Geomechanical Analysis of A Shale Resource Pilot Hole In North Sumatra Basin. Disertasi. Filosofi. University of Wisconsin-Madison.

Larsen, I., Fjaer, E., & Renlie, L. (2000). Static and Dynamic Poisson's ratio of Weak Sandstones. *ARMA North America Rock Mechanics Symposium*.

Linh, D., LOc, N., Tan, V., Huy, N., Trang, N., Tai, P., Abdurrahman, M. & Hidayat, F. (2021). Statistical Estimation of Frictional Coefficients of Faults Based on a Structural Dataset in The Tuy Hoa-Vung Tau Region, Viet Nam. Oil & Gas Science and Technology – Rev. *IFP Energies nouvelles*, 76(35), 1-15. https://doi.org/10.2516/ogst/2021016.

Liu, Y., Liu, S., Zhang, J., and Cao, J. (2025). Real-time estimation of geomechanical characteristics using drilling parameter data and LWD. *Geoenergy Science and Engineering, 244*. https://doi.org/10.1016/j.geoen.2024.213450

Lockner, D. (1995). Rock Failure. *American Geophysical Union*.https://www.researchgate.net/publication/313426883_Rock_failure.

Muchlis & Elder, C. (2020). Structural Style of The North Sumatra Basin, Offshore Aceh. *The 9th AIC 2019 on Sciences*

& Engineering (9thAIC-SE). http://dx.doi.org/10.1088/1757-899X/796/1/012038.

Nuraini, T. (2023). Ketahui Sejarah Lumpur Lapindo Sidoarjo Beserta Penyebab & Dampaknya Bagi Sekitar. https://www.merdeka.com/trending/ketahui-sejarah-lumpur-lapindo-sidoarjo-beserta-penyebab-dampaknya-bagi-sekitar-23578-mvk.html?page=4.

Osborne, M. & Swarbick, R. (1997). Mechanisms for Generating Overpressure in Sedimentary Basins: A Reevaluation. *AAPG Bulletin, V*, 81(6), 1023-1041. https://doi.org/10.1306/522B49C9-1727-11D7-8645000102C1865D.

Perras, M. & Diederichs, M. (2014). A Review of the Tensile strength of Rock: Concepts and Testing. *Geotechnical and Geological Engineering*, 32, 525-546. http://dx.doi.org/10.1007/s10706-014-9732-0.

Prasetyo, A. & Juventa. (2021). Karakterisasi Reservoir Berdasarkan Analisa Avo (Amplitude Versus Offset) Dan LMR (Lambda-Mu-Rho) Di Lapangan "Ap7" Formasi Keutapang Cekungan Sumatra Utara. *Jurnal Teknik Kebumian*, 6(2), 48-60. https://doi.org/10.22437/jtk.v6i02.21184.

Rozamuri, M., Ramdhan, A., & Setiawan, P. (2022). Geologi dan Analisis Geomekanika Terhadap Optimasi Injeksi Air Pada Lapangan "Sarina" Cekungan Sumatra Tengah, Indonesia. *Bulletin of Geology*, 6(3), 1040-1051. https://doi.org/10.5614/bull.geol.2022.6.3.2

Saadatnia, N., Sharghi, Y., Moghadasi, J., & Ezati, M. (2023). Coupled Hydro-mechanical Simulation in The Carbonate Reservoir of A Giant Oil Field in Southwest Iran. *Journal of Petroleum Exploration and Production Technology, 14, 59-83*. https://doi.org/10.1007/s13202-023-01695-2

Shaker, S. (2007). Calibration of Geopressure Predictions Using The Normal Compaction Trend: Perception and Pitfall. http://geopressureanalysis.com/nct_recorded.pdf_final_2pages.pdf.

Shen, S., Gao, Y., & Jia, L. (2024). A comparison of the Relationship between Dynamic and Static Rock Mechanical Parameters. *Applied Sciences, 14*. http://dx.doi.org/10.3390/app14114487

Soepardji, R.. (1983). Geology of The Arun Gas Field. *Society of Petroleum Engineers of AIME*. https://doi.org/10.2118/10486-PA.

Syarifuddin, I. & Ariyanto, P. (2018). Tectono-stratigraphy of Block A area, North Sumatra Basin: The impact of local tectonics and eustasy to accomodation space of the Tertiary interval. *Proceedings, Indonesian Petroleum Association.* http://dx.doi.org/10.29118/IPA18.586.G.

Tampubolon, R., Ozza, T., Arifin, T., Hidayatillah, A., Prasetio, A., & Furqan, T. (2017). A Review of Regional Geology of the North Sumatra Basin and its Paleogene Petroleum System. *Berita Sedimentologi*, 37(1), 23-29. https://doi.org/10.51835/bsed.2017.37.1.95.

Tandirerung, R. (2023). Analisis Geomekanika Batuan Berdasarkan 1D Mechanical Earth Model Sumur B Lapangan X Cekungan Tarakan Provinsi Kalimantan Utara. Skripsi. Program Studi Teknik Geologi. Universitas Hasanuddin. Makassar.

Verma, A., Deb, D., Dey, A., Roy, S., Singh, A., Avadhani, V. & Tiwari, R. (2021). Development of One Dimensional Geomechanical Model for a Tight Gas Reservoir. *Scientific Reports*. https://doi.org/10.1038/s41598-021-00860-z

Wardhana, B., Arsyi, H., Azransyah, T., Mawardi, F., Hafizh, I., & Mulyawan, M. (2021). Fractured Reservoir in Baong Formation, North Sumatra Basin, Indonesia. *Joint Convention Bandung 2021*. Journal.iatmi.or.id.

Wicaksono, A. (2021). Analisis Teknaan Luap dan Hubungannya Terhadap Akumulasi Hidrokarbon di Blok Nunukan, Subcekungan Tarakan. Tesis. Program Studi Teknik Geologi. Institut Teknologi Bandung. Bandung.

Wilson, M., Ansah, S., Nani, S., & Asante, D. (2022). Petrographic Studies And Physico-Mechanical Properties Of Birimian Granitoids – A Case Study Of Oyoko Granitoids Complex In Koforidua. *Geological Behavior*, 6(1), 16-21. http://dx.doi.org/10.26480/gbr.01.2022.16.21.

Yosandian, H. H., Irawan, H., Ulum, B. W. A., Tribuana, I. Y., & Embara, P. (2014). Overpressure Characteristic in the Langkat Field, North Sumatra Basin, Indonesia. *3rd International Conference in Geological and Environmental Sciences*, 73, 40-44.

Zain, M. & Henk, A. (2020). Building 1D and 3D Mechanical Earth Models for Underground Gas Storage – A Case Study from the Molasse Basin, Southern Germany. *Energies*, 13(21), 5722. http://dx.doi.org/10.3390/en13215722.

Zhang, J. (2013). Effective stress, porosity, velocity and abnormal pore pressure prediction accounting for compaction disequilibrium and unloading. *Marine and Petroleum Geology 45*, 2-11. https://doi.org/10.1016/j.marpetgeo.2013.04.007

SAŽETAK

Geomehanička analiza za određivanje maksimalne granice injekcije vode u formaciji Keutapangan, nalazište „ZA", bazen Sjeverna Sumatra

Polje „ZA" nalazi se u bazenu Sjeverne Sumatre i pretežno je pogođeno problemima geotlaka. Zbog toga je geomehanička analiza ključna tijekom bušenja kako bi se ublažile moguće opasnosti. Geomehanička analiza provedena u ovome istraživanju koristi se jednodimenzionalnim mehaničkim modelom Zemlje (1D MEM), koji uključuje sljedeće komponente: naprezanje nadtereta, porni tlak, čvrstoću stijene, elastična svojstva stijena i minimalno horizontalno naprezanje. Podatci korišteni u ovoj analizi prikupljeni su iz sljedećih izvora: mjerenja pomoću žične sonde za sve geomehaničke izračune, testovi tlaka za provjeru vrijednosti pornih tlakova, podatci o gradijentu loma za potvrdu krivulje minimalnoga horizontalnog naprezanja, testovi stupnjevitoga protoka za određivanje granice tlaka injekcije te izvješća s bušotina. Polje „ZA" pokazuje složen režim geotlaka, koji varira od podtlaka do nadtlaka, s prijelaznim zonama koje kombiniraju oba stanja. Nadtlak se uglavnom pripisuje mehanizmima opterećenja, dok je podtlak rezultat povijesne ekstrakcije fluida tijekom prethodnih bušenja. Litološka analiza pokazuje da se rezervoar sastoji od glinovitoga pijeska i sitnozrnatih formacija. Zbog male dubine zakopavanja, ove stijene ostaju slabo konsolidirane, što rezultira uskim sigurnim injekcijskim prozorom iznad pornoga tlaka. Ovo ograničenje prikazano je na primjeru jedne bušotine, gdje je maksimalni dopušteni tlak injekcije iznosio 7,63 MPa, s razmakom od samo 2 MPa iznad pornoga tlaka.

Ključne riječi:
1D MEM, porni tlak, čvrstoća stijena, elastična svojstva stijena, minimalni horizontalni napon

Author's contribution

Zahra Adinda Billqish (B.Sc, Physics, expertise in geophysics, geomechanical analysis) performed the data processing, data analysis, interpretation of the results, and wrote the original draft and edited. **Andika Wicaksono** (M.T., Geology, seismic exploration, petroleum geology) provided the data, data collection, interpretation and supervision. **Sismanto** (Dr in Geophysics, expertise in seismic exploration and rock physics) performed the interpretation and supervision. All authors have read and agreed to the published version of the manuscript.

RGNZ/MGPB

Study of the bactericidal-inhibitor properties of new reagents

Rudarsko-geološko-naftni zbornik
(The Mining-Geology-Petroleum Engineering Bulletin)
DOI: 10.17794/rgn.2026.2.2

Original scientific paper

Guseyn Gurbanov[1]*, Aysel Gasimzade[1]
[1] *Azerbaijan State Oil and Industry University, Department of Transportation and Storage Oil and Gas, Baku, Azadliq Avenue, 34, AZ1010.*

Abstract
It is well known that in oil-producing countries with advanced industrial development, one of the most pressing unresolved challenges is protecting the internal surfaces of equipment and facilities from the effects of aggressive corrosive environments, thereby extending their operational life. Based on this, the present article explores the results of numerous laboratory tests on the effects of the newly developed organic MARZA-4 reagent and a composition provisionally named HAK-2 against hydrogen sulfide, carbon dioxide, and sulfate-reducing bacteria, which are primary causes of internal surface corrosion in the oil industry. For the first time, the MARZA-4 reagent was studied for its effectiveness against sulfate-reducing bacteria in aggressive corrosive environments such as neutral, acidic, and alkaline media, as well as in the "Postgate-B" nutrient medium. It was determined that the MARZA-4 reagent possesses bactericidal-inhibitor properties at an optimal concentration of 20 mg/L. At this concentration, its corrosion protective effect in neutral, acidic, and alkaline environments was found to be 98%, 98%, and 94%, respectively. In the "Postgate-B" nutrient medium, the bactericidal effect against *Desulfovibrio desulfuricans* and *Desulfomicrobium* cells was 78% and 81%, respectively.

Keywords:
sulfate-reducing bacteria, inhibitor, hydrogen sulfide, carbon dioxide, aggressive environment

1. Introduction

Ensuring the reliability and long-term operation of field equipment and pipeline systems is one of the critical challenges in the development of oil and gas fields and the subsequent transportation of hydrocarbon resources. In this study, the term "aggressive environment" specifically refers to conditions that accelerate corrosion due to their chemical composition. These include acidic media (such as hydrochloric acid solutions), neutral chloride-containing media (such as 3.5% NaCl solution), alkaline media (sodium hydroxide solutions), and gas-rich environments containing hydrogen sulfide (H_2S), carbon dioxide (CO_2), or their combination-all of which are representative of actual conditions encountered in oil and gas production systems. While acidic and neutral media are commonly found in production and pipeline systems, alkaline conditions may arise in the oil industry during enhanced oil recovery (EOR) techniques – such as alkaline flooding – or during chemical treatments involving basic agents like sodium hydroxide. Furthermore, the presence of gases like H_2S, CO_2, and O_2 in these environments significantly intensifies corrosion aggressiveness under operational conditions (**Abdel-Gaber et al., 2011; Ansari et al., 2020**). Additionally, condensation formed during the cooling of oil in pipelines presents a major corrosion risk, as it creates a biphasic system where corrosion processes primarily occur in the aqueous phase (**Bao et al., 2012; Gurbanov and Gasimzade, 2023a**).

The detrimental effects of corrosion extend beyond the degradation of metals. Particularly concerning is hydrogen sulfide-induced stress corrosion cracking. Furthermore, dispersed corrosion products (iron sulfides and oxides) clog and corrode pumping equipment, leading to reduced productivity of oil reservoirs. Iron sulfides and oxides extracted with well fluids act as stabilizers of oil emulsions, complicating demulsification and increasing the costs associated with crude oil preparation (**Gurbanov et al., 2023b, Xu et al., 2016**).

It should be noted that CO_2 gas reacts with water in the corrosive environment to form carbonic acid (H_2CO_3). It is specifically in the presence of carbonic acid that the corrosion of iron (Fe) occurs. The following reactions take place in the presence of CO_2 gas.

The dissolution of carbon dioxide in water and subsequent formation of carbonic acid occurs according to the following **Equation 1**:

* Corresponding author: Guseyn Gurbanov
e-mail address: ebikib@mail.ru
Received: 22 January 2025. Accepted: 20 September 2025.
Available online: 13 March 2026

$$CO_2+H_2O\rightarrow H_2CO_3 \quad (1)$$

The dissociation of carbonic acid occurs in two steps, as shown in the following **Equations**:

$$H_2CO_3\rightleftharpoons H^++HCO_3^- \quad (2)$$

$$HCO_3^-\rightleftharpoons H^+ + CO_3^{2-} \quad (3)$$

The ionization of iron as the anodic reaction can be represented by the following **Equation 4**:

$$Fe\rightarrow Fe^{2+}+2e^- \quad (4)$$

The cathodic reaction, involving the reduction of hydrogen ions, proceeds according to the following **Equation 5**:

$$2H^++2e^-\rightarrow H_2\uparrow \quad (5)$$

As a result, Fe^{2+} ions react with carbonate ions to form iron(II) carbonate ($FeCO_3$), which constitutes a passivating layer, as shown in the following **Equation 6**:

$$Fe^{2+}+CO_3^{2-}\rightarrow FeCO_3\downarrow \quad (6)$$

The resulting $FeCO_3$ layer can act as a protective barrier; however, in some cases, it is unstable, breaks down, and corrosion continues (**Matamoros-Veloza et al., 2020**).

H_2S gas creates a mildly acidic environment in water and leads to the formation of iron sulfide (FeS), which contributes to corrosion. The reactions can be represented by the following **Equations**:

$$H_2S\rightleftharpoons H^++HS^- \quad (7)$$

$$HS^-\rightleftharpoons H^+ + S^- \quad (8)$$

$$Fe\rightarrow Fe^{2+}+2e^- \quad (9)$$

$$2H^++2e^-\rightarrow H_2\uparrow \quad (10)$$

Formation of iron sulfide through the reaction of Fe^{2+} ions with HS^- or S^{2-} ions can be expressed by the following **Equation 11**:

$$Fe^{2+}+HS^-\rightarrow FeS\downarrow+H^+ \quad (11)$$

As a result, FeS is black in color and may sometimes act as a protective layer; however, it can also form a porous structure that allows corrosion to continue (**Wang et al., 2021**).

The corrosion of steel well equipment, as well as trunk and process pipelines, not only shortens their service life and increases repair costs, but also causes severe environmental damage. Equipment damage results in soil salinization by aggressive groundwater, as well as contamination of soil and natural water bodies with oil and oil products. Therefore, significant attention is being paid to extending the service life of technological well equipment in oil fields (**Kalinina et al., 2016; Kashkovskiy et al., 2012**).

One of the most effective methods to combat corrosion in oil production is the use of corrosion inhibitors. These inhibitors, which can be individual compounds or compositions of various substances, are designed to significantly reduce metal corrosion losses in harsh environments involving aggressive gases such as H_2S, CO_2, and O_2, as well as salts in technological media (**Kuznetsov et al., 2000**). Inhibitor-based protection is considered one of the most widely adopted and economically justified methods of corrosion protection for field equipment and pipelines. By varying the inhibitor dosage or using inhibitors with different anti-corrosion properties, it is possible to reduce corrosion rates to acceptable levels without significantly altering existing technological schemes (**Lecante et al., 2011; Lusk, 2008**).

Sulfate-reducing bacteria (SRB), which cause severe corrosion, are microorganisms that live in anaerobic (oxygen-free) conditions and reduce sulfate (SO_4^{2-}) ions to produce hydrogen sulfide (H_2S).

As a result of SRB activity, the produced H_2S reacts with the metal surface to form iron sulfide (FeS) and other corrosion products, as shown in the following **Equation 12**:

$$Fe+H_2S\rightarrow FeS\downarrow+H_2\uparrow \quad (12)$$

It should be noted that the FeS layer is usually uneven and porous, and it does not fully protect the metal surface, resulting in the development of pitting corrosion. SRBs also accelerate corrosion through cathodic depolarization (**Wang et al., 2021**).

Normally, in metal corrosion, hydrogen ions (H^+) accept electrons to form molecular hydrogen (H_2). However, hydrogen molecules can accumulate on the metal surface, slowing down the corrosion process. Sulfate-reducing bacteria (SRBs) consume this hydrogen, preventing its accumulation and thereby increasing the rate of corrosion, as shown in **Figure 1** and represented by the following **Equation 13**:

$$4H_2+SO_4^{2-}\rightarrow S^{2-}+4H_2O \quad (13)$$

The mechanism presented in **Figure 1** illustrates the microbiologically influenced corrosion (MIC) process initiated by sulfate-reducing bacteria (SRB). These anaerobic microorganisms utilize sulfate as a terminal electron acceptor, reducing it to hydrogen sulfide (H_2S), which subsequently reacts with metallic iron to form iron sulfide (FeS) corrosion products. This biogenic process not only deteriorates the protective oxide layer but also promotes localized corrosion through cathodic depolarization. The described mechanism is consistent with the model proposed by **Matamoros-Veloza et al. (2020)**.

Oil production companies impose high requirements on inhibitor compositions, demanding universal effects, including reducing hydrogen sulfide, carbon dioxide, and microbiological corrosion while mitigating hydrogenation of structural materials. Furthermore, it is ex-

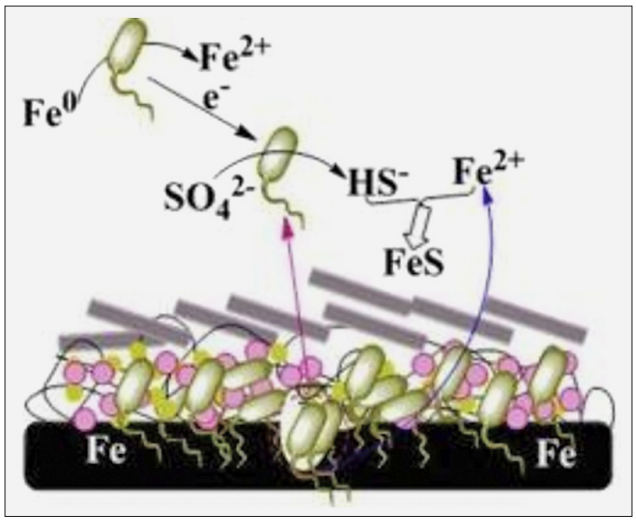


Figure 1. Mechanism of metal corrosion under the influence of sulfate-reducing bacteria (**Matamoros-Veloza et al., 2020**)

pected that their concentrations in operation environments should not exceed 100-200 mg/L. However, nearly all commercially produced corrosion inhibitors have narrow optimal application ranges (**Martens and Berner 1974; Milovzorov et. al., 2012**).

The development, research, and application of locally produced similar inhibitors not only address the issue of import substitution but also solve the problem of reducing the dependency on foreign products in the domestic market. Thus, the development of universal inhibitors capable of reducing hydrogen sulfide, carbon dioxide, and microbiological corrosion, as well as mitigating hydrogenation of construction materials, remains one of the most pressing issues in the oil industry (**Morris and Richard, 2002**).

One promising approach to the search for such inhibitors is the creation of new multifunctional compositions from substances with individual inhibitory properties (**Salasi et al., 2007**). By jointly enhancing protective properties, these compositions aim to increase the effectiveness of corrosion protection (**Starosvetsky et al., 2010; Talybov et al., 2020**).

In conclusion, protecting the internal surfaces of equipment and pipelines in the oil industry from the effects of aggressive electrochemical corrosion environments with varying compositions necessitates the development of effective individual reagents and compositions. The study of their properties in laboratory conditions remains one of the most urgent tasks of our time (**Taraneh et al., 2008; Zafari et al., 2020**).

Objective of the Study: This research investigates the protective and bactericidal effects of the MARZA-4 reagent in neutral, acidic, alkaline environments, and in conditions where sulfate-reducing bacteria (SRB) are active. SRB activity results in the formation of FeS, $Fe(OH)_2$, and H_2S on metal surfaces, promoting pitting corrosion. The release of H_2S, a highly toxic and hazardous gas, presents a serious risk to pipelines and oil-gas equipment. SRB-induced corrosion is a common problem in oil and gas production facilities, pipelines, and underground storage systems.

The primary objective of this study is to evaluate the corrosion protection performance of a newly developed reagent, HAK-2, and its composition under laboratory conditions. The research aims to compare the effectiveness of MARZA-4 and HAK-2 inhibitors, examine their chemical interaction mechanisms, and determine their overall impact on corrosion rates under different environmental conditions relevant to oil and gas operations.

2. Method

It is known that the equipment and installations used in the oil industry are primarily made from steel of grade Ct3. Therefore, in laboratory conditions, samples made of Ct3 steel were used to study the corrosion rate on metal specimens. The chemical composition of Ct3 steel is presented in **Table 1**.

Table 1. The elemental content of Ct3 steel (%)

	C	Mn	Si	P	S	Cr	Ni	Cu	Fe
Ct3	0.2	0.5	0.15	0.04	0.05	0.3	0.2	0.2	98.4

As seen in **Table 1**, Ct3 steel contains nine chemical elements in various percentages, with the main component being 98.36% iron. Specimens of Ct3 steel measuring 30x20x1 mm were used to conduct laboratory experiments. It should be noted that to determine the efficiency of the reagent's corrosion inhibition, the experiments were carried out under room conditions for a duration of six hours. The MARZA-4 reagent and a new composition, conditionally named HAK-2, consisting of MARZA-4 and chloroprene in a 1:1 ratio, were used as corrosion agents. MARZA-4 is an organic chemical compound, and its molecule comprises carbon, hydrogen, oxygen, halogen atoms, and a triple bond. MARZA-4 is a reagent produced in Azerbaijan, and its chemical formula is not disclosed by the manufacturers for commercial purposes (**Pashayeva, 2022**). In industry, this reagent is produced using methane gas, unsaturated monohydric alcohols, and halides as raw materials.

The experiments related to sulfate-reducing bacteria were carried out following the sequence outlined in RD-39-3-973-83. It should be noted that the laboratory tests were conducted in the "Postgate-B" medium, which provides an optimal environment for the growth of sulfate-reducing bacteria, at temperatures ranging from 28°C to 30°C (**Zhang et al., 2009; Zhao et al., 2020**).

The corrosion rate in an aggressive environment was determined using the gravimetric method outlined in RD-39-3-973-83. Metal coupons were exposed to the corrosive environment for a specified duration, after

Table 2. Composition of the "Postgate-B" nutrient medium, g/l

"Postgate-B"	NH_4Cl	K_2HPO_4	$MgSO_4 \times 7H_2O$	$CaSO_4$	lactate-Ca	Na_2S	Na_2SO_3	$FeSO_4$ (5% solution in 1% HCl)
	1,0	0,5	2,0	1,0	2,6	0,2	2,0	0,5

which they were cleaned and re-weighed to quantify the mass loss.

The protective effect of the MARZA-4 inhibitor was studied in acidic, neutral, and alkaline environments. The acidic environment was created using an HCl solution, resulting in a pH of 3. The alkaline environment was prepared with a NaOH solution, yielding a pH of 11. The neutral environment was created using a 3.5% NaCl solution, with a pH of 7. The pH values in the environments were measured and verified using a Hanna Instruments HI 2211 model pH meter. The metal sample surfaces were polished with #800 grit sandpaper, washed with distilled water, and dried. The effects of the MARZA-4 inhibitor at concentrations of 5, 10, 15, and 20 mg/L on corrosion environments were investigated. The corrosion rate K (g/m²·hour), retardation coefficient (γ), and protective efficiency (Z, %) were calculated.

Surface Preparation and Experimental Setup: before starting the experiments, the surfaces of the steel specimens were cleaned. Initially, the surfaces of the steel specimens were ground on a grinding machine. Then, the surfaces were wiped with acetone and alcohol, and their weights were determined using an analytical balance. Corrosion rate tests were conducted in two environments: the first being an aggressive corrosive environment, and the second being the same environment with the addition of an inhibitor.

After completing the laboratory experiments conducted at room temperature, the steel specimens were removed from the aggressive corrosion environment, and corrosion products were removed from their surfaces. Hydrochloric acid, 40% formalin, and cotton were used to clean the surfaces of the steel specimens. After chemical treatment, the specimens were rinsed with running water and then dried with acetone. The specimens were kept in a desiccator for two hours before and after the experiments. The purpose of storing the steel specimens in the desiccator was to bring them to a stable weight. After this process, the steel specimens were weighed again using an analytical balance to determine their final weights (**Postgate, 1984**).

The rate of corrosion in aggressive environments under laboratory conditions is calculated, as given in **Equation 14**, as follows (**Pashayeva, 2022**):

$$K = \frac{m_1 - m_2}{S \cdot \tau} \quad (14)$$

Where: m_1 – mass of the steel sample before the experiment, g; m_2 – mass of the steel sample after removing the corrosion products from its surface, g; S – surface area of the steel sample, m²; τ – duration of the experiment, hours.

The term "retardation coefficient" (γ) is also used in corrosion processes and is calculated as shown in **Equation 15**, as follows (**Pashayeva 2022**):

$$\gamma = \frac{K_0}{K_{inh}} \quad (15)$$

Where: K_0 – corrosion rate without reagents; K_{inh} – corrosion rate with the presence of the reagent (g/m²·hour). The retardation coefficient (γ) is a dimensionless quantity.

The protective effect of the reagents used in the experiment is calculated, as shown in **Equation 16**, as follows (**Pashayeva, 2022**):

$$Z = \frac{K_0 - K_{inh}}{K_0} 100\% \quad (16)$$

Where: K_0 – corrosion rate without reagents; K_{inh} – corrosion rate with the presence of the reagent (g/m²·hour).

One of the terms used in corrosion processes is the penetration factor (K_p), which is calculated as shown in **Equation 17**, as follows (**Pashayeva 2022**):

$$K_p = \frac{8760 K_m}{\rho} \cdot 10^{-3} \text{ mm/year} \quad (17)$$

Where: K_m – corrosion rate, g/m²·hour; ρ – density of the metal being studied, g/cm³; 8760- a constant representing the number of hours in a year.

All chemicals used in the experiments (HCl, NaCl, NaOH, ethanol, acetone, chloroprene, etc.) were of analytical grade (AR) and were officially supplied to the Azerbaijani market by well-known manufacturers such as "Sigma-Aldrich" and "Merck."

Corrosion tests based on mass loss were conducted using the gravimetric method, in accordance with the ASTM G31-21 and GOST 9.905-82 international standards.

Bactericidal Studies: the bactericidal properties of the reagents against sulfate-reducing bacteria were investigated in the "Postgate-B" nutrient medium (see **Table 2**).

In the laboratory, each experiment was repeated five times, and the standard deviation was calculated to ensure the reliability of the results. During the experiments, carbon dioxide (CO_2) was continuously introduced into the environment at a specific flow rate. Initially, the gases were introduced into the corrosive medium through controlled gas injection, simulating real-world conditions where gases interact with the metal surface (see **Table 3**).

The concentration of H_2S was set at 0.015 psi, representing typical field conditions where low levels of H_2S can significantly impact the corrosion rate. The CO_2 con-

centration was set at 10%, which is commonly found in pipeline systems. During the experiments, the pH of the solution was monitored, as the dissolution of CO_2 leads to the formation of carbonic acid, which lowers the pH. Initially, the pH was 6.5, and it decreased to approximately 5.2 in the presence of CO_2.

Corrosion rates were measured using both weight loss and potentiodynamic polarization methods. Both gases were maintained in the experimental environment for 24 hours. The simultaneous application of CO_2 and H_2S was performed to analyze their joint influence on corrosion, with flow rates carefully controlled during their introduction. These techniques provided real-time data on the influence of H_2S and CO_2 on corrosion behavior.

Finally, the impact of the inhibitors MARZA-4 and HAK-2 on H_2S and CO_2 environments was assessed. The results demonstrated that higher concentrations of these inhibitors significantly reduced corrosion rates.

Bactericidal Activity Calculation: For the growth and development of sulfate-reducing bacteria, the "Postgate-B" nutrient medium is used, and the research is conducted based on the NACE standard methodology. The number of sulfate-reducing bacterial cells in 1 ml of the initial suspension which is calculated as shown in **Equation 18**, as follows (**Pashayeva 2022**):

$$M = \frac{1000an}{hs} \quad (18)$$

Where: M – the number of cells in 1 ml of the suspension; a – the average number of cells in the square grid; h – the depth of the chamber (in mm); S – the area of the square grid (in mm^2); n – the dilution rate of the suspension; 1000 mm^3 = 1 ml.

The growth rate of sulfate-reducing bacteria (N,%) with the involvement of the bactericide which is calculated as shown in **Equation 19**, as follows (**Pashayeva 2022**):

$$N,\% = \frac{100(n_0 - n_{inh})}{n_0} \quad (19)$$

Where: n_0 – the number of microorganisms in the reagent-free medium; n_{inh} – the number of microorganisms in the reagent-containing medium.

The bactericidal effect (S,%) of the reagent based on the amount of hydrogen sulfide which is calculated as shown in Equation 20, as follows (**Pashayeva 2022**):

$$S,\% = \frac{C_0 - C_{inh}}{C_{inh.}} 100 \quad (20)$$

Where: C_0 – the concentration of biogenic hydrogen sulfide in the reagent-free medium; C_{inh} – the concentration of biogenic hydrogen sulfide in the reagent-containing medium.

The change in biogenic hydrogen sulfide concentration was measured using the methylene blue spectrophotometric method, a well-established technique for detecting H_2S in sulfate-reducing bacteria cultures. This method involves the reaction of H_2S with N,N-dimethyl-p-phenylenediamine and $FeCl_3$ under acidic conditions, forming methylene blue, which was quantified at 667 nm wavelength. The use of this method ensures high sensitivity and accuracy in detecting even minor changes in H_2S levels. The decrease in H_2S production directly correlates with the bactericidal efficiency of MARZA-4. The methodology aligns with similar studies on SRB inhibition (**Postgate, 1984; Muyzer and Stams, 2008**).

Scanning Electron Microscopy (SEM) Analysis: surface morphology and microstructural changes of the steel specimens before and after exposure to the corrosive medium were investigated using scanning electron microscopy (SEM). The SEM analysis was performed using a JEOL JSM-7001F field emission scanning electron microscope operating at an accelerating voltage of 15 kV under high vacuum conditions. Prior to imaging, all samples were cleaned with ethanol, air-dried, and then coated with a thin layer of gold (approx. 10 nm) using a sputter coater (Quorum Q150R ES) to enhance surface conductivity and imaging resolution.

The SEM investigation was carried out at various magnifications (ranging from ×500 to ×10,000) to assess surface degradation features such as pit formation, crack propagation, and corrosion product morphology.

All images were captured with a calibrated scale bar, and the micrographs were analyzed using ImageJ software to estimate the average pit diameter and surface coverage of corrosion products. Representative images were selected from at least three different areas on each specimen to ensure statistical reliability and reproducibility of the observations.

3. Results and discussions

Initially, the laboratory studies were conducted in three aggressive corrosion environments: neutral, acidic, and alkaline. It should be noted that the experiments for determining the corrosion rate were carried out in a U-shaped setup. The gravimetric method for determining the corrosion rate in a U-shaped setup was carried out in accordance with ASTM G31-72. It should be noted that the experiments for determining the corrosion rate were carried out in a U-shaped setup. The gravimetric method for determining the corrosion rate in the U-shaped setup was conducted in accordance with ASTM G31-72. During the experiments, there was no liquid flow in the system; however, to simulate real field conditions, a continuous flow of CO_2 and/or H_2S gases was introduced into the system at a controlled flow rate. The results of the numerous laboratory experiments lasting six hours are presented in **Table 3**.

The data presented in the table demonstrates the protective effectiveness of the MARZA-4 inhibitor under different environmental conditions: neutral, acidic, and

Table 3. The protective effectiveness of the MARZA-4 inhibitor in various aggressive environments

№	C_{inh} mg/L	K, g/m²-hour		SD (±)	Retardation coefficient, γ	Protective effect, Z%
		Without inhibitor	With inhibitor			
a) Protective effectiveness of MARZA-4 inhibitor in a neutral environment (pH=7)						
1	0	0.6248	-	-	-	-
2	5.0		0.0749	±0.002	8.34	88
3	10.0		0.0562	±0.0018	11.11	91
4	15.0		0.0249	±0.0012	25.09	96
5	20.0		0.0124	±0.0008	50.38	98
b) Protective effect of MARZA-4 inhibitor in acidic environment (pH=3)						
1	0	1.2364	-	-	-	-
2	5.0		0.1730	±0.004	7.14	86
3	10.0		0.1236	±0.003	10.00	90
4	15.0		0.0618	±0.0025	20.00	95
5	20.0		0.0247	±0.0015	50.05	98
c) Protective effect of MARZA-4 inhibitor in alkaline environment (pH=11)						
1	0	1.012	-	-	-	-
2	5.0		0.2024	±0.004	5.00	80
3	10.0		0.1619	±0.0035	6.25	84
4	15.0		0.1416	±0.0032	7.14	86
5	20.0		0.0607	±0.0016	16.67	94

alkaline. As the concentration of MARZA-4 increases, there is a consistent improvement in corrosion protection across all environments. This indicates that the inhibitor is effective in mitigating corrosion as its concentration rises.

In the neutral environment, the protective efficiency of MARZA-4 increases steadily with the concentration of the inhibitor. Initially, the corrosion rate without the inhibitor is relatively high. However, as the inhibitor is introduced, a significant reduction in corrosion is observed, with the protection efficiency rising considerably. The highest inhibitory efficacy in the neutral environment was achieved at a concentration of 20 mg/L, with a protection efficiency of 98%.

Similarly, in the acidic environment, the inhibitor exhibits a similar trend of increasing protection efficiency with higher concentrations. Acidic conditions typically accelerate corrosion, but MARZA-4 effectively counteracts this by reducing the corrosion rate as its concentration increases. Even at lower concentrations, there is a noticeable reduction in the corrosion rate, which continues to improve with higher inhibitor concentrations. At 20 mg/L, the protection efficiency reached its maximum in acidic conditions, with a value of 98%.

In the alkaline environment, while the overall corrosion rates are lower than those in acidic conditions, the inhibitor still proves effective. The pattern of increased protection efficiency with higher concentrations remains consistent, although the degree of improvement is slightly less pronounced compared to the acidic environment. At 20 mg/L, the highest protection efficiency in the alkaline environment was 94%. This suggests that the inhibitor performs better in acidic conditions but still provides significant protection in alkaline conditions.

Overall, the MARZA-4 inhibitor demonstrates strong protective properties across various environments, with higher concentrations offering more effective corrosion resistance. The results suggest that MARZA-4 is a versatile inhibitor capable of enhancing corrosion resistance in a range of pH conditions, with the highest efficacy observed at a concentration of 20 mg/L across all test environments.

It is known that the internal corrosion of oil pipelines is primarily due to formation water and sulfate-reducing bacteria present in the oil. It should be noted that corrosion caused by the activity of sulfate-reducing bacteria progresses rapidly, often resulting in leaks in pipelines within a short period. Therefore, the effect of MARZA-4 inhibitor on sulfate-reducing bacteria was also studied under laboratory conditions.

Figures 2–4 present the potentiodynamic polarization curves obtained for Ct3 steel in neutral, acidic, and alkaline environments with varying concentrations of the MARZA-4 inhibitor. The results clearly show that increasing the inhibitor concentration shifts the corrosion potential (E_{corr}) in a more positive direction and reduces the corrosion current density (I_{corr}), indicating a significant inhibition effect.

The inhibition performance of the MARZA-4 compound on Ct3 grade carbon steel was systematically evaluated using the potentiodynamic polarization method. Experiments were carried out in media of varying pH-neutral (pH = 7), acidic (pH = 3), and alkaline (pH =

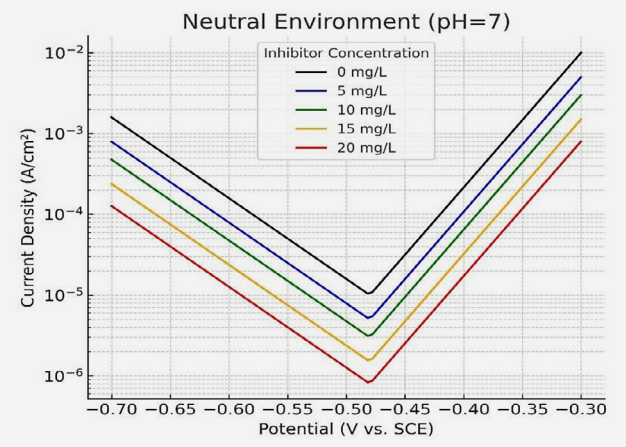


Figure 2. Potentiodynamic polarization curves of Ct3 steel in a neutral medium in the presence of the MARZA-4 inhibitor

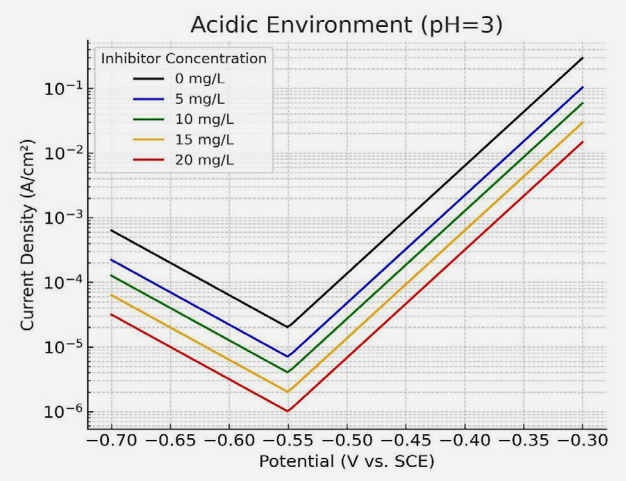


Figure 3. Potentiodynamic polarization curves of Ct3 steel in an acidic medium in the presence of the MARZA-4 inhibitor

11) – to assess the inhibitor's effectiveness under diverse corrosion environments. For each condition, polarization curves were constructed for inhibitor concentrations of 0, 5, 10, 15, and 20 mg/L (see **Figures 2–4**).

The electrochemical measurements were supported by gravimetric data, which provided estimated corrosion current densities (I_{corr}). These values were used to quantify the inhibitor's impact on the corrosion kinetics. Test parameters, including a metal surface area of 0.0013 m², density of 7850 kg/m³, and 6-hour immersion time, were maintained consistently across all systems to ensure comparability.

As observed from **Figures 2** to **4**, increasing the concentration of MARZA-4 led to:

- A progressive shift in corrosion potential (E_{corr}) toward more positive values, suggesting enhanced surface passivation,
- A substantial reduction in corrosion current density (I_{corr}), indicating effective suppression of electrochemical activity at the metal–electrolyte interface.

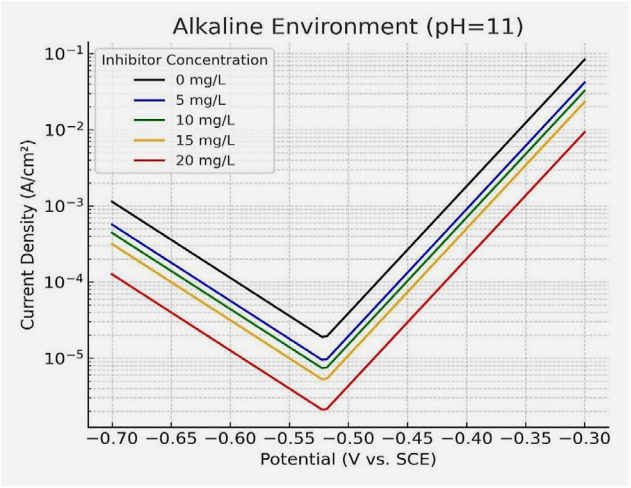


Figure 4. Potentiodynamic polarization curves of Ct3 steel in an alkaline medium in the presence of the MARZA-4 inhibitor

These trends confirm that MARZA-4 functions as a mixed-type inhibitor, affecting both anodic metal dissolution and cathodic hydrogen evolution or oxygen reduction reactions. This dual-mode inhibition likely arises from the formation of a protective adsorbed film on the steel surface, which acts as a physical and electrochemical barrier to charge and mass transfer.

The highest inhibition efficiency was observed in the acidic medium (pH = 3), where a reduction in I_{corr} of approximately 90–95% was recorded at 20 mg/L. This superior performance may be attributed to the enhanced adsorption of MARZA-4 molecules in acidic conditions, where protonation of functional groups can facilitate electrostatic interactions with the positively charged metal surface. The agreement between the electrochemical and gravimetric protection efficiencies (Z%) supports this interpretation.

In both neutral and alkaline environments, a similar concentration-dependent inhibition trend was observed, although the magnitude of protection was slightly lower. This suggests that MARZA-4 remains active across a broad pH spectrum, a critical feature for practical applications in variable oil and gas pipeline environments where pH conditions may fluctuate due to processing fluids or environmental ingress.

Collectively, the data demonstrate that MARZA-4 exhibits:

- Strong inhibition across all tested media,
- Enhanced activity in acidic environments,
- A mechanism consistent with adsorption-controlled inhibition,
- The characteristics of a passivating, mixed-type inhibitor capable of forming a stable barrier layer on steel surfaces.

These findings place MARZA-4 among the most promising candidates for corrosion control in oilfield environments, particularly where aggressive acid media are encountered. Compared to literature-reported inhibitors with similar structures and mechanisms (**Enning and Garrelfs, 2014; Gu et al., 2019**), MARZA-4 provides competitive or superior protection, affirming its potential for industrial-scale deployment.

The effect of MARZA-4 inhibitor on the growth of sulfate-reducing bacteria was examined over seven days. **Figure 5** presents the impact of the inhibitor on *Desulfovibrio desulfuricans* bacterial cells, while **Figure 6** shows its effect on *Desulfomicrobium* bacterial cells.

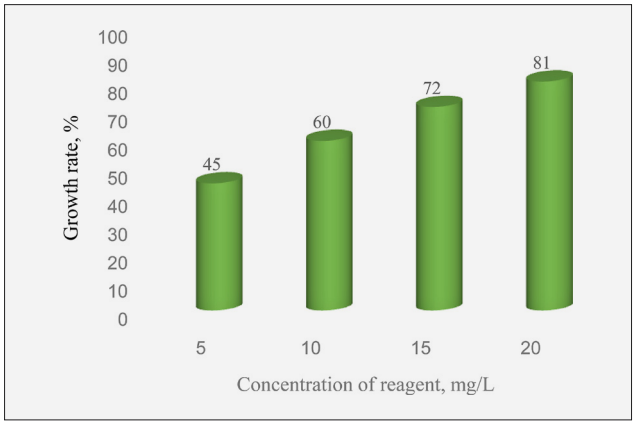


Figure 5. Effect of MARZA-4 reagent on the growth coefficient of *Desulfovibrio desulfuricans* bacterial cells (over 7 days)

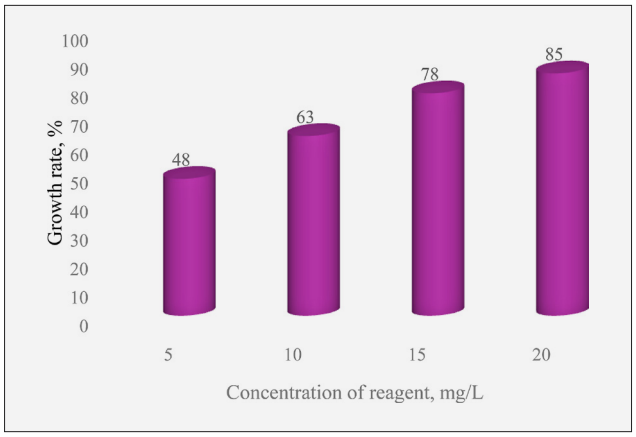


Figure 6. Effect of MARZA-4 reagent on the growth coefficient of *Desulfomicrobium* bacterial cells (over 7 days)

From the figures, it is evident that as the concentration of the MARZA-4 inhibitor increases in the nutrient medium, its inhibitory effect on the growth coefficient of bacterial cells also rises. Specifically, at concentrations of 5, 10, 15, and 20 mg/L, the inhibitory effect on the growth coefficient of *Desulfovibrio desulfuricans* bacterial cells is 45%, 60%, 72%, and 81%, respectively. For *Desulfomicrobium* bacterial cells, the corresponding inhibitory effects are 48%, 63%, 78%, and 85%. Thus, a concentration of 20 mg/L was found to be the most effective in suppressing bacterial growth in both strains tested.

In the "Postgate-B" nutrient medium, the bactericidal effect of the MARZA-4 inhibitor against *Desulfovibrio desulfuricans* and *Desulfomicrobium* cells was calculated based on changes in the concentration of biogenic hydrogen sulfide. The results for various concentrations of the MARZA-4 inhibitor are shown in **Figure 7** and **Figure 8**, respectively.

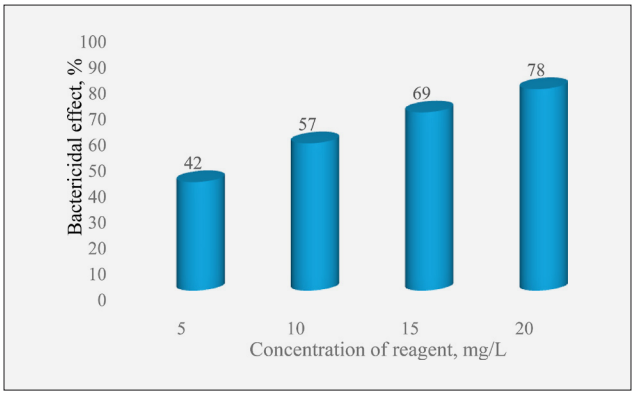


Figure 7. Bactericidal effect of the MARZA-4 reagent in a medium containing *Desulfovibrio desulfuricans* bacterial cells (over 7 days)

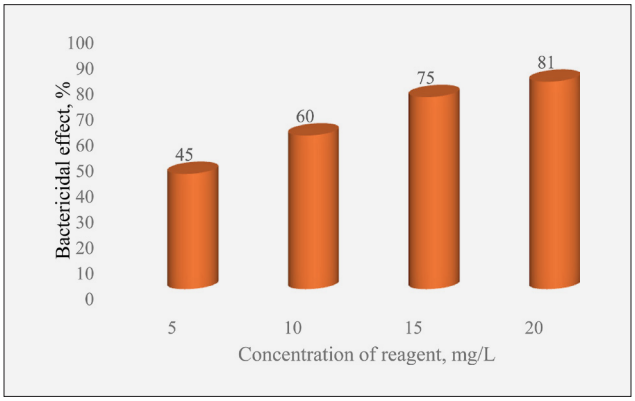


Figure 8. The bactericidal effect of MARZA-4 reagent in a medium containing *Desulfomicrobium* bacteria cells (over 7 days)

The experimental results presented in the figures provide insight into the bactericidal effects of the MARZA-4 inhibitor on Desulfovibrio desulfuricans and Desulfomicrobium bacterial cells in the "Postgate-B" nutrient medium. The data shows a clear trend in the increase of bactericidal activity with higher concentrations of MARZA-4.

In the case of Desulfovibrio desulfuricans, the inhibitor demonstrates a notable bactericidal effect, which intensifies as the concentration of MARZA-4 increases. The highest level of bactericidal activity is observed at a concentration of 20 mg/L.

For Desulfomicrobium bacterial cells, a similar pattern is observed, with increasing bactericidal effects cor-

responding to higher concentrations of MARZA-4. The results also indicate that the inhibitor's efficiency is higher against Desulfomicrobium than Desulfovibrio desulfuricans, as reflected in the overall percentages of bacterial inhibition at each concentration level.

These trends highlight the effectiveness of MARZA-4 as a bactericidal agent, with its efficacy improving at higher concentrations, and demonstrate the compound's potential in inhibiting the growth of sulfate-reducing bacteria in relevant industrial contexts. During the research process, a new composition, conditionally named HAK-2, was prepared under laboratory conditions using a 1:1 ratio of MARZA-4 inhibitor and chloroprene reagent, and its properties were studied. Laboratory tests were initially conducted in aggressive corrosion environments containing hydrogen sulfide, carbon dioxide, and both gases together.

Reagents based on chloroprene (2-chloro-1,3-butadiene), particularly compositions containing polychloroprene, are widely used as effective corrosion inhibitors in industrial applications. Their high anti-corrosion efficiency is attributed to the chemical structure of chloroprene and the functional groups facilitating adsorption onto the metal surface (**Zhang et al., 2021**).

The mechanism of action of chloroprene-based inhibitors, such as those found in the MARZA-4 reagent, can primarily be explained by the following factors:

Formation of an adsorption barrier: the unsaturated C=C bonds and the electronegative chlorine atom in the chloroprene structure strongly interact with the metal surface, promoting chemisorption. This leads to the formation of a uniformly distributed, dense adsorption layer, which acts as a physical barrier between the metal and the electrolyte, thereby limiting the ingress of oxygen and water molecules to the metal surface. MARZA-4 enhances this mechanism by including organic surfactants and polar functional groups (e.g. carboxylic and amine groups), which further increase adsorption density and stability on the steel surface (**Oginni et al., 2018; Gurbanov et al., 2022**).

Electrochemical passivation: due to the electron-withdrawing effect of the chlorine atom in chloroprene, the electron density on the metal surface is reduced, thereby suppressing anodic dissolution reactions (e.g. $Fe \rightarrow Fe^{2+} + 2e^{-}$). MARZA-4 contains halogenated organic compounds and stabilizers that complement this effect by forming complexation zones at anodic sites, contributing to decreased corrosion currents and reduced metal ion solubility (**Akinmoladun et al., 2018; Gurbanov et al., 2022**).

Jointly enhancing protective properties within the composition: the combination of chloroprene-based inhibitors with ionic and non-ionic surfactants in MARZA-4 improves the destabilization of oil-water emulsions, which is critical in corrosion-prone environments. Our experiments showed that the MARZA-4 mixture accelerated phase separation and enhanced the homogeneity of the adsorption film. This is attributed to its formulation, which includes emulsifiers and dispersants that increase surface coverage and minimize interfacial tension (**Xu et al., 2018; Gurbanov et al., 2022**).

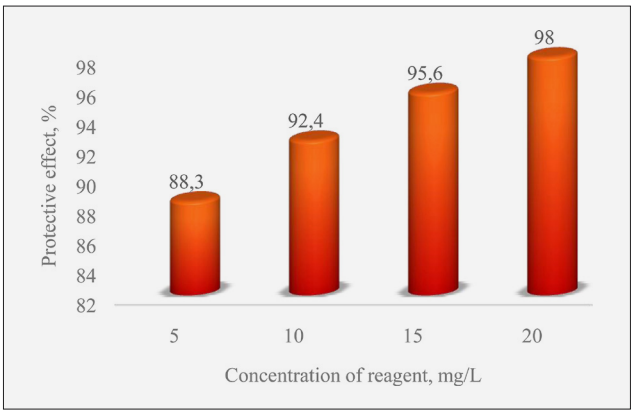


Figure 9. Dependence of the reagent concentration on the protective effect in an H_2S environment (t = 24 hours) for the HAK-2 composition

Prevention of microbiologically influenced corrosion: chloroprene-based compounds have been shown to suppress the metabolic activity of sulfate-reducing bacteria (SRB), a common source of MIC. MARZA-4 further improves this function through the incorporation of organic biocides and quaternary ammonium salts, which exhibit strong antimicrobial effects against SRB and acid-producing bacteria. This dual inhibition mechanism effectively mitigates both electrochemical and biological corrosion (**Popoola et al., 2017; Akinmoladun et al., 2018; Gurbanov et al., 2022**).

Analysis of our experimental results demonstrated that the application of the chloroprene-based composition significantly reduced the quantity of corrosion products on the metal surface. Moreover, the inhibitor efficiency, expressed as a percentage, was observed to be 10–15% higher compared to previously tested variants. These findings confirm that chloroprene provides a comprehensive protective effect through both physical barrier formation and chemical passivation mechanisms.

The corrosion rate was calculated using the gravimetric method. Subsequently, the composition's corrosion protective effect and penetration factorwere determined. For durations of 24 and 240 hours, the dependency of the composition's concentration on its protective effect in the hydrogen sulfide environment is presented in **Figures 9** and **10**. The dependency of the composition's concentration on its protective effect in the carbon dioxide environment is shown in **Figures 11** and **12**, and in environments containing both hydrogen sulfide and carbon dioxide, this relationship is shown in **Figures 13** and **14**.

As seen in **Figure 9**, in the hydrogen sulfide environment, the protective effect of the HAK-2 composition at concentrations of 5, 10, 15, and 20 mg/L is 83.3%, 92.4%, 95.6%, and 98%, respectively, over a 24-hour period.

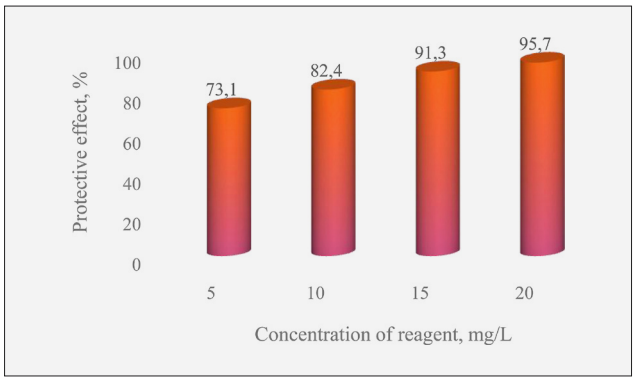


Figure 10. Dependence of the reagent concentration on the protective effect in an H_2S environment (t = 240 hours) for the HAK-2 composition

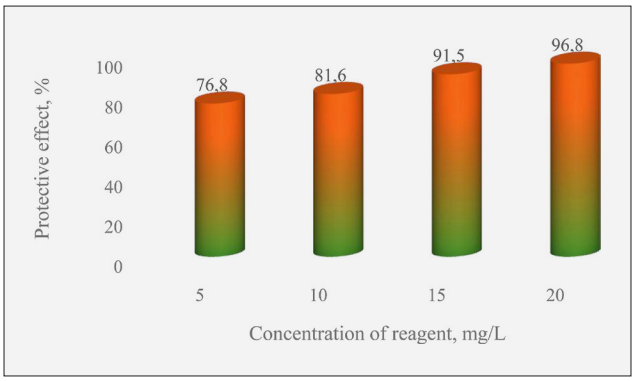


Figure 13. Dependence of reagent concentration on the protective effect in an $H_2S + CO_2$ environment (t = 24 hours) for the HAK-2 composition

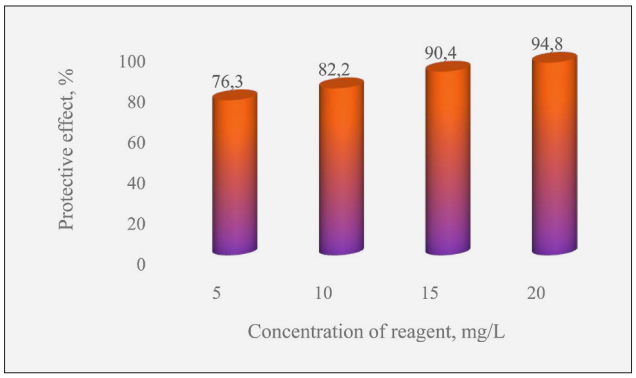


Figure 11. Dependence of the reagent concentration on the protective effect in a CO_2 environment (t = 24 hours) for the HAK-2 composition

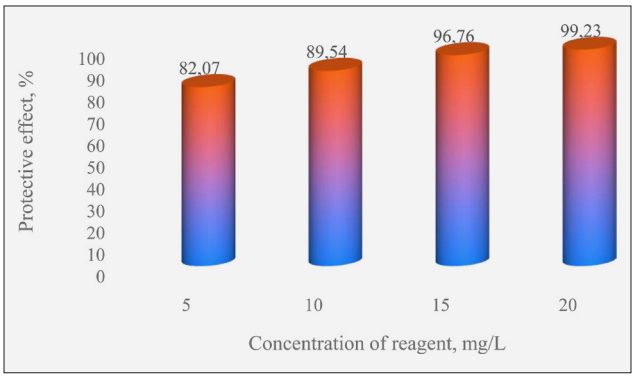


Figure 14. Dependence of reagent concentration on the protective effect in an $H_2S + CO_2$ environment (t = 24 hours) for the HAK-2 composition

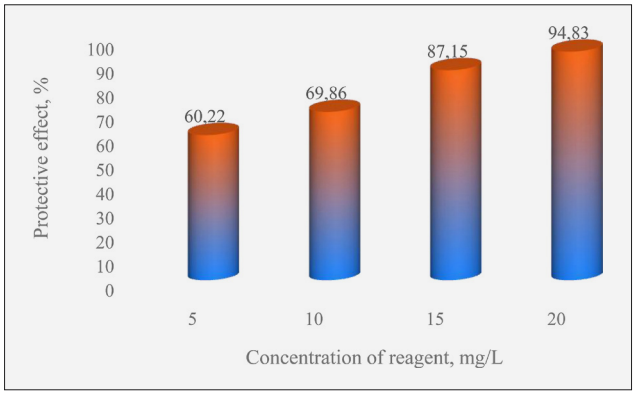


Figure 12. Dependence of the reagent concentration on the protective effect in a CO_2 environment (t = 240 hours) for the HAK-2 composition

As seen in **Figure 10**, in the hydrogen sulfide environment, the protective effect of the HAK-2 composition at concentrations of 5, 10, 15, and 20 mg/L is 73.1%, 82.4%, 91.3%, and 95.7%, respectively, over a 240-hour period.

As seen in **Figure 11**, in the carbon dioxide environment, the protective effect of the HAK-2 composition at concentrations of 5, 10, 15, and 20 mg/L is 76.3%, 82.2%, 90.4%, and 94.8%, respectively, over a 24-hour period.

As seen in **Figure 12**, in the carbon dioxide environment, the protective effect of the HAK-2 composition at concentrations of 5, 10, 15, and 20 mg/L is 60.22%, 69.86%, 87.15%, and 94.83%, respectively, over a 240-hour period.

As seen in **Figure 13**, in the H_2S+CO_2 environment, the protective effect of the HAK-2 composition at concentrations of 5, 10, 15, and 20 mg/L is 76.8%, 81.6%, 91.5%, and 96.8%, respectively, over a 24-hour period.

As seen in **Figure 14**, in the H_2S+CO_2 environment, the protective effect of the HAK-2 composition at concentrations of 5, 10, 15, and 20 mg/L is 82.07%, 89.54%, 96.76%, and 99.23%, respectively, over a 240-hour period.

The data from **Figures 6–11** clearly demonstrate that the corrosion protection efficiency of the HAK-2 composition increases proportionally with concentration across all test environments and time intervals. The most notable observation is that the highest corrosion inhibition in each environment was achieved at a concentration of 20 mg/L, validating this dosage as the most effective within the experimental range.

In the hydrogen sulfide environment (see **Figures 9** and **10**), the HAK-2 composition shows a consistently high level of protection. This may be due to the inhibitor's strong chemisorption onto the metal surface, form-

ing a dense protective film that resists the penetration of corrosive H_2S molecules. Over extended exposure (240 hours), although the protection slightly decreases compared to the 24-hour results, it still remains highly effective (up to 95.7%).

In carbon dioxide environments (see **Figures 11** and **12**), the efficiency is slightly lower, especially over the longer duration. This could be attributed to CO_2's ability to form carbonic acid in aqueous environments, which might partially compromise the integrity of the inhibitor layer. However, the inhibitor still achieves 94.83% protection at 20 mg/L after 240 hours, highlighting its resilience.

In mixed H_2S+CO_2 environments (see **Figures 13** and **14**), the inhibitor's performance is particularly impressive. Despite the aggressive nature of this combined corrosive environment, the HAK-2 composition delivers superior protection – up to 99.23% at 20 mg/L over 240 hours. This suggests a synergistic protective mechanism, where the inhibitor forms a dual-function barrier that limits both sulfide and acid gas attack.

The increasing efficiency with concentration can be explained by enhanced surface coverage and adsorption of the active components, which block corrosion-prone sites more effectively. Furthermore, the time-dependent data show that the protective layer formed by the inhibitor remains relatively stable over prolonged exposure, especially at the highest concentration.

These results confirm that 20 mg/L is the optimal concentration for the HAK-2 composition, ensuring robust corrosion resistance in acidic, CO_2-rich, and combined environments commonly encountered in the oil and gas industry.

Figure 15 shows the effect of the composition on the growth rate of *Desulfovibrio desulfuricans* bacterial cells, while **Figure 16** shows the effect on the growth rate of *Desulfomicrobium* bacterial cells.

As seen from the figures, as the concentration of the HAK-2 composition in the nutrient medium increases, the effect on the growth rate of bacterial cells also increases. Specifically, at concentrations of 5, 10, 15, and 20 mg/L, the effect of the composition on the growth rate of *Desulfovibrio desulfuricans* bacterial cells is 52%, 68%, 82%, and 89%, respectively, while the effect on the growth rate of *Desulfomicrobium* bacterial cells is 55%, 72%, 85%, and 94%, respectively.

These results clearly demonstrate that the HAK-2 composition exhibits strong bacteriostatic activity, particularly against sulfate-reducing bacteria, which are known to significantly accelerate microbiologically influenced corrosion (MIC) in oil and gas infrastructure. The data indicate a dose-dependent inhibitory effect: as the concentration of the composition increases, the ability of bacterial cells to proliferate diminishes substantially. This is likely due to the disruption of bacterial cell membranes and metabolic processes by the active components in the HAK-2 formulation.

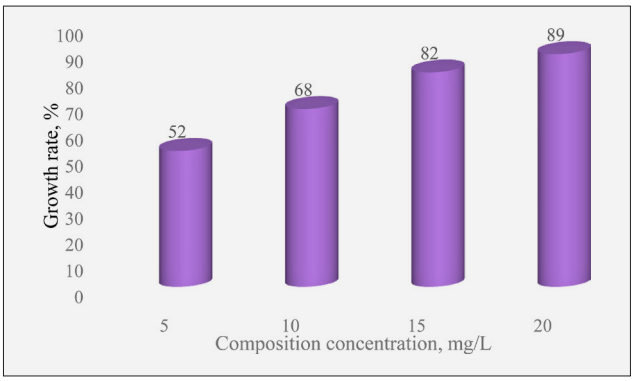


Figure 15. Effect of the HAK-2 composition on the growth rate of *Desulfovibrio desulfuricans* bacterial cells (over 7 days)

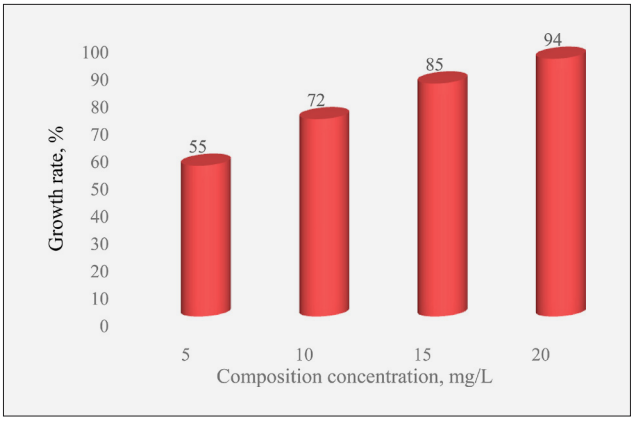


Figure 16. Effect of the HAK-2 composition on the growth rate of *Desulfomicrobium* bacterial cells (over 7 days)

At a concentration of 20 mg/L, the highest level of inhibition was achieved for both bacterial strains, with growth suppression reaching 89% for Desulfovibrio desulfuricans and 94% for Desulfomicrobium. These findings suggest that 20 mg/L is the optimal concentration for effectively controlling bacterial activity and preventing microbiological corrosion in operational environments. This bactericidal effect complements the corrosion protection function of the HAK-2 composition, making it a dual-purpose reagent suitable for use in oil and gas systems vulnerable to both chemical and biological corrosion mechanisms.

In the "Postgate-B" nutrient medium, based on the change in the concentration of biogenic hydrogen sulfide, the bactericidal effect of the HAK-2 composition on *Desulfovibrio desulfuricans* and *Desulfomicrobium* cells was calculated for different concentrations. The obtained results are shown in **Figure 17** and **Figure 18**, respectively.

The results presented in **Figures 17** and **18** demonstrate the bactericidal effectiveness of the HAK-2 composition in the "Postgate-B" nutrient medium against *Desulfovibrio desulfuricans* and *Desulfomicrobium* bacterial cells. As the concentration of HAK-2 increases, a

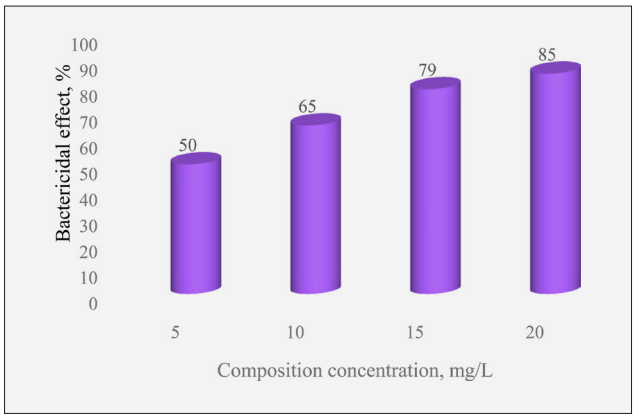


Figure 17. Bactericidal effect of the HAK-2 composition in a *Desulfovibrio desulfuricans* bacterial cell medium (over 7 days)

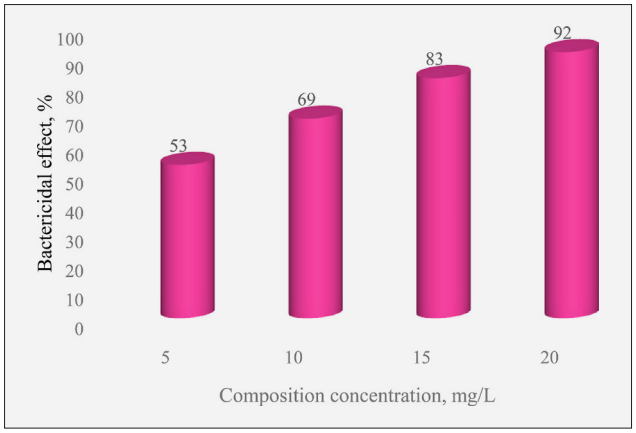


Figure 18. Bactericidal effect of the HAK-2 composition in a *Desulfomicrobium* bacterial cell medium (over 7 days)

significant enhancement in bactericidal activity is observed for both bacterial strains.

For *Desulfovibrio desulfuricans*, the bactericidal effect increases progressively with higher concentrations of the HAK-2 composition. The highest bactericidal efficiency is observed at the 20 mg/L concentration, indicating the composition's potential to effectively reduce bacterial growth.

Similarly, for *Desulfomicrobium*, the bactericidal effect follows the same trend, with higher concentrations resulting in greater bacterial inhibition. The inhibitor demonstrates more pronounced effectiveness against Desulfomicrobium than Desulfovibrio desulfuricans, as indicated by the greater inhibition at corresponding concentrations.

These findings highlight the potential of HAK-2 as a potent bactericidal agent, with its effectiveness improving as the concentration increases. The results suggest that HAK-2 can be an effective tool for controlling sulfate-reducing bacteria in industrial environments.

Thus, for the first time, the corrosion protective effect of the organic-origin MARZA-4 reagent, which can be produced from local raw materials, in neutral, acidic, and alkaline environments, as well as the new HAK-2 composition in aggressive corrosion environments with hydrogen sulfide, carbon dioxide, and both gases together, has been investigated. Their optimal consumption rates have been determined. Additionally, the effect of both reagents on sulfate-reducing bacteria in the "Postgate-B" nutrient medium has been studied. It has been established that, compared to the MARZA-4 reagent, the HAK-2 composition exhibits higher bactericidal-inhibitor properties. Therefore, it is proposed to use the HAK-2 composition as a widely applicable bactericidal-inhibitor reagent in the oil industry, especially in field conditions.

The observed bactericidal effectiveness of HAK-2 can be attributed to its ability to interfere with the metabolic processes and membrane integrity of sulfate-reducing bacteria. This inhibition is particularly important in mitigating microbiologically influenced corrosion (MIC), which poses a severe threat in oilfield operations. The consistent increase in bactericidal activity with concentration suggests a dose-dependent response, with 20 mg/L emerging as the most effective dose. The superior performance against Desulfomicrobium may be due to structural or physiological differences between the two bacterial species.

These findings highlight the potential of HAK-2 as a potent bactericidal agent. Its dual function as both a corrosion inhibitor and a biocide makes it highly valuable for industrial application in environments prone to both chemical and microbial corrosion.

Thus, for the first time, the corrosion protective effect of the organic-origin MARZA-4 reagent, which can be produced from local raw materials, in neutral, acidic, and alkaline environments, as well as the new HAK-2 composition in aggressive corrosion environments with hydrogen sulfide, carbon dioxide, and both gases together, has been investigated. Their optimal consumption rates have been determined. Additionally, the effect of both reagents on sulfate-reducing bacteria in the "Postgate-B" nutrient medium has been studied. It has been established that, compared to the MARZA-4 reagent, the HAK-2 composition exhibits higher bactericidal-inhibitor properties. Therefore, it is proposed to use the HAK-2 composition as a widely applicable bactericidal-inhibitor reagent in the oil industry, especially under field conditions.

As shown in **Figure 19**, the surface morphology of the Ct3 steel coupons significantly differs depending on the presence of the HAK-2 composite reagent and sulfate-reducing bacteria.

Figure 19a–d presents SEM images of steel surfaces after 360 hours of exposure to environments containing sulfate-reducing bacteria (SRB), specifically Desulfomicrobium and Desulfovibrio desulfuricans, both in the absence and presence of the HAK-2 composite reagent at its optimal concentration.

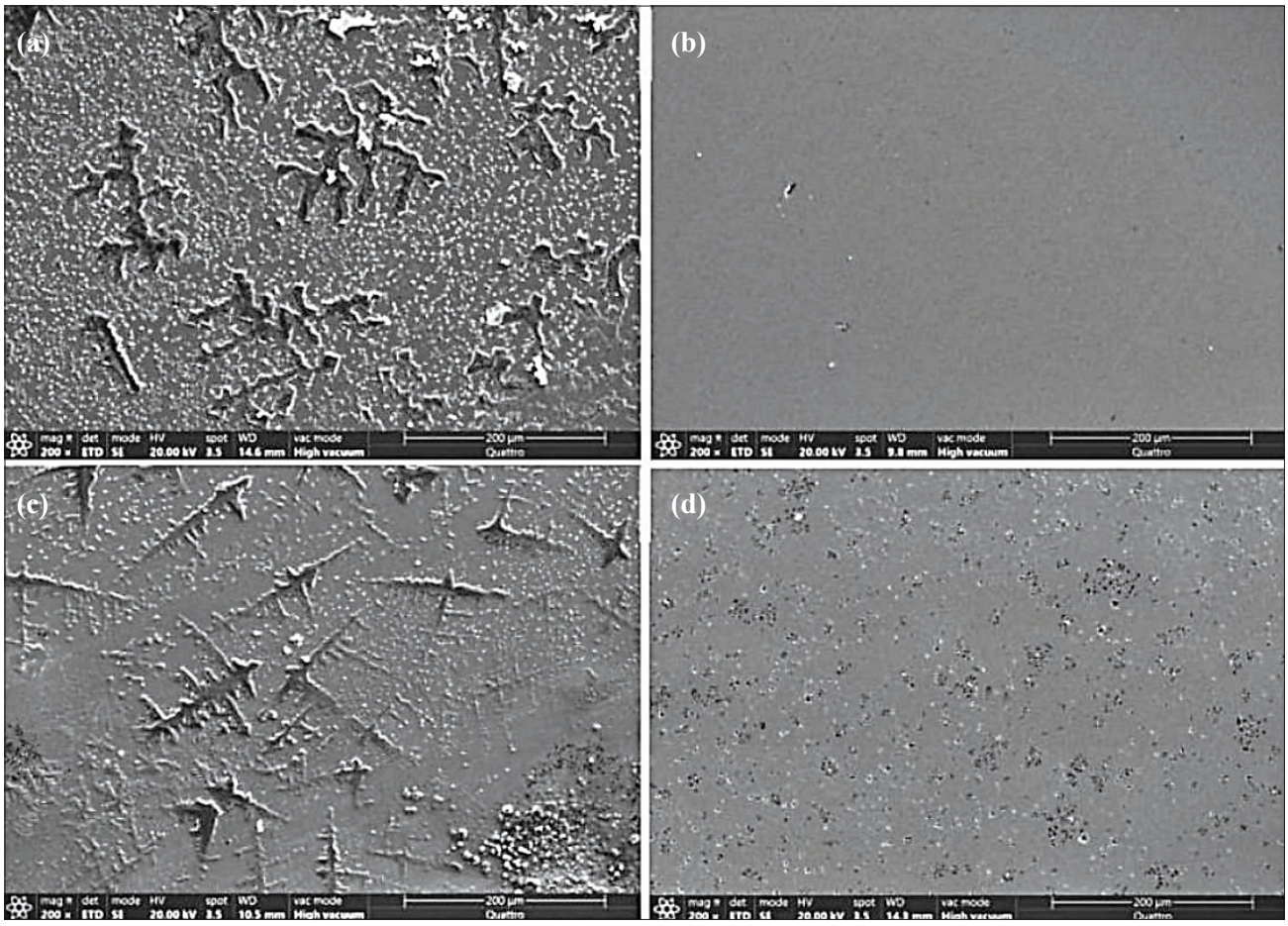


Figure 19. SEM images of corrosion on Ct3 grade steel coupons under the influence of sulfate-reducing bacteria and with the application of the HAK-2 composite reagent: a) Corrosion of steel in the presence of *Desulfomicrobium* species without any reagent applied; b) Corrosion of steel in the presence of *Desulfomicrobium* species with the addition of the HAK-2 composite reagent at its optimal concentration (C_{comp}=20 mg/L); c) Corrosion of steel in the presence of *Desulfovibrio desulfuricans* species without any reagent applied; d) Corrosion of steel in the presence of *Desulfovibrio desulfuricans* species with the addition of the HAK-2 composite reagent at its optimal concentration (C_{comp}=20 mg/L).

Figure 19a–d presents SEM images of steel surfaces after 360 hours of exposure to microbiologically active environments containing either Desulfomicrobium or Desulfovibrio desulfuricans species, with and without the addition of the HAK-2 composite reagent.

In the absence of any inhibitor (see **Figures 19a** and **19c**), severe corrosion damage is evident, with more aggressive surface degradation observed in the environment containing Desulfovibrio desulfuricans (**19c**).

In contrast, the addition of HAK-2 at its optimal concentration significantly reduces corrosion effects in both environments (see **Figures 19b** and **19d**). The surface exposed to Desulfomicrobium in the presence of HAK-2 (**25b**) appears smoother and more uniform, indicating strong inhibitory performance. However, in the case of Desulfovibrio desulfuricans (**19d**), although corrosion is mitigated, localized pitting remains visible – suggesting reduced effectiveness against this more aggressive SRB strain.

Overall, the HAK-2 composite demonstrates superior corrosion protection compared to individual reagents across both microbial environments, and the observed SEM results are in full agreement with the quantitative laboratory findings.

The SEM observations support the quantitative results obtained from corrosion rate measurements and bacteriological tests. The surface morphology clearly reveals that the 20 mg/L concentration of HAK-2 provides the most effective protection, minimizing corrosion damage and bacterial colonization. The significant decrease in pitting and corrosion product deposition confirms that HAK-2 disrupts both the microbial corrosion pathway and the electrochemical processes underlying steel degradation.

The optimal performance at 20 mg/L can be attributed to a saturation effect, where the active components of HAK-2 sufficiently adsorb onto the metal surface, forming a protective barrier while simultaneously neutralizing the metabolic byproducts of SRB. This dual mechanism ensures both inhibition of bacterial proliferation and stabilization of the metal surface.

These findings reinforce the earlier experimental data, showing that the HAK-2 composition exhibits superior

performance compared to MARZA-4, particularly in aggressive environments and in the presence of SRB. The clear reduction in corrosion damage at 20 mg/L suggests this dosage as the optimal operational concentration for field applications where MIC is prevalent.

This study investigates the corrosion protective and bactericidal-inhibitor properties of the organic-origin MARZA-4 reagent and the novel HAK-2 composition in various environmental conditions. The reagents were tested in neutral, acidic, and alkaline environments, as well as in aggressive environments containing hydrogen sulfide (H_2S), carbon dioxide (CO_2), and a combination of both gases. Furthermore, their effects on sulfate-reducing bacteria in the "Postgate-B" nutrient medium were evaluated.

The explanation can be expanded with more scientific details to better clarify why the 20 mg/L concentration of HAK-2 exhibits optimal performance. Below is the rationale based on scientific principles.

Saturation effect: the saturation effect occurs when the concentration of the inhibitor HAK-2 reaches a level at which the active components in the composition fully interact with the metal surface.When the concentration of HAK-2 is increased to 20 mg/L, a sufficient amount of inhibitor molecules adsorb to the steel surface, forming a stable and protective layer. This layer reduces the direct interaction between corrosive agents (such as hydrogen sulfide, carbon dioxide, or sulfate-reducing bacteria) and the metal, thereby preventing corrosion.

Adsorption mechanism: the adsorption of HAK-2 molecules onto the metal surface is an important process in corrosion inhibition. Inhibitors like HAK-2 typically contain functional groups that can bond with the steel surface, creating a physical barrier that prevents further oxidation or chemical degradation. At 20 mg/L, there is enough of the active ingredient to form a dense, continuous film on the steel surface, offering maximum protection.

Bactericidal action on SRB: the sulfate-reducing bacteria (SRB), such as Desulfovibrio desulfuricans and Desulfomicrobium, are known to produce hydrogen sulfide (H_2S) and other corrosive metabolites, which accelerate the corrosion process. At lower concentrations of HAK-2, the number of bacteria is not sufficiently controlled, allowing them to continue their metabolic activity. However, at 20 mg/L, the bactericidal properties of HAK-2 become more effective, leading to a noticeable reduction in SRB proliferation. This not only reduces the bacterial-induced corrosion but also prevents the generation of aggressive metabolic byproducts like H_2S, further mitigating corrosion.

Dual protective mechanism: the dual mechanism of HAK-2 is particularly important. First, it inhibits the microbial activity of SRB, which prevents them from producing corrosive metabolites. Second, the inhibitor provides electrochemical protection by forming a barrier that reduces the interaction of corrosive species with the steel surface. This combined action leads to the significant reduction of both microbial-induced corrosion (MIC) and electrochemical corrosion.

Optimal concentration: the 20 mg/L concentration represents a threshold concentration where the beneficial effects of HAK-2 are maximized. Concentrations above this level may lead to diminishing returns in terms of additional protective effects, as the surface may become saturated, and any excess inhibitor might not further enhance performance. Conversely, concentrations below 20 mg/L might not fully protect the metal surface or control bacterial activity, leading to reduced effectiveness.

Field applications: in field conditions, especially in environments prone to microbiologically influenced corrosion (MIC), 20 mg/L of HAK-2 is the optimal dosage that balances cost and performance. Higher concentrations might be wasteful, while lower concentrations may fail to prevent the harmful effects of SRB and corrosion. Therefore, 20 mg/L is recommended for industrial applications in environments where corrosion and bacterial degradation are significant concerns, ensuring both long-term protection and efficient use of the inhibitor.

This scientific reasoning ties together the experimental observations (SEM images, corrosion rates, and bacterial growth inhibition) and explains why the 20 mg/L concentration of HAK-2 offers the best balance between bactericidal activity, corrosion inhibition, and efficiency.

In conclusion, this study demonstrates that HAK-2 not only provides superior corrosion protection, but also offers more potent bactericidal-inhibitor effects compared to MARZA-4. These findings support the potential application of HAK-2 in mitigating both corrosion and microbial activity in the oil and gas industry, particularly under challenging operational conditions.

4. Conclusions

1. For the first time, the corrosion protective effect of the organic-origin MARZA-4 reagent in neutral, acidic, and alkaline environments, as well as the new HAK-2 composition in aggressive environments with hydrogen sulfide, carbon dioxide, and both gases together, has been investigated. Additionally, their effect on sulfate-reducing bacteria in the "Postgate-B" nutrient medium has been studied. It has been determined that both reagents, at an optimal concentration of 20 mg/L, possess bactericidal-inhibitor properties.
2. It has been established that the bactericidal-inhibitor MARZA-4 reagent, at concentrations of 5, 10, 15, and 20 mg/L in neutral, acidic, and alkaline environments, provides corrosion protective effects of 88%, 91%, 96%, 98%, 86%, 90%, 95%, 98%, and 80%, 84%, 86%, 94%, respectively. In the "Postgate-B" nutrient medium, the bactericidal effect against *Desulfovibrio desulfuricans* and

Desulfomicrobium cells is 42%, 57%, 69%, 78%, and 45%, 60%, 75%, 81%, respectively.

3. The corrosion protective effect of the HAK-2 composition in hydrogen sulfide, carbon dioxide, and both gases together in aggressive corrosion environments, as well as its effect on sulfate-reducing bacteria in the "Postgate-B" nutrient medium, has been studied. It has been determined that, compared to the MARZA-4 reagent, the HAK-2 composition exhibits higher bactericidal-inhibitor properties. Therefore, the HAK-2 composition is proposed for widespread use as a bactericidal-inhibitor reagent in the oil industry, particularly in field conditions.

Acknowledgement

We would like to thank Azerbaijan State Oil and Industry University for its support and resources provided during the course of this research.

5. References

Abdel-Gaber, A.M., Abd-El-Nabey, B.A., Khamis, E. (2011). A natural extract as scale and corrosion inhibitor for steel surface in brine solution. *Desalination*, *278*(1-2), 337-342. https://doi.org/10.1016/j.desal.2011.05.048

Akinmoladun A. J., Akinmoladun O.A., Oginni S.O. (2018). Inhibition of sulfate-reducing bacteria (SRB) and corrosion of mild steel in oilfield conditions by chloroprene-based reagents. *Biochemical Engineering Journal*, 137, 35-43. https://doi.org/10.1016/j.bej.2018.05.003

Ansari, K.R., Chauhan, D.S., Quraishi, M.A., Mazumder, M.A.J., Singh, A. (2020). Chitosan Schiff Base: An Environmentally Benign Biological Macromolecule as a New Corrosion Inhibitor for Oil & Gas Industries. *International Journal of Biological Macromolecules.* 144, 305–315. https://doi.org/10.1016/j.ijbiomac.2019.12.106

Bao, Q., Zhang, D., Wang, P. (2012). Effects of two main metabolites of sulphate-reducing bacteria on the corrosion of Q235 steels in 3.5 wt.% NaCl media. *Corrosion Science*, 65, 405–413. https://doi.org/10.1016/j.corsci.2012.08.044

Enning, D., Garrelfs, J. (2014). Corrosion of iron by sulfate-reducing bacteria: New views of an old problem. Applied and Environmental Microbiology, 80(4), 1226–1236. https://doi.org/10.1128/AEM.02848-13

Gu, T., Jia, R., Unsal, T., Xu, D. (2019). Toward a better understanding of microbiologically influenced corrosion caused by sulfate reducing bacteria. Journal of Materials Science & Technology, 35(4), 631–636. https://doi.org/10.1016/j.jmst.2018.10.026

Gurbanov, G.R., Gasimzade, A.V. (2023a). Research of physical and chemical influence on rheological parameters of highly paraffinic oil. *ChemChemTech, 66*(5), 80-86. https://doi.org/10.33070/etars.2.2024.03

Gurbanov, G.R., Gasimzade, A.V., Abbasova, L.A. (2023b). Study of a new multifunctional inhibitor under laboratory condition. *ChemChemTech, 66*(8), 106-112. https://doi.org/10.6060/ivkkt.20236608.6764

Gurbanov, H.R., Gasimzade, A.V., Shikhiyeva, L.M. (2022). The study of the effect of individual and compositional agents on the physical-chemical parameters of oils. *Azerbaijan Oil Industry Journal*, (12), 38–45. https://doi.org/10.37474/0365-8554/2022-12-38-45

Kalinina, A.S., Polkovnikov, I.S., Shein, B.A. (2016). Protection against corrosion of low-carbon steel in acidic environments by inhibitors of the Soling series. *ChemChemTech, 59*(2), 70-73. https://doi.org/10.17072/2223-1838-2021-4-254-262

Kashkovskiy, R., Kuznetsov, Yu.I., Leonid, K. (2012). Inhibition of hydrogen sulfide corrosion of steel in gas phase by tributylamine. *Corrosion Science*, 64, 126-136. https://doi.org/10.1016/j.corsci.2012.07.010

Kuznetsov, Yu.I., Andreev, N.N., Ibatullin, K.A., Oleinik, S.V. (2000). Volatile inhibitor of carbon dioxide corrosion of steels. *Protection of metals, 36*(3), 266-270. https://doi.org/10.1007/BF02758397

Lecante, A., Robert, F., Blandinières, P.A. (2011). Anti-corrosive properties of S. tinctoria and G. ouregou alkaloid extracts on low carbon steel. *Current Applied Physics, 11*(3), 714-724. https://doi.org/10.1016/j.cap.2010.11.038

Lusk, D., Gupta, M., Boinapally, K. (2008). Armoured against corrosion. *Hydrocarb Eng,* 13, 115–118.

Martens, C.S., Berner, R.A. (1974). Methane production in the interstitial waters of sulfatedepleted marine sediments. *Science,* 185. 167-169. https://doi.org/10.1126/science.185.4157.1167

Matamoros-Veloza, A., Barker, R., Vargas, S., & Neville, A. (2020). Mechanistic insights of dissolution and mechanical breakdown of $FeCO_3$ corrosion films. *Corrosion Science*, 170, 108693. [Online]. Available: https://doi.org/10.1016/j.corsci.2020.108693

Milovzorov, G.V., Makletsov, V.G., Trefilova, T.V. (2012). The use of inhibitors - bactericides in the conditions of hydrogen sulfide corrosion of steel. *Bulletin of Udmurt University,* 3, 44-47.

Morris, W., Richard, R. (2002). Ethnicity and Genomics Social Classifications as Proxies of Biological Heterogeneity Genome Res. Microbiol, 12, 844-850. https://doi.org/10.1101/gr.99202

Muyzer, G., Stams, A. J. M. (2008). The ecology and biotechnology of sulphate-reducing bacteria. *Nature Reviews Microbiology*, 6(6), 441–454.

Oginni O.M., Okanlawon S.O., Badmus A.M. (2018). Corrosion inhibition of mild steel in acidic media by chloroprene-based surfactants. *Journal of Applied Electrochemistry*, 48(2): 223–234.

Pashayeva, S. M. (2022). Application of effective technology in the storage-transportation system of high paraffin well products. Applicant dissertation, Speciality: 3354.01 - Construction and exploitation of oil-gas pipelines, bases and storage. Field of science: Technical sciences, 140.

Popoola F.L.T., Oginni S.O., Akinyemi A.A. (2017). Electrochemical studies of chloroprene-based corrosion inhibitors for mild steel. *Corrosion Science*, 121, 89-97. https://doi.org/10.1016/j.corsci.2017.03.001

Postgate, J. R. (1984). The Sulphate-Reducing Bacteria. 2nd ed. Cambridge University Press.

Salasi, M., Sharabi, T., Roayaei, E. (2007). The electrochemical behavior of environment-friendly inhibitors of silicate and phosphonate in corrosion control of carbon steel in soft water media. *Materials Chemistry and physics, 104*(1), 183-190. https://doi.org/10.1016/j.matchemphys.2007.03.008

Starosvetsky, D.J., Armon, R., Ein-Eli, Y. (2010). A peculiar cathodic process during iron and steel corrosion in sulfate reducing bacteria (SRB) media. *Corrosion Science, 52*(4), pp. 1536-1540. doi:10.1016/j.corsci.2010.01.013

Talybov, G.M., Azizbeyli, A.R., Mammadbeyli, E.G., Gurbanov, G.R. (2020). Alkoxyhalogenation of dichlorostyrenes in the medium of unsaturated C3-alcohols. *Journal of Organic Chemistry, 56*(1), 47-51. https://doi.org/10.1134/S1070428020010066

Taraneh, J.B., Rahmatollah, G., Hassan, A., Alireza, D. (2008). Effect of wax inhibitors on pour point and rheological properties of Iranian waxy crude oil. *Fuel Process. Technol,* 89, 973-977. https://doi.org/10.1016/j.fuproc.2008.03.013

URL 1. https://aak.gov.az/upload/dissertasion/texnika_elml_ri/SAIDA__PASAYEVA_-AVTOREF_-17__05_221.pdf

Wang, S., Liu, H., & Zhang, Y. (2021). Formation and characterization of iron sulfide films on carbon steel in H_2S-containing environments. *Corrosion Science*, 183, 109316. [Online]. Available: https://doi.org/10.1016/j.corsci.2021.109316

Xu L.L., Zhang X.H., Cao C.L. (2018). Synergistic corrosion inhibition by anionic surfactants and organic inhibitors in oilfield environments. *Journal of Petroleum Science and Engineering*, 169, 169-179. DOI: 10.1016/j.petrol.2018.05.009.

Xu, D., Li, Y., Gu, T. (2016). Mechanistic modeling of biocorrosion caused by biofilms of sulfate reducing bacteria and acid producing bacteria. *Bioelectrochemistry,* 110, 52–58. https://doi.org/10.1016/j.bioelechem.2016.03.003

Zafari, S., Niknam Shahrak, M., Ghahramaninezhad, M. (2020). New MOF-Based Corrosion Inhibitor for Carbon Steel in Acidic Media. *Metals and Materials International,* 26, 25–38. https://doi.org/10.1007/s12540-019-00307-1

Zhang, L., Li, Y., et al. (2021). Study on the adsorption behavior of chloroprene-based corrosion inhibitors on carbon steel in saline environments. *Corrosion Science*, 190, 109665. [Online]. Available: https://doi.org/10.1016/j.corsci.2021.109665

Zhang, S., Li, Q., Fan, J., Kang, W., Hu, W., Yang, X. (2009). Novel Composite Films Prepared by Sol–gel Technology for the Corrosion Protection of AZ91D Magnesium Alloy. *Progress in Organic Coatings,* 66, 328–335. https://doi.org/10.1016/j.porgcoat.2009.08.011

Zhao, Q., Guo, J., Cui, G., Han, T., Wu, Y. (2020). Chitosan Derivatives as Green Corrosion Inhibitors for P110 Steel in a Carbon Dioxide Environment. *Colloids and Surfaces B: Biointerfaces,* 194, 111150. https://doi.org/10.1016/j.colsurfb.2020.111150

SAŽETAK

Istraživanje inhibitorskih svojstava novih reagensa na djelovanje bakterija

Opće je poznato da je u industrijski razvijenim zemljama proizvođačima nafte jedan od najvećih neriješenih izazova, kojim se ujedno produljuje radni vijek opreme i postrojenja, zaštita unutarnjih površina opreme i postrojenja od korozije. S obzirom na navedeno, ovaj rad analizira rezultate brojnih laboratorijskih ispitivanja učinaka novorazvijenoga organskog reagensa MARZA-4 i sastava privremeno nazvanoga HAK-2 na bakterije koje reduciraju sumporovodik, ugljikov dioksid i sulfate, koji su primarni uzroci korozije unutarnjih površina u naftnoj industriji. Prvi put istraživana je učinovitost djelovanja reagensa MARZA-4 protiv bakterija koje reduciraju sulfate u agresivnim korozivnim okruženjima kao što su neutralni, kiseli i alkalni mediji te u hranjivome mediju „Postgate-B". Utvrđeno je da reagens MARZA-4 posjeduje inhibitorska svojstva pri optimalnoj koncentraciji od 20 mg/L. Pri toj koncentraciji njegov zaštitni učinak od korozije u neutralnim, kiselim i alkalnim okruženjima utvrđen je na 98 %, 98 % i 94 %. U hranjivoj podlozi „Postgate-B" baktericidni učinak protiv stanica *Desulfovibrio desulfuricans* i *Desulfomicrobium* bio je 78% odnosno 81%.

Ključne riječi:
bakterije koje reduciraju sulfate, inhibitor, sumporovodik, ugljikov dioksid, agresivno korozivno okruženje

Author's contribution

Guseyn R. Gurbanov (Professor, Doctor of Science in Chemistry): methodology development and validation. **Aysel Gasimzade** (PhD, Associate Professor): conceptualization, investigation and software.
All authors have read and agreed to the published version of the manuscript.

RGNZ/MGPB

Optimization of Stope Dimensions in a Geotechnically Complex Mine Using Automated Stability Analysis

Rudarsko-geološko-naftni zbornik
(The Mining-Geology-Petroleum Engineering Bulletin)
DOI: 10.17794/rgn.2026.2.3

Original scientific paper

Mohammad Army[1] ✉, Tri Karian[1]* ✉, Takashi Sasaoka[2] ✉, Akihiro Hamanaka[2] ✉, Firly Rachmaditya Baskoro[1] ✉, Budi Sulistianto[1] ✉, Hideki Shimada[2] ✉

[1] *Mining Engineering Department, Faculty of Mining and Petroleum Engineering, Institut Teknologi Bandung, Jalan Ganesha No.10, Bandung 40132, Indonesia.*

[2] *Earth Resources Engineering Department, Faculty of Engineering Department, Kyushu University, 744 Motooka, Nishi-ku, Fukuoka 819-0395, Japan.*

Abstract

Stope stability is a critical factor in underground mining, directly influencing safety, productivity, and overall mining efficiency. Traditional stope design methods often employ uniform stope lengths, disregarding geotechnical variability and thereby increasing the risk of instability or suboptimal dimensions. This study introduces an automated stability analysis approach that iteratively evaluates multiple stope dimension scenarios based on the Modified Stability Number (N') to identify the optimum stable configuration. By conducting detailed stability assessments for each stope wall, the method provides a more accurate representation of geotechnical conditions compared to the conventional methods with uniform stope length. The case study demonstrates that this approach effectively reduces the total number of stopes while maintaining geotechnical stability, in contrast to conventional methods where 14%–40% of stopes exhibit instability. Furthermore, the optimization method achieves a balanced outcome between dilution control and operational efficiency resulted in lower stope production cost. The optimized configurations generated by the proposed method deliver the lowest total production cost, with estimated savings of approximately USD 1.6–2.4 million compared to conventional designs. These findings confirm that the optimization framework not only enhances geotechnical stability but also provides a demonstrable economic advantage, underscoring the importance of integrating geotechnical variability into stope design.

Keywords:
stope stability, Modified Stability Number N', stope dimension optimization, automated analysis

1. Introduction

The stope stability during mining operations is a critical factor that directly influences both the safety and efficiency of underground mining activities (**Diederichs & Kaiser, 1996; Patanwar et al., 2025; Putra et al., 2024; Zhang et al., 2024**). Ensuring that the stope remains stable throughout the extraction process is essential to minimize the risks of ground failures, protect workers, and maintain uninterrupted production (**Adoko, 2025**).

The stability of a stope is significantly affected by its dimensions and the geotechnical characteristics of the surrounding rock mass (**Adoko, 2025; Cui et al., 2024; Li, Liu et al., 2024; Rinne et al., 2024; Sabao et al., 2022**). Larger stopes, while potentially lowering mining cost and increasing production efficiency, tend to be more susceptible to instability. In contrast, smaller stopes may enhance stability but can lead to higher costs (**Li et al., 2024; O'Hara & Suboleski, 1992**). Therefore, determining the optimum stope dimensions is crucial to achieving a balance between economic efficiency and geotechnical stability.

Traditionally, several mining operations adopt a simplified approach by applying a uniform stope dimension across different areas of the mine (**Chen et al., 2024; Guo & Miao, 2022; Heidarzadeh et al., 2019; Patanwar et al., 2025; Phaisopha et al., 2023; Zhao & Zhou, 2023**). These uniform dimensions are determined based on the general geomechanical properties of the rock mass (**Cui et al., 2024; Heidarzadeh et al., 2020; Kang et al., 2021; Nhleko & Musingwini, 2022**). This method was used due to its straightforward implementation, minimal computational requirements, and lack of necessity for detailed geotechnical data. Nevertheless, by generalizing stope dimensions across the entire mining area, this approach neglects the spatial variability of the rock mass, overlooking local differences in geomechanical characteristics. Such simplification can result in

* Corresponding author: Tri Karian
e-mail address: tri_karian@itb.ac.id
Received: 6 July 2025. Accepted: 1 October 2025.
Available online: 13 March 2026

Table 1. Advantage and disadvantage comparison

Method	Advantages	Disadvantages
Uniform stope dimension (Conventional method)	Simple implementation; low computational demand; widely adopted in practice	Ignores geotechnical variability of rock-mass; may cause local instability;
Stope dimension optimization using automated stability analysis (New method)	Considers spatial variability of the rock-mass; improves stability and cost efficiency	Detailed geotechnical data requirements; increased computational workload

suboptimal stope dimensions or even localized instability around individual stopes (**Zhou et al., 2023**).

In mining environments characterized by complex geotechnical conditions, the use of generalized stope dimensions can result in significant instability, particularly in areas of locally weak rock mass (**Cakrabuana et al., 2024; Zadhesh & Majdi, 2022; Zulfahmi et al., 2023**). This instability may lead to stope collapse and excessive overbreak, as documented in several case studies addressing dilution and overbreak in weak rock masses (**Clark, 1998**). For instance, at the Obuasi Mine in Ghana, local zones of poor rock mass and unfavourable structural conditions were identified as primary triggers for instability and excessive dilution (**Amedjoe & Agyeman, 2015**). Similarly, in the Dongguashan Copper Mine, China, unfavourable rock-mass structures, low mechanical properties, and excessive stope hydraulic radius were the leading causes of tall stope collapse (**Zhang et al., 2024**). Conversely, in a gold mine in Western Australia, the application of uniform stope dimensions, based on pessimistic assumptions, resulted in suboptimal design outcomes in areas with strong rock mass (**Stephenson & Sandy, 2013**). These cases underscore the necessity of addressing local ground weaknesses while optimizing stope dimensions in regions of stronger rock mass through the incorporation of spatial rock mass variability in both stability analysis and stope design.

This paper introduces an automated stability analysis method aimed at improving stope stability assessments and identifying optimum stope dimensions in a spatially distributed manner. The method involves iterating through various possible stope dimensions to determine the most stable configuration at each location within the mining area. To implement this method, an algorithm based on Modified Stability Number N' by **Potvin (1988)** will be used to streamline the analysis.

While this approach demands increased computational resources and more detailed geotechnical data, it offers significant potential benefits (**Dolatshahi & Molladavoodi, 2024; Sugianti & Tohari, 2023**). These include improved accuracy in stope stability assessments, reduced dilution rates, a decrease in the total number of required stopes, and, consequently, lower stope production costs. **Table 1** summarizes the principal advantages and disadvantages of the proposed automated stability analysis method in comparison with conventional uniform stope dimensioning practices.

The objective of this paper is to develop and validate an automated stability analysis method for optimizing stope dimensions in underground mining by incorporating spatial variability of rock mass properties into the design process. This approach aims to improve geotechnical stability, minimize the risk of stope failure, and achieve a balance between dilution control and operational efficiency. By iteratively evaluating multiple stope dimension scenarios using the Modified Stability Number (N'), the proposed method seeks to identify the most stable and cost-effective configurations, demonstrating significant economic benefits and enhanced safety compared to conventional designs that rely on uniform stope lengths.

2. Methods

2.1. Modified Stability Number

The stability analysis method utilized in this study is based on the modified stability number (N') introduced by **Potvin (1988)**, which builds based on the stability number developed by **Mathews et al. (1980)**. This original stability number is derived by adjusting the Q' value to account for factors such as induced stresses, the orientation of geological discontinuities, and the angle of the stope wall. The modified stability number, N', is calculated using **Equation 1**.

$$N' = Q' \times A \times B \times C \tag{1}$$

The rock stress factor (A) represents the strength of rock and the stress around the stope excavation. The joint orientation factor (B) assesses how the orientation of the primary joint set relates to the excavation surface, and the gravity adjustment factor (C) represents the influence of gravity on the stope wall stability. The values of these factors can be obtained using the chart shown in **Figure 1**.

An empirical approach is utilized to evaluate the stability or potential failure of stopes, wherein the hydraulic radius is correlated with the modified stability number (N'). This method is based on an extensive compilation of case histories originally developed by **Mathews et al. (1980)** and later refined by **Potvin (1988)**. The relationship is graphically represented in **Figure 2**, which categorizes stope conditions into three zones: stable, transition, and collapse. By plotting the N' value against the hydraulic radius, the chart provides a practical frame-

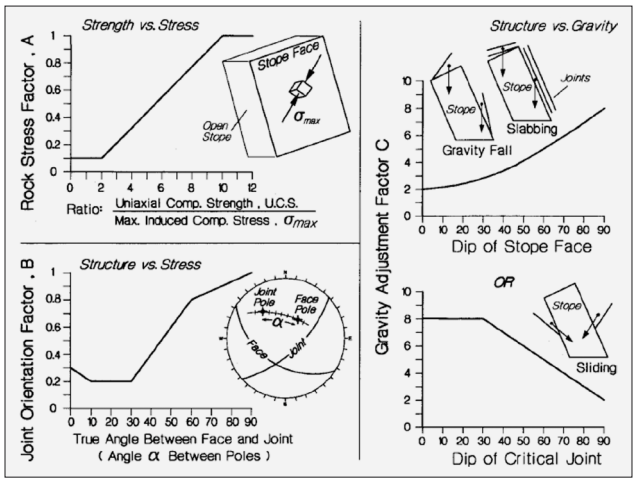


Figure 1. Factors A, B, and C by **Potvin (1988)**

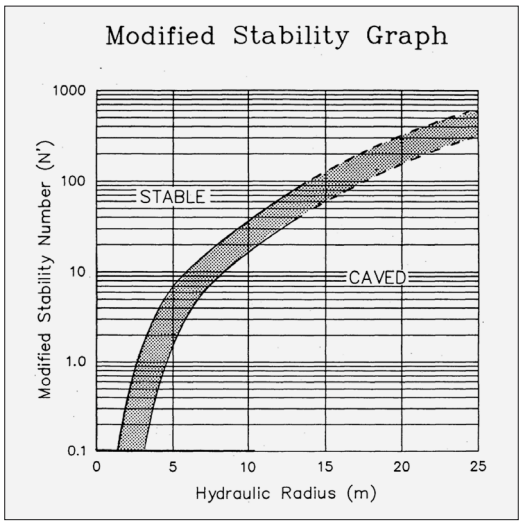


Figure 2. Modified stability graph by **Potvin (1988)**

work for assessing stope stability. This enables engineers to determine safe design dimensions for stope excavation.

2.2. Digitizing Graph Data

The linear approximation method will be used in this research to reconstruct several graphs from **Potvin (1988)** into mathematical functions. Most graphs were piecewise linear functions, making linear interpolation particularly suitable for accurately reproducing the trends without introducing artificial curvature. This method was chosen because the original datasets were only available as graphical plots, and linear interpolation offers simplicity, robustness, and low computational cost compared with higher-order polynomial or spline method, which can overfit local noise or produce unrealistic oscillations (**Press et al., 2007**). A sufficient number of points were sampled from each graph to ensure fidelity, and functions were constructed using **Equation 2** (**Salomon, 2006**). To determine the value of $f(x)$ using the interpolation method, find i such that $x_i \leq x \leq x_{i+1}$, then interpolate the value using **Equation 2**.

$$f(x) = f_i + \frac{x - x_i}{x_{i+1} - x_i}(f_{i+1} - f_i) \tag{2}$$

The accuracy of the digitization was evaluated using the Mean Absolute Error (MAE) for each function, summarized in **Table 2**. MAE values were below 0.5% in all cases, confirming that the reconstructed functions reliably represent the original graphs and are suitable for subsequent analysis. To further increase the accuracy of this method, additional sampling points can be incorporated, particularly in regions where the function changes rapidly (**Salomon, 2006**). Minor deviations may still occur due to image resolution or scaling effects.

Table 2. Number of Sampled Point and Mean Absolute Error (MAE)

Function	$f_N(HR)$	$f_A(SSR)$	$f_B(\alpha)$	$f_{Cj}(\alpha)$
Number of Sampled Point	8	10	6	200
Meam Absolute Error (MAE)	0.0%	0.0%	0.0%	0.4%

3. Stope Dimensions Optimization

As a mine can consist of dozens of stopes, with each stope containing dozens of possible dimensions, manually determining the stability of hundreds to thousands of possible stope dimensions is time-consuming (**Army & Karian, 2024**). To address this challenge, an algorithmic approach is implemented in this research**.** This process consists of several steps executed using Deswik, Python, and FLAC3D. The general workflow of the optimization process is illustrated in **Figure 3**.

The stope dimension optimization begins by discretizing a mineable stope boundary into individual slices, with the slice length corresponding to the minimum feasible blasting advanced. Each slice is first evaluated for stability, and unstable slices are excluded to prevent potential collapse during stopping (**Villaescusa, 2014**). Stable slices are then sequentially merged to progressively extend the stope geometry. After each merge, the stability of the resulting stope is assessed. If the stope remains stable, merging continues; if the addition of a slice induces instability, the merging process is terminated, and the last unstable slice is excluded. A new stope is subsequently initiated from the following slice. This merge–evaluate–terminate process is repeated until all the slices are assigned. Geometric discretization and modelling are performed in Deswik, iterative control is implemented in Python, and geomechanical parameters required for stability evaluation are derived from FLAC3D stress modelling. Details of the algorithm used in the optimization process are presented in **Section 3.1**,

while the stability assessment procedure is described in **Section 3.2**.

In this section, several terms and parameters were used; **Table 3** and **Figure 4** summarizes the notations and parameters that were used for the subsequent sections.

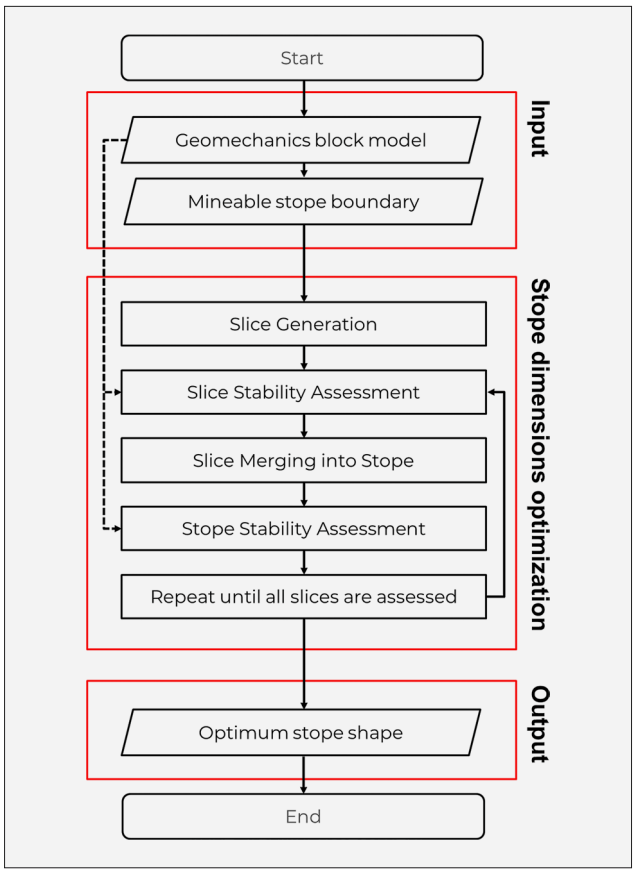


Figure 3. General workflow of the optimization process

3.1. Stope Shape Determination

Iterations will be conducted to determine the optimum stope shape. The objective of this optimization is to make the stope with the longest possible length, as described in **Equation 3**.

$$Objective\ function: Max(L_s) \tag{3}$$

Stope length is constrained by the stability of the stope, as a longer stope is more prone to instability. So, the optimum stope length must be verified as stable through a stability analysis, as described in **Equation 4**. The stope shape parameters, denoted as Shp_s comprise a numerical list representing the geometric and geotechnical attributes of the stope wall. The function f_{sta} serves as a binomial indicator of stope stability classification, where $f_{sta} = 1$ signifies the stope shape parameters resulted in stable stope, and $f_{sta} = 0$ mean stope shape parameters resulted in unstable stope. As previously outlined, the principal constraint in the optimization process is stope stability, necessitating that the resulting stope configuration satisfies $f_{sta}(shp_s) = 1$. Details about the stability analysis will be discussed in **Section 3.2**.

$$Constrain: f_{sta}(shp_s) = 1 \tag{4}$$

Based on the objective function and constraints, the pseudocode for the iteration is described in **Algorithm 1**. In the present algorithm, stability analysis is performed at each iteration to rigorously assess stope configurations. The computational complexity of this algorithm is O(N), where N represents the total number of stope slices, indicating a direct relationship between the process count and the number of slices evaluated. This systematic approach provides a robust framework for

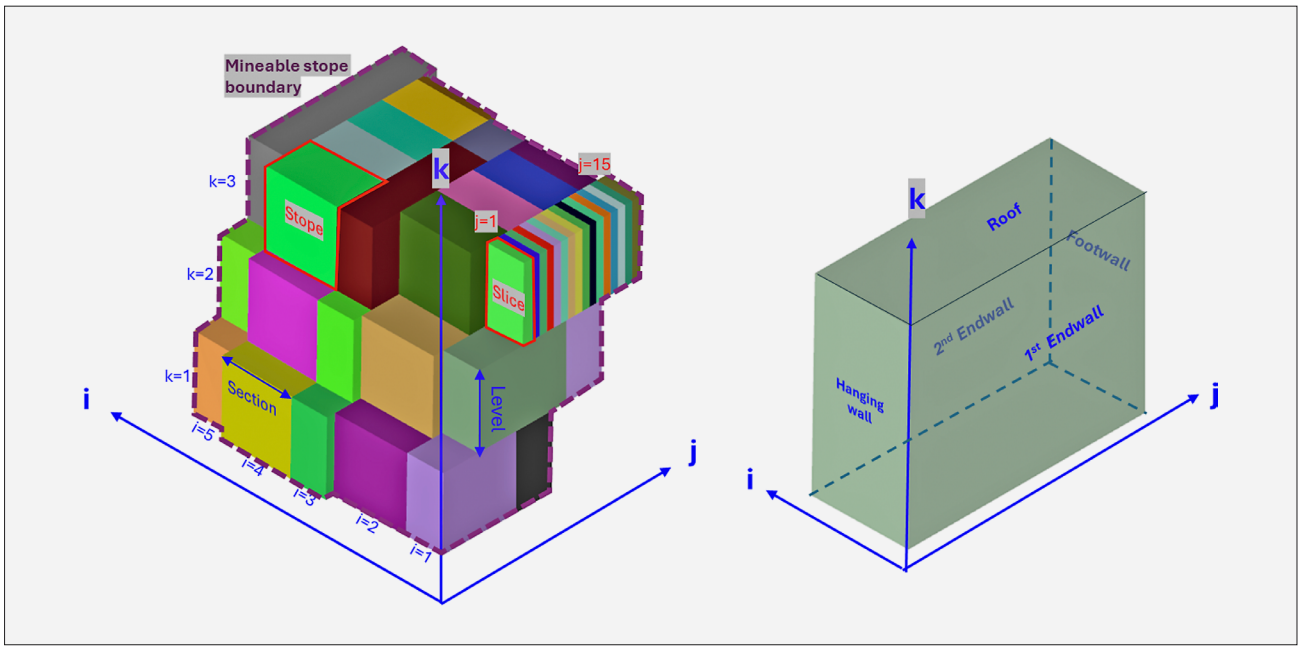


Figure 4. Notations and Parameters

Table 3. Notations and parameters

Symbol	Description
Notation	
x	Index of stope type. 1: Primary Stope 2: Secondary Stope
r	Index of block.
s	Index number of stope .
i	Index number of section.
j	Index number of Slice.
k	Index number of levels.
w	Index of stope wall. 0 : Hangingwall 1: Footwall 2 : Roof 3 : 1st End wall 4 : 2nd End wall
Parameters	
Sta_s	Stability of the stope s $[0,1]$. 1: $Stable\ stope\ shape$ 0: $Unstable\ stope\ shape$
sta_s^w	Stability of the wall w at stope s $[0,1]$. 1: $Stable\ stope\ wall$ 0: $Unstable\ stope\ wall$
shp_s	Shape of stope s.
$slice_{i,j,k}$	Shape of slice with index position of i,j,k
$st_{i,j,k}$	Stope number that belong to slice tag i,j,k. $st_{i,j,k} = -1$ mean slice won't be mined.
N_i	Number of section.
N_j	Number of slice.
N_k	Number of level.
Q_r	Q' value in block.
UCS_r	UCS in block.
Si_r	Induced stress in block.
Dd_r	Domain of discontinue orientation in block.
m_r^w	Proportion of the block influenced the stope wall *w*. $0 \le m_r^w \le 1$.
Wo_s^w	Norm vector of wall orientation of Stope *s* in wall *w*.
Wp_s^w	Perimeter of Stope *s* in wall *w*.
Wa_s^w	Area of Stope *s* in wall *w*.
Q_s^w	Q' value of Stope *s* in wall *w*.
UCS_s^w	UCS of Stope *s* in wall *w*.
Si_s^w	Induced stress of Stope *s* in wall *w*.
Dd_s^w	Domain of discontinue orientation of Stope *s* in wall *w*.
$\boldsymbol{Dd_{s,jo}^w}$	Normal vector of *jo*th discontinue of Stope *s* in wall *w*.
A_s^w	Factor A value of Stope *s* in wall *w*.
B_s^w	Factor B value of Stope *s* in wall *w*.
C_s^w	Factor C value of Stope *s* in wall *w*.
N_s^w	N value of Stope *s* in wall *w*.

optimizing stope geometry while upholding structural stability throughout the evaluation process.

The proposed algorithm can be classified as a heuristic, constructive iterative algorithm designed to optimize stope geometry under explicit stability constraints. It operates by progressively merging stope slices and performing stability checks at each step, halting expansion once instability is detected. This rule-based process emphasizes computational efficiency and practical feasibility rather than exhaustive exploration of all possible configurations and therefore does not guarantee a globally optimal solution. Instead, it produces a locally optimal configuration that is inherently dependent on the sequence in which slices are evaluated. Due to the absence of backtracking, enumeration, or global search strategies, the algorithm is best described as greedy-like and heuristic, making it particularly suitable for practical applications in large scale mining scenarios where speed, simplicity, and reliable stability verification are prioritized over theoretical global optimality.

Algorithm 1: Stope Shape Iteration	
$s \leftarrow 1$	Initiation of stope number
$shp_s \leftarrow [\ \ ]$	Initiation of stope shape with blank shape
$for\ i = 1\ to\ N_i$	
$for\ k = 1\ to\ N_k$	
$for\ j = 1\ to\ N_j$	
$shp_s \leftarrow merge\,(\,shp_s, slice_{i,j,k})$	Merge the stope slice
$if\ f_{sta}(shp_s) = 1$	If stope shape stable
$st_{i,j,k} \leftarrow s$	Assign stope number s to slice tags i,j,k
$else$	
$shp_s \leftarrow slice_{i,j,k}$	
$s \leftarrow s + 1$	
$if\ f_{sta}(shp_s) = 1$	If slice stable
$st_{i,j,k} \leftarrow s$	Assign stope number s to slice tags i,j,k
$else$	
$st_{i,j,k} \leftarrow -1$	Assign -1 (unmined) to slice tags i,j,k
$shp_s \leftarrow [\ \ ]$	
$s \leftarrow s + 1$	
$shp_s \leftarrow [\ \ ]$	
$s \leftarrow s + 1$	

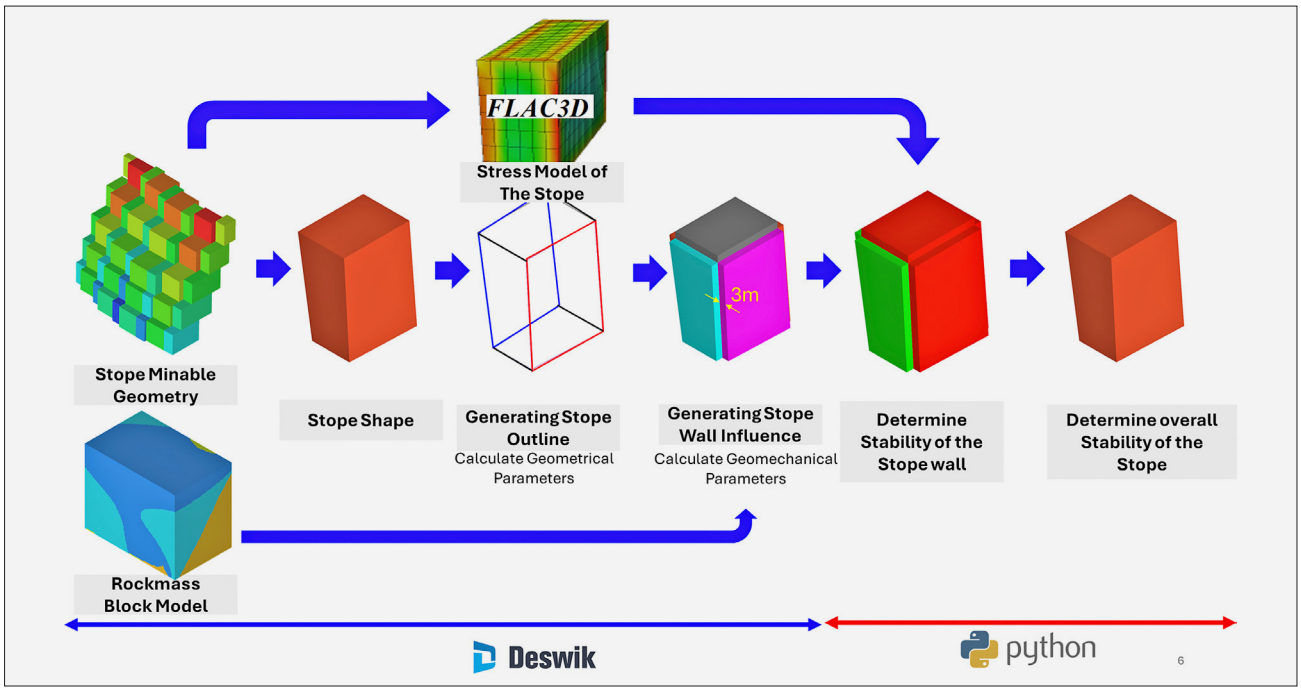


Figure 5. Stope shape stability workflow

3.2. Stability Evaluation

Based on the generated stope shape (Shp_s), several parameters will be generated to evaluate the stability of the stope. To determine these parameters, the outline of each stope wall will be generated to determine wall orientation, perimeter, and area. To define the representative rock mass properties for each stope wall, an n-meter boundary extension from the stope wall was applied, corresponding to the expected overbreak depth. Since the resulting stope is expected to be stable, the overbreak is anticipated to be less than 3 m (classified as large overbreak) based on **McFadyen et al. (2024)**. Therefore, the default value of n will be set to 3 m. This value remains consistent with the case study used in this research, considering the influence of stope geometry, stress conditions, and rock mass quality (**Cepuritis et al., 2007; Villaescusa, 2014**).

Subsequently, using the modelled stress of the stope, the wall orientation, and the rock mass properties of the stope wall, the N' value for each slice wall will be determined. This value is then used to evaluate the stability of each stope wall. The algorithm's general workflow is presented in the **Figure 5**, and the details of the stability evaluation will be discussed in this section.

As mentioned before, the stability of the stope is the function of several parameters, as described in **Equation 5**.

$$sta_s = f_{sta}(shp_s) = \\ = f_{sta}(Wo_s^w, Wp_s^w, Wa_s^w, Q_s^w, UCS_s^w, Si_s^w, Dd_s^w) \quad (5)$$

Wo_s^w, Wp_s^w, Wa_s^w are the geometrical parameters of the stope wall and the other parameter is the geotechnical parameters of the stope wall. The geotechnical parameters were generated from the block models and stress models using **Equations 6-9**.

$$Q_s^w = \frac{\sum Q_r \times tr \times m_r^w}{\sum tr \times m_r^w} \quad (6)$$

$$UCS_s^w = \frac{\sum UCS_r \times tr \times m_r^w}{\sum tr \times m_r^w} \quad (7)$$

$$Si_s^w = \frac{\sum Si_r \times tr \times m_r^w}{\sum tr \times m_r^w} \quad (8)$$

$$\boldsymbol{Dd_s^w} = \left\{ a \in \boldsymbol{Dd_r^w} \;\middle|\; \frac{\sum_{\boldsymbol{Dd_r^w}=a} tr \times m_r^w}{\sum tr \times m_r^w} > 0.1 \right\} \quad (9)$$

Given that $f_N(HR)$ is the function of stable boundary of minimum N' value for each HR from **Potvin (1988)** digitized graph. So, the stope wall stability can be determined using **Equations 10-12**.

$$N_s^w = Q_s^w \times A_s^w \times B_s^w \times C_s^w \quad (10)$$

$$HR_s^w = \frac{Wa_s^w}{Wp_s^w} \quad (11)$$

$$sta_s^w = \begin{cases} 1, & N_s^w \geq f_N(HR_s^w) \\ 0, & N_s^w < f_N(HR_s^w) \end{cases} \quad (12)$$

Equation 13 is then used to assess the stability of the stope.

$$sta_s = \begin{cases} sta_s^0 \times sta_s^1 \times sta_s^2 \times sta_s^3 \times sta_s^4, \ j = 1 \ and \ x = 1 \\ sta_s^1 \times sta_s^2 \times sta_s^3 \times sta_s^4, \ j > 1 \ and \ x = 1 \\ sta_s^0 \times sta_s^1 \times sta_s^2, \ j = 1 \ and \ x = 2 \\ sta_s^1 \times sta_s^2, \ j > 1 \ and \ x = 2 \end{cases} \quad (13)$$

3.3. Factor A determination

Given that $f_A\left(\frac{UCS}{\sigma_{max}}\right)$ is the function of Rock Stress factor **from Potvin (1988)** digitized graph, so the Factor A can be determined using **Equation 14**.

$$A_s^w = f_A\left(\frac{UCS_s^w}{Si_s^w}\right) \quad (14)$$

3.4. Factor B determination

Given that:

- $f_B(\alpha)$ is the function of the joint orientation factor from **Potvin (1988)** digitized graph
- $Dd_{s,jo}^w$ is the the norm vector of joint jo

So, Factor B can be determined using **Equations 15-16**.

$$\alpha_{s,jo}^w = cos^{-1}\left(\frac{\boldsymbol{Wo}_s^w \cdot \boldsymbol{Dd}_{s,jo}^w}{\| \boldsymbol{Wo}_s^w \| \| \boldsymbol{Dd}_{s,jo}^w \|}\right) \quad (15)$$

$$B_s^w = min\left(f_B\left(\alpha_{s,jo}^w\right) \forall \, jo \in \{0,1,2,3, \dots\}\right) \quad (16)$$

3.5. Factor C determination

Given that:

- $f_{Cs}(\alpha)$ is the function of the gravity adjustment factor of Stope face from **Potvin (1988).**
- $f_{Cj}(\alpha)$ is the function of the gravity adjustment factor of critical joint from **Potvin (1988)** digitized graph
- $\boldsymbol{Vo} = [\mathbf{0}, \mathbf{0}, \mathbf{1}]$ is the vector of vertical plane orientation.

So, Factor C can be determined using **Equations 17-22**.

$$f_{Cs}(\alpha) = 8 - 7 \times \cos(\alpha) \quad (17)$$

$$\alpha s_s^w = cos^{-1}\left(\frac{\boldsymbol{Wo}_s^w \cdot \boldsymbol{Vo}}{\| \boldsymbol{Wo}_s^w \| \| \boldsymbol{Vo} \|}\right) \quad (18)$$

$$\alpha j_{s,jo}^w = cos^{-1}\left(\frac{\boldsymbol{Vo} \cdot \boldsymbol{Dd}_{s,jo}^w}{\| \boldsymbol{Vo} \| \| \boldsymbol{Dd}_{s,jo}^w \|}\right) \quad (19)$$

$$Cs_s^w = f_{Cs}(\alpha s_s^w) \quad (20)$$

$$Cj_s^w = min\left(f_{Cj}\left(\alpha j_{s,jo}^w\right) \ \forall \, jo \in \{0,1,2,3, \dots\}, \ \alpha_{s,jo}^w < 30^0\right) \quad (21)$$

$$C_s^w = Q \, min(\{Cs_s^w, Cj_s^w\}) \quad (22)$$

4. Results

4.1. Geotechnical Data

This research utilizes a case study from a copper mine to demonstrate the proposed method. This case study was chosen because it highlights the importance of optimizing stope dimensions in areas where high productivity is required despite relatively poor ground conditions. Several geotechnical parameters were simplified and stored in the block model. The maximum dimensions of a regular block model are 10m × 10m, with parameter values estimated from drill hole data and laboratory test results. The geotechnical parameters considered in this study include:

- Geotechnical Domain
- Uniaxial Compressive Strength (UCS) (MPa)
- Q' Value
- Major Joint Orientation

The major joint orientation parameters are represented as integers that correspond to specific joint set codes. For example, joint set 1 represents a joint set with an orientation of 220°/45° NE. **Figure 6** illustrates the section view of the block model.

The copper deposit is hosted within a vein geotechnical domain, with 15 to 80 meters of apparent thickness. The vein generally trends about N 50° E and dips between 60° and 80°. The footwall belongs to a marble geotechnical domain, while the hanging wall consists of a diorite geotechnical domain.

The planned stopes are distributed across five levels, with 20 meters of vertical spacing between each level. The surface elevation is approximately 595 meters above sea level, placing the depths of the stope between 395 meters and 295 meters of elevation.

The geotechnical condition is relatively complex, with high variability in rock mass strength as summarized in **Table 4**. This variability results in significant differences in stope stability conditions, leading to a wide range of optimal stope dimensions.

4.2. Mining Method and Stope Sequence

The mining method used in this study is transverse longhole stoping with a primary and secondary stope sequence. This method is typically applied to ore bodies that are tabular and either vertical or steeply dipping. It is most effective when both the ore and the surrounding waste rock have fair to good rock quality (**SME, 2011**).

In this method, the stope design consists of two types of stopes: primary stopes and secondary stopes. The primary stopes are mined first and then backfilled with cemented backfill, serving as pillars when the secondary stopes are later mined, as presented in the **Figure 7**. Different sizes of primary and secondary stopes are applied in this study, and their dimensions are presented in **Table 5**.

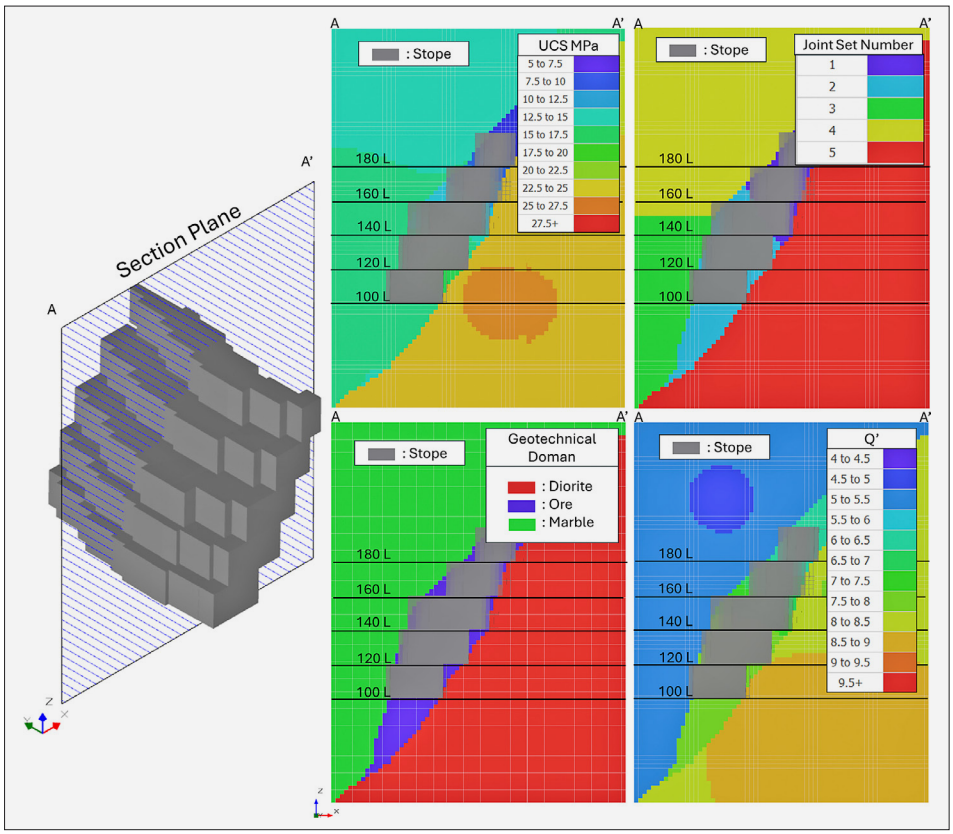


Figure 6. Block model of geotechnical data

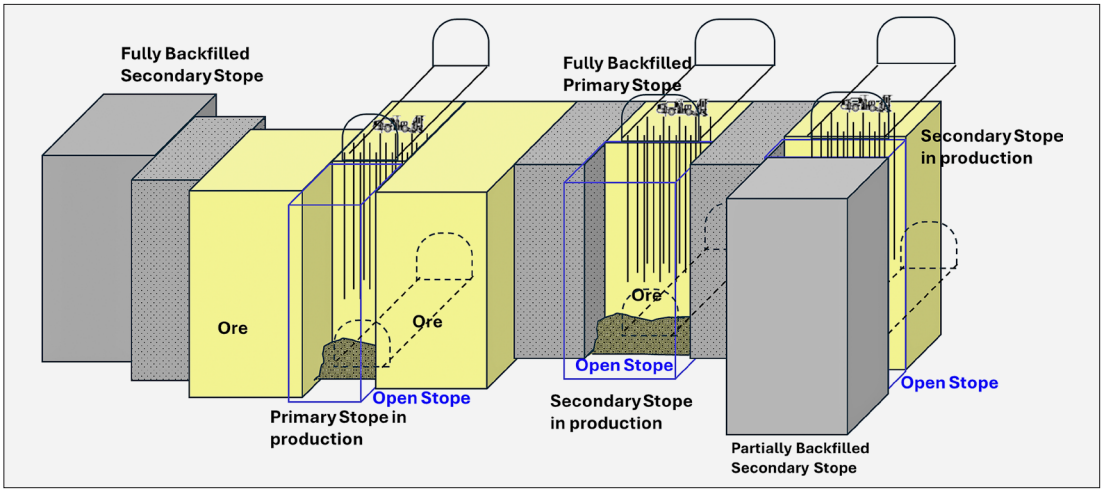


Figure 7: Mining method

Table 4. Summary of the rock mass properties

Parameters	Symbol	Minimum	Maksimum
UCS (MPa)	UCS_r	5.1	28.5
Q'	Q_r	4.4	9.2
Rock Domain	Rd_r	{Diorite, Ore, Marble}	
Joint Set Domain	Dd_r	{1,2,3,4,5}	

Table 5. Stope dimension

Stope	Width (m)	Height (m)
Primary	10	20
Secondary	20	20

This method was selected because the ore body thickness exceeds 60 meters, necessitating an efficient, large-scale mining approach. A partial backfill stope approach is implemented in certain areas where the ore body is too thick to be mined in a single stope sequence. In these cases, the stope is divided into multiple sections, and each section must be backfilled before mining the next section.

The stope sequence follows an overhand stoping sequence, meaning that a stope can only be mined once the stope below it has already been mined and backfilled. Additionally, a primary-secondary stoping dependency is enforced, where a secondary stope can only be mined

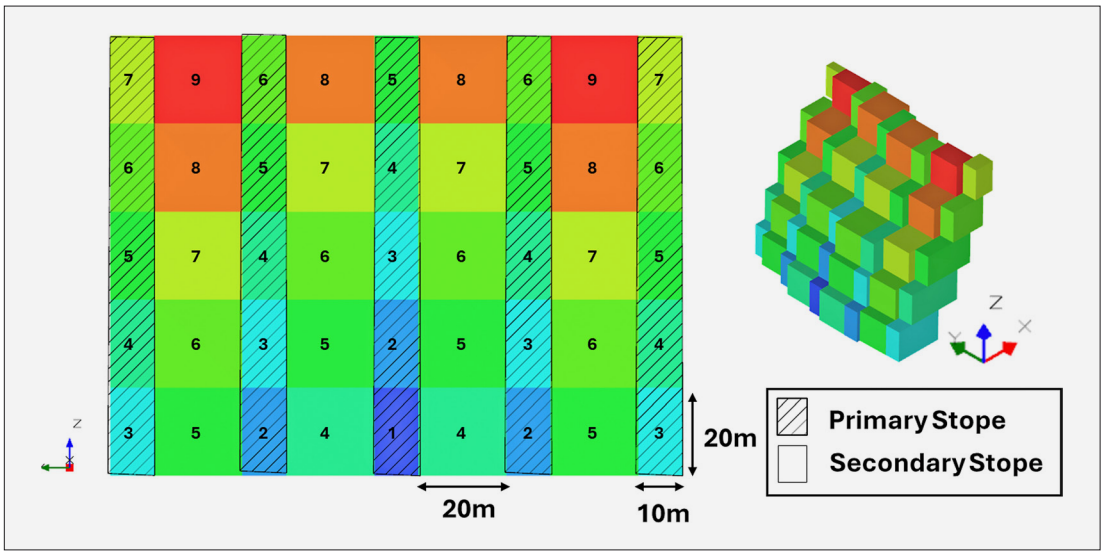


Figure 8. Stopping sequence

Table 6. Material properties of the model

Property	Granodiorite (Footwall)	Marble (Hanging wall)	Ore body	Cemented tailings (Backfill)
Unit weight (kN//m³)	28	28	30	22.1
Uniaxial Compressive Strength (MPa)	23	17	15	3.5
Tensile Strength (MPa)	1.0	0.8	1.7	0.5
Cohesion (MPa)	6.0	2.1	4.3	0.65
Internal Friction angle (°)	43	40	41	35
Young's Modulus (MPa)	7800	18600	39000	1000
Poisson's Ratio	0.16	0.26	0.31	0.30

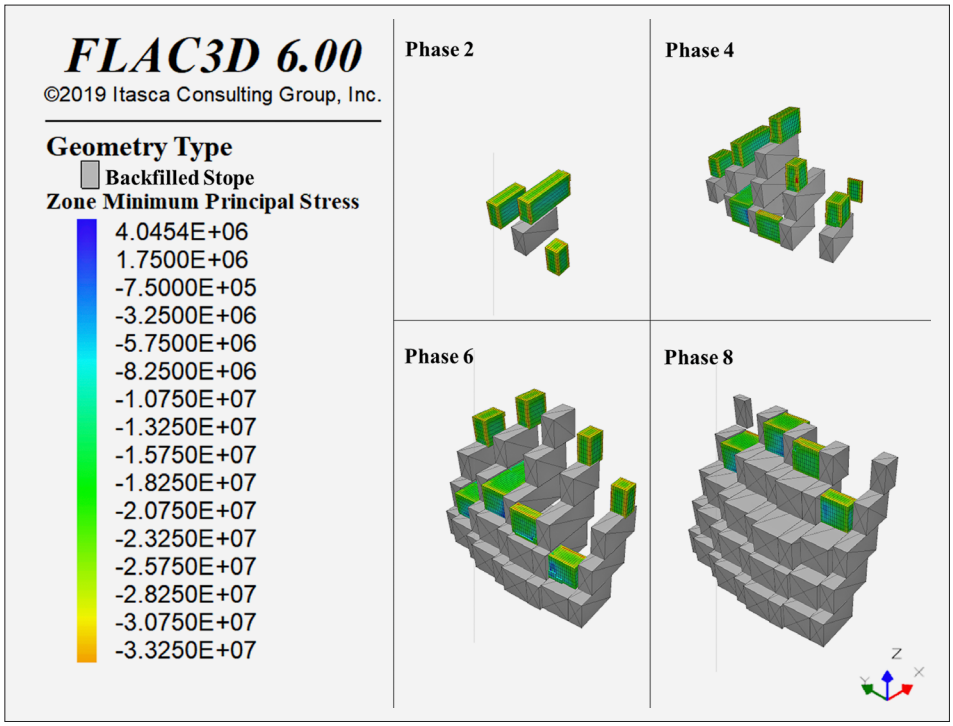


Figure 9. Stress model result

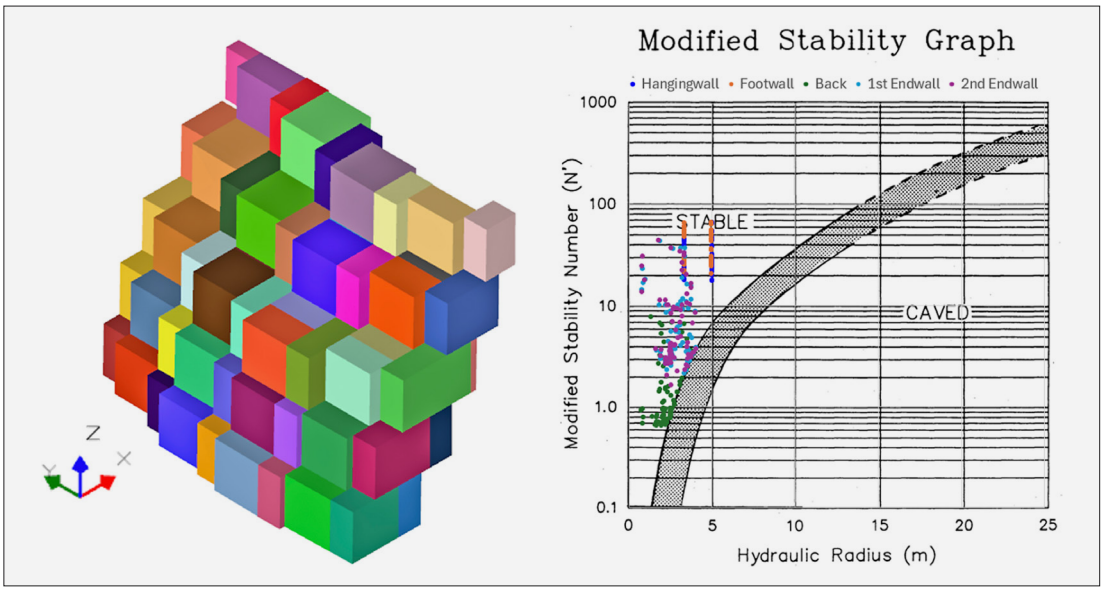


Figure 10. Final stope geometry (left) and Stability analysis (Right)

after the primary stopes in the three levels above have been mined and backfilled. The stope sequence used in this case study is illustrated in **Figure 8**. The sequence is divided into nine phases, with each phase required to be mined in the specified order.

4.3. Stress Model Result

To capture the stress changes during the stope extraction and backfilling process, stress modelling was performed using FLAC3D. The analysis was based on the representative properties of the rock mass and backfill materials. The material properties applied in the stress modelling are summarized in **Table 6**.

The modelling was performed in eight phases, following the stope mining and backfilling sequence. The maximum and minimum principal stress on each stope wall was then queried. These stress values were subsequently used to represent the stress component in the N' stability number analysis. An example of stress results from several phases is shown in **Figure 9**.

4.4. Stope Final Result

The analysis shows that the optimized stope design produced a total of 83 individual stopes, consisting of 51 secondary stopes and 32 primary stopes, shown in **Figure 10**. The stability analysis results show that all walls of each stope were in a stable condition. Several stope walls also reached their critical hydraulic radius.

The computation of the stope final results required approximately 32 minutes for the algorithm to complete the entire process, corresponding to an average of 3.1 seconds per stope slice. This computation time is deemed feasible for implementation in larger and more complex mining scenarios. The analysis was conducted on a personal computer equipped with an AMD Ryzen 9 270 (8-core) processor, an NVIDIA GeForce RTX 5080 GPU, and 16 GB of GDDR7 memory. Notably, the algorithm's running time may vary depending on the mine's complexity, the number of generated stope slices, and the device specifications.

5. Discussion

5.1. Stope Dimension Sensitivity Analysis

As described in **Section 4.1**, the geotechnical conditions are relatively complex, with high variability in rock mass strength. This variability leads to significant differences in stope stability, resulting in a wide range of optimal stope dimensions. To investigate the relationship between rock mass variability and stope geometry, a sensitivity analysis is presented in this section.

The sensitivity analysis was conducted using the calculated N' values for each stope wall orientation, as shown in **Figure 11**. The results indicate that N' values ranged from 0.5 to 90, reflecting the wide variability in potential stope dimensions. **Figure 11** further presents the percentage of samples that resulted in unstable stopes at different stope lengths. The analysis shows that stope lengths should be limited to less than 8 m to ensure that 90% of stopes remain stable. Applying a uniform stope length across all stopes would lead to higher costs and reduced production efficiency. These findings highlight the necessity of further optimization that accounts for the spatial distribution of rock mass strength, allowing stope lengths to vary according to local geotechnical conditions.

5.2. Stope Geometry Analysis

Based on the **Figure 12**, the majority of the secondary stopes have reached their maximum dimension at the

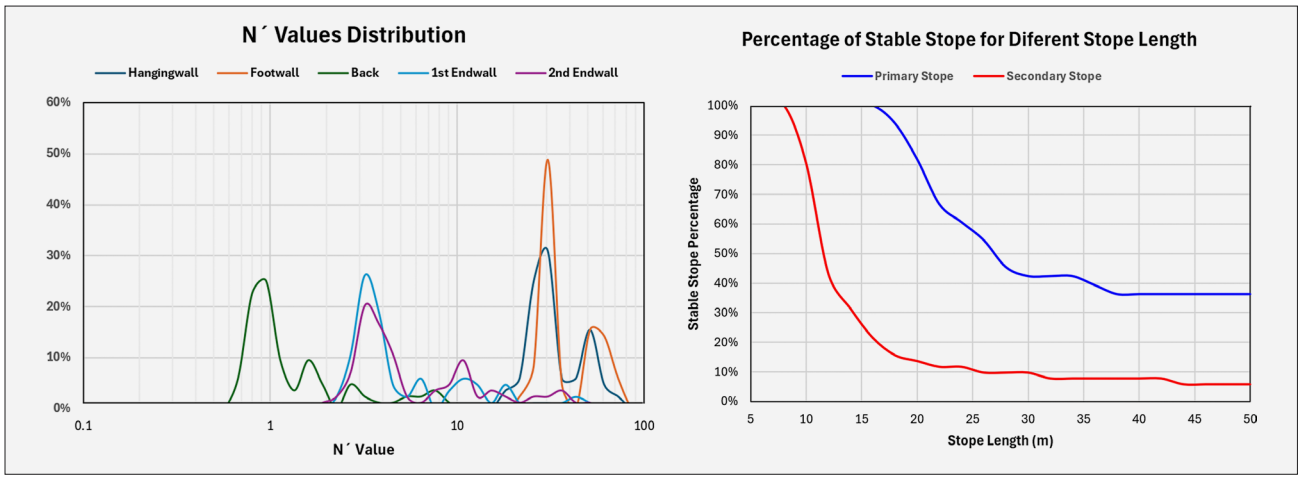


Figure 11. N' Values Distribution (left) and Percentage of Stabel Stope (right)

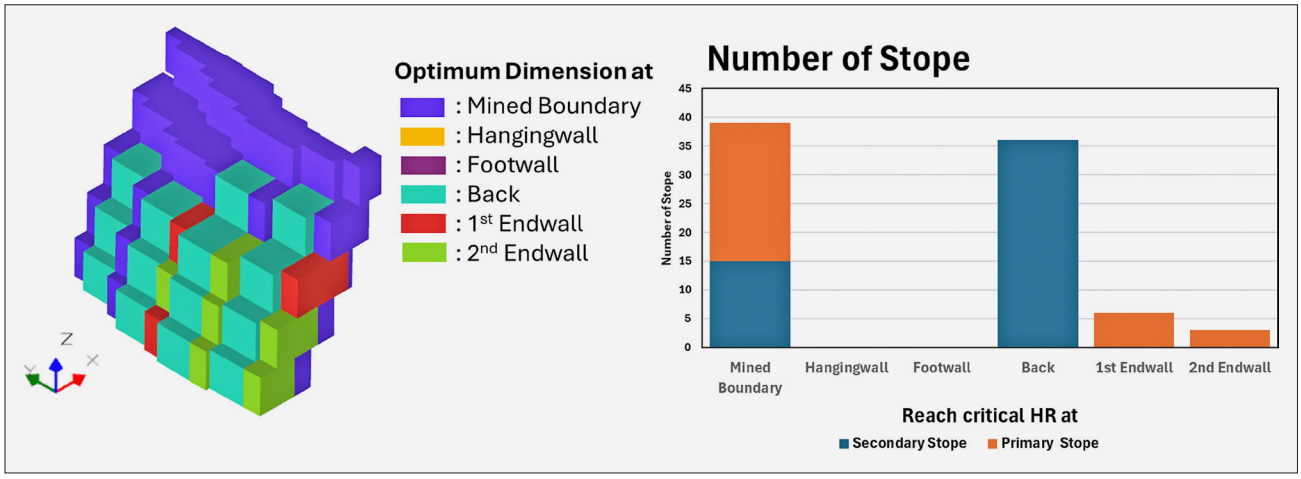


Figure 12. Critical wall of stope

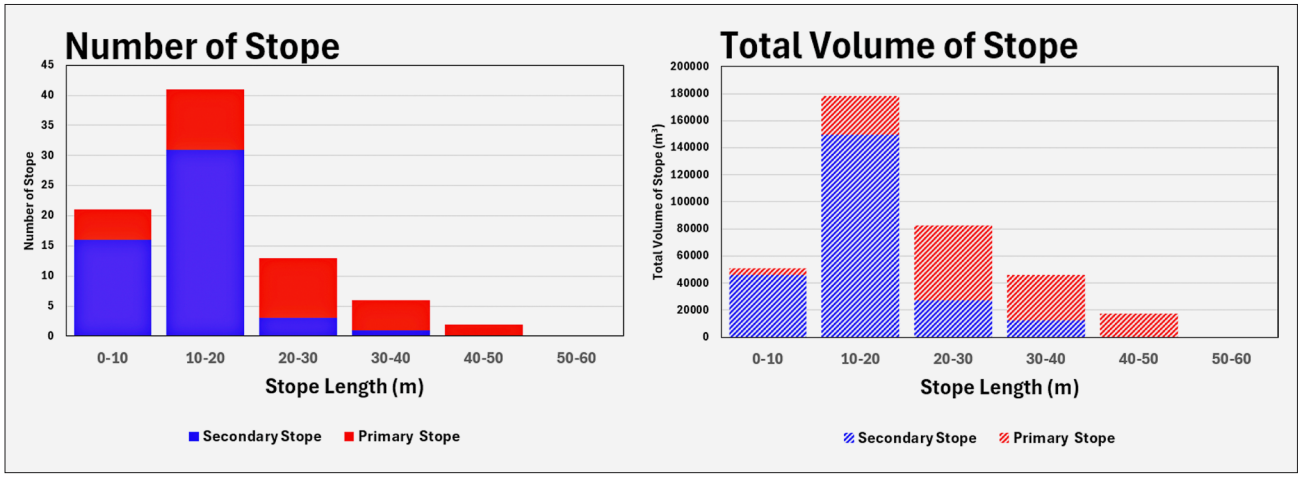


Figure 13. Distribution of Stope length

back. Meanwhile, for the primary stopes, most have reached their maximum dimension due to the mined boundary. The results also show that no stope has reached its maximum dimension at the hanging wall or footwall.

Figure 13 shows that several stopes (13% of the total volume) have a total length of less than 10 meters. Based on this result, further analysis can be conducted to evaluate the economic feasibility of these short stopes. Min-

ing small stopes can be uneconomical due to increased mining costs (**Samanta et al., 2024**).

5.3. Result Comparison

To further evaluate the effectiveness of the proposed optimization approach, a series of simulations were conducted in comparison with conventional stope design methods. These simulations incorporated varying stope length scenarios as dictated by standard design practices. The outcomes of this comparative analysis are summarized in **Table 7**, which details the performance metrics of both the conventional and optimization-based methodologies.

Table 7. Stope stability result

Method	Number of Stope	Unstable Stope
Stope produced by optimization	83	0 (0%)
Stope with regular 10m length	123	17 (14%)
Stope with regular 20m length	62	25 (40%)
Stope with regular 20m length of Primary Stope and 10m length of Secondary Stope	90	18 (20%)

The results show that the new method produces a more stable stope geometry while requiring fewer stopes. In contrast, the conventional methods, which applies a uniform stope length, results in either a more number of stopes or the presence of unstable stopes. The distribution of the unstable stopes is shown in **Figure 14**. **Figure 15** shows that most unstable face walls in regular stope scenarios occur at the back and endwall. In contrast, stopes designed using the optimization method have more adaptable HR based on the N' value, enhancing stope stability.

Stope instability frequently leads to overbreak of stope walls (**Villaescusa, 2014**), resulting in higher mining costs due to increased ore dilution. Consequently, unstable stopes are typically associated with greater dilution percentages. The empirical relationship between the hydraulic radius (HR), the modified stability number (N'), and the anticipated stope dilution is presented in **Equation 23** (**Roux, 2017**).

$$Stope\ dilution = \begin{cases} 0.6305\ln(HR) - 0.9575, & N' < 4 \\ 0.5090\ln(HR) - 0.8596, & 4 \le N' < 11 \\ 0.4144\ln(HR) - 0.4673, & 11 \le N' < 21 \\ 0.6357\ln(HR) - 1.1934, & N' \ge 21 \end{cases} \quad (23)$$

Although longer stopes are generally more susceptible to instability and increased dilution, their use can significantly reduce overall stoping costs and streamline the mining sequence. By employing longer stopes, the total number of individual stopes is minimized, which in turn lowers the requirements for slot raises and filling barricade constructions. This approach not only optimizes operational efficiency but also leads to more cost-effective production. The cost parameters utilized to compare the conventional and optimization methods are presented in **Table 8**, providing a comprehensive assessment of total stope production costs for each approach.

Table 8. Stope cost parameters

Parameters	Value	Unit
Mining cost	35.8	$/Ton
Stope slot raise and filling barricade cost (Stope Fix Cost)	43,314	$/Stope

Empirical dilution, as presented in **Equation 23** and supported by the cost parameters in **Table 8**, was utilized to calculate the expected total stope production cost for both conventional and optimization methods. **Table 9** offers a direct comparison of ore tonnage, dilution tonnage, and total stope production costs between these approaches. The results indicate that smaller stopes with a regular length of 10 meters more effectively control dilution compared to other stope dimensions, albeit at the

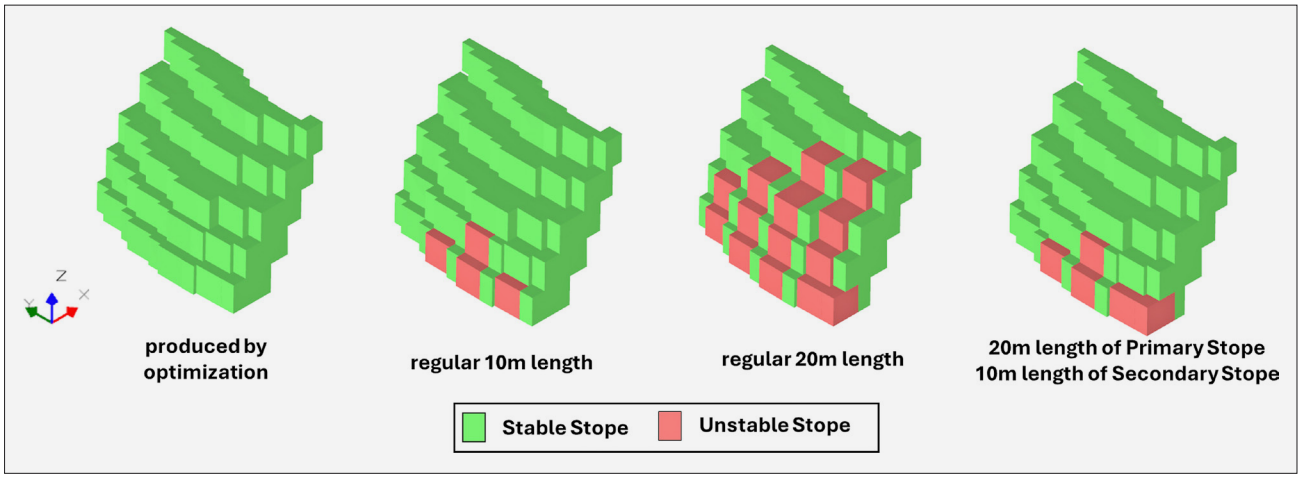


Figure 14. Distribution of Unstable Stopes

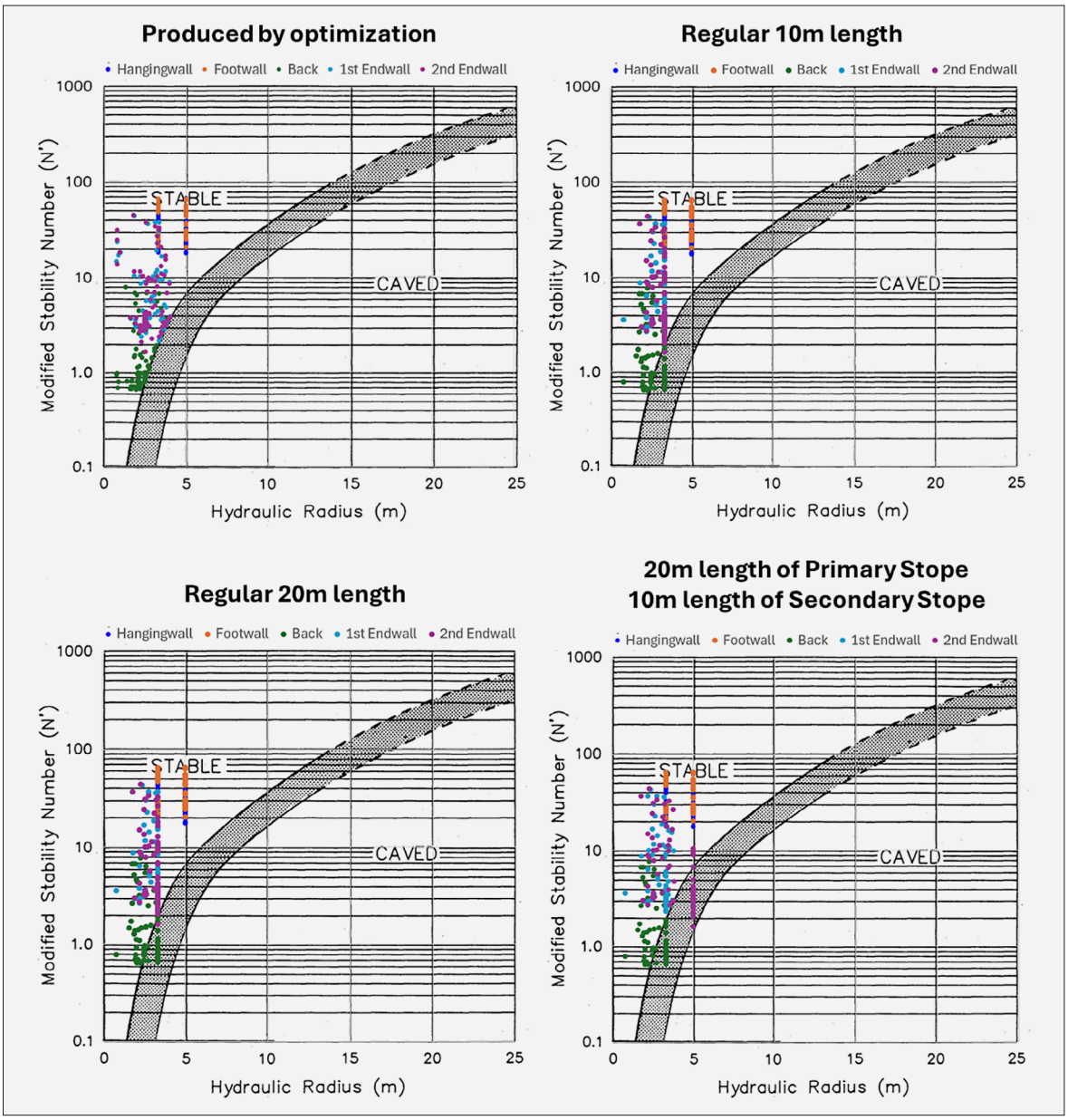


Figure 15. Stope stability analysis

Table 9. Stope dilution and production cost result

Method	Ore Tonnage	Dilution Tonnage	Average Dilution	Total Tonnage	Number of Stope	Total Stope Production Cost ($)
Stope produced by optimization	956,046	35,554	3.7%	991,600	83	39,094,326
Stope with regular 10m length	956,046	30,510	3.2%	986,556	123	40,646,328
Stope with regular 20m length	956,046	116,413	12.2%	1,072,459	62	41,079,495
Stope with regular 20m length of Primary Stope and 10m length of Secondary Stope	956,046	94,911	9.9%	1,050,956	90	41,522,490

expense of an increased number of separate stopes. Conversely, stopes configured with a 20-meter regular length exhibit the highest percentage of expected dilution, yet result in the smallest number of stopes overall. Notably, stopes produced through the optimization method demonstrate a balanced outcome in terms of dilution percentage and number of stopes. The optimized stope shapes yield the lowest total production cost, with a reduction of approximately 1.6 to 2.4 million dollars relative to the conventional method. This finding supports

the conclusion that the optimization method produces more cost-efficient stope configurations.

Stope production cost calculations, as reflected in **Table 9**, primarily account for production aspects; however, they often overlook the broader implications arising from unstable stopes. In practice, stope collapse can lead to increased expenses due to necessary rehabilitation, loss of ore reserves, and potential delays in production. Furthermore, the safety risks associated with such collapses are considerable, as they may result in equipment damage or, in extreme cases, serious injury and even fatalities. These consequences underscore the critical importance of ensuring stope stability, a goal that can be effectively achieved through optimization method. Indeed, the application of optimized stope design not only mitigates geotechnical and safety risks but may also deliver greater economic benefits than those indicated solely by the value presented in **Table 9**.

6. Conclusions

The new method shown in this research provides a more cost-efficient and adaptable approach to stope stability analysis compared to conventional method. By using an iteration on the stope dimension and conducting detailed stability assessments on each stope wall, this method allows for a more accurate evaluation of geotechnical conditions and the determination of optimized stope dimensions. Comparative analysis reveals that the proposed approach effectively reduces the total number of stopes while maintaining geotechnical stability. In contrast, traditional methods employing uniform stope lengths are prone to producing a significant proportion of unstable stopes; specifically, findings indicate that between 14% and 40% of stopes generated by conventional techniques exhibit instability. Conversely, the optimization method consistently yields stopes that satisfy stability criteria.

Furthermore, the comparative analysis underscores the ability of the optimization method to achieve an effective balance between dilution control and operational efficiency. While smaller, uniformly dimensioned stopes (e.g. 10 m length) exhibit superior dilution performance, they substantially increase the total number of stopes, thereby elevating overall production costs. In contrast, larger uniform stopes (e.g. 20 m length) minimize the number of the stopes but incur the highest dilution percentages, resulting in significant cost escalation due to increased handling of waste material. The optimized stope configurations generated by the proposed method deliver a more favourable outcome by achieving the lowest total production cost, with estimated savings of approximately USD 1.6–2.4 million compared to conventional approaches. These findings confirm that the optimization method not only enhances geotechnical stability but also provides a demonstrable economic advantage.

While the demonstrated optimization method exhibits clear advantages over conventional approaches, it is important to note that the optimization in this study was restricted to stope length. Future research can consider a comprehensive three-dimensional optimization framework that incorporates stope width and stope height, as such an approach may offer enhanced utility and further improvements in stope stability and cost efficiency.

Acknowledgement

The authors sincerely acknowledge DESWIK for granting access to their mining software, which was essential for carrying out this research.

Funding

This research was funded by Institut Teknologi Bandung through the Program Penelitian, Pengabdian Masyarakat dan Inovasi ITB.

Competing Interests

The authors have no conflicts of interest to disclose.

7. References

Adoko, A. C. (2025). Discussion on “Refined Approaches for Open Stope Stability Analysis in Mining Environments: Hybrid SVM Model with Multi optimization Strategies and GP Technique” Rock Mech Rock Eng (2024). *Rock Mechanics and Rock Engineering*. https://doi.org/10.1007/s00603-024-04348-w

Amedjoe, C. G., & Agyeman, J. (2015). Assessment of effective factors in performance of an open stope using cavity monitoring system data: A case study. *Journal of Geology and Mining Research*, *7*(3), 19–30. https://doi.org/10.5897/JGMR2014.0216

Army, M., & Karian, T. (2024). Stope Dimension Analysis Based on Geomechanical Properties Using Brute Force Algorithm. *IOP Conference Series: Earth and Environmental Science*, *1437*(1), 12032. https://doi.org/10.1088/1755-1315/1437/1/012032

Cakrabuana, W., Sadisun, I. A., Tohari, A., Dinata, I. A., Martireni, A. P., Mahmud, H. Z., & Atmojo, H. T. (2024). Andesite Slope Stability Analysis Using Rock Mass Rating (RMR) and Slope Mass Rating (SMR) in Gunung Batu and Graha Puspa Areas, West Bandung Regency, West Java, Indonesia. *Rudarsko-Geološko-Naftni Zbornik*, *39*(4), 137–151. https://doi.org/10.17794/rgn.2024.4.11

Cepuritis, P. M., Villaescusa, E., & Lachenicht, R. (2007). Back analysis and performance of Block A long hole open stopes – Kanowna Belle Gold Mine. In E. Eberhardt, D. Stead, & T. Morrison (Eds.), *Rock Mechanics: Meeting Society’s Challenges and Demands* (pp. 1431–1439). Taylor & Francis.

Chen, Q., Gan, Q., Wang, H., & Liu, C. (2024). A New Combined Mining Method: The Stope Limit Length Calculation of Considering Bulk Support Boundary. *Rock Me-*

chanics and Rock Engineering, *57*(9), 6909–6925. https://doi.org/10.1007/s00603-024-03865-y

Clark, L. M. (1998). *Minimizing dilution in open stope mining with a focus on stope design and narrow vein longhole blasting*. https://open.library.ubc.ca/collections/831/items/1.0081111

Cui, X., Yang, S., Zhang, N., & Zhang, J. (2024). Optimization of stope structure parameters by combining Mathews stability chart method with numerical analysis in Halazi iron mine. *Heliyon*, *10*(4). https://doi.org/10.1016/j.heliyon.2024.e26045

Salomon, D. (2006). Linear Interpolation. In D. Salomon (Ed.), *Curves and Surfaces for Computer Graphics* (pp. 49–69). Springer New York. https://doi.org/10.1007/0-387-28452-4_2

Diederichs, M. S., & Kaiser, P. K. (1996). Rock instability and risk analyses in open stope mine design. *Canadian Geotechnical Journal*, *33*(3), 431–439. https://doi.org/10.1139/t96-064

Dolatshahi, A., & Molladavoodi, H. (2024). Prediction of Rock Tensile Fracture Toughness: Hybrid ANN-WOA Model Approach. *Rudarsko-Geološko-Naftni Zbornik*, *39*(3), 1–12. https://doi.org/10.17794/rgn.2024.3.1

Guo, Y., & Miao, Y. (2022). Study on stope stability in continuous mining of long-dip, thin orebody by room–pillar method. *Sustainability*, *14*(15), 9601.

Heidarzadeh, S., Saeidi, A., & Rouleau, A. (2019). Evaluation of the effect of geometrical parameters on stope probability of failure in the open stoping method using numerical modeling. *International Journal of Mining Science and Technology*, *29*(3), 399–408. https://doi.org/10.1016/j.ijmst.2018.05.011

Heidarzadeh, S., Saeidi, A., & Rouleau, A. (2020). Use of probabilistic numerical modeling to evaluate the effect of geomechanical parameter variability on the probability of open-stope failure: a case Study of the Niobec Mine, Quebec (Canada). *Rock Mechanics and Rock Engineering*, *53*(3), 1411–1431.

Kang, Q., Wang, Y., Zhang, S., Pu, C., & Zhang, C. (2021). Prediction of Stope Stability Using Variable Weight and Unascertained Measurement Technique. *Geofluids*, *2021*(1), 8821168. https://doi.org/10.1155/2021/8821168

Li, C., Liu, G., Guo, L., Zheng, D., & Yuan, X. (2024). A New CRITIC-GRA Model for Stope Dimension Optimization Considering Open Stoping Stability, Mining Capacity and Costs. *Applied Sciences*, *14*(12). https://doi.org/10.3390/app14125249

Mathews, K. E., Hoek, E., Wyllie, D. C., & Stewart, S. B. V. (1980). Prediction of stable excavations for mining at depths below 1000 metres in hard rock. *Canmet Report*, *802*, 1571.

McFadyen, B., Grenon, M., Woodward, K., & Potvin, Y. (2024). Optimising stope design through economic and geotechnic assessments of predictions made at a meter scale resolution using the sites' reconciled data. *International Journal of Rock Mechanics and Mining Sciences*, *178*, 105778. https://doi.org/10.1016/j.ijrmms.2024.105778

Nhleko, A. S., & Musingwini, C. (2022). Optimisation of Three-Dimensional Stope Layouts Using a Dual Interchange Algorithm for Improved Value Creation. *Minerals*, *12*(5). https://doi.org/10.3390/min12050501

O'Hara, T. A., & Suboleski, S. C. (1992). Chapter 6:3: Costs and Cost Estimation. In H. L. Hartman (Ed.), *SME Mining Engineering Handbook* (2nd ed., Vol. 1, pp. 405–424). Society for Mining, Metallurgy, and Exploration (SME).

Patanwar, Y. K., Mohanto, S., & Deb, D. (2025). Stability Analysis of Deep Underground Stopes with Transverse Method of Extraction Using 3-Dimensional Numerical Modelling Technique. In A. K. Gorai, S. Ram, R. M. Bishwal, & S. Bhowmik (Eds.), *Sustainable and Innovative Mining Practices* (pp. 427–441). Springer Nature Switzerland.

Phaisopha, S., Shimada, H., Sasaoka, T., Hamanaka, A., Pongpanya, P., Shorin, S., & Senthavisouk, K. (2023). A Stope Mining Design with Consideration of Hanging Wall When Transitioning from Open Pit Mining to Underground Mining for Sepon Gold Mine Deposit, Laos. *Mining*, *3*(3), 463–482. https://doi.org/10.3390/mining3030027

Potvin, Y. (1988). *Empirical open stope design in Canada* [University of British Columbia]. https://doi.org/10.14288/1.0081130

Press, W. H., Teukolsky, S. A., Vetterling, W. T., & Flannery, B. P. (2007). *Numerical Recipes: The Art of Scientific Computing* (3rd ed.). Cambridge University Press.

Putra, D., Karian, T., Sulistianto, B., & Heriawan, M. N. (2024). Integrating Mathews Stability Chart into the Stope Layout Determination Algorithm. *Mining, Metallurgy & Exploration*, *41*(3), 1351–1364. https://doi.org/10.1007/s42461-024-00993-5

Rinne, M., Janiszewski, M., Pontow, S., Uotinen, L., Kiuru, R., Kangas, L., Laine, I., & Leveinen, J. (2024). Improvements in Rock Mass Description for Stope Design by Geophysical and Geochemical Methods. *Applied Sciences*, *14*(3). https://doi.org/10.3390/app14030957

Roux, P. J. (2017). Value creation in a mine operating with open stoping mining methods. *Journal of the Southern African Institute of Mining and Metallurgy*, *117*, 133–142. https://doi.org/10.17159/2411-9717/2017/v117n2a4

Sabao, A. R., Munemo, P., & Kolapo, P. (2022). Investigating the causes of stope instability at Golden Valley Mine. *Journal of Sustainable Mining*, *21*(2), 128–140.

Samanta, G., Sinha, S., & Dey, T. (2024). A Case Study on Economic Impact Assessment of Developing Single Drill Level in Sublevel Stoping Method. *Journal of The Institution of Engineers (India): Series D*, *105*(1), 119–125. https://doi.org/10.1007/s40033-023-00453-2

SME. (2011). *SME Mining Engineering Handbook, Third Edition* (D. Peter, Ed.). Society for Mining, Metallurgy, and Exploration.

Stephenson, R. M., & Sandy, M. P. (2013). Optimising stope design and ground support – a case study. In Y. Potvin & B. Brady (Eds.), *Ground Support 2013: Proceedings of the Seventh International Symposium on Ground Support in Mining and Underground Construction* (pp. 387–400). Australian Centre for Geomechanics.

Sugianti, K., & Tohari, A. (2023). The Impact of Geological and Rainfall Characteristics on Slope Stability Analysis in

Shallow Landslide Modelling using the TRIGRS Model. *Rudarsko-Geološko-Naftni Zbornik*, *38*(4), 147–166. https://doi.org/10.17794/rgn.2023.4.12

Villaescusa, E. (2014). *Geotechnical Design for Sublevel Open Stoping*. https://doi.org/10.1201/b16702

Zadhesh, J., & Majdi, A. (2022). Estimation of Rock Joint Trace Length Using Support Vector Machine (SVM). *Rudarsko-Geološko-Naftni Zbornik*, *37*(3), 55–64. https://doi.org/10.17794/rgn.2022.3.5

Zhang, Q., Huang, M., & Guo, J. (2024a). A Simulation Analysis of the Stability of Tall and Collapse-Prone Stopes: A Case Study of the Dongguashan Copper Mine. *Applied Sciences*, *14*(22). https://doi.org/10.3390/app142210608

Zhao, X., & Zhou, X. (2023). Design Method and Application of Stope Structure Parameters in Deep Metal Mines Based on an Improved Stability Graph. *Minerals*, *13*(1). https://doi.org/10.3390/min13010002

Zhou, X., Zhao, X., Qu, Q., & Shi, J. (2023). Stope Structural Parameters Design towards Green and Deep Mining: A Review. *Processes*, *11*(11). https://doi.org/10.3390/pr11113125

Zulfahmi, Z., Sarah, D., Novico, F., & Susilo, R. B. (2023). Assessment of Rock Slope Stability in a Humid Tropical Region: Case Study of a Coal Mine in South Kalimantan, Indonesia. *Rudarsko-Geološko-Naftni Zbornik*, *38*(2), 109–125. https://doi.org/10.17794/rgn.2023.2.8

SAŽETAK

Optimizacija dimenzija komora u geotehnički složenome rudniku primjenom automatizirane analize stabilnosti

Stabilnost komora i stupova jedan je od ključnih čimbenika u podzemnoj eksploataciji mineralnih sirovina pomoću komorno-stupne metode jer izravno utječe na sigurnost, produktivnost i ukupnu ekonomsku učinkovitost proizvodnje. Tradicionalne metode projektiranja komora često se temelje na uniformnim dimenzijama, pri čemu se zanemaruje geotehnička varijabilnost ležišta, što povećava rizik od pojave nestabilnosti ili neoptimalnih dimenzija komora i stupova. U ovome radu predlaže se pristup automatizirane analize stabilnosti koji iterativno procjenjuje različite varijante dimenzioniranja komora na temelju modificiranoga koeficijenta stabilnosti (N') s ciljem određivanja optimalne stabilne konfiguracije. Provođenjem detaljnih analiza stabilnosti za svaki zid komore i međustup, metoda omogućuje znatno precizniju procjenu stvarnih geotehničkih uvjeta u usporedbi s konvencionalnim metodama uniformnih dimenzija. Studija slučaja pokazala je da predloženi pristup omogućuje smanjenje ukupnoga broja komora uz održavanje potrebne razine stabilnosti za razliku od klasičnih metoda kod kojih 14 – 40 % komora pokazuje znakove nestabilnosti. Nadalje, optimizacija omogućuje postizanje povoljnoga kompromisa između kontrole razrjeđenja i operativne učinkovitosti, što rezultira nižim troškovima eksploatacije po komori. Optimizirane konfiguracije ostvarile su najniži ukupni trošak proizvodnje uz procijenjene uštede od približno 1,6 – 2,4 milijuna USD u odnosu na konvencionalne projekte. Dobiveni rezultati potvrđuju da okvir optimizacije ne samo da poboljšava geotehničku stabilnost komorno-stupnoga sustava, već donosi i znatne ekonomske prednosti naglašavajući važnost uvažavanja geotehničke varijabilnosti u projektiranju komora i stupova.

Ključne riječi:
stabilnost komora, komorno-stupna metoda, modificirani faktor stabilnosti N', optimizacija dimenzija komora, automatizirana analiza

Author's contribution

Mohammad Army (MS Scholar): Conceptualization, writing – review and editing, software, visualization, and project administration. **Tri Karian** (PhD, Lecturer): validation, methodology, formal analysis, writing – review and editing. **Firly Rachmaditya Baskoro** (PhD, Lecturer)**, Takashi Sasaoka** (PhD, Lecturer) and **Akihiro Hamanaka** (PhD, Lecturer): resources, writing – review and editing, validation, supervision, and funding acquisition. **Budi Sulistianto** (PhD, Lecturer) and **Hideki Shimada** (PhD, Lecturer): validation, resources, supervision, writing – review and editing.
All authors have read and agreed to the published version of the manuscript.

RGNZ/MGPB

Feasibility analysis of granitic rocks for use in the dimension stone industry

Rudarsko-geološko-naftni zbornik
(The Mining-Geology-Petroleum Engineering Bulletin)
DOI: 10.17794/rgn.2026.2.4

Original scientific paper

CC BY

Ekin Köken[1]*
[1] *Materials Science and Nanotechnology Engineering Department, Abdullah Gül University, 38100, Kayseri, Türkiye.*

Abstract
This study presents two objective evaluation tools for assessing the feasibility of granitic rocks in dimension stone applications. The developed methods integrate fundamental physical and mechanical properties, including dry density (ρ_d), effective porosity (n_e), P-wave velocity (V_p), uniaxial compressive strength (UCS), and Böhme abrasion value (BAV). Feasibility analyses based on the conditional formatting (CF) and ranking method RM reveal that the adopted input parameters are essential for determining the suitability of granitic rocks as dimension stones. The strong relationship between the CF and RM results highlights their consistency and broad applicability. Both methods exhibit good agreement with the recommendations of the American standard for granitic rocks. Consequently, the suggested methods provide practical guidance for selecting suitable rock exposures in field studies, also offering a time- and energy-efficient decision-making framework for the dimension stone industry. To comprehensively evaluate the strengths and limitations of the proposed approaches, it is recommended that these tools be applied to a wider range of dimension stone types and geological settings.

Keywords:
granitic rocks, dimension stones, rock feasibility, conditional formatting, ranking method

1. Introduction

Dimension stones have been environmentally friendly construction and building materials for centuries due to their durability and aesthetic properties. They play a significant role in preserving historical and cultural considerations in several ways, linked to geographical diversity, architectural traditions, and cultural significance (**Cassar et al., 2014**; **Pereira, 2023**). Additionally, the appropriate use of dimension stones contributes to both regional and global economies (**Stone, 2015**). In this context, high-quality dimension stones are highly preferred in most engineering projects for several reasons. For example, dimension stones like granite and basalt often exhibit higher durability and strength properties compared to many other construction and building materials, such as wood, tile, and standard concrete mixtures.

The relative quality of dimension stones is primarily associated with physical and mechanical rock properties such as water absorption by weight (w_a), dry density (ρ_d), flexural strength (FS), uniaxial compressive strength (UCS), and Böhme abrasion value (BAV) (**Çobanoğlu et al., 2015; Bellopede et al., 2015; Strzałkowski et al., 2020; Amirkiyaei et al., 2021; Ahmed et al., 2021; Briševac et al., 2023; Çelik et al., 2025**). These properties provide a solid basis for assessing the durability of dimension stones. In some cases, geometric quality is also essential for obtaining desirable rock blocks in dimension stone manufacturing (**Hazrathosseini and Mahdevari**, **2019**). Dimension stones can be specified for particular areas based on previous experiences and some national and international specifications. For example, American standards (**ASTM 615-03 2004; ASTM 503-08a 2008**) for dimension stones specify certain technical requirements based on different rock lithologies (see **Table 1**). On the other hand, European standards do not define any requirements for dimension stones based on various physical and mechanical rock properties. They would rather define some testing methods to evaluate the quality of dimension stones.

In this context, **Strzałkowski et al. (2023)** put forward some evaluation criteria for assessing natural stone products based on some European standards (see **Table 2**). Additionally, dimension stones also have dimensional standards for various applications. Some dimensional standards for granitic dimension stones are given in **Table 3**. Apart from these standards, impact resistance is another crucial mechanical property in dimension stones, such as granite, marble, limestone, and sandstone, which are cut to specific sizes for use in construction and decoration.

* Corresponding author: Ekin Köken
e-mail address: ekin.koken@agu.edu.tr
Received: 18 August 2025 Accepted: 1 October 2025.
Available online: 13 March 2026

Table 1. American standards for marble and granite dimension stones

Rock type	Dry density, ρ_d (g/cm^3)	Water absorption by weight (w_a, %)	Uniaxial compressive strength, UCS (MPa)	Flexural strength, FS (MPa)	Standard
Granite	≥ 2.56	≤ 0.40	≥ 131	≥ 8.27	**ASTM 615-03 (2004)**
Marble	≥ 2.59 (limestone) ≥ 2.80 (Dolomite)	≤ 0.20	≥ 52	≥ 7.00	**ASTM 503-08a (2008)**

Table 2. Quantitative classification for dimension stones (**Strzałkowski et al., 2023**)

Criterion I ρ_d (g/cm^3)	Criterion II n_e (%)	Criterion III BAV (cm^3/50cm^2)	Criterion IV UCS (MPa)	Criterion V FS (MPa)	Classification
< 1.5	> 16.0	> 55	< 15	< 4	Very low
1.5 – 1.8	11.0 – 16.0	40 – 55	15 – 50	4 – 8	Low
1.8 – 2.2	6.0 – 11.0	25 – 40	50 – 120	8 – 12	Moderate
2.2 – 2.6	1.0 – 6.0	10 – 25	120 – 200	12 – 16	High
> 2.6	< 1.0	< 10	> 200	> 16	Very high

Explanations: ρ_d: Dry density, n_e: effective porosity, BAV: Böhme abrasion value, UCS: Uniaxial compressive strength, FS: Flexural strength

Table 3. Nominal thickness of dimension stones offered by major authorities (**ASTM C1528, 2008**)

Thickness (mm)	Application
10	Floor tile thickness
20	Interior cladding, interior flooring, or furniture applications
30/32	Minimum thickness suitable for most exterior applications
40/50	Applicable to exterior cladding for standard panels
80	Applicable to exterior cladding for large panels
100	Appropriate thickness for landscape purposes (curbs, coping, steps or foundations)
150/200	Appropriate thickness for cubic materials.

It describes the ability of a natural stone to absorb sudden shocks or loads without fracturing (**Sariisik, 2012; Sariisik et al., 2016**). In the British standards (BS EN 1467 2005; BS EN 1469 2006), the impact resistance of natural stones (≥ 6 MPa) has been emphasised to measure their relative quality.

Tables 1–3 provide a solid basis for quantifying the quality of dimension stones and identifying potential usage areas based on their dimensions. However, it is worth reminding that while a rock type may meet one quantitative specification, such as w_a, it may fall short of others like UCS and BAV. Under these circumstances, additional laboratory studies or objective decision-making tools are required to determine whether related rock types should be further investigated for their potential use in the industry. Engineering judgment for material selection should be based on the feasibility assessments that consider the determination of physical and mechanical rock properties. Therefore, additional laboratory tests or objective quantitative approaches help stakeholders make informed decisions.

Multi-decision evaluation tools can save time and energy, ensuring the efficient use of natural resources. Moreover, they play a crucial role in environmental protection by guiding decisions on the further utilization of specific rock types (**Esmaeilzadeh et al., 2025**).

Essentially, due to various constraints or a lack of opportunities, it may not always be feasible to conduct detailed laboratory tests to assess rock suitability, particularly in field studies. In cases of limited quantitative data, objective evaluation methods can offer valuable insights into rock feasibility. Based on the above description, this study proposes two quantitative approaches to evaluate the feasibility of dimension stones. As a case study, granitic rocks are adopted since they are among the most desirable rock lithologies, together with basalt and marble, in the dimension stone industry. A comprehensive literature survey is conducted to collect quantitative data on granitic rocks. Then, several assessment criteria are adopted to thoroughly investigate the suitability of granitic rocks for use as dimension stones. In the last part, the findings obtained from the two methods are compared.

2. Materials and methods

2.1. Data gathering

Previous research articles in rock mechanics and engineering geology have been reviewed to gather quantitative data on granitic rocks. As a result of this survey, 134 granitic rock samples were considered. It is worth

Table 4. Collected data for granitic rocks

Country	ρ_d (g/cm³)	n_e (%)	V_p (km/s)	UCS (MPa)	BAV (cm³/50cm²)	n	Reference
Portugal	NR	0.51 – 6.15	2.32 – 4.78	38.92 – 159.8	NR	8	Vasconcelos et al. (2008)
China	2.77	0.66	NR	135.73	NR	1	Tan et al. (2011)
Turkey	2.60 – 2.64	0.32 – 0.43	NR	155.9 – 168.0	4 – 4.7	2	Ersoy et al. (2005)
Turkey	NR	NR	4.05 – 5.35	94.0 – 141.5	NR	12	Er and Tuğrul (2016)
China	2.54	0.33	3.66	159.42	NR	1	Xu et al. (2021)
India	2.62	0.12	5.49	68.08	NR	1	Gautam et al. (2018)
Turkey	2.61 – 2.67	0.6 – 1.09	NR	111.77 – 155.98	NR	3	Karaca et al. (2012a)
Turkey	2.63	0.54	5.53	155.33	6.83	1	Çobanoğlu and Çelik (2017)
Iran	2.54 – 2.85	0.84 – 3.26	NR	97.2 – 152.2	NR	14	Farhadian et al. (2021)
Turkey	2.57 – 2.75	0.27 – 1.21	NR	NR	10.08 – 21.42	13	Teymen (2024)
Turkey	2.72	1.03	NR	131.44	4.34	1	Karaca et al. (2010)
Turkey	2.56 – 2.76	0.12 – 0.70	NR	118.53– 181.41	3.05 – 5.17	4	Karaca et al. (2012b)
Sweden	2.74	NR	NR	227	NR	1	Nicksiar and Martin (2012)
Malaysia	2.05 – 2.76	NR	2.70 – 8.55	15.0 – 204.9	NR	46	Armaghani et al. (2015)
Saudi Arabia	NR	0.16 – 2.05	4.11 – 5.21	156 - 198	2.25 – 10.2	26	Alsaiari and El Aal (2021)
NR: Not reported.					Total	134	

Table 5. Statistical descriptions of the variables involved in the analyses

Variable	n	Mean	St. Dev	Minimum	First quartile, Q_1	Third quartile, Q_3	Maximum
ρ_d (g/cm³)	88	2.626	0.107	2.05	2.59	2.67	2.85
n_e (%)	75	1.181	0.871	0.115	0.668	1.50	6.15
V_p (km/s)	95	4.848	1.017	2.32	4.32	5.37	8.55
UCS (MPa)	121	127.53	45.494	15.00	96.60	164.00	227.00
BAV (cm³/50cm²)	47	8.103	3.707	2.25	5.25	10.26	21.420

Explanations: ρ_d: Dry density, n_e: Effective porosity, UCS: Uniaxial compressive strength, V_p: Pulse wave velocity, BAV: Böhme abrasion value, n: number of datasets

noting that the number of datasets (n) for adopted studies varies. This variation may arise from factors such as data availability, the focus of previous studies, and the specific parameters measured. The collected data are presented in **Table 4**, and descriptive statistics derived from this data are listed in **Table 5**. The dataset has been used to evaluate the feasibility of granitic rocks for their potential application as dimension stones.

2.2. Development of assessment criteria

Several standards and technical recommendations are considered in this study to develop quality classifications. Accordingly, seven different quality classification systems (Class I – VII) are reviewed (see **Table 6**) for dimension stones. Class I and II are based on the n_e of rocks. Classes III and V are based on the UCS of rocks. The ρ_d is adopted only in Class IV. The V_p and BAV are other essential parameters for Class VI and VII, respectively.

Focusing on these quality classifications, five different evaluation criteria (EC1–EC5) are defined (see **Table 7**). The technical parameters and corresponding threshold values are crucial in determining whether granitic rock types are suitable for further investigation.

2.3. Data analysis methods

2.3.1. Conditional Formatting (CF)

CF is a practical feature in spreadsheet software such as Microsoft Excel or Google Sheets that allows users to for-

Table 6. Assessment criteria adopted in this study

Quality classification I		**Quality classification II**	
Parameter	**Moos and Quervain (1948)**	Parameter	**Strzałkowski et al. (2023)**
n_e (%)	Identification	n_e (%)	Identification
< 1*	Very low porosity	< 1*	Very high quality
1 – 2.5	Low porosity	1 – 6	High quality
2.5 – 5	Moderate porosity	6 – 11	Moderate quality
5 – 10	High porosity	11 – 16	Low quality
10 – 20	Very high porosity	> 16	Very low quality
> 20	Extremely high porosity		
Quality classification III		**Quality classification IV**	
Parameter	**ASTM C615-03 (2004)**	Parameter	**ASTM C615-03 (2004)**
UCS (MPa)	Identification	ρ_d (g/cm^3)	Identification
≥ 131	Appropriate for use as dimension stone	≥ 2.56*	Appropriate for use as dimension stone
Quality classification V		**Quality classification VI**	
Parameter	**Strzałkowski et al. (2023)**	Parameter	**Anon (1979)**
UCS (MPa)	Identification	V_p (km/s)	Identification
< 15	Very low quality	< 2.5	Very low quality
15 – 50	Low quality	Low quality	Low quality
50 – 120	Moderate quality	3.5 – 4.0	Moderate quality
120* – 200	High quality	4.5* – 5.0	High quality
> 200	Very high quality	> 5.0	Very high quality
Quality classification VII		Note: *The thresholds (e.g. 120 MPa for assessment criteria V) are utilized to evaluate the suitability of granitic rocks for dimension stone applications.	
Parameter	**Strzałkowski et al (2023)**		
BAV (cm^3/50 cm^2)	Identification		
< 10*	Very high quality		
10 – 25	High quality		
25 – 40	Moderate quality		
40 – 55	Low quality		
> 55	Very low quality		

Table 7. Evaluation criteria adopted in CF analyses

Evaluation criterion	**Adopted quality classification**	**Threshold value**
EC1	I, II	$n_e \leq 1\%$
EC2	V	UCS ≥ 120 MPa
EC3	IV	$\rho_d \geq 2.56$ g/cm^3
EC4	VI	$V_p \geq 4.5$ km/s
EC5	VII	BAV ≤ 10 cm^3/50 cm^2

mat, classify, and redesign cells based on specific conditions or criteria. Although CF has been primarily adopted in the social sciences (**Abramovich and Sugden, 2004; Sugden et al., 2015**), it can also be applied in various engineering disciplines. In this study, CF is implemented in the Microsoft Excel environment to assess the feasibility of using granitic rocks as dimension stones. In the context of CF analyses, several if-then rules and countable commands (e.g. COUNTA) are used in conjunction.

Before running the CF methodology, if–then rules should be identified based on the ECs in **Table 7**. Then, three steps are defined to run CF in the Microsoft Excel environment. First, all cells that are to be analysed should be selected (Step 1). Next, the conditional formatting button should be activated to manage the rules (Step 2).

Finally, the output should be formatted to consider the font and shades that can make it more visible (Step 3). These steps are also illustrated in **Figure 1**.

After performing the CF, each evaluation criterion (EC1–EC5) is divided into two categories as a result: "suitable" and "unsuitable". When assessing the feasibility of granitic rocks for their use as dimension stones, the sum of rows indicating the definition of "suitable" is considered. By implementing the "COUNTA" command in Microsoft Excel, the sum of rows indicating the definition of "suitable" and the results counted by the COUNTA command are compared. If this ratio (number of suitable cases/cases counted by COUNTA) is higher than 0.65, then the investigated granitic rock can be further investigated (continue to investigate: CTI). Otherwise, further investigation may be abandoned (FIMA) for the specific rock type being investigated.

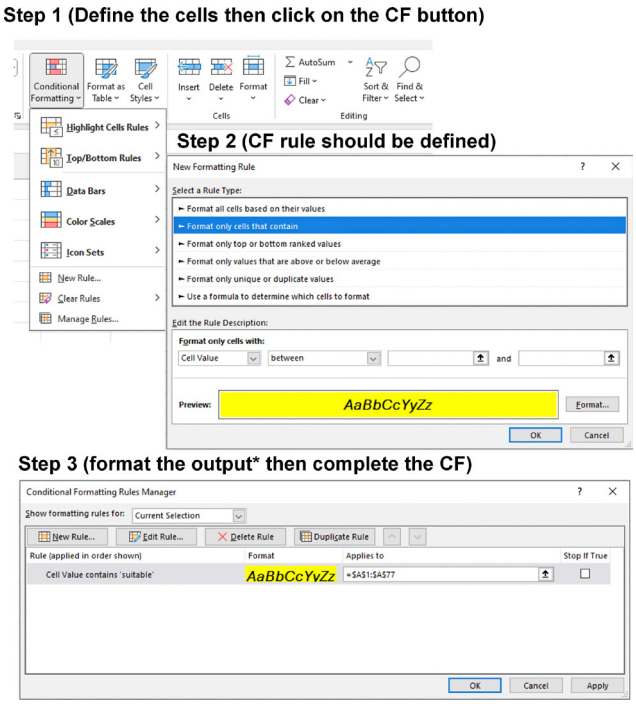


Figure 1. Steps for running the CF feature in Microsoft Excel

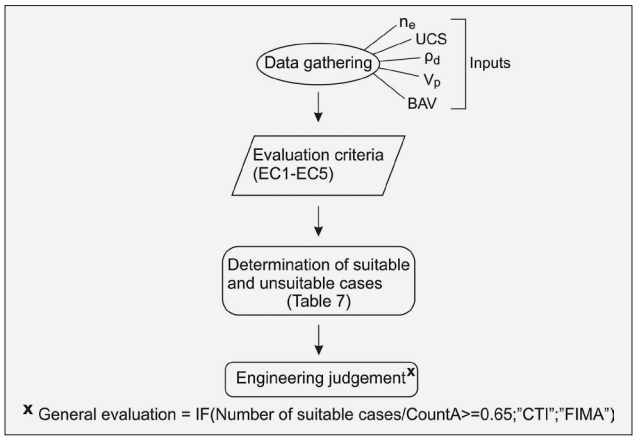


Figure 2. Flowchart of the CF process. (CTI: Continue to investigate, FIMA: Further investigation may be abandoned)

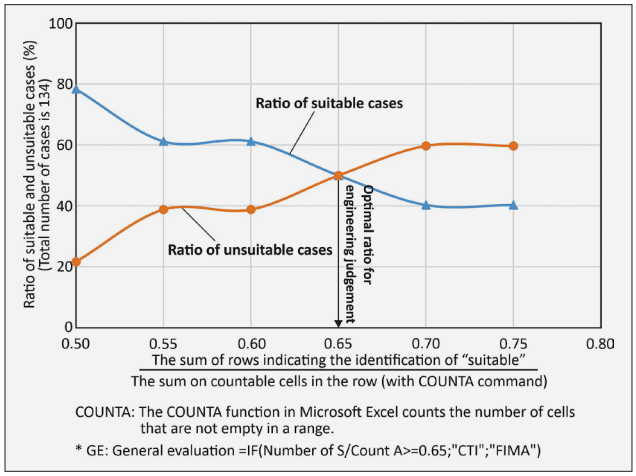


Figure 3. Optimization of the threshold value for engineering judgement in CF

The flowchart of this process is given in **Figure 2**. This approach can speed up decision-making processes during field studies that focus on exploring rock types that can be evaluated as potential dimension stone resources. The optimisation of the threshold value (0.65) was determined by considering several simulations. More profoundly, it was found by attempting different threshold values until a balanced evaluation (50% suitable and 50% unsuitable cases) was reached. The goal behind this was to identify a threshold value that yielded a balanced assessment, where the cases were evenly divided between 50% suitable and 50% unsuitable classifications (see **Figure 3**).

This approach ensured that the threshold value minimised bias in the evaluation process and provided a fair representation of the dataset's characteristics. By achieving this balance, the selected threshold value enhanced the reliability of the model and ensured its applicability to real-world scenarios.

2.3.2. Ranking method (RM)

The RM in engineering judgement offers several advantages that make it a valuable tool for decision-making processes (**Milanovic et al., 2010; Chang and Ku, 2021**). It is mainly used in decision contexts, including project selection, risk assessment, and performance evaluation. RM is easy to comprehend, making it accessible to a wide range of users, including engineers, managers, and stakeholders. In the RM, each independent variable (i.e. ρ_d, n_e, UCS, V_p, and BAV) is identified as a novel mathematical function (see **Table 8**). Thanks to these equations, each rock type has a rating point (RP), depending on each evaluation criterion.

Table 8. Mathematical functions for RM

Evaluation criterion	Formula
EC_1	$RP_1 = \exp(-0.154 n_e)$
EC_2	$RP_2 = 0.0013 UCS^{1.248}$
EC_3	$RP_3 = 0.004 \rho_d^5$
EC_4	$RP_4 = 0.054 \exp(0.42 V_p)$
EC_5	$RP_5 = \exp(-0.052 BAV)$

Then, the average of these RPs is defined as the basic point (BP). Using the CF methodology, suitable (S) and unsuitable (US) cases are identified based on these BPs. Probability density functions (PDFs) based on Gamma, logistic, Weibull, and normal distributions are employed to establish the ranges for CMI and FIMA cases. The optimal threshold value in the RM is determined by averaging the intersection values obtained from the PDFs shown in **Figure 4**. In this study, the threshold value in the RM is found to be 0.53. Accordingly, BPs greater than 0.53 can be regarded as CTI.

The intersection of these PDFs in **Figure 4** provides a threshold value that can be used to distinguish different

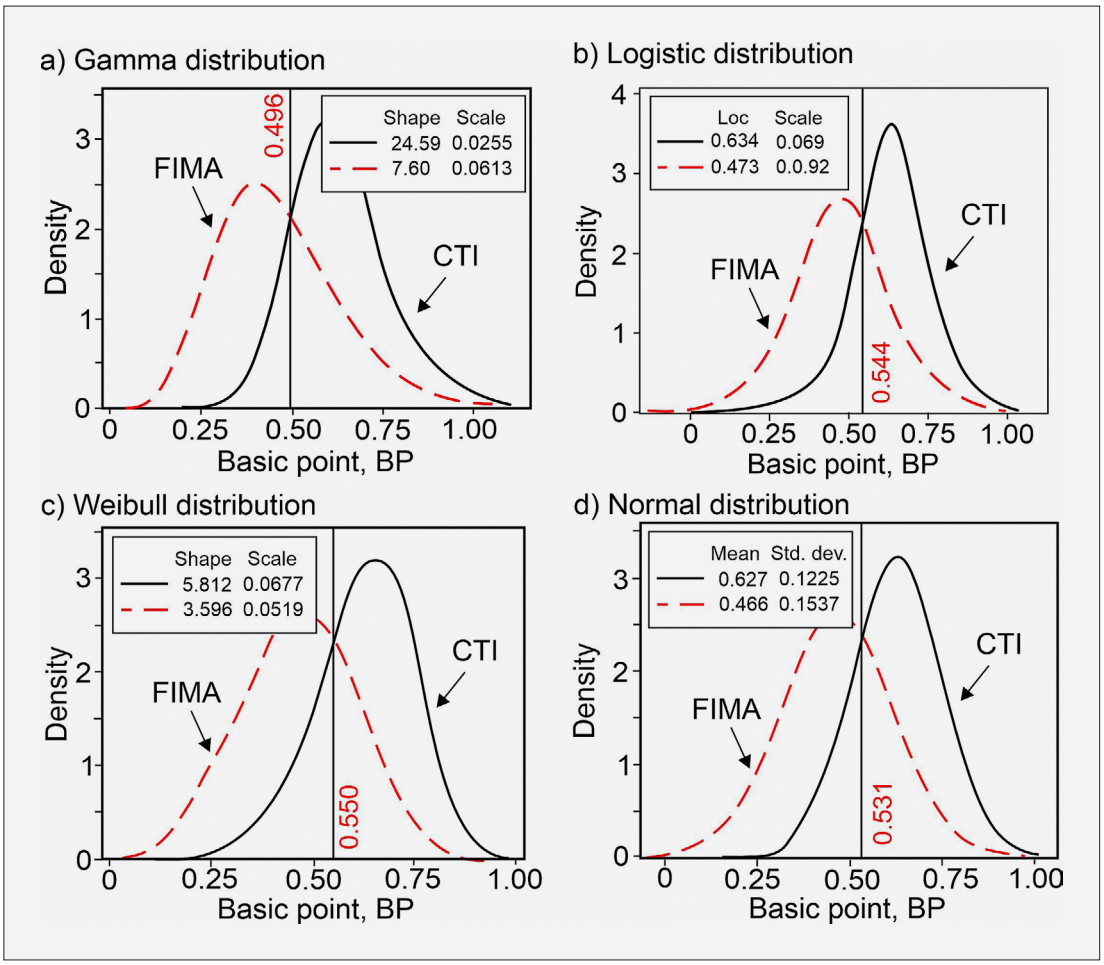


Figure 4. Probability density functions (PDFs) of the suitable and unsuitable cases based on different distributions a) Gamma b) Logistic c) Weibull d) Normal.

feasibility categories. This critical value (0.53) was used to assess the feasibility of granitic rocks. Although the referred value is crucial in determining the feasibility of rocks, it is essential to note that such intersections in PDFs are frequently encountered in statistics and probability theory when analysing decision-making processes (**Fox and Sturdivant, 2022**). The following section compares the findings obtained from the two proposed methods.

3. Results and Discussion

3.1. CF analysis results

CF analysis results for selected case studies are listed in **Table 9**. Accordingly, the investigated granitic rocks can be easily characterised in terms of their potential use as dimension stones. As shown in **Table 9**, sufficient input data enables a reliable feasibility assessment in some cases, whereas limited input data can negatively impact the performance of the CF method. In such cases, it is recommended to conduct additional tests (at least three measurable rock parameters as described in this study) before reapplying the CF methodology. The initial results in **Table 9** highlight the importance of comprehensive datasets in evaluating rocks for dimension stone applications. Rocks with well-documented properties can be assessed more confidently using the CF approach, while those with limited input data may yield uncertain evaluations, necessitating further testing to determine their suitability.

Nonetheless, in most cases, the CF methodology is easy to implement and can be effectively used to assess the feasibility of rocks for potential use as dimension stones. However, it is important to note that the threshold value (0.65) used in the CF methodology may be somewhat conservative, especially when limited data are available. This strict boundary could exclude certain rock types that may still deserve further investigation. Therefore, to apply the proposed methodology effectively, at least three measurable evaluation criteria must be satisfied.

3.2. RM analysis results

The RM analysis results are presented in **Table 10**. Accordingly, granitic rocks with BP values greater than the threshold value (0.53) may deserve further investiga-

Table 9. CF analysis results for some cases

Case	Parameter					Evaluation criterion					Number of S (x)	Count A (y)	x/y	GE*	Reference
	n_e (%)	UCS (MPa)	ρ_d (g/(cm3)	V_p (km/s)	BAV (cm^3/50cm^2)	EC1	EC2	EC3	EC4	EC5					
1	0.32	155.90	2.60	NR	4.70	S	S	S	NA	S	4	4	1	CTI	Ersoy et al. (2005)
2	0.87	146.70	NR	4.00	NR	S	S	NA	US	NA	2	3	0.67	CTI	Vasconcelos et al. (2008)
3	1.50	97.2	2.70	NR	NR	US	US	S	NA	NA	1	3	0.33	FIMA	Farhadian et al. (2021)
4	1.33	124.80	2.66	NR	NR	US	S	S	NA	NA	2	3	0.67	CTI	
5	0.60	118.50	2.67	NR	3.61	S	US	S	NA	S	3	4	0.75	CTI	Karaca et al. (2012b)
6	NR	124.5	2.60	4.43	NR	NA	S	S	US	NA	2	3	0.67	CTI	Armaghani et al. (2015)
7	NR	147.1	2.61	6.48	NR	NA	S	S	S	NA	3	3	1	CTI	
8	1.88	164.0	NR	4.32	9.42	US	S	NA	US	S	2	4	0.50	FIMA	Alsaiari and El Aal (2021)
9	1.13	175.0	NR	4.61	5.64	US	S	NA	S	S	3	4	0.75	CTI	
10	NR	227.0	2.74	NR	NR	NA	S	S	NA	NA	2	2	1	CTI	Nicksiar and Martin (2012)
11	0.99	NR	2.59	NR	10.29	S	NA	S	NA	US	2	3	0.67	CTI	Teymen (2024)
12	1.21	NR	2.58	NR	12.98	US	NA	S	NA	US	1	3	0.33	FIMA	
13	1.03	131.44	2.72	NR	4.34	US	S	S	NA	S	3	4	0.75	CTI	Karaca et al. (2010)
14	0.54	153.33	2.63	5.53	6.83	S	S	S	S	S	5	5	1	CTI	Çobanoğlu I. and Çelik (2017)
15	NR	95.0	NR	4.32	NR	NA	US	NA	US	NA	0	2	0	FIMA	Er and Tuğrul (2016)
16	NR	124.0	NR	5.35	NR	NA	S	NA	S	NA	2	2	1	CTI	

NR: Not reported, NA: Not available, S: Suitable, US: Unsuitable, CTI: Continue to investigate, FIMA: Further investigation may be abandoned.
Count A: The COUNTA function in Microsoft Excel counts the number of cells in a range that are not empty.
* GE: General evaluation =IF (Number of S/Count A=>0.65;"CTI";"FIMA")

Table 10. RM analysis results for some cases

Case	Parameter					Evaluation criterion					BP	Threshold	GE*	Reference
	n_e (%)	UCS (MPa)	ρ_d (g/(cm3)	V_p (km/s)	BAV (cm^3/50cm^2)	EC1	EC2	EC3	EC4	EC5				
1	0.32	155.90	2.60	NR	4.70	0.95	0.71	0.48	NA	0.78	0.73	0.53	CTI	Ersoy et al. (2005)
2	0.87	146.70	NR	4.00	NR	0.87	0.66	NA	0.29	NA	0.61	0.53	CTI	Vasconcelos et al. (2008)
3	1.50	97.2	2.70	NR	NR	0.79	0.39	0.57	NA	NA	0.59	0.53	CTI	Farhadian et al. (2021)
4	1.33	124.80	2.66	NR	NR	0.81	0.54	0.53	NA	NA	0.63	0.53	CTI	
5	0.60	118.50	2.67	NR	3.61	0.91	0.50	0.54	NA	0.83	0.70	0.53	CTI	Karaca et al. (2012b).
6	NR	124.5	2.60	4.43	NR	NA	0.54	0.48	0.35	NA	0.45	0.53	FIMA	Armaghani et al. (2015)
7	NR	147.1	2.61	6.48	NR	NA	0.66	0.48	0.82	NA	0.65	0.53	CTI	
8	1.88	164.0	NR	4.32	9.42	0.75	0.76	NA	0.33	0.61	0.61	0.53	CTI	Alsaiari and El Aal (2021)
9	1.13	175.0	NR	4.61	5.64	0.84	0.82	NA	0.37	0.75	0.69	0.53	CTI	
10	NR	227.0	2.74	NR	NR	NA	1.13	0.62	NA	NA	0.88	0.53	CTI	Nicksiar and Martin (2012)
11	0.99	NR	2.59	NR	10.29	0.86	NA	0.47	NA	0.59	0.64	0.53	CTI	Teymen (2024)
12	1.21	NR	2.58	NR	12.98	0.83	NA	0.46	NA	0.51	0.60	0.53	CTI	
13	1.03	131.44	2.72	NR	4.34	0.85	0.57	0.60	NA	0.80	0.70	0.53	CTI	Karaca et al. (2010)
14	0.54	153.33	2.63	5.53	6.83	0.92	0.69	0.50	0.55	0.70	0.67	0.53	CTI	Çobanoğlu I. and Çelik (2017)
15	NR	95.0	NR	4.32	NR	NA	0.38	NA	0.33	NA	0.36	0.53	FIMA	Er and Tuğrul (2016)
16	NR	124.0	NR	5.35	NR	NA	0.53	NA	0.51	NA	0.52	0.53	FIMA	

NR: Not reported, NA: Not available, CTI: Continue to investigate, FIMA: Further investigation may be abandoned.
* GE: General evaluation = IF (BP=>Threshold value (0.53);"CTI";"FIMA")

tion. In this context, the results obtained from the RM analysis are in good agreement with those obtained from the CF methodology. However, it is worth noting that each evaluation criteria (EC1 – EC5) are weighted equally in the RM.

To address the dominance of input parameters, it is possible to assign the relative weights of input parameters based on the specific engineering context of dimension stones. Since each rock type has pros and cons depending on its inherent nature, by carefully assigning appropriate weights to each input parameter according to their relative importance, the dominance of any single input parameter can be regulated. This approach helps mitigate biases and ensures that the RM can accurately reflect the suitability of granitic rocks for dimension stone applications based on comprehensive and well-balanced evaluation criteria.

3.3. Discussion

Dimension stone quality assessment is conducted based on the quantitative rock properties. In this context, it has been noted that the fundamental input parameters can be defined as ρ_d, w_a, UCS, FS, and BAV for assessing rock feasibility (**Strzałkowski et al., 2023; Strzałkowski and Köken, 2024**). However, geochemical and textural properties become prominent in assessing the quality of granitic rocks (**Ersoy and Acar, 2016; Lasheen et al., 2023; Waqar et al., 2025**). To observe the long-term behaviour and performance of granitic rocks, rock weathering effects, including freezing–thawing, heating–cooling, drying–wetting, and salt crystallisation, should be considered (**Bao and Zhao, 2008; Heidari et al., 2013; Abad et al., 2016; Liu et al., 2022; Ghasera and Rashid, 2024, Maričić et al., 2025**).

When evaluating the adopted methods used to assess rock feasibility, physical and mechanical rock properties are essential components in both the CF and RM. They define the evaluation criteria, influence analytical outcomes, and facilitate effective data interpretation. The selection and application of these properties should be carefully chosen in consideration of the specific requirements of dimension stone applications to ensure accurate and meaningful results. **Table 11** presents the results of the proposed approaches, considering the available input parameters.

The table clearly demonstrates that the combined use of physical and mechanical parameters leads to more reliable and comprehensive outcomes.

In this context, the CF and RM-based methods exhibit strong coherence in their results and effectively complement each other, enhancing the overall robustness of the assessment process. In general, CF may have numerous practical implications, enabling one to interpret large datasets. It enables geoscientists and mining engineers to identify patterns, anomalies, and thresholds in raw tables without requiring any additional computa-

Table 11. Comparison of the suggested methods

Case	Methodology		Input parameter						American specifications for granitic dimension stones (Table 1) [1]			References
	CF	RM	n_e	UCS	ρ_d	V_p	BAV		Criterion I (ρ_d, g/cm^3)		Criterion II (UCS, MPa)	
1	CTI	CTI	+	+	+	–	+		2.60	Suitable	155.9	Suitable	**Ersoy et al. (2005)**
2	CTI	CTI	+	+	–	+	–		NA	NA	146.70	Suitable	**Vasconcelos et al. (2008)**
3	FIMA	CTI	+	+	+	–	–		2.70	Suitable	97.2	Unsuitable	**Farhadian et al. (2021)**
4	CTI	CTI	+	+	+	–	–		2.66	Suitable	124.80	Unsuitable	
5	CTI	CTI	+	+	+	–	+		2.67	Suitable	118.50	Unsuitable	**Karaca et al. (2012b)**
6	CTI	FIMA	–	+	+	+	–		2.60	Suitable	124.5	Unsuitable	**Armaghani et al. (2015)**
7	CTI	CTI	–	+	+	+	–		2.61	Suitable	147.1	Suitable	
8	FIMA	CTI	+	+	–	+	+		NA	NA	164.0	Suitable	**Alsaiari and El Aal (2021)**
9	CTI	CTI	+	+	+	+	+		NA	NA	175.0	Suitable	
10	CTI	CTI	–	+	+	–	–		2.74	Suitable	227.0	Suitable	**Nicksiar and Martin (2012)**
11	CTI	CTI	+	–	+	–	+		2.59	Suitable	NA	NA	**Teymen (2024)**
12	FIMA	CTI	+	–	+	–	+		2.58	Suitable	NA	NA	
13	CTI	CTI	+	+	+	–	+		2.72	Suitable	131.44	Suitable	**Karaca et al. (2010)**
14	CTI	CTI	+	+	+	+	+		2.63	Suitable	153.33	Suitable	**Çobanoğlu and Çelik (2017)**
15	FIMA	FIMA	–	+	–	+	–		NA	NA	95.0	Unsuitable	**Er and Tuğrul (2016)**
16	CTI	FIMA	+	+	–	+	–		NA	NA	124.0	Unsuitable	

[1] **ASTM 615-03 (2004)** CTI: Continue to investigate, FIMA: Further investigation may be abandoned, NA: Not available

tional software. On the other hand, RM is used to help inform multi-criteria decisions. Since RM avoid bias from different units/scales, every input parameter is put on a comparable scale, which makes its use much easier. In the natural stone industry, both CF and RM can be reliably used to analyse large datasets from different perspectives, including quality evaluation, usage area addressing, and determination of the appropriate rock exposures for dimension stone manufacturing.

The validity of the suggested approaches is further supported by comparison with results based on the American standard (see **Table 11**) for granitic rocks. The findings indicate that the cases identified as CTI by the proposed methods are largely consistent with those suitable for use as dimension stones, according to the American standard. This strong correlation highlights the reliability of the RM and CF methodologies in distinguishing between suitable and unsuitable cases, supporting their applicability in practical evaluation scenarios.

Consequently, the adoption of these objective, data-driven methods can help standardize the assessment of dimension stones and support informed decision-making in both industrial and engineering contexts.

Particularly, the implementation of CF seems to be easier than that based on RM. However, the RM can be coded in any programming language, such as MATLAB or Python, to implement it more effectively. On the other hand, the most significant challenge in any decision-making task is the availability of input parameters. Therefore, the appropriate use of these methods heavily relies on the presence of input parameters adopted in this study.

Nevertheless, it should be mentioned that at least three measurable rock properties should be identified to run the CF more effectively. On the other hand, RM can be successfully applied to assess the feasibility of dimension stones by considering the input parameters adopted. The suggested method based on RM can also be arranged or modified by considering different input parameters. This flexibility increases its potential use in the dimension stone industry. Finally, although the proposed methods are in good agreement with the American Standard (**ASTM 615-03, 2004**), they should be applied to different granitic rocks to observe their advantages and limitations.

4. Conclusions

This study presents two objective evaluation tools for assessing the feasibility of using granitic rocks as dimension stone. The feasibility analysis reveals that the selected input parameters (ρ_d, n_e, V_p, UCS, and BAV) are crucial for accurately determining the suitability of rocks as dimension stones. The results indicate that the proposed CF and RM approaches offer practical support for selecting appropriate rock exposures in field studies. Additionally, these methodologies provide a time- and energy-efficient solution, enhancing decision-making within the dimension stone industry. The strong agreement between the CF and RM methods highlights their consistency and wider applicability. Furthermore, both techniques show good compatibility with the American standard recommendations for granitic rocks, supporting their validity and relevance in real-world applications.

Beyond technical robustness, integrating CF and RM tools can promote more sustainable resource management by lowering unnecessary quarrying activities, including laboratory testing and analysis, and minimising economic and environmental risks. Their flexibility makes them especially useful for preliminary assessments where quick yet reliable results are needed, such as in early exploration, project planning, and investment decisions. However, to better understand the strengths and possible limitations of these methods, it is recommended to test them on a wider variety of dimension stone types and geological settings. Future research should focus on validating and refining these tools through more case studies to demonstrate their robustness and versatility for various applications within the natural stone industry, while also investigating the potential for digital integration with technologies like GIS, machine learning, and remote sensing to further improve prediction accuracy and practical use.

5. References

Ahmed I., Basharat M., Sousa L., and Mughal M.S. (2021). Evaluation of building and dimension stone using physico-mechanical and petrographic properties: a case study from the Kohistan and Ladakh batholith, Northern Pakistan. Environmental Earth Sciences, 80, 1−17.

Amirkiyaei V., Ghasemi E., and Faramarzi L. (2021). Estimating uniaxial compressive strength of carbonate building stones based on some intact stone properties after deterioration by freeze-thaw. Environmental Earth Sciences, 80(9), 352.

Abramovich S., and Sugden S. (2004).Spreadsheet conditional formatting: An untapped resource for mathematics education." Spreadsheets in Education, 1(2), 104–124.

Anon (1979). Classification of rocks and soils for engineering geological mapping. Part I—rock and soil materials. Bulletin of International Association for Engineering Geology, vol 19, 364–371.

Alsaiari M.A., and El Aal A.A., (2021). Influence of composition on the physico-mechanical properties of granitic rocks used in floor covering and building cladding in Najran Region, Saudi Arabia. Arabian Journal of Geosciences, 14(20), 2100.

Armaghani J.D., Tonnizam Mohamad E., Momeni E., Narayanasamy M.S., and Mohd Amin M.F. (2015). An adaptive neuro-fuzzy inference system for predicting unconfined compressive strength and Young's modulus: a study on Main Range granite. Bulletin of Engineering Geology and the Environment, 74, 1301-1319.

Abad S.V.A.N.K., Tugrul A., Gokceoglu, C. and Armaghani, D.J. (2016). Characteristics of weathering zones of granit-

ic rocks in Malaysia for geotechnical engineering design. Engineering Geology, 200, 94−103.

ASTM C1528 (2008). Standard Guide for Selection of Dimension Stone for Exterior Use, ASTM International.

ASTM 615-03 (2004). Standard Specification for Granite Dimension Stone, ASTM International.

ASTM 503-08a (2008). Standard Specification for Marble Dimension Stone, ASTM International.

Bao Z., and Zhao Z. (2008). Geochemistry of mineralization with exchangeable REY in the weathering crusts of granitic rocks in South China. Ore Geology Reviews, 33(3-4), 519-535.

Bellopede R., Marini P., and Collaro L. (2015). Size effect in flexural strength test on dimension stones. In Engineering Geology for Society and Territory-Volume 5: Urban Geology, Sustainable Planning and Landscape Exploitation, 303 – 307.

Briševac Z., Maričić A., Kujundžić T., and Hrženjak P. (2023). Saturation Influence on Reduction of Compressive Strength for Carbonate Dimension Stone in Croatia, Minerals, 13(11), 1364.

Chang T.Y., and Ku C.C.Y. (2021). Fuzzy filtering ranking method for multi-criteria decision making. Computers & Industrial Engineering, 156, 107217.

Cassar, J., Winter, M.G., Marker, B.R., Walton, N.R., Entwisle, D.C., Bromhead, E.N., Smith, J.W. (2014). Introduction to stone in historic buildings: characterization and performance. Geological Society, London, Special Publications, 391(1), 1−5.

Çelik, S. B., Çobanoğlu, İ., & Gireson, K. (2025). Prediction and classification of flexural strength of rock materials used as dimension stones. Bulletin of Engineering Geology and the Environment, 84(1), 44.

Çobanoğlu I., (2015). Prediction and identification of capillary water absorption capacity of travertine dimension stone. Arabian Journal of Geosciences, 8, 10135-10149.

Çobanoğlu I. and Çelik S.B., (2017). Assessments on the usability of Wide Wheel (Capon) test as reference abrasion test method for building stones, Construction and Building Materials, 151, 319-330.

Er S. and Tuğrul A., (2016). Correlation of physico-mechanical properties of granitic rocks with Cerchar Abrasivity Index in Turkey, Measurement, 91, 114-123.

Ersoy A., Buyuksagic S., and Atici U., (2005). Wear characteristics of circular diamond saws in the cutting of different hard abrasive rocks, Wear, 258(9), 1422−436.

Ersoy, H., & Acar, S. (2016). Influences of petrographic and textural properties on the strength of very strong granitic rocks. Environmental Earth Sciences, 75(22), 1461.

Esmaeilzadeh, A., Akhyani, M., Kashtiban, Y. J., Mikaeil, R., Zinno, R., & Haghshenas, S.S. (2025). Selecting Appropriate Dimension Stone in Processing Plants using the Fuzzy Delphi Analytic Hierarchy Process. Spectrum of Engineering and Management Sciences, 3(1), 238-252.

Farhadian A., Ghasemi E., Hoseinie S.H., and Bagherpour R. (2021). Development of a new test method for evaluating the abrasivity of granite building stones during polishing process based on weight loss of abrasive tool. Construction and Building Materials, 303, 124497.

Fox, W.P., and Sturdivant, R.X. (2022). Probability and Statistics for Engineering and the Sciences with Modelling using R, Chapman and Hall/CRC, ISBN: 9781003317906.

Gautam, P.K., Verma A.K., Jha M.K., Sharma P., and Singh T.N. (2018). Effect of high temperature on physical and mechanical properties of Jalore granite, Journal of Applied Geophysics, 159, 460-474

Ghasera, K.M., and Rashid, S.A. (2024). Influence of microscale factors in weathering and elements mobility: Evidence from a comparative study of granite and basalt weathering profiles across India. Catena, 235, 107680.

Hazrathosseini A., and Mahdevari S. (2019). Geometric quality assessment of in situ blocks in dimension stone quarries. Bulletin of Engineering Geology and the Environment, 78, 2377−2385.

Heidari M., Momeni, A.A., and Naseri, F. (2013). New weathering classifications for granitic rocks based on geomechanical parameters. Engineering geology, 166, 65-73.

Karaca Z., Deliormanli A.H., Elci H., and Pamukcu C. (2010). Effect of freeze–thaw process on the abrasion loss value of stones." International Journal of Rock Mechanics and Mining Sciences, 47(7), 1207-1211.

Karaca Z., Yılmaz N.G., and Goktan R.M. (2012a). Abrasion wear characterization of some selected stone flooring materials with respect to contact load, Construction and Building Materials, 36, 520-526.

Karaca Z., Günes-Yılmaz N., and Goktan R.M. (2012b) Considerations on the European Standard EN 14157 test methods: abrasion resistance of natural stones used for flooring in buildings. Rock mechanics and rock engineering, 45, 103-111.

Lasheen, E. S. R., Rashwan, M. A., & Azer, M. K. (2023). Effect of mineralogical variations on physico-mechanical and thermal properties of granitic rocks. Scientific Reports, 13(1), 10320.

Liu, X., Zhang, X., Kong, L., Wang, G., and Liu, H (2022). Chemical weathering indices and how they relate to the mechanical parameters of granite regolith from southern China. Catena, 216, 106400.

Maričić, A., Briševac, Z., & Barudžija, U. (2025). Resistance to salt crystallization of thin-bedded or platy limestone from the town of Benkovac in Croatia. Mining of mineral deposits, 19(1), 98-106.

Milanovic D.L., Milanovic D.D., and Misita M.Z. (2010). Application of ranking method in evaluation of engineering investment projects. International Journal of Industrial Engineering, 17(4), 310 – 318, 2010

Moss A.V. and Quervain F.D. (1948). Technische Gesteinkunde. Verlag Birkhauser, Basel.

Nicksiar, M., and Martin, C.D. (2012). Evaluation of methods for determining crack initiation in compression tests on low-porosity rocks. Rock mechanics and rock engineering, 45, 607-617.

Pereira, D. (2023). The Value of Natural Stones to Gain in the Cultural and Geological Diversity of Our Global Heritage. Heritage, 6, 4542–4556.

Sariisik, G. (2012). Determining performance of marble finished products on their usage areas by a new impact-resistance test method. Journal of Testing and Evaluation, 40(6), 945-951.

Sariisik, G., Özkan, E., Kundak, E., & Akdaş, H. (2016). Classification of parameters affecting impact resistance of natural stones. Journal of Testing and Evaluation, 44(4), 1650-1660.

Strzałkowski P., Kaźmierczak U., and Wolny M. (2020). Assessment of the method for abrasion resistance determination of sandstones on Böhme abrasion test apparatus. Bulletin of Engineering Geology and the Environment, 79(9), 4947–4956.

Strzałkowski P., Köken E. and Sousa L. (2023). Guidelines for natural stone products in connection with European standards, Materials, 16, 6885.

Strzałkowski, P., and Köken, E., (2024). A novel evaluation methodology for dimension stone quality. Mining Science, 31, 119−143.

Stone, D. (2015). The dimension stone sector: New perspectives on the global market and on the reporting of international mining standards. European Geologist, pp. 24

Sugden S., Baker J.E., and Abramovich S. (2015). Conditional formatting revisited: A companion for teachers and others." Spreadsheets in Education, 8(3), 18 pp.

Tan X., Chen W., Yang J., and Cao J. (2011). Laboratory investigations on the mechanical properties degradation of granite under freeze-thaw cycles. Cold Regions Science and Technology, 68(3), 130−138.

Teymen, A. (2024). Assessment of Bohme surface abrasion resistance of natural stones by simple and nonlinear multiple regression methods. Construction and Building Materials, 411, 134195.

Vasconcelos G., Lourenço P.B., Alves C.A.S., and Pamplona J. (2008). Ultrasonic evaluation of the physical and mechanical properties of granites, Ultrasonics, 48(5), 453−466.

Xu J., Kang Y., Liu F., Liu Y., Wang Z., and Wang X. (2021). Mechanical properties and fracture behaviour of flawed granite under dynamic loading, Soil Dynamics and Earthquake Engineering, 142, 106569.

Waqar, M. F., Guo, S., Qi, S., Karim, M. A. M., Zada, K., Ahmed, I., & Shang, Y. (2025). Influence of Mineralogical and Petrographic Properties on the Mechanical Behavior of Granitic and Mafic Rocks. Minerals, 15(7), 747.

SAŽETAK

Analiza upotrebljivosti granitnih stijena u industriji arhitektonsko-građevnoga kamena

Ovom studijom predstavljena su dva objektivna alata za ocjenjivanje upotrebljivosti granitnih stijena u industriji arhitektonsko-građevnoga kamena. Razvijene metode integriraju temeljna fizička i mehanička svojstva, uključujući suhu gustoću (ρ_d), efektivnu poroznost (n_e), brzinu P-valova (V_p), jednoosnu tlačnu čvrstoću (UCS) i Böhmeov indeks abrazije (BAV). Analize pogodnosti temeljene na uvjetnome formatiranju (CF) i metodi rangiranja (RM) pokazale su da su odabrani ulazni parametri ključni za određivanje primjene granitnih stijena kao arhitektonsko-građevnoga kamena. Snažna povezanost između rezultata CF i RM potvrđuje njihovu konzistentnost i široku primjenu. Obje metode pokazale su dobro slaganje s preporukama američkoga standarda za granitne stijene. Slijedom toga, predložene metode pružaju praktične smjernice za odabir prikladnih stijenskih izdanaka u terenskim istraživanjima nudeći pritom vremenski i energetski učinkovit okvir za donošenje odluka u industriji arhitektonsko-građevnoga kamena. Za cjelovitiju procjenu prednosti i ograničenja predloženih pristupa preporučuje se primjena ovih alata na širi spektar tipova arhitektonsko-građevnoga kamena i različite geološke uvjete.

Ključne riječi:
granitne stijene, arhitektonsko-građevni kamen, upotrebljivost stijena, uvjetno formatiranje, metoda rangiranja

Author's contribution

Ekin Köken (PhD): conceptualization, investigation, data curation, software. The author has read and agreed to the published version of the manuscript.

RGNZ/MGPB

Facies Architecture and Sedimentary Provenance of the Miocene Ombilin Formation: Interplay of Tectonics and Eustasy in a Neogene Intermontane Basin, Central Sumatra, Indonesia

Rudarsko-geološko-naftni zbornik
(The Mining-Geology-Petroleum Engineering Bulletin)
DOI: 10.17794/rgn.2026.2.5

Original scientific paper

Aurio Erdi[1]*, Syahreza S. Angkasa[2], Eko Suwarno[2], Aswan[3]
[1] *Research Centre for Geological Resources, National Research and Innovation Agency (BRIN), Indonesia.*
[2] *Directorate of Geothermal, Ministry of Energy and Mineral Resources, Indonesia.*
[3] *Geological Engineering, Faculty of Earth Science and Technology (FITB), Institut Teknologi Bandung, Indonesia.*

Abstract
The Early–Middle Miocene Ombilin Formation in the intermontane Ombilin Basin, Central Sumatra, records a critical interval of paleoenvironmental change shaped by regional tectonics and global sea-level fluctuations. Despite its significance, the formation's sedimentological architecture, provenance, and sea-level history have been poorly constrained. This study integrates detailed outcrop-based sedimentary logging and petrographic analysis to address these gaps. Ten lithofacies are identified and grouped into three facies associations: open marine, tidal-influenced channels, and intertidal mixed tidal flats deposits. Their vertical distributions show normal and inverse transitions. The normal transition indicates a shift from sublittoral to tidally dominated environments, interpreted as a result of seaward progradation driven by increased sediment supply from the uplifting Barisan Mountains and short-term global sea-level falls (e.g. SEA34–SEA46). The inverse transition, however, indicates a transgression occurred in the Ombilin Basin. Petrographic analysis in the Ombilin Formation show arkosic sandstones sourced primarily from a magmatic arc, consistent with contemporaneous volcanism west of the basin, with minor reworking of marine units and older clastic materials. Stratigraphic evidence suggests an initial regression, likely driven by the uplifting of Barisan Mountain and global sea-level fall, which occurred in the Ombilin Basin during Early Miocene. This event was followed by deposition aligned with global transgressive trends. These findings provide new insight into the sedimentary evolution, provenance, and tecto-no-eustatic interplay controlling Ombilin Basin development during the Early–Middle Miocene.

Keywords:
tidal-related deposits, Sinamar sub-basin, sedimentology, provenance, tectonics

1. Introduction

The Ombilin Basin has been classified as one of the intermontane basins (**Koesoemadinata, 2020**) within the Barisan Mountain Range in Central Sumatra, Indonesia (**e.g. Koesoemadinata and Matasak, 1981; Habrianta et al., 2018**). Owing to this unique tectonic location, the basin has been infilled with a substantial thickness of Cenozoic sediments, which has been interpreted as a response to the region's dynamic tectonic setting, particularly its proximity to the active Sumatra Fault System and the Barisan Mountains (**Figure 1a,b; e.g. Howells, 1997; Barber et al., 2005**). Among the sedimentary successions, the Ombilin Formation has been highlighted as a crucial stratigraphic unit for interpreting the paleoenvironmental history of the basin during a phase characterized by regional transgression, the occurrence of the Barisan being uplifted (**e.g. Koesoemadinata and Matasak, 1981; Koning, 1985**), and/or a transition from a eustatic sea-level fall to a rise in the Early Miocene (**e.g. Zaim et al., 2012; Morley et al., 2021**).

Despite the recognized significance of the Ombilin Formation in recording tectonic activity and sea-level fluctuations, limited understanding has been established regarding its sedimentological characteristics, provenance, depositional environment, and their linkage to global eustatic changes. The formation has generally been interpreted as an Early Miocene marine deposit, distinguished by grey calcareous shales, clays, and locally developed bioclastic limestone layers, which have been associated with a transitional to neritic depositional environment (**e.g. Koesoemadinata and Matasak, 1981; Barber et al., 2005; Linggadipura et al., 2018**). This previous interpretation of the depositional environment was supported by a limited analysis of lithofacies variability, sedimentary structures, and fossils, constraining reconstructions of the paleoenvironments that prevailed during its formation. These previous studies, however, have not clearly defined the impact of the glob-

* Corresponding author: Aurio Erdi
e-mail address: auri002@brin.go.id
Received: 22 May 2025. Accepted: 2 October 2025.
Available online: 13 March 2026

al transition from eustatic fall to rise on the sedimentary dynamics of the Ombilin Formation during the Early Miocene age. Such a relationship is considered critical for a comprehensive paleoenvironmental reconstruction of the basin during this period. Moreover, provenance studies specifically addressing the Early Miocene Ombilin Formation have remained scarce (**Adhiperdana, 2010; Yeni, 2011**). The origin of the clastic material is regarded as a key element in deciphering the tectonic development of the basin and its relation to the adjacent geological domains during the Early Miocene.

In this study, the existing gaps in understanding the Ombilin Formation have been addressed through an integrated sedimentological and petrographic investigation conducted in the area adjacent to the Tanjung Ampalu Fault, situated within the Sinamar sub-basin of the Ombilin Basin. To achieve this, several research questions have been posed: (1) how can the lateral and vertical variability of facies and depositional environments within the Ombilin Formation be characterized?; (2) what does the provenance of the formation reveal about sediment sources?; and, (3) how are facies architecture and provenance related to regional tectonics in Sumatra and broader Miocene eustatic trends across Southeast Asia? Through the examination of sediment textural and compositional characteristics, new insight into the depositional processes and environmental conditions that governed the formation's development has been obtained. The provenance and potential sediment dispersal pathways into the basin have been inferred through petrographic analysis of framework grains. Ultimately, the integration of these findings has been employed to reconstruct the paleoenvironmental evolutions of the Ombilin Basin during the Early Miocene and to evaluate its linkage with regional tectonic activity in Sumatra and contemporaneous eustatic sea-level fluctuations across Southeast Asia.

2. Geological Settings

The study area is situated within the Ombilin Basin, a Cenozoic intermontane basin covering approximately 25 × 60 km² and aligned parallel to the NW–SE structural trend of Sumatra (**Figure 1; e.g. Koesoemadinata and Matasak, 1981; Anastasia et al., 2012; Habrianta et al., 2018**). This basin is located within the Bukit Barisan Mountain range, on the continental crust where the magmatic arc and the Sumatra Fault Zone (SFZ) are also present (**e.g. Van Bemmelen, 1949; Situmorang et al., 1991; Noeradi et al., 2005; Zaim et al., 2012**). The eastern margin of the basin is bounded by the Takung Fault, whereas its western and southern flanks are bordered by pre-Cenozoic lithologies composed of limestone, metamorphic, and granitic complexes, as well as by the NW-trending Barisan Fault System (**Figure 1b; e.g. Koesoemadinata and Matasak, 1981; Koning, 1985; Noeradi et al., 2005**). Toward the northwest, the basin is observed to transition into either the basement ridge of the Tungkar High or the active volcanic centers of Marapi and Malintang (**Koning, 1985**). Furthermore, the basin is transected centrally by N–S trending Tanjung Ampalu Fault, subdividing it into the Paleogene-aged Talawi sub-basin in the west and the Neogene-aged Sinamar sub-basin in the east (**Figure 1b; e.g. Koning, 1985; Situmorang et al., 1991; Barber et al., 2005**).

The Ombilin Basin has been filled with up to 4600 m of Eocene to Middle Miocene deposits, which overlie the pre-rift Pre-Cenozoic basement (**e.g. Koning, 1985; Whateley and Jordan, 1989**). The pre-Cenozoic basement units are exposed along the basin margins, represented by Permian to Upper Cretaceous granites, Middle to Late Triassic limestones, and Permo-Carboniferous limestones, and considered part of the Mergui and Woyla accretionary terrains (**e.g. Fletcher and Yarmanto, 1993; Noeradi et al., 2005**). The Eocene to Middle Miocene deposits, however, are believed to have been eroded for approximately 3600 meters in the western side of the basin (**Whateley and Jordan, 1989**). The Eocene to Middle Miocene deposits reflect tectonostratigraphic stages in the Ombilin Basin (see **Figure 2**).

The initial period of Ombilin Basin filling was reflected by the deposition of early syn-rift formations, unconformably overlying the Pre-Cenozoic Basement (**Figures 1b, d and 2; Koning, 1985; Fletcher and Yarmanto, 1993**). The early syn-rift formations consist of interfingering deposits of the alluvial fans, and the lake and lacustrine deposits of the Brani and Sangkarewang formation, respectively (**e.g. Whateley and Jordan, 1989; Koesoemadinata and Matasak, 1981**). Debates regarding age determination of these formations have arisen, with proposed ages ranging from Paleocene (**Koesoemadinata and Matasak, 1981; Whateley and Jordan, 1989**), Paleocene to Early Eocene (**Noeradi et al., 2005**), Eocene (**e.g. Fletcher and Yarmanto, 1993; Situmorang et al., 1991; Murray, 2020**), or Eocene to Oligocene (**Barber et al., 2005**). These formations were deposited during the formation of the graben (**Van Bemmelen, 1947; Barber et al., 2005**) and are associated with: (i) Middle Cretaceous to Early Cenozoic orogenesis (**e.g. Katili and Hehuwat, 1967; Koesoemadinata and Matasak, 1981**); (ii) the nucleation of the en-echelon array of the Sumatra Fault Zone (SFZ; **Koning, 1985; Situmorang et al., 1991**); or (iii) the extensional rifting of back-arc settings in response to subduction (**e.g. Fletcher and Yarmanto, 1993; Noeradi et al., 2005**).

The late syn-rift formation was deposited either unconformably (**Barber et al., 2005**) or conformably (**Koesoemadinata and Matasak, 1981; Noeradi et al., 2005**) above the early syn-rift formations and is represented by the fluvio-deltaic deposits of the Sawahlunto Formation (see **Figures 1b-d** and **2**). This formation is characterized by fining-upward sequences of interbedded fine to medium sandstones, shales, and coals (**What-**

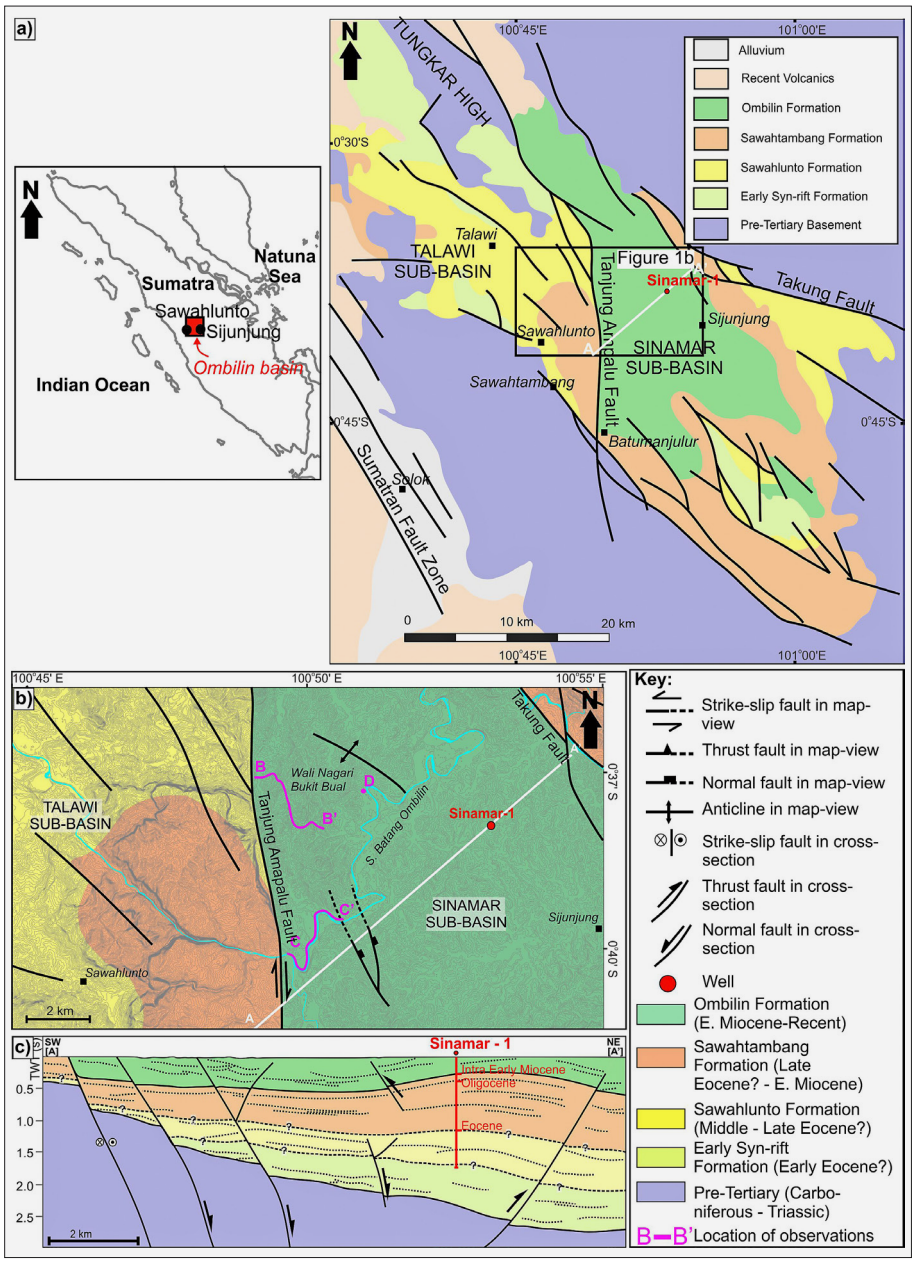


Figure 1. a) Regional map of Sumatra, showing the location of the Ombilin Basin. b) Simplified geological map of the study area in the Ombilin Basin (compiled from **Barber et al, 2005**; **Zaim et al., 2012**). c) Structural cross-sections across the study area (**Putra et al., 2021**).

eley and Jordan, 1989; Fletcher and Yarmanto, 1993), which transition upward into thick-bedded sandstones and shales (**Koesoemadinata and Matasak, 1981**), and laterally into glauconitic conglomeratic sandstones (**Noeradi et al., 2005**). Deposition of this formation has been interpreted to have occurred in meandering fluvial to deltaic environments (**Koesoemadinata and Matasak, 1981; Noeradi et al., 2005**), with the age variously assigned from the Eocene (**Koesoemadinata and Matasak, 1981; Whateley and Jordan, 1989**; **Murray, 2020**) to Oligocene–Early Miocene (**Bartram and Nugrahaningsih, 1990; Situmorang et al., 1991; Fletcher and Yarmanto, 1993; Noeradi et al., 2005**).

The late stage of basin infill in the Ombilin Basin has been marked by the deposition of post-rift successions. During the early post-rift phase, the Sawahtambang Formation was deposited either conformably (**Koesoemadinata and Matasak, 1981**) or unconformably (**Koning, 1985; Whateley and Jordan, 1989**) above the Sawahlunto Formation (see **Figures 1b-d** and **2**). The Sawahtambang Formation is characterized by thick, channelled and cross-bedded quartzose to feldspathic sandstones and conglomerates, transitioning upward into fine-grained sandstones, mudrocks, thin coal beds, and interbedded tuffs (**e.g. Noeradi et al., 2005; Barber et al., 2005**). This formation is interpreted to have been deposited within a fluvial-dominated environment (**Koesoemadinata and Matasak, 1981; Howells, 1997**). This event occurred between the Eocene to Early Miocene (**e.g. Koning et al., 1985; Noeradi et al., 2005**), when back-arc subsidence, magmatic arc activation, and strike-slip deformation along the Sumatra Fault System occurred (**Howells, 1997; Barber et al., 2005**).

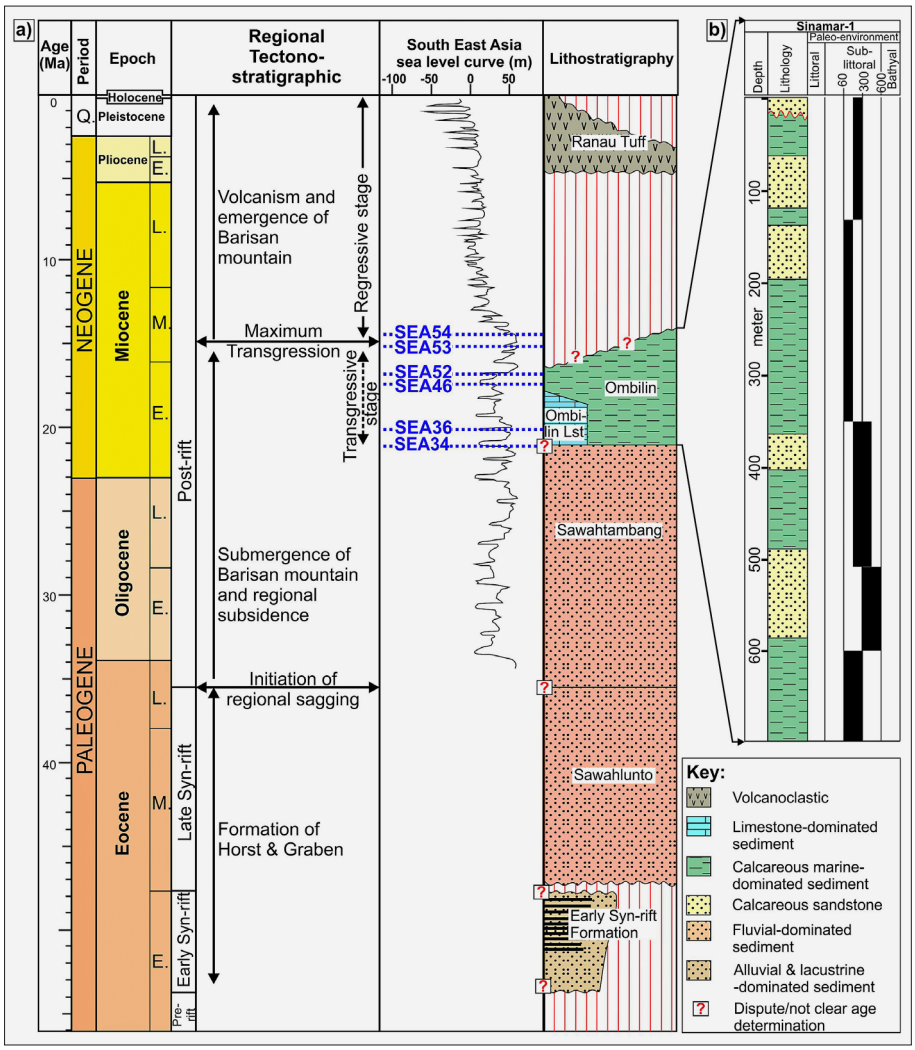


Figure 2. a) Simplified regional tectono- and lithostratigraphy in the Ombilin Basin according to **Noeradi et al (2005)** and **Barber et al (2005)**, modified to accommodate the latest published age of early syn-rift (Early Eocene) and Sawahlunto Formation (Middle-Late Eocene) from **Murray (2020)**. b) Mudlog of Sinamar 1, covering the Ombilin Formation and its paleoenvironment based on biostratigraphy data (**Koning, 1985**). See the location of Sinamar-1 in **Figure 1**.

During the late post-rift phase, the Ombilin Formation and Ranau Tuff were deposited (**Koesoemadinata and Matasak, 1981; Noeradi et al., 2005**), with the Ombilin Formation unconformably (**Koning, 1985; Whateley and Jordan, 1989**) or conformably (**Fletcher and Yarmanto, 1993; Noeradi et al., 2005**) overlying the Sawahtambang Formation (**Figures 1b-d** and **2**). Although initially reported only in the Sinamar sub-basin, which extends laterally from Batumanjulur near the Tanjung Ampalu Fault to the eastern margin of the sub-basin (**Koning, 1985; Anastasia et al., 2012**), the Ombilin Formation has also been identified in the Talawi sub-basin (**Linggadipura et al., 2018**). Seismic data indicate this formation has a thickness of approximately 2740–4000 m in the northern limb of the basin (**Koning, 1985; Anastasia et al., 2012**), while up to 692 m was encountered in the Sinamar-1 **(Fletcher and Yarmanto, 1993; Noeradi et al., 2005; Figure 2**). However, the true thickness of this formation remains uncertain due to post-depositional erosion. The lower part of the formation is marked by calcareous mudrock with limestone nodules and thin foraminiferal limestone lenses or beds (**Koesoemadinata and Matasak, 1981; Howells, 1997; Anastasia et al., 2012**), which grades upward into carbonaceous, calcareous, and silty to sandy mudrocks interbedded with sandstone and/or tuff (**Koesoemadinata and Matasak, 1981; Noeradi et al., 2005; Habrianta et al., 2018**). The sandstones are typically very fine- to fine-grained, calcareous, and glauconitic (**Noeradi et al., 2005**). The deposition of this formation has been interpreted as neritic to bathyal in the Sinamar Sub-basin, based on biostratigraphic data (e.g. **Koesoemadinata and Matasak, 1981; Koning, 1985**). In contrast, a transitional environment has been suggested for the Talawi Sub-basin (**Linggadipura et al., 2018**). Deposition of this formation coincided with the continued uplift of the Barisan Mountains (**Moss and Carter, 1996; Barber et al., 2005; Erdi et al., 2025**), volcanic activity in the basin's northeastern margin (**Koesoemadinata and Matasak, 1981**), and regional subsidence (**Howells, 1997**).

Following the deposition of the Ombilin Formation, the Ranau Tuff was locally deposited and is unconformably overlying the Ombilin Formation within the Ombilin Basin (**Figures 1b and 2; Koesoemadinata and Matasak, 1981; Habrianta et al., 2018**). This tuff unit has been interpreted to have been deposited during the Pleistocene (**Koesoemadinata and Matasak, 1981; Habrianta et al., 2018**), or from the Pliocene to Recent

(**Fletcher and Yarmanto, 1993**). It is composed of andesitic to basaltic lava flows, lahar deposits, and tuffs (**Fletcher and Yarmanto, 1993**).

3. Methods

Two methods were conducted in this study, consisting of sedimentary logging and petrographic analysis. The sedimentary logging was conducted to uncover sedimentary characteristics, while petrographic analysis was conducted to unravel sandstone characteristics and the provenance of the Ombilin Formations.

3.1. Sedimentary Logging

Geological data were collected through three measured outcrop sections located within a 12 km radius of Sijunjung, West Sumatra, specifically in the Sinamar Sub-basin (see **Figure 1b**). The outcrops, aligned with the regional N–S strike of the Tanjung Ampalu Fault, provided excellent vertical but limited lateral exposures. Two localities, which are Wali Nagari Bukit Bual and Sungai Batang Ombilin, were examined, and approximately 80 m of the Ombilin Formation was measured. In this study, higher-resolution logging was conducted to document sedimentary features for facies analysis, including grain size, sorting, roundness, color, sedimentary structures, bed thickness, fossil content, and bounding contacts. Facies and facies associations were interpreted based on lithology, sedimentary structures, and vertical stacking patterns following standard methodologies (**e.g. Anderton, 1985; Zakaria et al., 2013**).

3.2. Petrography, Sandstone Classifications and Provenance

Twenty petrographic samples were collected from the measured outcrop sections of the Ombilin Formation, of which seven were selected for detailed petrographic analysis. The seven samples were used to illustrate (1) non-calcareous, sand-rich sediments, (2) sandy calcareous sediments, and (3) limestone, which collectively reflect the sedimentary compositions of the Ombilin Formation. Thin sections were prepared from these samples, impregnated with blue-stained epoxy resin to enhance porosity visualization, and examined under a transmitted light petrographic microscope (Zeiss Axio Imager A2m). Detrital components (e.g. quartz, feldspars, lithic fragments), authigenic minerals (e.g. heavy and accessory minerals, silicates), biogenic materials (e.g. bioclasts), matrix, and cement were identified. Petrography was employed as a primary method for provenance analysis, in line with standard practices for initial sandstone provenance studies (**e.g. Augustsson, 2021**). Sandstone composition was recalculated using point counting to generate ternary plots for classification and provenance purposes (**e.g. Dickinson, 1985; Malaza et al., 2015**). These data were plotted on QFL diagrams of **Pettijohn (1975)**, **Folk (1980)**, and **Dickinson et al. (1983; 1985**) to infer sandstone classifications, tectonic settings, and sedimentary provenances.

4. Results

The methodology outlined previously was applied, and the results are presented in this chapter. The findings comprise descriptions of facies associations and petrographic characteristics of the Ombilin Formation.

4.1. Facies Associations of the Ombilin Formation

Ten lithofacies were identified based on distinctive features such as grain size, sorting, roundness, sedimentary structures, fossil content, and bedform-to-outcrop geometry (C1–C3 and S1–S7; **Figure 3 and Table 1**). These were grouped into three facies associations (FA1–FA3) according to their characteristics, occurrence, and vertical stacking patterns (see **Figure 3** and **Table 2**). FA1 were observed in sections C and D, situated southward and northeastward of section B. The FA2 and FA3, however, were recognized in sections B, located east of the Tanjung Ampalu Fault (see **Figure 1b**). Strike-projection onto a cross-section indicates that section B lies between sections C and D and is separated by subsurface normal faults, although no surface expression of these faults, such as repetition of sedimentary log, was observed during logging (see **Figure 1c**). This stratigraphic relationship suggests that FA1 in section C is older than the FA2 and the FA3, while FA1 in section D is younger than the FA2 and the FA3 in section B (see **Figure 3**). The three facies associations are described in detail below.

4.1.1. Facies Association 1 (FA1)

The FA1 is comprised of three lithofacies, being represented by alternations of calcareous mudrock (C1), calcareous ripple-stratified sandstone (C2), and stratified limestone (C3; **Figure 3** and **Table 2**). The C1 is defined by up to 8 m thick, dark grey, silt-grained, calcareous mudrocks, containing shell fragments and locally displaying parallel laminations (C1; **Figure 4a–c** and **Tables 1–2**). Sharp contacts are observed at both the base and top of the C1 with either the C2 or the C3 within FA1, while locally, the top surface is truncated by an erosional contact with the S1 of the FA2 (see **Figure 3**).

Facies C2 is observed in alternation with the calcareous mudrock of C1 within FA1 (see **Figure 3** and **Tables 1–2**). The C2 is defined by up to approximately 0.5 m thick, greenish light grey, well-sorted, rounded, very fine- to fine-grained calcareous sandstones containing glauconite and displaying internal parallel and ripple laminations (see **Figure 4d**). Sharp contacts are present at both the base and top of the C2, with the adjacent C1 within FA1.

The final facies within the FA1 is the C3, occurring as alternations with C1 (see **Figure 3** and **Tables 1-2**). It is

Table 1. Sedimentary facies of the Ombilin Formation

Facies name and code	Textures	Thickness (m)	Sedimentary structure	Trace fossils and biota	Interpretation
Calcareous, massive mudrock (C1)	Dark grey, lime mudrock, showing silt-grained mudrock (Fig. 9a-c).	0.3-8 m thick.	Structureless	Shell fragments	Combination of breakdown of calcareous bioclast (**Pratt, 2010**), suspension, and/or dynamic process of long-distance horizontal transport of mud aggregates (**Plint, 2010**).
Calcareous, ripple-stratified sandstone (C2)	Greenish light grey, rounded and well sorted, very fine to medium-grained sandstone, containing glauconite and bioclasts.	0.1 - 0.5 m thick	Parallel-, and commonly symmetric ripple laminations		Combination of breakdown of calcareous bioclasts and episodic oscillatory current (**e.g. Pratt, 2010**). The glauconite reflects the boundary condition of oxidizing seawater and reducing interstitial water at depths of down to 60 m (**e.g. Odin and Matter, 1981**).
Stratified limestone (C3)	Horizontally stratified, grain-supported, fine to medium-sized sandy skeletal limestone, being classified as packstone	up to 1.5 m thick	Parallel stratification		Depositional product of a deep ramp of a shallow carbonate platform, being controlled by subtidal cycles (**Jones, 2010**).
Amalgamated sandstone (S1)	Reddish brown, sub-rounded to rounded, poorly sorted, gravel-grained conglomerates. The conglomerates contain igneous rocks and mud clasts that contain plant and/or coal fragments	Up to 0.8 m thick; occurring close to the base of the sedimentary bed.	Vertically amalgamated and fining upward. Internally show coal stringer and parallel lamination at the top.	Plant fragments	Basal gravel-grained conglomerate reflects lag deposits, being related to migration of channel thalweg and dunes (**e.g. Plink-Bjorklund, 2005; Fakhruddin et al., 2023**). The amalgamated geometry indicates a high rate of sedimentary discharge (**e.g. Boggs, 2014**). The parallel lamination reflects the transition of upper flow into lower flow regime (**Boggs, 2014**). The laminated mudrock deposited due to suspension, while coal stringer reflects rapid accumulations of plant fragments and peats (**Plink-Bjorklund, 2005**).
	Reddish brown, sub-rounded to rounded, poorly sorted, fine to coarse-grained sandstones.	Up to 0.7 m thick.			
	White grey, claystone.	Laminated up to 1 cm thick; occurring at the top of the sandstones.			
Interbedded sandstone and mudrock (S2)	Reddish brown, sub-angular to sub-rounded, poorly sorted, fine to coarse-grained sandstones.	Up to 0.6 m thick.	Parallel lamination	-	Planar bed flows of the upper flow regime in point bars (**e.g. Plink-Bjorklund, 2005; Boggs, 2014**).
	Light yellowish grey, silt-grained mudrock, locally shows coal stringers.	Up to 0.3 m thick.			
Massive sandstone (S3)	Reddish brown, medium to thick bed, sub-rounded to rounded, poorly sorted, broadly fine to coarse-grained sandstones.	Up to 7 m thick.	Structureless	Occasionally plant fragments; Locally shell fragment.	High and rapid depositional rates and various intensity of high concentration and energy in depositional environments (**e.g. Olariu et al., 2010; Fakhruddin et al., 2023**).
Cross-stratified sandstone (S4)	Reddish brown to yellowish grey, sub-rounded to rounded, poorly sorted, fine to coarse-grained sandstones.	0.3-0.6 m thick.	Planar and herringbone cross stratifications	-	Planar cross-stratifications reflect downstream migration of 2D dunes and/or migration of longitudinal bars in channels; Herringbone cross-stratifications reflect migration of 3D dunes in channels, bidirectional currents of approximately equal strength (**e.g. Plink-Bjorklund, 2005; Fakhruddin et al., 2023**).

Table 1. Continued

Facies name and code	Textures	Thickness (m)	Sedimentary structure	Trace fossils and biota	Interpretation
Heterolithic bedding (S5)	Yellowish grey, rounded and well sorted of laminated and/or thin beds of reddish brown, fine to coarse-grained sandstone; Locally show coal stringers.	Laminated sandstones alternating with mudrock; Both occurs of up to 0.1 m thick.	Wavy lamination and/or flaser	Plant fragments	Depositions from reversing tidal currents (**Reineck and Singh, 1980**), suggesting an intertidal succession of decreasing current energy (**e.g. Dalrymple, 1992**).
	Light yellowish grey, claystone.				
Ripple-stratified sandstone (S6)	Yellowish grey, sub-rounded to rounded, poorly sorted, fine to coarse-grained sandstones	Up to 0.4 m thick.	Locally parallel and commonly symmetric ripple laminations	*Skolithos* and *Laevicyclus*	Symmetric rippled stratifications represent lower flow regime (**e.g. Simons and Richardson, 1963; Boggs, 2014; Fakhruddin et al., 2023**), being deposited during maximum tidal flow (**e.g. Plink-Bjorklund, 2005**); The locally parallel lamination reflects deposition from traction current (**e.g. Boggs, 2014; Plink-Bjorklund, 2005**). The *Skolithos* and *Laevicyclus* indicates deposition in shallow marine and/or nearshore environments, being influenced by tidal currents (**e.g. Desjardins et al., 2012; Knaust et al, 2018**).
Massive mudrock (S7)	Light yellowish grey, silt-grained mudrock. Locally show coal stringers.	Up to 2.7 m thick.	Structureless	-	Depositions from suspensions in low-energy environments (**e.g. Santos and Rossetti, 2006; Fakhruddin et al., 2023**).

characterized by up to 1.5 m thick, yellowish light grey, grain-supported, presence of carbonate mud, horizontally stratified limestone (see **Figure 4c**). Their character of grain-supported with carbonate mud is shown, suggesting packstone of **Dunham's (1962)** classification. Sharp contacts are observed at both the top and base of the C3 with the adjacent C1 facies within FA1 (see **Figures 3** and **4c**).

4.1.2. Facies Association 2 (FA2)

The FA2 is composed of four lithofacies, typically represented by alternations of amalgamated sandstone (S1), interbedded sandstone and mudrock (S2), massive sandstone (S3), and/or cross-stratified sandstone (S4) (see **Figure 3** and **Table 2**). The lithofacies S1 occurs interbedded with the S3 and/or the S4 and is characterized by conglomerate beds at the base, overlain by fining-upward, amalgamated sandstones (S1; **Figure 5a–c** and **Table 1-2**). The conglomerates, up to approximately 0.8 m thick, are reddish-brown, poorly sorted, and composed of sub-rounded to rounded gravel clasts, including igneous rock and mudrock fragments with plant remains and coal (see **Figure 6a**). The overlying sandstones are up to 0.7 m thick, reddish-brown, and similarly poorly sorted, containing fine- to coarse-grained, sub-rounded to rounded grains. Parallel lamination and local laminated mudrock and coal stringers occur at the top of the sandstone beds (see **Figure 6b**), with white-grey claystone being up to 1 cm thick. The basal contact of the S1 is typically erosional against the S2 and the S3 of the FA2, or calcareous mudrock (C1) of the FA1, but is sharp against the S4 within the FA2 (see **Figure 3**). Its overlaying contact is sharp with either S3 of the FA2 or the heterolithic bedding (S5) of Facies Association 3 (FA3).

Lithofacies S2 is defined by interbedded sandstone and mudrock and occurs alternating with S3 and/or S4 (S2; **Figures 3, 5b, d,** and **Tables 1-2**). The sandstones reach up to 0.6 m thick, are reddish-brown, poorly sorted, and composed of fine- to coarse-grained, sub-angular to sub-rounded particles, exhibiting parallel lamination (see **Figure 5b, d**). The mudrocks, up to 0.3 m thick, are light yellowish, massive, and composed of silt-grained materials. The basal contact of the S2 is sharply defined against the underlying S1, the S3 of the FA2, or the S5 of the FA3. The upper boundary of the S2, however, is sharp against the overlying S3 of the FA2 or ripple-laminated sandstones (S6) and massive mudrocks (S7) of the FA3 (see **Figure 3**).

Lithofacies S3 is defined by massive and structureless sandstones and occurs either as a singular facies or in alternation with S1, S2, and/or S4 (S3; **Figures 3, 5a, e,** and **Tables 1-2**). This lithofacies S3 is characterized by reddish-brown, massive, poorly sorted sandstones, up to 7 m thick, composed of fine- to coarse-grained, sub-rounded to rounded particles. The basal contacts of the S3 are sharply defined against the S1, the S2, or the S4 of the FA2, and the S7 of the FA3 (see **Figure 3**). The

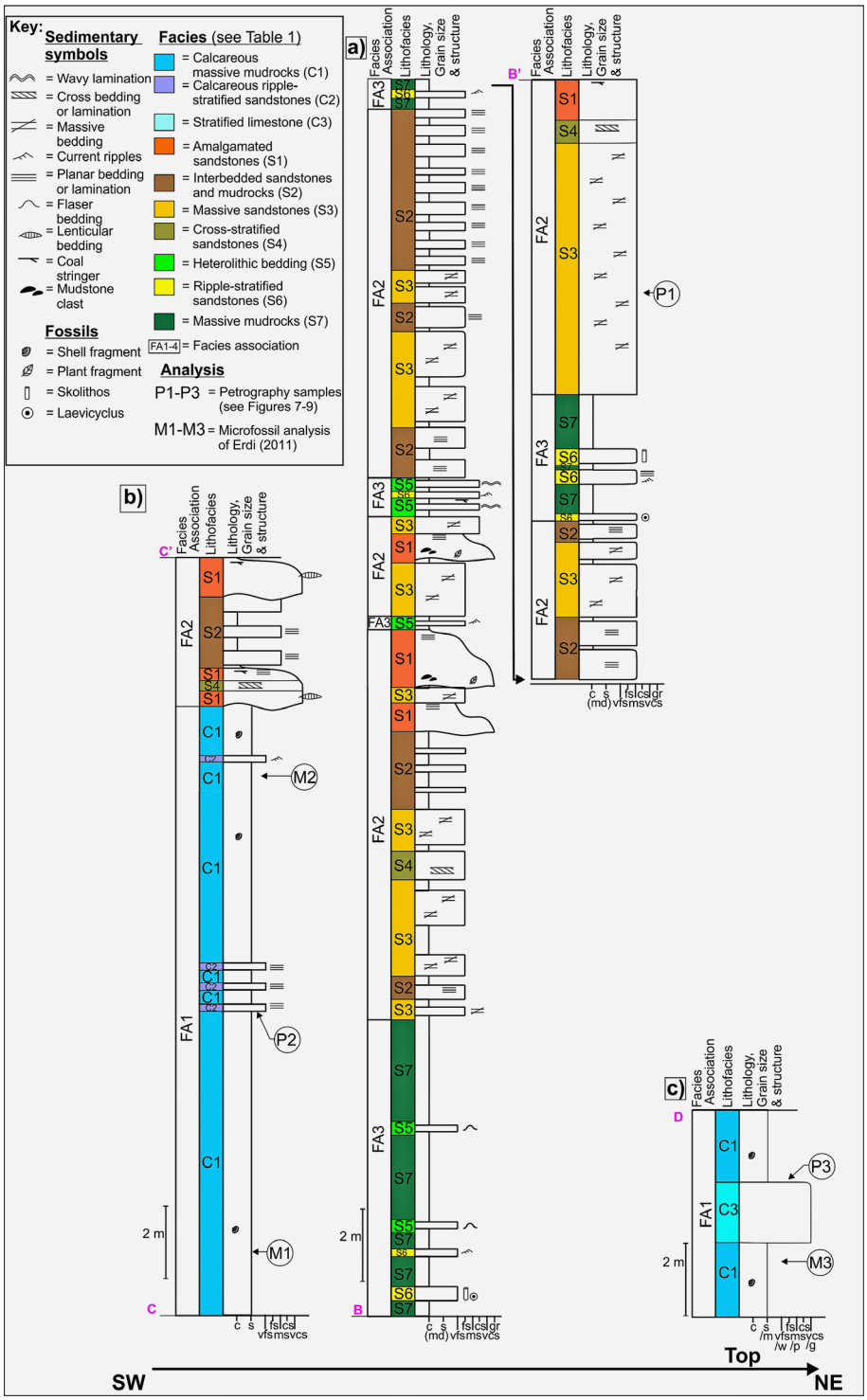


Figure 3. Sedimentary log of the Ombilin Formation in this study, being measured in Wali Nagari Bukit Bual, Sijunjung Province in section B-B' and D-D' (a, c) and Sungai Batang Ombilin in section C-C (b). Strike-projection of the measured log in **Figure 1b** onto A-A' section (see **Figure 1c**) shows that the measured log of C-C', B-B' and D reflect the Ombilin Formation from bottom to top. The petrographic samples are recorded on S_3, C_2, and C_3 for P_1, P_2, and P_3, respectively. The biostratigraphic samples of **Erdi (2011)** are recorded on C_1 for M_1 and M_2.

Table 2. Facies associations (FA) of the Ombilin Formation

Facies Association and code	Lithofacies	Interpretation
Facies Association 1 (FA1)	C1, C2, C2	Open marine
Facies Association 2 (FA2)	S1, S2, S3, S4	Tidal channel
Facies Association 3 (FA3)	S5, S6, S7	Mixed tidal flat

upper contacts of the S3 are also sharp, occurring against the S2 or the S4 of the FA2, or the S5 and the S7 of the FA3. Still, the S3 locally has erosion contact with the overlying S1 sandstones of the FA2.

The final facies within the FA1 is represented by lithofacies S4, being defined as cross-stratified sandstones and observed in alternation with S1, S2, and/or S3 (see **Figure 3** and **Tables 1-2**). This lithofacies S4 is characterized by reddish-brown, poorly sorted, fine- to coarse-grained sandstones up to 0.6 m thick, composed



Figure 4. Field photographs illustrating the characteristics of facies association 1 (FA1), showing: (a) thick sequence of calcareous mudrock (C1); (b) presence of shell fragments in the C1; (c) interbedding of the C1 and stratified limestone (C3); (d) presence of calcareous ripple-stratified sandstone (C2).

of sub-rounded to rounded grains (see **Figures 3** and **4e; Table 1**). Planar and herringbone cross-stratifications are present within the sandstones of the S4 (see **Figures 5e** and **6d**). The basal contact is sharp against the S3, while the upper boundary is sharply defined against either the S1 or the S3 within the FA2 (see **Figure 3**).

4.1.3. Facies Association 3 (FA3)

The FA3 is defined by three lithofacies, typically represented by a singular S5, or occasionally by alternations between heterolithic bedding (S5), ripple-laminated sandstones (S6), and/or massive mudrocks (S7; **Figure 3** and **Tables 1-2**). The S5 facies is marked by up to 2 m thick heterolithic bedding, composed of interlaminated sandstones and claystone. The sandstones are characterized by reddish-brown, well-sorted, rounded, fine- to coarse-grained laminations, each up to 1 cm thick, and internally display wavy and flaser bedding (see **Figure 6e; Table 1**). In contrast, the claystone is distinguished by light yellowish-grey, massive, clay-textured laminations of similar thickness. The base of the S5 is bounded sharply by either the S7 of the FA3 or the massive sandstones (S3) of FA2, while the top is typically in a sharp contact with either the S7 of FA3 or the S2 of FA2 (see **Figure 3**). Locally, the top contact is erosional, overlying the S1 of the FA2.

The S6 is made of symmetric ripple-laminated sandstones, typically occurring in alternation with S5 and/or S7 within FA3 (see **Figure 3; Tables 1–2**). This facies is characterized by up to 0.4 m thick, yellowish-grey, poorly sorted, sub-rounded to rounded, fine- to coarse-grained sandstones, internally showing symmetric ripple and parallel laminations, and locally containing abundant bioturbations (see **Figure 6f–h**). The bioturbations show cylindrical burrows of up to 0.5 cm in diameter, filled with fine-grained sand and enclosed by medium- to coarse-grained sands, interpreted as *Skolithos linearis* (**cf. Knaust, 2015; Knaust et al., 2018; Figure 6g**). Other bioturbations consist of cylindrical burrows with fine-grained sandy cores and surrounded by fine- to medium-grained friable sandstone, resembling *Laevicyclus*

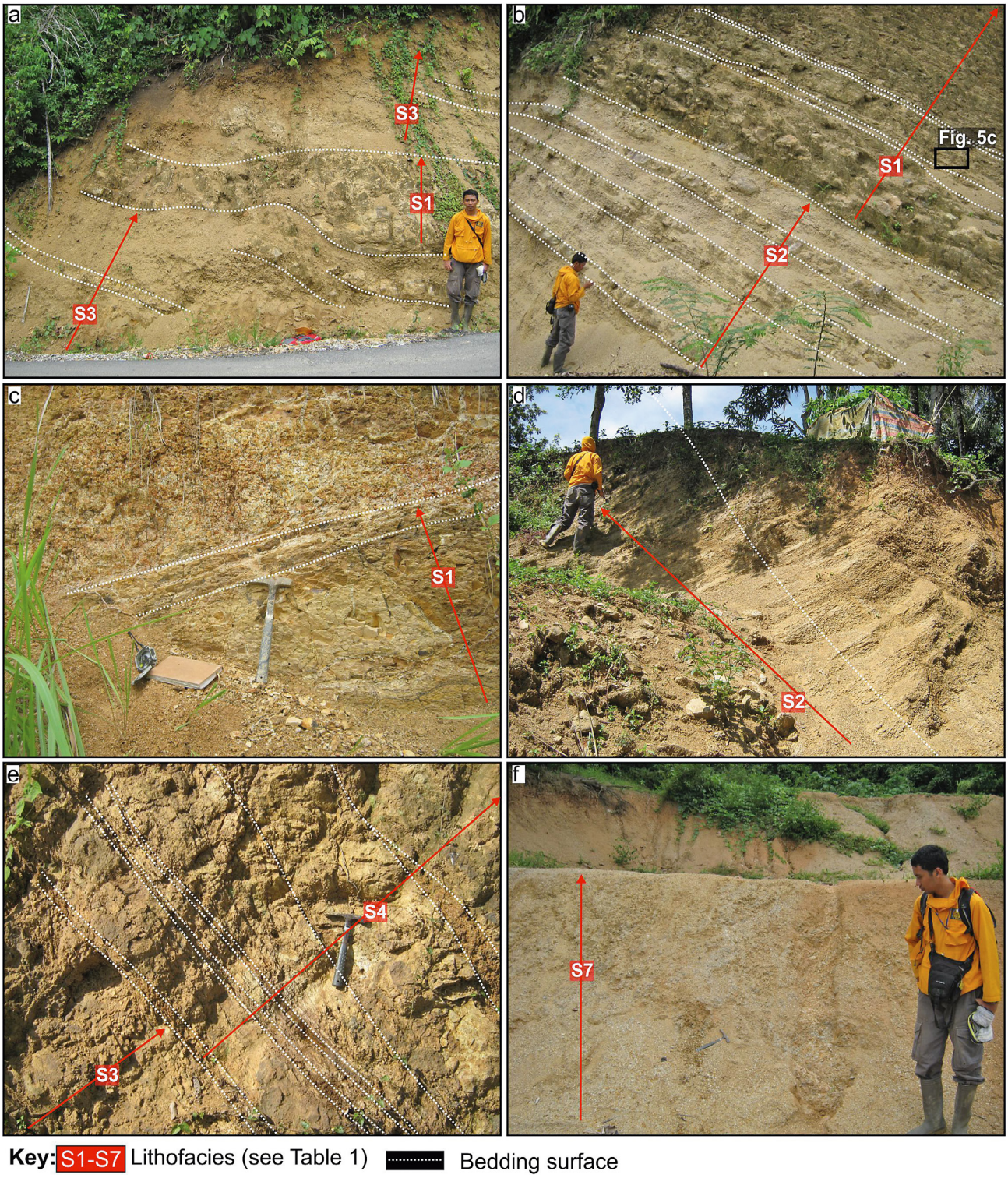


Figure 5. Field photographs illustrating the characteristics of: (a-e) facies association 2 (FA2) that consists of amalgamated sandstone (S1), interbedded sandstones and mudrocks (S2), massive sandstones (S3), cross-stratified sandstones (S4), and (f) facies association 3 (FA3) that consists of massive mudrocks (S7).

parvus (**cf. Knaust, 2015; Knaust et al., 2018; Figure 6h**). The base of the S6 is marked by a sharp contact with the S7 of FA3, while the top contact is sharp against either the S3 of FA2 or the S7 within FA3 (see **Figure 3**).

The final facies identified within FA3 is the S7, which is composed of massive mudrock (S7; **Figures 3, 5f,** and **Tables 1-2**). This facies alternates with S5 and S6. The S7 is characterized by up to 3 m thick, light yellowish-grey, massive, silt-grained mudrock. The base of the S7 is marked by a sharp contact with either the S2 or S3 of FA2, or with S5 or S6 within FA3. The top of the S7 is also similarly bounded by sharp contacts

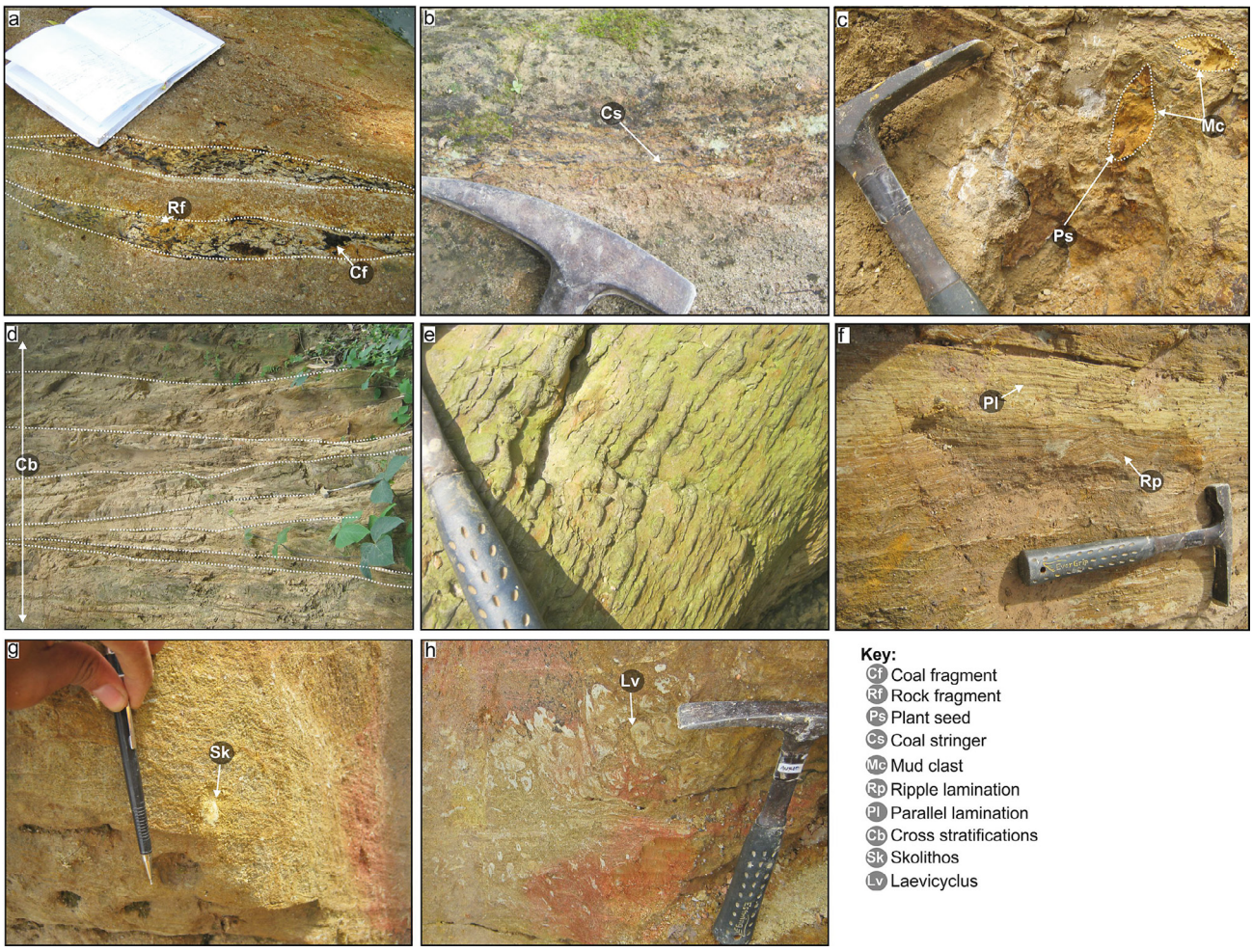


Figure 6. Characteristics of facies association 2 (FA2) and facies association 2 (FA3). The FA2 is characterized by: (a) mud clasts, including coal fragments, in S1; (b) parallel lamination with coal stringer in S1; (c) plant fragment in S1; and (d) herringbone structures in S4. The FA2, however, is characterized by: (e) flaser bedding in S5; (f) parallel and symmetric ripple laminations in S6; and trace fossils in S6 such as (g) *Skolithos* and (h) *Laevicyclus*.

with the S3 of FA2 or with S5 or S6 within FA3 (see **Figure 3**).

4.2. Petrography of the Ombilin Formation

Petrography analyses were conducted to unravel the texture and composition of sandstone and limestone in the Ombilin Formation. Three selected petrography analysis was presented, given these three samples reflect non-calcareous, sand-rich sediment, sandy calcareous sediments, and limestone. Petrography of non-calcareous, sand-rich sediment was reflected by the S3. On the other hand, the petrography of sandy calcareous sediments was illustrated by C2, while the limestone was reflected by the C3.

4.2.1. Petrography of C2

Petrographic analysis of the C2 facies within the FA1 was performed to determine the texture and composition of calcareous, ripple-stratified sandstones in the Ombilin Formation (P2; **Figure 3**). The C2 is consists of averages of 0.8% quartz, 30.8% feldspar, 5.3% lithic fragments, 30.1% bioclasts, 23.7% accessory minerals, 2.4% silicate minerals, 4.8% matrix, and 2.1% cement (see **Figure 7; Table 3-4**). Grain sizes range from 0.1 to 0.45 mm, indicating a very fine- to medium-grained sandstone according to **Wentworth's (1922)** classification.

Detrital minerals in the C2, including quartz, feldspar, and lithic fragments, exhibit compositional variability (see **Figure 7; Table 3**). The quartz is generally rare, with some samples completely lacking it. When present, the quartz contains monocrystalline grains. Feldspar, however, dominates the detrital framework. These grains are sub-rounded and usually display linear or point contacts. Lithic fragments are mostly of volcanic origin, characterized by sub-angular to sub-rounded shapes and long contacts with adjacent grains (see **Figure 7e–f**). Normalized point counting was conducted to determine percentages of QFL compositions in the C2, showing feldspar, quartz, and lithic fragments average making up 77.3%, 1.4% and 21.27% of the framework, respectively (see **Table 5**).

Table 3. Summary of composition and texture of petrography from the Ombilin Formation.

Sample	Composition		Textures and features
Calcareous, ripple-stratified sandstone (C2)	Quartz		Grain size: from 0.1 to 0.2 mm (very fine- to fine-grained)
			Shape: mostly sub-rounded
			Strained: high strained
			Contact: linear and point contact
	Feldspar		Grain size: from 0.1 to 0.45 mm (very fine- to medium-grained)
			Shape: mostly sub-rounded
			Contact: linear and point contact
	Lithic fragments	Volcanic fragment	Grain size: from 0.3 to 0.4 mm (medium-grained)
			Shape: sub-angular to sub-rounded
			Contact: long contact
	Bioclast		Grain size: from 0.18 to 0.3 mm (fine- to medium-grained)
			Occurrences: foraminiferal skeletal fragments
	Accessory mineral	Glauconite	Grain size: average of 0.2 mm (fine-grained)
			Occurrences: act as grains; commonly interlock with feldspars
		Chlorite	Grain size: average of 0.2 mm (fine-grained)
			Occurrences: as detrital monomineralic grains
	Silicate mineral	Pyroxenes	Grain size: average of 0.2 mm (fine-grained)
			Occurrences: act as grains; commonly form prismatic shape
	Matrix	Calcite	Occurrences: filling intergranular pore spaces; locally replaces bioclast shells
	Cement		
Stratified limestone (C3)	Quartz		Grain size: from 0.08 to 0.2 mm (very fine- to fine-grained)
			Shape: rounded
			Strained: moderate-high strained
			Contact: linear and point contact
	Feldspar		Grain size: from 0.08 to 0.2 mm (very fine- to fine-grained)
			Shape: rounded
			Contacts: linear and point contacts
	Bioclast		Grain size: from 0.18 to 0.3 mm (fine- to medium-grained)
			Occurrences: foraminiferal skeletal fragments
	Calcite		Occurrences: replacement of bioclast material
	Micrite		Occurrences: filling intergranular pore spaces
	Sparry calcite		
Massive sandstone (S3)	Quartz		Grain size: from 0.3 to 0.5 mm (fine- to coarse-grained)
			Shape: mostly sub-rounded
			Strained: moderate-high strained
			Contacts: linear and concave-convex contacts
	Feldspar		Grain size: from 0.2 to 0.6 mm (fine- to coarse-grained)
			Shape: sub-angular to sub-rounded; prismatic shapes
			Contacts: linear contacts
	Lithic fragments	Volcanic fragment	Grain size: from 0.4 to 0.6 mm (medium- to coarse-grained)
			Shape: sub-angular to sub-rounded
			Contacts: linear contacts
	Accessory Mineral	Muscovite	Grain size: from 0.2 to 0.3 mm (fine- to medium-grained)
			Shape: sub-rounded to rounded
			Alterations: expanding into pore spaces and grow from grains
		Opaque	Occurrences: commonly as coating and stains on quartz grains
	Matrix	Very fine lithic fragment and clay minerals	Occurrences: fill pore spaces and occur as coating on grains
	Cement	Very fine calcite	Occurrences: cement-filling grain contacts
		Very fine muscovite	
		Oxide mineral	

Table 4. Summary of point counting results of compositions in petrography samples from the Ombilin Formation. The compositions for sandstones are defined for **Zuffa (1980)** scheme. The Zuffa code reflect non-carbonate extrabasinal (NCE), carbonate intrabasinal (CI), non-carbonate intrabasinal (NCI), carbonate matrix (CMt), carbonate cement (CCm) and non-carbonate cement (NCCm).

Sample	Composition		Proportion (%)			Average (%)	Classifications of Zuffa (1980)		
			Sub-Sample						
			1	2	3		Spatial	Compositional	Zuffa (1980) code
Calcareous, ripple-stratified sandstone (C2)	Quartz		0	2	0.4	0.8	Extrabasinal	Non-carbonate	NCE
	Feldspar		31	30.6	30.8	30.8	Extrabasinal	Non-carbonate	NCE
	Lithic fragments	Volcanic fragment	5.5	5	5.4	5.3	Extrabasinal	Non-carbonate	NCE
	Bioclast		30.8	29.5	30	30.1	Intrabasinal	Carbonate	Cl
	Accessory mineral	Glauconite	20	21.4	20.5	20.63	Intrabasinal	Non-carbonate	NCl
		Chlorite	3	2.2	4	3.07	Extrabasinal	Non-carbonate	NCE
	Silicate mineral	Pyroxenes	2.7	2.5	2	2.4	Extrabasinal	Non-carbonate	NCE
	Matrix	Calcite	5	4.6	4.8	4.8	Intrabasinal	Carbonate	CMt
	Cement		2	2.2	2.1	2.1			CCm
Stratified limestone (C3)	Quartz		7			7			
	Feldspar		3			3			
	Bioclast		20			30			
	Calcite		20			10			
	Micrite		35			35			
	Sparry calcite		15			15			
Massive sandstone (S3)	Quartz		8.6	10.7	10.4	9.9	Extrabasinal	Non-carbonate	NCE
	Feldspar		58.6	57.8	55.1	57.17	Extrabasinal	Non-carbonate	NCE
	Lithic fragments	Volcanic fragment	15.6	14.8	12.3	14.23	Extrabasinal	Non-carbonate	NCE
	Accessory Mineral	Muscovite	3.2	2.3	3.9	3.13	Extrabasinal	Non-carbonate	NCE
		Opaque	5	7	6	6	Intrabasinal	Non-carbonate	NCl
	Matrix	Very fine lithic fragment and clay minerals	2	2.4	5	3.13	Extrabasinal	Non-carbonate	NCE
	Cement	Very fine calcite and muscovite	2	2.8	3	2.6	Intrabasinal	Carbonate and non-carbonate	CCm and NCCm
		Oxide	5	2.2	4.3	3.83	Intrabasinal	Non-carbonate	NCCm

Table 5. Average of normalized point counting results (percentage) for Petrographic sample from the Ombilin Formation.

Facies	Sample Number	Q	F	L	Avg. Q	Avg. F	Avg. L	Qm	Qp	Avg. Qm	Avg. Qp
C2	1	0	76.8	23.2	1.4	77.3	21.27	0	0	1.4	0
	2	3.1	78	18.9				3.1	0		
	3	1.1	77.2	21.7				1.1	0		
S3	4	9.8	73.3	16.9	11.67	70.87	17.5	8.2	1.6	9	2.6
	5	12.7	71.5	15.8				9.6	3.1		
	6	12.4	67.8	19.8				9.2	3.2		

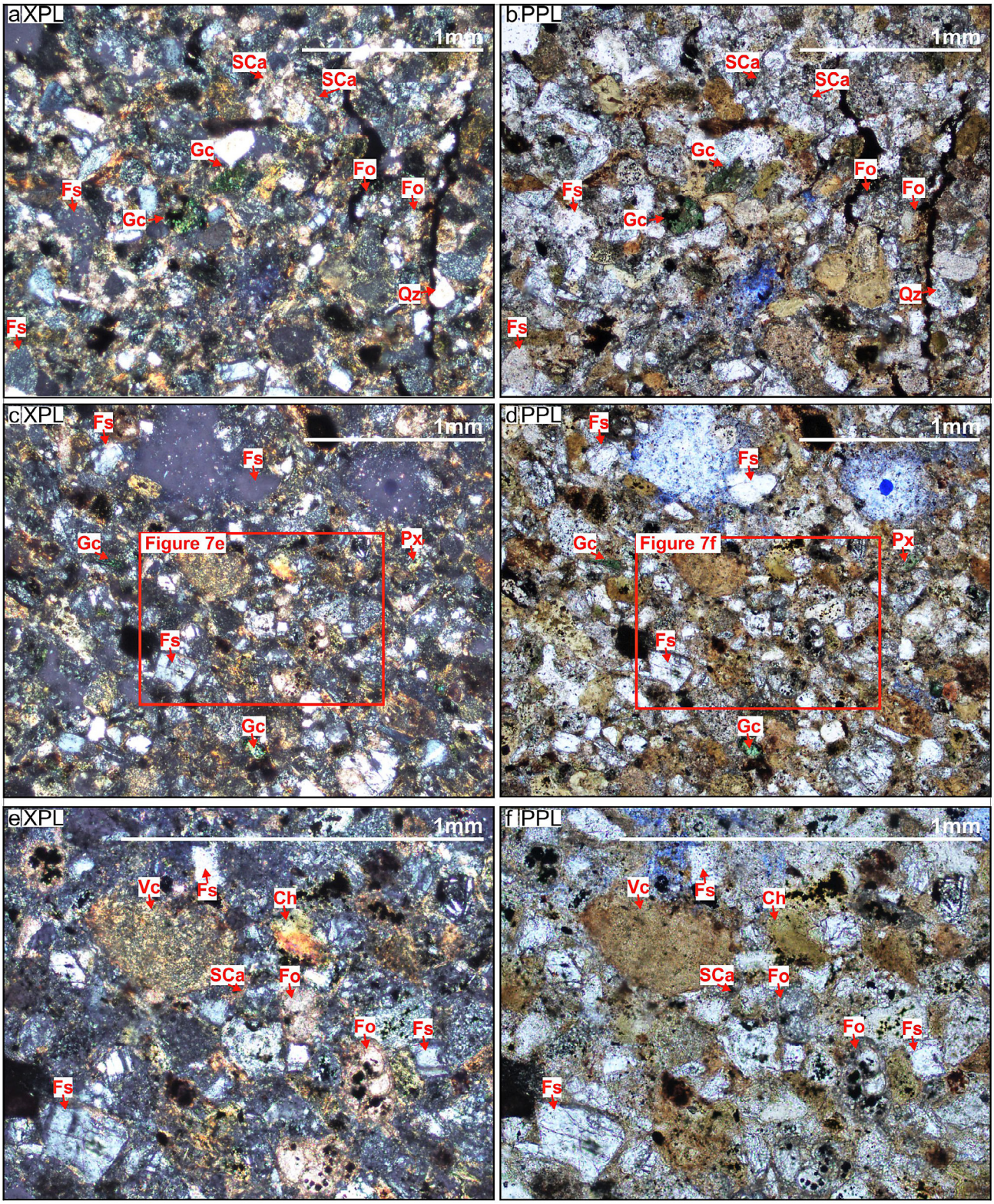


Figure 7. Photomicrographs from thin sections of calcareous ripple-stratified sandstones (C2) of facies association 1 (FA1) in the Ombilin Formation, being taken from P2 (see **Figure 3**). The thin sections show (a) cross- and (b) parallel- polarized with 10x magnifications, showing the characteristic of the C2. The C2 in (a) and (b) composed of quartz (Qz), feldspar (Fs), bioclast (Fo), glauconite (Gc) and sparry calcite (SCa). The thin sections also show (c) cross- and (d) parallel-polarized with 10x magnifications, and (e) cross- and (f) parallel-polarized with 25x magnifications. The (c-f) show volcanic fragments (Vr), chlorite (Ch), and pyroxene (Px) along sparry calcite (SCa).

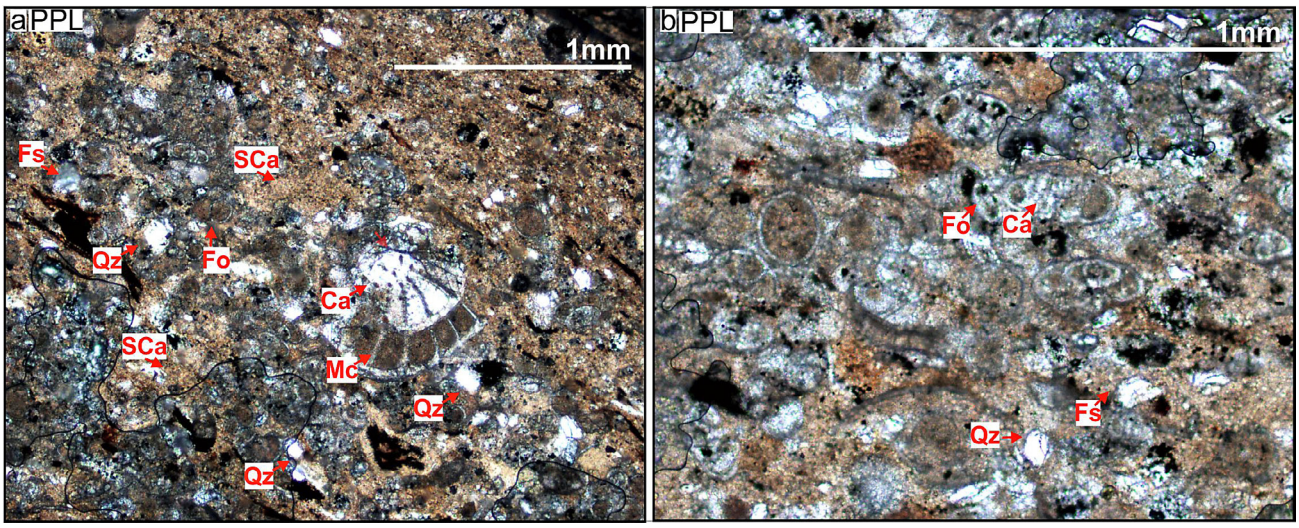


Figure 8. Photomicrographs from thin sections of stratified limestone (C3) of facies association 1 (FA1) in the Ombilin Formation, being taken from P3 (see **Figure 3**). The thin sections show parallel-polarized with (a) 10x and (b) 25x magnifications. The C3 is composed of quartz (Qz), feldspar (Fs), bioclast (Fo), calcite (Ca), along micrite (Mc) and sparry calcite (SCa) that fill the spaces between grains.

Bioclast fragments are abundant in lithofacies C2, with average grain sizes ranging from 0.3 mm to 0.18 mm. The bioclasts are primarily composed of foraminiferal skeletal fragments (see **Figure 7a-b, e-f**).

Accessory and silicate minerals are also present in the C2 (see **Figure 7**). The accessory minerals are dominated by glauconite and chlorite. Glauconite grains account for an average of 20.63% of the total framework content and average 0.2 mm in grain size (see **Table 3-4**). The chlorite, however, occurs as detrital monomineralic grains, averaging 3.07% of the total framework and also averaging 0.2 mm in size. These grains commonly interlock with feldspars. Silicate minerals are present in minor amounts, primarily represented by pyroxenes, which average 0.2 mm in grain size (see **Figure 7c–d**).

The matrix and cement are present for an average of 4.8% and 2.1% respectively, showing a ratio of 2 : 1 (see **Table 4**). They are predominantly composed of calcite (see **Figure 7**). The calcite commonly fills interstitial spaces between grains, but also locally replaces bioclast shells, contributing to the diagenetic fabric of the C2 facies.

4.2.2. Petrography of C3

Petrographic analysis of the C3 facies within FA1 was conducted to determine the texture and composition of limestone in the Ombilin Formation (P3; **Figure 3**). The C3 is identified as a poorly sorted, rounded grain, very fine to coarse calcarenite (0.08 to 0.7 mm) limestone, composing of approximately 20% bioclasts, 20% calcite, 10% detrital minerals, 35% micrite, and 15% sparry calcite of cement (see **Figure 8; Table 3-4**). Following **Folk (1959; 1980)** classification, the limestone is classified as intrasparite.

Bioclasts and calcite represent the most abundant components (see **Figure 8**). Although most bioclasts are difficult to identify taxonomically, some are interpreted as debris and skeletal fragments of foraminifera (**c.f. Flugel, 2004**). Calcite commonly appears as a replacement of bioclast material, indicating diagenetic alteration.

Detrital components are primarily represented by monocrystalline quartz of up to 7% and feldspar of up to 3% (see **Figure 8; Table 4**). These grains contribute to the minor clastic input within the limestone. Micrite and sparry calcite, however, are also significant, together comprising half of the rock volume, predominantly filling the spaces between grains, and contributing to the overall fabric and lithification of the C3 facies.

4.2.3. Petrography of S3

Petrographic analysis of the S3 facies within the FA2 was conducted to characterize the texture and composition of non-calcareous sandstones in the Ombilin Formation (P1; **Figure 3**). The S3 is primarily composed of quartz (average of 9.9%), feldspar (average of 57.17%), lithic fragments (average of 14.23%), accessory (average of 9.13%), matrix (average of 3.13%), and cement (average of 6.43%) (see **Figure 9; Table 3-4**). Grain sizes range from 0.2 to 0.6 mm, indicating a fine- to coarse-grained sandstone of **Wentworth's (1922)** classification.

The petrographic analysis revealed that the detrital framework in the S3 is dominated by feldspar, followed by quartz and lithic fragments, each showing diverse morphometric characteristics (see **Figure 9**). Feldspar is characterized by sub-angular to sub-rounded grains, prismatic shapes, and linear contacts with adjacent grains. Quartz is mostly sub-rounded and exhibits linear to convex-concave contacts with one another. Lithic fragments are predominantly volcanic in composition. The volcanic grains are sub-angular to sub-rounded and

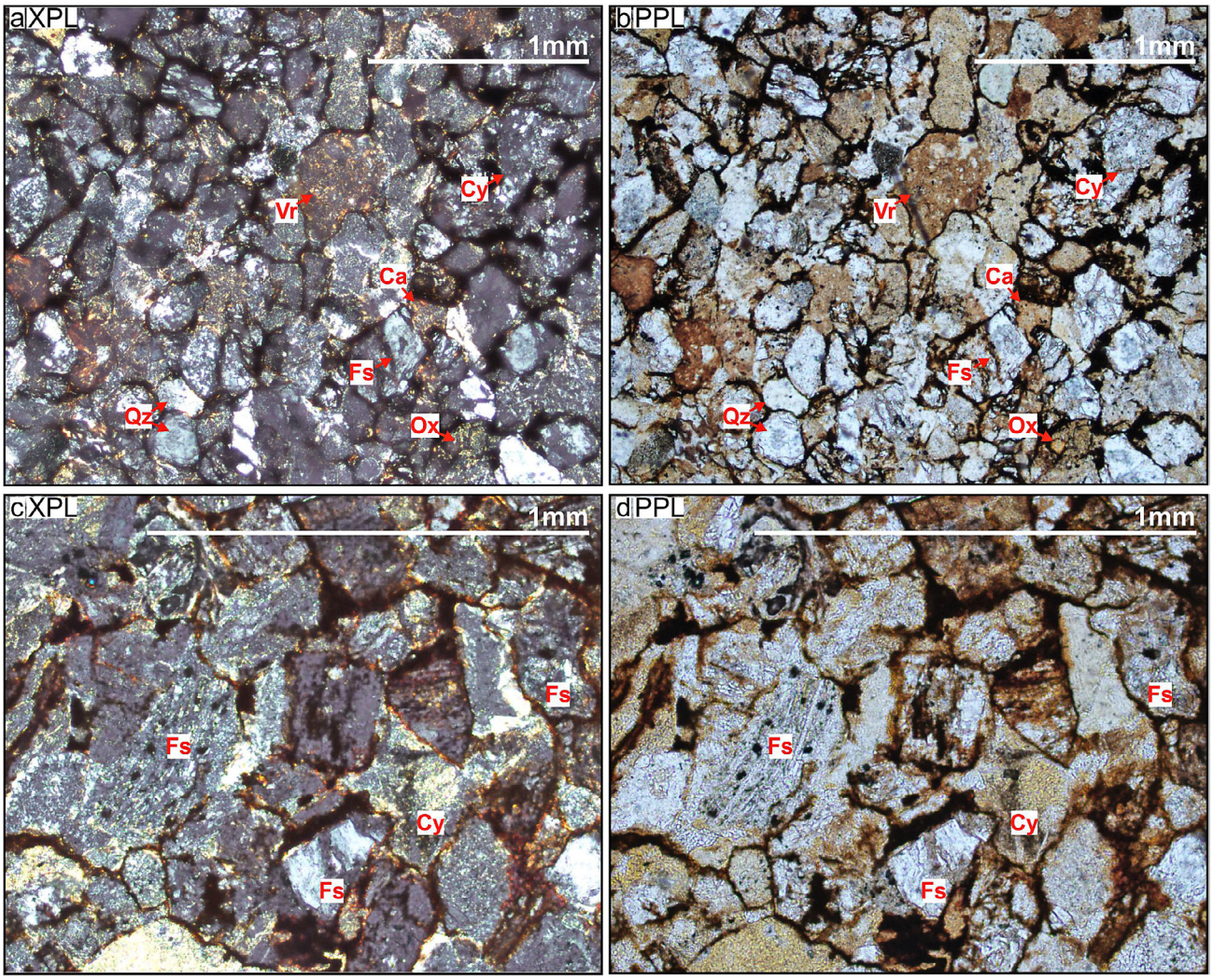


Figure 9. Photomicrographs from thin sections of massive sandstone (S3) of facies association 2 (FA2) in the Ombilin Formation, being taken from P1 (see **Figure 3**). The thin sections show (a) cross- and (b) parallel-polarized with 10x magnifications, and (c) cross- and (d) parallel-polarized with 25x magnifications. The S3 composed of quartz (Qz), feldspar (Fs), volcanic fragments (Vr) and clay (Cy) as matrix, and calcite (Ca) and oxide grains (Ox) as cements.

exhibit linear contacts with neighbouring grains. Normalized point counting was conducted to determine the percentage of QFL framework compositions in the S3. The framework compositions show that the feldspar, quartz, and lithic fragments average 70.87, 11.67, and 17.5% respectively (see **Table 5**). The quartz contains an average of 9% monocrystalline and 2.6% polycrystalline grains.

Accessory minerals include muscovite and opaque minerals (see **Figure 9**). Muscovite occurs with an average of 3.13%, while opaque minerals are present with an average of 6% of the sample. They commonly appear as coatings and stains on quartz grains.

The matrix and cement are present in relatively minor concentrations with an average of 3.13% and 6.43% respectively, showing the ratio of 1 : 2 (see **Figure 9**). The matrix consists of very fine lithic fragments and clay minerals, whereas the cement is mostly composed of very fine calcite, muscovite and oxide minerals. Both components fill pore spaces and occur as coatings on grains, contributing to the overall textural maturity of the S3.

5. Discussions

5.1. Sedimentology of the Ombilin Formation

The three facies that have been described above have been interpreted, indicating three depositional environments. The interpretations are described below.

5.1.1. Sedimentology of FA1: open marine

5.1.1.1. Lithofacies and facies association of FA1

The sedimentary processes and depositional environments of the FA1 have been inferred from the lithological characteristics, petrographic features, and sedimentary structures observed in C1 to C3. The character of lithology in the FA1 consists of calcareous, massive

mudrock (C1), calcareous, ripple-stratified sandstone (C2), and stratified limestone (C3). The C1 and C2 are similarly observed in Sinamar-1, showing calcareous sandstone and calcareous marine-dominated sediments (see **Figure 2; Koning, 1985**).

The fine-grained nature of the calcareous mudrock in the C1 is interpreted in this study as products of suspension setting under low-energy conditions (**e.g. Boggs, 2014; Fakhruddin et al., 2023**), and/or from long-distance horizontal transport of clay aggregates by dynamic processes (**Plint, 2010**). The calcareous composition of these sediments has been attributed to the breakdown of calcareous bioclasts (**Prat, 2010**). Still, the sparry calcite in petrography C3 was formed by precipitation from carbonate solution. Interpretation of the C1 is consistent with previous studies, showing biostratigraphic analysis of the C1 (M1–M3; **Figure 3**), suggesting a littoral marine setting (**Erdi, 2011; Loeblich and Tappan, 1994**), where it was located between high- and low-tide levels (**Hedgpeth, 1957**).

The calcareous ripple-stratified sandstone of the C2 is characterized by the presence of parallel and ripple laminations. These structures have been interpreted as indicators of contrasting flow regimes, with parallel lamination reflecting deposition under upper flow regime conditions, and ripple lamination indicating lower flow regime (**e.g. Simons and Richardson, 1963; Boggs, 2014**). The coexistence of both structures has been attributed to weak and episodic oscillatory currents operating in shallow marine environments (**Pratt, 2010; Longhitano et al., 2021**). Additionally, the occurrence of glauconite within the C2 has been interpreted as a product of early diagenesis, formed under conditions of oxidizing seawater and reducing pore water at depths reaching approximately 60 meters (**e.g. Odin and Matter, 1981; Rubio and Lopez-Perez, 2024**). When considered alongside the fine-grained nature of the sandstone, the presence of glauconite suggests deposition in a lower to middle shoreface setting. This interpretation aligns with analogues of glauconite-bearing very fine sands in shoreface environments, such as those observed along the coast of Rio Grande do Sul (**Plint, 2010**) or Lublin Basin, Poland (**Starzec et al., 2023**).

Within the FA1, the occurrence of the packstone has been identified in the C3. Petrographic observations are suggested for the C3 as intrasparite, that has high in allochemical rock and intraclast compositions, suggesting a shallow depth with sea level fluctuations of calm and high energy environment (**Folk, 1959; 1980**). Given this petrographic observation that suggest sea level fluctuations, this packstone of the C3 has been interpreted as having been deposited on the subtidal part of a carbonate ramp environment. This interpretation is also consistent with analogous occurrences of packstone in Utah, where it is distributed as subtidal cycles within carbonate ramps (**Jones, 2010**), and by Mesozoic packstone successions in Western Newfoundland and Southern Australia, where it is commonly found as a subtidal deposit (**e.g. James and Bone, 1994**; **Pratt, 2010**). The interpretation of the subtidal part of a carbonate ramp environment for the C3 is aligned with biostratigraphic data of the Ombilin Formation in the Sinamar-1 well, located northeast of Section D, which suggests deposition within a sublittoral marine zone (**Koning, 1985; Figures 1 and 2b**).

5.1.1.2 Vertical distributions and interpretation of FA1

The open marine deposits (FA1) are situated beneath the tidally influenced channels (FA2), as evidenced by an erosional contact between the C1 and the S1 (see **Figure 3**). This stratigraphic relationship is further supported by lateral facies changes, with a transition from mud-prone deposits in the central area (Section C) to sand-prone deposits toward the northeast (Section B; **Figure 1b and 3**). These vertical and lateral facies variations reflect a coarsening trend from the FA3 to the FA1 near Tanjung Ampalu (section C; **Figure 3**), indicating a transition from accumulation of suspended-load fines to bedload-dominated transport of tidal-influenced channel in this area. However, from this point northeastward (section B to D), the vertical and lateral facies show an inverse transition, illustrated by the bedload-dominated transport of tidal-influenced channel near Tanjung Ampalu to the accumulation of suspended-load fines in more distal open marine settings northeastward. The observations of normal and inverse transition are aligned with biostratigraphy data of **Erdi (2011)** and **Koning (1985)**, revealing a northeastward shift from littoral in Section C to sublittoral environments in the Sinamar-1 (c.f. **Figures 1b and 2b**). More particularly to the inverse transition, this observation indicates that transgression likely occurred during deposition of the FA1 in section D, which is likely deposited above FA2 and FA3 in section B (see **Figure 3**).

5.1.2. Sedimentology of FA2: tidal influenced channel

5.1.2.1. Lithofacies and facies association of FA2

The sedimentary processes and depositional environments of the FA2 have been interpreted based on lithological characteristics and sedimentary structures identified within facies S1 to S4. The basal conglomerates of the S1 have been interpreted as representing the early stage of channel development (**e.g. Bentham et al., 1993**). Alternatively, the basal conglomerate originated from lag deposits, being associated with thalweg and dune migration (**e.g. Kleinhans et al., 2002; Plink-Bjorklund, 2005; Fakhruddin et al., 2023**). The presence of coal fragments and mud clasts within these conglomerates have been attributed to erosion and transportation of muddy substrates at the channel base (**Li et al., 2017**), with tidal influence inferred from the abundance of mud clasts, consistent with estuarine fluvial settings

(**Dalrymple, 2010**). The amalgamated geometry of the S1 has been interpreted as an indicator of environments that contain a high rate of sedimentary discharge (**e.g. Boggs, 2014**). The occurrence of massive sandstones in the S3, however, have been interpreted as indicators of an environment that contain high depositional rates and rapid deposition (**e.g. Olariu et al., 2010; Olariu and Bhattacharya, 2006; Fakhruddin et al., 2023**). These S1 and S3 facies have been found in environments, such as tidal channels (**e.g. Plink-Bjorklund, 2005; Dalrymple, 2010**), distributary systems (**e.g. Olariu and Bhattacharya, 2006; Gani and Bhattacharya, 2007**), or delta fronts (**e.g. Olariu et al., 2010; Fakhruddin et al., 2023**). Parallel laminations in the S1 and the S2 have been linked to upper flow regime conditions and turbulent sediment transport (**Paola et al., 1989; Boggs, 2014**), possibly representing planar bed flows in lateral accretion sets (**e.g. Plink-Bjorklund, 2005**). Laminated mudrocks and coal stringers in the S1, alongside interbedded sandstone and mudrock in the S2, have been interpreted as rapid accumulation of organic matter near floodplains or in abandoned channels (**cf. Plink-Bjorklund, 2005**). Furthermore, planar cross-stratified sandstones in the S4 have been associated with dune or bar migration, while herringbone cross-stratification in the S4 has been interpreted as evidence for bidirectional currents and 3D dune migration under tidal influence (**Plink-Bjorklund, 2005; Fakhruddin et al., 2023**). Collectively, the presence of (i) basal conglomerates, which indicate early stage and migration of channels, (ii) amalgamated and massive sandstone, which indicates high energy environments, (iii) herringbone cross-stratified sandstones, which indicate bidirectional currents, support the interpretation that the FA2 represents tidally influenced channel deposits.

5.1.2.2. Vertical distributions and interpretation of FA2

The tidal-influenced channels (FA2) have been observed to overlie either mixed tidal flat deposits (FA3) or open marine deposits (FA1; **Figure 3**). The vertical transition from the mixed tidal flats to the tidally influenced channels has been interpreted as evidence for incision of channel systems into previously established intertidal, mixed tidal flat environments. In contrast, transitions from the open marine to the tidal-influenced channel deposits suggest an increase in sediment supply from proximal sources. Erosional surfaces at the base of these channels, particularly where they overlie the open marine deposits, is an indication of progradation of tidal channels into open marine settings.

5.1.3. Sedimentology of FA3: mixed tidal flats

5.1.3.1. Lithofacies and facies association of FA3

The sedimentary processes and depositional environments of the FA3 have been inferred from the lithological characteristics, sedimentary structures, and bioturbation features of S5 to S7. Wavy and flaser stratifications observed in the S5 have been interpreted as products of deposition by reversing tidal currents (**Reineck and Singh, 1980**), indicative of an intertidal setting characterized by diminishing current energy (**Dalrymple, 1992**). Symmetrical rippled laminations in the S6 have been associated with lower flow regimes (**e.g. Simons and Richardson, 1961; Boggs, 2014**), and are considered to have formed during phases of maximum tidal flow (**e.g. Plink-Bjorklund, 2005; Fakhruddin et al., 2023**). These interpretations are supported by the occurrence of *Skolithos linearis* and *Laevicyclus parvus*, which indicate deposition in shallow marine to nearshore environments under tidal influence (**Desjardins et al., 2012; Knaust et al., 2018**). The presence of *Laevicyclus parvus*, an ichnogenus of *Siphonicnus*, has been linked to marginal-marine settings, ranging from proximal offshore and shoreface to estuarine and lagoonal environments, often affected by variable salinity and freshwater influx (**Knaust, 2015; 2018**). Additionally, the rare occurrence of parallel lamination in the S6 has been interpreted as evidence of planar bed flows from traction current (**e.g. Boggs, 2014**; **Plink-Bjorklund, 2005**). In contrast, the massive mudrocks in the S7 are believed to have been deposited from suspension under low-energy conditions (**e.g. Santos and Rossetti, 2006; Fakhruddin et al., 2023**). Collectively, the presence of (i) wavy, flaser, and ripple stratifications, (ii) bioturbation by *Skolithos linearis* and *Laevicyclus parvus*, (iii) thick massive mudrock, and (iv) minor parallel lamination suggest that the FA2 represents intertidal, mixed tidal flat deposits.

5.1.3.2. Vertical distributions and interpretation of FA3

The mixed tidal flat deposits (FA3) are commonly positioned above or interbedded with tidally influenced channel deposits (FA2; **Figure 3**). Vertical transitions from the mixed tidal flats to the tidal channel deposits have been interpreted to reflect incisions of the tidal channel into the underlying mixed tidal flats. Conversely, upward transitions from the tidal channels into the mixed tidal flat deposits indicate lateral migration of the tidal channel over time.

5.2. Sandstone Maturity, Classification and Provenance

The C2 samples have provided insight into sediment maturity, sandstone classification, and provenance related to tectonic settings. Detrital and authigenic minerals exhibit sub-angular to sub-rounded shapes and poor sorting, indicating sub-mature to mature textural characteristics (**cf. Folk, 1980**), and suggesting limited transport from the source. Compositionally, C2 is dominated by feldspar (average of 77.3%) and lithic fragments (average of 21.27%), with minimal to absent quartz content

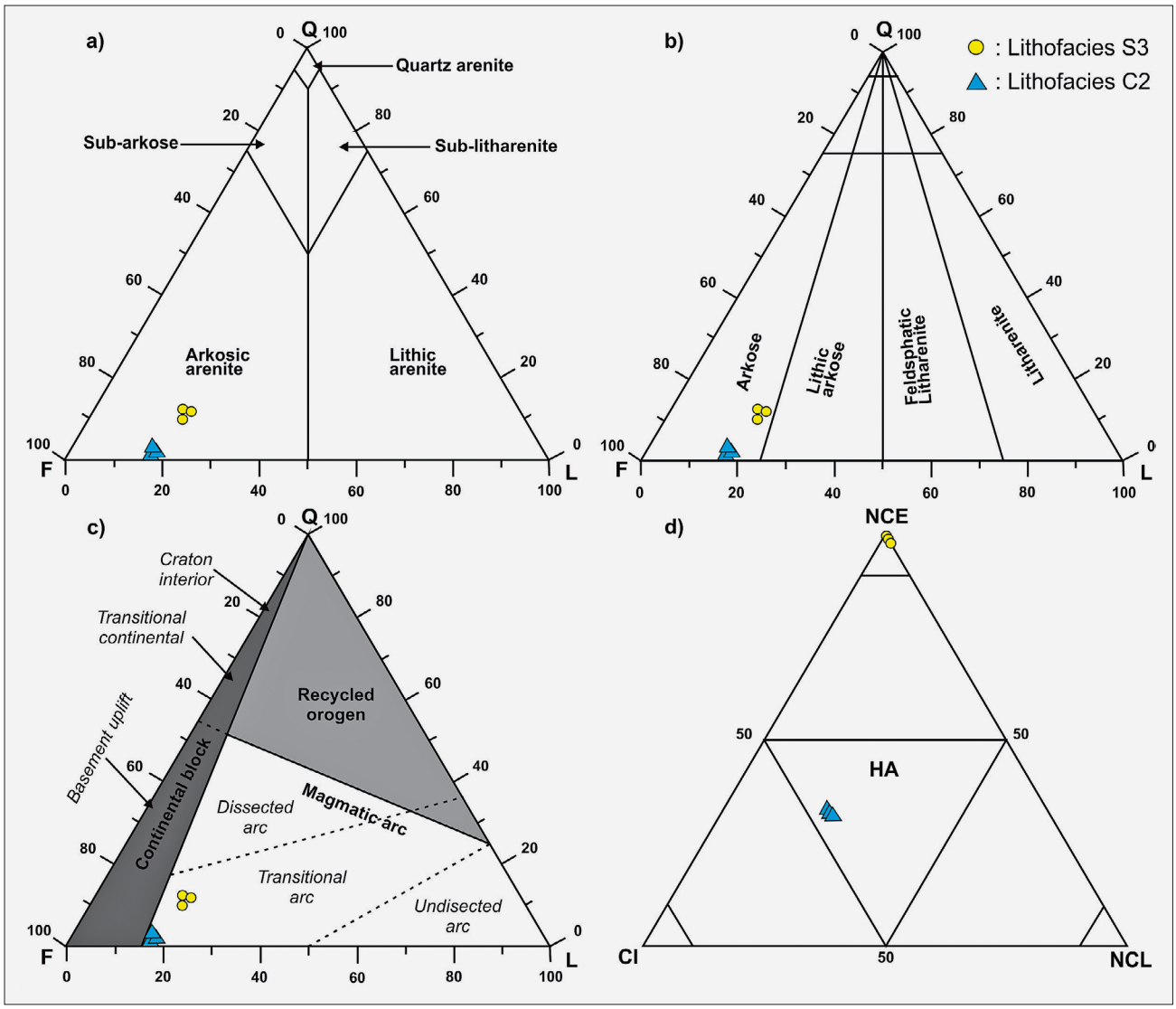


Figure 10. The sandstone composition from the petrography of the Ombilin Formation in the Ombilin Basin based on schemes proposed by (a) **Pettijohn (1975)** and **(b) Folk (1980)**. The sandstone in (a) represents arkosic arenite, while in (b) represents arkose sandstone. (c) The sandstone compositions are plotted on the diagram of **Dickinson et al (1983)** to indicate their provenance. The abbreviations of Q, F, L reflect standard plots of Quartz, Feldspar, and Lithic grains, respectively. (d) Compositions from the petrography are plotted to the schemes proposed by **Zuffa (1980)**. The abbreviation of NCE, CI and NCL reflects non-carbonate extrabasinal, carbonate intrabasinal and intrabasinal non-carbonate respectively in **Table 4**. The HA reflects region of hybrid arenite of **Zuffa (1980)**.

and a ratio of 2:1 for matrix (average of 4.8%) and cement (average of 2.1%) (see **Table 4-5**). These characteristics correspond to arkosic arenite (**Pettijohn, 1975**) or arkose (**Folk, 1980**) classifications (**Figure 10a, b**). Detrital chlorite grains are present, implying the inclusion of chlorite-bearing allogenic lithics derived from metamorphic or igneous sources (**Worden et al., 2020**). Provenance analysis using the **Dickinson et al. (1983)** diagram places the sandstones within the magmatic arc field (see **Figure 10c**), and the high feldspar content supports derivation from intermediate volcanic sources such as andesite (see **Table 4**). Additionally, the high content of bioclast (average of 30.1%) and glauconite (average of 20.63%), which illustrate the high composition of carbonate intrabasinal (CI) and non-carbonate intrabasinal (NCl) respectively, reflecting into the C2 is classified as a hybrid arenite (HA) in the triangular diagram of **Zuffa (1980)** (see **Figure 10d**). Some bioclasts show skeletal fragments, likely suggesting a rework of marine materials. These bioclasts were reported to have been deposited during N4-N5 of the Early Miocene age (**Erdi, 2011**). As such, it is speculated that the marine materials were derived from limestone of the Ombilin Basin, which are distributed along the basin margin (**e.g. Koning, 1985; Anastasia et al., 2012**). Consequently, the provenance of C2 is interpreted as a mixture of volcanic input and reworked marine materials. Such interpretations of a mixture of volcanic input and reworked marine materi-

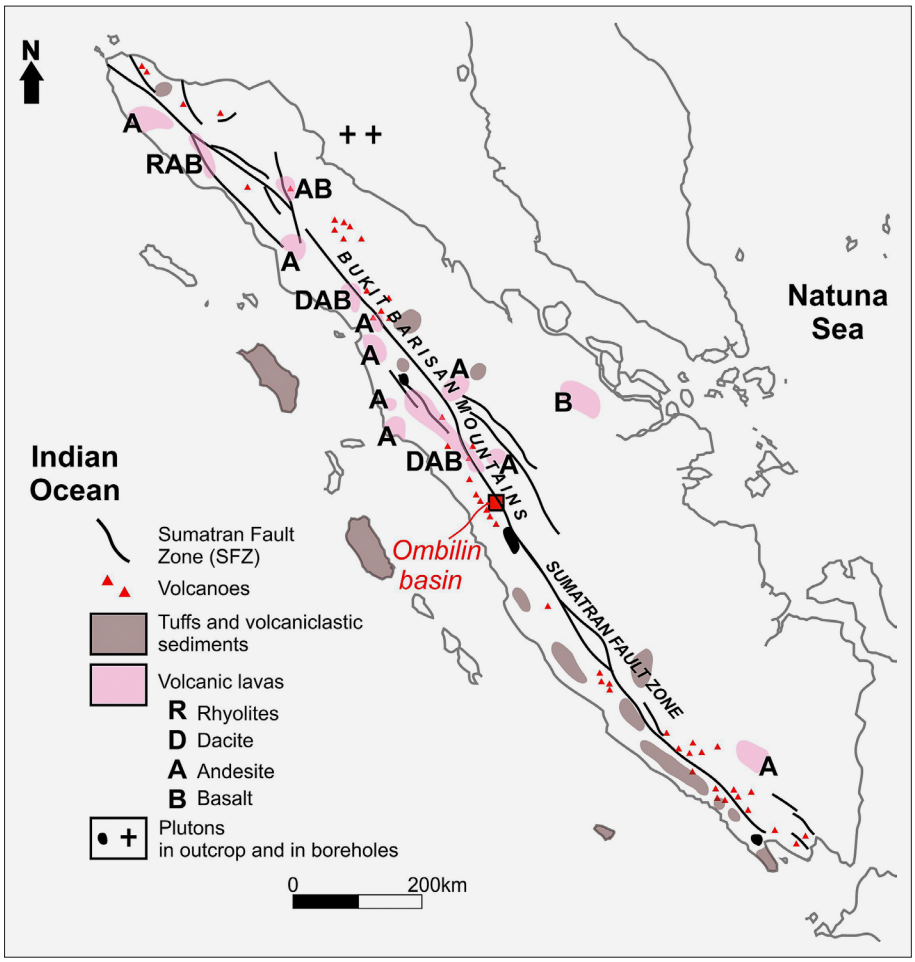


Figure 11. Distributions of Early-Middle Miocene volcanic units in Sumatra (modified from **Barber et al., 2005**). The provenance of the Ombilin Formation is speculated to come from the western part of the basin, where a volcanic chain is present.

als are aligned with earlier studies that link the Ombilin Formation to active volcanism and/or syn-sedimentary reworking (**Adhiperdana, 2010; Yeni, 2011**).

The S3 samples have also revealed information on sediment maturity, sandstone classification, and provenance related to tectonic settings. Detrital and authigenic grains exhibit sub-angular to sub-rounded shapes and poor sorting, indicating a sub-mature to mature texture (**cf. Folk, 1980**), and suggesting limited transport distance from the source. Compositionally, S3 is dominated by feldspar (average of 70.87%), with lower proportions of quartz (average of 11.67%) and lithic fragments (average of 17.5%) (see **Table 5**). Based on these compositions and combined with a ratio of 1:2 for matrix (average of 3.13%) and cement (average of 6.43%) (see **Table 4**), the sandstones have been classified as arkosic arenite (**Pettijohn, 1975**) or arkose (**Folk, 1980**; **Figure 10a, b**). Provenance analysis using the **Dickinson et al. (1983)** diagram places the S3 sandstones within the magmatic arc field (see **Figure 10c**). On the other hand, high non-carbonate extrabasinal (NCE) is shown by the triangular plot of **Zuffa (1980)** (see **Figure 10d**), suggesting extrabasinal origin of high feldspar, moderate lithic fragments, and low quartz, accessory, and heavy mineral content (see **Table 4**). Given the high feldspar content and the tectonic interpretation, the feldspathic assemblages in S3 are inferred to reflect an andesitic source, similar to the result of the C2.

The high feldspar content and a magmatic arc affinity in the S3 and the C2 have been interpreted as consistent with the distribution of Early–Middle Miocene volcanic lavas in Central Sumatra (see **Figure 11**). These volcanic products, predominantly andesitic in composition, were emplaced near the Sumatra Fault Zone and the Barisan Mountains during the emergence and uplift of the Bukit Barisan range in the Early Miocene (**Barber et al., 2005**). The provenance of the Ombilin Formation is therefore inferred to have been derived from volcanic sources situated to the west of the Ombilin Basin (see **Figure 11**). This pattern is similar to observations of provenance for the early syn-rift formations that were deposited during the Eocene in the Ombilin Basin (**Howells, 1997; Barber et al., 2005**).

The Ombilin Formation is underlaid by the Sawahtambang Formation. Several previous studies have illustrated the character of the Sawahtambang Formation. The conglomerate in this formation composed of sedimentary clasts, consisting of volcanic, sedimentary, plutonic and metamorphic fragments (**Howells, 1997**). The distribution of these clasts from this previous study show that

they are characterized by an upward increase in volcanic and sedimentary clast, whereas plutonic and metamorphic clast decrease from bottom to top of the formation. Petrographic analysis of sandstone in the Sawahtambang Formation show characteristic of poor sortation, subangular to sub-rounded grains and non-calcareous (**Erdi, 2011; Putri et al., 2024**). These previous studies show that the Sawahtambang Formation dominantly in quartz, with minor feldspar and sedimentary fragment, reflecting dominantly litharenite and lithic wacke, and minor feldsphatic wacke and arkosic arenite. Previous study has defined that the Sawahtambang Formation is recycled origin, suggesting its origin was related to long process of uplift and erosion (**Putri et al., 2024)**.

The sand-rich sediments in the Ombilin Formation, which is illustrated by the C2 and the S3, has different characteristics compare with the Sawahtambang Formation. Although texture, such as grain sized, sortation and roundness are similar, mineral compositions of the Ombilin Formation show they are relatively higher in feldspar than the Sawahtambang Formation. The presence of lithic fragments and quartz content in C2 and S3 may indicate a rework from underlying formations. We speculate that the Sawahtambang Formation as an origin of this minor mineral content, given that Sawahtambang has high levels of quartz and lithic fragments. As such, the provenance of C2 and S3 is speculatively a mixture of volcanic input, reworked marine materials and clastic materials derived from underlying formations.

5.3. Tectonic Settings and Paleoenvironments in Early-Middle Miocene of the Ombilin Basin

The Ombilin Formation has been defined by several previous studies, occurring as early as the Early Miocene (N4-N5). This formation was deposited during a regional transgression in Sumatra (**Koesoemadinata and Matasak, 1985; Fletcher and Yarmanto, 1993; Situmorang et al., 1991; Barber et al., 2005**), and/or global sea-level rise (**Zaim et al., 2012**). However, the transgression documented in these previous studies are in contradiction to global eustatic events of Mi-1a, Mi-1aa, and Mi-1b glaciation events (**Miller et al., 1998; Morley et al., 2021**). These events are illustrated by Early Miocene Southeast Asia sea-level curves in SEA34–SEA46 (**Morley et al., 2021; Figure 2**). These sea level curve and associated events suggest glacial episodes and associated sea-level falls occurred during the Early Miocene age in SEA34-SEA46, being driven by continental ice-sheet expansion (**Miller et al., 1998; Morley et al., 2021**). Still, global transgression did occur in Early-Middle Miocene, being initiated near SEA52 at the onset of the Middle Miocene Climate Optimum (MMCO) and peaking at SEA53 (**Figure 2; De Boer et al., 2010; Holbourn et al., 2013; Morley et al., 2021).**

The global sea-level fall events in the Early Miocene, during the uplifting of Barisan Mountain in Sumatra, are likely related to the present study that identifies tidal-influenced channels, mixed tidal flat and open marine depositional environment in the Ombilin Formation near Tanjung Ampalu Fault (see **Figure 1b**). The tidal influenced channel (FA2) and mixed tidal flat (FA3) reflect the sub-environment of the estuarine depositional environment near Tanjung Ampalu during the deposition of the Ombilin Formation. Such sub-environments of estuarine origin are also observed in Spitsbergen (**Plink-Bjorklund, 2005; Plink-Bjorklund and Steel, 2006**) and Seven River estuaries (**Dalrymple, 2010**). Such an estuarine depositional environment is also observed during the Early Miocene Bangko Formation in the Central Sumatra Basin, located 17 km northeast from the Ombilin Basin (**e.g. Hendra et al., 2018**). Particularly to the tidal influenced channel, this facies overlies the open marine deposits (FA1), indicating progradation of tidal channels into open marine settings. This observation suggests that regression occurred in the Ombilin Basin. This regression event might result from uplifting, given that isostatic uplifts result in increasing sediment supply and shoreline regressions (**e.g. Catuneanu, 2006; Tsunetaka et al., 2024**). This suggestion is consistent with the Barisan Mountain that underwent uplift in the Early Miocene (**Barber et al., 2005**). Alternatively, this regression might also relate to eustatic sea level fall, given that eustatic sea level fall might destroy accommodation space that induces regression and seaward migration of shoreline (**e.g. Pitman, 1979**; **Catuneanu, 2006**). This suggestion is also consistent with Southeast Asia sea-level curves during the Early Miocene, showing sea-level falls (SEA34–SEA46**; Morley et al., 2021**). As such, this paper suggests that uplifting of Barisan Mountain and sea-level falls occurred, resulting in the deposition of a tidal influenced channel (FA2) and mixed tidal flat (FA3) near Tanjung Ampalu Fault during Early Miocene (see **Figure 12a**). Furthermore, the depositional environment of the tidal-influenced channel and mixed tidal flat in the intertidal, in this study, are consistent with observations of tidal flat facies of calcareous shale and claystone intercalations and *Pelecypods* in Talawi Sub-basin (**Linggadipura et al., 2018**). It was speculated by this study that the Ombilin Formation in the Talawi sub-basin was deposited in the range of supratidal to intertidal environments (see **Figure 12a**). This suggestion is supported by the westward-trending biostratigraphy data, which indicate a landward shift to the west, as reflected by sub-littoral environments in the Sinamar-1 and littoral environment in the section C (**c.f. Koning, 1985** and **Erdi, 2011**).

The calcareous deposits of the Ombilin Formation have been interpreted as neritic to bathyal in origin, based on biostratigraphy data of **Koesoemadinata and Matasak, (1981)** and **Koning (1985**). This study, however, presents the first comprehensive documentation of the presence of tidal-influenced channel sandstones and mixed tidal flat deposits within the Ombilin Formation,

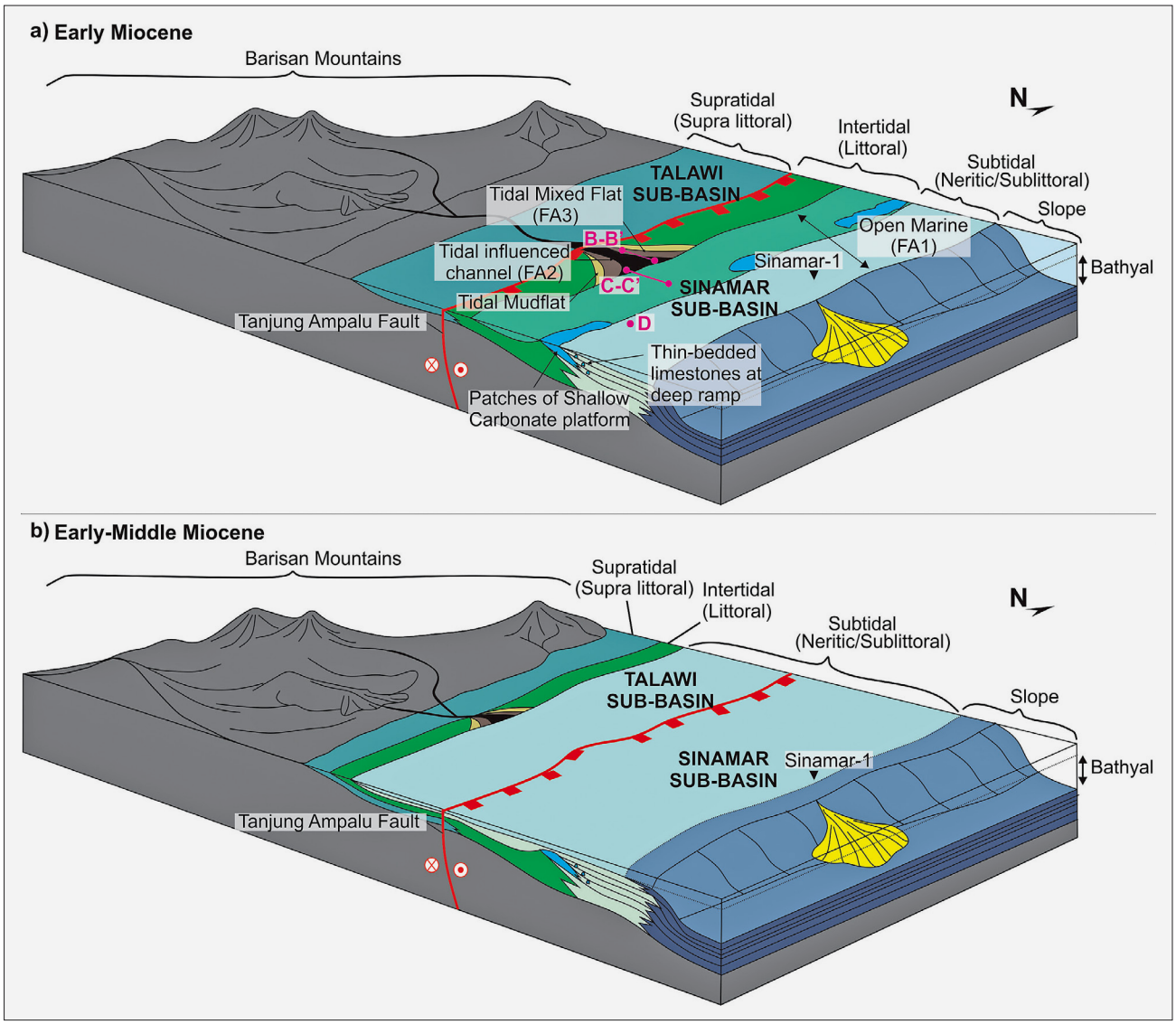


Figure 12. Paleoenvironment of the Ombilin Basin during: (a) Early Miocene, while regional subsidence and eustatic sea level fall occurred in Sumatra and; (b) Early-Middle Miocene, while regional subsidence occurred in Sumatra, eustatic sea level rise due to global transgression (SEA52-54 of **Morley et al., 2021**; **Figure 2**). The black arrow indicates the North (N) direction.

particularly around the basin margins and the Tanjung Ampalu Fault in the Early Miocene. This interpretation is supported by (1) the landward positioning of tidal-influenced deposits relative to calcareous mudrock, (2) the distribution of early limestone facies along basin margins (**Koning, 1985; Anastasia et al., 2012**), (3) increased clastic input attributed to uplift and erosion of the Barisan Mountains (**Barber et al., 2005**), and (4) the long-standing activity of N–S-trending faults such as the Tanjung Ampalu Fault since the mid-Oligocene (**Howells, 1997**). Additionally, volcanism in the western Ombilin Basin during the Early Miocene has been inferred as a major provenance source, despite the absence of direct age dating from these volcanic centres. This interpretation is supported by (1) radiometric dating of andesitic lavas around the Bukit Barisan indicating Early Miocene ages (**Barber et al., 2005; Figure 11**), and (2) the immature to sub-mature texture of Ombilin sandstones, suggesting short transport distances from volcanic sources.

Several previous studies have suggested that the Ombilin Formation continued to be deposited during the Early–Middle Miocene (**Fletcher and Yarmanto, 1993; Howells, 1997**). This event occurred in response to the continuation of a regional transgression in Sumatra (**Koesoemadinata and Matasak, 1985; Fletcher and Yarmanto, 1993; Situmorang et al., 1991; Barber et al., 2005**), and/or global sea-level rise (**Zaim et al., 2012**).

Although comparison between sedimentary log and cross-sections show that section D overlies section B (**c.f. Figure 1b-c** and **3a, c**), this study, however, did not find direct contact between them that indicates certainty of transgression. Nevertheless, based on observation

that the section D overlies section B, where the open marine deposit of FA1 overlie the tidal influenced channel deposits of FA2, this study is suggests that a transgression likely occurred (see **Figure 12b**). It is speculated that the calcareous mudrock of the Ombilin Formation, initially deposited in the deeper parts of the basin, began to accumulate in the study area near the Tanjung Ampalu Fault as a result of global transgression that occurred from SEA 52 to SEA 54 (**Morley et al., 2021**). Additionally, during this period, calcareous mudrocks may have been deposited in the Talawi Sub-basin. The erosional events during the Early–Middle Miocene were driven by ongoing uplift and inversion around the Barisan Mountains (**Barber et al., 2005**). This tectonic activity coincided with the global transgression until SEA 54, followed by regional and global regression extending to the present (**Barber et al., 2005; Morley et al., 2021**).

6. Conclusions

An integrated, detailed analysis of sedimentology and petrography has been provided for the Early-Middle Miocene Ombilin Formation in the Ombilin Basin. Sedimentological analysis of sedimentary logging identified ten lithofacies, being classified into three facies associations: a) open marine deposits (FA1); b) tidal-influenced channels (FA2); and c) intertidal mixed tidal flats (FA3). Their vertical distributions show that FA2-3 are distributed between FA1, reflecting normal and inverse transitions of suspended-load-fines and bedload-dominated transport. The normal transition shows that the FA2-FA3 reflect seaward progradation of tidal channels above open marine settings (FA1). The inverse transition, combined with their spatial distribution along the Tanjung Ampalu Fault, shows that the FA2-3 are likely overlaid by the FA1, speculating a transgression occurred in the Ombilin Basin. Petrographic analysis indicates a submature to mature arkosic composition, derived primarily from a nearby magmatic arc source, with contributions from reworked marine and clastic material derived from the underlying formation(s). The magmatic source is speculated to have originated from Early-Middle Miocene volcanoes located westward of the basin. The evolution of the Ombilin Basin during the Early-Middle Miocene is suggested by the analysis of the sedimentary logging and the petrography, and was influenced by both regional tectonics and global sea-level changes. An initial regression, likely driven by the uplift of Barisan Mountain and global sea level fall, which occurred in the Ombilin Basin during the Early Miocene (SEA34–SEA46). This event was followed by a global transgression that occurred during the Early-Middle Miocene (SEA 52 to SEA 54). This study enhances the understanding of paleoenvironmental evolution and the interplay of tectonic and sea-level controls on sedimentation not only in the intermontane setting of the Ombilin Basin, but also the Sumatra and South East Asia during the Early-Middle Miocene.

Acknowledgement

Some data in this paper is part of the bachelor thesis of the first authors, being supervised by the fourth author. The thesis was conducted in 2011, being sponsored by PT Radiant Bukit Barisan (now PT. Rizki Bukit Barisan Energi). As such, we wish to say thank you to the management of PT Radiant Bukit Barisan, especially to Litto Habrianta Tarigan. We also wish to thank all staff and students in Institut Teknologi Bandung for all their effort and cooperation.

7. References

Adhiperdana, B. G. (2010). A Preliminary Account Of The Framework Grain Composition And Provenance Of The Lower Tertiary Sandstone Outcropped In The Ombilin Basin, Central Sumatra. Bulletin of Scientific Contribution, 8(3), 141-157. https://doi.org/ https://doi.org/10.24198/bsc.v8i3.8252

Anastasia, S., Sitanggang, B. P., Lie, H. S., & Syafri, I. (2012). Ombilin Basin: A Prospect for Shale Gas In Indonesia. Proceedings Indonesia Petroleum Association, the 36th Annual Convention & Exhibition, Jakarta.

Anderton, R. (1985). Clastic facies models and facies analysis. Geological Society, London, Special Publications, 18(1), 31-47. https://doi.org/10.1144/GSL.SP.1985.018.01.03

Augustsson, C. (2021). Influencing Factors on Petrography Interpretations in Provenance Research – A Case-Study Review. Geosciences, 11(5).

Barber, A. J., Crow, M. J., & Milsom, J. S. (2005). Sumatra: Geology, Resources and Tectonic Evolution (Vol. 31). Geological Society, London.

Bartram, K. M., & Nugrahaningsih, L. (1990). A palynological study of the Sawahlunto Formation, Ombilin Basin, West Sumatra. Scientific Contributions/90 Special Issue.

Bentham, P. A., Talling, P. J., & Burbank, D. W. (1993). Braided stream and flood-plain deposition in a rapidly aggrading basin: the Escanilla formation, Spanish Pyrenees. Geological Society, London, Special Publications, 75(1), 177-194. https://doi.org/10.1144/GSL.SP.1993.075.01.11

Boggs, S. (2014). Principles of Sedimentology and Stratigraphy Pearson Education Limited.

Catuneanu, O. (2006). Principles of Sequence Stratigraphy. Elsevier, Amsterdam.

Dalrymple, R. W. (1992). Tidal depositional systems. In R. G. Walker & N. P. James (Eds.), Facies Model: Response to Sea Level Change (pp. 195-218). Geological Association of Canada.

Dalrymple, R. W. (2010). Tidal depositional systems. In N. P. James & R. W. Dalrympe (Eds.), Facies Model 4 (pp. 201-231). Geological Association of Canada.

De Boer, B., van de Wal, R. S. W., Bintanja, R., Lourens, L. J., & Tuenter, E. (2010). Cenozoic global ice-volume and temperature simulations with 1-D ice-sheet models forced by benthic δ18O records. Annals of Glaciology, 51(55), 23-33. https://doi.org/10.3189/172756410791392736

Desjardins, P. R., Buatois, L. A., Pratt, B. R., & MÁNgano, M. G. (2012). Sedimentological–ichnological model for tide-

dominated shelf sandbodies: Lower Cambrian Gog Group of western Canada. Sedimentology, 59(5), 1452-1477. https://doi.org/10.1111/j.1365-3091.2011.01312.x

Dickinson, W. R. (1985). Interpreting Provenance Relations from Detrital Modes of Sandstones. In G. G. Zuffa (Ed.), Provenance of Arenites (pp. 333-361). Springer Netherlands. https://doi.org/10.1007/978-94-017-2809-6_15

Dickinson, W. R., Beard, L. S., Brakenridge, G. R., Erjavec, J. L., Ferguson, R. C., Inman, K. F., Knepp, R. A., Lindberg, F. A., & Ryberg, P. T. (1983). Provenance of North American Phanerozoic sandstones in relation to tectonic setting. GSA Bulletin, 94(2), 222-235. https://doi.org/10.1130/0016-7606(1983)94<222:PONAPS>2.0.CO;2

Erdi, A. (2011). Geologi Daerah Bukitbual Dan Sekitarnya, Kabupaten Sijunjung, Provinsi Sumatera Barat [Institut Teknologi Bandung]]. Bandung.

Erdi, A., Setiawan, A., Zulmi, I., Inabuy, A. R., Zahra, R. H., Edwin, E., Andhika, I. P., Auliansyah, D., & E., W. (2025). Middle-Late Miocene Tidal-related Deposits of the Binio Formation: the Sedimentary and Stratigraphic Records during Inversion of the Central Sumatra Basin, Indonesia. Rudarsko-geološko-naftni zbornik, 40(1). https://doi.org/10.17794/rgn.2025.1.10

Fakhruddin, R., Sunardi, E., Adhiperdana, B. G., Zajuli, M. H. H., Ramli, T., Saleh, H. M., Putra, A. P., Sabra, E., & Arvyalin, G. G. (2023). Late Miocene to Pliocene delta-lacustrine to incised-valley fills sedimentation of the Ransiki Area, Bird's Head Papua, Indonesia: The sedimentary record of Lengguru Fold and Thrust Belt wedge-top depozone. Journal of Asian Earth Sciences, 242, 105497. https://doi.org/10.1016/j.jseaes.2022.105497

Fletcher, G., & Yarmanto. (1993). Post Convention Field Trip: Ombilin Basin Field Guide Book. Indonesian Petroleum Association.

Flügel, E. (2004). Microfacies of Carbonate Rocks. Springer, New York. https://doi.org/10.1007/978-3-662-08726-8

Folk, R. L. (1959). Practical Petrographic Classification of Limestones. AAPG Bulletin, 43(1), 1-38. https://doi.org/10.1306/0BDA5C36-16BD-11D7-8645000102C1865D

Folk, R. L. (1980). Petrology of Sedimentary Rocks. Hemphill Publishing Company, Texas.

Gani, M. R., & Bhattacharya, J. P. (2007). Basic Building Blocks and Process Variability of a Cretaceous Delta: Internal Facies Architecture Reveals a More Dynamic Interaction of River, Wave, and Tidal Processes Than Is Indicated by External Shape. Journal of Sedimentary Research, 77(4), 284-302. https://doi.org/10.2110/jsr.2007.023

Habrianta, L., Matthew, G., Fakhrurozi, F., Auliansyah, D., & Andhika, I. P. (2018). A Semi-Regional Play Analysis Of The Ombilin Basin To Understand The Tectono-Stratigraphic Framework And Identification Of Potential Exploration Opportunities. Proceedings Indonesian Petroleum Association, the 42nd Annual Convention & Exhibition, Jakarta.

Hedgpeth, J. W. (1957). Chapter 2: Classification of Marine Environments*. In J. W. Hedgpeth (Ed.), Treatise on Marine Ecology and Paleoecology (pp. 0). Geological Society of America. https://doi.org/10.1130/MEM67V1-p17

Hendra, H., Wulandari, R., Regina, A., Meilany, H., Gunawan, I. M., Hayatulah, M. S., Thamrin, M. H., Zainal, A. F., & Raihan. (2018). Bangko Shaly Sand Is The Key For The Future To Be Main Reservoir And Increase Oil Production With The Fracturing Stimulation In Beruk Field, Coastal Plan Pekanbaru Block, Central Sumatra Basin. Prosiding Simposium Ikatan Ahli Teknik Perminyakan Indonesia (IATMI) 2018, Padang.

Holbourn, A., Kuhnt, W., Frank, M., & Haley, B. A. (2013). Changes in Pacific Ocean circulation following the Miocene onset of permanent Antarctic ice cover. Earth and Planetary Science Letters, 365, 38-50. https://doi.org/https://doi.org/10.1016/j.epsl.2013.01.020

Howells, C. (1997). Tertiary response to oblique subduction and indentation in Sumatra, Indonesia: new ideas for hydrocarbon exploration. Geological Society, London, Special Publications, 126(1), 365-374. https://doi.org/10.1144/GSL.SP.1997.126.01.22

Irwansyah, Kurniadi, D., Habrianta, L., Reza, T., & Yogi, A. (2018). High Resolution Biostratigraphy And Correlation Accross Paleogene Boundaries In The Ombilin Basin, West Sumatra. Simposium Ikatan Ahli Teknik Perminyakan Indonesia 2018, Padang.

James, N. P., & Bone, Y. (1994). Paleoecology of Cool-Water, Subtidal Cycles in Mid-Cenozoic Limestones, Eucla Platform, Southern Australia. PALAIOS, 9(5), 457-476. https://doi.org/10.2307/3515136

Jones, B. (2010). Warm-Water Neritic Carbonates. In N. P. James & R. W. Dalrympe (Eds.), Facies Model 4 (pp. 341-370). Geological Association of Canada.

Katili, J. A., & Hehuwat, F. (1967). On the occurrence of large transcurrent faults in Indonesia. Journal of Geosciencese, 10, 5-16.

Kleinhans, M. G., Wilbers, A. W. E., De Swaaf, A., & Van Den Berg, J. H. (2002). Sediment Supply-Limited Bedforms in Sand-Gravel Bed Rivers. Journal of Sedimentary Research, 72(5), 629-640. https://doi.org/10.1306/030702720629

Knaust, D. (2015). Siphonichnidae (new ichnofamily) attributed to the burrowing activity of bivalves: Ichnotaxonomy, behaviour and palaeoenvironmental implications. Earth-Science Reviews, 150, 497-519. https://doi.org/10.1016/j.earscirev.2015.07.014

Knaust, D., Thomas, R. D. K., & Curran, H. A. (2018). Skolithos linearis Haldeman, 1840 at its early Cambrian type locality, Chickies Rock, Pennsylvania: Analysis and designation of a neotype. Earth-Science Reviews, 185, 15-31. https://doi.org/10.1016/j.earscirev.2018.05.009

Koesoemadinata, R. P. (2020). Geology of Indonesia Vol I: General Introduction and Part I Western Indonesia (Vol. 1). Ikatan Alumni Teknik Geologi ITB.

Koesoemadinata, R. P., & Matasak, T. (1981). Stratigraphy and sedimentation – Ombilin basin, Central Sumatra (West Sumatra Province). Proceedings Indonesian Petroleum Association, the 10th Annual Convention & Exhibition, Jakarta.

Koning, T. (1985). Petroleum geology of the Ombilin intermontane basin, West Sumatra. Proceedings Indonesian Petroleum Association, the 14th Annual Convention Jakarta.

Li, S., Shan, X., Gong, C., & Yu, X. (2017). Classification, formation, and transport mechanisms of mud clasts. International Geology Review, 59(12), 1609-1620. https://doi.org/10.1080/00206814.2017.1287014

Linggadipura, R. D., Fernando, R. E., Prasetyo, M. H., Krestanu, A., Addiansyah, M., & Susilo, B. K. (2018). Architectural, Facies, And Depositional Environment Analysis Of Paleogene To Neogene Deposit In The Northern Ombilin Basin: Implication Hydrocarbon Potential. Retrieved 2025 from https://geosriwijaya.com/wp-content/uploads/2017/11/Linggadipura-et-al-2018-Architectural-Facies-and-Depositional-Environment-Analysis-of-Paleogene-to-Neogene-Deposit.pdf

Loeblich, A. R., Jr., & Tappan, H. (1994). Foraminifera Of The Sahul Shelf And Timor Sea. In A. R. Loeblich, Jr. & H. Tappan (Eds.), Foraminifera of the Sahul Shelf and Timor Sea (Vol. 31, pp. 0). Cushman Foundation for Foraminiferal Research.

Longhitano, S. G., Rossi, V. M., Chiarella, D., Mellere, D., Tropeano, M., Dalrymple, R. W., Steel, R. J., Nappi, A., & Olita, F. (2021). Anatomy of a mixed bioclastic–siliciclastic regressive tidal sand ridge: Facies-based case study from the lower Pleistocene Siderno Strait, southern Italy. Sedimentology, 68(6), 2293-2333. https://doi.org/https://doi.org/10.1111/sed.12853

Longley Ian, M. (1997). The tectonostratigraphic evolution of SE Asia. Geological Society, London, Special Publications, 126(1), 311-339. https://doi.org/10.1144/GSL.SP.1997.126.01.19

MacEachern, J. A., Pemberton, S. G., Gingras, M. K., & Bann, K. L. (2010). Ichnology and Facies Models. In N. P. James & R. W. Dalrympe (Eds.), Facies Model 4 (pp. 19-58). Geological Association of Canada.

Malaza, N., Liu, K., & Zhao, B. (2016). Petrology and geochemistry of clastic sedimentary rocks as evidences for provenance of the Late Palaeozoic Madzaringwe Formation, Tshipise-Pafuri Basin, South Africa. Science China Earth Sciences, 59(12), 2411-2426. https://doi.org/10.1007/s11430-016-5274-z

Miller, K. G., Mountain, G. S., Browning, J. V., Kominz, M., Sugarman, P. J., Christie-Blick, N., Katz, M. E., & Wright, J. D. (1998). Cenozoic global sea level, sequences, and the New Jersey Transect: Results From coastal plain and continental slope drilling. Reviews of Geophysics, 36(4), 569-601. https://doi.org/https://doi.org/10.1029/98RG01624

Morley, R. J., Hasan, S. S., Morley, H. P., Jais, J. H. M., Mansor, A., Aripin, M. R., Nordin, M. H., & Rohaizar, M. H. (2021). Sequence biostratigraphic framework for the Oligocene to Pliocene of Malaysia: High-frequency depositional cycles driven by polar glaciation. Palaeogeography, Palaeoclimatology, Palaeoecology, 561. https://doi.org/10.1016/j.palaeo.2020.110058

Moss, S. J., & Carter, A. (1996). Thermal histories of Tertiary sediments in western central Sumatra, Indonesia. Journal of Southeast Asian Earth Sciences, 14(5), 351-371. https://doi.org/https://doi.org/10.1016/S0743-9547(96)00071-2

Murray, A. M. (2020). Early Cenozoic Cyprinoids (Ostariophysi: Cypriniformes: Cyprinidae and Danionidae) from Sumatra, Indonesia. Journal of Vertebrate Paleontology, 40(1), e1762627. https://doi.org/10.1080/02724634.2020.1762627

Noeradi, D., Djuhaeni, & Simanjuntak, B. (2005). Rift play in Ombilin basin outcrop, West Sumatra. Proceedings Indonesian Petroleum Association, the 30th Annual Convention, Jakarta.

Odin, G. S., & Matter, A. (1981). De glauconiarum origine. Sedimentology, 28(5), 611-641. https://doi.org/https://doi.org/10.1111/j.1365-3091.1981.tb01925.x

Olariu, C., & Bhattacharya, J. P. (2006). Terminal Distributary Channels and Delta Front Architecture of River-Dominated Delta Systems. Journal of Sedimentary Research, 76(2), 212-233. https://doi.org/10.2110/jsr.2006.026

Olariu, C., Steel, R. J., & Petter, A. L. (2010). Delta-front hyperpycnal bed geometry and implications for reservoir modeling: Cretaceous Panther Tongue delta, Book Cliffs, Utah. AAPG Bulletin, 94(6), 819-845. https://doi.org/10.1306/11020909072

Paola, C., Wiele, S. M., & Reinhart, M. A. (1989). Upper-regime parallel lamination as the result of turbulent sediment transport and low-amplitude bed forms. Sedimentology, 36(1), 47-59. https://doi.org/https://doi.org/10.1111/j.1365-3091.1989.tb00819.x

Pettijohn, F. J. (1975). Sedimentary Rocks (Third Edition ed.). Harper and Row, New York.

Pitman, W. C., III. (1979). The Effect of Eustatic Sea Level Changes on Stratigraphic Sequences at Atlantic Margins1. In Geological and Geophysical Investigations of Continental Margins (Vol. 29, pp. 0). American Association of Petroleum Geologists. https://doi.org/10.1306/M29405C30

Plink-BjÖRklund, P. (2005). Stacked fluvial and tide-dominated estuarine deposits in high-frequency (fourth-order) sequences of the Eocene Central Basin, Spitsbergen. Sedimentology, 52(2), 391-428. https://doi.org/https://doi.org/10.1111/j.1365-3091.2005.00703.x

Plint, A. G. (2010). Wave- and Strom-Dominated Shoreline and Shallo-Marine Systems. In N. P. James & R. W. Dalrympe (Eds.), Facies Model 4 (pp. 167-200). Geological Association of Canada.

Pratt, B. R. (2010). Peritidal Carbonate. In N. P. James & R. W. Dalrympe (Eds.), Facies Model 4 (pp. 401-420). Geological Association of Canada.

Putra, A. F., Abdullah, C. I., & Noeradi, D. (2021). Ombilin Basin as Inverted Oblique Rift in Barisan Mountains, Sumatra: Considerations on Subsidence Mechanisms and Fault Development. IAGI Journal.

Reineck, H. E., & Singh, l. B. (1980). Depositional Sedimentary Environments. Springer-Verlag, Berlin.

Rubio, B., & López-Pérez, A. E. (2024). Exploring the genesis of glaucony and verdine facies for paleoenvironmental interpretation: A review. Sedimentary Geology, 461, 106579. https://doi.org/https://doi.org/10.1016/j.sedgeo.2024.106579

Santos, A. E. A., & Rossetti, D. F. (2006). Depositional model of the Ipixuna formation (Late Cretaceous- Early Tertiary), Rio Capim area, northern Brazil. Latin Am. J. Sedimentol. Basin Analysis, 13.

Simons, D. B., & Richardson, E. V. (1963). Forms of Bed Roughness in Alluvial Channels. Transactions of the

American Society of Civil Engineers, 128(1), 284-302. https://doi.org/10.1061/TACEAT.0008730

Situmorang, B., Yulihanto, B., Guntur, A., Himawan, R., & Jacob, T. G. (1991). Structural Development of the Ombilin Basin West Sumatra. Proceedings Indonesian Petroleum Association, the 20th Annual Convention, Jakarta.

Starzec, K., Stadnik, R., Skiba, M., Bębenek, S., & Waśkowska, A. (2023). Origin and paleoenvironmental significance of Al-rich glauconite in the Ediacaran/Cambrian deposits of the Lublin Basin, Poland (SW margin of Baltica). Precambrian Research, 397, 107165. https://doi.org/https://doi.org/10.1016/j.precamres.2023.107165

Tsunetaka, H., Murakami, W., & Daimaru, H. (2024). Shoreline advance due to the 2024 Noto Peninsula earthquake. Scientific Reports, 14(1), 28026. https://doi.org/10.1038/s41598-024-79044-4

Van Bemmelen, R. W. (1949). General Geology of Indonesia and Adjacent Archipelagoes (Vol. I). Goverment Printing Office, The Hague.

Wentworth, C. K. (1922). A Scale of Grade and Class Terms for Clastic Sediments. The Journal of Geology, 30(5), 377-392. https://doi.org/10.1086/622910

Whateley, M. K. G., & Jordan, G. R. (1989). Fan-delta-lacustrine sedimentation and coal development in the Tertiary Ombilin Basin, W Sumatra, Indonesia. Geological Society, London, Special Publications, 41(1), 317-332. https://doi.org/10.1144/GSL.SP.1989.041.01.22

Worden, R. H., Griffiths, J., Wooldridge, L. J., Utley, J. E. P., Lawan, A. Y., Muhammed, D. D., Simon, N., & Armitage, P. J. (2020). Chlorite in sandstones. Earth-Science Reviews, 204, 103105. https://doi.org/https://doi.org/10.1016/j.earscirev.2020.103105

Yeni, Y. F. (2011). Perkembangan Sedimentasi Formasi Brani, Formasi Sawahlunto Dan Formasi Ombilin Ditinjau Dari Provenance Dan Komposisi Batupasir Cekungan Ombilin Proceedings JCM Makassar 2011, The 36th HAGI and 40th IAGI Annual Convention and Exhibition, Makassar.

Zaim, Y., Habrianta, L., Abdullah, C. I., Aswan, Rizal, Y., Basuki, N. I., & Sitorus, F. E. (2012). Depositional History and Petroleum Potential of Ombilin Basin, West Sumatra - Indonesia, Based on Surface Geological Data. AAPG International Convention and Exhibition, Singapore.

Zakaria, A. A., Johnson, H. D., Jackson, C. A. L., & Tongkul, F. (2013). Sedimentary facies analysis and depositional model of the Palaeogene West Crocker submarine fan system, NW Borneo. Journal of Asian Earth Sciences, 76, 283-300. https://doi.org/https://doi.org/10.1016/j.jseaes.2013.05.002

SAŽETAK

Organizacija facijesa i podrijetlo sedimenata miocenske formacije Ombilin: međudjelovanje tektonike i eustazije u neogenskome unutarplaninskom bazenu, Središnja Sumatra, Indonezija

Ranomiocenska ombilinska formacija u unutarplaninskome Ombilinskom bazenu, Središnja Sumatra, bilježi ključni interval paleoekoloških promjena uzrokovanih regionalnom tektonikom i globalnim fluktuacijama razine mora. Unatoč važnosti, raspored facijesa sedimentnih stijena, podrijetlo sedimenta i povijest oscilacija razine mora ove formacije slabo su istraženi. Ova studija integrira detaljno sedimentološko istraživanje i petrografsku analizu izdanaka s ciljem dobivanja novih spoznaja o navedenim nedostatcima. Identificirano je deset litofacijesa koji su grupirani u tri asocijacije facijesa: facijes otvorenoga mora, facijes plimnih kanala i facijes međuplimne zone s plimnom ravnicom. Njihov vertikalni raspored upućuje na postojanje normalnih i inverznih prijelaza. Normalni prijelaz upućuje na pomak od sublitoralnih do plimom dominiranih okoliša, što se tumači kao rezultat povećanoga donosa sedimenta s uzdignutih planina Barisan te kratkoročnim globalnim padom razine mora (npr. SEA34–SEA46). S druge strane, inverzni prijelaz upućuje na transgresiju koja se dogodila u Ombilinskome bazenu. Petrografska analiza u formaciji Ombilin uputila je na postojanje arkoznih pješčenjaka koji potječu ponajprije iz magmatskoga luka, što je u skladu s istovremenim vulkanizmom koji se odvija zapadno od promatranoga bazena, ali s manjom preradom marinskih naslaga i starijih klastičnih naslaga. Stratigrafski dokazi upućuju na početnu regresiju, vjerojatno uzrokovanu podizanjem planine Barisan i globalnim padom razine mora u bazenu Ombilin tijekom ranoga miocena. Nakon ovoga događaja uslijedilo je taloženje praćeno globalnim transgresivnim trendovima. Ovi nalazi pružaju nove znanstvene spoznaje o razvoju sedimentacije, podrijetlu i tektonsko-eustatičkoj interakciji koja je kontrolirala razvoj bazena Ombilin tijekom ranoga i srednjega miocena.

Ključne riječi:
naslage povezane s plimom, podbazen Sinamar, sedimentologija, podrijetlo, tektonika

Author's contribution

Aurio Erdi (PhD): conceptualization, data curation, formal analysis, methodology, project administration, resources, validation, visualization, writing – original draft, and writing – review and editing. **Syahreza Saidina Angkasa** (PhD): formal analysis, investigation, methodology, and writing – review and editing. **Eko Suwarno** (M. Sc): data curation, and writing – review and editing. **Aswan** (PhD): supervision, validation, and writing – review and editing.
All authors have read and agreed to the published version of the manuscript.

RGNZ/MGPB

The Effect of Calcium and Magnesium Ions on a Crude Oil-Brine-Carbonate Rock System for Enhanced Oil Recovery by Sophorolipid Solution

Rudarsko-geološko-naftni zbornik
(The Mining-Geology-Petroleum Engineering Bulletin)
DOI: 10.17794/rgn.2026.2.6

Original scientific paper

Indah Widiyaningsih[1,2] ✉, Ivan Kurnia[1] ✉, Harry Budiharjo Sulistyarso[2] ✉, Tutuka Ariadji[1] ✉, Taufan Marhaendrajana[1*] ✉

[1] *Department of Petroleum Engineering, Faculty of Mining and Petroleum Engineering, Institut Teknologi Bandung, Ganesha Street No. 10, Bandung 40132, Indonesia.*

[2] *Department of Petroleum Engineering, UPN Veteran Yogyakarta, Padjajaran Street, North Ring Road No.104, Ngropoh, Sleman Regency, 55283, Yogyakarta, Indonesia.*

Abstract

The interaction between crude oil, brine and carbonate rock systems is critical for implementing enhanced oil recovery (EOR). Surfactants, such as sophorolipid biosurfactants, incorporated in the displacing fluid are able to reduce the interfacial tension (IFT) and alter the wettability in these systems. However, the presence of divalent ions, especially calcium (Ca^{2+}) and magnesium (Mg^{2+}), complicates this interaction, affecting the effectiveness of EOR techniques. This study examines the influence of divalent ions on crude oil–brine–carbonate rock systems with the introduction of sophorolipids through experimental work. Interfacial tension and emulsion viscosity experiments evaluate the fluid-to-fluid interactions, while contact angle and static adsorption measurements characterize the interaction between the fluids and the rock, which are highly pertinent to the EOR mechanism. The Ca^{2+} and Mg^{2+} ions (2000 ppm) to sodium chloride (NaCl) solutions (10,000–15,000 ppm) with a 0.5 wt.% sophorolipid concentration at Critical Micelle Concentration (CMC) increased the water-wetness of the carbonate rock surface. In addition, while the ions reduced the interfacial tension (IFT), they did not significantly affect the viscosity of the oil–water emulsion of the NaCl solution with 0.5 wt.% sophorolipid. At low salinity (5000 ppm NaCl solution), these ions decreased the adsorption rate of the sophorolipid solutions on Indiana Limestone samples. The addition of these divalent ions to the injection solution significantly reduced the oil recovery efficiency, by about 28% for light oil and 32% for medium oil, during the biosurfactant flooding process.

Keywords:
Sophorolipids, divalent ions, carbonate, salinity conditions, enhanced oil recovery

1. Introduction

Carbonate reservoirs, which contain about 60% of the world's oil reserves, present unique challenges for oil extraction due to their complex pore structure and wettability characteristics (**Ayirala et al., 2021; Sheng, 2013**). Carbonate reservoirs are often heterogeneous, having varying degrees of porosity and permeability, which further complicates the oil production process (**Mogensen & Masalmeh, 2020; Nazari et al., 2019**). These reservoirs are usually oil-wet or mixed-wet, which reduces the effects of traditional water-flooding methods (**Hao et al., 2019; Mohammed & Babadagli, 2015**). This means large residual oil reserves are often left in carbonate rocks (**Mogensen & Masalmeh, 2020; Xu et al., 2020**), awaiting innovative solutions to increase oil recovery.

* Corresponding author: Taufan Marhaendrajana
e-mail address: tmarhaendrajana@itb.ac.id
Received: 18 June 2025. Accepted: 13 October 2025.
Available online: 13 March 2026

The injection of surfactants into carbonate rocks for enhanced oil recovery (EOR) is critical, but it has environmental impacts. Concerns about this have prompted research into sustainable alternatives, such as biosurfactants. Consequently, the use of sophorolipids as green surfactants has attracted increased research interest. Sophorolipids – a class of biosurfactants – have attracted interest for their potential in EOR applications owing to their biodegradability, low toxicity and relatively low cost (**Díaz De Rienzo et al., 2015; Ganji et al., 2020**). Sophorolipids can lower the interfacial tension (IFT) between crude oil and brine, mobilising trapped oil (**Esfandyari et al., 2021; Hou et al., 2021; Shekhar et al., 2015**). These biosurfactants can modify the wettability of carbonate rocks from oil-wet to water-wet, and reduce the surfactant adsorption by carbonate rock, hence improving oil recovery (**Akanji et al., 2021; Bhardwaj, 2013; Elshafie et al., 2015; Magri et al., 2018**).

Crude oil–brine–carbonate rock systems are common in petroleum engineering studies, and oil recovery can be significantly enhanced from these. The crude

oil–brine–carbonate rock system represents a complex interaction of multiple components that substantially affect the efficiency of EOR methods. Fluid-to-fluid interactions in biosurfactant injection processes impact the microemulsion viscosity and lower the IFT (**Marhaendrajana et al., 2025; Megayanti et al., 2023; Udoh & Vinogradov, 2019**). Changes in the wettability and the degree of rock adsorption are usually measured to evaluate fluid-to-carbonate rock interactions (**Bassir & Shadizadeh, 2020; Shaik et al., 2020**).

Salinity affects the interactions between fluids and the mechanisms of biosurfactant application in fluid-to-fluid and fluid-to-rock interactions. In specific instances, biosurfactants have demonstrated optimal performance at particular salinity levels, at which point the IFT reaches its minimum value (**Mohammadi et al., 2019; Yutkin et al., 2022**). The viscosity and stability of the microemulsion generated during the EOR biosurfactant process are influenced by salinity levels (**Iravani et al., 2025; Khodaparast & Johns, 2020**). The salinity level of the solution can potentially decrease biosurfactant adsorption, thereby increasing the availability of biosurfactant molecules to alter the rock-wetting properties (**Hou et al., 2022**). In elevated salinity conditions, the solubility of biosurfactants in the brine solution may decrease due to aggregate (e.g. micelle) formation or precipitation, and the biosurfactant's effectiveness may be reduced. Thus, the optimal salinity must be established for each reservoir, considering the intricate interactions between the biosurfactant and the carbonate rock (**Ghaedi et al., 2023**).

Elevated IFT between crude oil and brine can impede the mobilisation of entrapped oil. Incorporating surfactants, including sophorolipids, markedly decreases the IFT, promoting oil displacement (**Baccile & Kleinen, 2025; Esfandyari et al., 2021; Fu et al., 2024; Gazem et al., 2025**). Divalent ions reduce the IFT between oil and aqueous surfactant solutions, achieving very low values at optimal concentrations. This phenomenon is crucial for applications such as EOR (**Jha et al., 2018**). The presence of divalent ions can also improve the effectiveness of sophorolipids in reducing the IFT, these ions interacting with the surfactant molecules and the crude oil, leading to a more effective reduction in IFT (**Koh et al., 2016**).

Carbonate rocks are primarily composed of calcite ($CaCO_3$) minerals. In the formation of dolomite, magnesium ions (Mg^{2+}) replace some of the calcium ions (Ca^{2+}) in the limestone's mineral structure. The chemical formula for dolomite is $CaMg(CO_3)^2$. Derikvand (2020) discovered that including Mg^{2+} and Ca^{2+} in brine solutions can improve oil recovery by modifying the surface characteristics of the crude oil–brine–carbonate rock system (**Derikvand et al., 2020; Zheng et al., 2024**).

This modification has been ascribed to the capacity of these ions to engage both with the rock surface and the crude oil, thereby changing the wettability and IFT (**Derikvand et al., 2020; Eslahati et al., 2020**). Divalent ions, including Ca^{2+} and Mg^{2+}, are also essential in modifying rock wettability and thereby enhancing oil mobilisation (**Bai et al., 2021; Gandomkar & Reza, 2017; Marhaendrajana et al., 2018; Zaeri et al., 2019**). The presence of Ca^{2+} and Mg^{2+} significantly affects the adsorption rate (**Anachkov et al., 2015; Herawati et al., 2022; Hou et al., 2022**). The reactive properties of Ca^{2+} and Mg^{2+} are also strongly influenced by salinity (**Derikvand et al., 2020; Prabhakar & Melnik, 2018; Zaeri et al., 2019**).

The interaction of these three components can significantly impact the fluid movement mechanism in a reservoir and the oil recovery efficiency using sophorolipids. The objective of the study is to evaluate the effects of brine with various salinities (5000–15,000 ppm) and sophorolipid concentration (0–2 wt.%) on medium and light oil samples using Indiana Limestone (IL). In addition, the study investigates the role of divalent ions (Ca^{2+} and Mg^{2+}) in enhancing and optimising biosurfactant-based EOR system through IFT, oil–water emulsion viscosity, contact angle, static adsorption and core flooding tests. Incorporating sophorolipids into EOR represents an innovative approach to addressing the challenges associated with carbonate reservoirs. This strategy not only improves recovery efficiency but also provides environmental and operational benefits that align with the industry's incrceasing commitment on sustainable practices.

2. Experimental Methodology

2.1. Material and Sample Preparation

2.1.1. Crude Oil Sample

The crude oil samples used in this study were collected from two oil fields in Indonesia. The light oil properties presented in **Table 1** were cited by **Swadesi et al. (2015)**. The medium oil properties were obtained from laboratory analyses conducted by Lemigas. Based on API gravity, each sample represents the characteristics of light and medium oils.

Table 1. Crude Oil Characteristics

Property	Light Crude Oil	Medium Crude Oil
API Gravity (°API)	43.45	33.1
Saturates (%)	71.60	74.67
Aromatics (%)	25.49	24.07
Resins (%)	2.14	1.15
Asphaltenes (%)	0.78	0.106
Total Acid Number, TAN (mg KOH/g)	1.23	0.178
Viscosity (cP) at Corresponding reservoir temperature	0.9 (66°C)	4.38 (60°C)

Note. KOH, potassium hydroxide.

2.1.2. Sophorolipids

We used a sophorolipid biosurfactant purchased from Shanghai Yuchuang Chemical Technology Co., Ltd., which has a light yellow to brown liquid appearance, as shown in **Figure 1**. This product is water soluble and has the sophorolipid specifications shown in **Table 2**. Sophorolipids consist of hydrophilic sophorose groups covalently bonded to hydrophobic fatty acid groups. Two glucose units are linked by a glycosidic bond (β-1,2′) to form sophorose, a disaccharide (2-O-β-D-glucopyranosyl-β-D-glucopyr-anose) (**Pal et al., 2023**).

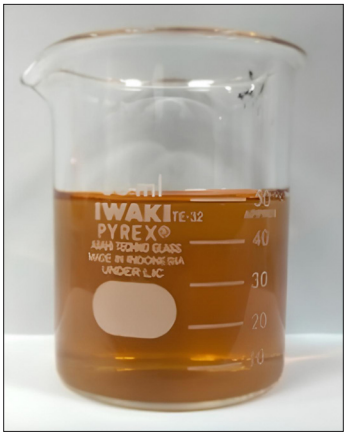


Figure 1. Example of a Sophorolipid Sample

Table 2. Sophorolipids Specification

Items	Specifications
Solid Content	51.50%
pH	3.95
Solubility (Water)	Soluble

2.1.3. Core Sample

Indiana Limestone was used for the rock-fluid test in this study. Based on laboratory testing, this limestone is characterized by 20% porosity and 135 mD permeability, as measured by a PORG-200 porosimeter and PERG using gas N2. The mineral composition based on X-ray diffraction data from IL, is shown in **Table 3**.

Table 3. Mineral Composition of Indiana Limestone

Items	Specifications
Quartz	0.84%
Calcite	94.08%
Clay	1.94%
Pyrite	1.61%
Dolomite	1.53%

2.2. Experiment Design

The overall fluid-to-fluid and fluid-to-carbonate rock testing involved synthetic brines with various compositions, as shown in **Table 4**. The scenarios totalled 90 tests, incorporating two samples of crude oil and five sophorolipid concentrations, from 0 to 2 wt.%.

Table 4. Synthetic Brine Composition

Number	Synthetic Brine		
	NaCl	$CaCl_2$	$MgCl_2$
1	5,000 ppm	-	-
2	5,000 ppm	2,000 ppm	-
3	5,000 ppm	-	2,000 ppm
4	10,000 ppm	-	-
5	10,000 ppm	2,000 ppm	-
6	10,000 ppm	-	2,000 ppm
7	15,000 ppm	-	-
8	15,000 ppm	2,000 ppm	-
9	15,000 ppm	-	2,000 ppm

Note. NaCl, sodium chloride; $CaCl_2$, calcium chloride; $MgCl_2$, magnesium chloride.

The technique of attributing reaction rates to the distance from equilibrium (X) becomes troublesome when dealing with magnesian calcites, and there has been debate regarding the precise definition of this equilibrium. Uncertainties in free energy values, the more general issue of whether magnesian calcites ever achieve a truly metastable equilibrium state, and the best way to depict this connection in thermodynamic calculations are some of the causes of this issue.

Thus, far more attention has been paid to the problem of how magnesium substitution impacts solubility than to the impact on dissolution rate alone. To address this issue, **Thorstenson & Plummer** (**1977**) proposed the concept of stoichiometric saturation. They suggested that the product of activities provides the equilibrium constant for a magnesian calcite with the composition $Ca(_{1-x})Mg_xCO_3$.

$$IAP_{mag\ cal} = (Ca^{2+})^{1-x}(Mg^{2+})^{x}(CO_3^{2-}) \qquad (1)$$

Where x = mole fraction of lattice magnesium. Magnesian calcite is thus assumed to react as a one-component phase having a fixed composition (**Morse & Arvidson, 2002; Thorstenson & Plummer, 1977**).

2.3. Procedure

2.3.1. Interfacial Tension Test

The IFT measurement was conducted using a spinning-drop tensiometer (see **Figure 2**) to determine the biosurfactant's ability to reduce the IFT between the oil and brine solutions. The measurement time was 30 min at 6000 rpm and a temperature of 60 ± 0.5°C.

2.3.2. Viscosity Emulsion

A Brookfield viscometer measures the torsional force exerted on a cylindrical rotor (spindle) immersed in a flu-

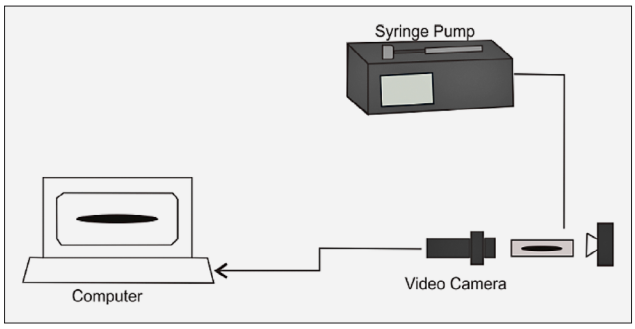


Figure 2. Schematic of the Spinning Drop Tensiometer

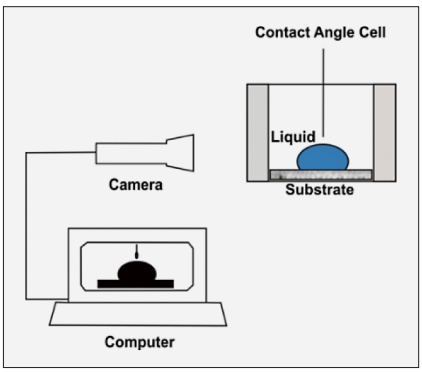


Figure 3. Schematic of the Optical Tensiometer Tool

id, which gives the measurement of viscosity. In this experiment, the viscometer was used to measure the viscosity of an oil–water emulsion. The sample mixture was 1:1, with 5 mL each of oil and sophorolipid solution, stirred for 10 min at 60 ± 0.5°C to promote emulsification.

2.3.3. Contact Angle Measurement

A Theta Lite Optical Tensiometer TL100 (OneAttention) tool was used to measure the contact angle on a thin-section of the IL. The IL thin-section was immersed in crude oil for 24 h at 60 ± 0.5°C to adjust the rock conditions to the initial wettability of the reservoir by inducing the adsorption of oil molecules and polar compounds, such as asphaltene and resins, onto the rock surface. During the procedure, water droplets were placed on the oil-soaked rock surface, and the contact angle was measured, as shown in **Figure 3**. A similar procedure had previously been used by **Abdallah et al. (2007)** and **Al-Maamari & Buckley (2003)**.

2.3.4. Static Adsorption

The adsorption test was performed to evaluate the adsorption efficacy of the sophorolipids on the IL and to ascertain whether other factors, such as the interaction of

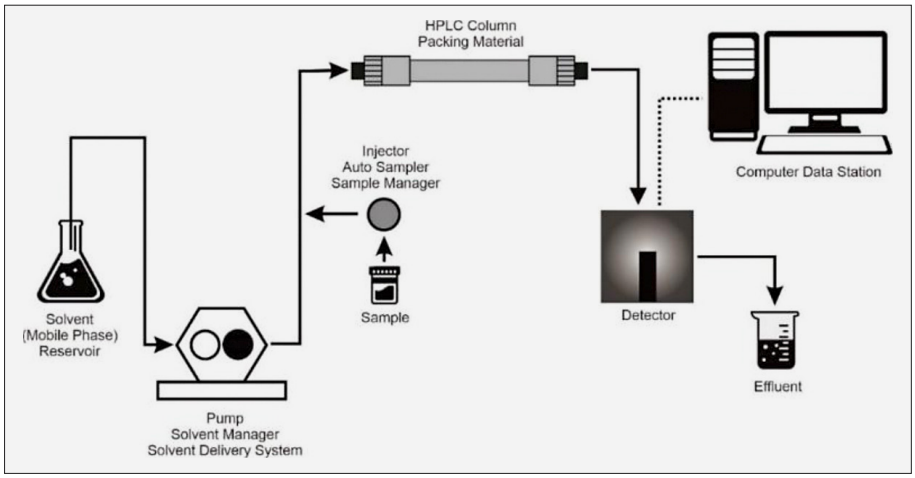


Figure 4. Schematic of The High-Performance Liquid Chromatography (HPLC) Apparatus

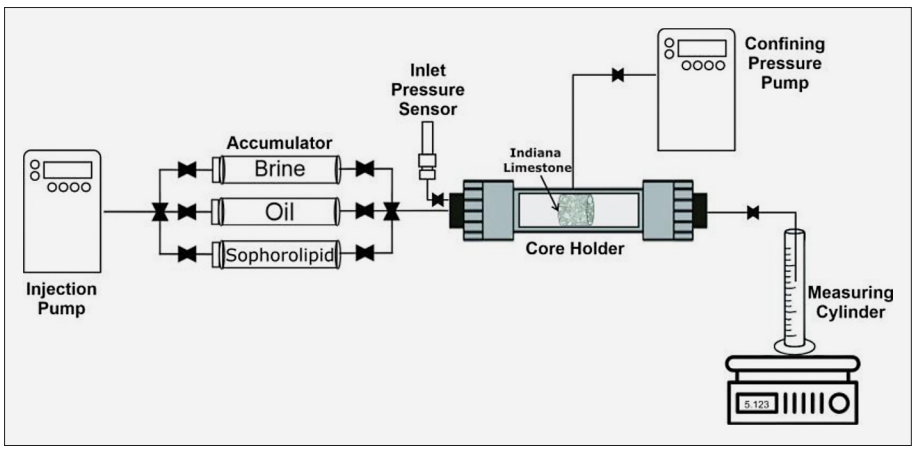


Figure 5. Schematic of the Core Flooding Apparatus

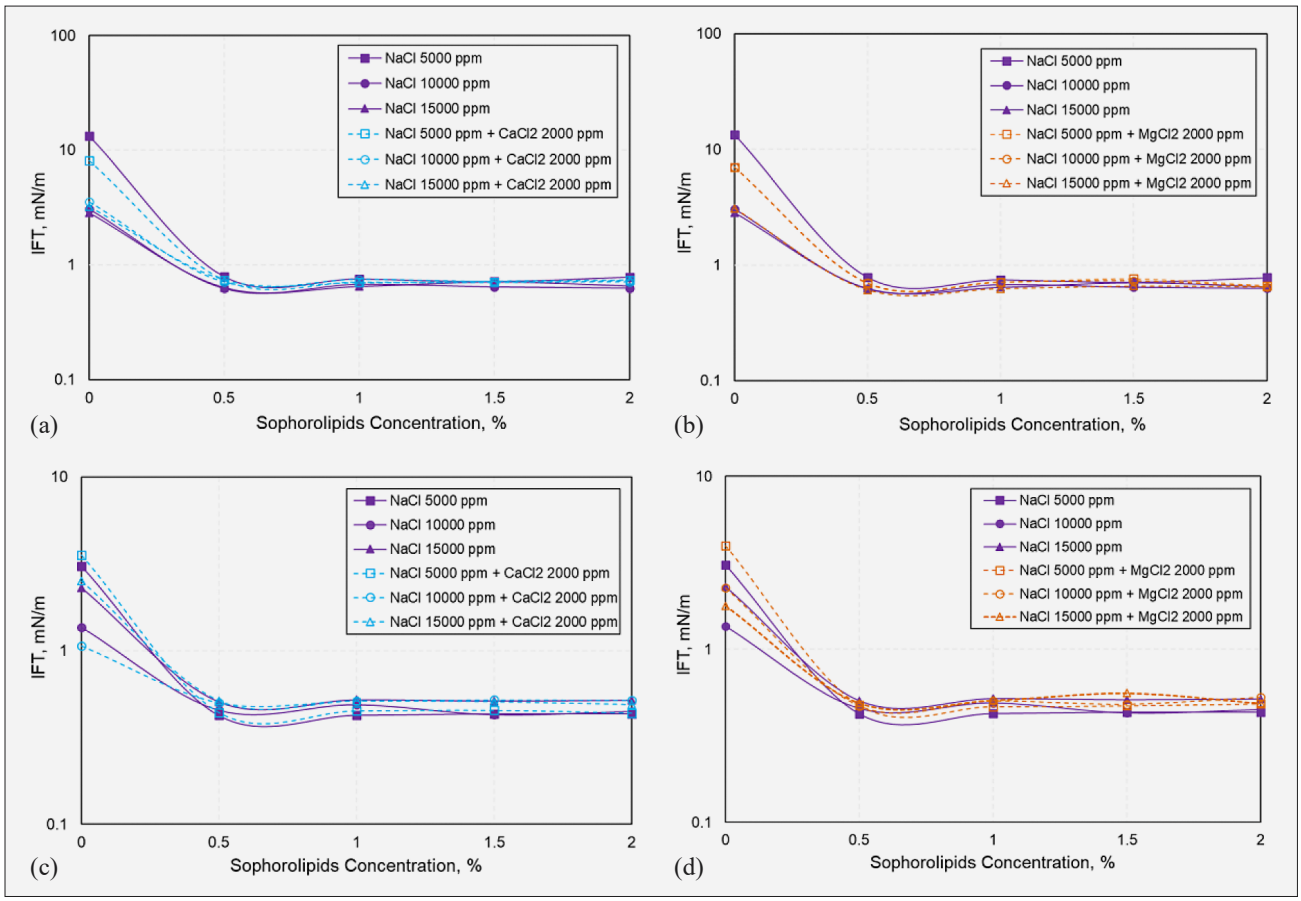


Figure 6. Oil-water Interface Tension vs. Various Sophorolipids Concentrations: (a and b) Medium Oil; and (c and d) Light Oil, both with Added $CaCl_2$ and $MgCl_2$.

water with the rock surface, changed the adsorption features. In a volumetric flask, a sample of IL grain (80 mesh) was soaked in a solution of sophorolipids at 0.5% and 2 wt.%. The mass ratio between the grain and the solution was 1:4. The flask was shaken for 48 h, and then the liquid was filtered through 4 micro-sized filter papers. The adsorption analysis was conducted using a high-performance liquid chromatography apparatus (see **Figure 4**). The test was performed by introducing the fluid (all particles analysed had to be in liquid form) into the injection port.

2.3.5. Core Flooding

The core flooding test involves fluid, or a combination of fluids, being injected into a rock sample. This test is commonly used to determine the optimal development options for oil reservoirs and often helps in evaluating the effects of injecting fluids specifically designed to enhance or increase oil recovery. A core plug sample of IL was immersed in crude oil for 24 h at 60 ± 0.5°C after water injection. The concentration of the sophorolipid solution was 0.5 wt.% under CMC conditions and the brine concentration was 10,000 ppm, representing the field conditions in Indonesia. Divalent ions were added to this fluid. The test was conducted using the core flooding apparatus, with a confining pressure of 100 psia and an injection rate of 0.3 cc/min, as shown in **Figure 5**.

3. Results

3.1. Interfacial Tension

Measurement of the IFT in sophorolipid solutions was carried out on 90 samples, with the effects of the addition of Ca^{2+} and Mg^{2+} ions, respectively in the forms of $CaCl_2$ or $MgCl_2$ at concentrations of 2000 ppm, to the solutions that had varying NaCl and sophorolipid concentrations. In general, the presence of $CaCl_2$ or $MgCl_2$ affected the IFT values in very subtle ways (see **Figure 6**). This suggests that the sophorolipids were not significantly affected by the divalent ions in either the medium crude oil (see **Figures 7a** and **b**) or light crude oil (see **Figures 6c** and **d**) cases. The sophorolipids were found to be optimum for reducing the oil–water IFT at a concentration of approximately 0.5 wt.%.

3.2. Oil-Water Emulsion Viscosity

In the oil–water emulsion viscosity test, observations were made at a sophorolipid concentration of 0.5 wt.%. In the medium oil (see **Figure 7a**), the Ca^{2+} caused an

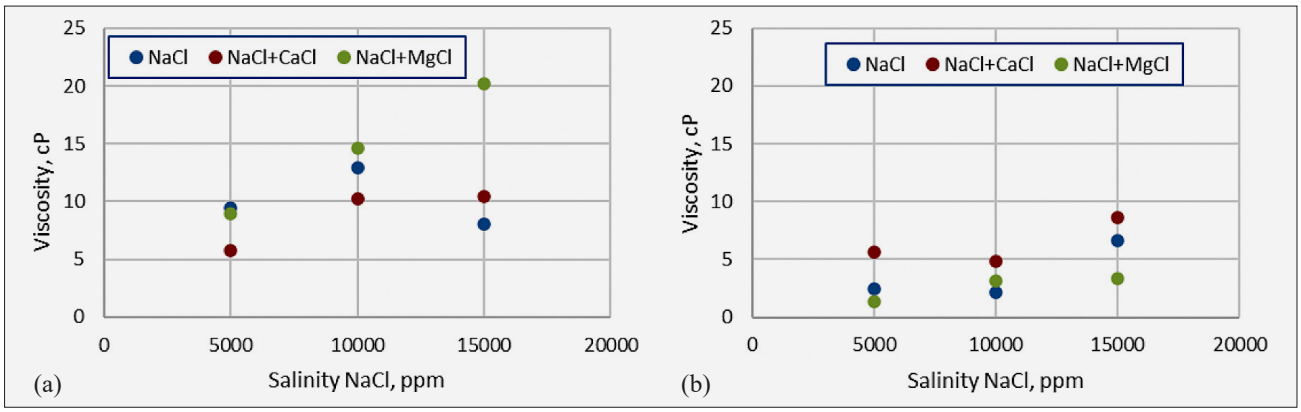


Figure 7. Mix Viscosity at Various Salinity of 0.5%w Sophorolipids: (a) Medium Oil; and (b) Light Oil with added $CaCl_2$ and $MgCl_2$

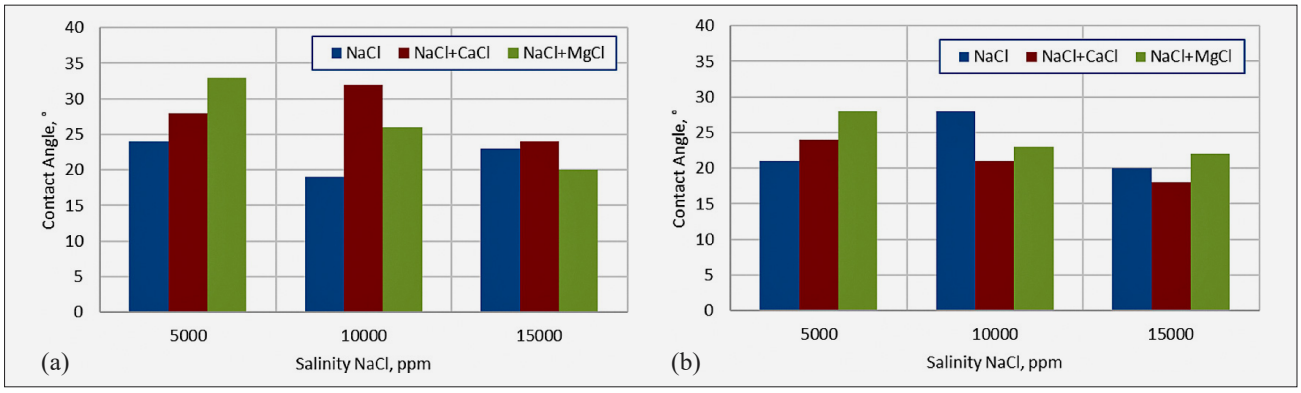


Figure 8. Effect of $CaCl_2$ and $MgCl_2$ on the Contact Angle of 0.5 %wt Sophorolipids in Various NaCl Concentrations: (a) Medium Oil; and (b) Light Oil

increase in the viscosity of the oil–water emulsion at high salinity (15,000 ppm) and the Mg^{2+} increased the viscosity even more, especially at medium to high salinities. In the light oil (see **Figure 7b**), the Ca^{2+} and Mg^{2+} effects were less critical, but both still increased the viscosity at a specific salinity. The impacts of the Ca^{2+} and Mg^{2+} were more significant in the medium oil than the light oil. In the light oil, the initial viscosity was lower, and the impact of the sophorolipids and additional ions was less pronounced. The structure of light oils tends to be simpler, which might explain this. Sophorolipids can affect the viscosity of oil–water emulsions depending on the oil type, optimum salt concentration, and the presence of divalent ions. Adding Ca^{2+} and Mg^{2+} increases the viscosity of medium oils in particular because the interaction between the ions and the sophorolipid micelles strengthens the structure, thus increasing flow resistance. The combination of NaCl and divalent ions showed synergistic effects in modifying the viscosity, especially at the Critical Micelle Concentration of sophorolipids.

3.3. Wettability Alteration

The influence of divalent ions on the alteration of wettability by sophorolipids is a complex subject that encompasses the interactions between biosurfactants and ionic compositions in aqueous solutions. Divalent ions, especially Ca^{2+} and Mg^{2+}, significantly influence the wettability of surfaces, particularly those altered by sophorolipids. In the case of 0.5 %wt sophorolipids concentration, Ca^{2+} and Mg^{2+} ions cause a significant increase in contact angle at NaCl salinity of 5,000 ppm and 10,000 ppm. At the same time, the effect is not noticeable at 15,000 ppm (see **Figure 8**).

The observation is almost similar for the light oil case. The contact angle increases at low salinity (5,000 ppm); it decreases at 10,000, and finally it tends to stabilize at 15,000 ppm. The effect of the addition of divalent ions on wettability alteration does not always have a clear pattern, but it is highly dependent on the specific conditions of the system and the combination of ions used (**Gandomkar & Reza, 2017**).

3.4. Static Adsorption

Static adsorption tests were conducted at 5000, 10,000 and 15,000 ppm NaCl salinity and 0.5 wt.% sophorolipid concentrations. At low NaCl salinity (5000 ppm), the presence of a divalent ion was able to reduce the adsorption (see **Figure 9**). At NaCl salinities of 10,000 and 15,000 ppm, the addition of Ca^{2+} or Mg^{2+} did not affect

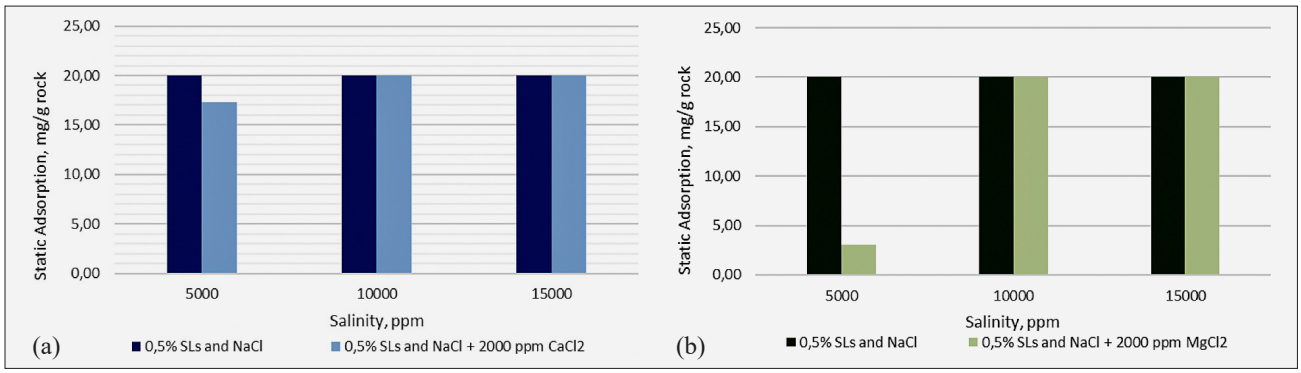


Figure 9. Static Adsorption of Sophorolipids on Carbonate Rocks-Effects of: (a) $CaCl_2$; and (b) $MgCl_2$

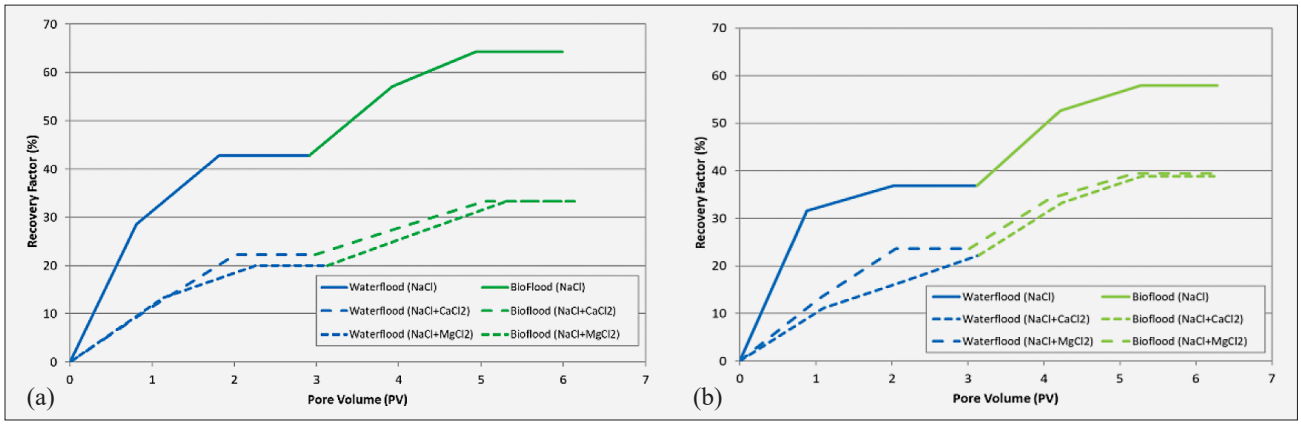


Figure 10. Effects of $CaCl_2$ and $MgCl_2$ on Waterflooding and Biosurfactant Flooding of 0.5 %wt sophorolipids in Various NaCl Concentrations: (a) Medium Oil; and (b) Light Oil.

the adsorption of sophorolipids. It is assumed that the sophorolipid molecules act directly on the surface, their distribution being more even under diverse ion circumstances (i.e. in the presence of Na^+, $Na^+ + Ca^{2+}$ or and $Na^+ + Mg^{2+}$), resulting in a consistent adsorption rate.

3.5. Core Flooding

The addition of Ca^{2+} and Mg^{2+} to the injection solution significantly decreased the oil recovery efficiency in both the water flooding and sophorolipid flooding processes, regardless of the crude oil grade, whether medium or light. During water flooding, the recovery factor decreased from approximately 44% to 20–23% for medium oil and from 37% to about 25% for light oil when divalent ions were added. In the biosurfactant flooding, the recovery factor decreased significantly, from approximately 65% to 33% for medium oil and from 58% to 40% for the light crude (see **Figure 10**). In carbonate rock reservoirs, the presence of divalent ions, such as Ca^{2+} and Mg^{2+}, has a more complex effect than in sandstone reservoirs. This is because carbonate rocks are composed mainly of calcite ($CaCO_3$), which can chemically interact directly with these ions. Divalent ions interact with the sophorolipid solution and the rock, causing a decrease in biosurfactant activity, an increase in adsorption, and the formation of mineral scales that inhibit permeability. Elevated divalent-ion concentrations (Ca^{2+}/Mg^{2+}) in carbonate systems alter surface charge and promote Ca^2-mediated surface complexation, which diminishes wettability alteration and reduces incremental recovery (**Mahani et al., 2015**).

4. Discussion

The interaction between divalent ions (Ca^{2+} and Mg^{2+}), sophorolipid molecules, and carbonate mineral surfaces plays a crucial role in determining the overall recovery performance. These ions are known to engage in surface complexation reactions with carbonate minerals, leading to changes in surface charge and electrostatic potential. At moderate salinity levels (5,000–10,000 ppm NaCl), Ca^{2+} and Mg^{2+} ions tend to compete with the carboxyl and hydroxyl functional groups of sophorolipid molecules for adsorption sites on the carbonate surface. This competition reduces biosurfactant adsorption, enhancing the availability of active sophorolipid molecules in solution and promoting water-wet conditions. Conversely, at higher salinities (≥15,000 ppm), the accumulation of these divalent ions at the mineral interface promotes the formation of Ca–CO_3 or Mg–CO_3 surface

complexes, which can hinder the ability of sophorolipids to interact effectively with the rock, thus diminishing wettability alteration efficiency. Mg^{2+} ions, due to their stronger hydration shell, induce greater charge shielding and restrict surfactant adsorption, resulting in more stable but less reactive interfaces. In contrast, Ca^{2+} can bridge between negatively charged sophorolipid headgroups and carbonate surfaces, promoting partial aggregation of micelles at the interface. This bridging effect explains the observed increase in emulsion viscosity for medium oils and the reduced recovery during coreflooding tests. These mechanistic insights align with previous findings by **Bai et al. (2021)** and **Derikvand et al. (2020)**, suggesting that the balance between ion concentration, salinity, and biosurfactant molecular structure must be optimized to achieve effective EOR performance in carbonate reservoirs.

5. Conclusions

The findings show that divalent ions – especially Ca^{2+} and Mg^{2+} – affect the interactions between crude oil, brine solutions, and carbonate rocks, to a certain degree, when biosurfactant sophorolipids are added to the brine as the EOR agent. These ions decrease the IFT between the brine and sophorolipid at least a tenth of the time, in both light and medium oil. Meanwhile, these ions tend to increase the water contact angle at low salinities (5000–10,000 ppm) and decrease the water contact angle at higher salinities (10,000–15,000 ppm). The adsorption of the sophorolipids onto the IL decreased in the presence of Ca^{2+} and Mg^{2+} at low salinities. These results suggest Ca^{2+} and Mg^{2+} can improve the performance of sophorolipids if used as an EOR agent in a carbonate reservoir. Incorporating Ca^{2+} and Mg^{2+} enhances the viscosity of the mixture, particularly in medium oils, due to the interaction of these ions with sophorolipid micelles, thereby fortifying the structure and augmenting flow resistance. This may potentially create a more stable displacement front for improved oil recovery.

The recovery factor in biosurfactant flooding decreased significantly, dropping from approximately 65% to 33% for the medium oil and from 58% to 40% for the light crude oil. In carbonate rocks, the adverse effects of divalent ions are more complex because they stabilize the carbonate minerals, reducing the potential for changes in wettability required to increase recovery. Increased divalent-ion concentrations (Ca^{2+}/Mg^{2+}) in carbonate systems modify surface charge and facilitate surface complexation, hence decreasing wettability alteration and limiting incremental recovery.

Acknowledgement

This study was funded by the Center of Higher Education Funding and Assessment, Ministry of Higher Education, Science, and Technology of the Republic of Indonesia through Grant No: 0742/J5.2.3/BPI.06/10/2021. The experiments were conducted in the Laboratory of Enhanced Oil Recovery (EOR), Institut Teknologi Bandung, and UPN Veteran Yogyakarta.

Funding

This research was funded by the Center of Higher Education Funding and Assessment, Ministry of Higher Education, Science, and Technology of the Republic of Indonesia, grant number 0742/J5.2.3/BPI.06/10/2021.

6. References

Abdallah, W., Buckley, J. S., Carnegie, A., Edwards, J., Herold, B., Fordham, E., Graue, A., Habashy, T., Seleznev, N., Signer, C., Hussain, H., Montaron, B., & Ziauddin, M. (2007). Fundamentals of wettability. *Oilfield Review*, *19*(2), 44–61.

Akanji, L. T., Rehman, R., Onyemara, C. C., Ebel, R., & Jamal, A. (2021). A novel technique for interface analysis : Behaviour of sophorolipids biosurfactant obtained from Meyerozyma spp . MF138126 during low-salinity heavy-crude experiments. *Fuel*, *297*(April 2020), 120607. https://doi.org/10.1016/j.fuel.2021.120607

Al-Maamari, R. S. H., & Buckley, J. S. (2003). Asphaltene precipitation and alteration of wetting: The potential for wettability changes during oil production. *SPE Reservoir Evaluation and Engineering*, *6*(4), 210–214. https://doi.org/10.2118/84938-PA

Anachkov, S. E., Tcholakova, S., Dimitrova, D. T., Denkov, N. D., Subrahmaniam, N., & Bhunia, P. (2015). Adsorption of linear alkyl benzene sulfonates on oil-water interface: Effects of Na+, Mg2+ and Ca2+ ions. *Colloids and Surfaces A: Physicochemical and Engineering Aspects*, *466*, 18–27. https://doi.org/10.1016/j.colsurfa.2014.10.059

Ayirala, S., Sofi, A., Li, Z., & Xu, Z. (2021). Surfactant and surfactant-polymer effects on wettability and crude oil liberation in carbonates. *Journal of Petroleum Science and Engineering*, *207*(June), 109117. https://doi.org/10.1016/j.petrol.2021.109117

Baccile, N., & Kleinen, J. (2025). Biosurfactants and bioamphiphiles, survey, perspectives and applicative potential from a colloid science point of view. *Current Opinion in Colloid and Interface Science*, *75*, 101891. https://doi.org/10.1016/j.cocis.2024.101891

Bai, S., Kubelka, J., & Piri, M. (2021). Wettability Reversal on Dolomite Surfaces by Divalent Ions and Surfactants: An Experimental and Molecular Dynamics Simulation Study. *Langmuir*, *37*(22), 6641–6649. https://doi.org/10.1021/acs.langmuir.1c00415

Bassir, S. M., & Shadizadeh, S. R. (2020). Static adsorption of a new cationic biosurfactant on carbonate minerals: Application to EOR. *Petroleum Science and Technology*, *38*(5), 462–471. https://doi.org/10.1080/10916466.2020.1727922

Bhardwaj, G. (2013). Biosurfactants from Fungi: A Review. *Journal of Petroleum & Environmental Biotechnology*, *04*(06). https://doi.org/10.4172/2157-7463.1000160

Derikvand, Z., Rezaei, A., Parsaei, R., Riazi, M., & Torabi, F. (2020). A mechanistic experimental study on the combined effect of Mg2+, Ca2+, and SO42- ions and a cationic surfactant in improving the surface properties of oil/water/rock system. *Colloids and Surfaces A: Physicochemical and Engineering Aspects*, *587*(September 2019), 124327. https://doi.org/10.1016/j.colsurfa.2019.124327

Díaz De Rienzo, M. A., Banat, I. M., Dolman, B., Winterburn, J., & Martin, P. J. (2015). Sophorolipid biosurfactants: Possible uses as antibacterial and antibiofilm agent. *New Biotechnology*, *32*(6), 720–726. https://doi.org/10.1016/j.nbt.2015.02.009

Elshafie, A. E., Joshi, S. J., Al-Wahaibi, Y. M., Al-Bemani, A. S., Al-Bahry, S. N., Al-Maqbali, D., & Banat, I. M. (2015). Sophorolipids production by Candida bombicola ATCC 22214 and its potential application in microbial enhanced oil recovery. *Frontiers in Microbiology*, *6*(NOV), 1–11. https://doi.org/10.3389/fmicb.2015.01324

Esfandyari, H., Moghani Rahimi, A., Esmaeilzadeh, F., Davarpanah, A., & Mohammadi, A. H. (2021). Amphoteric and cationic surfactants for enhancing oil recovery from carbonate oil reservoirs. *Journal of Molecular Liquids*, *322*, 114518. https://doi.org/10.1016/j.molliq.2020.114518

Eslahati, M., Mehrabianfar, P., Isari, A. A., Bahraminejad, H., Manshad, A. K., & Keshavarz, A. (2020). Experimental investigation of Alfalfa natural surfactant and synergistic effects of Ca2+, Mg2+, and SO42− ions for EOR applications: Interfacial tension optimization, wettability alteration and imbibition studies. *Journal of Molecular Liquids*, *310*, 113123. https://doi.org/10.1016/j.molliq.2020.113123

Fu, L., Ren, Z., Chen, W., Liu, Q., Ye, M., Qiu, X., Zhang, Y., Zheng, Y., Liao, K., & Shao, M. (2024). Polyetheramine enhanced biosurfactant/biopolymer flooding for enhanced oil recovery. *Journal of Molecular Liquids*, *411*(May), 125757. https://doi.org/10.1016/j.molliq.2024.125757

Gandomkar, A., & Reza, M. (2017). The impact of monovalent and divalent ions on wettability alteration in oil / low salinity brine / limestone systems. *Journal of Molecular Liquids*, *248*, 1003–1013. https://doi.org/10.1016/j.molliq.2017.10.095

Ganji, Z., Beheshti-Maal, K., Massah, A., & Emami-Karvani, Z. (2020). A novel sophorolipid-producing Candida keroseneae GBME-IAUF-2 as a potential agent in microbial enhanced oil recovery (MEOR). *FEMS Microbiology Letters*, *367*(17), 1–8. https://doi.org/10.1093/femsle/fnaa144

Gazem, A., Krishna, S., & Al-Yaseri, A. (2025). Low-salinity enhanced oil recovery using biosurfactant-ZnO nanoparticle-xanthan gum formulations: A comparative study of rhamnolipid and sophorolipid systems. *Journal of Molecular Liquids*, *432*(May), 127894. https://doi.org/10.1016/j.molliq.2025.127894

Ghaedi, A., Nabipour, M., Azdarpour, A., & Gandomkar, A. (2023). Mechanistic investigation of using low salinity alkaline surfactant solutions in carbonate reservoirs based on polarity of crude oil. *Journal of Molecular Liquids*, *390*(PB), 123098. https://doi.org/10.1016/j.molliq.2023.123098

Hao, J., Mohammadkhani, S., Shahverdi, H., Esfahany, M. N., & Shapiro, A. (2019). Mechanisms of smart waterflooding in carbonate oil reservoirs - A review. *Journal of Petroleum Science and Engineering*, *179*(January), 276–291. https://doi.org/10.1016/j.petrol.2019.04.049

Herawati, I., Permadi, P., Rochliadi, A., & Marhaendrajana, T. (2022). Adsorption of anionic surfactant on sandstone reservoir containing clay minerals and its effect on wettability alteration. *Energy Reports*, *8*, 11554–11568. https://doi.org/10.1016/j.egyr.2022.08.268

Hou, J., Du, J., Sui, H., & Sun, L. (2021). Surfactants enhanced heavy oil–solid separation from carbonate asphalt rocks-experiment and molecular dynamic simulation. *Nanomaterials*, *11*(7). https://doi.org/10.3390/nano11071835

Hou, J., Lin, S., Du, J., & Sui, H. (2022). Study of the Adsorption Behavior of Surfactants on Carbonate Surface by Experiment and Molecular Dynamics Simulation. *Frontiers in Chemistry*, *10*(April), 1–19. https://doi.org/10.3389/fchem.2022.847986

Iravani, M., Simjoo, M., & Chahardowli, M. (2025). Screening key parameters affecting stability of graphene oxide and hydrolyzed polyacrylamide hybrid: Relevant for EOR application. *Heliyon*, *11*(4), e42875. https://doi.org/10.1016/j.heliyon.2025.e42875

Jha, N. K., Iglauer, S., & Sangwai, J. S. (2018). Effect of Monovalent and Divalent Salts on the Interfacial Tension of n -Heptane against Aqueous Anionic Surfactant Solutions. *Journal of Chemical and Engineering Data*, *63*(7), 2341–2350. https://doi.org/10.1021/acs.jced.7b00640

Khodaparast, P., & Johns, R. T. (2020). A continuous and predictive viscosity model coupled to a microemulsion equation of state. *SPE Journal*, *25*(3), 1070–1081. https://doi.org/10.2118/190278-PA

Koh, A., Linhardt, R. J., & Gross, R. (2016). Effect of Sophorolipid n-Alkyl Ester Chain Length on Its Interfacial Properties at the Almond Oil-Water Interface. *Langmuir*, *32*(22), 5562–5572. https://doi.org/10.1021/acs.langmuir.6b01008

Magri, A., Baldo, C., Pedrine, M. A., & Celligoi, C. (2018). Review: Sophorolipids A Promising Biosurfactant and it's Applications Study of probiotics in different matrices View project Optimization and scale-up of liquid-liquid extraction process with ionic liquids (ILs) as a sustainable tool for the separation of. *International Journal of Advanced Biotechnology and Research(IJBR)*. http://www.bipublication.com

Mahani, H., Keya, A. L., Berg, S., Bartels, W.-B., Nasralla, R., & Rossen, W. R. (2015). Insights into the Mechanism of Wettability Alteration by Low-Salinity Flooding (LSF) in Carbonates. *Energy & Fuels*, *29*(3), 1352–1367. https://doi.org/10.1021/ef5023847

Marhaendrajana, T., Ridwan, M. G., Kamil, M. I., & Permadi, P. (2018). Wettability alteration induced by surface roughening during low salinity waterflooding. *Journal of Engineering and Technological Sciences*, *50*(5), 635–649. https://doi.org/10.5614/j.eng.technol.sci.2018.50.5.4

Marhaendrajana, T., Widiyaningsih, I., Kurnia, I., & Sulistyarso, H. B. (2025). Fluid-to-Fluid and Fluid-to-Rock Interaction on Sophorolipids Biosurfactant for Enhanced Oil Recovery: A Literature Review. *Scientific Contributions Oil and Gas*, *48*(1), 63–76. https://doi.org/10.29017/SCOG.48.1April.1688

Megayanti, R., Hidayat, M., Cahyaningtyas, N., Sanmurjana, M., Nur Muhammad Yahya, Z., Sagita, F., Kadja, G. T. M., & Marhaendrajana, T. (2023). Effect of Titanium Dioxide Nanoparticles on Surfactants and Their Impact on the Interfacial Properties of the Oil-Water-Rock System. *ACS Omega*, *8*(41), 38539–38545. https://doi.org/10.1021/acsomega.3c05365

Mogensen, K., & Masalmeh, S. (2020). A review of EOR techniques for carbonate reservoirs in challenging geological settings. *Journal of Petroleum Science and Engineering*, *195*(May). https://doi.org/10.1016/j.petrol.2020.107889

Mohammadi, S., Kord, S., & Moghadasi, J. (2019). The hybrid impact of modi fi ed low salinity water and anionic surfactant on oil expulsion from carbonate rocks : A dynamic approach. *Journal of Molecular Liquids*, *281*, 352–364. https://doi.org/10.1016/j.molliq.2019.02.092

Mohammed, M., & Babadagli, T. (2015). Wettability alteration: A comprehensive review of materials/methods and testing the selected ones on heavy-oil containing oil-wet systems. *Advances in Colloid and Interface Science*, *220*, 54–77. https://doi.org/10.1016/j.cis.2015.02.006

Morse, J. W., & Arvidson, R. S. (2002). The dissolution kinetics of major sedimentary carbonate minerals. *Earth-Science Reviews*, *58*(1–2), 51–84. https://doi.org/10.1016/S0012-8252(01)00083-6

Nazari, M. H., Tavakoli, V., Rahimpour-Bonab, H., & Sharifi-Yazdi, M. (2019). Investigation of factors influencing geological heterogeneity in tight gas carbonates, Permian reservoir of the Persian Gulf. *Journal of Petroleum Science and Engineering*, *183*(March), 106341. https://doi.org/10.1016/j.petrol.2019.106341

Pal, S., Chatterjee, N., Das, A. K., McClements, D. J., & Dhar, P. (2023). Sophorolipids: A comprehensive review on properties and applications. *Advances in Colloid and Interface Science*, *313*(February), 102856. https://doi.org/10.1016/j.cis.2023.102856

Prabhakar, S., & Melnik, R. (2018). Influence of Mg2+, SO42− and Na+ ions of sea water in crude oil recovery: DFT and ab initio molecular dynamics simulations. *Colloids and Surfaces A: Physicochemical and Engineering Aspects*, *539*(July 2017), 53–58. https://doi.org/10.1016/j.colsurfa.2017.12.009

Shaik, I. K., Song, J., Biswal, S. L., Hirasaki, G. J., Bikkina, P. K., & Aichele, C. P. (2020). Effect of brine type and ionic strength on the wettability alteration of naphthenic-acid-adsorbed calcite surfaces. *Journal of Petroleum Science and Engineering*, *185*(October 2019), 106567. https://doi.org/10.1016/j.petrol.2019.106567

Shekhar, S., Sundaramanickam, A., & Balasubramanian, T. (2015). Biosurfactant producing microbes and their potential applications: A review. *Critical Reviews in Environmental Science and Technology*, *45*(14), 1522–1554. https://doi.org/10.1080/10643389.2014.955631

Sheng, J. J. (2013). Review of Surfactant Enhanced Oil Recovery in Carbonate Reservoirs. *Advances in Petroleum Exploration and Development*, *6*(June), 1–10. https://doi.org/10.3968/j.aped.1925543820130601.1582

Swadesi, B., Marhaendrajana, T., Septoratno Siregar, H. P., & Mucharam, L. (2015). The effect of surfactant characteristics on IFT to improve oil recovery in tempino light oil field Indonesia. *Journal of Engineering and Technological Sciences*, *47*(3), 250–265. https://doi.org/10.5614/j.eng.technol.sci.2015.47.3.2

Thorstenson, D. C., & Plummer, L. N. (1977). Equilibrium criteria for two-component solids reacting with fixed composition in an aqueous phase; example, the magnesian calcites. *American Journal of Science*. https://doi.org/10.2475/ajs.277.9.1203

Udoh, T., & Vinogradov, J. (2019). A synergy between controlled salinity brine and biosurfactant flooding for improved oil recovery: An experimental investigation based on zeta potential and interfacial tension measurements. *International Journal of Geophysics*, *2019*. https://doi.org/10.1155/2019/2495614

Xu, Z. X., Li, S. Y., Li, B. F., Chen, D. Q., Liu, Z. Y., & Li, Z. M. (2020). A review of development methods and EOR technologies for carbonate reservoirs. *Petroleum Science*, *17*(4), 990–1013. https://doi.org/10.1007/s12182-020-00467-5

Yutkin, M. P., Radke, C. J., & Patzek, T. W. (2022). Chemical Compositions in Modified Salinity Waterflooding of Calcium Carbonate Reservoirs: Experiment. *Transport in Porous Media*, *141*(2), 255–278. https://doi.org/10.1007/s11242-021-01715-x

Zaeri, M. R., Shahverdi, H., Hashemi, R., & Mohammadi, M. (2019). Impact of water saturation and cation concentrations on wettability alteration and oil recovery of carbonate rocks using low-salinity water. *Journal of Petroleum Exploration and Production Technology*, *9*(2), 1185–1196. https://doi.org/10.1007/s13202-018-0552-2

Zheng, C., Wang, Z., Zhang, X., Wang, Y., & Zhang, L. (2024). Effect of salt ions (Na+, Ca2+ and Mg2+) and EOR anionic and nonionic surfactants on the dispersion stability of cellulose nanocrystals. *International Journal of Biological Macromolecules*, *282*(October). https://doi.org/10.1016/j.ijbiomac.2024.136761

SAŽETAK

Utjecaj iona kalcija i magnezija na sustav sirove nafte, slojne vode i karbonatnih stijena tijekom povećanja iscrpka nafte soforolipidnom otopinom

Interakcija između sirove nafte, slojne vode i karbonatnih stijena ključna je za primjenu metoda povećanja iscrpka nafte (engl. *Enhanced Oil Recovery*, EOR). Površinski aktivne tvari (surfaktanti), kao što su biosurfaktanti soforolipidi, koji su sastavni dio istiskivajućega fluida, mogu smanjiti međufaznu napetost (engl. *interfacial tension*, ITF) i promijeniti močivost takvih sustava. Međutim, prisutnost dvovalentnih iona, posebice kalcija (Ca^{2+}) i magnezija (Mg^{2+}), čini ovu interakciju složenijom, utječući na učinkovitost EOR metoda. U ovome je radu eksperimentalno ispitan utjecaj dvovalentnih iona na sustav sirova nafta – slojna voda – karbonatne stijene uz dodatak soforolipida. Izražen je utjecaj dvovoalentnih iona na uzorke srednje teške i lake nafte dodavanjem različitih koncentracija Ca^{2+} i Mg^{2+} iona u otopinu soforolipida u trima različitim uvjetima saliniteta. Eksperimenti s međufaznom napetošću i viskoznošću emulzije procjenjuju interakcije fluida, dok mjerenja kontaktnoga kuta i statičke adsorpcije karakteriziraju interakciju između fluida i stijene, što je vrlo važno za EOR mehanizam. Dodavanje Ca^{2+} i Mg^{2+} iona (2000 ppm) otopinama natrijeva klorida (NaCl) (10 000 – 15 000 ppm) s koncentracijom soforolipida od 0,5 % težinski pri kritičnoj micelnoj koncentraciji (engl. *Critical Micelle Concentration*, CMC) povećalo je močivost karbonatne stijene na vodu. Uz to, iako su ioni smanjili međufaznu napetost (ITF), nisu znatno utjecali na viskoznosti emulzije nafte u vodenoj otopini NaCl s 0,5 % (težinski) soforolipida. U uvjetima niskoga saliniteta (otopina s 5000 ppm NaCl) ovi su ioni smanjili brzinu adsorpcije u soforolipidnim otopinama na uzorcima vapnenaca iz Indiane. Dodavanje ovih dvovalentnih iona u otopinu za utiskivanje znatno je smanjilo učinkovitost istiskivanja nafte, za oko 28 % u slučaju lake nafte i 32 % u slučaju srednje teške nafte, tijekom navodnjavanja biosurfaktantima.

Ključne riječi:
soforolipidi, dvovalentni ioni, uvjeti saliniteta, povećanje iscrpka nafte

Author's contribution

Indah Widiyaningsih (Doctoral Student in Petroleum Engineering ITB): conceptualization, validation, formal analysis, investigation, data curation, writing-original draft, writing-review and editing, visualization. **Ivan Kurnia** (PhD in Petroleum Engineering ITB): conceptualization, validation, formal analysis, resources, data curation, writing-review, and editing. **Harry Budiharjo Sulistyarso** (PhD in Petroleum Engineering UPN Veteran Yogyakarta): conceptualization, validation, and formal analysis. **Tutuka Ariadji** (PhD, Professor in Petroleum Engineering ITB): conceptualization, validation, and formal analysis. **Taufan Marhaendrajana** (PhD, Professor in Petroleum Engineering ITB): conceptualization, validation, formal analysis, resources, data curation, writing-review and editing, supervision, and project administration.
All authors have read and agreed to the published version of the manuscript.

RGNZ/MGPB

Geodynamic and Paragenetic Evolution of the Jbel Houanite Mineralization (Sb-Au; Pb-Zn) Eastern High Atlas of Morocco

Rudarsko-geološko-naftni zbornik
(The Mining-Geology-Petroleum Engineering Bulletin)
DOI: 10.17794/rgn.2026.2.7

Original scientific paper

Jaouad Choukrad[1]* ✉, Abdelkhiar Ait ali[1] ✉, Mohammed Charroud[1] ✉, Nacir El moutaouakkil[2] ✉, Boubker Boukili[2] ✉, Amine talih[3] ✉

[1] *LaRSI, Science and Engineering Research Laboratory, Faculty of Sciences and Technics, Sidi Mohamed Ben Abdellah University, BP 2202, Fez, Morocco.*

[2] *Geoscience, Water and Environment Laboratory, Faculty of Sciences Rabat, Mohammed V University in Rabat, 4 Avenue Ibn Battouta, B.P. 1014 RP, Rabat, Morocco.*

[3] *Geo-Biodiversity and Natural Patrimony Laboratory (GEOBIO), Geophysics, Natural Patrimony and Green Chemistry Research Center (GEOPAC), Department of Geology and Remote Sensing, Scientific Institute, Mohammed V University, Avenue Ibn Battouta, P.B. 703, 10106 Rabat-Agdal, Morocco.*

Abstract

The district of Jbel Houanite is an important metallogenic province rich in polymetallic mineralization (Sb-Au-Pb-Zn-Ba-Fe-Cu) located in the northern part of the Eastern High Atlas of Morocco, along the North High Atlasic Fault. The earliest identified mineralization corresponds to quartz veins rich in antimony and gold hosted in the Paleozoic formations, while the later mineralization corresponds to Pb-Zn deposits hosted in the Liassic limestones. Geological reconnaissance and mineral exploration work in the Jbel Houanite region determined the presence of antimony mineralization in the form of Stibnite (Sb_2S_3) and Bindheimite ($Pb_2Sb_2O_6(O,OH)$), while the lead mineralization in the sedimentary cover consists of galena (PbS) and cerussite ($PbCO_3$). The lead anomalies are intimately linked to the presence of antimony, and this mineralization is the result of hydrothermal remobilization during the Atlas phases, which reactivated the basement faults, facilitating the establishment of lead mineralization in a Mississippi Valley Type (MVT) system. Petrographic and geochemical investigations of mineral parageneses allowed us to establish temporal relationships between mineralization events: the primary Sb-Au mineralization is linked to late Hercynian extensional tectonics, while the Pb-Zn mineralization is related to early Atlas compressional phases. This sequential evolution highlights a complex polyphase tectono-metallogenic history controlling ore deposition. These findings contribute to a better understanding of the genetic models of Sb-Au-Pb-Zn mineralization in the High Eastern Atlas and demonstrate the crucial role of tectonic inheritance and structural reactivation in ore formation and localization.

Keywords:
Antimony, lead, paragenetic evolution, Paleozoic basement, Meso-Cenozoic cover, Eastern High Atlas, Morocco

1. Introduction

The Eastern High Atlas of Morocco is an intracontinental chain that was formed during the Mesozoic and Cenozoic phases (**Mattauer et al., 1977; Laville et al., 2004; Choukrad, 2022**). This evolution is reflected in the development of pull-apart basins controlled by a network of major faults inherited from the Precambrian and Hercynian tectonic cycles. In this context, the Jbel Houanite mining district is located at the intersection of the North High Atlasic Fault and constitutes a pivotal zone between the Paleozoic structural domain of the Tamlelt inlier and the High Atlasic domain (see **Figure 1a**) (**e.g. Jacobshagen et al., 2005; Nouayti et al., 2023; Chellai et al., 2024**).

The Jbel Houanite region is distinguished by polymetallic mineralization that occurs in two distinct episodes: antimony and gold mineralization (see **Figure 1b**), of Hercynian age, and lead-zinc mineralization, linked to the Atlas orogeny. The former is located along NW-SE and NE-SW oriented fractures, while the latter develops preferentially along the E-W fracture systems intersecting the carbonate platform of the Lower and Middle Lias.

The Paleozoic Tamlelt formations begin with a Neoproterozoic and Cambrian carbonate platform composed of limestones and dolomites. The Cambrian period, marked by black or green pelites with sandstone and quartzitic intercalations, reflects a gradual deepening of the basin (**El Kochri, 1996; Houari, 2003; Houari & Hoepffner, 2003; El Hakour, 2005; Talih et al., 2022**).

* Corresponding author: Jaouad Choukrad
e-mail address: jaouad.choukrad@usmba.ac.ma
Received: 29 May 2025. Accepted: 2 October 2025.
Available online: 13 March 2026

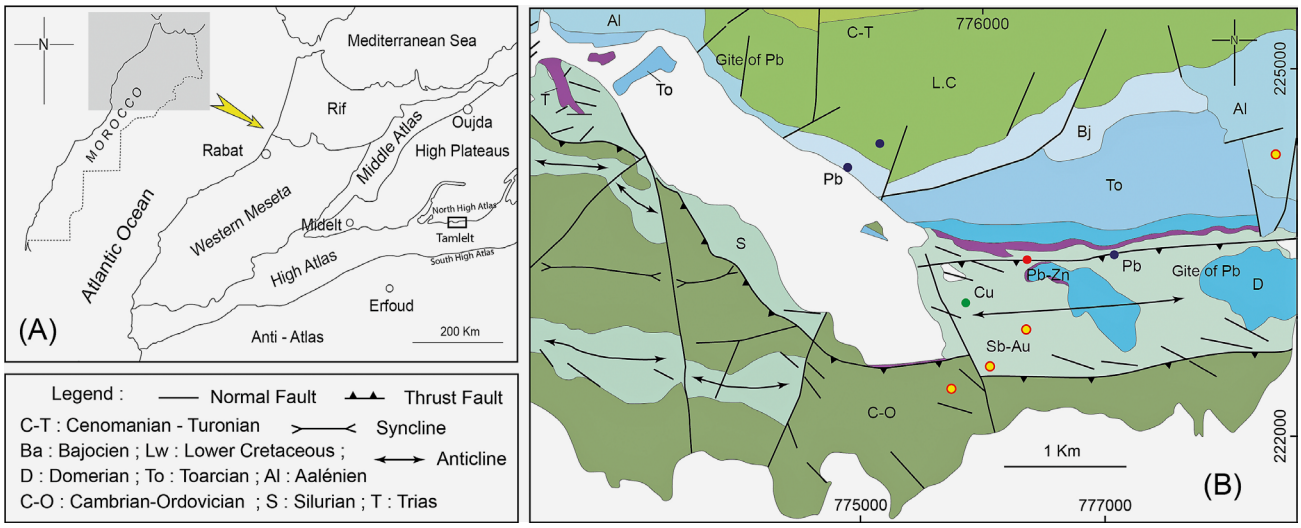


Figure 1. (a) Location of the study area district (b) geological map of Houanite District.

The Ordovician is defined by alternations of sandstone, clayey or silty schist, and quartzites, while the Silurian is represented by silty or clayey pelites (see **Figure 1b**).

The Mesozoic and Cenozoic cover is the result of a negative tectonic inversion initiated in the Triassic and continued during the Jurassic and Cretaceous periods, which led to the formation of sedimentary basins (see **Figure 1b**). The Triassic is characterized by coarse arkoses, conglomerates and sandstones of detrital origin. The Lias, particularly the Sinemurian (see **Figure 1b**), is represented by massive dolomites and limestones reflecting the development of a typical Atlasic carbonate platform (**Charroud et al., 1996; Bezar et al., 1998; Charroud, 2002; Blomeier & Reijmer, 2002; Verwer et al., 2009; Merino-Tomé et al., 2012**). This deposition is followed, between the Pliensbachian and Toarcian periods, by successions of limestone and marl, indicating tectonic activity and the dislocation of the platform (**El Kochri & Chorowicz, 1996; Laville et al., 2004; Choukrad et al., 2024**). The Middle Jurassic begins with Aalenian and Bajocian limestones associated with a reef environment, topped by Bathonian detrital formations (**Kaoukaya et al., 2001; Adil et al., 2004; Choukrad et al., 2022**). The Lower Cretaceous is represented by detrital formations (red sandstones, lacustrine carbonates) dated to the Upper Aptian-Baremian (**El Kochri & Chorowicz, 1988; Haddoumi et al., 1998; Charrière et al., 2005; Haddoumi et al., 2008**). The infra-Cenomanian and Cenomanian levels indicate a detrital-evaporitic environment of sandstone, clay and gypsum, followed by Turonian carbonate deposits.

This study aims to characterize the paragenetic evolution of Sb-Au-Pb-Zn mineralization in the Jbel Houanite region by highlighting the spatio-temporal relationships between the antimony-bearing mineralization of the Hercynian basement and the lead-zinc mineralization hosted in the Mesozoic cover. This analysis is based on a multidisciplinary approach that integrates geological mapping, structural analysis, petrographic studies, and geochemical data.

Despite the significant metallogenic potential of the Eastern High Atlas particularly in polymetallic systems (Sb, Au, Pb, Zn, Fe, Ba, Cu) antimony mineralization in this region remains poorly documented and largely underrepresented in scientific literature. Previous studies have primarily focused on Pb-Zn deposits hosted in the Mesozoic cover (**Adil et al., 2004; Verhaert et al., 2017; Choukrad et al., 2023**), while Sb-Au occurrences in the Paleozoic basement, particularly those associated with shear zones, have received little attention. However, comparable Sb-Au mineralizations located along major crustal structures are well known in other orogenic settings, such as the Massif Central (France) and the Bohemian Massif (Central Europe), where they are typically associated with late hydrothermal fluid circulation controlled by major tectonic structures (**Marcoux & Bril, 1986; Bril et al., 1991; Ashley & Craw, 2004; Craw et al., 2004; Faure et al., 2005**).

In this context, the Jbel Houanite District represents a valuable case study for investigating the genetic links between successive mineralization events, spanning from the Paleozoic Hercynian orogeny to the Cenozoic Atlas orogenic phases.

By comparing the Jbel Houanite system to other Sb-bearing provinces in accretionary orogens, this research provides new insight into the role of inherited structures in controlling polyphase metallogenic systems. It also offers a refined paragenetic framework and temporal constraints that may be applied to other poorly known or unexplored Sb-Au-Pb-Zn occurrences in the High Atlas and analogous geodynamic settings.

2. Methods

In order to identify and characterize the geological and mineralogical aspects, as well as to define the para-

genetic evolution and the modes of mineralization in the region of El Houanite (Eastern High Atlas of Morocco), an integrated methodological approach was adopted, combining field approaches, petrographic, mineralogical and geochemical analyses.

➢ Fieldwork and Geological Mapping

A series of fieldwork campaigns was carried out in order to identify the geological strata, in particular the Paleozoic formations of the schist quartzitic basement and their Meso-Cenozoic cover with predominantly carbonate (limestone and dolomite). The study focused on the geological units containing the Sb and Pb-Zn mineralized showings.

Detailed geological sections and logs were drawn along profiles crossing the mineralized structures. These data were integrated into a geographic information system using ArcGIS 10.8 software to spatialize mineralization in relation to host structures.

➢ Sampling

Twelve representative samples were collected in an area bounded between the coordinates 32°33'58.4"N; 02°27'39.56"W and 32°34'31.27"N; 02°26'23.39"W. These samples cover both the Paleozoic basement (schist and quartzite formations) and the Mesozoic and Cenozoic cover (carbonate formations). Polished thin sections were prepared from selected samples for SEM examination. Prior to SEM analysis, the sections were coated with a thin carbon film using a vacuum carbon coater to ensure electrical conductivity and to improve imaging and EDX signal quality. The carbon coating is necessary to avoid charge accumulation on non-conductive phases and may appear in EDX spectra as an artifact; this was taken into account during data interpretation.

The samples were also examined with the JSM-IT100 Scanning Electron Microscope (SEM), equipped with an Energy Dispersive X-ray (EDX) analysis system semi-quantitative chemical analysis.

The EDX analyses were performed in high-vacuum mode, with an accelerating voltage of 15–20 kV and a working distance of ~10 mm. Elemental mapping and spot analyses were conducted on specific mineral phases to identify their chemical composition and textural relationships.

➢ Mineralogical Analyses (XRD)

The major minerals were identified by X-ray diffraction (XRD), carried out at the laboratory of the University of Fez using a Philips PANalytical X'Pert Pro diffractometer (Cu-Kα radiation, λ = 1.5406 Å, voltage 40 kV, intensity 40 mA). The analyses were performed at room temperature on powders obtained after fine grinding of the samples at a 50 μm mesh sieve, in order to minimize the effects of texture and preferential orientation. Data processing was carried out via the X'Pert Data Collector software.

➢ Geochemical analyses (XRF and ICP-MS)

The twelve collected samples were also the subjected to geochemical analyses to quantify major, minor and trace elements. The major elements were determined by wavelength dispersive X-ray fluorescence (XRF, Axios model), according to the standardized PROT ELE03-v01 protocol, after drying and conditioning the samples in granular form.

We followed the NI 43-101 standards for mining work using quality control procedures on geochemical analyses that correspond to the use of one sample doubling for every 10 samples and certified blank samples to ensure the reliability of the results and geochemical analyses.

Trace elements were analyzed by inductively coupled plasma mass spectrometry (ICP-MS) using an Ultima 2 - Jobin Yvon spectrometer, according to the NF EN ISO 11885. The results of these analyses are summarized in **Table 1**.

➢ Structural data treatment

We have processed the different tectonic structural measurements using the "Win-Tensor" software developed by the structural geologist Dr. Damien Delvaux (**Delvaux & Sperner, 2003**), this program is widely adopted and redundant, having already been used in scientific publications worldwide for processing tectonic and structural data results.

➢ Objective of the integrated analytical approach

The combination of these different analytical techniques (mapping, optical and electron microscopy, X-ray diffraction, X-ray fluorescence, ICP-MS) has made it possible to establish a clear link between the types of mineralization and their geological context. This cross-referencing of the data has contributed to the reconstruction of the paragenetic evolution of the antimony mineralization of the basement and the lead-bearing mineralization of the cover.

3. Results

Houanite District is a polymetallic province known for various types of mineralization; the location of the mineralized bodies of the Houanite District and their hosted rock has allowed us to indicate the presence of stages of mineralization with a paragenetic relationship between them. The first ore bodies associated with N120 and N40 quartz veins and they are composed by antimony and gold hosted in the Paleozoic formations, while the second one is hosted in the Liassic limestones following the Atlasic fracturing and the karstification area.

3.1. The Paleozoic inlier ore deposit

The antimony mineralization (Sb) is mainly located along major fracture and fault systems affecting the Paleo-

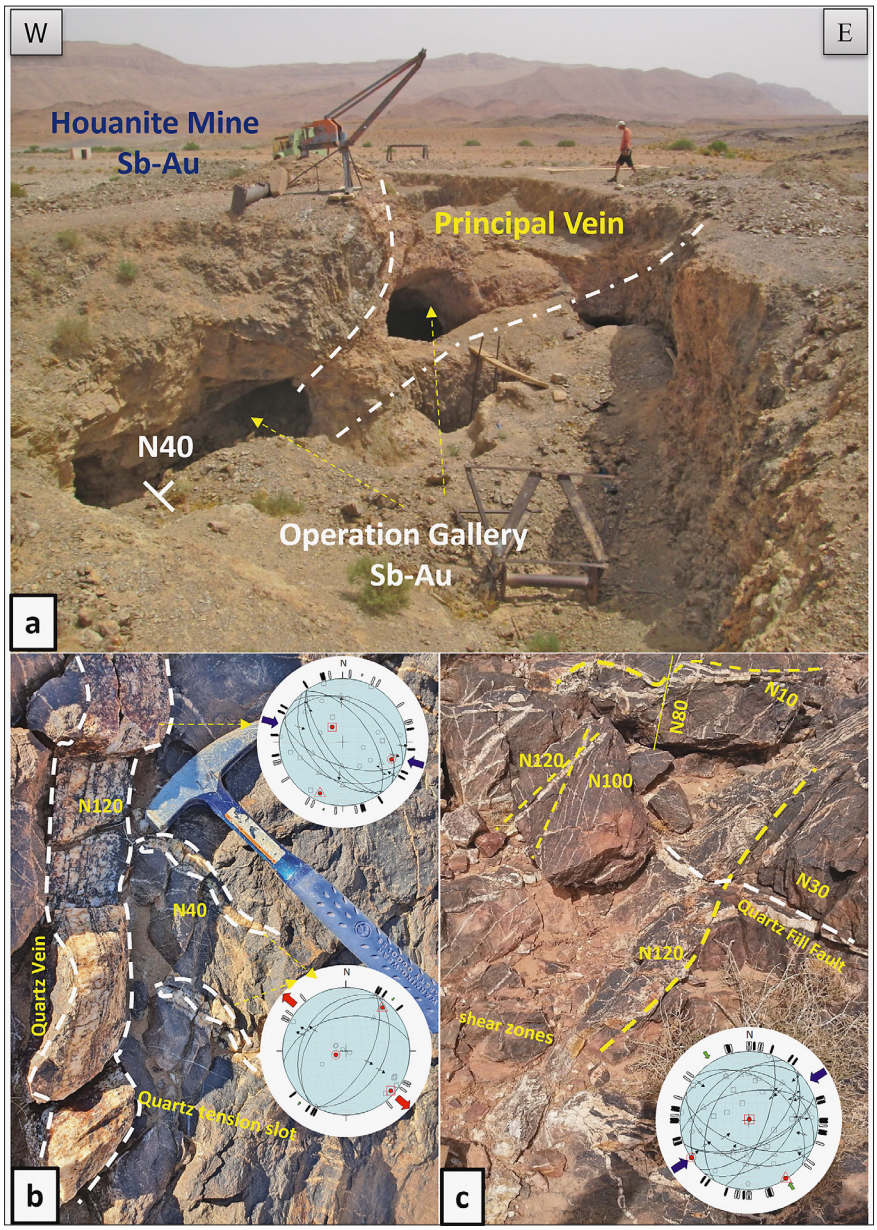


Figure 2. Detailed photos of the Houanite Au-Sb mining sector (a) the Houanite mine zone, (b) showing mineralization associated with quartz veins and stereographic representation of structural measurements (c) Deformation shear zone with the different generation of quartz rich in Sb-Au- and stereographic representation of structural measurements.

zoic basement (see **Figure 2a**). These structures have a dominant orientation between NW-SE and NE-SW, suggesting a polyphase tectonic heritage (**Ashley & Craw, 2004; Azza et al., 2019; Choukrad, 2022**). The structural ground analysis, coupled with the study of the spatial distribution of the orebodies, indicates that the mineralization is controlled by shear zones and deformation corridors associated with these large faults (see **Figure 2c**).

Three main episodes of deformation have been identified:

➢ Episode D_1: NW–SE Extension:

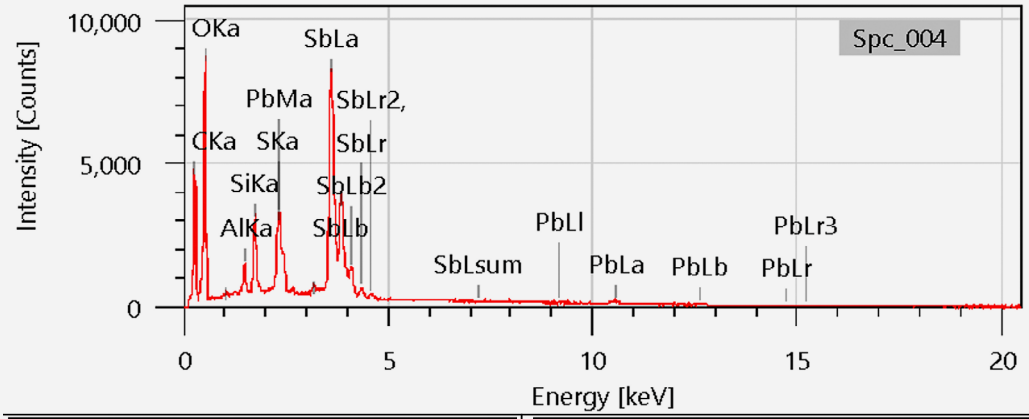
The first tectonic episode is characterized by an extensional regime-oriented NW–SE. This phase led to the formation of normal faults with apparent displacement along a N40° direction (approximately NE–SW) (see **Figure 2b**). These faults are commonly filled with quartz and, in some areas, show the presence of stibnite and gold-bearing mineralized bands.

➢ Episode D_2: NE–SW Compression:

The second episode corresponds to a compressive regime-oriented NE–SW, marked by reverse faults, open to tight folds, and ductile shear zones. Some of the earlier extensional structures were reactivated during this phase, displaying transpressive kinematics (see **Figure 2b).**

➢ Episode D_3: NW–SE Compression

A third compressive episode, oriented NW–SE, is also recognized. It is expressed by late-stage deformation features such as fault intersections and folding, which locally overprint earlier structures (see **Figure 2c**). This phase contributed to the development of fine-scale fracturing in previously deformed zones.



Element	Line	Mass%	Atom%
C	K	27.00±0.06	54.14±0.13
O	K	23.57±0.13	35.48±0.19
Si	K	0.43±0.03	0.37±0.02
S	K	0.79±0.03	0.59±0.02
Sb	L	46.75±0.27	9.25±0.05
Total		100.00	100.00
Spc_004			Fitting ratio 0.0440

Stibnite (Sb2S3) possibly Valentinite / Senarmontite (Sb_2O3)

Element	Line	Mass%	Atom%
C	K	27.00±0.06	54.14±0.13
O	K	23.57±0.13	35.48±0.19
S	K	0.79±0.03	0.59±0.02
Sb	L	46.75±0.27	9.25±0.05
Pb	M	1.47±0.010	1.17±0.01
Total		100.00	100.00
Spc_004			Fitting ratio 0.0440

Bindheimite ($Pb_2Sb_2O_6(O, OH)$) possibly Valentinite / Senarmontite (Sb_2O3)

Figure 3. Semi-quantitative compositions of Sb-bearing Paleozoic inlier ore samples from Houanite District (targeted sample)

The observed structural context suggests that the mineralizing episodes were multi-phased, with initial mineralization mainly related to the extensive D_1 phase, followed by reactivation and concentration events controlled by the D_2 and D_3 compressive phases. This polyphase tectonic control underscores the importance of shear corridors as major hosts of stibnite and gold deposits in this region.

The research and exploitation work by gallery, well, and open pit revealed the presence of polymetallic deposits (Sb-Au-As) in the basement (see **Figure 2a**). The general structures measured led to a typical dexterous shear zone. This zone is considered a transformation zone in Paleozoic times (**Piqué & Michard, 1989; Dill, 1998; Houari & Hoepffner, 2003; Azza et al., 2019; Jaouad et al., 2024**). The mineralization observed in the field is hosted in quartz veins intersecting middle Cambrian sandstone and quartzite.

In the field the folding belt ENE - WSW with regional development of the vertical axial plane cleavage. This deformation shows ductile faults associated with vertical foliation with mineralization of stibnite and chalcopyrite. The Sb-Au mineralization is emplaced in locally irregular 40-50 cm quartz veins (stockwork) (see **Figure 2c**). Quartz veins are observed in some places explaining the mode of emplacement of this mineralization in a shear-zone type shear zone.

Petrographic observation by optical microscopy of the samples indicated gold mineralization showing gold pipettes injected into the sub-automorphic quartz of the microgranites. While stibnite is disseminated in quartz and plagioclase, feldspars with chlorite with a very large portion in the rock. Thus, we can conclude that the paragenetic ores of the Paleozoic basement are composed of Sb-Pb (see **Figure 3**).

Scanning Electron Microscope (SEM) analysis combined with Energy-Dispersive X-ray Spectroscopy (EDS) was conducted on samples collected from mineralized quartz veins within the Paleozoic basement of the Houanite District. Multiple mineral assemblages were identified based on their chemical signatures. EDS spectra reveal the presence of antimony in association with lead, sulfur, oxygen, and silica (**Choukrad et al., 2022; Rajeshkumar et al., 2024; Sun et al., 2024**).

The EDS data display variable concentrations of sulfur and lead, reflecting local chemical heterogeneity within the mineralized zones. Complementary (XRD) analyses performed on the same samples allowed for the definitive identification of Stibnite (Sb_2S_3) and Bindheimite ($Pb_2Sb_2O_6(O,OH)$) (see **Figure 4a** & **d**). These mineral phases were further corroborated by ore microscopy observations, confirming their presence and textural relationships within the quartz veins.

The EDS spectra presented in **Figure 3** were initially interpreted as evidence of the presence of Stibine (Sb_2S_3) and Bindheimite. However, a reevaluation of the chemical data suggests the presence of an antimony oxide. Valentinite (Sb_2O_3), Secondary alteration product com-

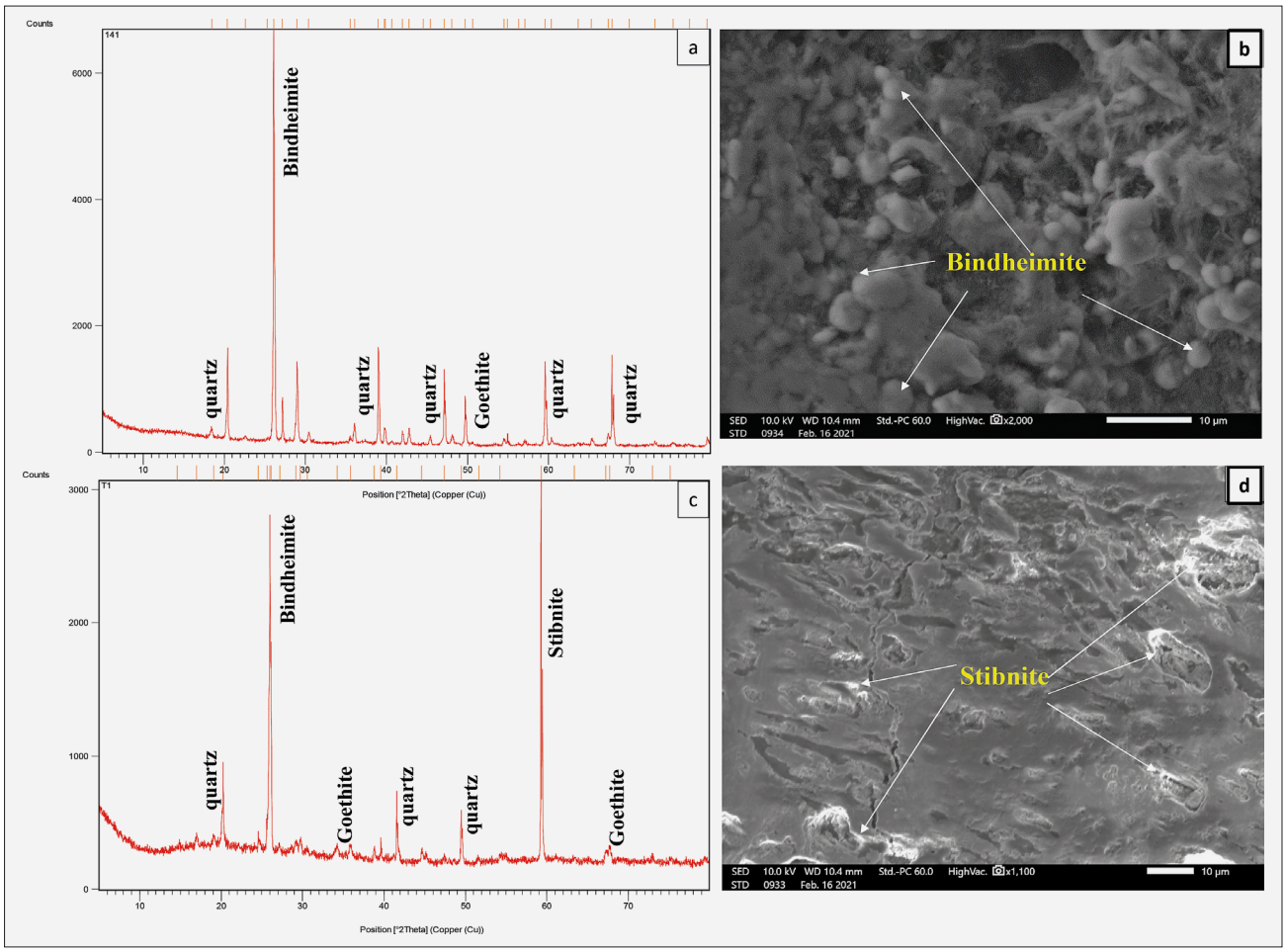


Figure 4. X-ray diffraction analysis of antimony samples from the Houanite basement; (a) X-Ray Diffraction, (b) Bindheimite scale microscope observation, (c): results of X-Ray Diffraction (d): stibnite scale microscope observation.

monly observed in oxidized zones of antimony deposits, was thus considered as a probable phase. In order to validate this hypothesis, additional X-ray diffraction (XRD) analyses were performed (see **Figure 4**). However, the obtained diffractograms do not confirm the presence of either Valentinite or Senarmontite, these two polymorphs share an identical chemical formula (Sb_2O_3). This absence of distinctive crystalline signals could indicate that the antimony oxide present is either amorphous or weakly crystallized, making its identification by XRD inconclusive.

3.2. The Mesozoic and Cenozoic cover ore deposit

The mineralization is embedded in the Mesozoic and Cenozoic cover of Jbel Houanite following faults of major directions varying from E-W to NW-SE structurally parallel to the North High Atlasic Accident (see **Figure 5, a** & **d**) and also to the Hercynian inheritance faults. The mineralization is mostly found in the limestones and dolomites of the Domerian and Toarcian, which are Mesozoic and Cenozoic formations (see **Figure 5b, c** & **e**). The mineralized structures are hosted in the fault N90 and follow the karstification area. The mineralization indicates the presence of Pb-Zn-Ba-Calcite (**Munoz & Moëlo, 1982; Leach et al., 2005; Wei et al., 2020; Lafforgue et al., 2021; Choukrad et al., 2022; Ait Ali et al., 2024; Choukrad et al., 2024; Sun et al., 2024; Ait Ali et al., 2025**).

During the Jurassic, the Mesozoic sedimentary cover of the region was affected by a major tectono-sedimentary phase attributed to the Atlas orogeny. Field observations indicate an extensive tectonic regime, evidenced by a dense network of normal faults and sub-vertical dislocations (see **Figure 5a**), oriented mainly NE–SW and NW–SE. These structures are associated with the development of karstic cavities and brecciated zones, locally filled with carbonate cement and sulfide mineralization.

Structural data reveal that E–W trending faults intersect and link the two main extensional systems. These faults show features suggesting their possible role as transfer zones or relay structures (see **Figure 5d**). The mineralized bodies are mainly hosted within fractured and karstified carbonate formations, spatially associated with these structural features.

The geometric relationships observed between mineralized zones, karst features, and fault systems suggest a

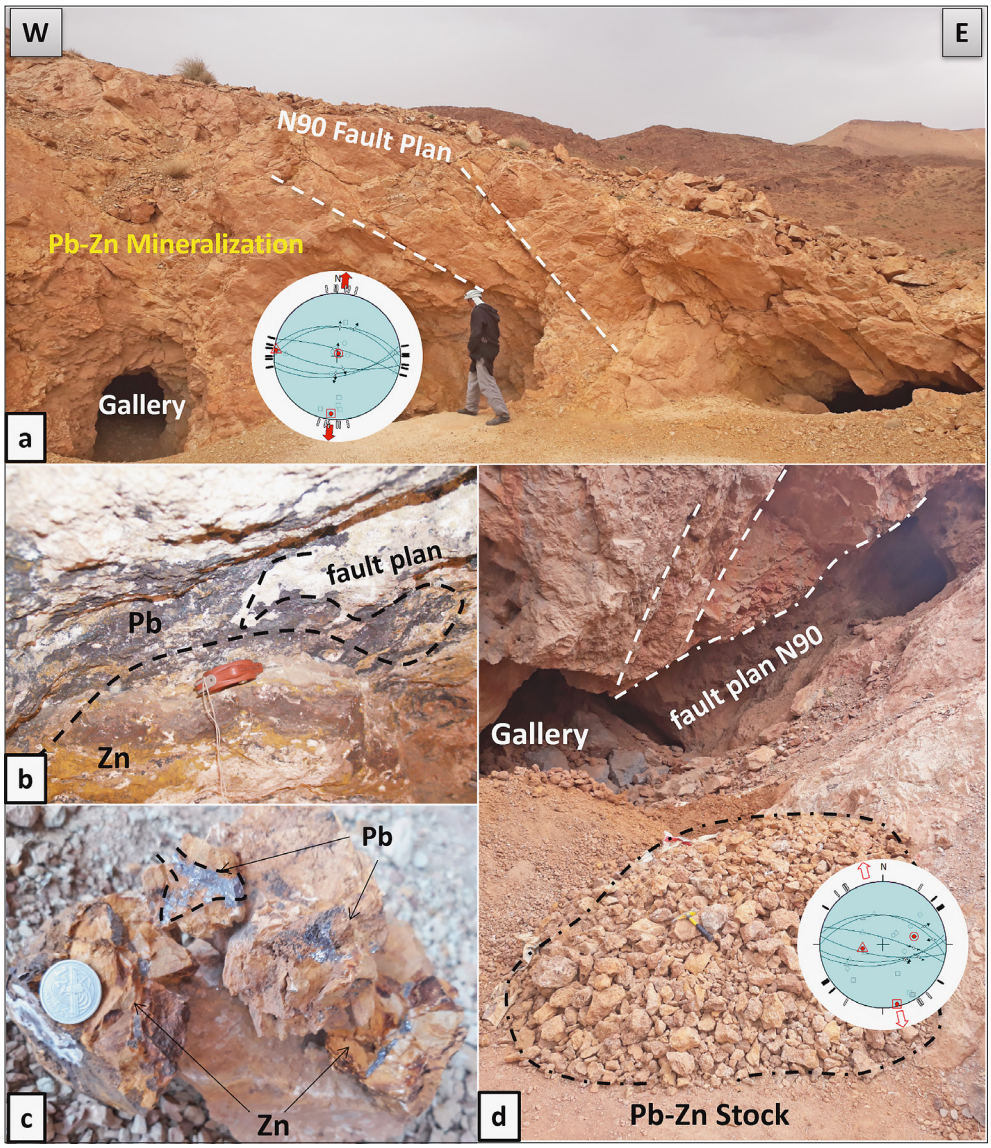


Figure 5. Pb-Zn mineralization of the El Houanite District (a) Pb-Zn- mine and mining gallery along the N90 normal fault with stereographic representation of structural measurements along the N90 fault. (b & c) samples of high-grade Pb-Zn mineralization from the Mezosoic canopy (d) Mined Pb-Zn suivant la faille normale N90 with stereographic representation of structural measurements.

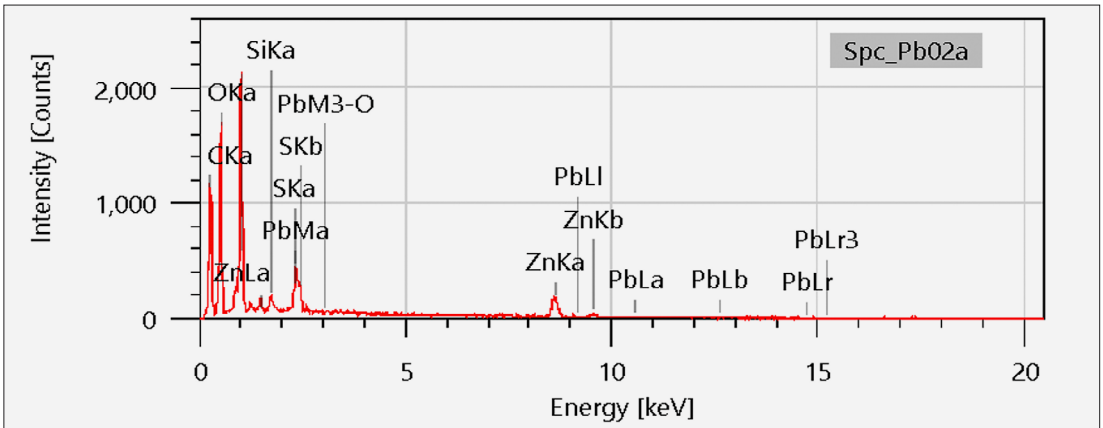
strong structural control on the spatial distribution of the Pb-Zn mineralization during this post-Liassic phase. Further implications regarding fluid migration, mineralization processes, and tectono-sedimentary interactions are discussed in the Discussion section.

Scanning Electron Microscope (SEM) analysis, coupled with Energy Dispersive X-ray Spectroscopy (EDS), performed on samples collected from the lead-zinc mineralized zones within the Mesozoic cover of the Jbel Houanite District, reveals the presence of several mineral assemblages, identified based on spectral peaks and elemental proportions. Lead is detected in association with sulfur, carbon, and oxygen, corresponding respectively to sulfide (galena, PbS) and carbonate (cerussite, $PbCO_3$) phases. These minerals are frequently associated with smithsonite ($ZnCO_3$).

It is important to note that the silica detected in some EDS spectra does not indicate the presence of lead silicate minerals. It most likely results from adjacent quartz grains included in the analyzed area, as the EDS beam interaction volume is large enough to encompass multiple mineral phases simultaneously. Therefore, the co-occurrence of Si and Pb peaks should not be interpreted as a direct chemical or mineralogical association.

The simultaneous detection of Pb and Sb peaks in certain samples (see **Figure 6**) may indicate either the coexistence of distinct Sb and Pb-bearing minerals within the same analyzed area, or partial remobilization of antimony into the lead-zinc mineralization system. However, these interpretations should be approached with caution, as EDS provides only bulk chemical data, and not direct mineralogical identification.

These interpretations were therefore cross-checked and confirmed by X-ray Diffraction (XRD) analyses, which allowed for the definitive identification of mineral phases such as galena and cerussite. The correlation between (EDS) and (XRD) data validates the presence of these mineral assemblages and reinforces their geological significance.



Element	Line	Mass%	Atom%
C	K	6.68±0.06	25.59±0.24
O	K	19.08±0.21	54.91±0.59
Al	K	0.41±0.04	0.70±0.06
Zn	K	4.95±0.25	3.49±0.17
Pb	M	68.88±0.44	15.31±0.10
Total		100.00	100.00
Spc_002			Fitting ratio 0.0624

Cerussite ($PbCO_3$) + Smithsonite ($ZnCO_3$)

Element	Line	Mass%	Atom%
C	K	6.50±0.05	27.63±0.21
O	K	14.59±0.14	46.55±0.45
Al	K	0.45±0.03	0.85±0.05
S	K	4.19±0.007	6.67±0.11
Pb	M	74.26±0.37	18.29±0.09
Total		100.00	100.00
Spc_002			Fitting ratio 0.0594

Galena (PbS) + Cerussite ($PbCO_3$)

Figure 6. SEM analyse with the semi-quantitative compositions of Pb-bearing Mesozoic cover ore samples from the Houanite District (targeted sample)

Observation of polished blades taken from mineralized structures in the Jbel Houanite District reveals the presence of several lead mineral phases, including galena (PbS) (see **Figure 7a** & **b**), anglesite ($PbSO_4$) and cerussite ($PbCO_3$) (see **Figure 7, c** & **d**). Other indices testify to the hydrothermal activity and its remobilization from the base up to the cover, which are arsenopyrite and the iron oxides. Moreover, the galena is surrounded by the iron oxide represented by hematite, indicating that the initial mineralization was followed by the alteration in an oxidizing environment.

The microscopic observation of twelve samples taken in the mineralized Mesozoic cover of Jbel Houanite has revealed a complex and polyphase paragenesis. Lead mineralization is mainly represented by Galena (PbS) (**Figure 7a** & **b**), often accompanied by its supergene alteration products (see **Figure 7c** & **d**). The occurrence of cerussite is consistent with the oxidation of primary galena in the presence of sulphate- and carbonate-rich fluids, under conditions typical of meteoric alteration environments. The coexistence of galena and cerussite suggests progressive oxidation under variable redox and pH conditions, characteristic of the supergene domain (**Chapman et al., 2022; Ece & Ercan, 2024; Choukrad et al., 2024**).

In contrast, the presence of iron oxides and arsenopyrite indicates the involvement of higher-temperature hydrothermal processes, possibly linked to earlier mineralizing phases. These minerals are generally associated with deeper fluid circulation during tectono-metamorphic evolution (**Oh et al., 2004 ; Iancu et al., 2005; Caddick & Thompson, 2008**). The observed vertical mineralization patterns, extending from the Paleozoic basement to the overlying formations, suggest that mineralizing fluids may have migrated upward along fracture systems or fault zones.

It is particularly noteworthy that Galena is frequently bordered or enclosed by iron oxides. This arrangement reflects post-mineralization hydrothermal alteration under oxidizing conditions. This mineralogical overprint indicates that after the deposition of the galena, a late episode of circulation of oxidizing fluids induced a partial transformation of the primary sulphides.

The entire mineralogical assemblage and the observed textural relationships support a mineralization model with two main phases: an early phase of hydrothermal sulphide deposition, followed by an episode of supergene alteration in an oxidative context. This evolution testifies to the interaction between deep hydrothermal processes and surface meteoric alteration phenomena, controlling the distribution of mineralization and the mobility of metals in the Jbel Houanite District.

3.3. Geochemical study

Geochemical analysis of twelve samples of the mineralized basement and cover structures shows significant concentrations of antimony and lead, according to **Table 1** noting that lead concentrations are closely related to that of antimony.

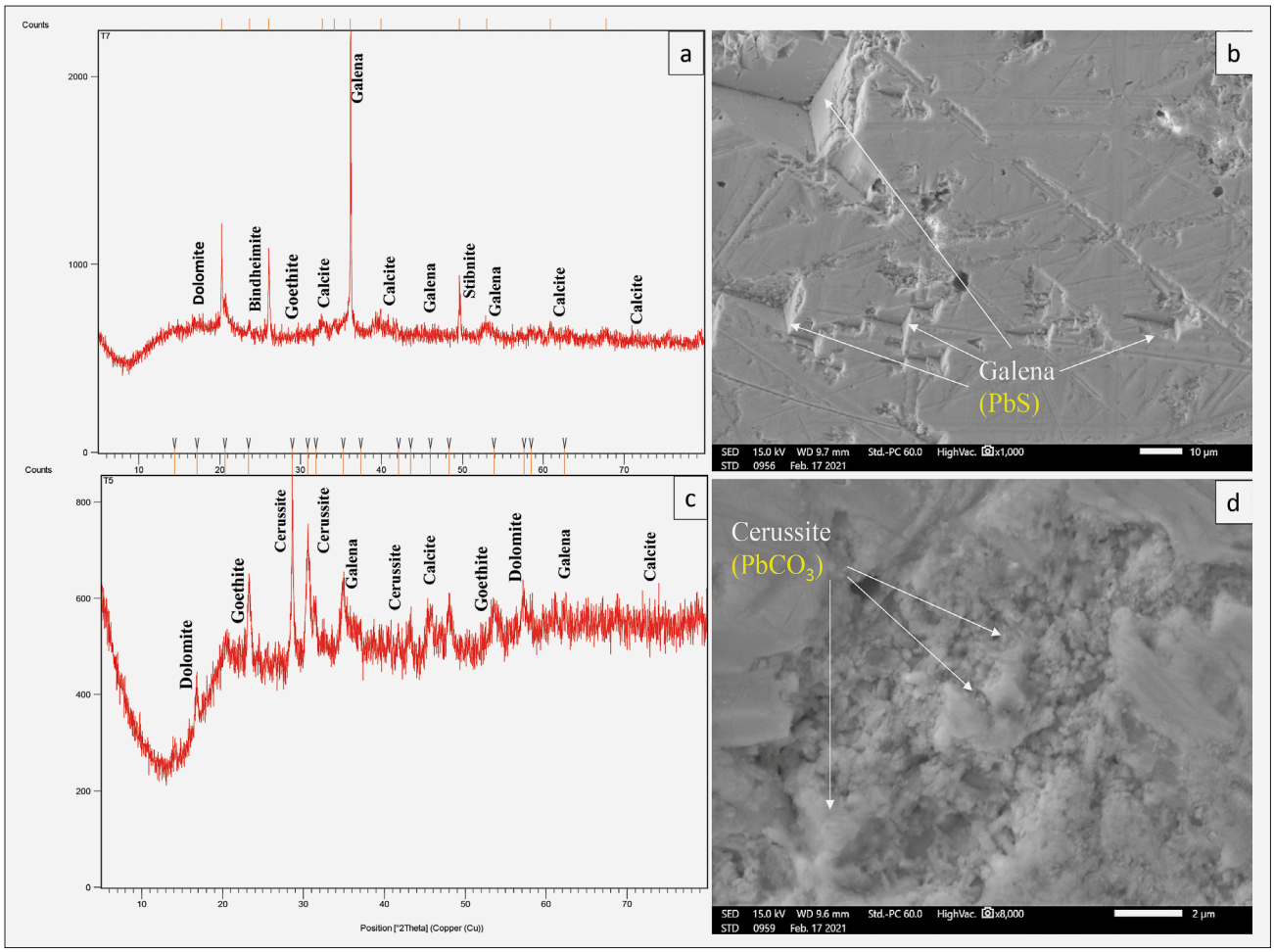


Figure 7. X-ray diffraction analysis of the Mesozoic cover ore deposit in the El Houanite District; (a) X-Ray Diffraction, (b) Galena scale microscope observation , (c): X-ray diffraction results (d): Cerussite scale microscope observation.

Table 1. Geochemical analysis by ICP-MS samples of Jbel Houanite

	Au (ppm)	Ag (ppm)	As (ppm)	Ba (ppm)	Cr (ppm)	Cu ppm)	Fe (%)	Pb (ppm)	S (%)	Sb (ppm)	Sn (ppm)	Te (ppm)	Ti (%)	Zn (ppm)
JH003	0.005	0.11	1.6	1140	1	16.6	23.7	4.6	0.24	2.13	0.2	0.07	0.005	40290
JH004	0.005	0.02	0.4	1800	2	29.2	0.35	5200	0.12	70000	0.2	-0.05	0.005	2
JH007	0.005	0.06	5	420	8	41.2	10.25	1450	0.01	2800	0.2	-0.05	0.005	32451
JH008	0.005	0.32	7.6	5250	7	10.1	37.1	2602	0.13	50000	0.2	-0.05	0.017	27
JH014	0.005	0.14	6.9	170	41	27.9	1.68	22100	0.01	56000	0.2	-0.05	0.062	58
JH017	0.005	0.07	2.9	20	34	13.1	0.77	12500	0.01	210000	0.2	-0.05	0.005	4
JH026	12.45	0.87	54.8	530	60	38.3	3.5	57200	0.12	220000	0.9	0.13	0.12	206
JH028	13.55	0.91	57.4	530	47	37.4	8.79	54300	0.33	390000	0.3	0.19	0.038	199
JH029	121	2.61	39.4	130	34	75	0.82	18400	0.05	400000	0.2	0.18	0.018	103
JH030	2.81	0.37	48.6	200	68	31.3	1.9	31300	0.45	450000	0.5	0.08	0.084	1909
JH031	0.156	0.3	102	390	75	30.1	2.32	1480	0.01	2150	1.2	-0.05	0.325	12500
JH032	0.005	0.88	113.5	1260	41	118	1.22	291	0.05	34.1	0.2	0.05	0.005	158

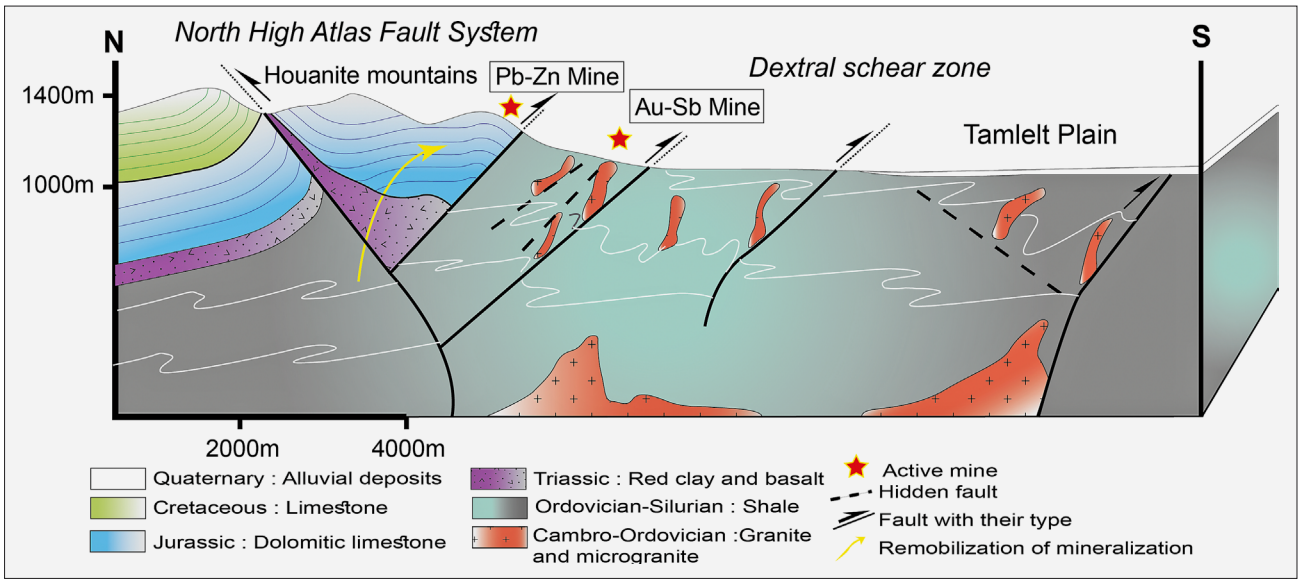


Figure 8. Geological section showing hydrothermal circulations and the passage of Au-Sb and Pb-Zn mineralization from the basement to the cover.

In particular, samples JH026, JH028, JH029 and JH030 show significant grades of Sb, Au, As and Pb (see **Table 1**). It is important to note that samples JH030 and JH031 are from the Meso-Cenozoic cover. The presence of gold provides evidence of paragenetic evolution and migration of mineralization from the basement to the cover, which resulted in the migration of gold and arsenic grains.

The results of the geochemical analyses made it possible to distinguish two sample populations:

- **Group 1**: samples from the Paleozoic basement rich in antimony (up to 45%), As, Au (trace values detected), accompanied by high Fe and S (see **Table 1**).
- **Group 2**: samples from the Mesozoic cover rich in Pb (up to 6%), Zn, Ba (trace values detected) (see **Table 1**).

ICP-MS analyses also revealed anomalous concentrations of trace elements such as Ag, Cu, Cr, Ti in the transition zones between the two types of mineralization, suggesting interactions between hydrothermal systems.

4. Discussion

Based on the various geochemical studies, petrographic and metallogenic observations and macroscopic examination of samples, two types of primary mineralization were determined. The Sb-Au mineralization in the basement related to large "shear zone" shear bands cemented by partially corroded quartz veinlets related to the Hercynian orogeny, and a second type of later Pb-Zn mineralization (see **Figure 8**) hosted in the Meso-Cenozoic cover related to the Atlas orogeny. The structural evolution, marked by successive extensional and compressive events (D_1 to D_3), played a significant role during the deposition of these mineralization types, controlling the fluid flow and ore localization. The D_1 extensional regime appears to have created permeable fault zones that facilitated the initial circulation of hydrothermal fluids and the deposition of stibnite- and gold-bearing mineralization. Subsequent compressive phases (D_2 and D_3) likely reactivated earlier structures, promoting remobilization and local concentration of mineralization within transpressive shear zones and structural traps (**Ashley & Craw, 2004**). This polyphase tectonic evolution highlights the critical role of structural inheritance and reactivation in ore system development (see **Figure 8**).

The mineralization is mainly located along major fractures and faults, with two dominant systems:

- NW-SE to NE-SW system, affecting the Paleozoic basement, hosting the stibnite (Sb_2S_3) bindheimite ($Pb_2Sb_2O_6(O,OH)$), and valentinite (Sb_2O_3) mineralization.
- E-W system, affecting Liasic carbonates, containing galena (PbS), anglesite (PbSO4), cerussite (PbCO3) and smithsonite (ZnCO3) mineralization.

Noting that the Pb, Sb mineralization's are intimately related to each other, while we have not observed a remarkable relationship between the grades of antimony and zinc, nor of lead and zinc, this explains the genetic relationship of the Pb/Sb mineralization's, and gives us a clear idea that these two types of mineralization are the result of a mineralogical evolution that has lasted for a long time (**Chovan et al., 1995; Dill, 1998; Clayton & Spiro, 2000**).

SEM-EDS analyses, combined with X-ray diffraction results, confirm the presence of Stibnite (Sb_2S_3) and Bindheimite ($Pb_2Sb_2O_6(O,OH)$) in the quartz veins. The

variability in lead and sulphur contents observed by EDS reflects local heterogeneity related to alteration processes. The presence of secondary antimony oxides, such as Valentinite and Senarmontite (Sb_2O3), is strongly supported by EDS data; however, it remains hypothetical pending confirmation by XRD. The silica detected by EDS likely corresponds to quartz micro-inclusions captured during analysis, without direct mineralogical association. Finally, the carbon detected in the EDS spectra is attributed to the conductive coating applied to the samples and is not considered a mineral component.

The presence of antimony in the form of Bindheimite ($Pb_2Sb_2O_6(O,OH)$, indicates an advanced stage of oxidation and remobilization of primary lead and antimony sulfides in a supergene environment (**Dill, 1998; Munoz & Moëlo, 1982; Sun et al., 2024**).

The transition towards secondary stibnite (Sb_2S_3) mineralization suggests a transformation under changing physicochemical conditions, particularly a decrease in oxygen activity and an increase in sulphur activity. This process likely involved the reduction of antimony, along with the release of lead and oxygen, possibly associated with a late hydrothermal or diagenetic event (**Dill, 1998; Munoz & Moëlo, 1982**).

The late overprinting of Stibnite (Sb_2S_3) by Bindheimite ($Pb_2Sb_2O_6(O,OH)$ highlights a complex paragenetic sequence (see **Table 2**), controlled by fluctuations in redox potential and geochemical conditions within the system.

The existence of Galena (PbS) and its alteration products reflects progressive oxidation under redox and pH conditions typical of the supergene environment, influenced by meteoric fluids enriched in sulfates and carbonates (**Chapman et al., 2022; Ece & Ercan, 2024**). The occurrence of arsenopyrite and iron oxides suggests an earlier high-temperature hydrothermal phase, likely associated with deep fluid circulation during a tectono-metamorphic event (**Oh et al., 2004; Iancu et al., 2005; Caddick & Thompson, 2008**). The vertical remobilization of mineralizing elements from the Paleozoic basement to upper stratigraphic levels suggests ascendent fluid migration, probably facilitated by fracture or fault systems.

On the basis of the various geochemical studies and petrographic and metallogenic observations and by macroscopic examination of the samples, the mineralization's of the Jbel Houanite District were formed in several successive stages, the first three correspond to the mineralization's deposited at the different phases of the Hercynian orogeny, these are the antimony, copper and arsenic mineralization, after remobilization of the latter in note the establishment of mineralization's at lead and zinc during the phases of the atlas orogeny (see **Figure 9**).

The results obtained through the different analysis methods (geological mapping, petrographic observations, XDR, SEM-EDX, XRF and ICP-MS analyses) have highlighted the lithological diversity, the characteristic mineralogical associations, as well as the paragenetic evolution of the Sb and Pb mineralization's in the Jbel Houanite District.

Observations under the light and electron microscope have identified several distinct mineral associations:

- **Sb-Au mineralization (Paleozoic basement):**
  - Main minerals: stibnite, bindheimite, pyrite, quartz.
  - Textures: fracture filling, vein and veinlet structure, local stibnite zonation, surface antimony oxide alteration.
  - Accompanying mineralogy: sericite, chlorite, sometimes native gold in the microscopic state.
  - The high oxygen content observed in some EDX spectra is likely related to the presence of valentinite and senarmontite (Sb_2O_3), an antimony oxide phase (see **Table 2**), although it was not identified by XRD.
- **Pb-Zn mineralization (Meso-Cenozoic cover):**
  - Main minerals: galena, cerussite, sphalerite, iron oxides, calcite.
  - Secondary minerals: dolomite, barite.
  - Textures: filling of karst cavities, cementation of sub-horizontal fractures, sometimes as a replacement for the host dolomite.

XRD analysis confirmed the predominance of carbonate phases (calcite, dolomite) in the host rock, with clear peaks of Stibnite and Galena in the mineralized samples.

The cross-analysis of textures, mineralogical relationships and structural contexts has made it possible to propose:

- **Phase 1 (Hercynian-Paleozoic):**
  - **Stage I:** The antimony mineralization in the basement, associated with a circulation of hydrothermal fluids along the NW-SE and NE-SW fractures. The environment is reductive, at moderate temperature, with precipitation of Stibnite (Sb_2S_3), quartz, pyrite, and calcite (see **Table 2**).
  - **Stage II:** Corresponds to a continuation of hydrothermal activity with precipitation of stibine (Sb_2S_3), galena (PbS), quartz and calcite, in an environment in transition to slightly oxidizing conditions. The appearance of bindheimite ($Pb_2Sb_2O_6(O,OH)$), valentinite and/or senarmontite (Sb_2O_3) and anglesite (PbSO4) affirms to an early alteration of lead sulphides (see **Table 2**). Although EDS data suggest the presence of antimony oxide, their formation is more likely related to later supergene alteration (phase III).
- **Phase 2 (Atlasic- Meso-Cenozoic):**
  - **Stage III:** It is manifested by the development of secondary antimony oxides, under the effect of oxidizing conditions in a subaerial context. On

Table 2. Paragenetic Sequence and Mineralogical Evolution in the Jbel Houanite District, Eastern High Atlas (Morocco).

MINERALS	STAGE- I	STAGE- II	STAGE- III
Stibnite (Sb_2S_3)	-- -- -- -- -- --	-- -- --	
Valentinite (Sb_2O_3)		-- ----	-- --
Sénarmontite (Sb_2O_3)		-- -- --	-- --
Bindheimite ($Pb_2Sb_2O_6(O,OH)$)		-- -- --	-- --
Gold (Au)	-- -- --	-- --	
Galena (PbS)		-- -- -- -- -- --	
Anglesite ($PbSO_4$)		-- -- --	-- -- -- --
Cerussite ($PbCO_3$)			-- -- -- -- -- --
Smithsonite ($ZnCO_3$)			-- -- --
Quartz (gangue)	-- -- -- -- -- --	-- -- -- --	
Calcite ($CaCO_3$)	-- -- --	-- -- --	-- --
Goethite ($FeO(OH)$)	-- -- --	-- -- --	-- -- -- --

-- -- presence of the mineral during the phase

the other hand, it corresponds to the deposition of lead mineralization in the carbonate cover, via cerussite (PbCO3) and smithsonite (ZnCO3) (see **Table 2**). enriched hydrothermal circulations, transported along the E-W faults. This phase is marked by an active tectono-sedimentary environment, with filling of karst cavities and hydrothermal replacement.

The contact zone between basement and cover locally shows a superposition of the two systems, suggesting a structural reactivation allowing the partial remobilization of the previous mineralization.

5. Conclusions

This study combines geochemical, petrographic, metallogenic, structural, and macroscopic analyses performed on samples from the Jbel Houanite area. The integrated results allowed the identification of antimony mineralization mainly in the form of stibnite (Sb_2S_3) and bindheimite ($Pb_2Sb_2O_6(O,OH)$) within the Paleozoic basement, as well as lead and zinc mineralization, notably galena (PbS) and cerussite ($PbCO_3$), occurring in the Meso-Cenozoic cover (see **Figure 9**).

Structurally, these mineralizations are closely associated with major fault zones and shear bands resulting from a polyphase tectonic evolution marked by the Hercynian and Atlas orogenies. Successive tectonic events alternating between extensional and compressional phases (D_1, D_2, D_3) controlled hydrothermal fluid circulation and ore deposition, with the initial extensional phase promoting fluid flow and mineral precipitation, while later compressional phases contributed to remobilization and local concentration of mineralization within transpressive shear zones and structural traps.

From a geodynamic perspective, the Sb-Pb deposits developed in accretionary orogenic settings, typically hosted in granitic, greenstone, and meta-sedimentary turbidite terrains. Their formation is temporally linked to the late stages of the Hercynian orogeny and the early phases of the Atlas orogeny (see **Figure 9**).

In the light of mineralogical and structural observations, a paragenetic evolution in several stages is proposed, illustrating a variation of the metal assemblies as a function of depth, with an enrichment of antimony in the upper levels.

Gold-bearing stibnite (Sb_2S_3) constitutes the primary phase of mineralization, developed in a hydrothermal context associated with a Hercynian fracture network, in a compressive to transpressive tectonic setting. The establishment of this mineralization is probably controlled by structural release zones, in connection with major discontinuities favorable to the circulation of antimoniferous sulphide fluids. A subsequent remobilization phase, linked to a late-Hercynian tectonic reactivation, allowed the local redistribution of Sb-Pb associations under the effect of the circulation of oxidizing fluids. This evolution led to the formation of secondary alteration minerals, including bindheimite ($Pb_2Sb_2O_6(O,OH)$), valentinite (Sb_2O_3) and/or senarmontite (Sb_2O_3) and anglesite (PbSO4), reflecting more oxidative conditions and transformation dynamics of the initial sulphide phases (see **Figure 9**). Thirdly, during the Atlas orogeny, supergene alteration processes affected the previous mineralizations. Under the effect of bicarbonate solution circulations, in the context of a wetter climate, a spatial dissociation of the elements Sb, Pb and S occurred, accompanied by the dissolution of galena (PbS) and the secondary precipitation of cerussite ($PbCO_3$) and smithsonite (ZnCO3) within the host carbonate formations. This late phase is characteristic of a shallow subaerial oxidation environment, where geochemical conditions favored the transformation of primary sulphides into secondary carbonates. This integrative framework, combining geochemical, structural, and geodynamic data, highlights the complexity of Sb-Au-Pb-Zn mineraliza-

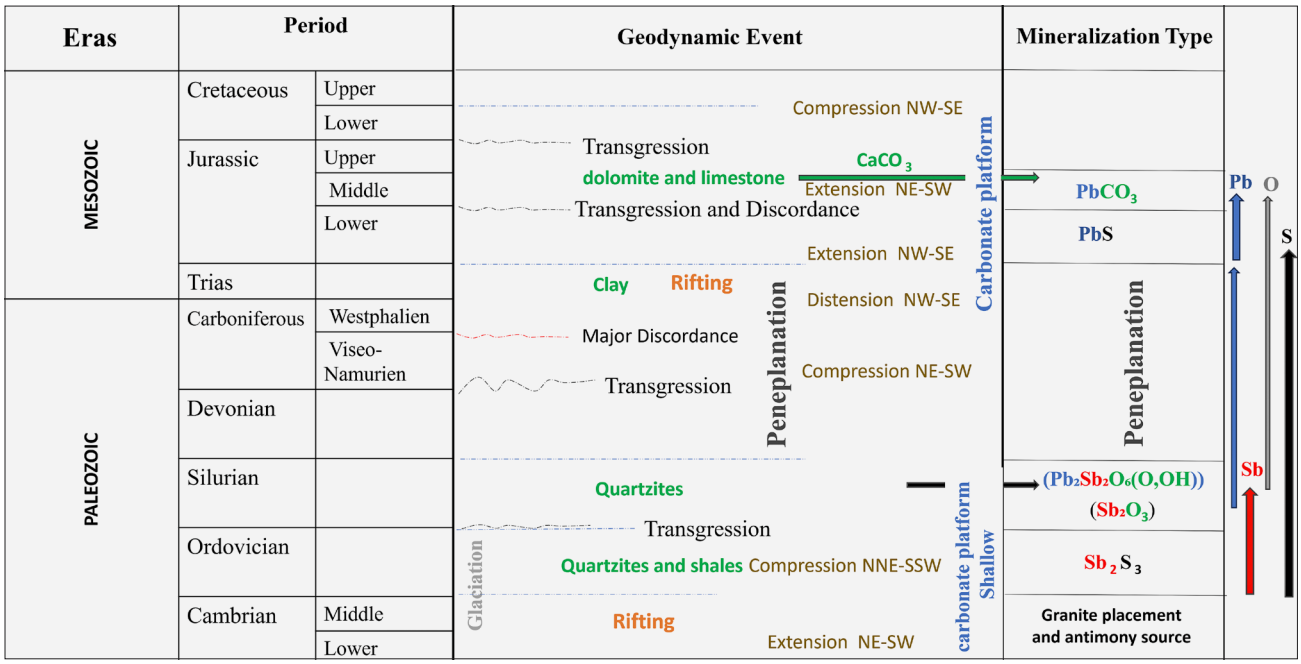


Figure 9. Conceptual model illustrating the paragenetic evolution of the Jbel Houanite mineralization (Sb-Au; Pb-Zn).

tion's in the High Eastern Atlas and underscores the fundamental role of tectonic inheritance and structural reactivation in the genesis and localization of these deposits.

Funding

The authors declare that they have received no funding.

6. References

Adil, S., Bouabdellah, M., Grandia, F., Cardellach, E., & Canals, À. (2004). Geochemistry of fluids associated to the Bou-Dahar Pb-Zn Mississippi Valley-type deposits (Morocco). *Comptes Rendus-Geoscience*, *336*(14), 1265–1272. https://doi.org/10.1016/j.crte.2004.06.010

Ait Ali, A., Choukrad, J., Ouahzizi, Y., Charroud, M., Si Mhamdi, H., Saoud, N., Mounir, S., & Mechaqrane, A. (2025). Integrated remote sensing and field data for lithological mapping and calcite exploration in the Middle Atlas, Morocco. *Scientific African*, *27*, e02521. https://doi.org/10.1016/j.sciaf.2024.e02521

Ait Ali, A., Mohammed, C., Choukrad, J., Ouahzizi, Y., Si Mhamdi, H., Saoud, N., nacer, E., & Mechaqrane, A. (2024). Identification, Characterization, and Deposit Model of Calcite Mineralization in the Middle Atlas Belts, Morocco. *Geosciences*, *14*. https://doi.org/10.3390/geosciences14060154

Ashley, P., & Craw, D. (2004). Structural controls on hydrothermal alteration and gold–antimony mineralisation in the Hillgrove area, NSW, Australia. *Mineralium Deposita*, *39*(2), 223–239.

Azza, A., Abdellah, B., & Moukadiri, A. (2019). Gold and Antimony Mineralizations of Jbel Haouanite (High Atlas, Morocco) in Their Geodynamic Context. *European Scientific Journal*, *15*, 1857–7881. https://doi.org/10.19044/esj.2019.v15n18p336

Bezar, B. S., de Lamotte, D. F., Morel, J. L., & Mercier, E. (1998). Kinematics of large scale tip line folds from the High Atlas thrust belt, Morocco. *Journal of Structural Geology*, *20*(8), 999–1011. https://doi.org/10.1016/S0191-8141(98)00031-5

Blomeier, D. P., & Reijmer, J. J. (2002). Facies architecture of an Early Jurassic carbonate platform slope (Jbel Bou Dahar, High Atlas, Morocco). *Journal of Sedimentary Research*, *72*(4), 462–475.

Bril, H., Bonhomme, M., Marcoux, E., & Baubron, J. (1991). Ages K/Ar des minéralisations de Brioude-Massiac (W-Au-As-Sb; Pb-Zn), Pontgibaud (Pb-Ag; Sn), et Labessette (As-Pb-Sb-Au): Place de ces districts dans l'évolution géotectonique du Massif central français. *Mineralium Deposita*, *26*(3), 189–198.

Caddick, M. J., & Thompson, A. B. (2008). Quantifying the tectono-metamorphic evolution of pelitic rocks from a wide range of tectonic settings: Mineral compositions in equilibrium. *Contributions to Mineralogy and Petrology*, *156*(2), 177–195.

Chapman, R. J., Moles, N. R., Bluemel, B., & Walshaw, R. D. (2022). *Detrital gold as an indicator mineral*. Geological Society Special Publication, 516. pp. 313-336. ISSN 0305-8719.

Charrière, A., Haddoumi, H., & Mojon, P.-O. (2005). Découverte de Jurassique supérieur et d'un niveau marin du Barrémien dans les «couches rouges» continentales du Haut Atlas central marocain: Implications paléogéographiques et structurales. *Comptes Rendus Palevol*, *4*(5), 385–394.

Charroud, M., (2002). Evolution géodynamique des Hauts Plateaux (Maroc) et de leurs bordures du Mesozoique au Cénozoique. *Université de Fes, These d'Etat.–315 Pp, Université de Fes, These d'Etat.–315 pp.*

Charroud, A., Charroud, M., Fedan, B., Laville, E., Rioult, M., Piqué, A., Du Dresnay, R., & Medina, F. (1996). Dynamique sédimentaire des formations triasiques du Moyen Atlas méridional. *Le Permien et Le Trias Du Maroc: État Des Connaissances, PUMAG, Marrakech*, 269–289.

Chellai, E. H., Youbi, N., Bamiki, R. E., Ettaki, M., Ibouh, H., Marzoqi, M., & Ait-Bihi, A. (2024). Evolution of the Atlasic Domain During the Alpine Cycle in the Broader Sense: General Outline of the Evolution of the Tethys. In *The Geology of North Africa* (pp. 187–220). Springer.

Choukrad, J. (2022). *Geological context of the emplacement of mineralizations in the Eastern High Atlas* [Doctorat]. Sidi Mohamed Ben Abdellah University.

Choukrad, J., Abdelkhiar, A. ali, Youssef, O., & Mohammed, C. (2022). Geology, Mineralogy, Geochemistry and deposit model of Iron and Manganese in Bouarfa mine, Eastern High Atlas, Morocco. *Scientific African*, e01401. https://doi.org/10.1016/j.sciaf.2022.e01401

Choukrad, J., Ali, A., Mhamdi, H. S., Ouahzizi, Y., El Moutaouakkil, N., & Charroud, M. (2023). Contribution of Landsat 8 OLI imagery to mapping of lithological series and lineaments: Implications for Pb-Zn mineralization exploration in the Boudahar Massif, Eastern High Atlas, Morocco. *Estudios Geológicos*, *79*(2), e159–e159.

Choukrad, J., Charroud, M., Mhamdi, H. S., Moutaouakkil, N. E., & Ali, A. A. (2024). Geodynamic, metallographic and geochemical characteristics of the Jbel Klakh copper deposit, Eastern High Atlas, Morocco. *Mining of Mineral Deposits*, *18*(4), 18–25. https://doi.org/10.33271/mining18.04.018

Chovan, M., Hurai, V., Sachan, H., & Kantor, J. (1995). Origin of the fluids associated with granodiorite-hosted, Sb-As-Au-W mineralisation at Dúbrava (Nízke Tatry Mts, Western Carpathians). *Mineralium Deposita*, *30*(1), 48–54.

Clayton, R., & Spiro, B. (2000). Sulphur, carbon and oxygen isotope studies of early Variscan mineralisation and Pb-Sb vein deposits in the Cornubian orefield: Implications for the scale of fluid movements during Variscan deformation. *Mineralium Deposita*, *35*(4), 315–331.

Craw, D., Wilson, N., & Ashley, P. (2004). Geochemical controls on the environmental mobility of Sb and As at mesothermal antimony and gold deposits. *Applied Earth Science*, *113*(1), 3–10.

Delvaux, D., & Sperner, B. (2003). New aspects of tectonic stress inversion with reference to the TENSOR program. *Geological Society, London, Special Publications*, *212*(1), 75–100.

Dill, H. (1998). Evolution of Sb mineralisation in modern fold belts: A comparison of the Sb mineralisation in the Central Andes (Bolivia) and the Western Carpathians (Slovakia). *Mineralium Deposita*, *33*(4), 359–378.

Ece, Ö. I., & Ercan, H. Ü. (2024). Global occurrence, geology and characteristics of hydrothermal-origin kaolin deposits. *Minerals*, *14*(4), 353.

El Hakour, A. (2005). Evaluation des ressources de J. Malek à fin décembre 2005, bordure Sud de la boutonnière de Tamlalt (Haut-Atlas oriental). *Unpublished Report (ONHYM)*, 15.

El Kochri, A. (1996). Géométrie et mécanismes de la déformation du Haut Atlas Centro-oriental (Maroc). *These Doctorat d'Etat, Univ. Med. V, Rabat*.

El Kochri, A., & Chorowicz, J. (1988). Tectonique synsedimentaire et style ejectif dans la couverture mesozoique du Haut Atlas oriental (Maroc); exemple de la boutonniere de Mougueur. *Bulletin de La Société Géologique de France*, *4*(4), 541–550.

El Kochri, A., & Chorowicz, J. (1996). Oblique extension in the Jurassic trough of the Central and Eastern High Atlas (Morocco). *Canadian Journal of Earth Sciences*, *33*, 84–92. https://doi.org/10.1139/e96-009

Faure, M., Mézème, E. B., Duguet, M., Cartier, C., & Talbot, J.-Y. (2005). Paleozoic tectonic evolution of medio-Europa from the example of the French Massif Central and Massif Armoricain. *Journal of the Virtual Explorer*, *19*(5), 1–25.

Haddoumi, H., Aiméras, Y., Bodergat, A.-M., Charrière, A., Mangold, C., & Benshili, K. (1998). Âges et environnements des Couches rouges d'Anoual (Jurassique moyen et Crétacé inférieur, Haut-Atlas oriental, Maroc). *Comptes Rendus de l'Académie Des Sciences-Series IIA-Earth and Planetary Science*, *327*(2), 127–133.

Haddoumi, H., Charrière, A., Andreu, B., & Mojon, P.-O. (2008). Les dépôts continentaux du Jurassique moyen au Crétacé inférieur dans le Haut Atlas oriental (Maroc): Paléoenvironnements successifs et signification paléogéographique. *Carnets de Géologie/Notebooks on Geology*, *A06*, 1–29.

Houari. (2003). *Etude structurale de la boutonnière paléozoïque de Tamlet (Haut Atlas oriental): Sa place dans la chaîne hercynienne du Maroc*.

Houari, M.-R., & Hoepffner, C. (2003). Late Carboniferous dextral wrench-dominated transpression along the North African craton margin (Eastern High-Atlas, Morocco). *Journal of African Earth Sciences*, *37*(1–2), 11–24. https://doi.org/10.1016/S0899-5362(03)00085-X

Iancu, V., Berza, T., Seghedi, A., Gheuca, I., & Hann, H.-P. (2005). Alpine polyphase tectono-metamorphic evolution of the South Carpathians: A new overview. *Tectonophysics*, *410*(1–4), 337–365.

Jacobshagen, V., Brede, R., Hauptmann, M., Heinitz, W., & Zylka, R. (2005). Structure and post-Palaeozoic evolution of the central High Atlas. In *The atlas system of Morocco: Studies on its geodynamic evolution* (pp. 245–271). Springer.

Jaouad, C., Mohammed, C., Nacir, E. M., Naoufal, S., Abdelkhiar, A. A., & Youssef, O. (2024). Geology, Mineralogy and Analysis of Tectonic Fracturing of Barite Mineralization's in Bateun Jeudari Paleozoic basement, Eastern High Atlas, Morocco. *Iraqi Geological Journal*, *57*(1D), 46–59. https://doi.org/10.46717/igj.57.1D.5ms-2024-4-15

Kaoukaya, A., Laadila, M., Fedan, B., & Saadi, Z. (2001). La plate-forme carbonatée liasique au NE d'Errachidia (Haut-Atlas oriental, Maroc): Modèle d'organisation des dépôts margino-littoraux. *Bulletin de l'Institut Des Sciences, Rabat*, *23*, 27–38.

Lafforgue, L., Dekoninck, A., Barbarand, J., Brigaud, B., Bouabdellah, M., Verhaert, M., Mouttaqi, A., & Yans, J. (2021). Geological and geochemical constrains on the genesis of the sedimentary-hosted Bou Arfa Mn(-Fe) deposit (Eastern High Atlas, Morocco). *Ore Geology Reviews*, *133*, 104094. https://doi.org/10.1016/j.oregeorev.2021.104094

Laville, E., Pique, A., Amrhar, M., & Charroud, M. (2004). A restatement of the Mesozoic Atlasic Rifting (Morocco). *Journal of African Earth Sciences*, *38*(2), 145–153. https://doi.org/10.1016/j.jafrearsci.2003.12.003

Leach, D. L., Sangster, D. F., Kelley, K. D., Large, R. R., Garven, G., Allen, C. R., Gutzmer, J., & Walters, S. (2005). *Sediment-hosted lead-zinc deposits: A global perspective*. Economic geology: One hundredth anniversary volume. 561-608. https://doi.org/10.5382/AV100.18

Marcoux, E., & Bril, H. (1986). Héritage et sources des métaux d'après la géochimie isotopique du plomb: Exemple des minéralisations filoniennes (Sb, Pb, Ba, F) du Haut-Allier (Massif Central, France). *Mineralium Deposita*, *21*(1), 35–43.

Mattauer, M., Proust, F., & Etchecopar, A. (1977). Lineation» a» et mecanisme de cisaillement simple lie au chevauchement de la nappe des schistes lustres en Corse. *Bulletin de La Société Géologique de France*, *7*(4), 841–847. https://doi.org/10.2113/gssgfbull.S7-XIX.4.841

Merino-Tomé, Ó., Porta, G. D., Kenter, J. A., Verwer, K., Harris, P., Adams, E. W., Playton, T., & Corrochano, D. (2012). Sequence development in an isolated carbonate platform (Lower Jurassic, Djebel Bou Dahar, High Atlas, Morocco): Influence of tectonics, eustacy and carbonate production. *Sedimentology*, *59*(1), 118–155.

Munoz, M., & Moëlo, Y. (1982). Etude paragénétique de la minéralisation sulfurée complexe (Sb-Pb-Zn...) de Bournac (Hérault, France). *Bulletin de Minéralogie*, *105*(6), 625–632.

Nouayti, A., Khattach, D., Nouayti, N., El Moudnib, L., Hilali, M., & Saadi, O. (2023). Structural modeling of the Paleozoic basement and hydrogeological study: Contribution of geology and aeromagnetic data of the Eastern High Atlas (Morocco). *Modeling Earth Systems and Environment*, *9*(1), 1199–1213.

Oh, C. W., Kim, S. W., Ryu, I., Okada, T., Hyodo, H., & Itaya, T. (2004). Tectono-metamorphic evolution of the Okcheon metamorphic belt, South Korea: Tectonic implications in East Asia. *Island Arc*, *13*(2), 387–402.

Piqué, A., & Michard, A. (1989). Moroccan Hercynides: A synopsis. The Paleozoic sedimentary and tectonic evolution at the northern margin of West Africa. *American Journal of Science*, *289*, 286–330. https://doi.org/10.2475/ajs.289.3.286

Rajeshkumar, R., Vignesh, S., Singh, L. K., & Srinivasan, A. (2024). Development of Mg-Sb-Sn and Mg-Sb-Ca Magnesium Alloys for Automotive Applications: Microstructure, Mechanical Properties, and Corrosion Behavior Analysis. *Journal of Materials Engineering and Performance*. https://doi.org/10.1007/s11665-024-09539-8

Sun, X., Li, R.-Y., Sun, H.-Y., Olin, P. H., Santosh, M., Fu, B., & Deng, J. (2024). Genesis of Pb–Zn-Ag-Sb mineralization in the Tethys Himalaya, China: Early magmatic-hydrothermal Pb–Zn(-Ag) mineralization overprinted by Sb-rich fluids. *Mineralium Deposita*, *59*(7), 1275–1293. https://doi.org/10.1007/s00126-024-01264-5

Talih, A., Aboussalam, Z., Becker, R., Saadi, M., & Benmlih, A. (2022). Stratigraphy and tectono-sedimentary processes of allochthonous and autochthonous Devonian deposits of the Tisdafine Basin, Eastern Anti-Atlas, Morocco. *Morocco Bulletin De L'institut Scientifique*, *44*(October), 43–69.

Verhaert, M., Bernard, A., Dekoninck, A., Lafforgue, L., Saddiqi, O., & Yans, J. (2017). Mineralogical and geochemical characterization of supergene Cu–Pb–Zn–V ores in the Oriental High Atlas, Morocco. *Mineralium Deposita*, *52*(7), 1049–1068. https://doi.org/10.1007/s00126-017-0753-5

Verwer, K., Merino-Tomé, O., Kenter, J. A., & Della Porta, G. (2009). Evolution of a high-relief carbonate platform slope using 3D digital outcrop models: Lower Jurassic Djebel Bou Dahar, High Atlas, Morocco. *Journal of Sedimentary Research*, *79*(6), 416–439.

Wei, H., Xiao, K., Shao, Y., Kong, H., Zhang, S., Wang, K., Li, Q., Chen, B., Xiang, J., & Wen, C. (2020). Modeling-based mineral system approach to prospectivity mapping of stratabound hydrothermal deposits: A case study of MVT Pb-Zn deposits in the Huayuan area, northwestern Hunan province, China. *Ore Geology Reviews*, *120*, 103368. https://doi.org/10.1016/j.oregeorev.2020.103368

SAŽETAK

Geodinamička i paragenetska evolucija mineralizacije Jbel Houanit (Sb-Au; Pb-Zn) u istočnome Visokom Atlasu, Maroko

Jbel Houanite važna je metalogenetska regija bogata polimetalnom mineralizacijom (Sb-Au-Pb-Zn-Ba-Fe-Cu) smještena u sjevernome dijelu istočnoga Visokog Atlasa u Maroku, uz sjeverni rasjed Visokoga Atlasa. Najranija identificirana mineralizacija odgovara kvarcnim žilama koje su bogate antimonom i zlatom te se nalaze u paleozojskim formacijama, dok kasnija mineralizacija odgovara Pb-Zn naslagama u lijaskim vapnencima. Geološkim rekognosciranjem i istraživanjem minerala u regiji Jbel Houanite utvrđena je prisutnost mineralizacije antimona u obliku stibnita (Sb_2S_3) i bindheimita ($Pb_2Sb_2O_6(O,OH)$), dok se olovna mineralizacija u sedimentnome pokrovu sastoji od galenita (PbS) i cerusita ($PbCO_3$). Anomalije olova blisko su vezane uz prisutnost antimona te je ova mineralizacija rezultat hidrotermalne remobilizacije tijekom faza Atlasa koje su reaktivirale rasjede u stijenama podine, olakšavajući nastanak mineralizacije olova u sklopu sustava tipa Mississippi Valley (MVT). Petrografska i geokemijska istraživanja mineralnih parageneza omogućila su uspostavljanje vremenskih odnosa između događaja mineralizacije: primarna Sb-Au mineralizacija povezana je s kasnohercinskom ekstenzijskom tektonikom, dok je Pb-Zn mineralizacija povezana s ranim atlaskim kompresijskim fazama. Ova sekvencijska evolucija upućuje na složenu polifaznu tektono-metalogenetsku povijest koja je kontrolirala nastanak orudnjenja. Rezultati ovih istraživanja doprinose boljem razumijevanju genetskih modela Sb-Au-Pb-Zn mineralizacije u istočnome Visokom Atlasu te pokazuju ključnu ulogu tektonike i strukturne reaktivacije u stvaranju i lokalizaciji orudnjenja.

Ključne riječi:
antimon, olovo, paragenetska evolucija, paleozojska podloga, mezokenozojski pokrov, istočni Visoki Atlas, Maroko

Author's contribution

Jaouad Choukrad (PhD Thesis in Mining and structural Geology): conceptualization, investigation, conceptualization, data curation, formal analysis, funding acquisition and software. **Ait Ali Abdelkhiar** (PhD Thesis in Economic Geology): conceptualization, investigation, conceptualization. **Mohammed Charroud** (Full Professor): supervision, validation, visualization, writing – original draft and writing – review & editing. **Nacir El moutaouakkil** (Professor): investigation, methodology, project administration. **Boubker Boukili** (Professor): investigation, software, investigation, methodology, and project administration, **Amine Talih** (PhD Thesis in Stratigraphy and Paleontology): resources, software.
All authors have read and agreed to the published version of the manuscript.

RGNZ/MGPB

Unveiling Shale Gas Reservoir Structures with Seismic and MT Data: WALDIM-Based Study from East Kalimantan Indonesia

Rudarsko-geološko-naftni zbornik
(The Mining-Geology-Petroleum Engineering Bulletin)
DOI: 10.17794/rgn.2026.2.8

Original scientific paper

Suharsono[1]*, Yustisio Dianwiyono[1], Edy Wijanarko[2], Wahyu Hidayat[1], Muhammad Fachrul Rozi Kurniawan[1], Yudha Agung Pratama[1]

[1] *Geophysical Engineering Department, Faculty on Mineral Technology and Energy, Universitas Pembangunan Nasional "Veteran" Yogyakarta, Jl Pajajaran 104, Condongcatur Depok, Sleman Yogyakarta, 55283, Indonesia.*

[2] *Testing Center for Oil and Gas "LEMIGAS", Indonesia, Jl. Ciledug Raya No. 109, South Jakarta, 12230, Indonesia.*

Abstract

The Pamaluan Formation, which has a Total Organic Carbon (TOC) value of up to 1.78% and varying degrees of thermal maturity, offers the Indonesian Kutai Basin considerable potential for shale gas production. This research integrates seismic and magnetotelluric (MT) geophysical techniques to improve the knowledge of shale gas prospectivity in the area. There are nine MT sounding locations and nine 2D seismic lines in the dataset. By creating a time structure map, the anticline and syncline structures that were detected by seismic interpretation were further examined. 2D resistivity inversion models were created by processing MT data using the rho variance approach and the Python WALDIM module. A dominant anticline-syncline structural trend oriented roughly 45° from true north is indicated by the data. With an average strike of 43.5°, MT analysis demonstrates a dominant two-dimensional (2D) geoelectrical dimensionality that is in good agreement with local geological trends. At depths of 500–1000 m in anticlines and 2000–3000 m in synclines, zones of low resistivity (1–5 Ohm.m) were found, with thicknesses varying from 2000 to 4000 m. Low resistivity anomalies are interpreted to represent potential shale gas-bearing intervals, consistent with the geological framework of the Kutai Basin. The integration of seismic and MT data successfully delineates folds, faults, and low-resistivity anomalies, interpreted as potential shale gas-bearing intervals, highlighting the significance of a multidisciplinary approach in mitigating exploration risk and enhancing shale gas prospectivity evaluation in the Kutai Basin.

Keywords:
shale gas, Kutai Basin, seismic, magnetotelluric, WALDIM

1. Introduction

The shale gas potential in the Kutai Basin, East Kalimantan, is considered to be highly promising based on various research findings. **Hamdani et al. (2019)** suggested that the Pulobalang Formation in this area exhibits a wide range of organic matter richness, with Total Organic Carbon (TOC) content varying from 0.2% to 4.27%, indicating a spectrum from poor to excellent quality. The dominant kerogen type identified within this Early Miocene formation is Type III, which typically has a strong potential for gas generation. The thermal maturity zone is relatively shallow, occurring at depths between 1,100 and 2,000 meters. Furthermore, the brittleness characteristics of the rock layers within the Pulobalang Formation support favorable conditions for hydraulic fracturing, with Brittleness Index (BI) values ranging from 0.6 to 0.91. The total estimated shale gas resource within this formation reaches approximately 2.78 trillion cubic feet (TCF). **Zajuli and Wahyudiono (2018)** proposed that TOC concentrations exceeding 1.5% and varying levels of thermal maturity across different depths are key factors influencing the shale gas potential in several Indonesian shale formations, including the Pamaluan Formation in the Kutai Basin. These findings reinforce the view that the Kutai Basin, with its favorable geological conditions, holds significant potential for the economically viable development of shale gas resources. Advanced geophysical methodologies are required to accurately analyze and quantify this shale gas potential, especially in geologically complicated basins like Kutai Basin.

Geophysical methods have been used extensively over the years to look for subsurface resources, especially hydrocarbons. Due to their great resolution and capacity to accurately simulate intricate subsurface geological features, seismic reflection techniques are the most popular among these approaches (**Susilo, 2020**). Seismic imaging reconstructs subsurface geometry by analyzing elastic wave propagation (**Bashir et al., 2021;**

* Corresponding author: Suharsono
e-mail address: harsonomgl@upnyk.ac.id
Received: 18 July 2025. Accepted: 22 October 2025.
Available online: 13 March 2026

Lixin, 2022). Delineating important geological structures, such as faults, stratigraphic boundaries, and structural traps, such as anticlines and synclines, is a crucial step in the interpretation phase of seismic data and is essential for evaluating hydrocarbon systems (**Zhang et al., 2022**). However, the effectiveness of seismic methods can be constrained in areas with complex geology, poor seismic data quality, or high acquisition costs. To overcome these limitations, researchers increasingly advocate for the integration of complementary geophysical methods. One such technique is magnetotellurics (MT), which measures natural variations in the Earth's electric and magnetic fields to infer subsurface resistivity distributions. MT is particularly sensitive to the fluid content and mineralogy of rocks, making it suitable for identifying potential hydrocarbon bearing formations (**Ledo and Jones, 2001**).

Prabowo et al. (2020) suggests that MT's benefits over other geophysical techniques include its deep penetration capabilities, limitless natural signal sources, and lack of the need for artificial wave transmitters. Furthermore, MT is more environmentally friendly, has higher resolution than gravity and magnetic approaches, and works well in places where seismic methods are scarce (**Likkason, 2014; Nabighian et al., 2005**). However, anthropogenic activity close to the survey location and natural phenomena like solar storms and local lightning can cause electromagnetic disturbances that affect MT results (**Hidayat et al., 2021; Hidayat and Hamdalah, 2019; Kumar and Rao, 2025; Prabowo et al., 2020**). MT interpretation has been made more reliable by the development of a number of analytical methods. The WALDIM (Weaver Agarwal Lilley Dimensionality) method is one such tool that uses seven impedance tensor invariants to calculate the dimensionality of MT data, represent one-dimensional (1D), two-dimensional (2D), or three-dimensional (3D) subsurface conditions (**Martí et al., 2009**). Furthermore, geoelectrical strike investigations based on MT impedance data offer important information about the direction and continuity of subsurface structural trends.

Several studies have demonstrated the effectiveness and complementary nature of integrating magnetotelluric (MT) and seismic data in subsurface investigations. **Miensopust et al. (2013)** emphasized that seismic and MT methods are complementary approaches. The limitations of seismic methods, which are less effective in areas with volcanic cover or zones characterized by complex heterogeneity, can be overcome through the application of MT, which is capable of detecting lithological variations as well as geological conditions at greater depths. Therefore, the integration of these two methods provides a more comprehensive representation of subsurface structures. **Tietze et al. (2019)** argued that the joint interpretation of seismic velocity and electrical resistivity data can significantly reduce ambiguities in subsurface models by offering independent yet mutually constraining physical property datasets. This approach is especially beneficial in shale gas exploration, where delineating both structural frameworks and lithological variations is critical for reservoir characterization. Further research supports the combination of seismic and MT techniques in geothermal and hydrocarbon exploration settings. **Cinti et al. (2015**) showed that the determination of reservoir limits in structurally complicated sedimentary basins was enhanced by the combination of MT resistivity and seismic reflection data. Similarly, **Ledo and Jones (2001)** demonstrated that MT can complement seismic amplitude anomalies by efficiently imaging resistivity contrasts linked to hydrocarbon saturation. Furthermore, to improve the accuracy of geological interpretation, joint inversion techniques, albeit more computationally intensive, are being used more and more to combine MT and seismic data into a single model framework (**Gallardo and Meju, 2004; Moorkamp et al., 2011**). Integrated geophysical techniques are being used more and more in the context of unconventional hydrocarbon resources like shale gas. Multimethod approaches are necessary to properly evaluate the potential of shale formations because of their complex heterogeneity and varying maturity levels. An integrated strategy combining seismic structural interpretation and MT resistivity imaging is required to comprehend the structural framework and detect low resistivity zones associated with organic rich shales. Overall, the reliability of hydrocarbon exploration results is increased by combining seismic and MT techniques, which improve the capacity to describe the geometry and physical characteristics of subsurface formations (**Irawati et al., 2022; Ledo and Jones, 2001; Tietze et al., 2019**). In the magnetotelluric (MT) method, geoelectric dimensionality analysis plays a crucial role in determining whether the data should be modeled using 1D, 2D, or 3D approaches. The WALDIM was developed to perform this dimensionality analysis more reliably through the use of rotational invariants criteria, without requiring prior assumptions of dimensionality, while also accounting for error propagation and establishing thresholds necessary for noisy real data (**Martí et al., 2009**). Nevertheless, many previous studies have tended to apply 1D, 2D, or 3D modelling and inversion directly, without being preceded by adequate dimensionality analysis, which may lead to biased interpretations, particularly in geologically complex regions. WALDIM-based dimensionality analysis is integrated with seismic and MT methods in order to overcome the limitations of each individual technique and to achieve a more accurate, consistent, and comprehensive reconstruction of subsurface structures.

2. Methods

2.1. Reflection Seismic

In this research, an integrated geophysical approach was employed by combining seismic reflection and magnetotelluric (MT) methods to delineate subsurface

geological structures. The seismic reflection technique provides detailed imaging of deeper stratigraphic horizons and structural configurations, enabling the identification of faults, folds, and potential traps. Complementing this, MT data offers insight into the distribution of subsurface electrical resistivity, which is particularly valuable for characterizing lithological variations and detecting fluid content. By integrating these complementary datasets, a more comprehensive and reliable understanding of the geological framework of the study area was achieved. The seismic reflection method is an active geophysical technique employed to delineate the Earth's subsurface structure by assessing the travel time of seismic waves that are reflected back to the surface upon encountering subterranean rock layers. Reflection seismic is an active geophysical method widely utilized to investigate deeper subsurface conditions (**Dragičević et al., 1991**). This method can be implemented both onshore and offshore, offering flexibility in various geological settings. Common applications of reflection seismics include petroleum exploration, identification of subsurface features such as faults, analysis of complex geological structures and stratigraphy, as well as the detection of earthquake sources. In the interpretation of seismic reflection data, a critical step often involves the construction of a Time Structure Map, which facilitates a comprehensive analysis of subsurface structural patterns and geometries. This map illustrates the distribution of geological structures and stratigraphic horizons within the time domain, enabling geoscientists to identify prospective zones and delineate the location and extent of subsurface features (**Sukmono and Arta, 2013**). Through the continuity of seismic reflectors and structural trends, the geometry and type of traps, such as anticlines or synclines, can be effectively recognized. Time structure maps play a vital role in identifying geological formations based on their seismic travel times, thereby supporting the detection of structural traps and enhancing resource exploration efforts (**Stark, 2008**). In order to identify subsurface structural features pertinent to the geological framework of the study area, two 2D seismic traces specifically, lines 93R-2100 Runtu Matra and K-8033 Ekali Geosin derived from Post Stack Time Migration (PSTM) processing were interpreted out of the nine seismic traces in this study.

2.2. Magnetotelluric

Magnetotellurics (MT) is a passive electromagnetic geophysical method used to estimate the subsurface electrical conductivity by measuring natural variations in the Earth's geomagnetic and geoelectric fields at the surface. The sources of these signals can be broadly categorized based on frequency: at low frequencies (below 1 Hz), the signals originate from the interaction between the solar wind and the Earth's magnetosphere, while at higher frequencies (above 1 Hz), they are primarily generated by thunderstorm, particularly concentrated near the equatorial region. The strength and quality of these MT signals vary with time and space and are susceptible to artificial noise, such as that produced by power lines, pipelines, and other man-made infrastructure. As a result, MT data acquisition typically requires long recording durations and sophisticated data processing techniques to ensure a high signal-to-noise ratio. The skin depth concept explains how the lower-frequency signals penetrate deeper into the Earth, whereas higher-frequency signals are restricted for imaging shallow structures. A broad frequency spectrum used in the MT data enables imaging subsurface from near-surface depths to several kilometers. The passive nature of MT offers significant advantages, including lower operational costs, lightweight equipment, and minimal environmental impact, especially when compared to active geophysical methods.

Synthetic modelling conducted by **Zhang et al. (2014)** demonstrated that MT is capable of delineating vertical discontinuities based on contrasts in resistivity. Therefore, in geological modelling, MT can significantly contribute to seismic inversion by clearly identifying geological features such as vertically oriented faults. In a reservoir system, MT successfully imaged anticline strucutures based on resistivity distribution. In certain settings, such as salt domes or thick volcanic sequences, MT has shown superior capability in resolving subsurface structures compared to conventional seismic methods (**Avdeeva et al., 2012; Mansoori et al., 2016; Patro, 2017**). Resistivity of rocks can be approximated by dividing the pore fluid resistivity by the fractional porosity, emphasizing the role of fluid conductivity and pore structure in governing the overall resistivity of a rock formation. This study uses nine MT data, including K03, KT04, KT05, KT06, KT07, KT08, KT09, KT10, and KT11 (see **Figure 1**).

2.2.1. Weaver Agarwal Lilley Dimensionality and Invariants Method (WALDIM)

The application of WALDIM in magnetotelluric (MT) data analysis offers several significant advantages in the preliminary stage of interpretation, particularly in geoelectric dimensionality analysis. Unlike classical methods such as *Swift's* and *Bahr's skews*, which are often unable to separate anisotropy effects from the regional structural strike, WALDIM relies on rotational invariants of the impedance tensor (**Kumar et al., 2021; Martí et al., 2009**). This approach allows for a more robust assessment without requiring prior assumptions about the dimensionality of the data (1D, 2D, or 3D), thereby reducing interpretation bias at the early stages of modelling. Another major advantage of WALDIM lies in its ability to differentiate anisotropic from isotropic media, a task that traditional techniques cannot adequately accomplish. The criteria applied in WALDIM, such as inconsistencies between the 2D regional strike direction and those derived from the impedance tensor columns, provide clear indicators of electrical anisotropy. This capability is particularly valuable in continental margins

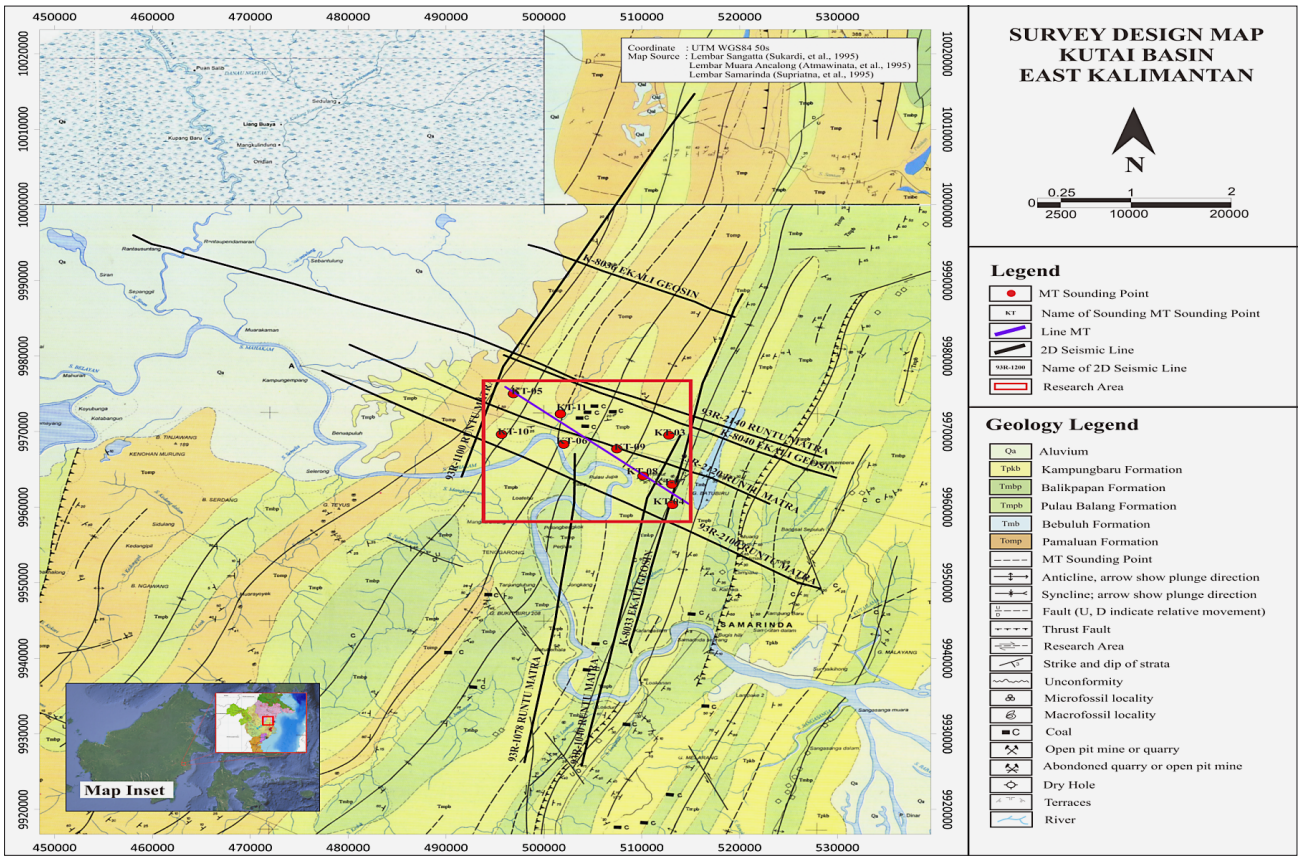


Figure 1. Design survey map The red box indicates the research region, black lines indicate seismic lines, and red dots indicate MT sounding stations overlay with geological maps sheet Samarinda (modified from **Supriatna et al., 1995**)

and tectonically active regions, where anisotropy is often associated with complex geological processes such as crustal deformation, fluid intrusions, and shear zones.

A further strength of WALDIM is its flexibility of application. The method can be applied to both synthetic and field MT data, yielding consistent results across different geological complexities. Dimensionality analysis based on invariants can also be grouped into frequency bands, enabling a more detailed characterization of variations in dimensionality with depth. Consequently, WALDIM not only assists in selecting the appropriate modelling approach (1D, 2D, or 3D) but also provides valuable guidance for data correction prior to inversion and forward modelling. Overall, WALDIM enhances the reliability of MT data interpretation, particularly in the identification of electrical anisotropy, which has important implications for understanding the evolution of geological structures, assessing economic resources, and interpreting hydrogeological systems. This advantage in detecting anisotropy makes WALDIM one of the most relevant and practical analytical tools in modern geophysical studies (**Martí et al., 2009**).

2.3. Design of MT data acquisition integrated with seismic lines

The MT sounding points are represented by red dots and labelled with their respective identifiers, while the seismic lines are depicted as black lines annotated with their corresponding names. As illustrated in **Figure 1**, the study area comprises three major geological formations: Balikpapan, Pulau Balang, and Pamaluan. The MT survey lines are oriented SE - NW, traversing the sounding points KT05, KT11, KT09, KT08, KT07, and KT04. In this study, the analysis is limited to seismic processing results confined within the boundaries of the research area. Seismic data processing involved fault and horizon picking, followed by time-structure analysis to generate a Time Structure Map. This map was subsequently employed to delineate anticline and syncline patterns developed across the study area. Magnetotelluric (MT) data processing began with Rho Variance analysis in the frequency domain. The next stage involved Crosspower editing using the MTEditor software, which generated two primary outputs: Tensor Impedance data in CSV format and inversion data in EDI format. Skin depth calculations were then performed on the Tensor Impedance dataset to determine which data should be retained or discarded. Subsequently, geoelectrical strike, twist, and shear were calculated using WALDIM, with the Swift method applied as a reference. The selected data were further utilized to compute the xi and eta parameters, which were then applied in constructing a Mohr Circle to interpret the real and imaginary components of each MT frequency. These parameters were also

used to calculate the WAL invariants, which were subsequently plotted for statistical evaluation. The invariants provided the basis for WAL dimensional classification and were visualized in bar charts. To improve robustness, Gaussian noise was incorporated into the invariants, supported by Mohr Circle interpretation, invariant distribution, and WAL bar chart analysis. The final stage comprised model inversion and the generation of depth resistivity maps, which were integrated with interpretations derived from the previously processed seismic data (**Martí et al., 2009**).

3. Results and Discussion

The integration of seismic and MT data serves as the primary approach in this discussion, as each method offers complementary strengths seismic data excels in spatial resolution and visualization of layer geometry, while MT data penetrates deeper into the subsurface and provides information on the physical properties of rocks through resistivity (**Moorkamp et al., 2011**). By leveraging the correlation between these methods, the resulting interpretation offers a more comprehensive understanding of the subsurface geological system, including the identification of structural traps, distribution of prospective zones, and characterization of hydrocarbon bearing layers such as black shale. This chapter presents the interpretation results step by step based on the output of each method, which are then correlated to achieve a more integrated understanding.

3.1. Seismic Interpretation

A structurally complex subsurface realm characterized by severe faulting and mild folding is highlighted by the interpreted 2D seismic section along the 93R-2100 Runtu Matra line (see **Figure 2**). Undulations on a continuous marker horizon, seen at depths of around 1500–2000 meters, indicate mild anticlinal and synclinal warping. Significant vertical displacements are caused by the numerous steeply dipping faults that cut across the strata and are primarily of normal type. The central and southeast portions of the line are dominated by these faults, suggesting areas of increased tectonic deformation and potential structural compartmentalization.

The high density and varied dip angles of the interpreted faults suggest a tectonic regime predominantly influenced by extensional forces, which may be associated with rifting events or post depositional tectonic reactivation. The observed vertical offsets and segmentation of the primary seismic horizon further indicate that these faults have played a significant role in controlling sedimentation patterns. Additionally, they may serve as either conduits or barriers for subsurface fluid migration, depending on their orientation, continuity, and fault rock properties. This seismic profile provides compelling evidence for the existence of multiple structural blocks, likely bounded by fault systems associated with regional

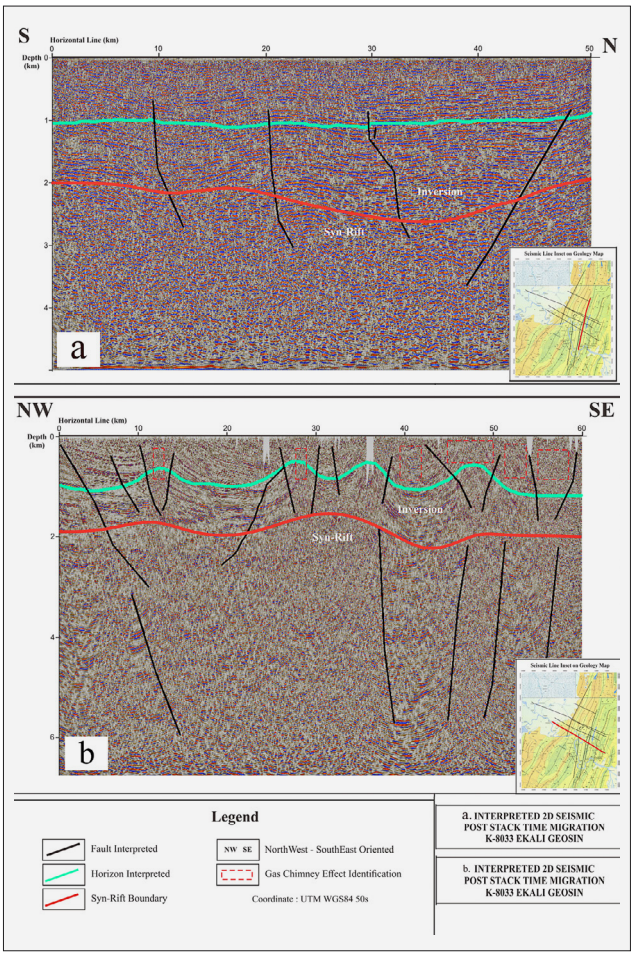


Figure 2. Interpretation of 2D Seismic Travel Time Migration Post-Stack Time Migration (PSTM). (a) 93R-2100 Runtu Matra seismic line, (b) K-8033 Ekali Geosin seismic line. The red line indicates the 93R-2100 seismic profile oriented N – S, while the K-8033 profile is oriented NW – SE. The red dashed box highlights the interpreted chimney effect, the solid black line delineates the interpreted fault, the green line represents the interpreted horizon, and the red line marks the interpreted Syn-Rift Boundary.

scale features such as the Buat Syncline and adjacent anticlinal structures. When correlated with regional structural mapping, these features contribute to a broader understanding of basin evolution, tectonostratigraphic development, and shale gas prospectivity. In particular, the identification of fault bounded compartments offers valuable insight into the localization of shale gas sweet spots, where structural complexity may enhance hydrocarbon trapping and preservation potential.

The interpreted 2D seismic section along the K-8033 Ekali Geosin line reveals several key subsurface structural features that contribute to the understanding of the regional geological framework. A prominent, continuous, and gently undulating seismic reflector is identified at an approximate depth of 1,000 meters. This reflector is interpreted as a major stratigraphic horizon, likely corresponding to a regionally extensive marker bed, and serves as a critical reference surface for subsequent

structural and stratigraphic mapping. Multiple normal faults, predominantly dipping westward, are observed to displace this horizon, extending to various depths within the subsurface. The geometry and distribution of these faults suggest the influence of extensional tectonic processes during the basin's development. The presence of these faults results in the segmentation of the subsurface into discrete structural blocks, which may play a significant role in controlling hydrocarbon migration and trap formation. Understanding the interaction between these faults and stratigraphic units is essential for evaluating the petroleum system elements and assessing the resource potential within the study area.

The observed vertical displacement and offset of seismic reflectors in proximity to the faults indicate evidence of active tectonism, which may have contributed to the development of anticlinal and synclinal features through differential fault movement. The seismic imagery also reveals thick, layered sedimentary sequences beneath the main stratigraphic horizon, which are characteristic of synrift to postrift depositional environments. This stratigraphic pattern suggests phases of extensional tectonics followed by relative tectonic quiescence and continued sediment accumulation. When correlated with other seismic profiles across the study area, these structural features exhibit continuity with regional scale tectonic elements, including the Tenggarong Anticline, Pembulan Anticline, and Buat Syncline. These features are further delineated and spatially constrained through the construction of the time structure map.

The seismic profile has features of a positive flower structure, which is a type of geological feature often found in transpressional regimes. In these regimes, strikeslip faulting is accompanied by compressional stress. This combination results in the upward displacement of rock units, forming a structure that resembles a palm or "push up" feature. Within an anticlinal framework, the development of a positive flower structure can lead to complex uplifted zones, which often act as effective structural traps for hydrocarbon accumulation. Furthermore, geological interpretations suggest that such features may originate from positive tectonic inversion a process in which preexisting extensional (normal) faults are reactivated under a compressive stress regime and converted into reverse faults, enhancing structural complexity and trap potential (**Pace et al., 2012**). The existence of chaotic seismic reflections in the anticlinorium zones in both seismic sections, in addition to the fault patterns that have been found, could be a sign of a gas chimney effect **Figure 2b** (red dashed box). Hydrocarbons, mostly in gaseous form, migrate vertically from deeper source rocks into the reservoir or possibly even to the surface in this phenomena. Usually, this kind of migration happens along permeable channels, such as fracture networks and faults. Reservoir overpressure, active fault systems that allow fluid migration, and structural deformation that causes the creation of new or reactivated fractures are some of the contributing variables that are frequently linked to the gas chimney effect (**Aminzadeh et al., 2002**).

3.2. Time Structure Map

The time structure map, generated through horizon and fault picking on the interpreted seismic sections, illustrates the development of key geological structures within the study area, including the Tenggarong Anticline, Pembulan Anticline, and Buat Syncline (see **Figure 3**). The Tenggarong Anticline is situated in the southwestern portion of the map and is represented by orange to yellow contour intervals with closely spaced lines, indicating a prominent structural high. In the central to eastern region, the Pembulan Anticline is identified as a secondary fold structure with a slightly lower elevation but still exhibiting significant structural potential. The Buat Syncline is seen on the map's eastern side. It is distinguished by blue to purple contour zones that indicate the deepest structural levels and a major sedimentary basin. The structural contours' overall arrangement shows a strong W - E folding trend, with possible faulting seen where there are sudden variations in contour spacing.

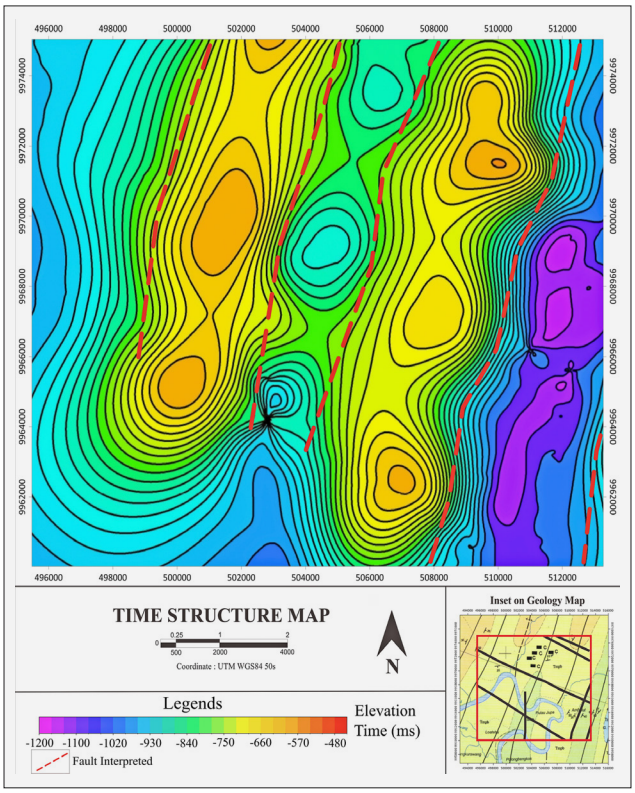


Figure 3. Time structure map research area

Figure 3 presents the time-structure map derived from horizon and fault picking on seismic sections, which illustrates the development of the main geological structures in the study area, namely the Tenggarong Anticline, Pembulan Anticline, and Buat Syncline. The fault boundaries are interpreted and represented by red dashed lines. The Tenggarong Anticline is located in the

Table 1. Presents the dimensionality classification with 0.05 and 0.15 noise of all MT point

Dimension	Noise	Point									Total
		KT03	KT04	KT05	KT06	KT07	KT08	KT09	KT10	KT11	
1D	*0.05*	6			1		9		9	1	26
	0.15	1					6		7	7	21
2D	*0.05*	26	24	49	52	23	48	34	24	32	312
	0.15	24	16	38	22	48	47	33	24	23	275
3D/2D twist	*0.05*			2		6			3	1	12
	0.15			1	4	1		4	3	3	16
3D/1D2D	*0.05*										0
	0.15										0
2D/1D	*0.05*										0
	0.15										0
3D/2D	*0.05*	4		1		4			2	1	12
	0.15	4		1	4				3	1	13
3D	*0.05*	17	22	7	4	13	1	24	14	23	125
	0.15	24	25	14	15	8	3	21	17	24	151
Undetermined	*0.05*	7	14	1	3	14	2	2	8	2	53
	0.15	7	19	6	15	3	4	2	6	2	64
Error	*0.05*	4.17	3.98	3.88	3.98	4.18	3.8	3.85	4.04	3.96	3.98
	0.15	12.7	12.47	12.15	11.97	11.95	11.71	11.25	11.68	12.47	12.034

southwestern part of the map, marked by orange - yellow colors and tightly spaced contours, indicating an uplifted structural high. In the Central - Eastern area, the Pembulan Anticline appears as a secondary fold with slightly lower elevation but still shows structural potential. Meanwhile, the Buat Syncline lies on the eastern side of the map, characterized by blue - purple colors representing the deepest area, serving as a sedimentary basin. The overall contour pattern suggests a dominant W – E folding trend, with indications of possible faulting in zones where abrupt contour changes occur. These structural features are significant not only in terms of conventional hydrocarbon trapping, but also in relation to shale gas potential. Anticlines such as Tenggarong and Pembulan may act as structural traps where shale formations are thermally mature and sufficiently pressured to retain gas. On the other hand, the Buat Syncline, being a deep and potentially thick sedimentary accumulation zone, may serve as a shale gas source and reservoir if the organic rich shale intervals are present and continuous. The combination of folding and faulting enhances the importance of these features as targets for unconventional gas exploration in the area.

3.3. Dimensionality of MT data

The dataset presented in **Table 1** and **Figure 4**, consisting of 540 frequency samples spanning from 320 Hz to 0.011 Hz, includes 60 analyzed frequency values at each measurement point. Overall, the average error is 3.982, while an additional analysis under higher noise conditions (0.15) yields a greater average error of 12.348. **Table 1** presents the dimensional classification results under both conditions in an integrated manner. Across the data, 2D remains the dominant dimensionality in the study area, indicating a prevailing complexity in subsurface structures that can generally be interpreted using 2D models. However, several points exhibit distinct behaviors. KT08 and KT10 show a strong dominance of 1D responses, suggesting homogeneous and laterally consistent subsurface characteristics at those locations. In contrast, KT04, KT09, and KT11 consistently display significant 3D classifications, pointing to complex geological conditions, likely influenced by galvanic distortion, local structural anomalies, or sharp resistivity contrasts.

The proportion of undefined dimensionality increases with higher noise levels, accompanied by a general decline in 1D and 2D classifications. Under these noisier conditions, 3D anomalies become more prominent, particularly at KT03, KT04, and KT11, where 3D classifications often exceed 2D. This suggests the presence of complex subsurface heterogeneity or enhanced resistivity anisotropy at depth. Despite these variations, 2D dimensionality remains the most dominant across the survey area, supporting its suitability for regional-scale interpretation while highlighting localized zones that may require more advanced 3D modelling. Results of the WAL analysis are illustrated in a bar chart, where colors represent different dimensional categories: red (1D), yellow (2D), brown (3D/2D twist), green (3D/1D2D), light purple (2D/1D), dark purple (3D/2D), blue (3D), and black (undefined). Dimensionality is classified using

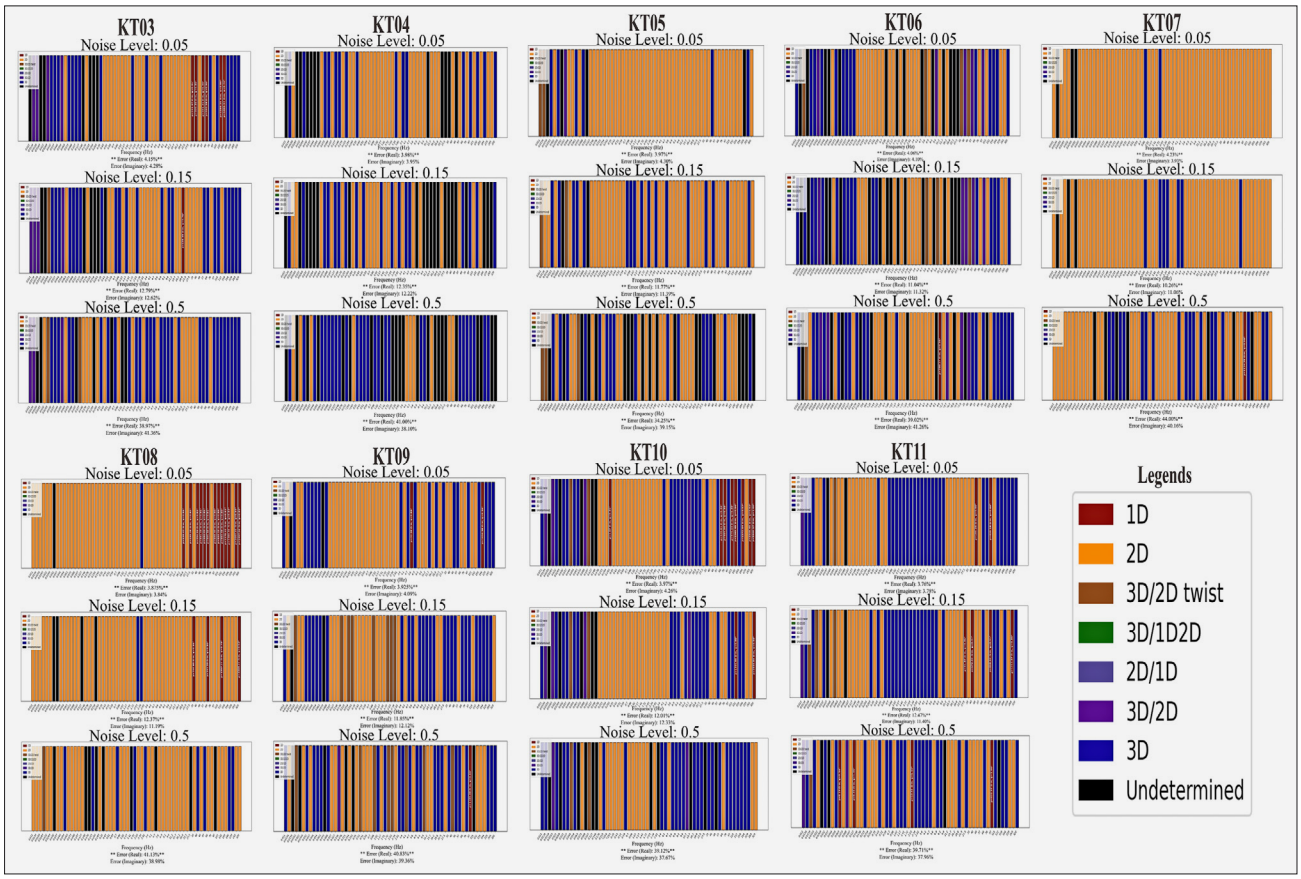


Figure 4. WALDIM bar chart dimensionality classification with 0.05, 0.15, and 0.5 noise of all MT point

threshold criteria from WALDIM (**Weaver et al., 2000**), and the resulting categories are examined both quantitatively and qualitatively to guide interpretation and inversion modelling. As shown in **Figure 5**, the chart is dominated by yellow, indicating that 2D anomalies are most common. Nonetheless, certain sites—such as KT05 and KT07—exhibit 3D characteristics at higher frequencies. At KT04 and KT06, 3D dimensionality is especially dominant in the mid-frequency range, while at KT08, high-frequency data are primarily 1D (red). Overall, anomalies display increasing inconsistency as frequency decreases, a trend observed across all measurement sites.

3.4. Geoelectrical strike of MT data

Geoelectrical strike refers to the dominant direction of resistivity anisotropy, which may differ from the orientation of the measured electric or magnetic fields. It plays a crucial role in determining the directional variability of subsurface resistivity within geoelectrical layers. According to **Groom and Bailey (1989)**, additional components contribute to the continuity of subsurface anomalies, namely twist and shear. As stated by **Martí et al. (2009)**, geoelectrical twist is a galvanic distortion parameter that represents the alteration in the orientation of the electric field due to localized distortions near subsurface structures. Twist quantifies the angular deviation between the measured electric field direction at a given point and the ideal geoelectrical strike direction. In this context, twist refers to the rotation or angular shift of the electric field orientation caused by surface irregularities or near-surface resistivity anomalies. Geoelectrical shear is another parameter associated with galvanic distortion, which describes the angular difference or shear in electric field orientation between two dominant directions. Shear indicates the presence of non-uniform resistivity distribution along these principal axes. **Table 2** presents the strike angle, which represents the predominant direc-

Table 2. Presents the geoelectrical strike, twist, shear of all MT point

Point	Average Angle (dominant)		
	Strike	Twist	Shear
KT03	47.42	-65.49	24.00
KT04	41.83	11.38	28.75
KT05	40.76	13.89	25.12
KT06	42.17	-38.97	23.45
KT07	44.71	-7.60	26.02
KT08	47.58	-11.04	26.98
KT09	40.67	-63.00	24.54
KT10	41.78	-38.03	25.16
KT11	44.73	20.66	26.00
Average	**43.52**	**-19.80**	**25.56**

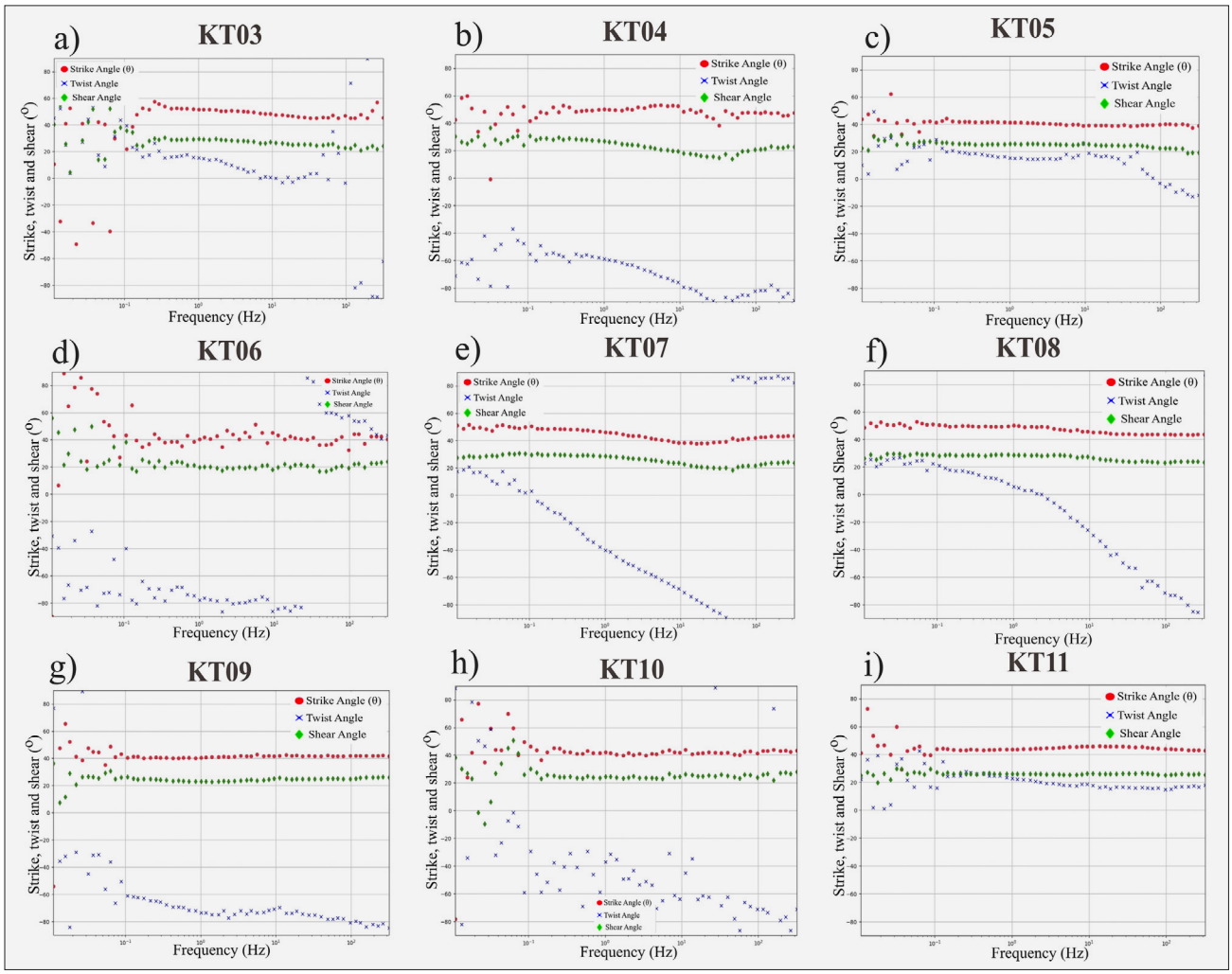


Figure 5. presents the plots of the relationships between the geoelectrical strike angle (q) (red), twist angle (green), and shear angle (blue) for each MT station: (a) MT point KT03, (b) MT point KT04, (c) MT point KT05, (d) MT point KT06, (e) MT point KT07, (f) MT point KT08, (g) MT point KT09, (h) MT point KT10, and (i) MT point KT11.

tion of subsurface resistivity anisotropy, with an average value of approximately 43.52°. This indicates that the subsurface structure exhibits a relatively consistent orientation across the measurement sites. The strike angle varies between 40.67° (KT09) and 47.42° (KT03), with locations such as KT03 and KT08 displaying relatively higher strike values. This suggests that these areas may possess more pronounced structural alignment or greater resistivity contrast compared to other sites. Given the overall consistency in strike orientation, it can be inferred that the electromagnetic field aligns with a uniform resistivity pattern, thereby supporting the validity of subsequent 2D inversion analysis.

Figure 5 illustrates the plots of the relationships between the electrical strike angle (red), twist angle (green), and shear angle (blue) for each MT station: (a) MT point KT03, (b) MT point KT04, (c) MT point KT05, (d) MT point KT06, (e) MT point KT07, (f) MT point KT08, (g) MT point KT09, (h) MT point KT10, and (i) MT point KT11. The results illustrate that the geoelectrical strike derived from the WALDIM analysis closely corresponds to the surface geological strike, with both orientations situated within the first quadrant. This correspondence reinforces the reliability of the subsurface resistivity model and indicates a strong structural control on the observed anisotropic properties. The consistency between the geophysical and geological strike directions further highlights the coherence between subsurface and surface features, thereby supporting a more comprehensive and integrated interpretation in the regional structural and tectonic framework.

3.5. 2D MT model inversion

Figure 6 presents a 2D resistivity model extending approximately 22 km laterally and reaching a depth of up to 15 km, illustrating a subsurface resistivity range between 1 and 300 Ohm.m. This resistivity range is categorized into three main zones: low resistivity (1–5 Ohm.m), represented by purple to light blue colors; moderate resistivity (6–135 Ohm.m), shown in green to yellow; and high resistivity (136–300 Ohm.m), indicat-

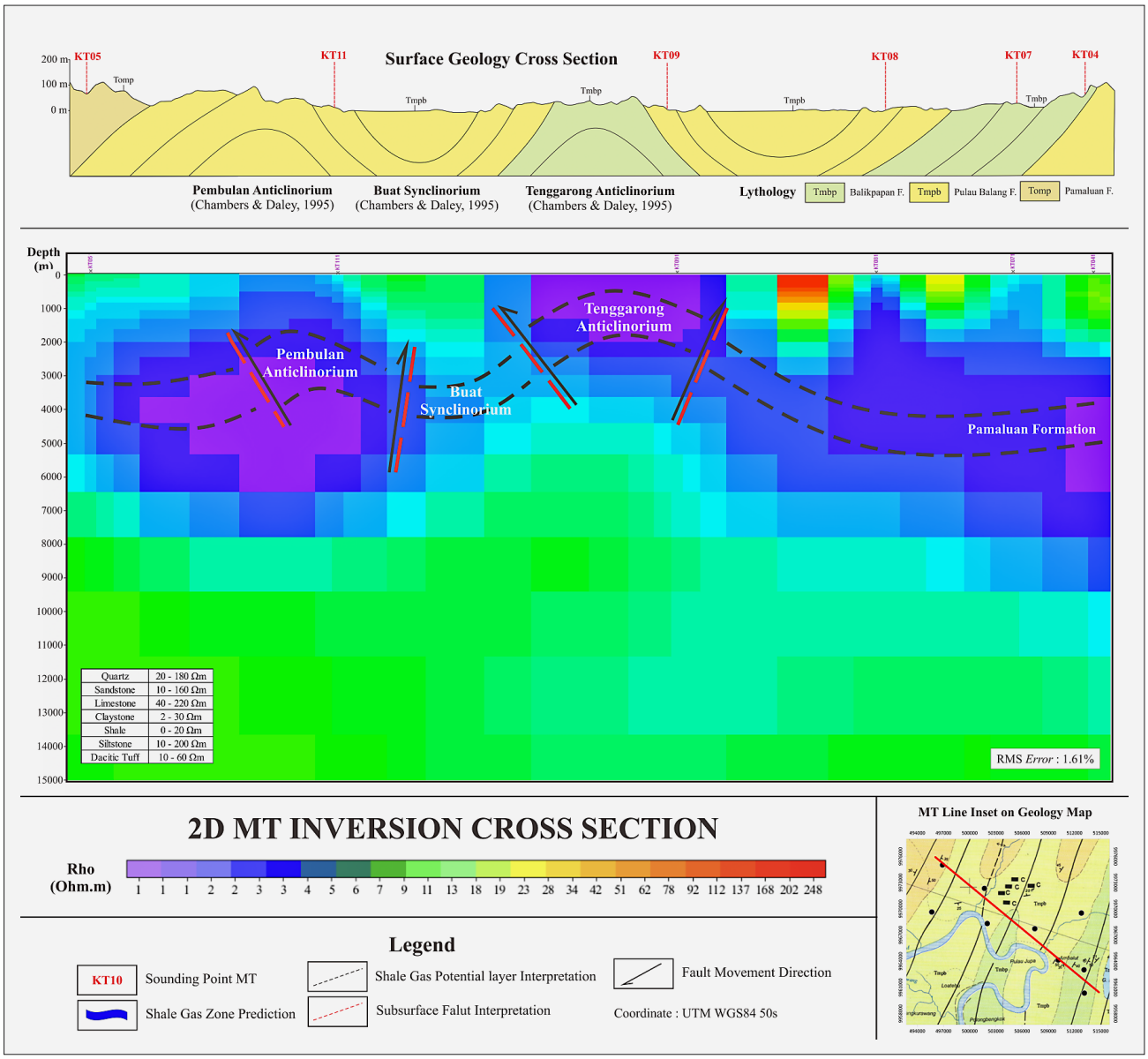


Figure 6. 2D MT model inversion with survey geological section

ed by orange to red tones. The resistivity values of rocks are interpreted as follows: quartz ranges from 20–180 Ohm.m, sandstone 10–160 Ohm.m, limestone 40–220 Ohm.m, claystone 2–30 Ohm.m, shale 0–20 Ohm.m, siltstone 10–200 Ohm.m, and dacitic tuff/alluvium 10–60 Ohm.m (**H. Hidayat et al., 2021**). Overall, the area is predominantly characterized by low to moderate resistivity zones. Based on the results of the 2D inversion model along the MT survey line, a low resistivity anomaly (1–5 Ohm.m) is observed, visualized in shades of purple and light blue in the crosssection of **Figure 6**. Based on the resistivity analysis, the Pamaluan Formation exhibits low-resistivity anomalies that can be interpreted as indications of shale gas presence. This anomaly is further interpreted as representing a black shale layer within the Pamaluan Formation (**Zajuli and Wahyudiono, 2018**). Such conditions are consistent with the general characteristics of high-potential source rocks, where organic-rich clay-rich layers are typically associated with unconventional petroleum systems. The anomaly pattern suggests that the layer has undergone deformation in the form of folding, resembling an anticlinal structure, consistent with features observed in the surface geological map. In addition to the fold structure, four fault lines previously unrecognized in the geological map were also identified. The MT survey line traverses several surface exposed geological formations, including the Pamaluan Formation (Tomp), the Pulau Balang Formation (Tmpb), and the Balikpapan Formation (Tmbp), as identified by **Umar et al. (2018)**. The Samarinda Anticlinorium within the study area comprises several major structural features, namely the Pembulan Anticline, Buat Syncline, Tenggarong Anticline, and Sebulu Anticline. According to **Chambers and Daley (1995)**,

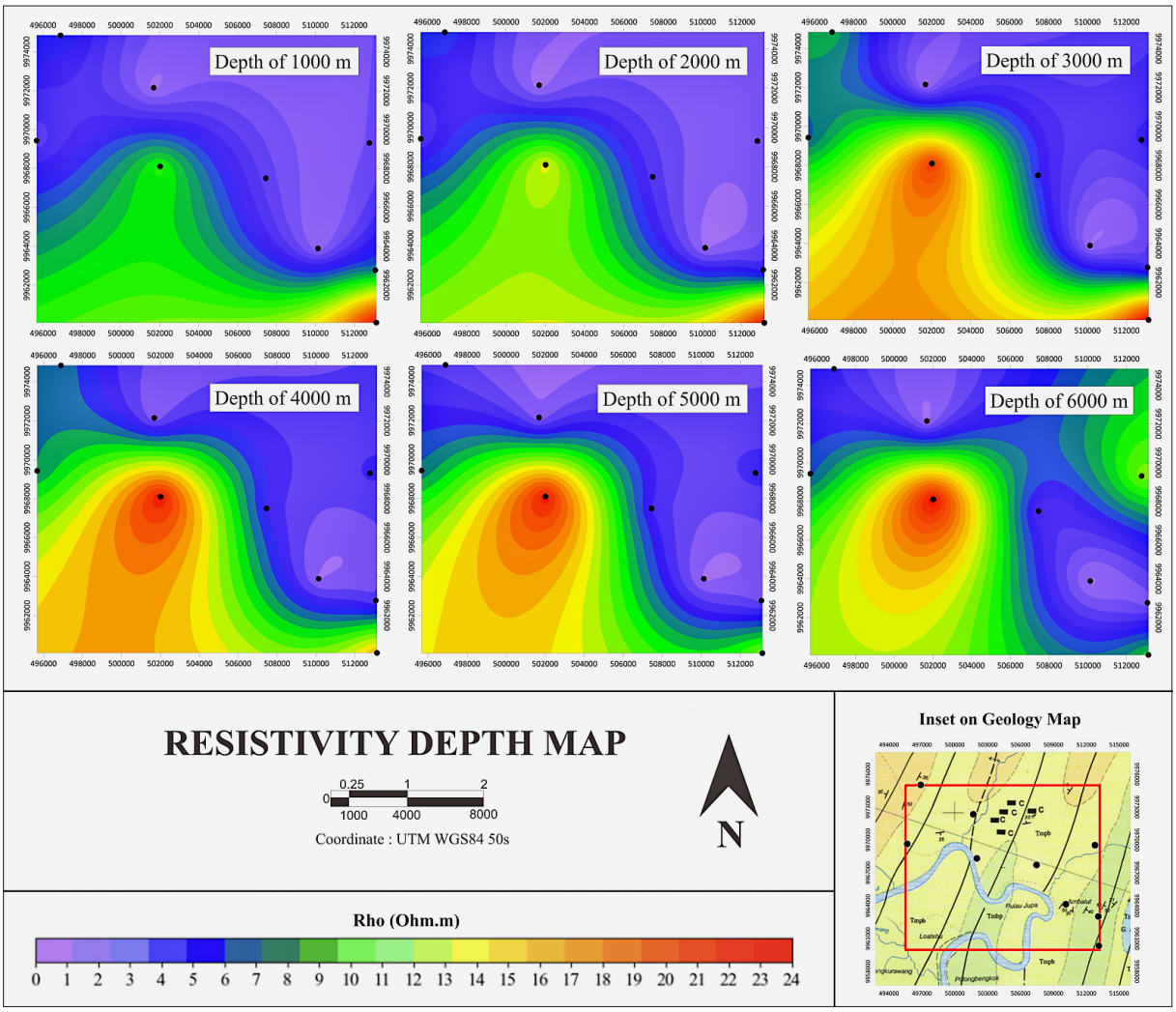


Figure 7. Resistivity depth map from 1000 to 6000 meters

interpretation of the MT survey line suggests that the black shale layer is associated with the structural features of the Pembulan Anticline, Buat Syncline, and Tenggarong Anticline, with an estimated thickness ranging from 2,000 to 4,000 meters. This layer begins to appear at depths of approximately 500 to 1,000 meters; however, due to folding and faulting processes, it is also detected at greater depths between 2,000 and 3,000 meters. The black shale is interpreted as acting as a reservoir within the anticlinal structures and as a potential gas generating source rock within the synclinal zones.

To estimate the shale gas resource potential, mapping the lateral distribution of shale gas is a crucial aspect. Magnetotelluric (MT) data can be visualized in the form of horizontal resistivity maps, which depict the electrical characteristics of various subsurface lithologies (see **Figure 7**). These maps are constructed based on measurements from nine MT sounding points distributed across three surface exposed geological formations: the Pamaluan Formation (Tomp), the Pulaubalang Formation (Tmpb), and the Balikpapan Formation (Tmbp). The interpolation method used for mapping is kriging. The complexity of structures and the depth of anomalies observed in the 2D resistivity sections served as the basis for generating resistivity maps at multiple depths namely 1,000 m, 2,000 m, 3,000 m, 4,000 m, 5,000 m, and 6,000 m. These maps reveal a resistivity range of 1–24 Ohm.m within the study area. The color classification is divided into three categories: low resistivity anomalies (1–5 Ohm.m) shown in purple to dark blue, moderate anomalies (6–15 Ohm.m) in dark green to yellow, and high anomalies (16–24 Ohm.m) in orange to red.

The different resistivity patterns with increasing depth are used to estimate the presence of shale gas. Low resistivity zones are widely dispersed at depths of 1,000 to 2,000 meters, especially in the study area's central and southern regions. This implies that the strata of shale gas are somewhat shallow and may be connected to faulting and bending, among other structural characteristics. Low resistivity anomalies are still discernible at depths of 3,000 to 4,000 meters, but they get smaller and begin to mix with moderate to high resistivity zones that show up in certain places. The presence of more compact or resistant rock formations, which change the resistivity

properties, or lithological changes may be connected to this phenomena. Low resistivity zones, on the other hand, become more localized and less extensive at depths of 5,000 to 6,000 meters, suggesting that the shale gas there may have experienced substantial compaction or thermal modification as a result of high subsurface pressures (**Hidayat et al., 2021; Zajuli and Wahyudiono, 2018**).

3.7. The correlation of seismic and magnetotelluric

In this research, seismic data are utilized as supporting information to identify fault patterns and stratigraphic horizons within the study area. Seismic data are employed due to their higher resolution compared to magnetotelluric (MT) data, making them a valuable reference for enhancing the interpretation. The seismic lines used are oriented linearly, parallel to the MT survey line, following a S- N direction. The specific seismic lines incorporated in the analysis are 93R-2100 Runtu Matra and K-8040 Ekali Geosin. **Figure 8a** presents a three-dimensional section of the seismic line, which serves as a primary reference for subsurface structural interpretation. **Figure 8b** shows the magnetotelluric (MT) resistivity section, correlated with fault systems and the syn-rift boundary as interpreted from the seismic section. In **Figure 8c**, a direct comparison between the seismic section and the MT profile is provided, illustrating the structural correspondence of folding and faulting features identified by both methods. Meanwhile, **Figure 8d** displays an overlay of the time structure map with the MT profile, reinforcing the geological interpretation and highlighting the delineation of major anticline–syncline structures within the research area. Spatially, this seismic line is located to the north of the MT survey line and shares a similar SE - NW orientation. Fault interpretation reveals the presence of several faults exhibiting various structural patterns. These faults are associated with folding structures, forming anticline–syncline configurations within the study area. Specifically, the faults create folded structures that resemble a positive flower structure pattern. Horizon interpretation is based on the reservoir depth within the Kutai Basin, which ranges between 500 and 600 meters. Within the anticline structures, irregular patterns indicative of gas chimney effects are observed.

The correlation between the resistivity data derived from the magnetotelluric (MT) method and the seismic data from line 93R-2100 Runtu Matra, as shown in **Figure 8d**, demonstrates a strong relationship in delineating subsurface structures. The seismic method, with its higher resolution, provides more detailed imagery of subsurface layering and faulting compared to the MT method. In the seismic section, reflection patterns suggest the presence of folds and possible faults that influence the distribution of subsurface lithologies. Hence, the folded layers shown in the seismic data seem to correspond with the low resistivity zones in the MT resistivity section, which are indicated by blue hues. This implies that lithologies with a high fluid content or shale gas deposits may be connected to the low resistivity zones.

Several geological features identified through seismic data show folding patterns that express as anticlines and synclines in the research area. Fold geometries that are congruent with a positive flower structure pattern have developed as a result of fault activity, which is the primary cause of these structural traits. **Figure 8c** shows the comparison of seismic and magnetotelluric (MT) resistivity data, which shows a good correlation in describing subsurface structures. Stratigraphic layering and fault structures are more precisely delineated by the seismic approach than by the MT method because of its higher resolution. The distribution of underlying lithologies is influenced by folding and potential faulting, which are shown by seismic reflection patterns.

The integration of both geophysical methods demonstrates that the major structural features observed in the seismic data, such as folds and faults, are also recognizable in the MT resistivity model. The low resistivity anomalies in the MT data are consistent with seismic reflections that indicate anticline and syncline structures throughout the area. Furthermore, several fault features identified in the seismic section correspond to changes in resistivity observed in the MT data, underscoring the MT method's capability in detecting potential reservoir or source rock zones. Although the MT method has lower resolution compared to seismic data, its ability to penetrate deeper into the subsurface provides valuable complementary information. Additionally, **Figure 8d** which overlays the Time Structure Map with MT data, reinforces the consistency between the datasets, showing coherent anticline–syncline patterns. This integrated interpretation strengthens the delineation of key fold structures such as the Tenggarong Anticline, Pembulan Anticline, and the associated synclinal features.

A similar fault pattern, known as a positive floral structure, is seen in both seismic sections. A positive floral structure is a type of geological formation that usually forms in transpressional tectonic settings, where rock layers are displaced upward by compressional force on strike-slip faults. This produces a structure that looks like a palm tree, often known as a "push-up structure." These characteristics are frequently seen in strike-slip fault zones, especially in regions with stepovers or restraining bends where compressive forces combine horizontal and vertical displacements. Positive floral structures help create intricate uplift zones in an anticlinorium and are frequently important structural traps for the buildup of hydrocarbons. Positive tectonic inversion, in which pre existing normal faults that were initially created under extensional regimes are reactivated as reverse faults due to compressional stress, is another way that these structures can emerge, according to earlier research (**Pace et al., 2012**). Despite the fault pattern, the gas chimney effect is responsible for the uneven reflec-

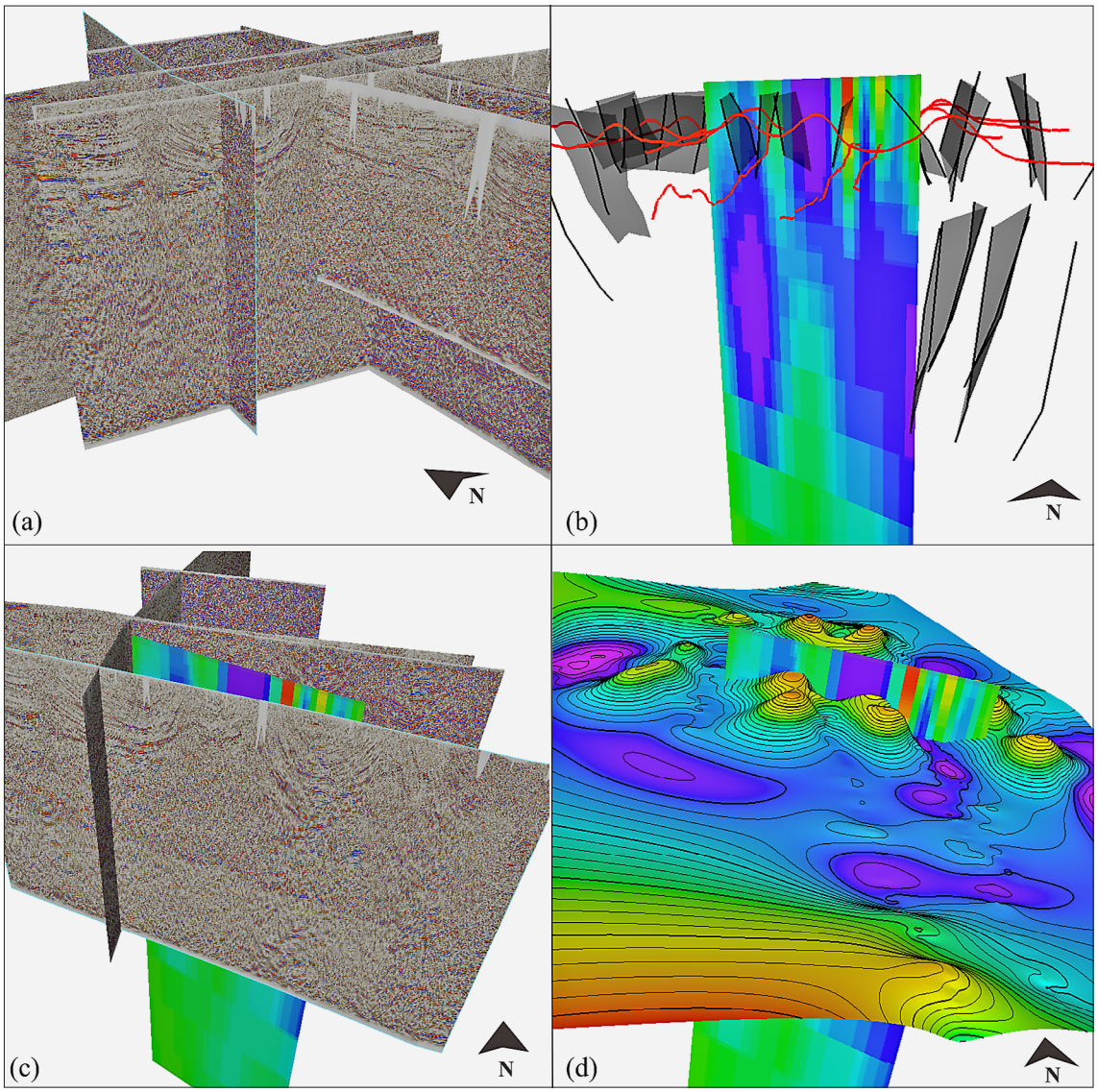


Figure 8. Correlation seismic section and MT interpretation; (a) corelation MT and selected fault horizon, (b) corelation MT and time structure map.

tion characteristics seen in the anticlinorial zones of both seismic sections. This phenomenon shows how hydrocarbons, especially gas, migrate vertically from source rocks to reservoirs or even to the surface via permeable channels like faults and fractures. Overpressure in the reservoir, migration routes along active faults, and structural deformation that creates new fracture networks are the main sources of this phenomenon. According to **Aminzadeh et al. (2002)**, gas chimneys are important markers of active hydrocarbon migration pathways.

5. Conclusions

The 2D Magnetotelluric (MT) resistivity modelling results reveal the presence of low-resistivity anomalies (1–5 Ohm.m), which are interpreted as black shale layers within the Pamaluan Formation. These anomalies exhibit folding patterns resembling anticlines and are influenced by several previously unmapped fault lines. Correlation with seismic data strengthens this interpretation, as folds and faults identified in seismic sections correspond with low-resistivity zones in the MT data. Major structural features in the study area, including the Pembulan Anticline, Tenggarong Anticline, and Buat Syncline, play a significant role in controlling the distribution of black shale. This layer appears at depths of 500–1,000 m and extends to 2,000–4,000 m due to folding and faulting processes. Resistivity depth maps (1,000–6,000 m) indicate that low-resistivity zones are predominant at shallow depths (1,000–2,000 m) but diminish with increasing depth as a result of compaction and thermal alteration. This suggests that shale gas potential is concentrated at shallow to intermediate depths. The integration of MT and seismic data also reveals positive flower structures (push-up structures) formed by transpressional strike-slip faulting. These structural

features act as hydrocarbon traps, while the occurrence of gas chimney effects indicates active hydrocarbon migration pathways from source rocks to reservoirs. Overall, the combined application of MT and seismic methods successfully delineates the relationship between folds, faults, and the distribution of black shale as both a source rock and a potential reservoir. Therefore, the study area demonstrates significant indications of shale gas prospectivity controlled by the major geological structures of the Kutai Basin.

Acknowledgement

We would like to express our gratitude to LEMIGAS for granting permission to use the data and for its support in this scientific publication. This paper represents one of the outcomes of the research collaboration agreement between LEMIGAS and UPN 'Veteran' Yogyakarta.

6. References

Aminzadeh, F., Connolly, D., & De Groot, P. (2002). Interpretation of gas chimney volumes. In *SEG Technical Program Expanded Abstracts 2002* (pp. 440–443). Society of Exploration Geophysicists.

Avdeeva, A., Avdeev, D., & Jegen, M. (2012). Detecting a salt dome overhang with magnetotellurics: 3D inversion methodology and synthetic model studies. *Geophysics*, *77*(4), E251–E263. https://doi.org/10.1190/geo2011-0167.1

Bashir, Y., Babasafari, A. A., Alashloo, S. M., Muztaza, N. M., Ali, S. H., & Imran, Q. S. (2021). Seismic wave propagation characteristics using conventional and advance modelling algorithm for d-data imaging. *Journal of Seismic Exploration*, *30*(1), 21–44.

Chambers, J. L., & Daley, T. E. (1995). *A tectonic model for the onshore Kutai Basin, East Kalimantan, based on an integrated geological and geophysical interpretation*.

Cinti, F., Pauselli, C., Livio, F., Ercoli, M., Brunori, C., Ferrario, M., Volpe, R., Civico, R., Pantosti, D., & Pinzi, S. (2015). Integrating multidisciplinary, multiscale geological and geophysical data to image the Castrovillari fault (Northern Calabria, Italy). *Geophysical Supplements to the Monthly Notices of the Royal Astronomical Society*, *203*(3), 1847–1863.

Dragičević, I., Andrić, M., & Blašković, I. (1991). Geological-geophysical exploration of the bauxite deposits application of the shallow seizmic reflection method. *Rudarsko-Geološko-Naftni Zbornik*, *3*(1), 23–28.

Gallardo, L. A., & Meju, M. A. (2004). Joint two-dimensional DC resistivity and seismic travel time inversion with cross-gradients constraints. *Journal of Geophysical Research: Solid Earth*, *109*(B3).

Groom, R. W., & Bailey, R. C. (1989). Decomposition of magnetotelluric impedance tensors in the presence of local three-dimensional galvanic distortion. *Journal of Geophysical Research: Solid Earth*, *94*(B2), 1913–1925.

Hamdani, A., Noeradi, D., Iskandar, Y., & Pusat Survey Geologi, Badan Geologi, ESDM. (2019). Potensi Gas Serpih Formasi Pulobalang, Cekungan Kutai, Kalimantan Timur. *Bulletin of geology*, *3*(2), 371–380. https://doi.org/10.5614/bull.geol.2019.3.2.5

Hidayat, H., H. Setiawan, J. J., Ibrahim, A., Marjiyono, M., & Lucki Junursyah, G. M. (2021). Studi Magnetotelurik (MT) untuk Mendelineasi Potensi Regional Gas Serpih Bawah Permukaan Berdasarkan Properti Tahanan Jenis di Cekungan Kutai, Kalimantan Timur. *Jurnal Geologi dan Sumberdaya Mineral*, *22*(2), 107–114. https://doi.org/10.33332/jgsm.geologi.v22i2.571

Hidayat, W., & Hamdalah, H. (2019). Analisa Geoelectrical Strike Metode AMT untuk Identifikasi Awal Potensi Sistem Panas Bumi di Daerah Gunung Pancar Bogor Jawa Barat. *Jurnal Offshore: Oil, Production Facilities and Renewable Energy*, *3*(1), 23–29.

Irawati, S. M., Hidayat, W. E., & Grandis, H. (2022). Integrated Magnetotelluric (MT), Gravity and Seismic Study of Lower Kutai Basin Configuration. *Journal of Engineering and Technological Sciences*, *54*(1). https://doi.org/10.5614/j.eng.technol.sci.2022.54.1.3

Kumar, A., & Rao, C. K. (2025). Electrical architecture across the Ridge-Fault structure in the seismically active Jind-Rohtak-Delhi regions, NW India: Imaged from magnetotellurics studies. *Journal of Asian Earth Sciences*, *277*, 106407. https://doi.org/10.1016/j.jseaes.2024.106407

Kumar, P. V., Rao, P. S., Singh, A., Kumar, A., & Rao, P. R. (2021). Dimensionality and directionality analysis of magnetotelluric data by using different techniques: A case study from northern part of Saurashtra region, India. *Journal of Earth System Science*, *130*(2), 102. https://doi.org/10.1007/s12040-021-01596-0

Ledo, J., & Jones, A. G. (2001). Regional electrical resistivity structure of the southern Canadian Cordillera and its physical interpretation. *Journal of Geophysical Research: Solid Earth*, *106*(B12), 30755–30769.

Likkason, O. K. (2014). Exploring and using the magnetic methods. *Advanced Geoscience Remote Sensing*, 141–174.

Lixin, Q. (2022). Full wave seismic exploration technology. *Petroleum Exploration and Development*, *49*(3), 586–595. https://doi.org/10.1016/S1876-3804(22)60048-X

Mansoori, I., Oskooi, B., Pedersen, L. B., & Javaheri, R. (2016). Three-dimensional modelling of magnetotelluric data to image Sehqanat hydrocarbon reservoir in south-western Iran. *Geophysical Prospecting*, *64*(3), 753–766. https://doi.org/10.1111/1365-2478.12328

Martí, A., Queralt, P., & Ledo, J. (2009). WALDIM: A code for the dimensionality analysis of magnetotelluric data using the rotational invariants of the magnetotelluric tensor. *Computers & Geosciences*, *35*(12), 2295–2303.

Miensopust, M. P., Queralt, P., Jones, A. G., & 3D MT modellers. (2013). Magnetotelluric 3-D inversion—A review of two successful workshops on forward and inversion code testing and comparison. *Geophysical Journal International*, *193*(3), 1216–1238.

Moorkamp, M., Heincke, B., Jegen, M., Roberts, A. W., & Hobbs, R. W. (2011). A framework for 3-D joint inversion of MT, gravity and seismic refraction data. *Geophysical Journal International*, *184*(1), 477–493.

Nabighian, M. N., Grauch, V., Hansen, R., LaFehr, T., Li, Y., Peirce, J. W., Phillips, J. D., & Ruder, M. (2005). The historical development of the magnetic method in exploration. *Geophysics*, *70*(6), 33ND-61ND.

Pace, P., Scisciani, V., Calamita, F., & Paltrinieri, W. (2012). Positive flower structures as reactivated normal faults along oblique thrust ramps: Examples from the Apulian structures, Central–Southern Apennines. *Rendiconti Online Società Geologica Italiana*, *21*, 47–49.

Patro, P. K. (2017). Magnetotelluric Studies for Hydrocarbon and Geothermal Resources: Examples from the Asian Region. *Surveys in Geophysics*, *38*(5), 1005–1041. https://doi.org/10.1007/s10712-017-9439-x

Prabowo, A., Junursyah, G. M. L., & Hidayat, W. (2020). Analisis Kualitas Data Magnetotelurik Berdasarkan Parameter Koherensi Pada Daerah Bandung, Jawa Barat. *Jurnal Mineral, Energi, Dan Lingkungan*, *4*(2), 78–84.

Stark, A. (2008). *Seismic methods and applications: A guide for the detection of geologic structures, earthquake zones and hazards, resource exploration, and geotechnical engineering*. Universal-Publishers.

Sukmono, S., & Arta, P. (2013). *Reevaluation of Miocene-Pliocene Carbonates Prospects in the Kutai Basin Using Integrated Well, Seismic and Gravity Analysis*.

Supriatna, Sukardi, & Rustandi. (1995). *Geological Map Of The Samarinda Sheet, Kalimantan 1:250.000*. Scale". Geological Research And Development Centre.

Susilo, A. (2020). Interpretasi data seismik dengan menggunakan software kingdom 6.7. 1. *petro: Jurnal Ilmiah Teknik Perminyakan*, *9*(4), 159–166.

Tietze, K., Ritter, O., Patzer, C., Veeken, P., & Dillen, M. (2019). Repeatability of land-based controlled-source electromagnetic measurements in industrialized areas and including vertical electric fields. *Geophysical Journal International*, *218*(3), 1552–1571. https://doi.org/10.1093/gji/ggz225

Umar, H., Pangeran, C., & Shodiqin, A. (2018). Geologi Dan Studi Struktur Geologi Berdasarkan Citra Satelit Daerah Muanglama, Kecamatan Samarinda Utara, Kota Samarinda, Provinsi Kalimantan Timur. *Jurnal teknik geologi: Jurnal Ilmu Pengetahuan Dan Teknologi*, *1*(1).

Weaver, J. T., Agarwal, A. K., & Lilley, F. (2000). Characterization of the magnetotelluric tensor in terms of its invariants. *Geophysical Journal International*, *141*(2), 321–336.

Zajuli, M. H. H., & Wahyudiono, J. (2018). Rock-Eval Characteristic of Oligosen Fine-grained Sedimentary Rocks from Pamaluan Formation, Gunung Bayan Area, West Kutai Basin, East Kalimantan: Implication for Hydrocarbon Source Rock Potential. *Jurnal Geologi Dan Sumberdaya Mineral*, *19*(2), 73–82.

Zhang, B., Tong, Y., Du, J., Hussain, S., Jiang, Z., Ali, S., Ali, I., Khan, M., & Khan, U. (2022). Three-dimensional structural modeling (3D SM) and joint geophysical characterization (JGC) of hydrocarbon reservoir. *Minerals*, *12*(3), 363. https://doi.org/10.3390/min12030363

Zhang, K., Wei, W., Lu, Q., Dong, H., & Li, Y. (2014). Theoretical assessment of 3-D magnetotelluric method for oil and gas exploration: Synthetic examples. *Journal of Applied Geophysics*, *106*, 23–36. https://doi.org/10.1016/j.jappgeo.2014.04.003

SAŽETAK

Otkrivanje struktura ležišta plinonosnih šejlova seizmičkim i MT podatcima: WALDIM studija iz Istočnoga Kalimantana, Indonezija

Pamaluanska formacija, s vrijednošću ukupnoga organskog ugljika (engl. *Total Organic Carbon*, TOC) od 1,78 % i različitim stupnjem termalne starosti, predstavlja izniman potencijal za proizvodnju iz plinonosnih šejlova u indonezijskome bazenu Kutai. Ovo istraživanje objedinjuje seizmičke i magnetotelurske (MT) geofizičke tehnike u svrhu povećanja znanja o potencijalima plinonosnih šejlova u tome području. U sklopu istraživanja obrađeni su podatci s devet lokacija MT sondiranja i devet linija 2D seizmičkih ispitivanja. Izrađenom strukturnom kartom dodatno su istražene antiklinale i sinklinale koje su utvrđene interpretacijom seizmičkih podataka. Obradom MT podataka, primjenjujući pristup varijance koeficijenta korelacije rho i modul WALDIM računalnoga programa Python, stvoreni su 2D modeli inverzije otpornosti. Podatci upućuju na dominantan smjer antiklinalnih i sinklinalnih struktura orijentiran otprilike 45° od pravoga sjevera. S prosječnim nagibom od 43,5° MT analiza pokazuje dominantnu dvodimenzionalnu (2D) geoelektričnu dimenzionalnost, koja se poklapa s lokalnim geološkim trendovima. Na dubinama od 500 do 1000 m u antiklinalama i 2000 do 3000 m u sinklinalama pronađene su zone niske otpornosti (1 – 5 Ohm·m), s debljinama koje variraju od 2000 do 4000 m. Anomalije niske otpornosti interpretiraju se kao potencijalni intervali plinonosnih šejlova, što je u skladu s geološkim karakteristikama bazena Kutai. Objedinjeni seizmički i MT podatci vjerno prikazuju bore, rasjede i anomalije niske otpornosti koji se tumače kao potencijalni intervali plinonosnih šejlova ističući važnost multidisciplinarnoga pristupa u ublažavanju rizika istraživanja i poboljšanju procjene perspektivnosti plinonosnih šejlova u bazenu Kutai.

Ključne riječi:
plinonosni šejlovi, bazen Kutai, seizmika, magnetotelurska metoda, WALDIM

Author's contribution

Suharsono: conceptualization, supervision, methodology, wriing and interpretation, **Yustisio Dianwiyono**: validation, processing and visualitation, **Edy Wijanarko:** data curation, software, resources supervision, and validation, **Wahyu Hidayat:** original draft and writing and review and editing. **Muhammad Fachrul Rozi Kurniawan:** project administration and review and editing, **Yudha Agung Pratama:** data curation and project administration.
All authors have read and agreed to the published version of the manuscript.

RGNZ/MGPB

Predicting Peak Particle Velocity Induced by Mining Blasting Using Optimized Deep Learning with Coronavirus Herd Immunity Algorithm

Rudarsko-geološko-naftni zbornik
(The Mining-Geology-Petroleum Engineering Bulletin)
DOI: 10.17794/rgn.2026.2.9

Original scientific paper

Davood Mohammadi Sargini[1], Mohammad Ataei[1], Reza Mikaeil[2]*, Akbar Esmaeilzadeh[2]

[1] *Faculty of Mining, Oil and Geophysics, Shahrood University of Technology.*

[2] *Faculty of Industries and Mining Technologies, Urmia University of Technology.*

Abstract

One of the most important economic sectors is mining. Open-pit mines are the most common form, and blasting is the most efficient method. This method can cause significant damage due to vibrations. Thus, monitoring and controlling vibrations is important. This research aims to predict vibrations based on the distance and quantity of explosives. To study this, vibrations were estimated using Peak Particle Velocity from seismograph devices. Measurements were done in two large Iranian mines, providing approximately 1000 data points. Considering the data complexity, a deep learning method was selected for modelling. Deep learning has numerous hyperparameters, and their correct adjustment impacts efficiency. The Coronavirus Herd Immunity Optimizer (CHIO) was used to find optimal values. Various criteria were used to test the model efficiency. The results indicate the optimization method improved predictions by at least 4%. The coefficient of determination for random forest, basic deep learning, and optimized methods was 0.861, 0.932, and 0.972. The root means square error values are 3.687, 2.338, and 1.146. The absolute mean percentage error indices are 0.169, 0.128, and 0.068. It is concluded that deep learning has acceptable performance. Its efficiency can be increased by optimization algorithms. The results show an excellent response to the integration of the CHIO method, demonstrating its good capability.

Keywords:
blasting, peak particle velocity, deep learning, herd immunity, coronavirus

1. Introduction

The increasing need of modern societies for diverse products has increased the dependence of manufacturing factories on the extraction of minerals, as the initial unit of the production chain. Open-pit mines are considered the largest supplier of mineral raw materials to production units. In these mines, minerals are extracted through drilling and blasting. Although this method leads to high-speed and large-scale production, it has significant drawbacks. This method generates significant vibrations that cause serious damage to buildings around the mine. These damages can be observed in the form of cracks or destruction of the building. Therefore, it is significantly important to control and manage these types of damage. To manage them, it is necessary to implement measures that are preceded by awareness of the magnitude of the vibration and its radius of effect. Considering the importance of the subject, this research attempted to record and collect data on the distance from the blasting site, the amount of explosive used for the blasting, and the corresponding vibration intensity generated in terms of Peak particle velocity in two large open-pit mines, resulting in a powerful tool for predicting the seismic situation of each blasting. Given the critical importance of controlling blasting vibrations, many researchers are dedicated to this field. A review of the work done in this field is provided as follows.

Armaghani et al. (2014) research developed a hybrid PSO-ANN model, which integrates Particle Swarm Optimization with an Artificial Neural Network, to provide simultaneous and accurate predictions for two critical blasting hazards: flyrock distance and ground vibration (PPV). The model was trained and validated using a robust dataset of 62 blasting events from a granite quarry, incorporating key design parameters such as burden, spacing, and powder factor. It demonstrated superior predictive performance, achieving notably high coefficients of determination of $R^2 = 0.957$ for flyrock and $R^2 = 0.988$ for PPV on the test dataset. A subsequent sensitivity analysis revealed that powder factor and stemming length were the dominant factors controlling flyrock, while maximum charge per delay was the paramount

* Corresponding author: Reza Mikaeil
e-mail address: reza.mikaeil@gmail.com
Received: 11 August 2025. Accepted: 22 October 2025.
Available online: 13 March 2026

variable for ground vibration. These findings robustly establish the proposed PSO-ANN model as an effective and reliable expert system, offering a practical tool for engineers to preemptively assess risks and design safer, more environmentally controlled blasting operations. **Dindarloo (2015)** investigated and predicted the vibration caused by the blasting using a genetic algorithm. In this study, 9 input variables were used to predict the vibration frequency at different distances from the blasting face. The high coefficient of determination with the absolute mean percentage error indicated the suitability of the algorithm in predicting the amount of vibration. **Ghasemi (2016)** presented a new hybrid approach based on the combination of adaptive neuro-fuzzy inference system and particle swarm optimization to predict the Peak particle velocity during the blasting stage in open pit mines. The models were trained and tested based on real data from 120 blasting cases in the Sarcheshmeh copper mine. The results obtained from the comparison of the models showed that the adaptive neuro-fuzzy inference system and particle swarm optimization model provided better results compared to other models. **Saghatforoush et al. (2016)** developed a hybrid Artificial Neural Network (ANN) model, optimizing it with the Ant Colony Optimization (ACO) algorithm, to predict and mitigate two critical blasting hazards: flyrock distance and back-break in a granite quarry. By employing ACO to refine the ANN's initial weights and biases, they significantly enhanced its predictive accuracy beyond that of a conventional, standalone ANN. Their results demonstrate the hybrid model's superior performance. For flyrock prediction, it achieved a coefficient of determination (R^2) of 0.964, markedly outperforming the standard ANN (R^2 = 0.934). Similarly, for back-break prediction, the hybrid ANN–ACO model delivered greater accuracy, with an R^2 of 0.980 compared to 0.960 for the conventional model. Consequently, this optimized tool allows engineers to proactively adjust key blasting design parameters—including burden, spacing, hole depth, and powder factor—before operations commence. This capability directly supports the minimization of hazardous side effects, thereby enhancing both safety protocols and economic efficiency at the site. **Hasanipanah et al. (2017)** studied the ground vibration caused by blasting in the Bakhtiari Dam area using a genetic algorithm. In their study, they developed equations to predict ground vibration using the mentioned algorithm. The maximum payload weight at each delay and the distance between the monitoring site and the blasting point, as well as the most influential parameters on ground vibration, were used as inputs for modelling. The Peak particle velocity parameter, as an indicator for evaluating ground vibration caused by the blasting, was also considered as an output or dependent variable for modelling. They measured the Peak particle velocity parameters accurately by considering 85 blasting cases and then compared the results with several empirical prediction models. The results showed that the genetic algorithm is an acceptable model compared to empirical prediction models for predicting the Peak particle velocity, considering the mean sum of squared error and multiple determination coefficient indices. In their study, **Asl et al. (2018)** attempted to design appropriate parameters for blast pattern design including overburden, spacing, hole depth, stemming, specific charge, charge at each delay time, and earth strength index to reduce inappropriate crushing and rock fly using artificial neural network and firefly algorithm. After collecting data and selecting the most effective parameters for rock fly and crushing, they developed an artificial neural network model and used the firefly algorithm for the optimization process. The results of modelling and optimization showed 42.9% and 32.9% reductions in rock fly and crushing, respectively. **Nguyen et al. (2019a)** compared the ground vibration and Peak particle velocity caused by open-pit coal mine blasting using boosted generalized additive models, an empirical equation, a support vector machine, and an artificial neural network. They used several statistical indicators, such as coefficient of determination, mean sum of squared error, and mean absolute error to evaluate the quality of each prediction model. The results showed that the proposed model had the highest accuracy, and the height difference between the blasting site and the monitoring site was one of the dominant parameters governing the Peak particle velocity prediction models. In their other work in same year, **Nguyen et al. (2019b)**, presented a new prediction model based on the Gaussian process regression approach to estimate ground vibration caused by blasting. They examined 210 blasting in an open-pit mine in Ghana, of which 130 data points were used for developing model training. The remaining 80 data points were used to evaluate the performance of the Gaussian regression model. Then, they compared the formulated model with other standard prediction methods, such as the generalized regression neural network, the radial basis function neural network, and the recurrent neural network, and with four conventional ground vibration predictors. The results showed that the proposed Gaussian process regression approach can predict ground vibration with much greater accuracy than the standard methods. **Bui et al. (2019)** studied the effects of blasting in an open-pit mine in Vietnam. During this study, 25 blasting were examined. In their study, they achieved a new hybrid model for predicting ground vibration caused by blasting by combining fuzzy clustering models and pseudo-recurrent neural networks. The results of the studies show that the new hybrid model has higher accuracy compared to old models, such as artificial neural networks, forest, and pseudo-recurrent neural networks. The proposed model could be used to control the adverse effects of ground vibration caused by blasting. **Fang et al. (2019)** considered ground vibration caused by blasting as the main objective in their study and presented a new artificial intel-

ligence system to predict ground vibration caused by blasting with high accuracy, which was based on the algorithm based on the five-rules and the imperialist competition algorithm, and they called it the imperialist competition hybrid method based on the five-rules. In the research, the imperialist competition algorithm was considered to optimize the "five-rules" concept. To evaluate the efficiency of the new hybrid method presented, they selected the "classical five-rules" and the support vector machine as benchmark methods. In addition, they used two empirical equations to develop models based on experimental data sets to predict ground vibration caused by blasting for comparison with the proposed new hybrid model. They also conducted their study on an open-pit mine in Vietnam using experimental models, support vector machines and extended random models based on 125 blasting cases. Then, evaluated the accuracy using the mean absolute error, the mean sum of squared error, and coefficients of determination. The research findings indicated that the proposed new hybrid model provides the highest accuracy compared to other methods. **Yang et al. (2020)** studied the prediction of ground vibration caused by blasting using hybrid artificial intelligence methods. Their study was based on optimized support vector regression with the firefly algorithm, genetic algorithm, and particle swarm optimization algorithm. In addition, they used spindle-face, artificial neural network-based models, and some well-known empirical models. During this research, they used 90 datasets collected from two open-pit mines. Their comparison results based on several statistical criteria indicated that the hybrid method has significantly higher efficiency than other hybrid models based on support vector machines. **Azimi et al. (2019)** proposed a new evolutionary artificial neural network that is optimized with a genetic algorithm for predicting Peak particle velocity. The proposed artificial neural network-based genetic algorithm is a hybrid method that provides a systematic and automated approach to find the appropriate ANN architecture, number of neurons, activation functions, training algorithm, and number of cycles. The dataset consisting of maximum load weight at each delay, horizontal distance, radial distance, and new modified radial distance between the monitoring station and the blasting station at the Songun copper mine site in Iran was used for the proposed validation.

The approach of comparing the performance of the proposed ANN-based genetic algorithm hybrid model with statistical indicators shows the superiority of the ANN-based genetic algorithm hybrid model over empirical predictors and the neuro-fuzzy inference system. Finally, the results indicate that the proposed ANN-based genetic algorithm hybrid method is effective in finding the optimal architecture of the ANN while predicting the Peak particle velocity. **Nguyen et al. (2020)** used an artificial neural network to predict air blasts caused by blasting in the open-pit coal mine of Diona, Vietnam. The parameters used in these models included charge per delay, overburden, spacing, stemming length, specific charge, air humidity, and monitoring the station distance. The results of the research showed that the multilayer neural network model has the most accurate prediction compared to previous models. **Al-Bakri et al. (2021)** confirmed the superiority of Artificial Neural Networks (ANNs) in predicting and optimizing blast-induced impacts such as vibrations and flyrock. Their findings show ANN models achieve greater accuracy and efficiency than traditional empirical approaches, making them critical for safety and environmental management in blasting projects.

Zhang et al. (2021a) investigated the effect of the Peak particle velocity caused by blasting in underground coal mines. This study discussed the relationship between the magnitude of mining events and the Peak particle velocity with the resulting stress increase, which is of important reference significance for studying the mechanism and early warning of rock bursting. **Zhang et al. (2021b)** predicted the Peak particle velocity caused by open-pit mining using an artificial intelligence-based method. In this paper, a combination of extreme machine learning and multiverse optimization methods is presented to predict the Peak particle velocity from 137 blasting events. As a result, better accuracy was achieved compared to traditional models. **Zeng et al. (2021b)** investigated and predicted the Peak particle velocity using hybrid machine learning. They concluded that a combination of boosting models can identify the most effective parameters affecting the Peak particle velocity values and predict them with high accuracy. **Hanifehnia et al. (2024)** focuses on predicting the distance of blast-induced flyrock, an undesirable environmental phenomenon in open-pit mines, using artificial intelligence methods and statistical techniques; they employ an _Artificial Neural Network (ANN-MLP)_ and a hybrid _ICA-ANN_ model (ANN optimized by the Imperialist Competitive Algorithm) to forecast flyrock distance considering parameters such as number of holes, hole spacing, burden, total charge, specific drilling, charge per hole and specific charge, and report that the ANN achieved RMSE = 9.31 m, MAE = 7.10 m, R2 = 0.81 while the ICA-ANN improved predictions to RMSE = 5.66 m, MAE = 4.60 m, R2 = 0.89; sensitivity analysis indicates explosive consumption and number of holes have the greatest impact. **Khosravimanesh et al. (2024)** noted that directly measuring the Rate of Penetration (ROP) in drilling is costly and time-consuming, making predictive models a valuable alternative. In their study, they evaluated linear, lasso, and ridge regression models on a dataset of 492 samples. Their comprehensive comparison, based on multiple error metrics, ultimately identified the Ridge regression model as the most reliable and accurate predictor for ROP.

Taiwo et al. (2024) presented new research about blasting process in a granite quarries. This study suc-

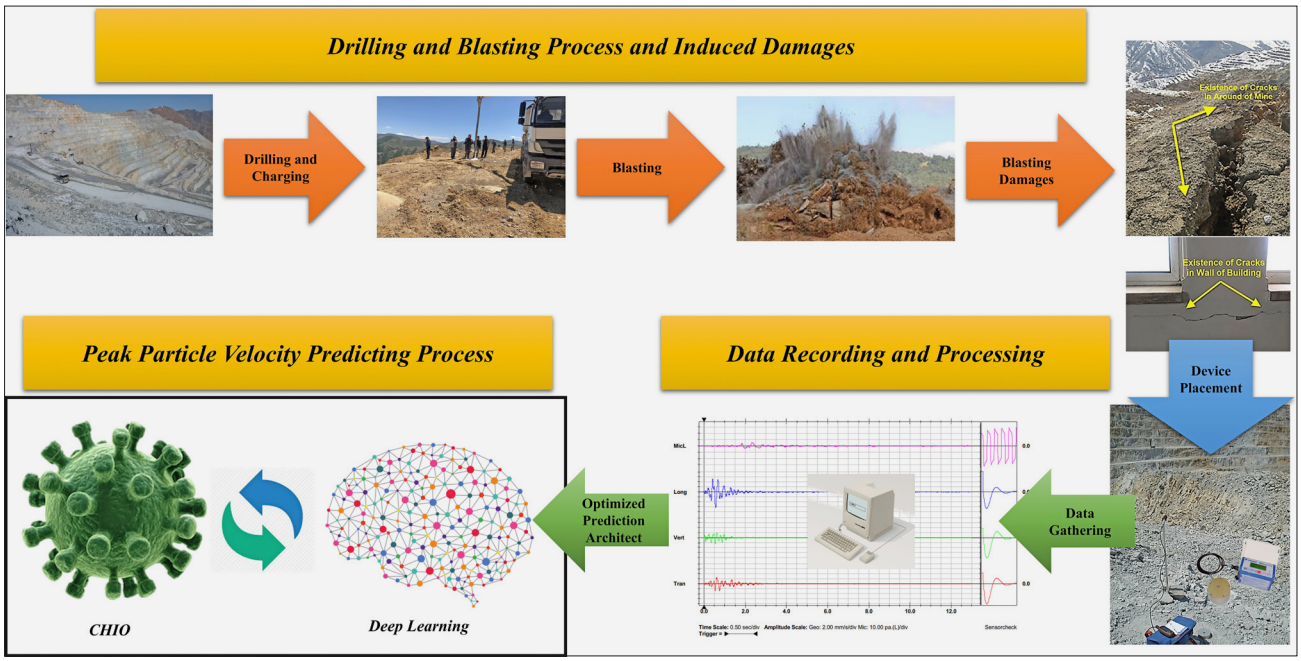


Figure 1. A schematic overview of the research stages

cessfully used an Artificial Neural Network (ANN) to predict profitability in Nigerian granite quarries, directly linking financial outcomes to blast design. By analyzing fragmentation data, it identified a 2m x 2m blast pattern as optimal and correlated higher blast efficiency with a better uniformity index. The research confirms the ANN model as a highly accurate profit forecasting tool, demonstrating the value of merging operational and financial data. **Taiwo et al. (2023)** in the other research, applied advanced ML models, including LSTM and SVR variants, to forecast flyrock in the Akoko Edo quarries. From their data, burden distance and charge amount were critical factors influencing projections. The LSTM model proved superior in accuracy, significantly outperforming other algorithms and providing a reliable tool for risk assessment. Further demonstrating the value of machine learning in mining, a study on the Dongri-Buzurg mine utilized a hybrid artificial neural network (ANN) to predict blast-induced Peak Particle Velocity (PPV). By integrating optimization techniques, the model improved prediction accuracy, which led to optimized blasting parameters and reported benefits in safety, environmental protection, and operational efficiency (**Bisoyi et al., 2025**). **Ebrahimabadi et al. (2025)** investigated the prediction of Roadheader performance, specifically the Instantaneous Cutting Rate (ICR), which is critical for optimizing excavation in tunneling and mining. To forecast ICR based on rock and machine parameters at the Tabas coal mine, they employed and evaluated three models: a Support Vector Machine (SVM), the Firefly Algorithm (FA), and the Bat Algorithm (BA). Their results demonstrated that all models performed satisfactorily, but the Bat Algorithm (BA) proved superior, achieving the highest coefficient of determination (R^2 = 0.9421) and the lowest error metrics, thereby offering the most precise and realistic predictions.

Considering the research conducted and the existing research gaps, in this present research work, an attempt was made to first create a suitable database including the distance and amount of explosives as input variables and the Peak particle velocity as an indicator of the amount of vibration as a dependent variable using a seismograph in two large-scale open-pit mines, Songun and Golgohar. Then, the deep learning method was used as a predictive tool. Given the number of hyperparameters in this method and the uncertainty of the random and trial-and-error selection, the predictive method was augmented by integrating a herd immunity-based optimization algorithm to obtain a reliable hybrid method. It is also worth noting that the adverse effect of vibrations on the lives of people working in mines or people living in areas near the mine shows the necessity of using such research. Accurate assessment of vibration intensity is critical for ensuring correct mining developing direction.

2. Methodology

The occurrence of blasting in open-pit mines for mineral extraction is essential and inevitable. With the occurrence of a blasting, vibrating waves move rapidly in all directions and, when they collide with buildings, transfer their kinetic energy to them, causing various damages to them. These damages are the source of many life and financial risks. These risks affect all buildings located in the range of motion of seismic waves. These buildings can include mining facilities or residential houses around mining areas. These vibrations, along with other negative effects caused by mining blasting,

are considered one of the most important negative consequences. Therefore, studying and investigating this phenomenon and then controlling and managing it is very important. Considering this issue, a path was drawn and implemented in this research work to provide this important information. The research path for this work includes recording and collecting the desired study data, analyzing and pre-processing the collected data, creating a predictive model, and optimizing the final model. **Figure 1** shows the overall research process taken to achieve the research goal in this study.

2.1. Developing Database

Considering the nature of the research subject as well as the implementation of the study on two open-pit mining sites, access to real data is inevitable. For this purpose, data on blasting in the two open-pit mines of Sungun Ahar and Golgohar Sirjan were monitored and recorded (see **Figure 2**). At this stage, by planning and replacing the Instantel Minimate Plus seismometer at important locations, various data related to the blasting and its seismic results were recorded and collected during the blasting operation. More than 1000 observations were recorded. This data included various information about the conditions of the blast holes and the distance from the blast site. Since the study aimed to investigate the relationship between the distance between the seismometer location and the center of gravity of the blasting and the amount of explosive used with the Peak particle velocity as an indicator of the magnitude of vibration, only this part of the data was used. **Figure 3** shows a sample of the content captured for blasting event number 27.

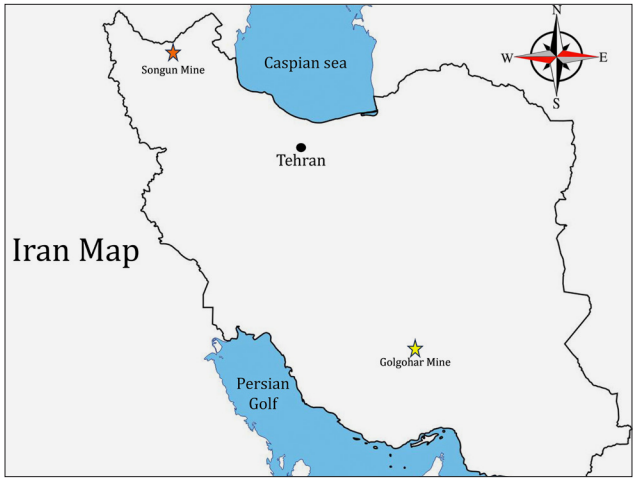
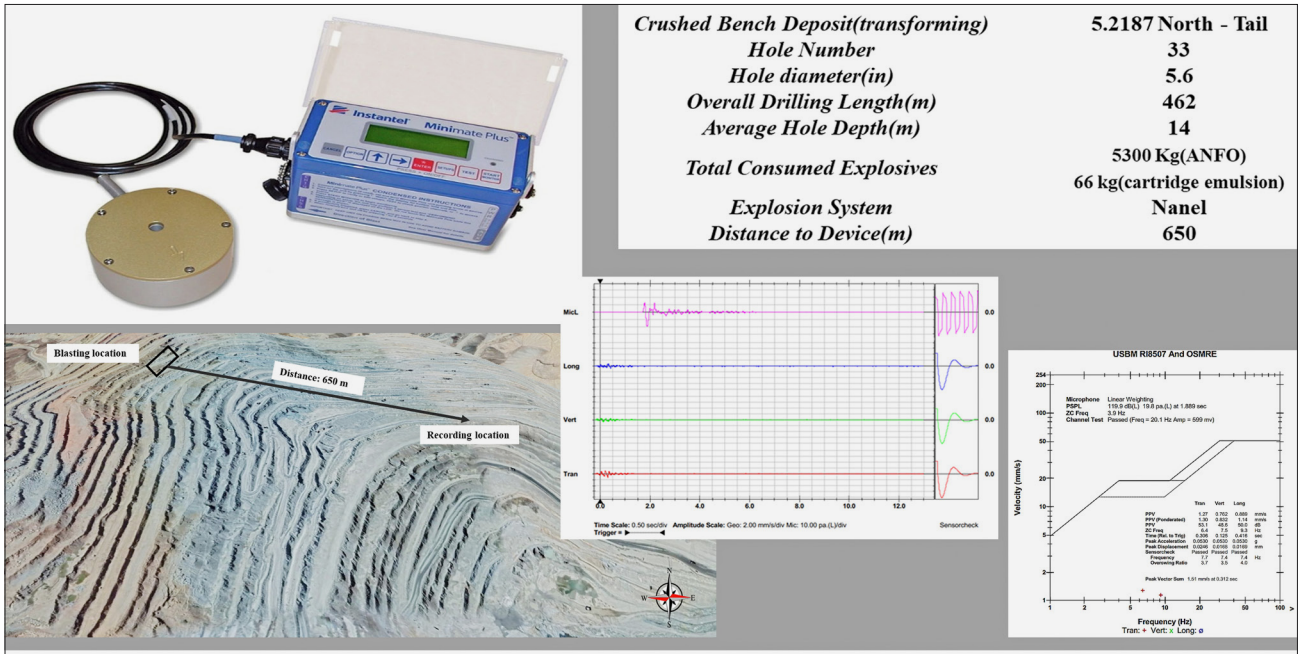


Figure 2. Location of the studied mines

2.2. Deep learning

Predictive modelling of diverse phenomena enables enhanced accuracy in operational planning. Artificial intelligence, which relies on its various tools, can provide acceptable predictions. Machine learning is one of the most important subsets of artificial intelligence-based methods offering a wide range of useful tools for prediction, including artificial neural networks. Among the subsets of neural network-based methods, deep learning techniques are considered to be one of the most efficient artificial intelligence tools. Deep learning refers to more complex and larger networks based on artificial neural networks. These networks differ from simple artificial neural networks in terms of characteristics. The frame-



Trigger	Tran Peak (mm/s)	Vert Peak (mm/s)	Long Peak (mm/s)	Mic Peak (dB)	PVS (mm/s)	Peak Acceleration(g)	Peak Displacement (mm)
Tran	1/27	0/762	0/889	119/9	1/51	0/0530	0/0246 Tran

Figure 3. An overview of the recorded data along with the location of blasting event number 27

work and architecture of these networks in deep learning give them high flexibility in dealing with complex problems and large volumes of data. Factors such as the type of network framework, the number of hidden layers, the number of neurons in each layer, activation functions, weight functions, optimization functions, and various other hyperparameters play an important role in defining and establishing a deep learning network.

The earth's condition, which involves facing a natural and self-made environment, does not allow any control and management over its key parameters. In conditions where there is no control over important environmental parameters, predicting behaviour is very difficult and complex. Therefore, facing and behaviour study of such environments for prediction requires the use of tools with high flexibility and power. On the other hand, as mentioned in the previous section regarding the nature of data, the number of data points collected is approximately 1000, which is a considerable number. Considering the above, the deep learning method was chosen to find the behavioural pattern between the input parameters, namely the distance from the blasting site and the amount of explosive, and the output parameter, namely the Peak particle velocity. Deep learning has various frameworks, among which the feedforward framework is the best option for working with tabular data. Other frameworks are used for working with time series data image data, etc. The architecture used for deep learning consists of an input layer containing two input parameters, followed by seven hidden layers, and finally, an output layer containing one output parameter. **Figure 4** shows the general scheme of the designed network architecture.

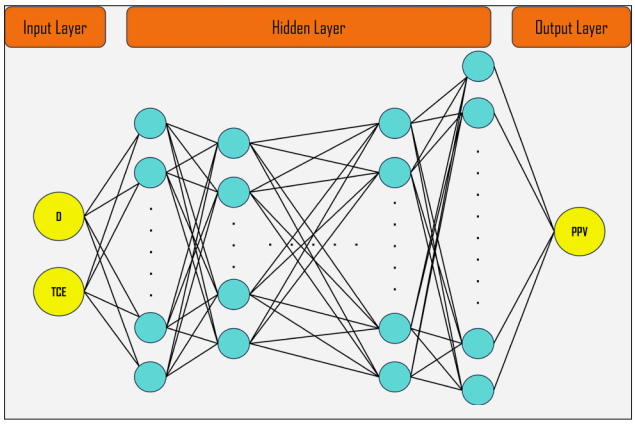


Figure 4. Overview of a deep learning network architecture

When applying deep learning methods, a portion of the data is designated as training data, while the remainder is reserved as test data. Typically, 70% of the data is allocated for training, and 30% is used for testing. This standard approach was adopted in this research.

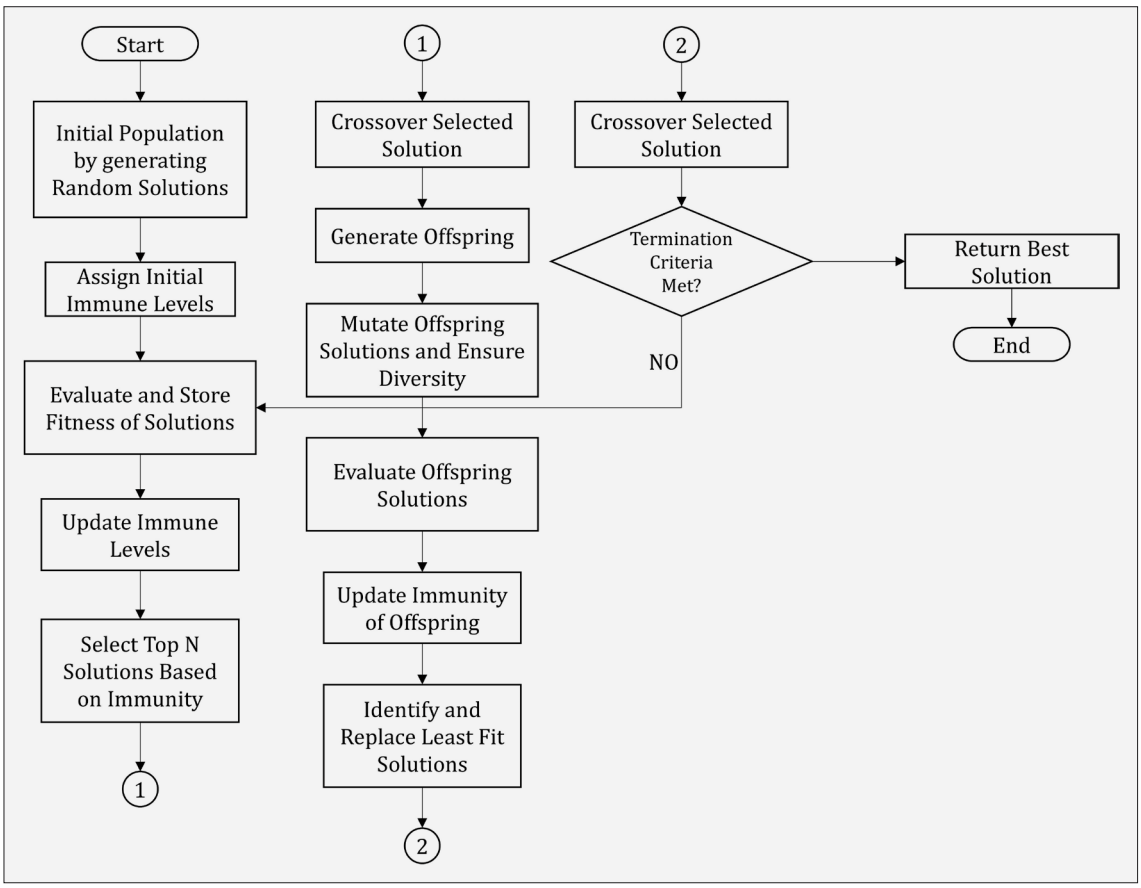


Figure 5. Flow chart of Corona Herd Immune Algorithm

2.3. Coronavirus Herd Immunity Optimizer (CHIO)

The coronavirus herd immunity optimizer, introduced by **Albetar et al. (2021)**, is a novel optimization algorithm based on human biological structure, classified under the subclass of nature-inspired optimization methods. This algorithm works on the coronavirus pandemic with the concept of herd immunity. The speed of the spread of the coronavirus infection depends on how directly infected individuals come into contact with other members of the community, which are modelled based on optimization concepts. The coronavirus herd immunity optimizer mimics the herd immunity strategy as well as social distancing concepts. This is a robust optimization algorithm that can solve optimization problems in a wide range of optimization domains. The different steps of the coronavirus herd immunity optimization process are given below. The flow chart of the coronavirus herd immunity optimizer algorithm is shown in **Figure 5**.

As can be seen from **Figure 5**, this algorithm, like other metaheuristic algorithms, creates a population of possible solutions by accepting the ranges of change of each input variable, and then by inserting them into the defined cost function, the best solution of that generation from the population is calculated and considered as the best solution up to that stage of the algorithm. Then, in the next stage, the second generation of the population of possible solutions is calculated based on the computational characteristics defined for this algorithm. After that, the cost function values are calculated again for each, and the best solution is selected and compared with the best solution of the entire process. In this way, the second iteration ends. The iterations of this algorithm continue until the defined stopping criterion is satisfied. For more information about this algorithm, refer to the source. For a more detailed explanation of optimization algorithm's calculation steps, different CHIO steps have been brought in following:

CHIO Algorithm Calculation Steps:

Initialization:

Initialize the population (individuals) with random solutions (HIS=15).

Define parameters:

Herd Immunity Rate (HIR=0.5)

Basic Reproduction Rate (BR=0.01)

Maximum Infected Cases Age (Max_age=3)

Fitness Evaluation

Evaluate fitness for each individual.

Virus Spread (Update Solutions)

For each individual, update its position based on infected cases:

If (rand ≤ BR), modify solution using:

$$X_i^{new} = X_i + r \cdot \left(X_i - X_j\right) \cdot I \quad (1)$$

Where:

X_i – current individual,

X_j – randomly selected infected neighbor,

r – random number,

I – binary infection indicator.

Herd Immunity (Crossover-like Update)

If (rand > BRR), update using herd immunity:

$$X_i^{new} = X_i + r \cdot (X_i - X_k) \cdot (1 - I) \quad (2)$$

Where X_k: a healthy (immune) individual.

Fitness Comparison & Replacement

Replace X_i with X_i^{new} only if the fitness is better.

Update Infection Rates

Adjust BR dynamically:

$$BR(t+1) = BR(t) \cdot \left(1 - \frac{t}{Max\_Iter}\right) \quad (3)$$

Termination

Repeat until Max_Iter (=1000) is reached or convergence is achieved.

The values enclosed in parentheses for each CHIO algorithm parameter and control parameter represent those utilized during the CHIO optimization process. These values were obtained through several trial-and-error attempts.

2.4. Date preprocessing

The first stage of the present research examines the data. To have acceptable results from predictive modelling, the quality of the input data is very crucial. The best models and algorithms cannot meet the lowest expectations when faced with poor-quality inputs. Therefore, monitoring and refining the data before importing them into the model is one of the most important steps in accessing a good model. This stage is called data pre-refining. The different stages of the preprocessing stage are presented in **Figure 6** below.

2.5. Optimization philosophy

Accessing the optimal value of the target variable has always been of interest in various engineering and non-engineering problems. The optimal value is a value that, for values other than that, the target function will provide more or less values. Consistent with the present study, the aim is to reach the most accurate tool for predicting the Peak particle velocity and, consequently, the target vibration level. The indicators that evaluate the accuracy and precision of the prediction methods in this study have been previously introduced. For example, considering the coefficient of determination index, the best performance of the prediction method occurs when this index has values close to one. In other words, one is the best value for the coefficient of determination. Therefore, the performance quality of the prediction method is the closeness of the coefficient of determination to the value of one. However, the target method in this study is a deep learning network. This method has various hyper-

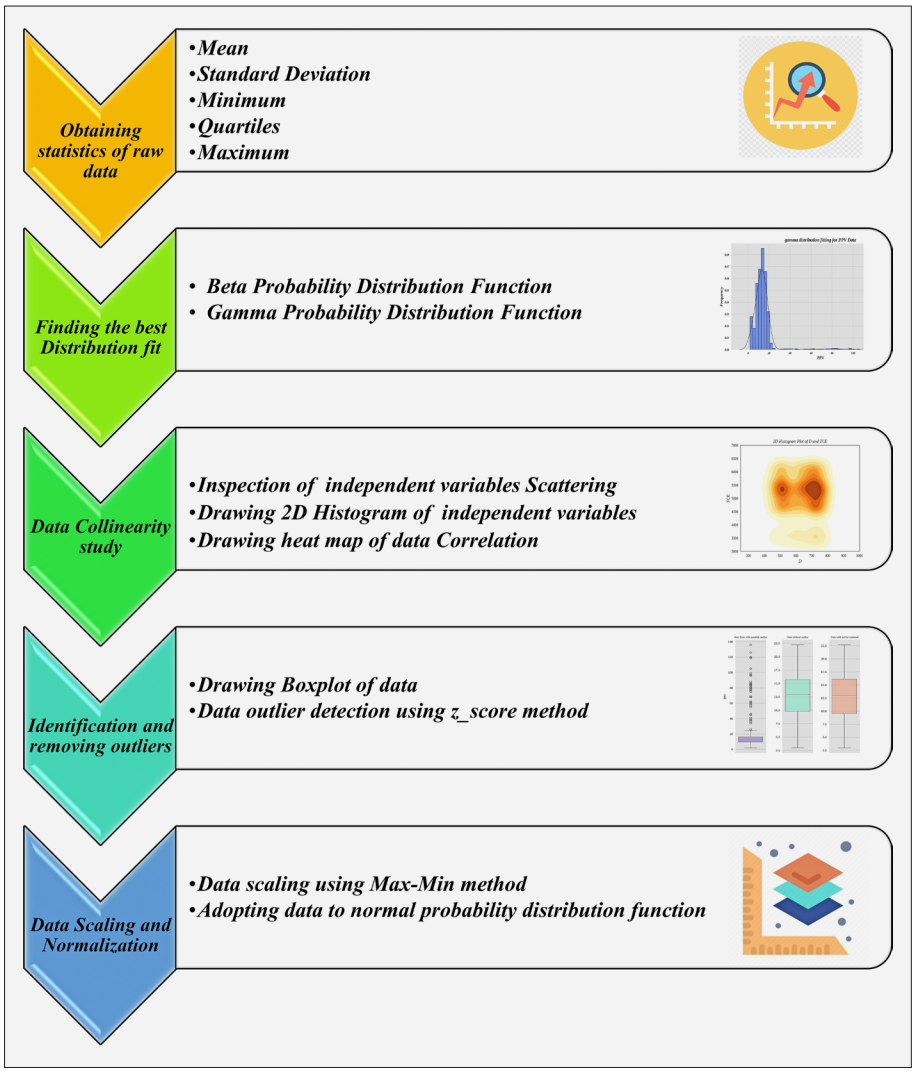


Figure 6. Various stages of data preprocessing to prepare it for entry into a deep learning model

parameters that affect its performance. The most important hyperparameters of this method include the number of hidden layers, the number of neurons in each layer, the types of functions involved in the layers, etc. The number of hyperparameters of a deep learning network is high. The values assigned to each of these hyperparameters have a direct impact on the performance quality of the deep learning network. **Figure 7** shows the effect of the number of neurons in the first hidden layer and the learning rate on the performance quality of the deep learning network by monitoring two indices: root mean square error and absolute percentage of average error. It is clear from all four figures that by changing the values of the two hyperparameters mentioned above, the change in the performance quality of the deep learning model is evident, indicating the high impact of the model behaviour on the values of the hyperparameters. Therefore, the selection of hyperparameter values is of considerable importance in discovering the optimal deep-learning network.

In the selection step of values for these hyperparameters, a random trial and error procedure can be used. This procedure provides the most accessible solution. Due to the lack of complete monitoring of the possible values, the space of each hyperparameter presents considerable uncertainty regarding the best performance of the deep learning network. On the other hand, due to the large number of hyperparameters, manual adjustment is very time-consuming. In another procedure, the best values are selected for the hyperparameters using optimization processes. In this method, by integrating prediction and optimization methods, a new hybrid method is created that provides the best results, considering the limitations of the optimization process.

2.6. Optimization process

As mentioned in the previous section on the necessity of the optimization process, the number of hyperparameters of a deep learning network is significant. Therefore, in this research work, the hyperparameters of the number of neurons in the hidden layers, the activation, the regulator and bias functions, and the learning rate were selected as the target hyperparameters for optimization. To create an optimized deep learning hybrid net-

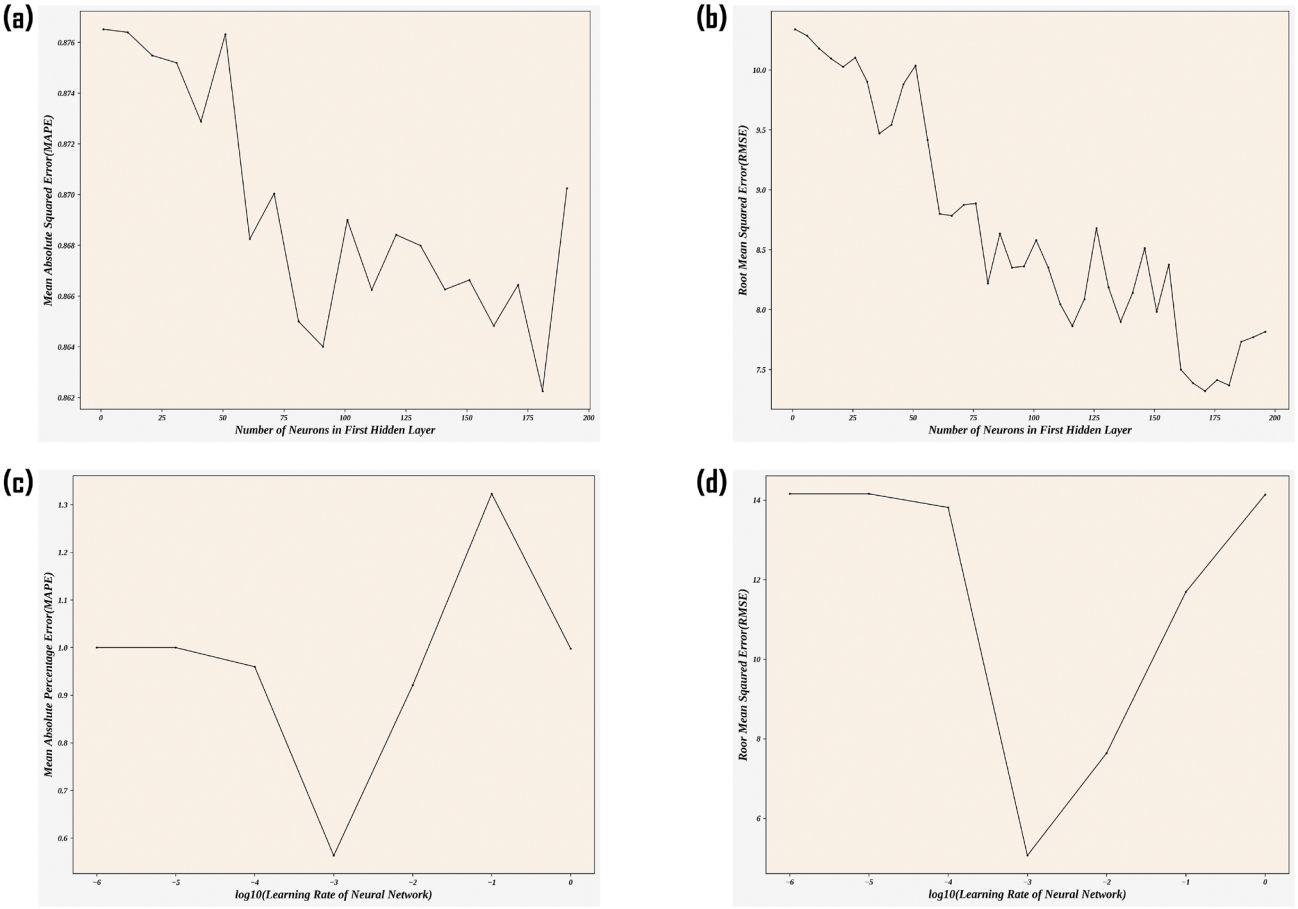


Figure 7. The effect of hyperparameters variation on deep learning network performance

work, the optimization process must be located and coordinated within the predictive process. The location, connection, and integration of the optimizer method into the predictive method are of great importance. To streamline exposition and facilitate comprehension of the optimization algorithm's integration with the deep learning architecture, a schematic representation of the workflow was presented. **Figure 8**, shows the view process of the optimized deep-learning hybrid network.

3. Results and discussion

3.1. Convergence curve

The computational structure of metaheuristic algorithms is based on searching the space of possible solutions. These algorithms randomly select a set of solutions at each stage and obtain the value of the objective function for each of them, considering the best solution available at each stage as the temporary solution to the problem at that stage. This process is repeated in subsequent stages. These iterations create a set of the best solutions. The geometric location of these solutions, in terms of the number of iterations, forms a graph that shows the state of changes in the best solutions obtained during the different stages of the algorithm. This graph is known as the convergence curve to the optimal solution or, in short, the convergence graph. The convergence graph shows the progress of the computational stages of the algorithm and the improvement of the objective function values while searching for the solution. In general, the convergence graph displays the overall behaviour of the optimization algorithm, whether the algorithm converges toward the final solution or diverges, and if it converges, the graph shows how this convergence occurs. The shape of convergence graphs can be gradual or stepwise, depending on the type of optimization process. In the stepwise type, the optimal solution value remains constant for successive iterations, and the algorithm cannot discover new optimal values in each iteration and stage, which is directly related to the computational structure of the optimization process and the type of optimization problem. The stepwise or gradual shape of the convergence graph cannot be the sole basis for judging the performance of the optimization algorithm. One of the important features of this graph is its decreasing slope. The higher the decreasing slope of the graph, the faster the algorithm discovers optimal solutions and its intelligent performance in searching for better solution space. Another important feature of this

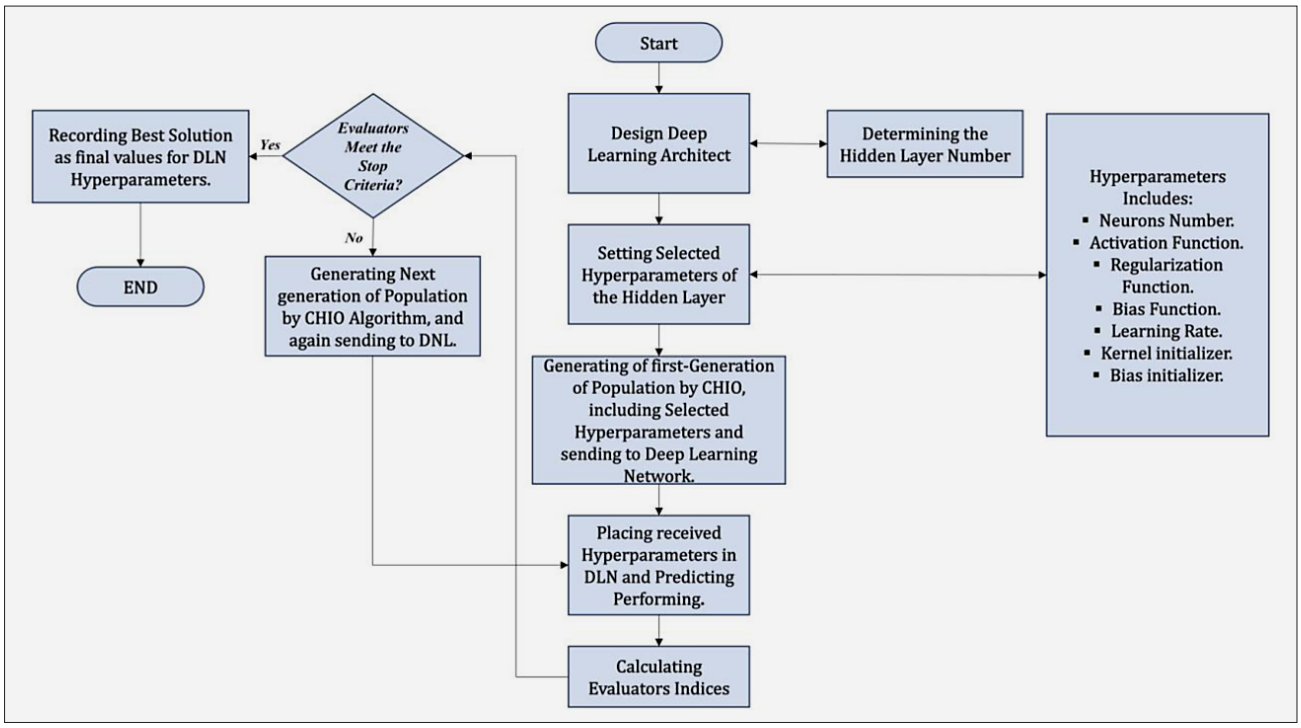


Figure 8. Process Overview of the steps taken to create an optimal deep learning network

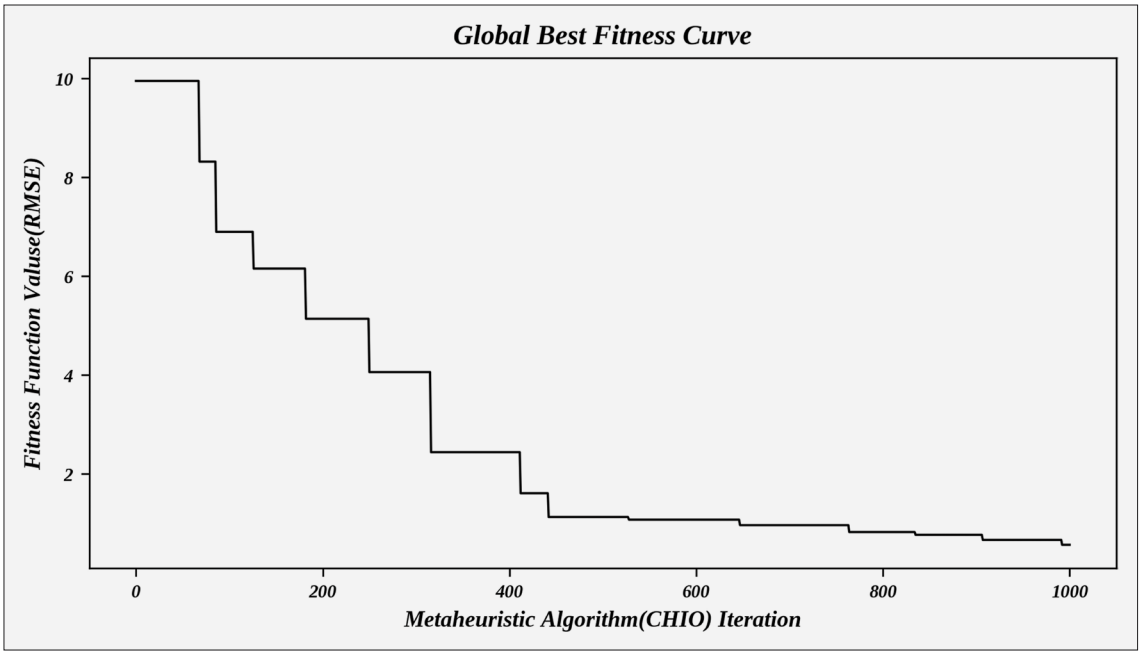


Figure 9. Convergence graph of the optimization algorithm with its iterations

graph is the final horizontal section of the graph, which indicates the stopping of the process of discovering a new optimal solution, and the iterations performed in that interval are useless calculations; to reduce the calculation time and avoid unnecessary use of the computer's computational capacity, those iterations can be ignored in the next stages. Of course, it must be ensured that the horizontal section must form the last part of the graph. The presence of oscillations in the convergence graph is generally not a good sign. These oscillations can indicate the algorithm's confusion in choosing an appropriate partition of the solution space to search for the optimal solution, which is considered a weakness of the optimization algorithm. In this case, the probability of the algorithm getting stuck in local extrema increases.

One of the important uses of this graph is to compare the performance of different optimization algorithms with each other. By considering this graph, various algo-

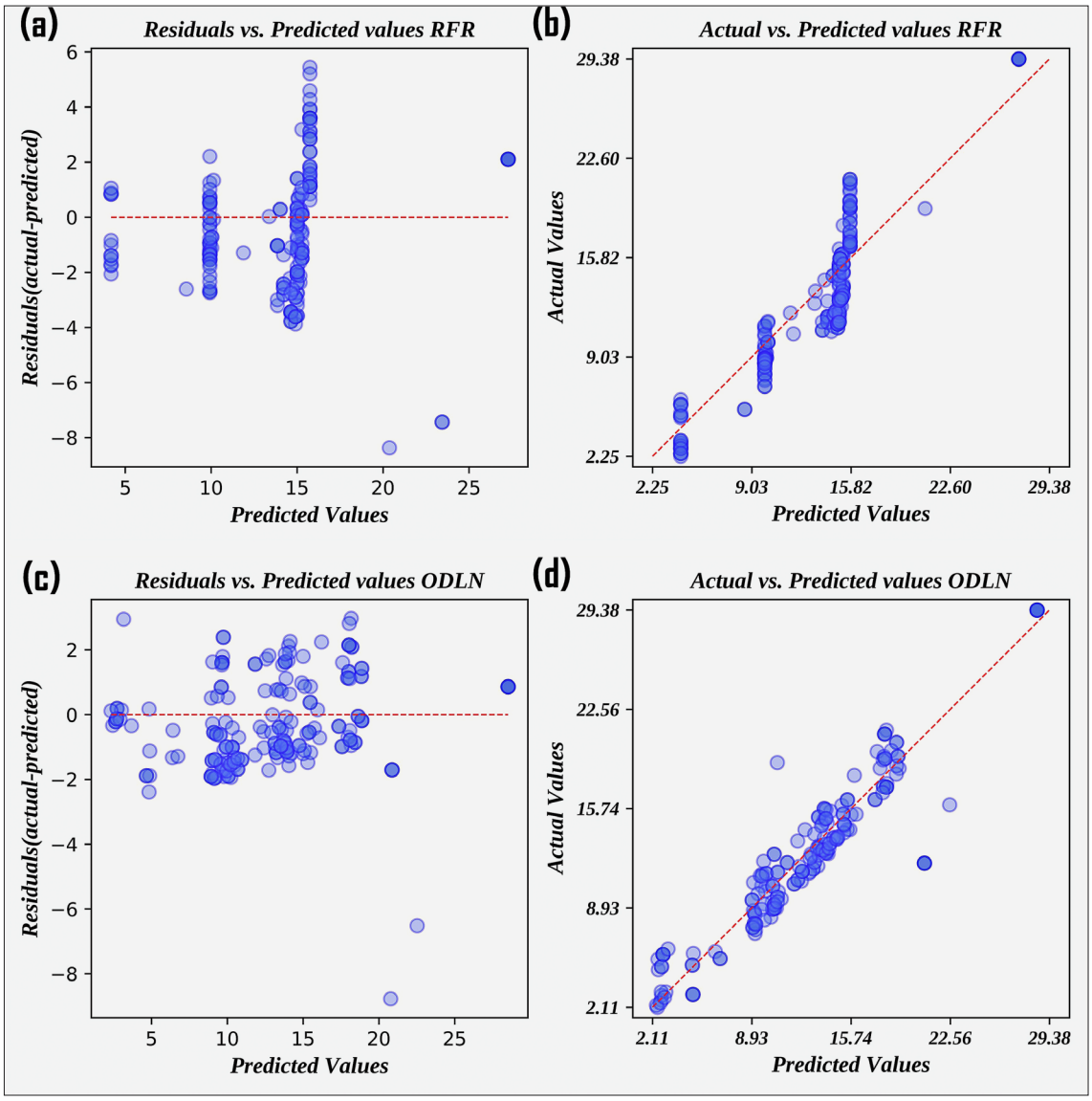


Figure 10. Correlation status of actual and predicted values (a. Random Forest, b. Optimized Deep Learning) and error value of each observation (a. Random Forest, b. Optimized Deep Learning)

rithms can be compared in terms of convergence and divergence to the optimal solution, as well as the convergence speed and shape of convergence. Furthermore, the convergence graph of the optimization algorithm can be used to adjust the hyperparameters and reach the optimal solution. This graph can also help identify problems in the optimization process and its slowness. Considering the above, drawing the convergence graph of the optimization process is very important. For this reason, the convergence pattern of the coronavirus herd immunity optimization process, which is used to optimize the deep learning network for predicting the Peak particle velocity, is plotted and given in **Figure 9**.

According to **Figure 9**, the optimization process converges to a specific solution. This indicates the correct performance of the optimized deep-learning network. The shape of the convergence graph is a step-down, indicating that the optimal solution is not reached at each step of the optimized deep learning hybrid network calculations. The size of the convergence graph platforms indicates that the speed of movement towards the optimal solution is high in the initial iterations and decreases as time passes and approaches the optimal solution, which is a normal behaviour of an optimization process. This also indicates that the number of iterations of the optimization process is sufficient. No fluctuations are observed in the pattern, which is due to the correct orientation of the optimization process in the problem solution space.

3.2. Correlation of Actual and Predicted Data

The evaluation of performance quality of behavioural models adapted to data can be evaluated from various aspects. One of the most common methods for testing the efficiency of models is the use of numerical criteria.

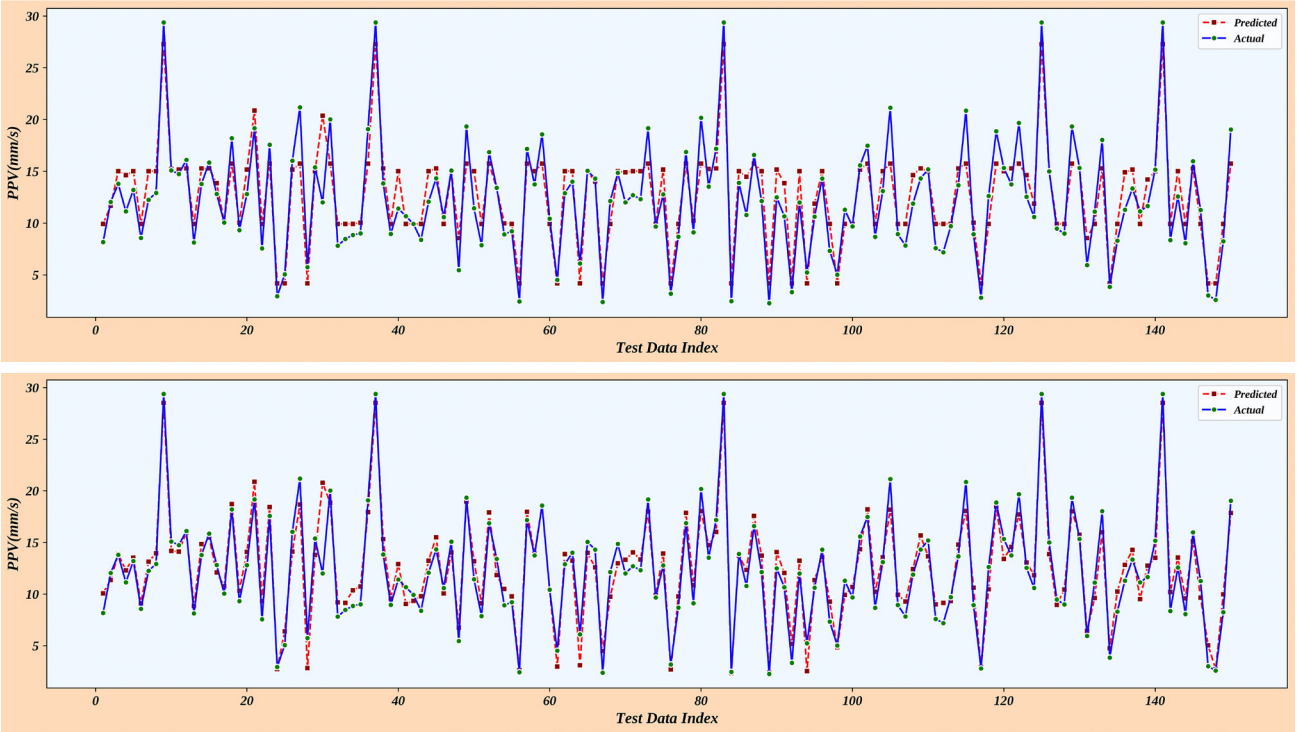


Figure 11. Compare actual and predicted values correspondingly

These criteria, according to their computational structure, evaluate and report the efficiency of a predictive model from various aspects. In addition to the weaknesses of these numerical parameters, which were mentioned in the previous section, only relying on this form of indicators can be misleading. To prevent partial judgment of the model's performance and ensure access to its real performance, in addition to using numerical criteria, graphical and diagrammatic observation of the model's performance can be beneficial. Accordingly, in this part of the present study, the efficiency of models has also been examined graphically. The residual error of each prediction is one of the most important indicators indicating the efficiency of each model, and it is not possible to make a correct and complete judgment of the quality of the model by studying its values or even its average. One of the most important graphical tools for examining the model performance is displaying the residual errors of each prediction. For this display, the data index is displayed on the horizontal axis and the residual errors of each prediction are displayed on the vertical axis. The residual error is the distance between the predicted value and the actual value. In this graph, if the model has acceptable performance, the data dispersion will have two characteristics. The residual error values of each prediction for a model with acceptable performance will have a high density around the horizontal axis, which represents zero error. However, in such models, the dispersion of the residual errors around the horizontal axis is symmetrical and their dispersion does not follow a specific pattern. Such a graphical display can show the overall performance of the model at once and help make a correct judgment. In addition to this graph, a correlation graph of the actual data and the predicted data is also presented. These two graphs together depict the model's performance. In this research work, the two aforementioned graphs have been depicted to complete the judgment process. **Figure 10** shows the prediction accuracy graphs for the stochastic gradient descent, support vector machine, adaptive reinforcement, and deep learning network models. Looking carefully at **Figure 10**, it is clear that the data density around the zero-error line for the deep learning-based model is better than other models. Also, the data symmetry around the zero-error line is more acceptable for the deep learning-based model than other models. Considering the correlation graph of the actual data and the predicted data, it also seems that the performance of the deep learning-based model is better than other models. Using the graph method helps to study the model's performance instantly and simultaneously.

Figure 11, is a line graph that graphs two datasets labeled "Predicted" and "Actual" over a test data index range from 0 to 140, with the two graphs repeated twice, likely to attract attention or for reproducibility purposes. The x-coordinate is the test data index, and the y-coordinate plots some unknown quantitative quantity between 0 and 30. The "Predicted" line is a line of constant value 25, which is an ideal or target value that is constant for all test indices. In contrast, the "Actual" line starts at 0 for the initial test index and rises slowly over time but never reaches the "Preferred" value, plateauing at 20-22—3-5

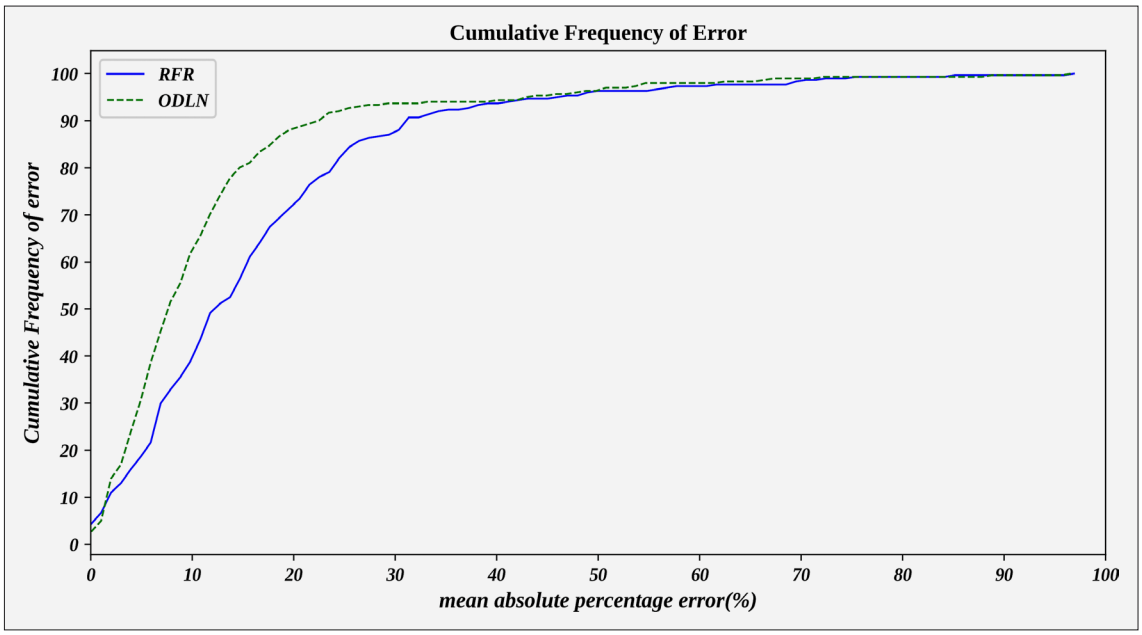


Figure 12. Cumulative frequency chart of model errors

units short of the target each time. This recurring shortage is an indicator of system underperformance, with the deficiency largest on first test indices and decreasing slowly but still considerable even on subsequent indices. The flattening of the "Actual" line is indicative of a saturation effect where decreasing returns or internal constraints make further convergence with the "Preferred" value unrealistic. The reasons may be errors in calibration (e.g. a predictive model underestimating the outcomes consistently), external constraints (e.g. lack of resources), or measurement noise. Recommendations are to verify the root cause of the plateau (e.g. model bias, feature omissions, or training issues), rescale systems as needed, and find out if the gap is tolerable or needs to be optimized further. The absence of axis markers and contextual details (e.g. domain knowledge) limits more detailed interpretation but suggests an obvious need for corrective action based on the visual trend to align "Actual" results with "Preferred" objectives. Additional context could refine the analysis further.

Examining the statistical status of errors resulting from prediction by a behavioural model can help provide confidence in the model's performance from various aspects. One of the important aspects of error in the discussion of behavioural data models is paying attention to the overall frequency of errors occurring in the prediction process. According to the definition of frequency, it refers to the number of data repetitions in defined intervals. Determining the frequency of errors in different intervals and identifying intervals with high frequency is a good reflection of the more accurate performance of the model. In this regard, using the relative cumulative frequency chart of the error population can be very helpful. About this type of criterion, it can be said that for models that perform better, the relative cumulative frequency of errors is in intervals containing the lowest errors. The graphical manifestation of this phenomenon is the stretching of the relative cumulative frequency chart towards values close to one in intervals of error values close to zero. In other words, the more the model's chart in the low error ranges moves above the charts of other models, the better the model's performance. In this research work, to complete the process of evaluating predictive models, the relative cumulative frequency of errors has been plotted against the mean absolute error. **Figure 12** shows the state of the relative cumulative frequency curve of errors based on the mean absolute error. As is clear from **Figure 12**, the curve of the deep learning-based model in the lower error ranges has presented a higher relative cumulative frequency and has moved to the upper part of the graph, indicating its better performance than the other selected models. This criterion also confirms the more stable and accurate performance of the deep learning-based model compared to other models.

3.3. Numerical results

The use of graphical methods, along with their strengths, also have weaknesses. The main weakness of graphical methods is the non-quantitative comparison of outputs. The only way to compare graphs, since they are based on visual indicators, is highly influenced by personal taste and judgment. The quality of using graphical indicators depends on the experience and knowledge of the person using them. This makes it difficult to use these types of graphs for judgment. To overcome this weakness, using a graphical criterion and matching it with a numerical index can be very useful. For this purpose, displaying actual and predicted data simultane-

ously is a common tool. To achieve such a graph, actual and predicted data are plotted based on a data index, indicating the degree of data matching. If the model performs well, the two lines passing through the actual and predicted data will be very close to each other and the distance between them will be small. However, in the event of large errors, the degree of separation between the two graphs will increase. This same criterion can be used to quantitatively compare the performances of models. For this purpose, after drawing lines passing through the actual data and the predicted data, the size of the area between the two lines was used as a quantitative indicator to compare the performance of the models and compare the graphs. Accordingly, the lines passing through the actual data and the predicted data for the different selected models are shown in **Figure 11**. In **Figure 11**, it is clear that the deep learning network-based model performs better and the separation between lines appears to be less than other models. However, for a more accurate judgment, the area between the two lines has been calculated. Based on the calculated values, it is also clear that the separation between the lines for the model based on the deep learning is equal to 30.459, which is the best condition compared to other models. This indicates a high agreement between the actual output data and the predicted data, which is a reliable criterion for measuring and selecting the best model.

3.4. The mean absolute percentage error

The mean absolute percentage error is one of the most common statistical measures for studying the behaviour of predictive models. The computational nature of this measure comes with certain characteristics that, while reflecting the degree of deviation of predicted values from actual values, sometimes should be interpreted with caution. This indicator can be easily calculated which is one of its strengths. Equation 4 shows its computational formula.

$$MAPE = \frac{1}{n}\sum_{i=1}^{n}\left|\frac{y_i - \hat{y}_i}{y_i}\right| \quad (4)$$

Where:

y_i – measured values (mm/s),

$\hat{y}_i$ – predicted values (mm/s),

n – amount of data.

The mean absolute percentage error is a measure of the model's accuracy. Since this measure is reported in percentage terms, it is easier to interpret and present than other indicators. Despite the strengths stated, this indicator has its unique weaknesses that must be considered while interpreting the results. The mean absolute percentage error, due to its computational structure, loses its computational power when faced with real zero values since division by zero has no mathematical meaning. This indicator sometimes evaluates models of poor quality that lack sufficient accuracy and precision as good models by calculating their low values. One of the main limitations of this indicator is that as the actual and predicted values approach zero, despite the closeness of the actual and predicted values, the error-index value moves towards high values. This measure is sensitive to the scale in which the data is located. Therefore, using this index for non-scalar data can lead to errors in evaluating the actual performance of the predictive model. Accordingly, using this index to compare the performance of a model when faced with different data is not logical. Therefore, it is always recommended to use other indices, along with this criterion, for a comprehensive evaluation of the predictive model.

In this research, the average absolute error percentage was calculated to evaluate the efficiency of the deep learning-based model. **Figure 13a** shows the average absolute error percentage values obtained for the deep learning model and the support vector machine, adaptive boosting, and stochastic gradient descent models. Considering the average absolute error percentage value, 0.068, it is clear that the deep learning-based model has provided the lowest average absolute error percentage. In the meantime, the support vector machine-based model has provided better performance by a minimal distance. According to the results obtained for these models, and considering the processed nature of the data, the deep learning model has shown acceptable performance in predicting the amount of vibration generated based on the distance and amount of explosives used.

3.5. Coefficient of determination

A high correlation between measured values and predicted values by models is an indication of their acceptable performance. To study the amount of both behaviour and correlation between predicted and actual data, there is an index called the coefficient of determination (R^2). The coefficient of determination; in its basic definition, is a measure of the quality of the data fit to a behavioural model. However, in the behavioural prediction workspace, it indicates how close the actual values and predicted values are, or more precisely, the degree of their correlation. To calculate the value of the coefficient of determination, we can use **Equation 5**.

$$R^2 = 1 - \frac{\sum_{i=1}^{n}(y_i - \hat{y}_i)}{\sum_{i=1}^{n}(y_i - \bar{y})} \quad (5)$$

Where:

$\bar{y}$ – mean of the actual data values (mm/s).

The rest of the parameters have been previously introduced. The coefficient of determination indicates to what extent the observed values match the predicted behavioural model. In general, the values of the coefficient of determination range from 1 to negative infinity. Values close to one usually indicate acceptable performance of the behavioural model, and values close to zero and even negative values indicate unacceptable performance of

the model in predicting the behaviour of the data. This index, like other criteria for measuring the efficiency of predictive behavioural models, has its weaknesses and limitations. Factors such as data scale, data nature, and data preprocessing methods are among the factors affecting the behaviour of the coefficient of determination index. Accordingly, in some cases, high values of this index can be due to errors in the model. The presence of outliers indicates the unreliability of the coefficient of determination. Because the coefficient of determination is very sensitive to the presence of outliers. The co-linearity phenomenon between sharp input data can cause the coefficient of determination to be high, and as a result, cover the real weakness of the model. It should also be noted that the coefficient of determination does not provide any interpretation for the cause of the model behaviour and the roots and origins of errors. Therefore, the quality of the predictive model can be examined by this index and others. Given the importance of this index and its limitations, the coefficient of determination for the selected predictive models has been calculated and its values are presented in **Figure 13b**. In **Figure 10b**, it is clear that the behavioural model based on deep learning, with a coefficient of determination of 0.972, has performed best. Considering the data scaling and the removal of outliers and the examination of the absence of the co-linearity phenomenon, it can be stated that the coefficient of determination value is a reliable expression and reflection of the model performance.

3.6. Root mean squared error

The scatter of measured data around the predicted behavioural model is also important in studying the quality of a predictive behavioural model. The root mean square error index is a measure of the behaviour of the model. The root mean square error index is an index that reflects the standard deviation of the residuals of the actual values from the predicted values. This measure is a parameter that is not standardized in terms of the scale of errors that occurred in the prediction process, however, the coefficient of determination is a standardized index. The values of the root mean square error index start from zero and move towards positive infinite values. Naturally, considering the type of index, values close to zero are considered desirable values. To calculate the value of the root mean square error-index, **Equation 6** can be used.

$$RMSE = \sqrt{\sum_{i=1}^{n} \frac{(y_i - \hat{y}_i)^2}{n}} \quad (6)$$

In addition to providing conditions for the alignment of actual and predicted data, the root mean square error-index, by emphasizing and magnifying large model errors, helps identify areas of the data where the model does not behave acceptably. Due to this feature, this index takes a more conservative approach compared to other indices and is considered more reliable. The root mean square error considers more weight for larger errors. This index separates the root mean square error from the mean absolute error and makes it more sensitive to outliers. The root mean square error index results from squaring the distance between the actual values and the predicted values. Of course, it should be noted that the root mean square error is also non-equilibrium and the data has a negative effect. The root mean square error was used to evaluate the performance of the model. Accordingly, **Figure 13a** shows different values of the root mean square error for the selected predictive models. Considering **Figure 13a**, the optimized deep learning-based model has provided more acceptable performance than the other models. The root mean square error value for the deep learning-based model is 0.836, which is an indicator of the smaller computational errors of the behavioural model.

3.7. Model Bias and variance

Bias and variance of predictive models are among the most important evaluation indicators, indicating the degree of generalizability. Bias is an indicator that shows the model's accuracy in tracking the general behaviour of the data. A low bias value indicates that the model has successfully determined the general trend of the data by overcoming data noise. On the other hand, if the model fails to track the general trend of the data, data noise is high and the model is unable to overcome it, thus, the model has a high level of variance. The interaction of these two parameters and reaching the equilibrium point of variance and bias is important for having a good predictive model. As the bias increases, the model's performance in predicting values for both training and test data will be poor. As the complexity of the model and its fit to the data increase, the bias will move towards lower values. The model performance variance is examined in the model training process, indicating the data fluctuation. A high variance indicates overfitting of the model in the training phase and the dominance of outlier data over the model behaviour. It shows that the model performs very well in the training phase but very poorly on tests and new data.

Given the nature of these two model parameters, it will provide reliable and generalizable results providing the minimum possible value for the two bias and variance indices. It is worth noting that with increasing model complexity, the model bias decreases, but, causes prefitting of the model, thus, the model variance will increase, which is undesirable for the model. Therefore, reaching an equilibrium point where both the bias and variance of the model have the lowest possible values is very important.

Considering the above explanations in this research work, to achieve a better judgment regarding the perfor-

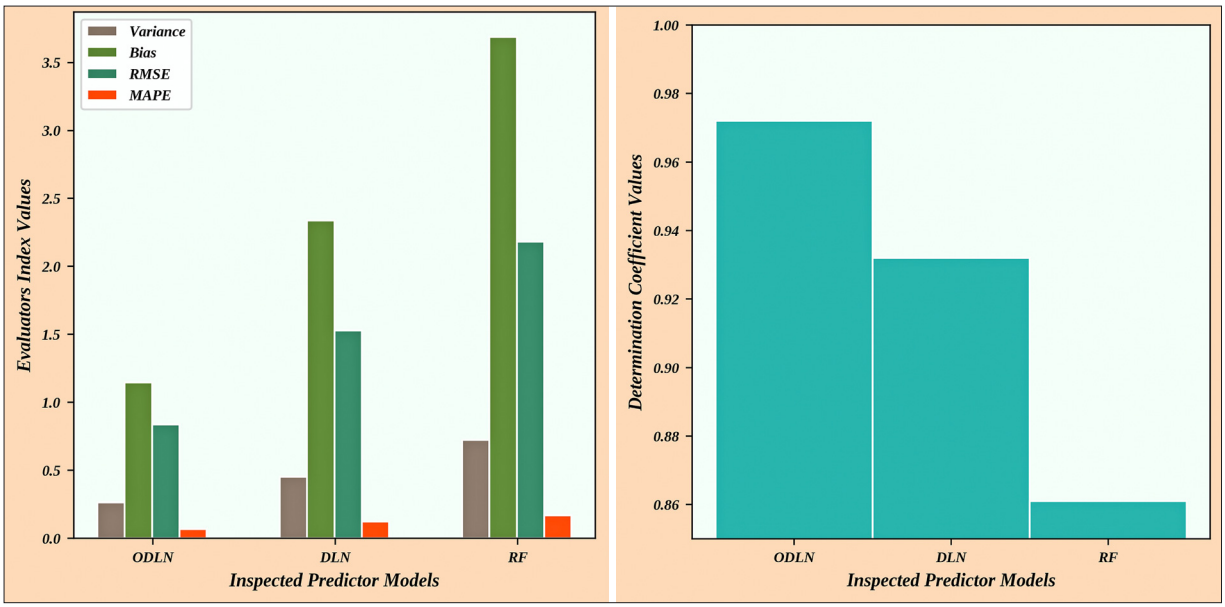


Figure 13. Values of various model evaluation indicators

mance of the models, the bias and variance of the models were also calculated. **Figure 13a** shows the values obtained for the three models. The model based on the optimal deep learning network presented the lowest point of balance of bias and variance, which is another proof of its better and more stable performance.

4. Conclusions

This study developed and validated a new hybrid model to predict blast-induced peak particle velocity (PPV) by combining a deep learning (DL) network with the Coronavirus Herd Immunity Optimizer (CHIO), a metaheuristic algorithm. The key innovation is using CHIO to automatically tune the DL model's hyperparameters—such as the number of hidden layers, neuron layout, activation functions, and learning rate—replacing slow, manual trial-and-error tuning. This automated search produced a more reliable model with better generalization. We tested the model on a strong dataset of more than 1,000 blast records from the Songun Ahar and Golgohar Sirjan mines. The hybrid approach outperformed standard methods, achieving an R^2 of 0.972, RMSE of 1.146, and MAPE of 0.068—at least a 4% improvement in accuracy compared with benchmarks like Random Forest and a non-optimized DL network. Practically, this tool can help mine engineers predict vibration levels more accurately, design safer blast patterns, and reduce environmental impacts while meeting strict safety standards. Methodologically, the work offers a useful blueprint for tackling other complex, nonlinear geomechanical problems where classic empirical formulas don't suffice. We also outlined paths for future research. The current model mainly uses distance and explosive charge as inputs; adding geomechanical variables (for example, rock mass rating and joint properties) and blast-design parameters (such as delay timing and stemming) should improve performance. The model should also be validated across different geological settings and mining methods to confirm its scalability and robustness. Overall, this research lays the groundwork for next-generation AI decision-support systems in mining and points toward integrating these models with real-time sensors and IoT platforms for smarter, dynamic excavation management.

5. References

Al-Bakri, A. Y., & Sazid, M. (2021). Application of artificial neural networks (ANNs) for prediction and optimization of blast-induced impacts. Mining, 1(3), 315–334. https://doi.org/10.3390/mining1030020

Armaghani, D. J., Hajihassani, M., Mohamad, E. T., Marto, A., & Noorani, S. A. (2014). Blasting-induced flyrock and ground vibration prediction through an expert artificial neural network based on particle swarm optimization. Arabian Journal of Geosciences, 7, 5383–5396. https://doi.org/10.1007/s12517-013-1174-0

Asl, P. F., Monjezi, M., Hamidi, J. K., & Armaghani, D. J. (2018). Optimization of flyrock and rock fragmentation in the Tajareh limestone mine using the firefly algorithm. Engineering with Computers, 34(2), 241–251. https://doi.org/10.1007/s00366-017-0535-9

Azimi, Y., Khoshrou, S. H., & Osanloo, M. (2019). Prediction of blast-induced ground vibration using a hybrid GA–ANN model. Measurement, 147, 106874. https://doi.org/10.1016/j.measurement.2019.106874

Bisoyi, N., Rath, R., Gupta, S., Rai, R., & Chatterjee, S. (2025). Predicting blast-induced peak particle velocity using a hybrid artificial neural network and its application in optimizing blasting parameters at Dongri-Buzurg mine.

Natural Resources Research. https://doi.org/10.1007/s11053-025-10447-y

Bui, X. N., Choi, Y., Atrushkevich, V., Nguyen, H., Tran, Q. H., Long, N. Q., & Hoang, H. T. (2019). Prediction of blast-induced ground vibration intensity using UAV and intelligent systems. Natural Resources Research, 29(2), 771–790. https://doi.org/10.1007/s11053-019-09573-7

Dindarloo, S. R. (2015). Prediction of blast-induced ground vibrations via genetic programming. International Journal of Mining Science and Technology, 25(6), 1011–1015. https://doi.org/10.1016/j.ijmst.2015.09.020

Ebrahimabadi, A., & Afradi, A. (2025). Performance prediction of Roadheaders using Support Vector Machine (SVM), Firefly Algorithm (FA) and Bat Algorithm (BA). Rudarsko-geološko-naftni zbornik, 40(3), 67–82. https://doi.org/10.17794/rgn.2025.3.6

Fang, Q., Nguyen, H., Bui, X. N., & Nguyen-Thoi, T. (2019). Prediction of blast-induced ground vibration using ICA and M5Rules. Natural Resources Research, 29(2), 791–806. https://doi.org/10.1007/s11053-019-09577-3

Ghasemi, E. (2016). Particle swarm optimization for forecasting backbreak induced by bench blasting. Neural Computing and Applications, 28, 1855–1862. https://doi.org/10.1007/s00521-016-2182-2

Khosravimanesh, S., Esmaeilzadeh, A., Akhyani, M., Mikaeil, R., & Asl, M. M. (2024). Accurate prediction of drill bit penetration rate in rock using supervised machine learning techniques base on laboratory test data. Rudarsko-geološko-naftni zbornik, 39(1), 115-130. https://doi.org/10.17794/rgn.2024.1.10

Hanifehnia, J., Esmaeilzadeh, A., Mikaeil, R., & Atalou, S. (2024). Prediction of blast-induced flyrock by using neural-imperialist competitive method (Case Study: Sungun Copper Mine). Rudarsko-geološko-naftni zbornik, 39(5), 109-120. https://doi.org/10.17794/rgn.2024.5.8

Hasanipanah, M., Faradonbeh, R. S., Amnieh, H. B., Armaghani, D. J., & Monjezi, M. (2017). Forecasting blast-induced ground vibration with CART. Engineering with Computers, 33(2), 307–316. https://doi.org/10.1007/s00366-016-0475-9

Nguyen, H., & Bui, X.-N. (2019a). Predicting air overpressure using ANN and random forest. Natural Resources Research, 28(3), 893–907. https://doi.org/10.1007/s11053-018-9424-1

Nguyen, H., Bui, X.-N., Nguyen-Thoi, T., Ragam, P., & Moayedi, H. (2019b). Flyrock prediction in open-pit mines using EANN. Applied Sciences, 9(21), 4554. https://doi.org/10.3390/app9214554

Nguyen, H., Bui, X. N., Bui, H. B., Cuong, D. T., et al. (2020). ANN-based model for predicting air overpressure. Acta Geophysica, 68(4), 1145–1157. https://doi.org/10.1007/s11600-019-00396-x

Saghatforoush, A., Monjezi, M., Shirani Faradonbeh, R., & J. Armaghani, D. (2016). ANN + ACO for flyrock and back-break. Engineering with Computers, 32(2), 255–266. https://doi.org/10.1007/s00366-015-0415-0

Taiwo, B. O., Famobuwa, O. V., Mata, M. M., Sazid, M., Fissha, Y., Jebutu, V. A., ... & Abubakar, O. (2024). Granite downstream production dependent size and profitability assessment: an application of mathematical-based artificial intelligence model and WipFrag software. Journal of Mining and Environment, 15(2), 497–515. https://doi.org/10.22044/jme.2023.13731.2543

Taiwo, B. O., Hosseini, S., Fissha, Y., Adebayo, B., Adesida, P. A., Famobuwa, V., ... & Akinlabi, A. A. (2023). Safe small scale mine blasting operation: An application of soft computing techniques to predict blast-induced flyrock distance, Research Square (preprint). https://doi.org/10.21203/rs.3.rs-3066450/v1

Yang, H., Hasanipanah, M., Tahir, M. M., & Bui, D. T. (2020). Intelligent prediction of blasting-induced ground vibration with ANFIS–GA–PSO. Natural Resources Research, 29(2), 739–750. https://doi.org/10.1007/s11053-019-09515-3

Zeng, J., Roussis, P. C., Mohammed, A. S., Maraveas, C., Fatemi, S. A., Armaghani, D. J., & Asteris, P. G. (2021). Prediction of peak particle velocity caused by blasting through the combinations of boosted-CHAID and SVM models with various kernels. Applied Sciences, 11(8), 3705. https://doi.org/10.3390/app11083705

Zhang, W., Ma, N., Ren, J., & Li, C. (2021a). Peak particle velocity of vibration events in underground coal mine and their caused stress increment. Measurement, 169, 108520. https://doi.org/10.1016/j.measurement.2020.108520

Zhang, X., Nguyen, H., Choi, Y., Bui, X. N., & Zhou, J. (2021b). Novel extreme learning machine-multi-verse optimization model for predicting peak particle velocity induced by mine blasting. Natural Resources Research, 30(6), 4735-4751. https://doi.org/10.1007/s11053-021-09960-z

SAŽETAK

Procjena vršne brzine čestica izazvane miniranjem primjenom optimiziranoga dubokog učenja s algoritmom optimizacije kolektivnog imuniteta koronavirusa

Rudarstvo je jedan od najvažnijih gospodarskih sektora. Površinski kopovi najčešći su oblik eksploatacije, a miniranje je najučinkovitija metoda razaranja stijenske mase. Međutim, ovaj postupak može uzrokovati znatna oštećenja uslijed vibracija. Stoga su praćenje i kontrola vibracija od ključne važnosti. Cilj je ovoga istraživanja procjena razine vibracija na temelju udaljenosti od mjesta miniranja i količine upotrijebljenoga eksploziva. U tu svrhu vibracije su procjenjivane pomoću najveće brzine čestica (*Peak Particle Velocity* – PPV) mjerene seizmografima. Mjerenja su provedena u dvama velikim površinskim kopovima u Iranu, u kojima je prikupljeno približno 1000 podataka. S obzirom na složenost prikupljenih podataka, za modeliranje je primijenjena metoda dubokoga učenja (*deep learning*). Ova metoda sadržava velik broj hiperparametara, čija pravilna prilagodba znatno utječe na učinkovitost modela. Za određivanje optimalnih vrijednosti korišten je algoritam optimizacije kolektivnoga imuniteta koronavirusa (*Coronavirus Herd Immunity Optimizer* – CHIO), algoritam inspiriran biološkim principima imunološkoga odgovora populacije na virusne infekcije. Učinkovitost modela ispitana je primjenom različitih kriterija. Rezultati pokazuju da je primjenom metode optimizacije točnost predviđanja poboljšana za najmanje 4 %. Koeficijent determinacije za modele slučajne šume (*random forest*), osnovnoga dubokog učenja i optimiziranoga modela iznosio je 0,861, 0,932 i 0,972. Vrijednosti korijenske srednje kvadratne pogreške (RMSE) bile su 3,687, 2,338 i 1,146, dok su indeksi prosječne apsolutne postotne pogreške (MAPE) iznosili 0,169, 0,128 i 0,068. Zaključeno je kako metoda dubokoga učenja pokazuje zadovoljavajuću izvedbu, a njezina se učinkovitost može dodatno povećati primjenom algoritama optimizacije. Dobiveni rezultati potvrđuju izvrsnu učinkovitost integracije CHIO metode i njezinu visoku primjenjivost u procjeni vibracija uzrokovanih miniranjem.

Ključne riječi:
miniranje, vršna brzina čestica, umjetna inteligencija, duboko učenje, kolektivni imunitet, koronavirus

Authors' contribution

Davood Mohammadi Sargini; (PhD Candidate, Shahrood University of Technology): participated in all work stages such as sample presentation, experimental tests, data analysis, writing and editing the article, and all project costs. **Mohammad Ataei**; (Professor, Shahrood University of Technology): shared contributions throughout the whole process and data analyses. **Reza Mikaeil** (Associate Professor, Urmia University of Technology): supervised the project and contributed to the writing and editing of the paper. **Akbar Esmaeilzadeh** (Assistant Professor, Urmia University of Technology): participated in all work stages such as sample presentation, experimental tests, data analysis, writing and editing the article.
All authors have read and agreed to the published version of the manuscript.

RGNZ/MGPB

Hydraulic Connectivity Between the Sava River and Lake Jarun During Drought: A High-Resolution Monitoring and Time Series Approach

Rudarsko-geološko-naftni zbornik
(The Mining-Geology-Petroleum Engineering Bulletin)
DOI: 10.17794/rgn.2026.2.10

Original scientific paper

Jelena Parlov[1]*, Filip Šegović[2], Kristijan Posavec[1], Zoran Kovač[1]
[1] *University of Zagreb, Faculty of Mining, Geology and Petroleum Engineering, Pierottijeva 6, HR10000 Zagreb, Croatia*
[2] *Croatian Geological Survey, Sachsova 2, 10000 Zagreb*

Abstract
This study offers the first detailed insight into the hydraulic relationship between the Sava River and Lake Jarun, an urban lake formed from a former river meander in Zagreb, Croatia. The main objective was to quantify and understand the temporal variability of their hydraulic connectivity under drought conditions. Continuous, high-resolution (hourly) water level monitoring of Lake Jarun, established in April 2022, was combined with interpolated Sava River water levels derived from national gauging stations. Using a suite of statistical tools – Pearson correlation, linear regression, cross-correlation, and the sliding window correlation method – the study assessed the strength, direction, and timing of river–lake interactions. The results revealed a clear but dynamic subsurface connection, with the lake typically responding to river fluctuations after a delay of five to six days. During the exceptional drought in the summer of 2022, this response weakened significantly, and the time lag extended beyond 21 days, indicating reduced hydraulic connectivity. The sliding window approach further revealed temporal variability, with sharp declines in correlation during low-flow periods and rapid recovery during high-water events. These findings highlight the non-stationary nature of hydraulic connectivity in regulated floodplains and the sensitivity of such systems to hydrological extremes. In addition to providing the first high-resolution dataset for Lake Jarun, this study introduces a time-adaptive analytical framework that enhances the understanding of short-term river–lake interactions and supports future management of urban water systems under increasing climatic pressure.

Keywords:
Hydraulic connectivity, River–lake interaction, Cross-correlation, Sliding window analysis, Drought impact

1. Introduction

Until 1899, the Sava River in the Zagreb region was an unregulated, meandering watercourse. Characterized by dynamic erosion and accumulation processes, the river frequently changed its course, eroding banks and forming new channels, oxbow lakes, sandbanks and islands. The course of the river in Zagreb was not a single, stable channel as we know it today, but rather a complex network of smaller streams and river arms whose position was constantly changing. The beginning of river regulation and the construction of embankments resulted in some of these channels and oxbow lakes being permanently cut off from the main riverbed. As a result, numerous artificial and semi-natural lakes were formed in the Zagreb area, which are directly related to the regulation of the Sava River and the gravel excavation for the embankment construction. However, no systematic monitoring of water levels or studies on the relationship between these lakes and the Sava River has been established.

Among these lakes, Jarun has a special significance for the City of Zagreb. Lake Jarun was originally created as part of the river regulation and has since developed into an important sport, recreational and cultural centre for the city's inhabitants. It is frequently used for water sports, leisure activities and events, making it an important social and environmental asset for the local community. The lake not only enhances the quality of life of Zagreb's residents but also plays an important role in the urban ecology by contributing to biodiversity and providing a green space that promotes both physical and mental well-being. Its continuing role in the city's urban water landscape highlights the need to understand its hydrological function, particularly in relation to the nearby Sava River.

In recent times, investigation of hydrological and hydrogeochemical characteristics of lakes, rivers and groundwater, their relationship, as well as their response to climate change, has been the focus of numerous research studies (**García-Alix et al., 2022; Kieu & Nguyen, 2024; Rex et al., 2024; Damanik et al., 2024; Mus-**

* Corresponding author: Jelena Parlov
e-mail address: jelena.parlov@rgn.unizg.hr
Received: 10 September 2025. Accepted: 1 November 2025.
Available online: 13 March 2026

tonen et al., 2024; Zhou et al., 2024; Hassan et al., 2024; Dialameh et al., 2025; Caroni et al., 2025). Lakes and wetlands that appear disconnected from rivers or surface water systems are often referred to as geographically isolated wetlands (**Tiner, 2003; Leibowitz, 2015**) and yet may be functionally connected via subsurface flow paths or episodic surface flooding (**Mushet et al., 2015; Rains et al., 2016**). Crucially, functional isolation cannot be inferred from geographic or morphological features alone, especially in complex floodplain systems where hydrogeological features allow for delayed or attenuated interactions (**Zhang et al., 2021**). Furthermore, the hydraulic connection between river and lake is not static, but exhibits pronounced temporal and spatial variability, influenced by both climatic events and anthropogenic changes (**Ward, 1989; Cohen et al., 2016; Leibowitz et al., 2018**). These dynamics form a continuum that determines how, when and to what extent one water body influences another.

Since the Sava once meandered through the area of the city of Zagreb and deposited sediments that today form the city's aquifer, and the river is still embedded in this aquifer today, it can be assumed that there is a hydraulic connection between the river and the nearby lakes. This is consistent with previous research done in the study area which showed that the Sava River is in a dynamic relationship with the Zagreb aquifer and it presents the main source of recharge (**Parlov et al., 2019; Buškulić et al., 2025**). It can also be assumed that recent lake sedimentation, characterised by the accumulation of fine-grained, organically enriched or silty material, clogs the bottom of the lake and weakens its connection with the surrounding waters. This semi-permeable layer significantly reduces hydraulic conductivity and prevents subsurface water exchange with neighbouring aquifers or the river system (**Packman et al., 2006**). As a result, it likely delays or dampens the hydraulic response of the lake to river water level fluctuations and weakens functional connectivity, especially at low water levels.

Despite many hydrogeological and hydrogeochemical studies conducted in the Zagreb area, no research has yet systematically examined the temporal variability of hydraulic connectivity between the Sava River and adjacent urban lakes. This represents a clear research gap, as understanding such temporal dynamics is essential for evaluating how urban floodplain systems respond to natural hydrological fluctuations and anthropogenic regulation.

Although different hydrogeological and hydrogeochemical studies have been done in the study area (**Parlov et al., 2019; Buškulić et al., 2023; Kovač et al., 2023; Buškulić et al., 2025**), the focus was not on the evaluation of the Sava River influence and its connectivity with lakes in the city of Zagreb. Accordingly, the main goal of this study is to quantify and characterise the dynamic hydraulic relationship between the Sava River and Lake Jarun using high-resolution water level data, with particular emphasis on drought and low-flow conditions. Specifically, the study aims to determine the temporal variability and responsiveness of the lake system to river fluctuations through advanced time-series analyses. This is extremely important because it can provide new insight into the variations of hydrological regime (**Chen et al., 2025**). By explicitly addressing this research gap, the study contributes to a better understanding of surface water interactions in a regulated, alluvial environment and provides a scientific foundation for the adaptive management of urban water resources under changing climatic conditions. Although this study builds on the authors' previous research on the hydrogeological and isotopic characteristics of the Zagreb aquifer system (**Parlov et al., 2019; Buškulić et al., 2023; Kovač et al., 2023; Buškulić et al., 2025**), it introduces a distinct focus and methodological advancement. Unlike earlier works, which primarily addressed groundwater recharge and geochemical processes, this paper explicitly quantifies and characterises the temporal dynamics of hydraulic connectivity between the Sava River and Lake Jarun using newly collected high-resolution (hourly) water level data and a time-adaptive sliding window correlation analysis. This approach and dataset are entirely novel and provide the first empirical evidence of river–lake interaction in this urban alluvial setting.

To empirically investigate this relationship and establish a foundation for long-term assessment, systematic monitoring of lake water levels was first initiated by **Šegović (2022)**. Building upon this, a continuous monitoring system was established at Lake Jarun with automatic water level gauge that have been recording hourly changes since April 7th, 2022. This represents the first long-term high-resolution (hourly) dataset available for Lake Jarun, providing a unique basis for assessing its hydraulic connectivity with the Sava River. In parallel, hourly water level data for the Sava River was obtained from the Croatian Meteorological and Hydrological Service (DHMZ). This double data set enabled a comprehensive statistical analysis of the hydraulic interaction between the two systems. The study uses a combination of established statistical techniques, namely correlation, linear regression and cross-correlation, to assess the direction, strength, and timing of the lake's response to river fluctuations. An important innovation in this context is the introduction of the sliding window correlation method. It was originally developed in fields such as climatology and neuroscience to analyse dynamic relationships between time series (**Bailly-Comte et al., 2011; Hutchison et al., 2013; Allen et al., 2014; Delbart et al., 2014; Vergara et al., 2019; Schrunner et al., 2025**). However, the sliding window correlation has rarely, if ever, been used to quantify the hydraulic interactions between rivers and lakes. By calculating Pearson correlation coefficients within successive, overlapping time windows, this method allows the detection of temporal variations in the strength of the lake–river connection. It

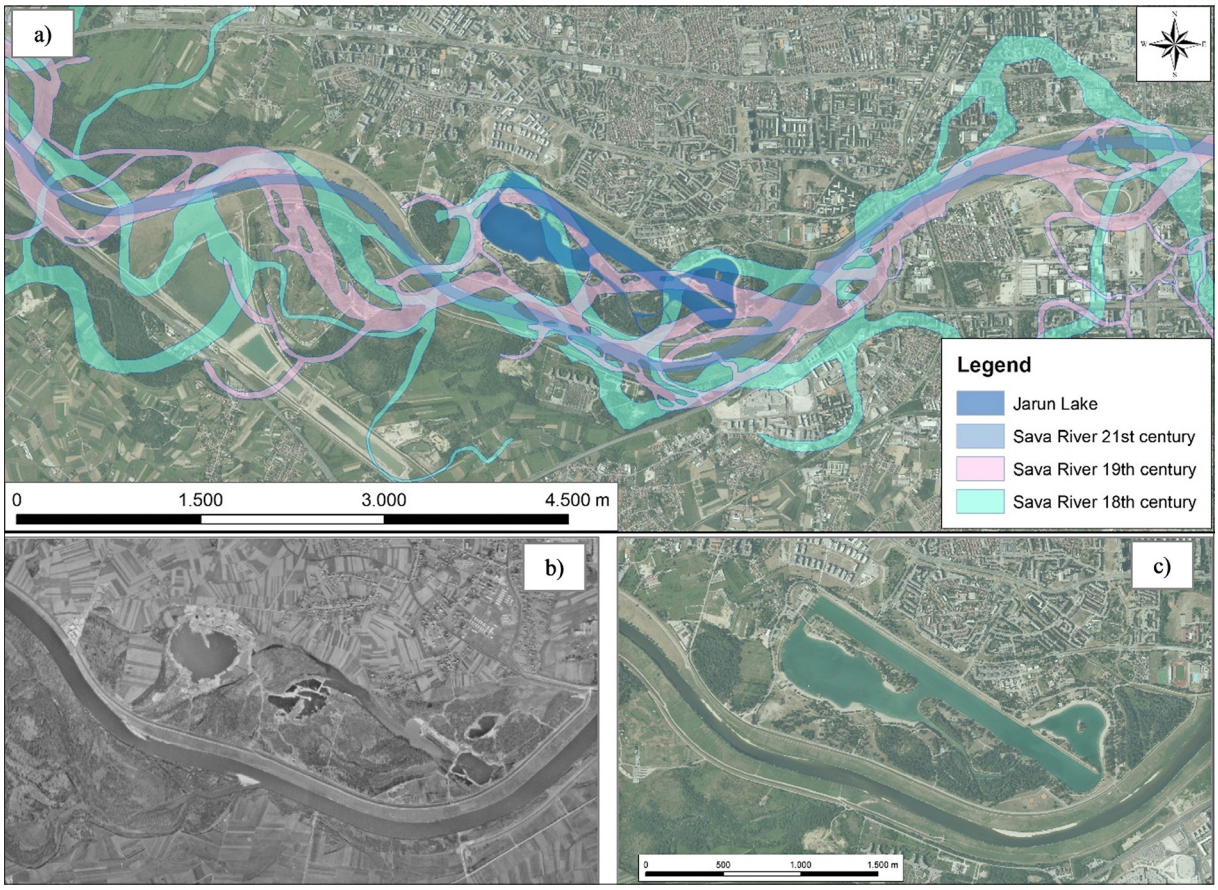


Figure 1. Lake Jarun (present state) in relation to the courses of the Sava River in the 18th, 19th and 21st centuries (a), Lake Jarun area on the aerial photograph from 1968 (b), Lake Jarun today (c)

is particularly useful in determining how droughts or high-water pulses affect the responsiveness of the lake system. The application of the sliding window correlation method provides new insight into the dynamic nature of river–lake hydraulic relationships in regulated, alluvial environments. In contrast to previous studies that primarily relied on temporally aggregated or static analyses of river–lake interactions, this research introduces a time-adaptive analytical framework based on the sliding window approach. This methodology enables the quantification of short-term variations and evolving correlations between hydrological systems, providing a more refined understanding of transient connectivity processes. By explicitly addressing the temporal dynamics of hydraulic coupling, the study advances current methodological practice and reinforces the importance of high-frequency monitoring data for capturing non-stationary hydrological behaviour. These findings offer a stronger empirical basis for adaptive management of urban water systems under increasing climatic and hydrological variability.

2. Materials and Methods

The methodological framework of this study was developed to investigate the hydraulic connection between the Sava River and Lake Jarun. As there has been no systematic monitoring of the lake to date, it was first necessary to reconstruct the broader historical and hydrogeological context of the area, followed by the establishment of a monitoring system that provides a comprehensive basis for quantifying the assumed river-lake interaction.

2.1. Historical Evolution and Regulation of the Sava River in the Zagreb Area

The current morphology and position of the Sava River in the Zagreb region differs considerably from its natural state before human intervention. In the past, the river meandered through a wide area bordered by the Medvednica Mountain, the Samobor Hills and the Vukomeričke Gorice, forming a dynamic river system. Over the last 10,000 years, these natural processes have led to the formation of three different alluvial terraces through the deposition of sediments transported from upstream. Today, these deposits form the so-called Zagreb alluvial aquifer. Through frequent lateral migration and channel shifts, the Sava River created numerous side channels, oxbow lakes, floodplains and gravel banks, thus forming a complex river landscape. Before regulation, the meandering course of the river through the city

of Zagreb is well documented in historical topographical maps, on which the wide, shallow and branched channel is clearly recognisable (see **Figure 1a**).

It is important to note that the main channel of the Sava River once ran along the site of today's Lake Jarun (**Šimunjak, 2022**). As part of river regulation works in the early 20th century, this section was cut off from the active river regime by the construction of flood protection embankments and the straightening of the channel. This hydromorphological intervention transformed a formerly dynamic river corridor into an isolated remnant that later developed into a managed urban lake system (see **Figures 1b and 1c; URL 1**).

The first systematic regulatory measures were initiated in response to rapid industrialisation and a series of devastating floods, particularly in the spring and autumn of 1895. Official work began in 1899 and lasted until 1918. By 1900, significant infrastructure had already been completed, including embankments along the left bank of the river. This marked the beginning of the Sava's transition to its current linear form. By 1914, the river had transformed from a wide, shallow watercourse into a narrower and deeper channel. Most of the embankments had been completed before the outbreak of the First World War, but further development was interrupted by both world wars. The newly regulated canal significantly improved the water flow and reduced the frequency of flooding. However, in the absence of continuous embankments, extreme rainfall events still led to flooding in the areas south of the railway line in Zagreb (**Slukan Altić, 2010**).

The last major phase of river regulation, which included the construction of reinforced embankments, was carried out after the flood disaster of 1964, which inundated large parts of Zagreb. By 1967, the Jarun area had been secured with protective embankments that effectively protected it from future flooding. In 1984, the concept for the Jarun Sports and Recreation Centre (RSC Jarun) was officially presented as part of Zagreb's bid to host the 1987 Summer Universiade. This event marked the beginning of extensive construction work with the aim of transforming the former floodplain into a multifunctional complex for sports, recreation and water management. The development continued until the start of the Universiade in 1987, making Jarun an important part of Zagreb's modern urban landscape.

2.2. Hydrogeological Context of the Lake Jarun Area

During the Holocene, the hydrogeological and geomorphological development of the Zagreb Plain changed considerably. As climatic conditions became more favourable and tectonic activity altered drainage patterns, the Sava River established its present course through the region and began depositing extensive alluvial sediments in the floodplain (**Velić and Durn, 1993**). These Holocene deposits, which consist mainly of gravels and sands with intercalated silts and clays, today form the upper and most permeable aquifer system in this area. These deposits, which are characterised by high hydraulic conductivity - especially in the western parts of the aquifer where values exceed 3,000 m/day - were deposited by the Sava River during alternating periods of intense sediment transport and flooding (**Bačani and Posavec, 2014**). The river actively interacts with this aquifer system: when the water level is high, the Sava River recharges the aquifer along its entire course in the Zagreb area, while during prolonged low water levels it can act as a drainage axis and lower the groundwater level. This dynamic relationship between the river and the aquifer depends on factors such as the permeability of the sediments in the riverbed and the height of the groundwater table (**Posavec, 2006**).

Lake Jarun lies directly in this Holocene alluvium, which formed in a section of the former main channel of the river. Due to its location on highly permeable, gravel-dominated sediments and its origin as an abandoned meander, with no surface inflows and observed higher water levels during high Sava River levels and vice versa, a justified hypothesis is that Lake Jarun has a strong hydraulic connection with the Sava River. This hydraulic connection is most likely dominantly maintained via subsurface flow through the shared alluvial substrate, especially during periods of elevated river water levels. However, the strength of the hydraulic connection remains unconfirmed as there are currently no direct measurements or long-term data sets to confirm the presence, direction or extent of water exchange between the lake and the river. Given the geomorphological context of the lake and the known permeability of the surrounding sediments, Jarun is theoretically expected to behave as part of the broader Holocene alluvial system, in which interactions between river, lake and groundwater occurs. In this conceptual model, the water level of the lake responds - albeit with a time lag and attenuation - to fluctuations in the hydrological regime of the Sava River, presumably with a longer time lag under extreme hydrological conditions such as droughts or floods.

2.3. Establishment of Water Level Monitoring at Lake Jarun

Despite the importance of Lake Jarun for the hydrological and urban system of Zagreb, no systematic or long-term monitoring of its water level was carried out in recent decades prior to this study. In April 2022, a continuous water level monitoring programme was launched, which represents the first recorded hydrometric observation of Lake Jarun in recent history. An automatic water level logger was installed on April 7th, 2022, and has been operating continuously since then, collecting water level data every hour. The logger was installed in the centre of a bridge spanning the lake. It is housed in a protective PVC pipe that has been securely fastened to a concrete

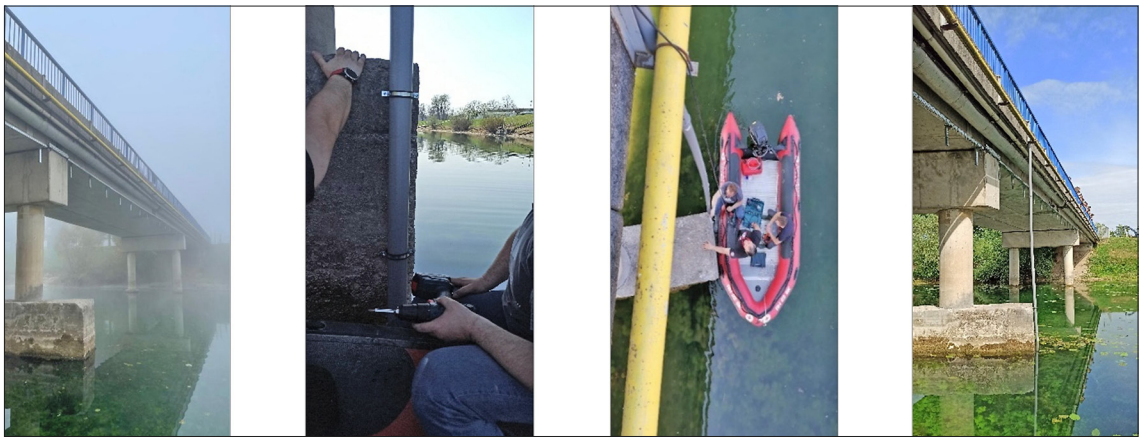


Figure 2. Installation of the automatic water level logger in Lake Jarun

platform and bridge pier to ensure physical stability and protection from external damage (see **Figure 2**).

This site was chosen for its accessibility, its protection from waves and its suitability for recording representative water levels in the main basin of the lake. The monitoring station provides high temporal resolution data, which is crucial for the assessment of seasonal and event-related fluctuations, especially during low water or drought, as well as for the study of the hydraulic relationship between the Lake Jarun and the nearby Sava River.

2.4. Approach for Verification and Quantification of the Hypothesized Hydraulic Connection

Although observations, the geomorphological features and sediment composition suggest a possible strong hydraulic connection between the Sava River and Lake Jarun, no analysis have yet been made to empirically quantify this interaction. The assumption of such a strong connection is primarily based on the location of the lake within a former main channel of the Sava River and the presence of highly permeable Holocene alluvial deposits shared by the river and the lake basin. Further, it can be observed that water level in the Lake Jarun rises when Sava River levels are high and vice versa.

A targeted observation campaign was launched to investigate this hypothesis and quantify Sava River - Lake Jarun hydraulic connection, using daily and hourly water level data. The water level data for the Sava was obtained from the Croatian Meteorological and Hydrological Service (DHMZ). The focus of the analysis was on low water level periods, which are defined as periods when the river level falls below the 10th percentile of observed values within the study period. To support this classification and ensure objective identification of low water level periods, a long-term water level duration curve (WLDC) was created based on historical water level data from the Sava, from 2000 to 2020.

2.5. Statistical Analysis of River–Lake Interaction

As Lake Jarun has not been monitored in recent decades, this study is the first attempt to confirm the existence of a hydraulic connection and to quantify the river–lake interactions in this area. The extreme hydrological conditions are particularly important to test for possible disruption of the river-lake connection or attenuation of the hydraulic response. The following methods were used to investigate the existence and characteristics of a possible hydraulic connection:

1. The correlation or statistical association describes the degree of interdependence between two measurable variables. In hydrological contexts, correlation analysis can be used to quantify the strength of the relationship between water systems (e.g. river and lake levels) and their boundary conditions. The strength of this connection can provide information on which system exerts a dominant influence or indicates the sensitivity of a lake or aquifer to external hydrological inputs and outputs. The correlation coefficient is a dimensionless statistical indicator that quantifies the strength and direction of a linear relationship between two variables, regardless of the units of measurement. In this analysis, the Pearson correlation coefficient was used, which was calculated using the CORREL function in Microsoft® Excel.

The coefficient ranges from +1 to −1, where +1 indicates a perfect positive linear relationship, −1 a perfect negative (inverse) relationship and values close to 0 indicating a weak or no linear association. Normally, correlation coefficients above 0.8 are considered strong, while values below 0.5 indicate weak relationships (**Davis, 2002**).

2. While correlation reveals the presence and direction of relationships, regression analysis is used to model and quantify these relationships, especially when the behaviour of a dependent variable is to be predicted on the basis of one or more independent variables. For example, the water level of a lake, dependent variable, can be predicted from the water level of a river, independent variable, using a simple linear regression:

$$y = \beta_0 + \beta_1 x + \varepsilon \quad (1)$$

where y is the dependent variable (e.g. lake level), x is the independent variable (e.g. river stage), β_0 and β_1 are

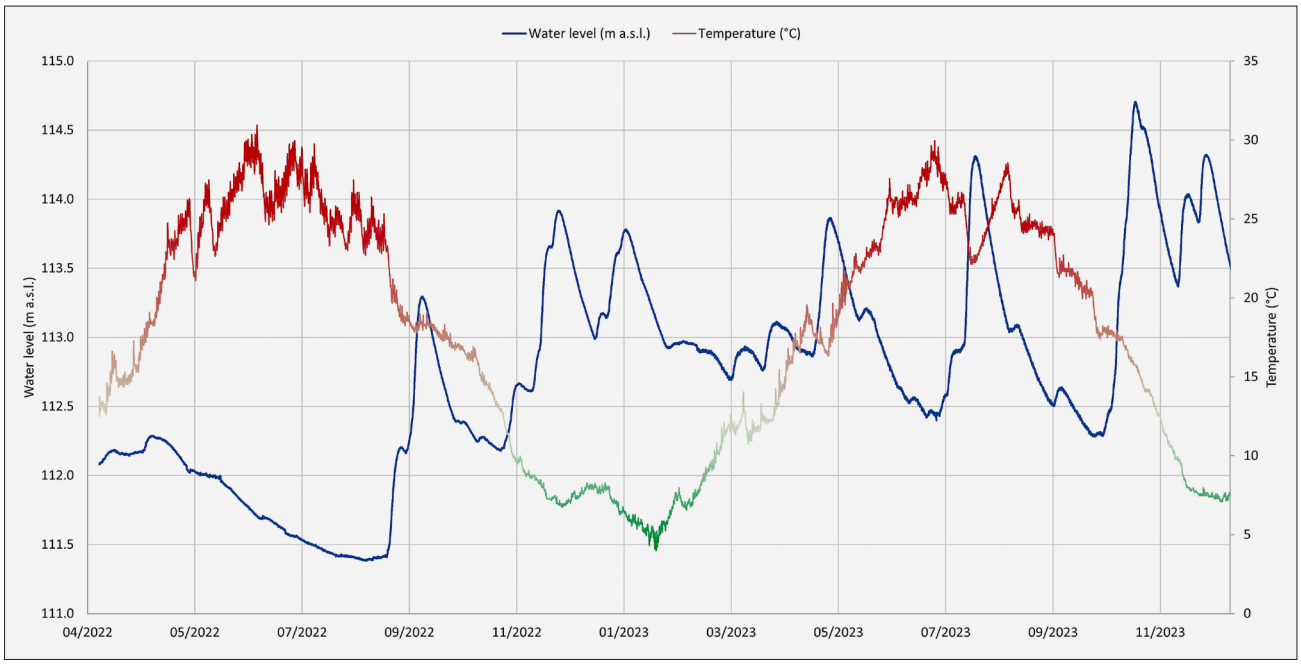


Figure 3. Hourly time series of water level and water temperature in Lake Jarun

regression coefficients, and ε is the random error term. This allows for assessing the influence of river input on lake level variation and is particularly valuable for forecasting and management (**Davis, 2002**).

3. Cross-correlation is used to analyse the time-delayed relationships between hydrological systems. This method is used to investigate how shifts in one time series (e.g. river levels) correspond to delayed responses in another (e.g. lake levels), revealing not only the strength but also the timing of their interaction. This is crucial when system responses are often delayed due to storage, flow paths or geological influences. In mathematical terms, cross-correlation quantifies the degree to which two data sets correlate depending on the time lag between them. The correlation coefficient r_{lag} is calculated for each time lag (positive or negative lag) so that the lag at which the maximum correlation occurs can be determined. This lag is interpreted as the transmission time of pressure changes through the aquifer system (**Davis, 2002**).

$$r_{lag} = \frac{cov_{xy}}{\sigma_x \sigma_y} \tag{2}$$

where r_{lag} is the correlation coefficient for each match position, cov_{xy} is the covariance between the two variables, and σ_x and σ_y are the standard deviations of the two-time series x and y, respectively.

The results are usually presented using a cross-correlogram, a graphical representation of the correlation coefficients over a series of time intervals. The first positive peak in the correlation diagram indicates the most likely lag in the response time between the variables, which is crucial for identifying cause-effect relationships in hydrogeological systems and supporting predictive modelling. A freely available VBA code in Excel published by **Posavec et al. (2017)** was used for the cross-correlation analysis.

4. To assess the temporal variability in the relationship between the water levels of river and lake, a sliding window Pearson correlation analysis was performed. The continuous time series was divided into overlapping windows of different lengths: 5, 10, 15, 20, 25, 30 and 35 days. Within each window, the Pearson correlation coefficients between the water levels of river and lake were calculated. This approach allowed the detection of changes in the strength of the correlation over time and provided insight into whether the lake's response to river fluctuations was consistent or varied under different hydrological conditions. Particular attention was given to periods of lower correlation that coincided with lower river levels, indicating possible changes in hydraulic connectivity or responsiveness of the lake system during low water level periods.

These complementary approaches aim to provide both statistical evidence and hydrological interpretations of the hypothesised river-lake interaction. Together, they represent not only a first but also a structured step towards understanding river-lake dynamics in the Holocene alluvial system of western Zagreb.

3. Results and discussion

The installed measuring system has been providing a continuous data set with hourly water level and water temperature measurements for Lake Jarun since April 7th, 2022. This long-term monitoring covers both low water and high water periods and provides valuable in-

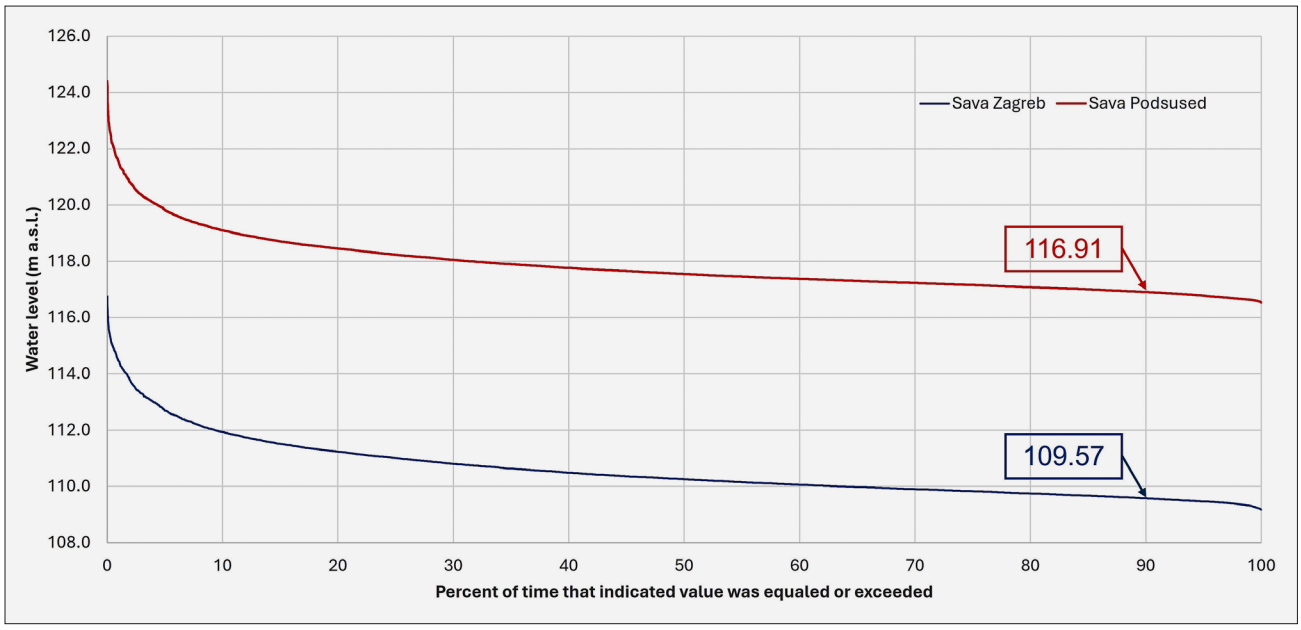


Figure 4. The water level duration curves (WLDC) created using the long-term historical water level data from 2000 to 2020

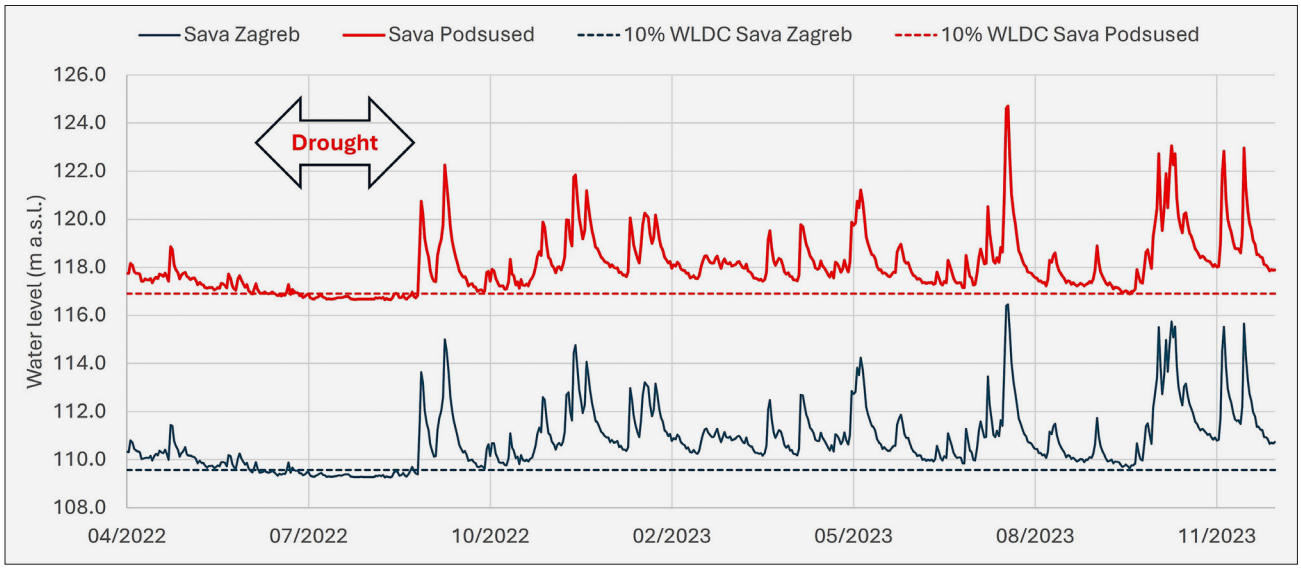


Figure 5. Water levels of the Sava at the Zagreb and Podsused stations with threshold values that indicate extreme drought in 2022

sight into the lake's response to a range of hydrological conditions. The recorded water levels show the expected seasonal and short-term fluctuations, with the fluctuations being more pronounced during high water events. In parallel, the water temperature data clearly reflect the seasonal transitions and show a consistent change between warmer and colder periods of the year. These patterns are illustrated in **Figure 3**, which shows the temporal dynamics of both variables from April 7th, 2022, to December 2023.

This extended dataset provides a solid basis for further correlation analyses aimed at characterising the hydraulic interaction between Lake Jarun and the Sava River across different hydrological regimes. Given the assumption that a strong hydraulic connection exists, supported by past observations, geological, historical and geomorphological evidence, the data provide the opportunity to empirically test and quantify this interaction, particularly during stress conditions such as drought. In order to conduct a meaningful correlation analysis focussing specifically on low water level conditions, it was first necessary to objectively define what constitutes a drought or low water level period for the Sava River in the study area. For this purpose, water level duration curves (WLDC) were created based on long-term historical water level data from 2000 to 2020,

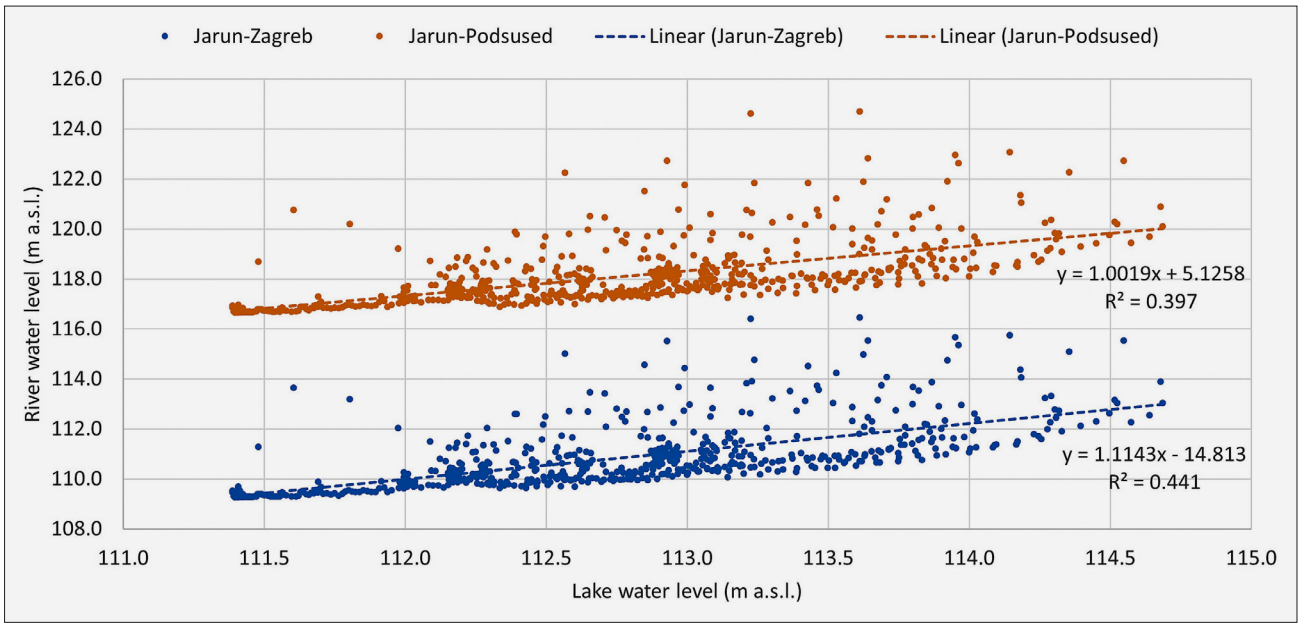


Figure 6. Linear regression between the water levels of the river Sava and Lake Jarun

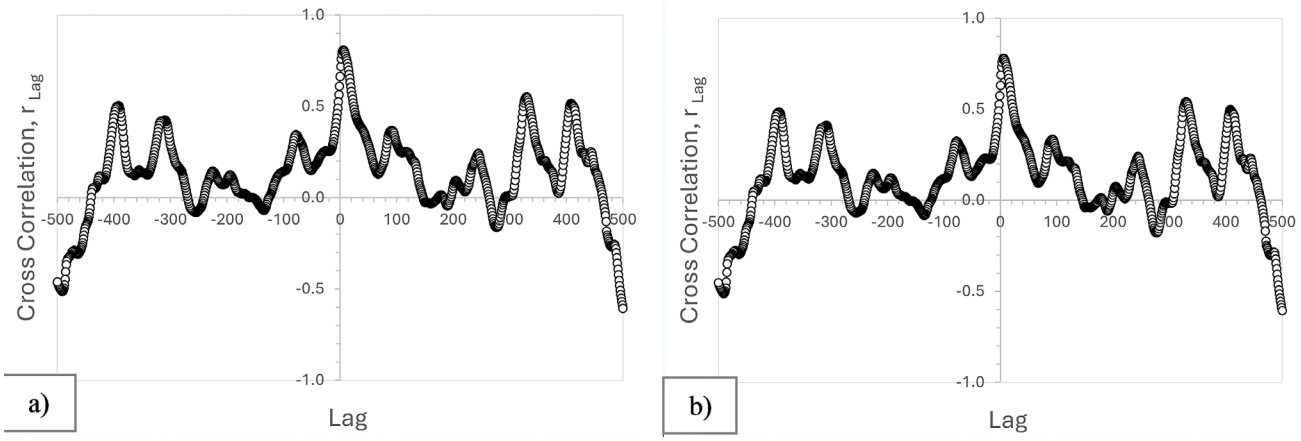


Figure 7. Cross-correlogram of Zagreb-Jarun (a) and Podsused-Jarun (b) – daily values

obtained from two nearby gauging stations (Zagreb and Podsused) and provided by the Croatian Meteorological and Hydrological Service (DHMZ). These curves are shown in **Figure 4**.

As already described in the theoretical framework, low water level periods are defined as intervals in which the river level falls below the 10th percentile of the observed values. Based on the WLDC analysis, this threshold corresponds to a water level of 116.91 m a.s.l. at the Podsused station and 109.57 m a.s.l. at the Zagreb station. The determined 10-percentile threshold values served as objective reference values for recognising extremely low water levels. These threshold values made it possible to determine specific time intervals in which extreme dryness prevailed. This is illustrated in **Figure 5**, which shows the daily water level time series of the Sava at both stations together with the respective threshold lines. It can be seen from the graph that a prolonged period of extremely low water levels occurred between June and September 2022, representing one of the most hydrologically stressed intervals within the monitoring period. It must be emphasized that drought happened in 2022 has been identified as one of the most severe in other parts of the world (**Chen et al., 2025**). This identified drought window was then used as a focus for a detailed correlation analysis between the Sava River and Lake Jarun.

In a first step, the relationship between the Sava River and Lake Jarun was assessed using the complete set of the daily water level data from the official gauging stations Zagreb and Podsused and the corresponding daily mean values from the automatic logger of Lake Jarun for the period from 04/2022 until 11/2023. Pearson correlation coefficients were calculated to assess the linear relationships. The values obtained were 0.66 for Zagreb and 0.63 for Podsused, indicating a moderate correlation between river and lake water levels on the daily scale. Linear regression analyses were also performed. The results

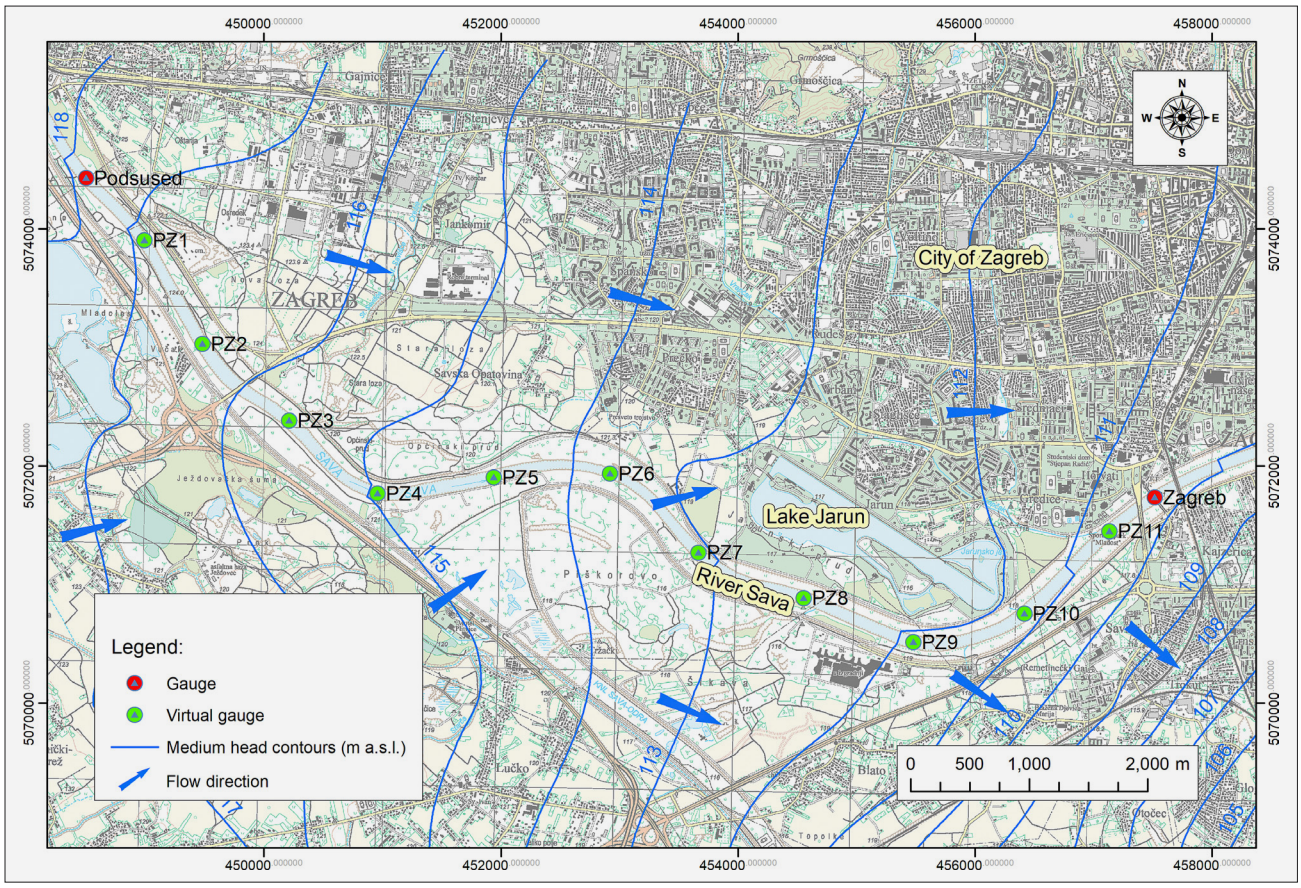


Figure 8. Virtual gauging stations and medium head contours near Lake Jarun

are presented in **Figure 6**, which shows scatter plots with regression lines and coefficients of determination (R^2) for both combinations of station and lake. In addition, a cross-correlation analysis was performed to investigate possible delayed responses between river and lake levels over daily time scales. The results showed that the maximum correlation between Jarun and the Zagreb station occurred with a lag of six days, as well as with the Podsused station, with corresponding coefficients of 0.806 and 0.781, respectively. The cross-correlation curves are shown in **Figure 7**. The correlation and regression analyses based on the daily data from the Zagreb and Podsused gauging stations showed moderate positive correlations with the lake level as well as relatively strong cross-correlation peaks with a lag of six days. These results indicate a delayed but stable interaction under typical hydrological conditions. They reflect subsurface flow processes through the common alluvial aquifer and the time required for pressure signals to propagate through the unconfined Holocene alluvial aquifer that underlies both the river and the lake. The presence of such a time lag is consistent with earlier results by **Posavec et al. (2017)**, who performed a cross-correlation analysis between the Sava River and nearby groundwater levels in the area between the river and Lake Jarun. Their work also showed delayed responses, supporting the hypothesis of indirect but functional hydraulic connectivity determined by the dynamics of the unconfined alluvial aquifer.

Although the Zagreb and Podsused gauging stations provide reliable long-term data, both are located at a considerable distance from Lake Jarun, which limits their representativeness for local hydraulic assessments. To improve the spatial resolution and better represent the river conditions in the vicinity of the lake, in the second step, a series of virtual gauging stations were set up along the Sava River between upstream Podsused and downstream Zagreb gauging stations. These virtual stations were positioned at 1,000 metre intervals between the Zagreb and Podsused stations (see **Figure 8**). For each position, the corresponding water level was estimated by linear interpolation of the measured values at the two reference stations. Linear interpolation method provided a reasonable estimate of water levels since no natural or artificial barriers like waterfalls, weirs or dams in the Sava watercourse between Zagreb and Podsused stations exist. This method provided a continuous spatial profile of water levels along the interpolated river section. Taking into account predominant general groundwater flow direction between the Sava River and Lake Jarun, i.e. from west to east, as well as the relative location of Lake Jarun within the interpolated section, the station labelled PZ6 (see **Figure 8**) was selected as the reference point for further correlation analysis, where

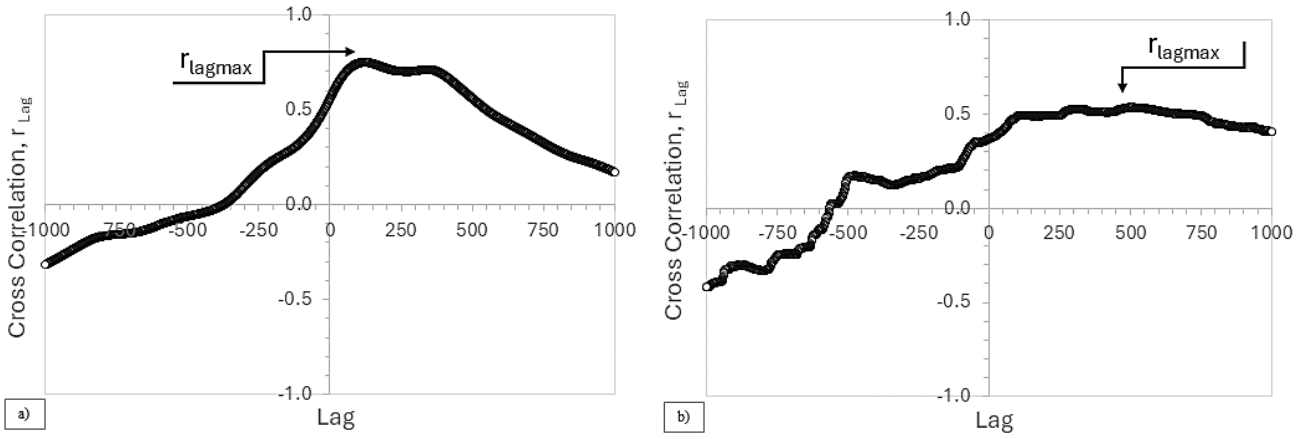


Figure 9. Cross-correlogram of PZ-6-Jarun – hourly values: all data (a), drought period (b)

the figure also shows the medium head contours illustrating the general groundwater flow pattern. This allowed for a more detailed investigation of the potential hydraulic interactions between the Sava River and Lake Jarun during the extreme drought period in 2022.

Further, in order to investigate possible short-term hydraulic reactions between the Sava River and Lake Jarun, a cross-correlation analysis was carried out using hourly water level data from the virtual station PZ6 and the lake. The analysis was performed in two phases. First, the entire available monitoring period was analysed to capture the general pattern of lagged interactions. The resulting cross-correlation function showed a maximum correlation at a delay of 120 hours (5 days) with a correlation coefficient of 0.748 (see **Figure 9a**), which corresponds exactly to the delay of six days observed in the daily data. This consistency between the different temporal resolutions emphasises the robustness of the identified relationship. Subsequently, in the second phase the same method was applied to a more hydrologically critical period - the extreme drought window from June 15th to September 15th, 2022. During this period, the cross-correlation showed a maximum at a lag of 504 hours (21 days) with a coefficient of 0.54 (see **Figure 9b**), indicating that the lake becomes more disconnected from the river system under hydrological stress conditions. This longer delay can be attributed to several factors, including a lower hydraulic gradient between the river and the lake during low water levels as well as the fact that during low water levels of the lake, groundwater–lake interaction predominantly occurs through the bottom of the lake which is mudded while during higher water levels in the lake, groundwater–lake interaction occurs also through the lake shores which are made of sand and gravel, making interactions stronger due to higher hydraulic conductivities of sands and gravels. As mentioned in the introduction, recent sedimentation, particularly of fine-grained, organically enriched material, can form a semi-permeable layer on the lake bottom (**Packman et al., 2006**). This layer reduces permeability, impedes subsurface flow and reduces the responsiveness of the lake to external fluctuations. In fact, during a drought, the system behaves more like a geographically isolated lake, which is geographically close to a large river but functionally more disconnected. As **Leibowitz (2018)** and **Zhang et al. (2021)** emphasise, the appearance of isolation can be misleading, since hydraulic connectivity is often governed by subtle subsurface processes that can weaken or strengthen over time. The Jarun-Sava system vividly illustrates this complexity. This behaviour clearly shows how sensitive the hydraulic connectivity is to external stressors, especially prolonged periods of low flow levels and limited recharge.

To investigate the temporal variability of the hydraulic relationship between the Sava River and Lake Jarun, a Pearson correlation analysis with sliding windows was performed for the entire data set of hourly water levels. The correlation coefficients were calculated in overlapping time windows of 5, 10, 15, 20, 25, 30 and 35 days. The results for all window lengths are shown in **Figure 10**, which shows the development of the correlation values over time on different temporal scales. The analysis revealed clear periods of decreasing correlation, especially in the summer months of 2022, which coincided with the previously identified extreme drought period. During these periods, the correlation coefficients decreased significantly across all window sizes, indicating a weakening hydraulic connection or a delayed response of the lake system at low river levels. This observation is consistent with the results of the cross-correlation analysis, which indicates longer lag times under drought conditions. Conversely, a strong increase in correlation strength was observed when river levels rise, indicating a rapid hydraulic response of the lake to rising river levels. This pattern was particularly evident in shorter time windows (5-10 days), highlighting the sensitivity of lake-river interaction to sudden hydrological influences. The sliding window approach therefore provides a dynamic view of the system's behaviour and shows that the strength and consistency of the hydraulic connection varies considerably over time, mainly due to the river's flow regime.

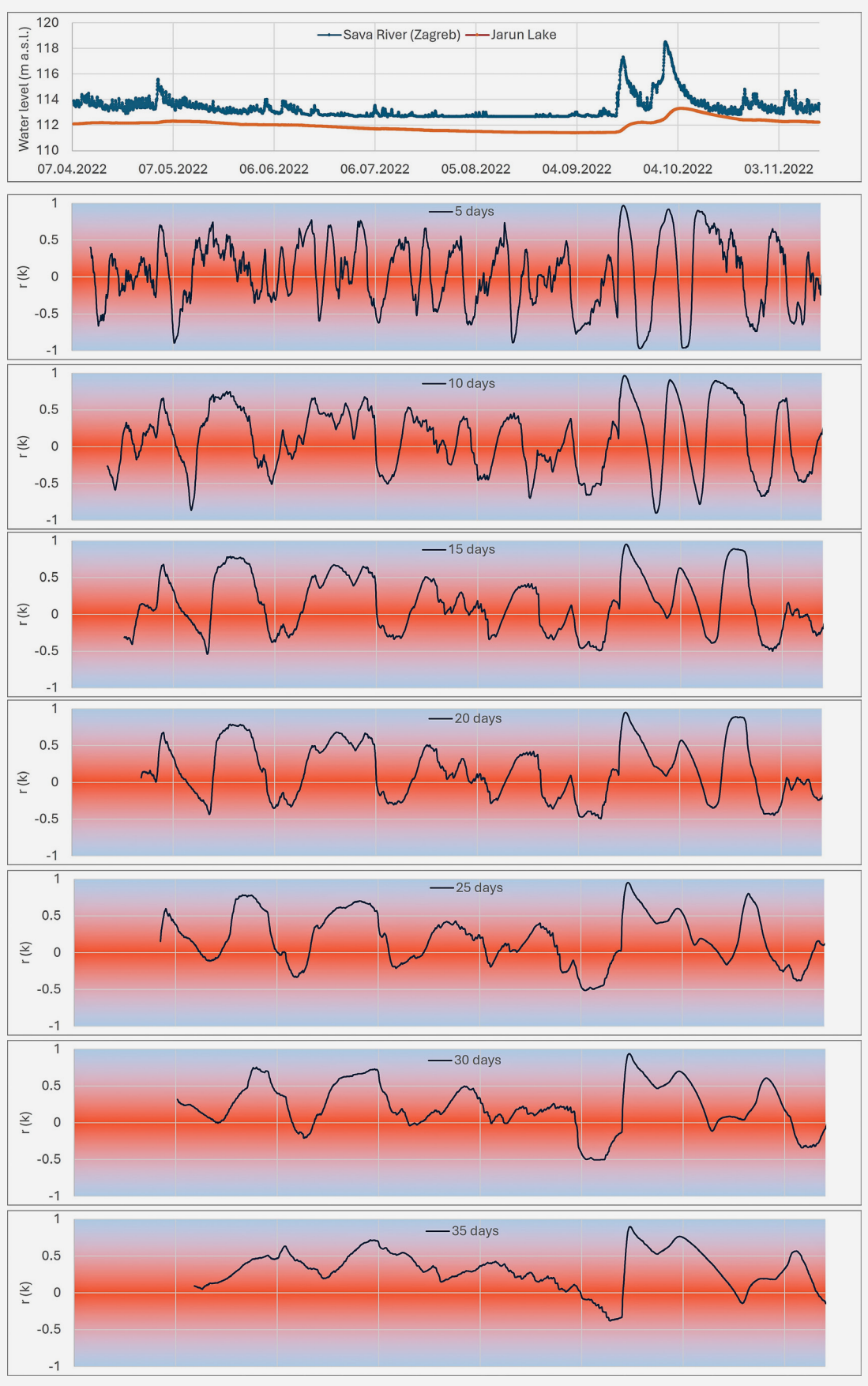


Figure 10. Sliding window correlation between the water levels of the Sava River and Lake Jarun for different window lengths (5, 10, 15, 20, 25, 30 and 35 days)

These findings reinforce a growing recognition in hydrological science that connectivity is not static but varies at both spatial and temporal scales (**Ward, 1989; Cohen et al., 2016**). With this in mind, Lake Jarun exhibits the same characteristics as so-called geographically isolated wetlands, i.e. systems that have no surface outflows or inflows but have episodic or permanent subsurface connectivity depending on climatic conditions. As **Mushet et al. (2015)** and **Rains et al. (2016)** have noted, such systems play an important hydrological and ecological role, even if their connections are only subtle or temporary. Lake Jarun seems to fit into this conceptual framework, particularly in times of hydrological stress.

The results of this study provide convincing evidence of a measurable, albeit temporally variable, hydraulic relationship between the Sava River and Lake Jarun. By combining long-term monitoring data with statistical methods, the study has successfully characterised how this relationship manifests itself under different hydrological regimes, with a particular focus on low flow conditions (drought). However, under extreme drought, the lake's response becomes delayed, weakened and less predictable - typical characteristics of isolated or weakly connected systems.

The differences in response times and correlation strength between the different hydrological regimes emphasise the importance of both spatial and temporal resolution in hydrological studies. While coarse resolution data is sufficient for general connectivity assessments, higher resolution time series in combination with spatially refined representations such as virtual stations are crucial to detect subtle or time-sensitive interactions. The results of this study highlight the vulnerability of shallow lake–aquifer systems in urban floodplains, especially given the projected increase in the frequency of droughts due to climate change.

To summarise, this study not only characterizes the strength of a hydraulic connection between the Sava River and Lake Jarun under normal flow conditions, but also shows that this connection becomes weaker and more delayed during extreme low flow events. These results have practical implications for future monitoring strategies and the management of water resources in urban alluvial areas. The observed variability in lag time and correlation strength highlights the sensitivity and vulnerability of river–lake interactions to hydrological extremes, with potential implications for groundwater recharge dynamics and aquifer sustainability in future climate-induced stress periods.

In addition, the planned dredging and cleaning of the lake bottom, which aims to remove accumulated sediments and increase the depth of the lake, raises important questions about the future hydraulic behaviour of the system. Such interventions are likely to alter the physical structure and permeability characteristics of the lake bottom sediment, potentially enhancing or disrupting current subsurface flow pathways that facilitate interaction with the Sava River. A deeper and potentially more permeable lakebed could increase the sensitivity of the system to prolonged droughts, as larger amounts of stored water could become more vulnerable to seasonal fluctuations. It remains to be seen whether this intervention strengthens or weakens the hydraulic connection, but it clearly emphasises the need for continuous high-resolution monitoring and reassessment of lake–river dynamics following anthropogenic changes.

4. Conclusions

This study presents the first detailed, data-driven assessment of hydraulic connectivity between the Sava River and Lake Jarun, combining continuous, high-resolution water level measurements with correlation-based time series analyses. The monitoring system, established in April 2022, has provided the first uninterrupted hourly dataset for Lake Jarun, covering both low- and high-water periods. By applying correlation, regression, and cross-correlation analyses to daily and hourly data, the study confirms a measurable but variable subsurface connection between the river and the lake.

Under typical hydrological conditions, a consistent response lag of approximately five to six days was identified between the river and the lake, reflecting the propagation of pressure signals through the shared unconfined alluvial aquifer. During the extreme drought in the summer of 2022, this connection weakened and the response lag increased to around 21 days, indicating reduced hydraulic gradients and a temporary decline in connectivity. The longer delay can be attributed to changes in groundwater–lake exchange pathways: during low lake levels, the exchange occurs mainly through the fine-grained, low-permeability lake bottom, whereas under higher levels, the water exchange extends to the sandy and gravelly shores with higher hydraulic conductivities, resulting in a stronger and faster response.

The introduction of the sliding window correlation method provided new insight into the temporal variability of hydraulic connectivity. This approach revealed clear fluctuations in correlation strength, with pronounced decreases during low-flow periods and rapid recovery during high-flow events. These results demonstrate that hydraulic connectivity between the river and lake is not constant but evolves dynamically under changing hydrological conditions. The use of virtual gauging stations between the Zagreb and Podsused sites further improved the spatial resolution of the analysis and confirmed that local river levels near Jarun exert the dominant control on lake fluctuations.

These findings provide the empirical basis for a new, time-adaptive framework to quantify dynamic river–lake interactions in urban floodplain settings. However, the study is limited by its relatively short monitoring period and its focus on a single site. Future research should

therefore extend the temporal coverage, incorporate isotopic and hydrogeochemical tracers, and include simultaneous groundwater observations to fully capture the river–aquifer–lake continuum.

With planned interventions to dredge and deepen the lake bottom, continuous hydrometric monitoring will be essential to reassess connectivity and manage potential changes in lake–river exchange. Overall, this research establishes Lake Jarun as a model system for understanding time-variable hydraulic interactions in regulated floodplains and demonstrates that the Sava–Jarun connection, though persistent, is sensitive to drought and climatic extremes. Sustained high-resolution observation and the use of adaptive analytical approaches remain key to ensuring informed, resilient management of urban water systems.

Funding

"This research was funded by institutional project of Faculty of Mining, Geology and Petroleum Engineering, MoNItoring VOdostaja zagrebačkih jezera (NIVO)."

5. References

Allen, E.A., Damaraju, E., Plis, S.M., Erhardt, E.B., Eichele, T., Calhoun, V.D. (2014). Tracking whole-brain connectivity dynamics in the resting state. Cerebral Cortex. 24(3): 663-76. https://doi.org/10.1093/cercor/bhs352

Bačani, A. and Posavec, K. (2014). Elaborat o zonama zaštite izvorišta grada Zagreba. Sveučilište u Zagrebu Rudarsko-geološko-naftni fakultet, Zagreb.

Bailly-Comte, V., Martin, J.B., Screaton, E. J. (2011). Time variant cross correlation to assess residence time of water and implication for hydraulics of a sink-rise karst system. KIP Articles. 6782. https://doi.org/10.1029/2010WR009613

Buškulić, P., Parlov, J., Kovač, Z., Nakić, Z. (2023): Estimation of nitrate background value in groundwater under the long-term human impact. Hydrology 10, 3, 63, https://doi.org/10.3390/hydrology10030063.

Buškulić, P., Kovač, Z. Matiatos, I., Parlov, J. (2025): Tracing nitrate contamination sources and dynamics in an unconfined alluvial aquifer system (Velika Gorica well field, Croatia). Environmental Science-Processes & Impacts 27, 1, 154-171, https://doi.org/10.1039/D4EM00527A.

Caroni, R., Greife, A.J., Bresciani, M., Giardino, C., Tellina, G., Carrea, L., Liu, X., Simis, S., Albergel, C., Pinardi, M. (2025): Examining global trends of satellite-derived water quality variables in shallow lakes. Remote Sensing Applications: Society and Environment 38, 101565, https://doi.org/10.1016/j.rsase.2025.101565.

Chen, H., Jin, G., Tang, H., Wu, J., Wang, Y-G., Zhang, Z., Deng, Y., Zhang, S. (2025): Spatiotemporal variations of water levels and river-lake interaction in the Poyang Lake basin under the extreme drought. Journal of Hydrology: Regional Studies 57, 102165, https://doi.org/10.1016/j.ejrh.2024.102165.

Cohen, M.J., Creed, I.F., Alexander, L., Basu, N.B., Calhoun, A.J.K., Craft, C., D'Amico, E., DeKeyser, E., Fowler, L., Golden, H.E., Jawitz, J.W., Kalla, P., Kirkman, L.K., Lane, C.R., Lang, M., Leibowitz, S.G., Lewis, D.B., Marton, J., McLaughlin, D.L., Mushet, D.M., Raanan-Kiperwas, H., Rains, M.C., Smith, L., Walls, S.C. (2016). Do Geographically Isolated Wetlands Influence Landscape Functions? Proceedings of the National Academy of Sciences. 113: 1978–1986. https://doi.org/10.1073/pnas.1512650113

Damanik, A., Janssen, D.J., Tournier, N., Stelbrink, B., von Rintelen, T., Haffner, G.D., Cohen, A., Cahyarini, S.Y., Vogel, H. (2024): Perspectives from modern hydrology and hydrochemistry on a lacustrine biodiversity hotspot: Ancient Lake Poso, Central Sulawesi, Indonesia. Journal of Great Lakes Research 50, 102254, https://doi.org/10.1016/j.jglr.2023.102254.

Davis, J. C. (2002). Statistics and Data Analysis in Geology, Third Edition. John Wiley & Sons Inc., New York.

Delbart, C., Valdes, D., Barbecot, F., Tognelli, A., Richon, P., Couchoux, L. (2014). Temporal variability of karst aquifer response time established by the sliding-windows cross-correlation method. Journal of Hydrology. 511: 580-588. https://doi.org/10.1016/j.jhydrol.2014.02.008

Dialameh, B., Ghane, E., Youssef, M. (2025): DRAINMOD predicted impact of climate change on hydrology, corn yield, and drainage design in the Western Lake Erie Basin, United States. Agricultural Water Management 318, 109641, https://doi.org/10.1016/j.agwat.2025.109641.

García-Alix, A., Jimenez-Moreno, G., Gazquez, F., Monedero-Contreras, R., Lopez-Aviles, A., Jimenez-Espejo, F., Rodríguez-Rodríguez, M., Camuera, J., Ramos-Roman, M.J., Anderson, R.S. (2022): Climatic control on the Holocene hydrology of a playa-lake system in the western Mediterranean. Catena 214, 106292, https://doi.org/10.1016/j.catena.2022.106292.

Hassan, W.H., Khazal, S.T., Al-Shammari, M.H. (2024): Effect of Climate Change on Wetland Areas in West Iraq Using Satellite Data and GIS Techniques. Civil Engineering Journal 10 (9), http://dx.doi.org/10.28991/CEJ-2024-010-09-013.

Hutchison, R.M., Womelsdorf, T., Allen, E.A., Bandettini, P.A., Calhoun, V.D., Corbetta, M., Penna, S.D., Duyn, J.H., Glover, G.H., Gonzalez-Castillo, J., Handwerker, D.A., Keilholz, S., Kiviniemi, V., Leopold, D.A., de Pasquale, F., Sporns, O., Walter, M., Chang, C. (2013). Dynamic functional connectivity: Promise, issues, and interpretations. NeuroImage. 80: 360-378. https://doi.org/10.1016/j.neuroimage.2013.05.079

Kieu, L.D., Nguyen, P.Q. (2024): Groundwater Quality Assessment in the Middle-Upper Pleistocene Aquifer. Civil Engineering Journal 10 (7), http://dx.doi.org/10.28991/CEJ-2024-010-07-018.

Kovač, Z., Bačani, L., Ružičić, S., Parlov, J., Posavec, K., Buškulić, P. (2023): Using Water Stable Isotopes and Cross-Correlation Analysis to Characterize Infiltration of Precipitation through Unsaturated Zone at the Velika Gorica Site of Zagreb Aquifer. Journal of Hydrologic Engineering, 28, 4, 1-18, https://doi.org/10.1061/JHYEFF.HEENG-5806.

Leibowitz, S.G. (2015). Geographically Isolated Wetlands: Why We Should Keep the Term. Wetlands. 35:997–1003. https://doi.org/10.1007/s13157-015-0691-x

Leibowitz, S.G., Wigington, P.J.Jr., Schofield, K.A., Alexander, L.C., Vanderhoof, M.K., Golden, H.E. (2018). Connectivity of streams and wetlands to downstream waters: An integrated systems framework. J Am Water Resour Assoc. 54(2):298-322. https://doi.org/10.1111/1752-1688.12631

Mushet, D.M., Calhoun, A.J.K., Alexander, L.C., Cohen, M.J., DeKeyser, E.S., Fowler, L., Lane, C.R., Lang, M.W., Rains, M.C., Walls, S.C. (2015). Geographically Isolated Wetlands: Rethinking a Misnomer. Wetlands. 35:423–431. https://doi.org/10.1007/s13157-015-0631-9

Mustonen, K-R., Marttila, H., Lehosmaa, K., Chapman, J., Juutinen, S., Koivunen, I., Korkiakoski, M., Lohila, A., Welker, J., Jyvasjarvi, J. (2024): From thaw till fall: Interacting hydrology, carbon cycle, and greenhouse gas dynamics in a subarctic stream-lake continuum. Science of the Total Environment 957, 177434, https://doi.org/10.1016/j.scitotenv.2024.177434.

Packman, A.I., Marion, A., Zaramella, M., Chen, C., Gaillard, J.F., Keane, D.T. (2006). Development of Layered Sediment Structure and its Effects on Pore Water Transport and Hyporheic Exchange. Water Air Soil Pollut: Focus 6, 433–442. https://doi.org/10.1007/s11267-006-9057-y

Parlov, J., Kovač, Z., Nakić, Z., Barešić, J. (2019): Using Water Stable Isotopes for Identifying Groundwater Recharge Sources of the Unconfined Alluvial Zagreb Aquifer (Croatia). Water 11, 10, 2177, https://doi.org/10.3390/w11102177.

Posavec, K. (2006). Identifikacija i prognoza minimalnih razina podzemne vode zagrebačkoga aluvijalnog vodonosnika modelima recesijskih krivulja. Doktorska disertacija, RGN fakultet, Zagreb: Arhiv Rudarsko-geološko-naftnog fakulteta. Sveučilište u Zagrebu.

Posavec, K., Vukojević, P., Ratkaj, M. & Bedeniković, T. (2017). Cross-correlation modelling of surface water – Groundwater interaction using the excel spreadsheet application. Rudarsko-geološko-naftni zbornik. 32. 25-32. https://doi.org/10.17794/rgn.2017.1.4

Rains, M.C., Leibowitz, S.G., Cohen, M.J., Creed, I.F., Golden, H.E., Jawitz, J.W., Kalla, P., Lane, C.R., Lang, M.W., McLaughlin, D.L. (2016). Geographically Isolated Wetlands Are Part of the Hydrological Landscape. Hydrological Processes. 30:153–160. https://doi.org/10.1002/hyp.10610

Rex, C.L., Tyler, J.J., Nagaya, K., Staff, R.A., Leng, M.J., Yamada, K., Kitaba, I., Kitagawa, J., Kojima, H., Nakagawa, T. (2024): The contemporary stable isotope hydrology of Lake Suigetsu and surrounding catchment (Japan) and its implications for sediment-derived palaeoclimate records. Quaternary Science Advances 13, 100145, https://doi.org/10.1016/j.qsa.2023.100145

Schrunner, S., Pishrobat, P., Janssen, J., Jenul, A., Cao, J., Ameli, A.A., Welch, W.J. (2025). A Gaussian sliding windows regression model for hydrological inference, Journal of the Royal Statistical Society Series C: Applied Statistics, https://doi.org/10.1093/jrsssc/qlaf009

Slukan Altić, M. (2010). Povijest regulacije rijeke Save kod Zagreba i njezine posljedice na izgradnju grada. Hrvatske Vode, 18, 73; 205-212

Šegović, F. (2022). Definiranje odnosa zagrebačkih jezera i rijeke Save. Diplomski rad, RGN fakultet, Zagreb: Arhiv Rudarsko-geološko-naftnog fakulteta. Sveučilište u Zagrebu.

Šimunjak, F. (2022). Reconstruction of the Sava course in the wider Zagreb area in the eighteenth and nineteenth centuries. Ekonomska i ekohistorija, 18 (1), 52-69. https://hrcak.srce.hr/310161

Tiner, R.W. (2003). Estimated Extent of Geographically Isolated Wetlands in Selected Areas of the United States. Wetlands. 23:636–652. https://doi.org/10.1672/0277-5212(2003)023[0636:EEOGIW]2.0.CO;2

Velić, J. & Durn, G. (1993). Alternating Lacustrine-Marsh Sedimentation and Subaerial Exposure Phases during Quaternary: Prečko, Zagreb, Croatia. Geologia Croatica, vol. 46, no. 1, str. 71-90.

Vergara, V.M., Abrol, A., Calhoun, V.D. (2019): An average sliding window correlation method for dynamic functional connectivity. Hum Brain Mapp 40, 2089-2103, https://doi.org/10.1002/hbm.24509.

Ward, J.V. (1989). The Four-Dimensional Nature of Lotic Ecosystems. Journal of the North American Benthological Society. 8:2–8. https://doi.org/10.2307/1467397

Zhang, Y., Huang, C., Zhang, W., Chen, J., Wang, L. (2021). The concept, approach, and future research of hydrological connectivity and its assessment at multiscales. Environ Sci Pollut Res 28, 52724–52743. https://doi.org/10.1007/s11356-021-16148-8

Zhou, Y., Tian, H., Hu, D., Hu, H., Shen, Q. (2024): Spatial-Temporal Characteristics of Green Development Level in River Basin. HighTech and Innovation Journal 5 (4), http://dx.doi.org/10.28991/HIJ-2024-05-04-014.

URL 1. https://geoportal.kulturnadobra.hr/geoportal.html?lang=cro#/ (accessed 1st August 2025)

SAŽETAK

Hidraulička povezanost rijeke Save i jezera Jarun tijekom suše: pristup visokorezolucijskoga monitoringa i analize vremenskih nizova

Ovo istraživanje donosi prvi detaljan uvid u hidraulički odnos između rijeke Save i jezera Jarun, urbanoga jezera nastaloga iz nekadašnjega riječnog meandra u Zagrebu. Glavni cilj bio je kvantificirati i razumjeti vremensku promjenjivost njihove hidrauličke povezanosti, osobito u uvjetima suše. Kontinuirano, visokorezolucijsko (satno) praćenje razine vode u jezeru Jarun, započeto u travnju 2022. godine, kombinirano je s interpoliranim razinama vode rijeke Save dobivenima iz nacionalnoga monitoringa. Primjenom niza statističkih metoda – Pearsonove korelacije, linearne regresije, kroskorelacije i metode korelacije pomičnoga prozora – procijenjena je jačina, smjer i vremenski odaziv interakcije između rijeke i jezera. Rezultati su pokazali jasnu, ali dinamičnu podzemnu povezanost, pri čemu je razina jezera uobičajeno reagirala na promjene vodostaja rijeke s odgodom od pet do šest dana. Tijekom iznimne suše u ljeto 2022. godine ta je povezanost znatno oslabjela, a vremenska se odgoda produljila na više od 21 dan, što upućuje na smanjenje hidrauličke povezanosti. Metoda korelacije pomičnoga prozora dodatno je otkrila vremenske varijacije, s izraženim padom korelacije tijekom razdoblja niskih voda i brzim oporavkom tijekom visokih voda. Ovi rezultati naglašavaju nestacionarnu prirodu hidrauličke povezanosti u reguliranim poplavnim ravnicama te osjetljivost takvih sustava na hidrološke ekstreme. Uz to što pruža prvi visokorezolucijski skup podataka za jezero Jarun, ovo istraživanje uvodi vremenski prilagodljiv analitički okvir koji produbljuje razumijevanje kratkoročnih interakcija rijeke i jezera te podupire buduće upravljanje urbanim vodnim sustavima pod sve većim klimatskim pritiscima.

Ključne riječi:
hidraulička povezanost, odnos rijeka – jezero, kroskorelacija, analiza pomičnoga prozora, utjecaj suše

Author's contribution

Jelena Parlov (Professor): conceptualization, formal analysis, writing – original draft and writing. **Filip Šegović** (Expert associate): investigation, visualization and writing – review & editing. **Kristijan Posavec** (Professor): writing – review & editing. **Zoran Kovač** (Associate professor): investigation, resources and writing – review & editing.
All authors have read and agreed to the published version of the manuscript.

RGNZ/MGPB

The Effect of Kaolinite on Calcium Carbonate Water-Based Drilling Fluid

Rudarsko-geološko-naftni zbornik
(The Mining-Geology-Petroleum Engineering Bulletin)
DOI: 10.17794/rgn.2026.2.11

Original scientific paper

Mohammed Abdalraheem[1]* ✉, Basfar S[1] ✉, Elkatatny S[1] ✉
[1] *College of Petroleum and Geoscience, KFUPM, Dhahran 31261, KSA.*

Abstract
This study evaluates the effect of kaolinite addition on calcium carbonate water-based drilling fluids (WBM) through systematic laboratory testing. Kaolinite was incorporated at concentrations of 42.8 kg/m³ (15 lb/bbl), 85.6 kg/m³ (30 lb/bbl), and 128.4 kg/m³ (45 lb/bbl) into a standard $CaCO_3$-based WBM, and its influence on density, pH, filtration, rheology, and viscoelastic behavior was analyzed. The density of the base mud (10.15 g/cm³) increased to 11.00 g/c cm³ with 128.4 kg/m³ (45 lb/bbl) kaolinite, while pH rose proportionally with kaolinite content. Filtration tests at 93°C (200°F) and 2.07 MPa (300 psi) revealed that the base sample produced a filter cake thickness of 0.0098 in, which increased progressively with kaolinite addition. Rheological measurements showed Bingham plastic behaviour across all samples, with apparent viscosity increasing from 25 cP in the base mud to 33 cP at 128.4 kg/m³ (45 lb/bbl). Yield point and gel strength also exhibited consistent growth, indicating improved suspension capacity. Viscoelastic testing confirmed enhanced storage modulus (G') and gelling effect with higher kaolinite concentrations. These results demonstrate that kaolinite significantly enhances the density, filtration control, and rheological stability of $CaCO_3$ WBMs, supporting its application as a cost-effective and multifunctional additive in drilling operations.

Keywords:
drilling fluids, kaolinite, calcium carbonate, WBM

1. Introduction

Drilling fluids are indispensable in hydrocarbon extraction, serving critical functions such as transporting cuttings, stabilizing the wellbore, cooling and lubricating the drill bit, and maintaining formation pressure (**Adams 1985; Bourgoyne et al. 1986; Rabia 2001**). Depending on the base fluid, drilling fluids are broadly categorized into oil-based muds (OBMs) and water-based muds (WBMs). OBMs offer superior thermal stability and lubricity but face limitations due to high costs and strict environmental regulations (**Antia 2022; Mahmoud et al. 2024**). Consequently, WBMs have gained increasing attention as more sustainable and cost-effective alternatives (**Ahmed et al. 2021; Asad et al. 2024**).

Typical WBMs are composed of water, bentonite, and various polymers and salts to control rheology, fluid loss, and wellbore stability (**Dong et al. 2019; Gamal et al. 2019**). However, in shale formations which account for more than 75% of drilled reservoirs these fluids often induce swelling and dispersion, causing wellbore instability and drilling inefficiencies (**Muhammed et al. 2021; Ai et al. 2024**). Therefore, continuous efforts are directed toward developing additives that improve the performance of WBMs under demanding conditions.

Calcium carbonate ($CaCO_3$) is widely used in WBMs as a weighting and bridging agent due to its acid solubility, cost-effectiveness, and environmental compatibility (**Ryabtsev et al. 2022; Basfar & Elkatatny 2023**). It contributes to fluid-loss control and filter-cake formation, especially when appropriately sized (**Dehghani et al. 2019; Villada et al. 2022**). Meanwhile, kaolinite, a non-swelling clay mineral derived from feldspar and mica weathering, has shown potential for modifying drilling fluid properties without inducing the severe hydration issues associated with smectite clays (**Ameloko et al. 2020; Zhang et al. 2020**). Its platy structure and chemical stability make it an attractive candidate for improving fluid rheology and filtration characteristics (**Omotioma et al. 2024; Uwaezuoke et al. 2024**).

While previous studies have explored the use of kaolinite and other clays as viscosifiers or loss-control agents (**Omary et al. 2023; Omotioma et al. 2024**), limited research has focused on the combined performance of kaolinite with calcium carbonate in WBM formulations. The potential synergy between kaolinite's rheological influence and $CaCO_3$'s bridging effect has not been fully characterized, particularly in terms of density, pH, filtration, rheological, and viscoelastic properties.

* Corresponding author: Mohammed Abdalraheem
e-mail address: midoaltieng@gmail.com
Received: 16 June 2025. Accepted: 1 November 2025.
Available online: 13 March 2026

The achievements of this work include the experimental characterization of kaolinite $CaCO_3$ WBM systems, the quantification of dose response relationships showing how increasing kaolinite concentrations systematically alter fluid properties, and the identification of a novel synergistic interaction between kaolinite and $CaCO_3$ that enhances filter-cake formation and viscoelastic performance. Unlike previous laboratory studies, this work establishes a new baseline for optimizing environmentally friendly and cost-effective WBMs.

In this study, we systematically investigate the influence of kaolinite addition on the performance of $CaCO_3$-based WBMs. A comprehensive experimental program was designed to measure density, pH, filtration behaviour, rheological parameters, and viscoelastic properties across varying kaolinite concentrations.

2. Experimental Section

This section provides a detailed description of the materials used in the preparation of the drilling fluids. The study focuses on formulating water-based muds (WBMs) using kaolinite as a key additive. Each component was carefully selected based on its function in improving rheological and filtration properties. The specific purpose of each material and its role in this research are outlined below.

2.1. Materials

The present study focuses on water-based drilling muds (WBMs) formulated and tested to evaluate the effect of kaolinite as an additive on mud performance. WBMs were selected because they are the most widely used type of drilling fluid due to their environmental compatibility, cost-effectiveness, and ease of handling compared to oil-based muds (OBMs).

Water base mud: although water-based drilling fluids (WBDF) are frequently utilized with good technical and economic performance (**Ahmed et al. 2021**), their usage in extremely deep, divergent, and unconventional wells calls for particular considerations to conform to the high temperature and pressure circumstances (**Khashay et al. 2025**). The water-based system is the mud system that is most frequently employed in the sector (**Alcheikh & Ghosh 2017**). Water is the continuous phase, but the discontinuous phase may also include air or oil (emulsion muds or aerated mud) (**M-I Swaco 2009**).

Defoamer: a substance added to mud to reduce interfacial tension and allow trapped gas to more easily escape (**Bourgoyne et al. 1986**). Along with defoamer, mechanical degassing equipment is frequently employed. Defoamers include octyl alcohol, aluminum stearate, different glycols, silicones, and sulfonated hydrocarbons.

XC-Polymer: anionic XC-Polymer with fair tolerance for hardness ions and tolerance for salinity (**Blkoor & Fattah 2013**). XC is a finely ground substance that can vary in the amount of lingering bacterium debris and how easily it dissolves in water (**Hamed & Belhadri 2009; Davoodi et al. 2024**).

Starch: starch can act as an addition that can increase and improve the mud's viscosity while also regulating fluid loss (**Talukdar et al. 2018; Joel et al. 2023**). There are two significant ingredients in it: amylose and amylopectin (**Taiwo et al. 2011**).

KCl: drilling fluids containing potassium chloride are widely utilized to keep well bores stable (**Al-Bazali 2021**). To purchase additional time before water absorption caused the shales to collapse into the well bore, the potassium ion fits into the silicon tetrahedron matrix of clays and helps maintain the structure together (**Muhammed et al. 2021; Ai et al. 2024**).

KOH: potassium hydroxide is sometimes known as KOH informally. In potassium-based water muds, caustic potash is used to boost pH and alkalinity as well as to aid in maintaining the K+ ion concentration (**Otitigbe 2021**). It is extremely caustic, as the name suggests, and when dissolved in water, it produces heat. It is dangerous to use caustic potash without the right training and tools (**M-I Swaco 2009**).

Polymers like Polyanionic Cellulose (PAC) and Carboxymethyl Cellulose (CMC) are also common additives for filtration control and rheology modification (**Saadi et al. 2025; Khan et al. 2024; Li et al. 2020a; Li et al. 2020b**).

Calcium carbonate $CaCO_3$: oil- and water-based drilling fluids, work-over fluids, and completion fluids all use $CaCO_3$ as a bridging agent and/or weighing material (**Ryabtsev et al. 2022; Basfar & Elkatatny 2023**). There are several different particle sizes available, ranging from 325 mesh (35 μm) to 30 mesh (550 μm). Applications can also be sized to order. During drilling, workover, and completion operations, it is utilized to keep fluid from entering permeable zones and to prevent circulation loss (**Siddig et al. 2020**). Both aqueous and non-aqueous drilling fluids can use calcium carbonate (**Villada et al. 2022; Dehghani et al. 2019**).

Kaolinite: a common clay mineral used in drilling fluids, sometimes as a primary viscosifier or as a contaminant from drilled formations (**Ameloko et al. 2020; Omary et al. 2023; Omotioma et al. 2024; Zhang et al. 2020; Basfar et al. 2025; Uwaezuoke et al. 2024**).

Sodium solfite: effective removal of soluble oxygen from water-based drilling fluid systems is made possible by sodium sulfnite (**Rabia 2001**). By removing factors that encourage organic polymers' heat deterioration, sodium sulfnite also contributes to their longevity (**Davoodi et al. 2024**).

In this study, four water-based mud samples were prepared using the chemical precipitation method, following the procedures outlined in the American Petroleum Institute (API) standards (**API, 2010; API, 2014**). The final compositions of the drilling fluids are presented in **Table 1**.

Table 1. The WBDF Formulation

Component	Function	Ingredients	Mixing Time
Water	Base Fluid	308 ml	-
Defoamer	Antifoam	0.1 ml	1
XC-Polymer	Viscosifier	1.5 g	20
Starch	Fluid loss controller	6 g	20
KCL	Shale swelling controller	80 g	10
KOH	pH controller	0.3 g	1
Sodium Solfite	Scavenge soluble oxygen	0.25 g	1
$CaCO_3$ (50 M)	Weighting material	80 g	10

2.2. Drilling Fluid Preparation

To prepare drilling fluid, kaolinite clay with different concentrations 42.8 kg/m³ (15 lb/bbl), 85.6 kg/m³ (30 lb/bbl), and 128.4 kg/m³ (45 lb/bbl), were added to the base drilling fluid, and mixed with electric stirrer. Using a filter press apparatus, according to API requirements (American Petroleum Institute 2014), the filtration properties of drilling fluid, such as fluid loss and filter cake thickness, were measured using a filter pressure set at 2.07 MPa (300 psi) and 93°C (200°F), fluid loss over time was observed. **Table 1** shows the formulation of the WBDF.

To examine the effect of the kaolinite additive, SEM images of the filter cake were taken for the base drilling fluid and for drilling fluids with different kaolinite concentrations (**Rugang et al. 2014**). Although the primary focus of this study is the overall influence of kaolinite on drilling mud parameters, the SEM analysis was conducted to provide supporting evidence through the observation of filter-cake morphology following API standards (**American Petroleum Institute 2010; American Petroleum Institute 2014**).

3. Characterization of drilling fluids

This section describes the experimental methodology used to evaluate the performance of the prepared water-based drilling fluids. All procedures were conducted in accordance with the American Petroleum Institute (API) standards to ensure consistency and reliability of results. Tests were performed to measure rheological, density, and filtration properties, as well as pH control. The experimental design aims to quantify how varying kaolinite concentrations affect overall drilling fluid performance.

3.1. Particle Size Analysis

The analysis of the kaolinite powder revealed that the particle size distribution ranged from D_{10} = 0.68 µm, D_{50} = 2.8 µm, to D_{90} = 10.63 µm, with a median (D_{50}) value of 2.8 µm. Particle size measurements were performed using a laser diffraction particle size analyzer, which employs a dual-laser system with two detectors to accurately characterize a broad range of particle sizes, from fine to coarse fractions. Prior to measurement, all samples underwent wet dispersion to ensure proper deagglomeration and to improve measurement accuracy. The particle size distribution (PSD) of the sample is illustrated in **Figure 1**.

Figure 2 illustrates the morphology of kaolinite. The synthesized $CaCO_3$ made up semi-spherical particles with a particle size of less than 10 µm.

The XRD analysis (see **Figure 3**) reveals the mineral composition of kaolinite, with oxygen as the predominant element at 57.4 wt%. This is followed by silicon (24.1 wt%) and aluminum (10.8 wt%), consistent with the expected SiO_2 and Al_2O_3 components of kaolinite. Minor constituents include iron (5.6 wt%) and potassium (2.2 wt%).

4. Results and Discussion

The results obtained from the laboratory experiments are presented and discussed in this section. The data il-

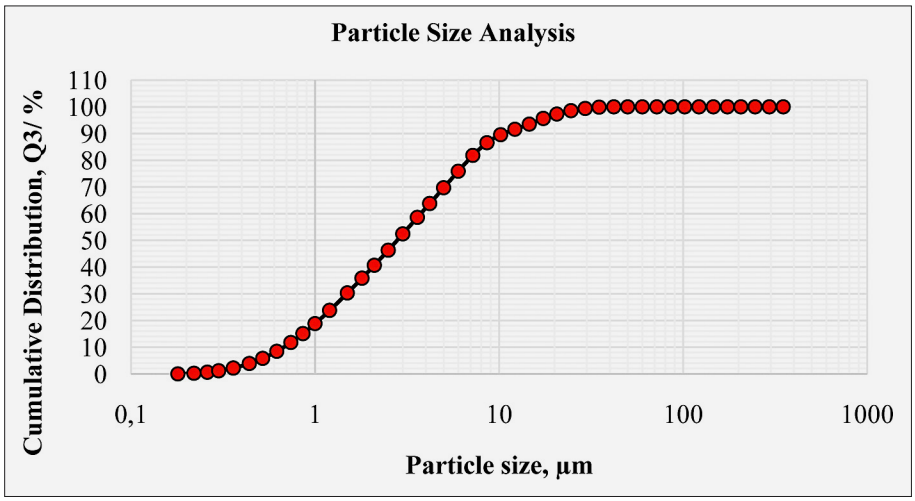


Figure 1. PSD Curves of The Drilled Cutting

lustrate how the addition of kaolinite influences the key physical and chemical properties of the water-based drilling muds. Comparisons are made between the base mud and the kaolinite-modified muds to assess changes in rheology, density, and filtration behaviour. The findings are further analyzed to identify correlations and practical implications for drilling operations.

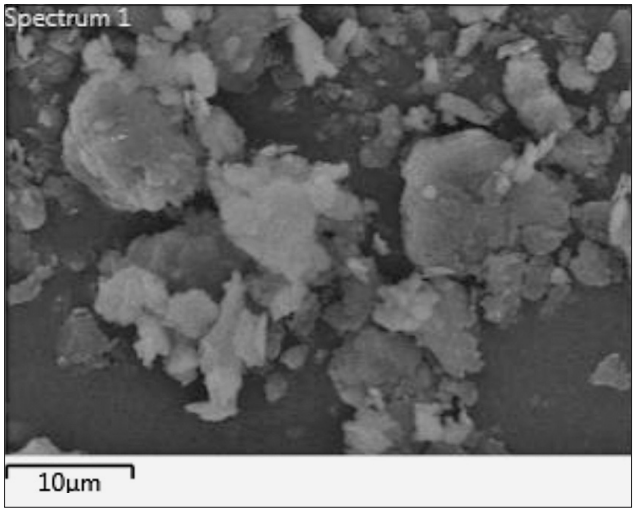


Figure 2. Kaolinite Particles Shape from SEM Image

4.1. Density and pH Measurement

The density (weight) of the base mud, measured using a mud balance apparatus at room temperature, was 1,216 kg/m³ (10.15 Ibm/gal). Introducing kaolinite led to a proportional increase in fluid density, reaching 1,318 kg/m³ (11.00 Ibm/gal) at a concentration of 128.4 kg/m³ (45 lb/bbl). Furthermore, **Figure 4** and **Figure 5** illustrate that the addition of kaolinite enhanced the pH of the base fluid.

4.2. Drilling Fluids Filtration

Filtration tests performed at 93°C (200°F) and 2.07 MPa (300 psi) over 30 minutes demonstrated a direct correlation between filtration cake thickness and both the duration of the test and the concentration of kaolinite. This indicates that higher kaolinite concentrations lead to a thicker filter cake. The relationship between filtration volume and time is visually represented in **Figure 6**.

In drilling, a thin filter cake is crucial for borehole stability and minimizing fluid loss. Filtration tests re-

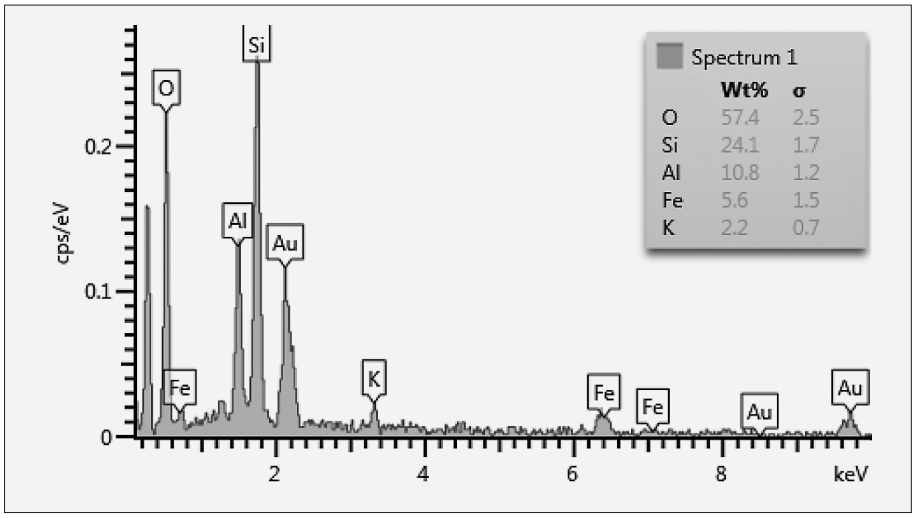


Figure 3. XRD Chart Showing the Mineral Composition of Kaolinite

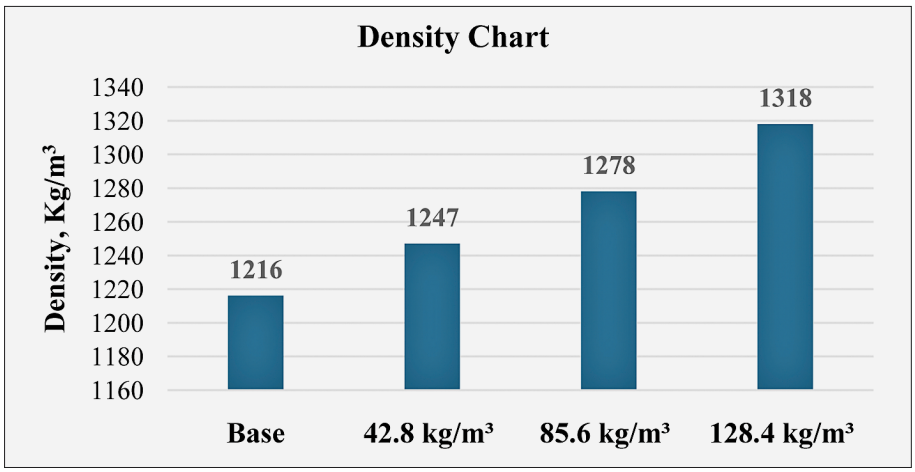


Figure 4. The Results of Density Measurements

vealed that the base sample exhibited a filtration volume of 0.5 cubic in and a cake thickness of 0.0098 in. However, as shown in **Figures 6** and **7**, the addition of kaolinite led to an increase in both filtration volume and filter cake thickness, deviating from the desired thin and low-permeable characteristics.

Expanding on the filtration test results, **Figure 8** provides visual evidence of the filter cake thickness immediately after the experiments. These photos, depicting the base sample and samples with varying kaolinite concentrations, further illustrate the increasing trend in filter cake thickness with higher kaolinite content, complementing the quantitative data presented in **Figure 6**.

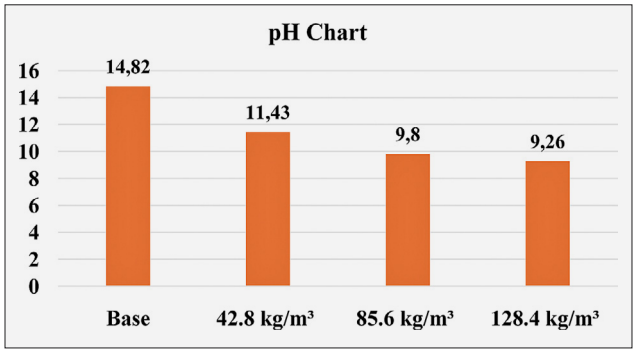


Figure 5. The Results of pH Measurements

4.3. Rheological Test

The rheological behaviour of drilling fluid with kaolinite concentrations of 42.8 kg/m³ (15 lb/bbl), 85.6 kg/m³ (30 lb/bbl), and 128.4 kg/m³ (45 lb/bbl) was evaluated at 93°C (200°F), as depicted in **Figure 9**. All fluids exhibited Bingham plastic behaviour, typical of drilling fluids. While improvements were observed in filter cake thickness and filtration, the rheological properties showed no significant alteration. This lack of substantial change may be attributed to the low kaolinite concentrations required to achieve the noted filtration enhancements. Notably, the addition of kaolinite at these concentrations had a negligible effect on the drilling fluid's pH and mud density.

Although several rheological models have been developed to describe the flow behaviour of drilling fluids, such as the Herschel–Bulkley, Vom Berg, and Hahn–Eyring models, the present study employs the Bingham

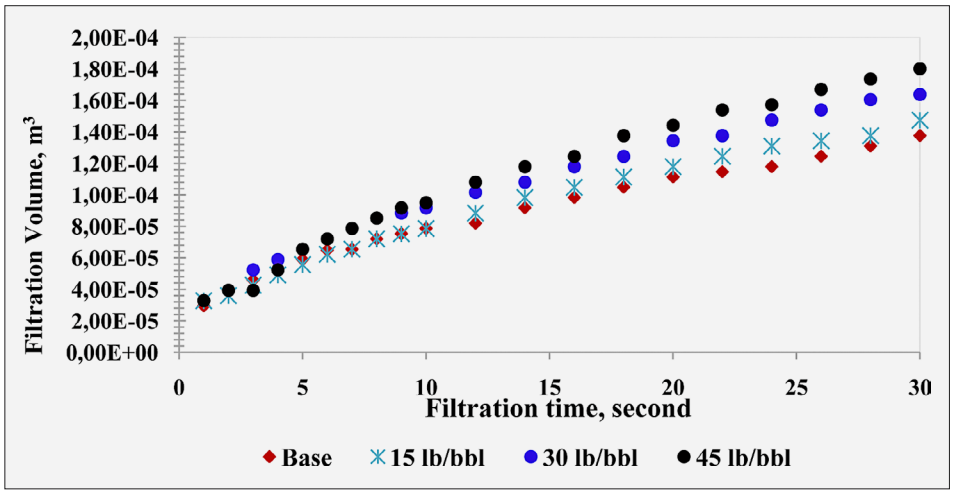


Figure 6. Filtration Time vs. Filtration Volume for the Drilling Fluids Samples

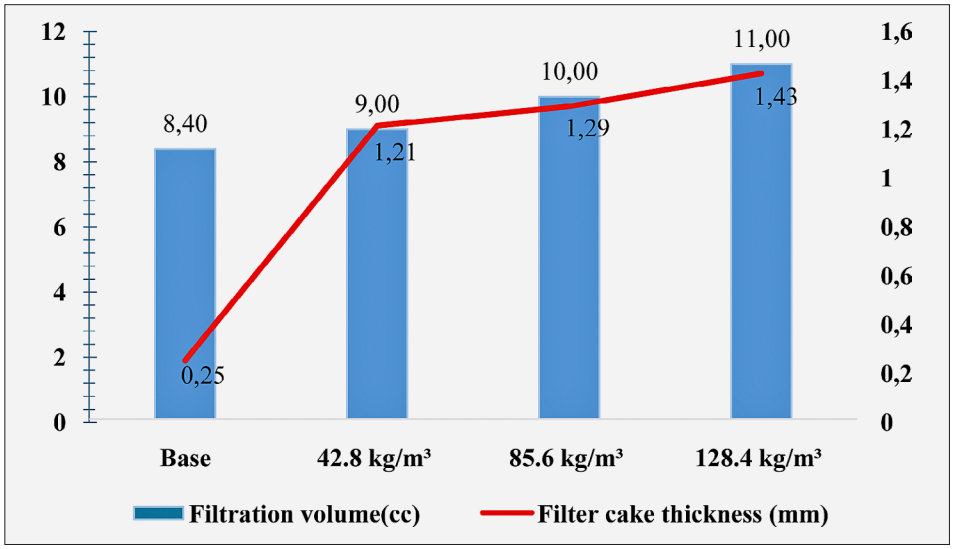


Figure 7. Filtration Volume and Cake Thickness

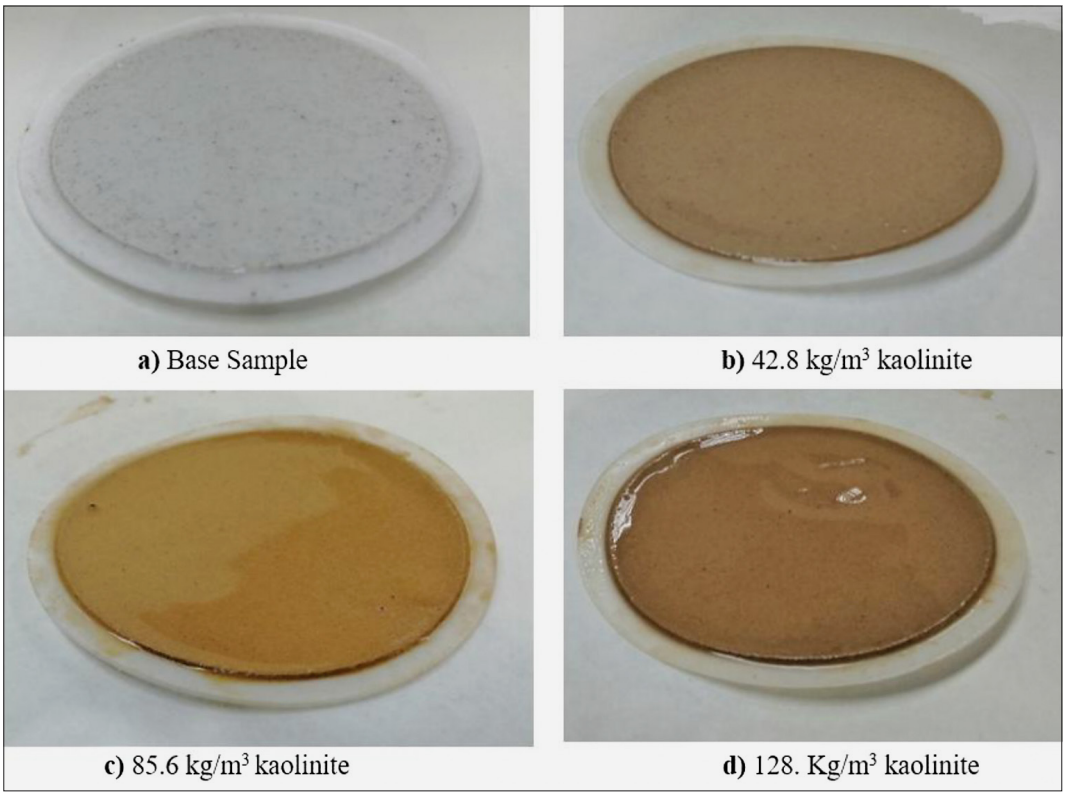


Figure 8. Filter Cake Thickness

Plastic model because it is the most commonly applied and recommended by the American Petroleum Institute (**API RP 13D 2010**) for field and laboratory analyses. The Bingham model provides a simple and practical approximation for water-based muds exhibiting moderate yield-stress behaviour under standard testing conditions. However, other advanced models have been shown to provide a more accurate representation of non-Newtonian and viscoplastic fluids. For example, the Vom Berg model (**Vom Berg 1981; Coussot et al. 2002**) has been successfully applied to describe drilling muds and other complex fluids by incorporating both yield stress and shear-thinning characteristics, often achieving higher correlation coefficients than the Bingham or Herschel–Bulkley models. Similarly, the Hahn–Eyring model (**Hahn & Eyring 1937**) has been used to represent the viscoelastic and plastic deformation behaviour of complex fluid systems and has demonstrated improved prediction of viscosity variation with shear rate. Recent investigations (**Ahmed et al. 2021**) have further confirmed that such advanced rheological models can provide more realistic characterization of water-based drilling fluids, particularly under high-pressure and high-temperature (HPHT) conditions. Therefore, while the Bingham Plastic model was adopted in the present study for its simplicity and industry relevance, future work should include a comparative evaluation using the Vom Berg and Hahn–Eyring models to achieve a more comprehensive understanding of the rheological behaviour of kaolinite-modified calcium carbonate muds.

Plastic Viscosity (PV), a parameter in the Bingham plastic model, refers to the flow resistance resulting from mechanical friction within the fluid. Experts in drilling fluids often consider PV a crucial indicator of the mud's solids content. Yield Point (YP) quantifies the minimum stress required to initiate fluid flow, reflecting the electrochemical and/or attractive forces between particles due to their orientation and concentration (colloidal size) (**Ahmed et al. 2021**). Apparent Viscosity (AV), based on the Bingham plastic rheology model, is determined using a direct-indicating rotational viscometer at 600 rpm (≈ 62.8 rad/s) (a shear rate of 1,022 s^{-1}) and is calculated as half of the dial reading. For example, a dial reading of 50 at 600 rpm corresponds to an AV of 25 mPa·s (25 cP). The results of this analysis, presented in **Figure 10**, illustrate the increasing trends of apparent viscosity, yield point, and plastic viscosity with increasing kaolinite concentration.

Figure 11 illustrates the relationship between gel strength and time for all drilling fluid samples. It suggests that the base sample exhibits a relatively small gelling effect over time in terms of viscoelasticity. However, the addition of kaolinite at different concentrations to the base sample clearly increases this gelling effect.

4.4. Amplitude, frequency and time sweep tests

To complement the rheological and filtration analyses, Scanning Electron Microscopy (SEM) was employed to investigate the surface morphology of the filter cakes. SEM images provide visual confirmation of the

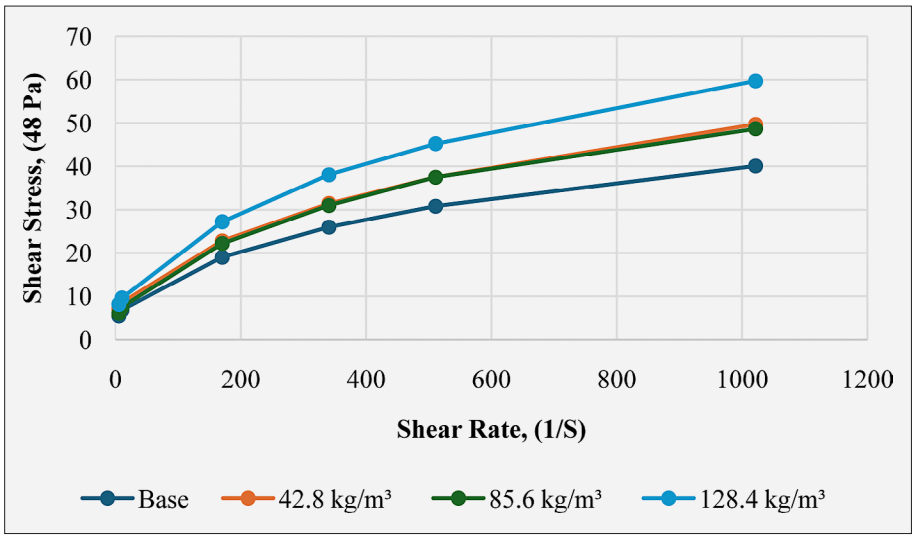


Figure 9. Rheological Behaviour of Both Drilling Fluids Samples

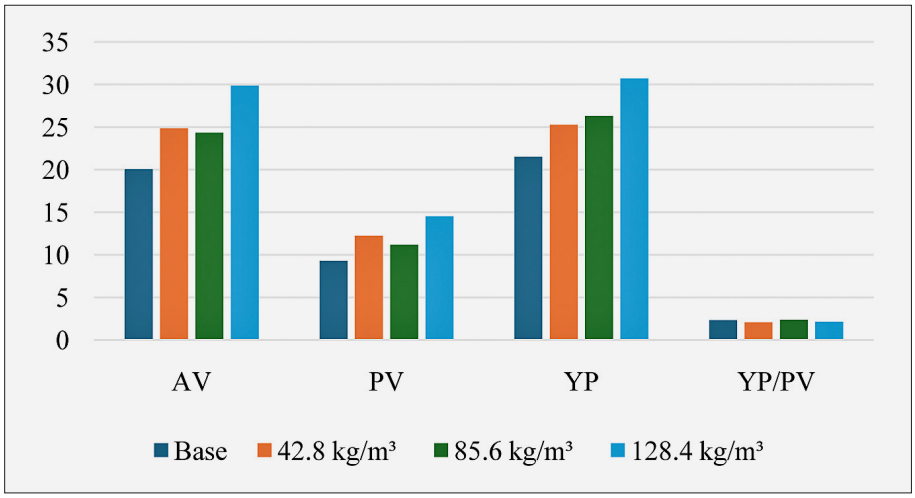


Figure 10. AV, PV, and YP for All Drilling Fluids Samples

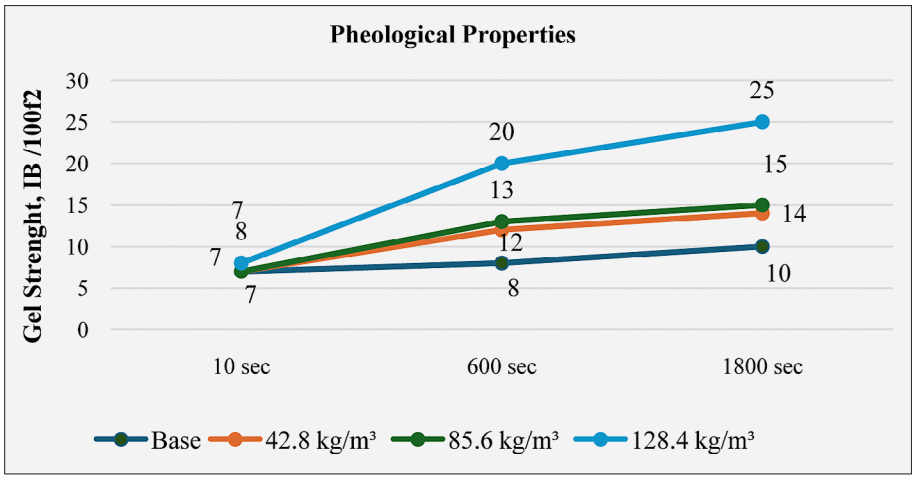


Figure 11. Gel Strength Over Time for All Drilling Fluid Samples

microstructural changes caused by the addition of kaolinite. This analysis helps to better understand how kaolinite particles influence the compactness and uniformity of the filter cake, which are important for controlling fluid loss and maintaining wellbore stability. The key observations are presented and discussed in the following figures.

4.4.1. Amplitude Test

Amplitude sweep tests were conducted to determine the linear viscoelastic domain by increasing the amplitude over time at a constant frequency. This can be performed using either controlled stress or controlled strain. Amplitude sweep is also known as strain sweep or stress

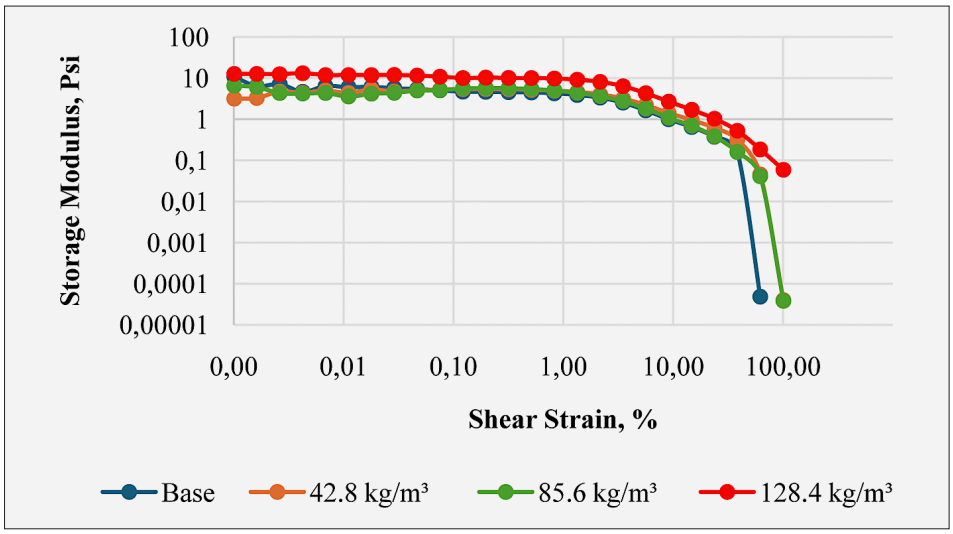


Figure 12. The Relationship Between Storage Modulus and Shear Strain

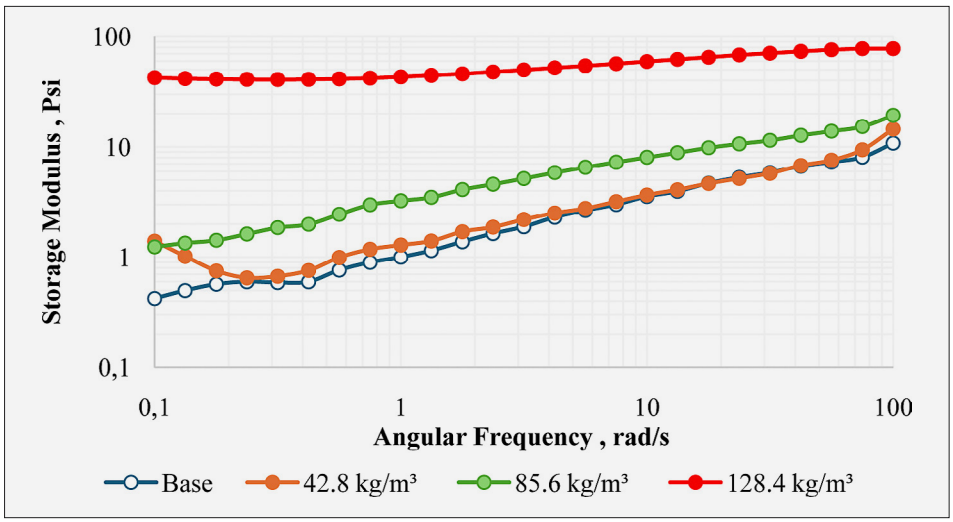


Figure 13. FRQ Sweep Plot

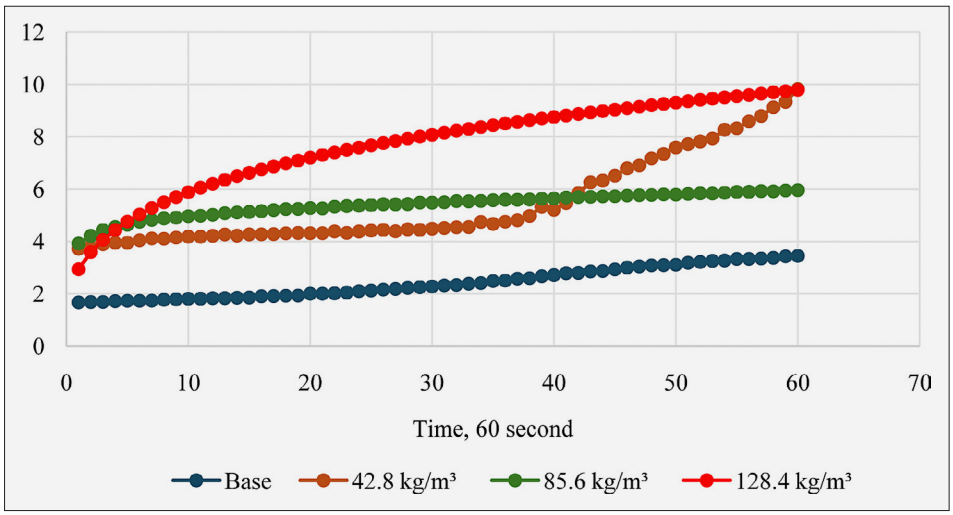


Figure 14. Time of Sweep

sweep. The linear viscoelastic range is defined as the stress or strain amplitude range within which the material's internal structure remains unchanged.

The linear viscoelastic (LVE) range was determined by plotting the storage modulus (G') and loss modulus (G") against strain (or stress) on logarithmic scales for both axes (see **Figure 12**). Within the LVE range, G' and G" exhibit constant values, indicating their independence from the stress or strain amplitude. Based on the results of this test, the LVE was found to be 1.94.

4.4.2. FRQ Sweeps

Frequency sweep tests, another type of oscillatory test, involve varying the frequency while maintaining a constant amplitude to investigate the time-dependent viscoelastic properties of the material. Typically, the frequency is scanned from high to low values. High-frequency oscillations probe short-term behavior, whereas low-frequency oscillations examine long-term behaviour. The results of this test, shown in **Figure 13**, indicate that increasing the kaolinite concentration in the fluid enhances its viscoelasticity, as evidenced by an increase in the storage modulus.

4.4.3. Time Sweep

Time sweep tests were conducted to monitor the evolution of the fluid's structure over time. By tracking changes in the elastic modulus, the formation and development of a gel-like structure can be studied. The results of this test, as shown in **Figure 14**, indicate that the base sample exhibits a limited gelling effect over time in terms of its viscoelastic viscosity.

5. Conclusions

This research provides a comprehensive investigation into the efficacy of kaolinite as a cost-effective, high-performance additive in calcium carbonate ($CaCO_3$) water-based drilling fluids (WBMs). While often viewed as a contaminant, this study reframes kaolinite as a valuable multifunctional material for enhancing drilling fluid properties. An extensive experimental program was conducted to quantify the effects of varying kaolinite concentrations on the rheological and filtration characteristics of a $CaCO_3$ WBM.

- The results demonstrate that the addition of kaolinite yields significant improvements in key performance indicators. A systematic increase in kaolinite concentration leads to a desirable enhancement of the rheological profile, including increased Plastic Viscosity, Yield Point, and gel strengths. This improved rheology is essential for efficient hole cleaning and suspension of solids. More critically, the study reveals that kaolinite acts as a superior filtration control agent, substantially reducing both API and HTHP (High-Temperature, High-Pressure) fluid loss. This effect is attributed to the synergistic interaction between the platy kaolinite particles and the $CaCO_3$ bridging particles, which co-operate to form a thin, robust, and low-permeability filter cake.
- A comparative analysis positions our findings within the context of existing literature, highlighting the unique advantages of kaolinite over conventional additives. Unlike swelling clays like bentonite, kaolinite provides controlled viscosity without excessive gelation, and it exhibits greater stability in certain ionic environments. Compared to excellent viscosifiers like attapulgite that offer poor fluid loss control, kaolinite demonstrates a dual functionality that is highly advantageous. Furthermore, it presents a thermally stable and significantly more economical alternative to synthetic polymers like polyanionic cellulose (PAC).
- The novel contribution of this work lies in its detailed characterization of the kaolinite/$CaCO_3$ synergy and the establishment of a clear dose-response relationship, offering a valuable baseline for fluid engineering. The practical implications for the drilling industry are substantial. The use of kaolinite is particularly applicable for drilling in cost-sensitive areas, through depleted or high-permeability zones where fluid loss control is paramount, and in formulating more environmentally benign fluid systems. The tangible benefits include significantly reduced drilling fluid costs, improved wellbore stability by minimizing shale hydration, enhanced operational efficiency through better hole cleaning, and minimized formation damage, ultimately contributing to safer and more economical drilling operations.

List of Terms Glossary

WBM	*Water Based Mud*
OBM	*Oil Based Mud*
$CaCO_3$	*Calcium Carbonate*
pH	*Potential of Hydrogen*
AMP	*Amplitude*
FRQ	*Frequency Sweep*
PSD	*Particle Size Distribution*
XRD	*X-Ray Diffraction*
KCL	*Potassium Chloride*
KOH	*Potassium Hydroxide*
API	*American Petroleum Institute*
SEM	*Scanning Electron Microscopy*
PV	*Plastic Viscosity*
YP	*Yield Point*
AV	*Apparent Viscosity*
LVE	*Linear Viscoelastic*

Acknowledgement

The authors would like to express their sincere gratitude to King Fahd University of Petroleum and Minerals, and specifically the College of Petroleum and Geoscience, for providing access to their laboratory facilities which made this research possible. We also extend our deepest appreciation to Professor Selah Elkatatny for his invaluable supervision and guidance throughout this project. Furthermore, we would like to thank Dr. Salim Basfar for his kind assistance and support in the laboratory. This work would not have been successfully completed and published without their generous support and contributions.

6. References

Adams NJ (1985). Drilling Engineering A Complete Well Planning Handbook. PennWell Books, Tulsa

Ahmed A, Alsaihati A, Elkatatny S (2021). An overview of the common water-based formulations used for drilling onshore gas wells in the Middle East. Arabian Journal for Science and Engineering 46(7): 6867–6877. https://doi.org/10.1007/s13369-021-05561-x

Ai E, Li Q, Liu Z, Zhang B, Wang L, Ma C (2024). Advanced trends in shale mechanical inhibitors for enhanced wellbore stability in water-based drilling fluids. Minerals 14(12): 1197. https://doi.org/10.3390/min14121197

Al-Bazali T (2021). Insight on the inhibitive property of potassium ion on the stability of shale: a diffuse double-layer thickness (κ−1) perspective. Journal of Petroleum Exploration and Production Technology 11: 2709–2723. https://doi.org/10.1007/s13202-021-01221-2

Alcheikh IM, Ghosh B (2017). A comprehensive review on the advancement of nondamaging drilling fluids. International Journal of Petrochemistry and Research 1 (1): 61–72. https://doi.org/10.18689/ijpr-1000111

Ameloko AA, Ogologo CE, Daramola OC, Babalola AO (2020). Assessment of clay materials for suitability in drilling mud formulation from part of Ondo State, South-West Nigeria. Journal of Petroleum Exploration and Production Technology 10: 2815–2828. https://doi.org/10.1007/s13202-020-00947-9

American Petroleum Institute (API) (2010). Rheology and hydraulics of oil-well fluids, API recommended practice 13d, sixth edition. API Publishing Services, Washington DC

American Petroleum Institute (API) (2014). Recommended practice for field testing water-based drilling fluids (API RP 13B-1 / ISO 10414-1:2008), 4th edn. Errata 1, August 2014

Antia M (2022). Environmental and public health effects of spent drilling fluid. Environmental Challenges 8: 100576. https://doi.org/10.1016/j.envc.2022.100576

Asad MS, Jaafar MT, Rashid FL, Togun H, Rasheed MK, Al-Obaidi MA, Al-Amir QR, Mohammed HI, Sarris IE (2024). Sustainable Drilling Fluids: A Review of Nano-Additives for Improved Performance and Reduced Environmental Impact. Processes 12(10): 2180. https://doi.org/10.3390/pr12102180

Basfar S, Elkatatny S (2023). Micronized calcium carbonate to enhance water-based drilling fluid properties. Scientific Reports 13: 18295. https://doi.org/10.1038/s41598-023-45776-y

Basfar S, Shokry A, Iqbal A, Elkatatny S, Alajmi S (2025). Evaluation of the effects of kaolin clay on the performance of barite-weighted oil-based drilling fluid. ACS Omega 10(10): 9976–9985. https://doi.org/10.1021/acsomega.4c07376

Blkoor SO, Fattah KA (2013). The influence of XC-polymer on drilling fluid filter cake properties and formation damage. Journal of Petroleum & Environmental Biotechnology 4(5): 157. https://doi.org/10.4172/2157-7463.1000157

Bourgoyne AT Jr, Millheim KK, Chenevert ME, Young FS Jr (1986). Applied Drilling Engineering. Society of Petroleum Engineers, Richardson, TX

Coussot P, Tocquer L, Lanos C, Ovarlez G. (2002). Rheological modeling of yield stress fluids: from Bingham to advanced viscoplastic models. Journal of Non-Newtonian Fluid Mechanics 102(2): 165–178.

Davoodi S, Al-Shargabi M, Wood DA, Rukavishnikov VS, Minaev KM (2024). Synthetic polymers: A review of applications in drilling fluids. Petroleum Science 21: 475–518. https://doi.org/10.1016/j.petsci.2023.08.015

Dehghani F, Kalantariasl A, Saboori R, Sabbaghi S, Peyvandi K (2019). Performance of carbonate calcium nanoparticles as filtration loss control agent of water-based drilling fluid. SN Applied Sciences 1: 1466. https://doi.org/10.1007/s42452-019-1446-8

Dong W, Pu X, Ren Y, Zhai Y, Gao F, Xie W (2019). Thermoresponsive bentonite for water-based drilling fluids. Materials 12(13): 2115. https://doi.org/10.3390/ma12132115

Gamal H, Elkatatny S, Basfar S, Al-Majed A (2019). Effect of pH on rheological and filtration properties of water-based drilling fluid based on bentonite. Sustainability 11(23): 6714. https://doi.org/10.3390/su11236714

Hamed SB, Belhadri M (2009). Rheological properties of biopolymers drilling fluids. Journal of Petroleum Science and Engineering 67(3–4): 84–90. https://doi.org/10.1016/j.petrol.2009.04.001

Hahn E, Eyring H. (1937). Theory of plastic deformation and flow in solids. Journal of Chemical Physics 5(11): 745–753.

Joel OF F, Ndubuisi EC (2023). Evaluation of local starch as a filtration control additive in water-based mud as substitute for imported samples for drilling operations in Nigeria. IOSR Journal of Engineering (IOSRJEN) 13(11): 42-48.

Khan MA, Li MC, Lv K, Sun J, Liu C, Liu X, Shen H, Dai L, Lalji SM, et al. (2024). Cellulose derivatives as environmentally-friendly additives in water-based drilling fluids: A review. Carbohydrate Polymers 342: 122355. https://doi.org/10.1016/j.carbpol.2024.122355

Khashay M, Zirak M, Sheng JJ, Ganat T, Esmaeilnezhad E (2025). Elevated temperature and pressure performance of water based drilling mud with green synthesized zinc oxide nanoparticles and biodegradable polymer. Scientific Reports 15: 11930. https://doi.org/10.1038/s41598-025-96900-z

Li MC, Tang Z, Liu C, Huang R, Koo MS, Zhou G, Wu Q (2020). Water-redispersible cellulose nanofiber and polyanionic cellulose hybrids for high performance waterbased drilling fluids. Industrial & Engineering Chemistry Research 59 (32): 14352–14363. https://doi.org/10.1021/acs.iecr.0c02644

Li MC, Wu Q, Han J, Mei C, Lei T, Lee SY, Gwon J (2020). Overcoming salt contamination of bentonite water-based drilling fluids with blended dual-functionalized cellulose nanocrystals. ACS Sustainable Chemistry & Engineering 8 (31): 11569–11578. https://doi.org/10.1021/acssuschemeng.0c02774

M-I Swaco (2009). Drilling Fluids Engineering Manual, Version 2.2. M-I Swaco - A Schlumberger Company, Houston

Mahmoud H, Mohammed AAA, Nasser MS, Hussein IA, El-Naas MH (2024). Green drilling fluid additives for a sustainable hole-cleaning performance: a comprehensive review. Emergent Materials 7: 387–402. https://doi.org/10.1007/s42247-023-00524-w

Muhammed NS, Olayiwola T, Elkatatny S (2021). A review on clay chemistry, characterization and shale inhibitors for water-based drilling fluids. Journal of Petroleum Science and Engineering 206: 109043. https://doi.org/10.1016/j.petrol.2021.109043

Omary PM, Ricky EX, Kasimu NA, Madirisha MM, Kilulya KF, Lugwisha EHJ (2023). Potential of kaolin clay on formulation of water based drilling mud reinforced with biopolymer, surfactant, and limestone. Tanzania Journal of Science 49(1): 218–229. https://dx.doi.org/10.4314/tjs.v49i1.19

Omotioma M, Nkemdilim Dorothy O, Mbah GO, Okechukwu ES, Azuka EJ (2024). Effects of process factors on the characteristics of water based mud viscosified by kaolin and bentonite. World Scientific News 192: 270-288.

Otitigbe FE (2021). Evaluation of pH of drilling fluid produced from local clay and additives. Journal of Applied Sciences and Environmental Management 25(4): 561-566. https://dx.doi.org/10.4314/jasem.v25i4.11

Rabia H (2001). Well Engineering and Construction. Entrac Consulting Limited, London.

Rugang Y, Guancheng J, Wei L, Tianqing D, Hongxia Z (2014). Effect of water-based drilling fluid components on filter cake structure. Powder Technology 262: 11-18. https://doi.org/10.1016/j.powtec.2014.04.060

Ryabtsev P, Kuksov V, Khomutov A (2022). Smart bridging agent enhanced well productivity in depleted production formation. Paper AADE-22-FTCE-052 presented at the AADE Fluids Technical Conference and Exhibition, Houston, Texas, 19-20 April.

Saadi R, Hamidi H, Wilkinson D (2025). Optimizing filtration properties of water-based drilling fluids: Performance of PAC variants and synergistic effects. Colloids and Surfaces A: Physicochemical and Engineering Aspects 715: 136590. https://doi.org/10.1016/j.colsurfa.2025.136590

Siddig O, Mahmoud AA, Elkatatny S (2020). A review of different approaches for water-based drilling fluid filter cake removal. Journal of Petroleum Science and Engineering 192: 107346. https://doi.org/10.1016/j.petrol.2020.107346

Taiwo A, Joel O, Kazeem A (2011). Investigation of local polymer (Cassava Starches) as a substitute for imported sample in viscosity and fluid loss control of water-based drilling mud. ARPN Journal of Engineering and Applied Sciences 6(12): 43–48

Talukdar P, Kalita S, Pandey A, Dutta U, Singh R (2018). Effectiveness of different starches as drilling fluid additives in non damaging drilling fluid. International Journal of Applied Engineering Research 13(16): 12469-12474.

Uwaezuoke N, Chukwuebuka UC, Muhammed AA, Duru U (2024). Evaluation of kaolin clay polymeric nanoparticles for improved water-based mud properties. International Journal of Oil, Gas and Coal Engineering 12(1): 36-45. https://doi.org/10.11648/ogce.20241201.15

Villada Y, Busatto C, Casis N, Estenoz D (2022). Use of synthetic calcium carbonate particles as an additive in water-based drilling fluids. Colloids and Surfaces A: Physicochemical and Engineering Aspects 652: 129801. https://doi.org/10.1016/j.colsurfa.2022.129801

Vom Berg R. (1981). A new rheological model for non-Newtonian fluids applied to drilling muds. Journal of Petroleum Technology 33(3): 657–662.

Zhang JR, Xu MD, Christidis GE, Zhou CH (2020). Clay minerals in drilling fluids: functions and challenges. Clay Miner 55(1): 1–11. https://doi.org/10.1180/clm.2020.10

SAŽETAK

Utjecaj kaolinita na isplaku na bazi vode koja sadržava kalcijev karbonat

Ovim je istraživanjem sistematskim laboratorijskim ispitivanjima analiziran utjecaj dodavanja kaolinita na isplaku na bazi vode (engl. *Water Based Mud*, WBM) koja sadržava kalcijev karbonat. Kaolinit je u standardni WBM na bazi $CaCO_3$ dodavan u koncentracijama od 42,8 kg/m³ (15 lb/bbl), 85,6 kg/m³ (30 lb/bbl) i 128,4 kg/m³ (45 lb/bbl) te je analiziran njegov utjecaj na gustoću, pH, filtracijska i reološka svojstva te viskoelastično ponašanje isplake. Sa 128,4 kg/m³ (45 lb/bbl) kaolinita gustoća osnovne isplake (10,15 g/cm³) povećala se na 11,00 g/cm³, dok je pH rastao proporcionalno s udjelom kaolinita. Filtracijski testovi na 93,3 °C (200 °F) i 2,07 bar (300 psi) pokazali su da uzorak osnovne isplake proizvodi debljinu filtarskoga kolača od 0,0098 in, koja se progresivno povećavala s dodatkom kaolinita. Mjerenja reoloških svojstava pokazala su Binghamovo plastično ponašanje u svim uzorcima, s prividnom viskoznošću koja se povećavala od 25 cP u osnovnoj isplaci do 33 cP pri 128,4 kg/m³ (45 lb/bbl) dodanoga kaolinita. Točka tečenja i čvrstoća gela također su pokazale dosljedan rast, što upućuje na poboljšani kapacitet suspenzije. Ispitivanja viskoelastičnosti potvrdila su povećan modul pohrane (engl. *enhanced storage modulus*) (G') i učinak geliranja pri višim koncentracijama kaolinita. Ovi rezultati pokazuju da kaolinit znatno poboljšava gustoću, kontrolu filtracije i reološku stabilnost $CaCO_3$ WBM-ova, što ide u prilog njegovoj primjeni kao isplativoga i multifunkcionalnoga aditiva u operacijama bušenja.

Ključne riječi:
isplaka, kaolinit, kalcijev karbonat, isplaka na bazi vode (WBM)

Author's contribution

Mohammed Abdalraheem (M.Sc. in Petroleum Engineering from Institut Teknologi Bandung – ITB): conceptualization, methodology, theoretical modelling, simulation, writing – original draft preparation, literature review, experimental investigation, data analysis, and visualization. **Basfar** (Postdoctoral Researcher, Department of Petroleum Engineering, King Fahd University of Petroleum and Minerals – KFUPM): supervision, project administration, methodology, validation, writing – review and editing, and technical guidance in drilling fluid research. **Elkatatny** (Professor, Department of Petroleum Engineering, KFUPM; Associate Editor for Journal of Energy Resources Technology and Arabian Journal for Geosciences): conceptual supervision, provision of advanced laboratory facilities and research infrastructure, review and editing, technical oversight in drilling fluid and reservoir engineering, and strategic support for research implementation.
All authors have read and agreed to the published version of the manuscript.

RGNZ/MGPB

Management of Frame-Anchor Fastening Parameters for Preparatory Excavations in Monorail-Based Heavy Cargo Delivery

Rudarsko-geološko-naftni zbornik
(The Mining-Geology-Petroleum Engineering Bulletin)
DOI: 10.17794/rgn.2026.2.12

Original scientific paper

Andrii Herasymenko[1], Leonid Shyrin[1], Rostyslav Yegorchenko[1], Ivan Iniutkin[1], Yuliya Pazynich[2,3]*

[1] *Dnipro University of Technology, Department of transport systems and energy-mechanical complexes, 19 Yavornytskoho Ave., 49-005, Dnipro, Ukraine.*

[2] *AGH University of Krakow, Faculty of Management, al. Mickiewicza 30, Krakow, 30059, Poland.*

[3] *Dnipro University of Technology, Department of philosophy and pedagogy, 19 Yavornytskoho Ave., 49-005, Dnipro, Ukraine.*

Abstract

This article presents a comprehensive study on the management and optimization of frame-anchor support systems for seam preparatory excavations designed for the transportation of large-tonnage cargo via suspended monorail transport. With the intensification of underground mining operations and the increasing use of heavy mechanized transport, ensuring the stability and safety of mine workings under dynamic load conditions has become a critical challenge for engineering. The research proposes an innovative support technology based on the combined fastening of monorail systems to the crowns of metal arches and directly to the roof using deep-embedded anchors. This approach aims to reduce dynamic impacts on the excavation roof and improve the overall reliability of the support system. To evaluate the effectiveness of the proposed support design, a numerical modelling method was employed to simulate the interaction of components within the dynamic system "suspended monorail – support – rock mass." The stress-strain behaviour of the frame-anchor structure under real load scenarios was analyzed using SolidWorks Simulation software. During the simulation, various parameters were systematically varied, including the spacing of support frames, the length and anchorage depth of the rock bolts, and the mechanical properties of the surrounding rock mass. The results of the analysis enabled the identification of rational design parameters that minimize deformation and enhance load-bearing capacity. In particular, optimal combinations of frame spacing and anchor configurations were found to significantly reduce stress concentrations and improve the stability of preparatory workings under dynamic loading from moving monorail trains. The study demonstrates that effective management of support system parameters can lead to improved safety, reduced material consumption, and faster development of mining panels. The findings have practical significance for the design of underground transport routes and can be incorporated into normative documents governing support systems in dynamically loaded mine environments.

Keywords:

Frame-anchor fastening, Monorail transportation, Heavy cargo delivery, Stress–strain analysis, Mining infrastructure managemen, Dynamic load distribution

1. Introduction

The implementation of suspended monorail tracks as the primary transportation system in the development of mineral deposits plays a crucial role in accelerating the progress of seam-level district excavations (**Herasymenko et al., 2023**). This method enhances logistical efficiency and reduces the time required for preparatory operations (**Rastsvietaiev et al., 2015**). However, when monorail systems are mounted using traditional fastening schemes, typically attached directly to arch supports, the dynamic behaviour of the surrounding rock mass under stress becomes a significant concern. Intense deformation of the rock mass can lead to alterations in the stress distribution, which, in turn, negatively impacts the technical condition and reliability of the transportation infrastructure (**Herasymenko et al., 2023; Rastsvietaiev et al., 2015; Kononenko et al., 2024**). As a result, effective management of support systems becomes essential to maintain the stability and safety of both the monorail structures and the surrounding excavation (**Babets et al., 2023**). An optimized management approach should include continuous monitoring, adaptive reinforcement strategies, and the integration of innovative fastening technologies to ensure consistent performance under variable geological and loading conditions (**Rastsvietaiev et al., 2015; Aitkazinova et al., 2022**).

* Corresponding author: Yuliya Pazynich
e-mail address: jpazynich@ukr.net

Received: 8 September 2025. Accepted: 1 November 2025.
Available online: 13 March 2026

Studies (**Herasymenko et al., 2023**) have shown that the transportation of large-tonnage cargo along deformed monorail tracks generates dynamic loads that can lead to the failure of arch supports and even roof collapses. These loads intensify the degradation of structural elements and significantly compromise the safety of underground workings. Under conditions of intensified mining operations, traditional technological schemes for auxiliary transportation prove to be particularly vulnerable to changes in the geomechanical environment (**Rastsvietaiev et al., 2015; De Borst et al., 2012**). Their limited adaptability to evolving stress conditions and deformation zones makes them unsuitable for high-performance and safe mining systems (**Rastsvietaiev et al., 2015; Tereshchuk et al., 2018**). Effective management of transportation infrastructure is essential, requiring a proactive approach to monitoring, maintenance, and reinforcement of support systems (**Aitkazinova et al., 2022; De Borst et al., 2012; Tereshchuk et al., 2018; Khomenko et al., 2023**). To address these challenges, innovative technical solutions must be developed and implemented to enhance the structural resilience, operational stability, and adaptability of monorail-based transport systems under dynamic loading conditions (**Herasymenko et al., 2023; Rastsvietaiev et al., 2015; Tereshchuk et al., 2018; Khomenko et al., 2023; Bondarenko et al., 2021**).

One of the critical tasks is the safe and efficient transportation of large-tonnage equipment, such as sections of mechanized roof supports, shearer components, and other heavy machinery, to designated installation chambers (**Rastsvietaiev et al., 2015; Khomenko et al., 2018**). Traditional transportation methods, particularly overground rail systems, often lack the necessary flexibility and adaptability to function effectively under such conditions (**Bondarenko et al., 2021; Khomenko et al., 2018; Kononenko et al., 2023**). Their performance is typically constrained by irregular layouts, limited turning radii, and unstable ground surfaces inherent to the mine environment (**Herasymenko et al., 2023; Kononenko et al., 2024; Zienkiewicz et al., 2013**). This lack of adaptability can lead to delays, increased labor costs, and heightened safety risks for personnel and equipment. Feasibility of implementing such innovative solutions is particularly relevant during the preparation of new mining panels, as well as during installation and dismantling operations (**Kononenko & Khomenko, 2010**). These stages of mine development involve complex logistical challenges and increased operational risks, especially in confined underground environments. Therefore, the management of transportation systems in these critical phases must focus on adopting more resilient and adaptable technologies, such as suspended monorail systems, to ensure operational continuity and safety.

In international mining practice, the development of coal seams using high-performance mining complexes encounters similar challenges related to transportation and infrastructure stability (**Rastsvietaiev et al., 2015**). These challenges are typically addressed by introducing alternative types of auxiliary transportation and implementing methods to maintain their technical condition in response to specific geological and operational conditions (**Rastsvietaiev et al., 2015; Moldabayev et al., 2021**). Ensuring the continuous functionality of transportation systems under dynamic mining environments is critical for both productivity and safety (**Kononenko & Khomenko, 2010; Moldabayev et al., 2021; Kovalevska et al., 2020**). One of the most promising developments in this area is the adoption of suspended monorail diesel locomotives, which offer enhanced maneuverability and load-bearing capacity in confined underground spaces (**Khomenko et al., 2023**; **Yegorchenko et al., 2022**). To ensure their effective application, it is essential to evaluate their operational performance based on the integrated behaviour of components within the transport-technological system "suspended monorail – mine support – rock mass." Such system-level analysis allows for the rational management of technical parameters and supports the development of robust, adaptive transportation infrastructure in modern mining operations.

It has been experimentally confirmed that, at present, the interaction parameters between the components of the technological system "suspended monorail – mine support – rock mass" remain insufficiently studied and poorly understood (**Herasymenko et al., 2023**). This knowledge gap limits the ability to predict system behaviour under varying mining conditions and complicates the development of effective transport management strategies (**Sala & Bieda, 2021**). As mining operations become more dynamic and equipment loads increase, the lack of comprehensive data on these interactions poses risks to both infrastructure integrity and operational safety (**Rastsvietaiev et al., 2015**; **Khomenko, Kononenko & Bilegsaikhan, 2018**). The issues of operational monitoring of the technical condition of suspended monorail tracks in district workings are of critical importance. Particular attention must be given to determining the maximum allowable dynamic loads that the system can safely withstand under real underground conditions (**Falshtynskyi et al., 2020**). Addressing these challenges requires a combination of in-situ field observations, numerical modelling, and theoretical justification to develop reliable criteria for design, maintenance, and safety management (**Herasymenko et al., 2023; Rastsvietaiev et al., 2015; Babets et al., 2023; Vlasov et al., 2022**).

Based on in-mine research into the interaction between suspended monorail components and arch supports, it was established that zones of deformed roof rock tend to form around the crowns of load-bearing arches to which the monorail system is attached during the transportation of large-tonnage cargo through seam-level district workings (**Rastsvietaiev et al., 2015**).

These deformations compromise both the structural integrity of the support system and the safety of underground operations (**Kosenko et al., 2025**). The primary cause of such deformation has been identified as dynamic loading, particularly at the joints between monorail beams and in sections of the track characterized by alternating elevation profiles (**Babets et al., 2023; Khomenko et al., 2023; Yegorchenko et al., 2022; Kosenko et al., 2025**). These areas are especially prone to stress, concentration and fatigue due to the uneven distribution of loads (**Babets et al., 2023; Bondarenko et al., 2021; Moldabayev et al., 2021; Kovalevska et al., 2020; Kononenko et al., 2016**). Additionally, emergency braking scenarios introduce sudden dynamic overloads, which are transferred from the monorail beams to the arch supports, exacerbating structural instability (**Babets et al., 2023; Kovalevska et al., 2020; Tokarczyk, 2016**). The comprehensive understanding of these interactions is essential for the effective management and design of support systems capable of withstanding the operational demands of modern monorail transport in underground mining environments (**Rastsvietaiev et al., 2015; Khomenko et al., 2023; Lewicka & Lewicka, 2019**).

Such disturbances in the technical condition of the monorail support, along with increased dynamic loads on the arch supports and surrounding rock mass, have a negative impact on the transportation process and reduce the throughput capacity of haulage workings. Therefore, the aim of this study is to develop innovative technological schemes involving combined frame-anchor support for preparatory workings and an improved monorail support system for suspended monorails. The objective is to justify and determine the optimal parameters of these systems to ensure the safe and efficient transportation of large-tonnage cargo under complex and dynamic operational conditions.

Literature Review on Frame-Anchor Fastening Parameters for Preparatory Excavations in Monorail-Based Heavy Cargo Transportation.

Efficient management of underground mining operations critically depends on the stability and reliability of preparatory excavations, especially when heavy cargo transport is involved (**Rastsvietaiev et al., 2015; Vladyko et al., 2025**). Frame-anchor fastening systems have emerged as a fundamental component in maintaining the structural integrity of mine workings subjected to dynamic loads from suspended monorail transport (**Herasymenko et al., 2023; Rastsvietaiev et al., 2015; Khomenko et al., 2018; Kumbasaroglu, 2010**). Studies emphasize the importance of optimizing fastening parameters, such as anchor length, spacing, and depth, to ensure load distribution and prevent excessive deformation or failure of supports (**Kononenko & Khomenko, 2010; Mackiewicz et al., 2022**). Effective mine management integrates monitoring of these parameters to minimize downtime and enhance safety during material handling operations (**Dychkovskyi et al., 2024**).

The transportation of large-tonnage cargo via suspended monorail systems generates complex dynamic loads that interact with the rock mass and support structures (**Kononenko & Khomenko, 2010; Kang et al., 2020**). Research has shown that traditional fastening schemes may not adequately address the dynamic effects, leading to accelerated wear and failure of arch supports and anchors (**Kononenko & Khomenko, 2010; Moldabayev et al., 2021; Kang et al., 2020; Carrascal et al., 2007**). Consequently, investigations focus on developing combined fastening techniques, such as frame-anchor systems, that better absorb and redistribute stress (**Kang et al., 2020; Carrascal et al., 2007; Dychkovskyi et al., 2024**). These studies highlight the need for adaptive support designs tailored to site-specific geomechanical conditions and operational demands.

Recent advancements in artificial intelligence (AI) and neural networks have opened new horizons for predictive management and optimization of mine support systems (**Psyuk & Polyanska, 2024**). These technologies offer the capability to process and interpret large volumes of data collected from sensors embedded throughout the underground mine environment (**Rastsvietaiev et al., 2015; Blinov et al., 2025**). By continuously monitoring parameters such as stress levels, displacement, vibration, and load distribution, AI-driven models can provide real-time assessments of support integrity and detect early signs of potential failure (**Psyuk & Polyanska, 2024; Chen & Chen, 2024**). Neural networks are highly effective in simulating complex, nonlinear interactions between suspended monorail loads, structural support elements, and the surrounding rock mass under dynamic operating conditions (**Psyuk & Polyanska, 2024; Zapukhliak et al., 2019**). These models enable the identification of hidden patterns and relationships that traditional analytical methods may overlook. As a result, intelligent systems can facilitate the dynamic adjustment of fastening parameters, such as anchor length, spacing, and installation angles, based on changing geomechanical and operational conditions (**Sosnowski et al, 2024**). The integration of AI into mine supports design and monitoring significantly enhances operational reliability, safety, and the overall efficiency of transportation systems in deep and structurally complex mining environments (**Rastsvietaiev et al., 2015; Kononenko & Khomenko, 2010; Zapukhliak et al., 2019; Sosnowski, Dyczko & Kamiński, 2024; Polyanska et al., 2024**).

Sustainable mining practices increasingly demand that support and transportation systems are designed not only for operational efficiency but also for minimal environmental impact (**Khomenko et al., 2018; Lewicka & Lewicka, 2019; Bashynska et al., 2024**). Frame-anchor

fastening systems must be evaluated in terms of both their mechanical performance and their influence on the surrounding geological and hydrogeological environment (**De Borst et al., 2012**; **Myronova et al., 2025**). Improperly designed or overloaded support systems can result in excessive deformation, leading to ground subsidence, fracture propagation, or contamination of groundwater resources (**Moldabayev et al., 2021; Kononenko et al., 2023**). Such consequences pose significant environmental risks and may compromise the long-term stability of the mine and its surrounding ecosystem (**Lewicka & Lewicka, 2019**; **Lapshyn et al., 2025**). To address these challenges, recent research has focused on integrating environmental monitoring with structural management strategies, including the use of predictive modelling and geotechnical feedback systems (**Lewicka & Lewicka, 2019**; **Kononenko et al., 2023; Lapshyn et al., 2025; Fedoreiko et al., 2025**). This holistic approach helps to balance the goals of resource extraction with the need for environmental protection, thereby contributing to the long-term sustainability and regulatory compliance of mining operations.

Innovations in fastening materials, including high-strength alloys, fiber-reinforced composites, and corrosion-resistant coatings, have been extensively investigated to enhance the durability and load-bearing capacity of frame-anchor systems in mining environments (**Lewicka & Lewicka, 2019**; **Kumbasaroglu, 2010, Symanovych et al., 2015**). These advanced materials are designed to withstand the harsh conditions of underground operations, including exposure to moisture, aggressive geochemistry, and fluctuating mechanical loads (**Kononenko et al., 2023; Kononenko et al., 2016; Kumbasaroglu, 2010; Stöcklein & Kaliske, 2022**). In parallel, research has focused on improving installation techniques, such as deep embedding, prestressed anchoring, and chemical grouting, to increase the overall quality and reliability of anchorage, particularly under dynamic loading conditions generated by suspended monorail transport (**Herasymenko et al., 2023; Rastsvietaiev et al., 2015; Kononenko & Khomenko, 2010; Beshta et al., 2015**). The performance of these materials and installation methods under cyclical and impact loading is a key area of study, as it directly informs the development of technical standards and guidelines for the selection and application of fastening systems in preparatory mine workings (**Kumbasaroglu, 2010; Symanovych et al., 2015; Jiang et al., 2025**). Ultimately, the integration of advanced materials with optimized installation practices contributes to safer, more efficient, and longer-lasting support structures in modern underground mining operations.

Numerical methods and finite element modelling play a crucial role in understanding the stress-strain behaviour of combined frame-anchor support under dynamic conditions. Simulation tools allow researchers to vary design parameters systematically and predict their impact on system stability and deformation patterns (**Stöcklein & Kaliske, 2022; Sobolev et al., 2025**). This approach supports the design of fastening schemes that optimize load transfer and minimize risks of failure, facilitating evidence-based decision-making in mine management (**Vladyko et al., 2025; Zhai et al., 2025**). Despite progress, challenges remain in fully characterizing the complex interactions in the "suspended monorail – mine support – rock mass" system, especially under varied geological conditions and intensified operational loads. Issues such as real-time monitoring under harsh underground environments, integration of AI models with existing mine management systems, and scaling laboratory findings to field applications require ongoing research (**Kosenko et al., 2025; Psyuk & Polyanska, 2024**, **Zapukhliak et al., 2019**; **Campos Zabala, 2023**). Addressing these gaps is essential for developing robust fastening solutions adaptable to evolving mining demands.

The current body of literature indicates a clear need for comprehensive studies that combine experimental field data, predictive modelling, and advanced computational simulations to refine frame-anchor fastening parameters specifically for monorail-based heavy cargo transportation. The purpose of this research is to develop innovative technological schemes and establish optimal fastening configurations that ensure safe, efficient, and environmentally sustainable transportation in complex underground mining conditions. This work aims to contribute to improved management practices by integrating multidisciplinary approaches for enhanced operational resilience.

2. Methods

The methodology of this study is based on an integrated approach combining numerical modelling, structural simulation, and field data analysis to determine optimal parameters for frame-anchor fastening systems in preparatory mine workings used for monorail-based heavy cargo transportation (**Herasymenko et al., 2023; Rastsvietaiev et al., 2015; Babets et al., 2023; Carrascal et al., 2007**). The study begins with the development of a conceptual model of the transport-technological system "suspended monorail – frame-anchor support – rock mass," taking into account the dynamic interaction between these components under operational conditions. Using SolidWorks Simulation software, finite element analysis (FEA) was conducted to evaluate the stress-strain behaviour of various support configurations under dynamic loading generated by moving large-tonnage cargo (**Rastsvietaiev et al., 2015; Babets et al., 2023; Carrascal et al., 2007; Zapukhliak et al., 2019; Sala & Bieda, 2024**). Key parameters, such as anchor length, spacing, depth of anchorage, and arch frame pitch, were systematically varied to assess their influence on support stability and rock mass deformation (**Babets et al., 2023**, **Tereshchuk et al., 2018; Bondarenko et al., 2021; Ko-**

valevska et al., 2020). Dynamic loads from train movement and emergency braking scenarios were simulated to reflect realistic mine conditions.

Field observations were conducted in an active underground coal mine where suspended monorail transport is routinely used for the delivery of mechanized support components. Instrumentation, including displacement sensors and vibration monitors, was installed along selected sections of district workings to record real-time deformation and load responses during monorail operation. Laboratory testing of fastening elements, including high-strength anchors and steel arch frames, was also carried out to determine material behaviour under cyclic and impact loading (**Herasymenko et al., 2023; Rastsvietaiev et al., 2015; Yegorchenko et al., 2022; Bashynska, 2025**). The combination of numerical modelling, field monitoring, and lab-based mechanical testing enabled a comprehensive validation of simulation results and informed the development of rational design parameters. This methodology ensures the reliability, safety, and performance of the support system under dynamic operational loads.

As it had been mentioned to determine rational schemes of frame-anchor support for preparatory mine workings that ensure the safe transportation of large-tonnage cargo via suspended monorail systems, a comprehensive research methodology was developed. The methodology focused on analyzing the stress–strain state of components within the transport-technological system "suspended monorail – mine support – rock mass" using numerical modelling in the SolidWorks Simulation environment (**Yegorchenko et al., 2022**). The modelling aimed to simulate and assess the behaviour of support structures under dynamic loading conditions typical of underground mining operations.

At the initial stage, parametric 3D models of the frame-anchor support system were constructed. These included various configurations of steel arch frames and anchors of differing lengths and anchoring types (**Khomenko et al., 2018**). The geometrical and mechanical parameters of the models reflected typical dimensions of preparatory mine workings and the mining-geological conditions of sites where suspended monorail transport is operationally implemented (**De Borst et al., 2012; Ravichandran, 2020**). The rock mass was modelled as a solid continuum with variable mechanical properties to reflect realistic stratified and fractured media.

To analyze the stress–strain state (SSS) of the support structure under dynamic loading conditions, the Static Study module of SolidWorks Simulation was utilized, applying the finite element method (FEM) (**Zienkiewicz et al., 2013; Lewicka & Zakrzewska-Bielawska, 2019**). This computational approach allowed for accurate modelling of the mechanical response of the combined frame-anchor support system under realistic operational stresses generated by monorail-based heavy cargo transport. The simulation aimed to evaluate structural stability, deformation behaviour, and stress distribution in both the support elements and the surrounding rock mass (**Moldabayev et al., 2021; Sun et al., 2009**).

The numerical analysis considered several key input conditions. Material properties were defined based on standard specifications: steel (according to DST 27772-2015 or DIN EN 10025) was used for the arch frame elements, while the rock mass was modelled as a conditionally fractured medium with variable strength parameters, including elastic modulus and Poisson's ratio (**DST 27772-2015. Rolled steel for construction purposes; DIN EN 10025-1:2019. Hot rolled products of structural steels**). Boundary conditions involved fixing the periphery of the model to simulate confinement by the surrounding geological environment and applying external loads that represented both mining pressure and dynamic impulses from moving monorail vehicles (**Moldabayev et al., 2021; Lewicka & Zakrzewska-Bielawska, 2019; Vosoughifar, Madadi & Rabiefar, 2017**).

Contact conditions were defined to reflect realistic interactions between system components, either frictional or adhesive, depending on the type of anchor-rock and frame-rock connections being modelled (**Sakurai, 2010**). As a result of the numerical modelling, distributions of stress, displacement, and safety factors were obtained for various frame-anchor support schemes. Special attention was given to three key indicators:

- Maximum stresses that may induce strength loss or plastic deformation;
- Displacements and deflections of frame elements, particularly at monorail load application points;
- Zones of stress concentration in anchor elements, indicating areas at high risk of rock failure or slippage.

Further simulations involved a series of parametric studies to optimize frame spacing, anchor length, and anchorage depth. Various anchor geometries and placement schemes were evaluated to determine their effect on the overall load distribution and support system performance. Model identification (**Kononenko et al., 2024**) was carried out by solving boundary value problems for fractured rock masses using a linear anisotropic constitutive model. A key aspect of this identification involved reproducing the principal tensile and compressive stress fields that develop around load-bearing arches under dynamic monorail loading. These stresses were then used to define loading parameters for secondary anchor levels.

The geometric dimensions of the model were determined using the following dynamic loads:

$$B = h + 4D_{eq}, \text{ m} \quad (1)$$

Where:

h – height of the mine working [m],

D_{eq} – equivalent diameter of the mine working [m], calculated as:

$$D_{eq} = \sqrt{4\frac{S_c}{\pi}}, \text{ m} \quad (2)$$

Where S_c is the cross-sectional area of the working [m²].

This approach makes it possible to accurately determine the characteristic geometric parameters of the excavation for further numerical modelling under dynamic loading conditions. Such precision is essential for correctly reproducing the stress–strain state of the rock mass and its interaction with the support elements. As a result, the developed model provides a reliable foundation for assessing the stability and safety of the entire "suspended monorail – mine support – rock mass" system.

The required length of the second-level anchors was computed as:

$$l_{anchor} = l_I + l_{emb} + l_{lock}, \text{ m} \quad (3)$$

Where:

l_I – design length of first-level roof anchors,

l_{emb} – embedding depth of the suspension anchors above the first-level anchors (≥ 0.5 m for roof type II; ≥ 1.0 m for types I, III, IV),

l_{lock} – locking section length.

Initial loads and boundary constraints were applied in the simulation, along with finite element meshing. The maximum load on the "monorail support – mine support" subsystem was calculated according to **Herasymenko et al. (2023)** using the following equation:

$$P = \frac{P_s^{max} k_d}{bC_s}, \text{ kN} \quad (4)$$

Where:

P_s^{max} – maximum static load on one monorail suspension [kN],

C_s – distance between suspensions [m],

k_d – dynamic load coefficient.

b – correction factor related to the width of the monorail support structure.

The simulation results were validated through comparison with data obtained from technical documentation and in-situ observations of support system behaviour under similar mining conditions. This validation step was essential for verifying the accuracy of the computational model and ensuring that it adequately represented the real-world performance of the frame-anchor support system. Based on the observed deviations and structural responses, necessary adjustments were made to the model parameters, which enhanced their reliability and applicability for conducting further variant calculations and scenario-based analyses.

Given the complexity of the overall transport-technological system, the interaction between the suspended monorail, the mine support, and the surrounding rock mass was examined by splitting the system into three interrelated subsystems: (1) "rolling stock – monorail support," (2) "monorail support – mine support," and (3) "mine support – rock mass." This modular approach allowed for a more focused and systematic analysis of individual stress transfer mechanisms at each interface. By isolating the influence of dynamic loads at each subsystem level, it became possible to identify structural vulnerabilities and develop targeted improvements in fastening design, particularly in areas prone to deformation, stress concentration, or progressive failure under cyclic monorail loading

3. Results

According to the research program and methodology developed for analyzing the interaction mechanisms within the "suspended monorail – mine support – rock mass" system, each of the designated subsystems was examined step by step as an independent structural entity. This modular approach allowed for a clearer understanding of load transfer processes and the localized effects of dynamic forces at each interaction level. In particular, the current article presents the results of a detailed study focused on the stress–strain state of components within the "Monorail Support – Mine Support" subsystem. The analysis emphasizes how dynamic loading, induced by monorail movement and braking, affects the mechanical performance and deformation behaviour of the fastening structures. The findings contribute to optimizing the frame-anchor support configuration and improving the structural reliability of preparatory mine workings under operational transport conditions.

According to the developed methodology, for modelling the interaction conditions within the "monorail support – mine support" subsystem using SolidWorks Simulation consists of several key stages. These include model identification, the creation of input data for geometric modelling, and the assignment of material properties for all structural components. Load parameters, boundary constraints, and finite element meshing are then defined to simulate operational conditions. Finally, the results are analyzed with particular attention to dynamic loads on anchors, focusing on stress variations around the crowns of load-bearing arches.

The obtained interaction parameters of elements within the "monorail support – mine support" subsystem served as the basis for developing a database to simulate changes in their technical condition under dynamic loads. This database enabled the formulation of innovative engineering solutions aimed at mitigating adverse effects on arch crowns and the mine roof. Operational studies of suspended monorail systems under atypical and extreme mining conditions (**Rastsvietaiev et al., 2015**) revealed that, to reduce the negative influence of rolling stock on both arch supports and the surrounding rock mass, dynamic loads must be evenly redistributed via the monorail support structure across all interacting components. To achieve this, the integration of deep-embedded anchors into exist-

ing frame-anchor fastening schemes is recommended, allowing the monorail support to be fixed directly to these anchors. This configuration effectively transfers part of the dynamic loading from the rolling stock onto the load-bearing arches and secondary anchorage points, thereby enhancing system stability.

The methodology for assessing dynamic loads acting on second-level anchors involves modelling the development of the stress–strain state of anchor elements under extreme operational conditions. According to engineering guidelines (**Aitkazinova et al., 2022**), this process includes several stages. Initially, a dataset is compiled to determine the technical condition of second-level anchors. This dataset includes the spatial orientation of anchors within the working, their physical and mechanical properties in situ, and environmental factors adversely affecting their performance. Such factors include vibration intensity, cyclic loading, and shock impulses, which deteriorate the structural integrity of mine support systems over time.

The primary sources of data include design specifications, construction and maintenance documentation (**Bondarenko et al., 2021**), as well as the results of dedicated investigations focused on dynamic load effects (**Zienkiewicz et al., 2013**) on subsystem elements during large-tonnage cargo transportation. Following the approved research methodology, a comprehensive stress–strain analysis of the subsystem components was performed. Critical zones with the highest stress concentrations were identified, and their actual load-bearing capacity was assessed to verify compliance with normative safety standards. Experimental observations confirmed that recurring dynamic loads, especially those generated as rolling stock pass over deformed joints in the monorail track, contribute to wear, fatigue, and damage in the supports of preparatory workings.

Building on the developed simulation methodology (**Moldabayev et al., 2021**) for evaluating suspended monorail operating regimes, data from experimental studies were incorporated into models simulating the behaviour of deep-embedded anchors under dynamic conditions during large-tonnage transport. In the modelling process, the second-level anchors and mine working were jointly analyzed as an integrated system within SolidWorks Simulation. Utilizing the finite element method (FEM) (**Khomenko et al., 2023**), structural analysis of system performance under dynamic loads was conducted, allowing predictions of anchor behaviour under realistic mining conditions. The objective of this methodology was to determine the maximum permissible stress levels in the anchor support elements using parametric CAD-based models (**Tereshchuk et al., 2018; Otey et al., 2018**), thereby ensuring both safety and operational reliability in transport-intensive underground environments.

The modelled mine section incorporated second-level anchors with a length of 3.4 meters, specifically designed to support suspended diesel locomotives (SDLs). These anchors are fabricated from high-strength wire rope steel and do not include additional protective coatings or corrosion-resistant treatments. The selection of material reflects typical in-mine operating conditions and mechanical loading scenarios associated with monorail transport. The physical and mechanical properties assigned to these elements in the CAD-based finite element models are summarized in **Table 1**.

Table 1. Main properties of wire rope steel

Property	Value	Unit
Elastic modulus	190000	N/mm²
Shear modulus	75000	N/mm²
Density	8000	kg/m³
Tensile strength limit	517	N/mm²
Poisson's ratio	0.29	
Yield strength	206	N/mm²
Thermal conductivity	16	W/(m·K)
Specific heat	500	J/(kg·K)

Table 2. Geometric dimensions of the model for simulation

Property	Value	Unit
Model height, B	24	m
Depth of occurrence, H	300	m
Average rock density, γ	2600	kg/m³
Poisson's ratio μ	0.25	
Mine working width, b	4460	mm
Mine working height, h	3800	mm
Inclination angle of second-level anchors, β	70	degrees
The length of second-level anchors, l_{anchor}	3400	mm

To simulate the interaction conditions of the elements within the technical subsystem "monorail support – mine support" in a CAD environment, a reference section was selected from an existing preparatory working at the Stepova mine operated by DTEK Pavlohradvuhillia, based on its current operational conditions. The selection of this site provided realistic boundary and loading conditions for accurate numerical modelling.

Based on the results of the mathematical simulation of subsystem behaviour, the model dimensions were determined while ensuring that the influence of external geometry on the simulation results was minimized. The model geometry was constructed at a 1:1 scale (**Kovalevska et al., 2020**), in accordance with the specifications provided in **Table 2**.

To determine the geometric dimensions of the model, a set of analytical expressions was used, including **Equation 1** for calculating the overall width of the modelled domain. The equivalent diameter of the mine working was obtained using **Equation 2**, which accounts for

Table 3. Physical and mechanical properties of rocks

	Elastic modulus, N/mm²	Poisson's ratio	Tensile strength limit, N/m²	Compressive strength, N/m²	Humidity, %	Fracturing
Siltstone	16600	0,394	18	381	2.0	1-3
Argillite	21200	0,41	25	280	2.6	4-5
Sandstone	27100	0,41	150	680	5.2	1-3
Coal	4700	0,33	14	300	4.4	10-15

the cross-sectional area of the excavation. These expressions ensured that the model reflected the actual geometry of the underground environment with sufficient accuracy for finite element simulation. In addition, the length of the second-level anchors was calculated using **Equation 3**, which considers the combined depth of primary anchorage, the embedding section, and the locking zone. These parameters were critical for replicating the interaction between the support system and the surrounding rock mass under dynamic loading conditions. Together, the applied equations formed the basis for building a physically representative CAD model suitable for stress-strain analysis using numerical methods.

The initial material properties used in the numerical model were defined based on the physical and mechanical characteristics of rock types commonly encountered in the mines of the Western Donbas region (**Khomenko et al., 2018**). These properties include parameters such as density, compressive strength, Young's modulus, and Poisson's ratio, which are essential for simulating the stress–strain behaviour of the rock mass under load. The selected values reflect average conditions derived from geological surveys and laboratory testing of core samples collected from operating mine sites. **Table 3** presents a summary of these average material properties, which were used as input for the finite element analysis. These values were further verified and calibrated to ensure compatibility with the dynamic loading conditions associated with suspended monorail operations. Incorporating realistic geomechanical data into the model was crucial for obtaining accurate simulation results and reliable safety assessments of the support system.

In practice, monorail support is suspended to the crowns of metal arch supports or to anchors. The proposed combined suspension system is simultaneously fixed to the crowns of the arch support and to deep-embedded anchors using chains. Suspension segments are interconnected in a way that ensures even distribution of dynamic loads from the transportation of heavy cargo between both types of support. This engineering solution allows each type of support to be considered individually, taking into account the nature of dynamic load transfer, which improves the reliability of the entire support system of the mine roadway.

The next stage of the modelling process involved defining the initial load P, applying boundary constraints, and generating the finite element mesh to discretize the model geometry. According to the recommendations presented in **Herasymenko et al. (2023)**, the load acting on the subsystem element "monorail support – mine support" is calculated using **Equation 4**. This equation accounts for the maximum static load on individual suspensions, the spacing between suspensions, and a dynamic load coefficient that reflects operational conditions. Proper implementation of these parameters is critical to accurately simulate dynamic interactions within the system and assess the resulting stress distribution.

According to the assessment of the technical condition of suspended monorail track support systems, the most deformation-prone areas are located at the junction between the crown of the arch support and the attachment points of the second-level anchors. Theoretical studies of the interaction conditions between the elements of the technical subsystem "monorail support – mine support" during the transportation of heavy loads have shown that the monorail track is divided into characteristic zones with the highest levels of dynamic loading (see **Figure 1**). To calculate the load and deformation in the characteristic nodes of the elements of the technical subsystem "monorail - fastening of the workings", the deep-seated anchor zones were divided into element-by-element grids using the FEM (**Kononenko et al., 2023**).

The application of SolidWorks Simulation software for modelling the technical condition of the monorail track enabled the determination of equivalent stresses and the tensile strength limits of second-level anchors during large-tonnage cargo transport. According to manufacturer specifications, the permissible tensile strength of the second-level anchors is 240 MPa. Simulation results were obtained for two different spatial arrangements of deep-embedded anchors, incorporating the dynamic load coefficient and assuming uniform load distribution among the frame-anchor support elements. The key findings of these analyses are summarized in **Table 4**.

Figure 2 illustrates the distribution of von Mises stresses generated in the deep-embedded anchors due to dynamic loads from the transportation of large-tonnage cargo weighing 8, 12, and 16 tons. These stress values reflect the complex interaction between the moving load and the support elements under realistic operational conditions. The calculated von Mises stress intensities, expressed in megapascals (MPa), serve as critical indicators for evaluating the structural integrity and safety margins of the anchors. By comparing these stress levels with the permissible tensile strength of the anchor material, it is possible to assess the reliability and durability of the fas-

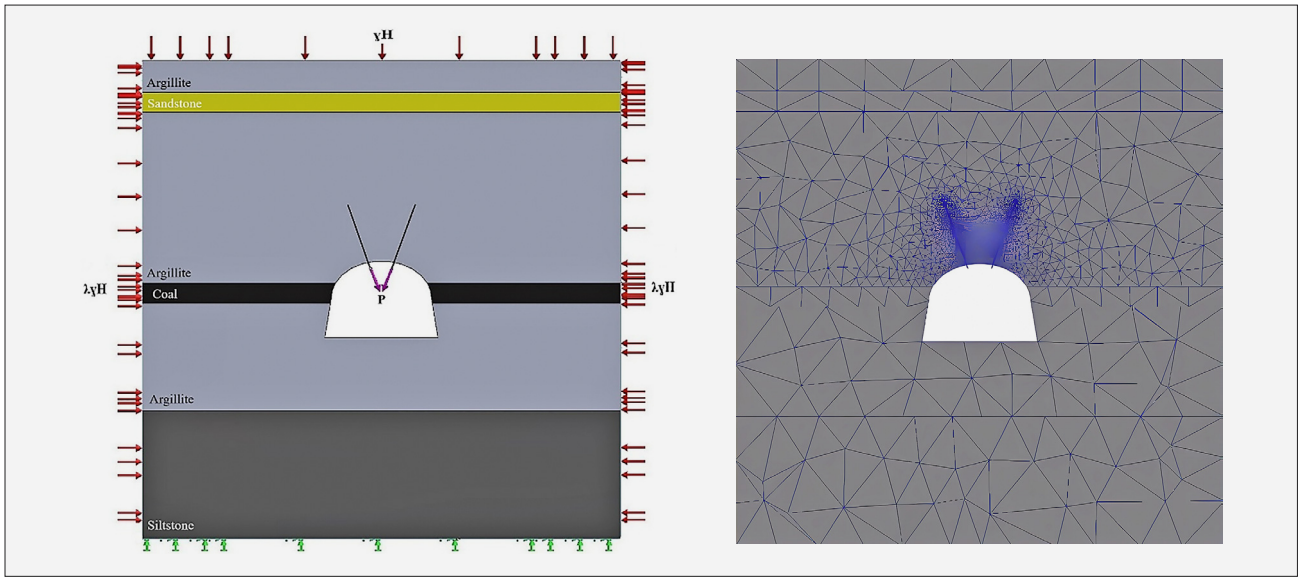
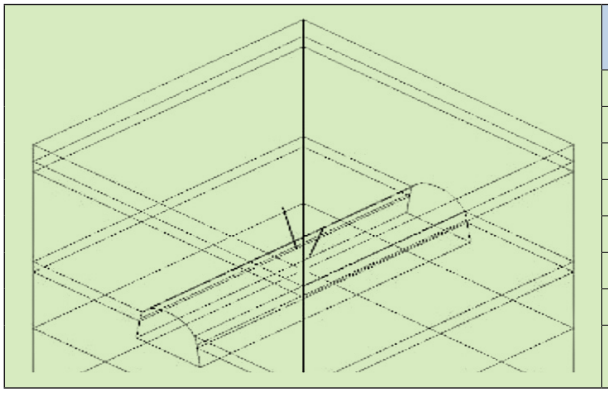


Figure 1. Initial constraints, applied loads, and finite element mesh of the model

Table 4. Simulation results for stress in deep-embedded anchors under dynamic loading



Cargo mass (tons)	Von Mises stress σ_{von} Mises (MPa)
2	63
4	95
6	127
8	159
10	190
12	222
14	255
16	287

tening system. This analysis provides essential data to guide the design and optimization of anchor placement to ensure safe and efficient mine transport operations.

The developed software package allows us to establish (see **Figure 2**) the possibility of safe transportation of high-tonnage cargo weighing up to 12 tons without destroying the structure of the proposed fastening system. The conducted simulations confirm the reliability of the system under various loading and dynamic impact conditions. This provides a solid basis for further optimization of the design parameters and practical implementation of the technology in real mining environments.

After approximating the maximum values shown in **Figure 3**, an empirical relationship was established describing how the von Mises stress intensity $\sigma_{von\ Mises}$ in the second-level anchor varies with the mass of the large-tonnage load P This dependence provides a quantitative basis for predicting stress responses in the anchor under different cargo weights. The derived formula enables engineers to estimate stress levels for various operational scenarios, facilitating risk assessment and design optimization. Such insights are critical for ensuring the structural integrity and safe performance of the anchoring system in mining transport applications.

For the anchors of the second level, the magnitude of the von Mises stresses depending on the mass of the large-tonnage load is determined by the equation:

$$\sigma_{\text{von Mises}} = 21P - 0{,}19P^2 \text{ MPa},$$
$$\text{attached to } R^2 = 0{,}9987 \quad (5)$$

Where P – cargo mass, tons; R^2 – reliability of approximation.

The second level anchor strength check is performed under the following conditions

$$\sigma_{\text{von Mises}} < [\sigma_y] \text{ MPa} \quad (6)$$

Where σ_y – yield strength of anchor material, MPa.

According to theoretical studies, the destruction of the anchor fastening will occur when the load weight

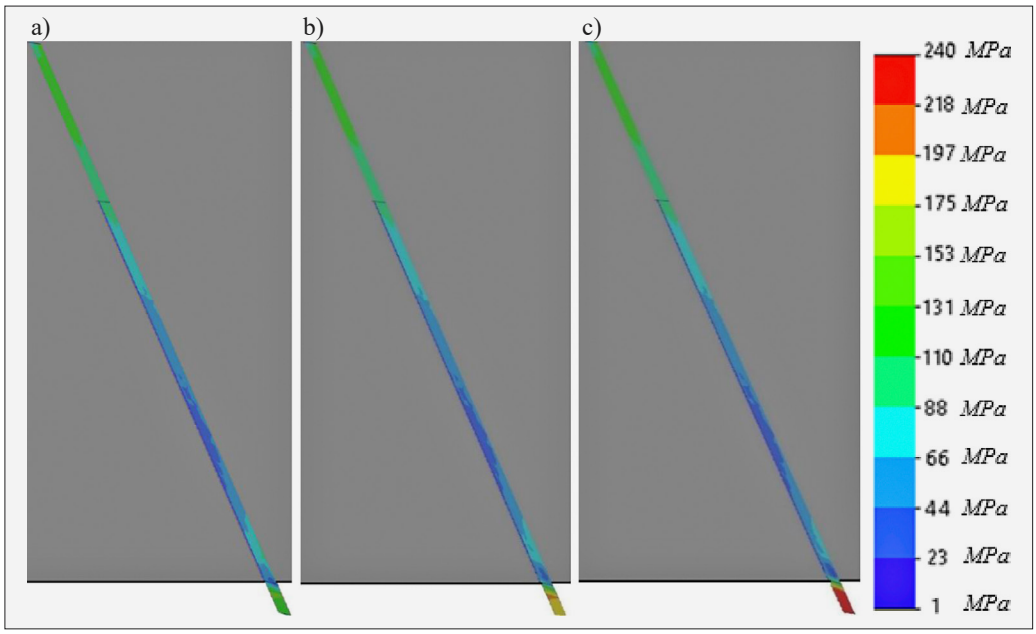


Figure 2. Von Mises stress intensities in deep-embedded anchors depending on cargo mass: a – 8 t; b – 12 t; c – 16 t

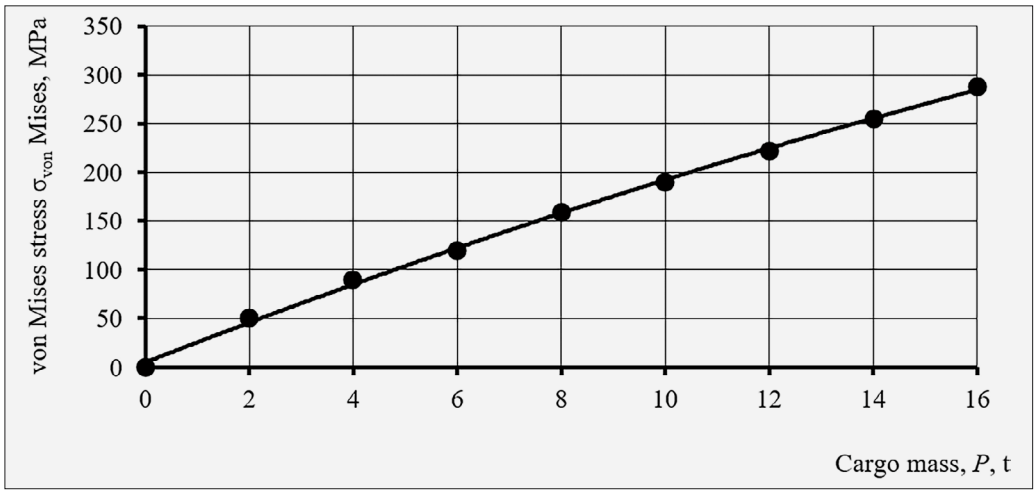


Figure 3. Graph of von Mises stress intensity in a second-level anchor versus cargo mass *P*

reaches 13 tons or more. This critical value determines the upper safety limit for the proposed fastening system under operational conditions. Exceeding this threshold may lead to structural deformation and a loss of load-bearing capacity. Therefore, it is recommended to maintain the operating load within the safe range identified to ensure long-term system reliability and stability.

4. Discussion

The predicted relationship between the von Mises stress intensity $\sigma_{von\ Mises}$ in deep-embedded anchors and the mass *P* of large-tonnage cargo is presented in **Table 5**. This data provides a clear overview of how increasing load mass affects the stress distribution within the anchoring system. Such predictions are essential for assessing the safety margins and optimizing the design of mine support structures under varying operational conditions.

The analysis of the simulation results for the interaction conditions within the "monorail support – mine support" subsystem demonstrates that employing a combined frame-anchor fastening, where the monorail support is simultaneously secured to second-level anchors and the crowns of arch supports, can significantly enhance system performance. Under the specific operational conditions of the Western Donbas mining region, this fastening approach facilitates the expansion of potential reserves for diesel suspension monorail roads. This method improves the stability and load-bearing capacity of the support system, thereby increasing the efficiency and safety of underground transport infrastructure.

Table 5. Prediction of the dependence of the stress intensity against the $\sigma_{von\ Mises}$ background of deep-seated anchors on the mass *P* of a large-tonnage cargo.

Cargo mass (tons)	Von Mises stress σ_{von} Mises (MPa)
1	39
2	63
3	81
4	95
5	111
6	127
7	143
8	159
9	175
10	190
11	206
12	222
13	239
14	255
15	270
16	281

The interaction indicators obtained through computer modelling of the "monorail support – mine support" subsystem demonstrate that dynamic loads can be significantly mitigated by effectively redistributing the mass of large-tonnage cargo across multiple elements within the complex dynamic transport-technological system "suspended monorail – mine support – rock mass." The implemented innovative technical solutions have raised the maximum permissible operational thresholds for suspended monorail tracks transporting heavy loads, thereby enhancing overall system reliability. This advancement also expands the potential for broader application of suspended monorail systems under the challenging geological and operational conditions characteristic of the Western Donbas region.

5. Conclusions

This research successfully employed a modular approach to analyze the interaction mechanisms within the "suspended monorail – mine support – rock mass" system, focusing specifically on the "monorail support – mine support" subsystem. The use of finite element modelling through SolidWorks Simulation enabled a comprehensive evaluation of the stress–strain states under dynamic loads typical for large-tonnage cargo transport. The study identified critical stress concentration zones, particularly at the junctions of anchors and arch crowns, providing valuable insight to optimize frame-anchor fastening designs and thereby enhance the structural reliability and operational safety of preparatory mine workings.

Numerical simulations demonstrated that integrating deep-embedded second-level anchors into combined frame-anchor fastening schemes effectively redistributes dynamic loads from the suspended monorail rolling stock across multiple support elements. This redistribution leads to a significant reduction in peak stress and deformation risks in vulnerable zones of the support system. Furthermore, the establishment of empirical relationships between cargo mass and von Mises stress in anchors allows for precise prediction of stress responses, ensuring that operational loads remain within permissible strength limits. These findings support the development of more resilient support systems capable of withstanding the challenging mining conditions prevalent in the Western Donbas region.

The simulation results also revealed that the tensile strength limit of second-level anchors, specified at 240 MPa, is reached when transporting cargo exceedingly approximately 13 tons. This threshold defines the upper safe operational boundary for suspended monorail transport under current design parameters. The combined fastening scheme, whereby the monorail support is anchored simultaneously to second-level anchors and arch crowns, facilitates a more uniform distribution of dynamic loads and reduces stress intensities in critical structural zones, thereby extending the service life and safety of the support system.

The practical recommendations derived from this research can be directly applied to the design and modernization of preparatory mine workings equipped with suspended monorail transport systems. The proposed innovative fastening solutions improve mining efficiency by accelerating panel preparation, minimizing maintenance and repair costs, and enhancing overall system reliability. Moreover, these solutions are highly adaptable for implementation in mines of Western Donbas as well as other mining regions with comparable geomechanical and operational conditions.

In conclusion, the developed technical framework provides a robust engineering basis for increasing the maximum allowable operational thresholds of suspended monorail tracks transporting heavy loads. By improving load management and reinforcing system stability, the study contributes to safer and more efficient underground transport infrastructures. These advancements also lay the groundwork for future development, standardization, and broader adoption of suspended monorail transport technologies in the global mining industry.

Further research is planned to be devoted to the unification of all subsystems into a single complex system "suspended monorail – mine support – rock mass" and the analysis of its operation. This approach will make it possible to comprehensively evaluate the mutual influence of mechanical, structural, and geological components. The obtained results are expected to form the basis for optimizing design parameters and improving the overall stability and efficiency of the system.

6. References

Aitkazinova, S., Sdvyzhkova, O., Imansakipova, N., Babets, D., & Klymenko, D. (2022). Mathematical modeling the quarry wall stability under conditions of heavily jointed rocks. *Naukovyi Visnyk Natsionalnoho Hirnychoho Universytetu*, (6), 18–24. https://doi.org/10.33271/nvngu/2022-6/018

Babets, D., Sdvyzhkova, O., Hapieiev, S., Shashenko, O., & Vasyl, V. (2023). Multifactorial analysis of a gateroad stability at goaf interface during longwall coal mining – A case study. *Mining of Mineral Deposits, 17*(2), 9–19. https://doi.org/10.33271/mining17.02.009

Bashynska, I. Ethical aspects of AI use in the circular economy. AI & Society (2025). https://doi.org/10.1007/s00146-025-02436-1

Bashynska, I., Niekrasova, L., Ivliev, D., Dudek, M., Kosenkov, V., & Yakimets, A. (2024). Justification for Transitioning Equipment to Direct Current for Smart Small Enterprises with Sustainable Solar Power Autonomy. 2024 IEEE 5th KhPI Week on Advanced Technology (KhPIWeek), 1–6. https://doi.org/10.1109/khpiweek61434.2024.10878001

Beshta, O., Albu, A., Balakhontsev, A., & Fedoreyko, V. (2015). Universal model of the galvanic battery as a tool for calculations of electric vehicles. *Power Engineering, Control and Information Technologies in Geotechnical Systems*, 7–11. https://doi.org/10.1201/b18475-2

Blinov, I., Radziukynas, V., Shymaniuk, P., Dyczko, A., Stecuła, K., Sychova, V., Miroshnyk, V., & Dychkovskyi, R. (2025). Smart Management of Energy Losses in Distribution Networks Using Deep Neural Networks. *Energies*, 18(12), 3156. https://doi.org/10.3390/en18123156

Bondarenko, V., Kovalevska, I., Cawood, F., Husiev, O., Snihur, V., et al. (2021). Development and testing of an algorithm for calculating the load on support of mine workings. *Mining of Mineral Deposits, 15*(1), 1–10. https://doi.org/10.33271/mining15.01.001

Campos Zabala, F. J. (2023). Integrating AI into Existing Systems and Processes. *Grow Your Business with AI*, 413–431. https://doi.org/10.1007/978-1-4842-9669-1_18

Carrascal, I. A., Casado, J. A., Polanco, J. A., & Gutiérrez-Solana, F. (2007). Dynamic behaviour of railway fastening setting pads. *Engineering Failure Analysis*, 14(2), 364–373. https://doi.org/10.1016/j.engfailanal.2006.02.003

Chen, Z., & Chen, Y. (2024). Advancing AI-Driven BETC Models for Transformative Educational Data Mining and Learning Analytics. Proceedings of the 2024 International Symposium on Artificial Intelligence for Education, 495–500. https://doi.org/10.1145/3700297.3700382

De Borst, R., Crisfield, M. A., Remmers, J. J. C., & Verhoosel, C. V. (2012). *Nonlinear finite element analysis of solids and structures*. John Wiley & Sons, 544 p.

DIN EN 10025-1:2019. Hot rolled products of structural steels – Technical delivery conditions.

DST 27772-2015. Rolled steel for construction purposes. Technical conditions.

Dychkovskyi, R., Dyczko, A., & Borojević Šoštarić, S. (2024). Foreword: Physical and Chemical Geotechnologies – Innovations in Mining and Energy. *E3S Web of Conferences*, 567, 00001. https://doi.org/10.1051/e3sconf/202456700001

Dychkovskyi, R., Saik, P., Sala, D., & Cabana, E. C. (2024). The current state of the non-ore mineral deposits mining in the concept of the Ukraine reconstruction in the post-war period. *Mineral Economics*, 37(3), 589–599. https://doi.org/10.1007/s13563-024-00436-z

Falshtynskyi, V., Dychkovskyi, R., Khomenko, O., & Kononenko, M. (2020). On the formation of a mine-based energy resource complex. *E3S Web of Conferences*, 201, 01020. https://doi.org/10.1051/e3sconf/202020101020

Fedoreiko, V., Zahorodnii, R., Lutsyk, I., Rutylo, M., & Bureha, N. (2025). Modelling of resource-saving control modes of a bioheat generator using neuro-fuzzy controllers. *IOP Conference Series: Earth and Environmental Science*, 1457(1), 012005. https://doi.org/10.1088/1755-1315/1457/1/012005

Herasymenko, A. O., Rastsvietaiev, V. O., & Shyrin, A. L. (2023). Selection of the means of auxiliary transportation facilities and adaptation of their parameters to specific operation conditions. *Naukovyi Visnyk Natsionalnoho Hirnychoho Universytetu*, (2), 40–46. https://doi.org/10.33271/nvngu/2023-2/040

Jiang, Y., Duan, P., Liu, W., Du, Z., & Chen, R. (2025). Dynamic performance analysis of suspended monorail vehicles under various operating conditions. *International Journal of Vehicle Systems Modelling and Testing*, 1(1). https://doi.org/10.1504/ijvsmt.2025.10071184

Kang, H., Yang, J., Gao, F., & Li, J. (2020). Experimental Study on the Mechanical Behavior of Rock Bolts Subjected to Complex Static and Dynamic Loads. *Rock Mechanics and Rock Engineering,* 53(11), 4993–5004. https://doi.org/10.1007/s00603-020-02205-0

Khomenko, O., Kononenko, M., & Bilegsaikhan, J. (2018). Classification of theories about rock pressure. *Solid State Phenomena*, 277, 157–167. https://doi.org/10.4028/www.scientific.net/ssp.277.157

Khomenko, O., Kononenko, M., Kovalenko, I., & Astafiev, D. (2018). Self-regulating roof-bolting with the rock pressure energy use. *E3S Web of Conferences, 60*, 00009. https://doi.org/10.1051/e3sconf/20186000009

Khomenko, O., Rudakov, D., Lkhagva, T., Sala, D., Buketov, V., & Dychkovskyi, R. (2023). Managing the Horizon-oriented In-Situ Leaching for the Uranium Deposits of Mongolia. *Rudarsko-Geološko-Naftni Zbornik*, 38(5), 49–60. https://doi.org/10.17794/rgn.2023.5.5

Kononenko, M., & Khomenko, O. (2010). Technology of support of workings near to extraction chambers. In *New Techniques and Technologies in Mining,* 193–197. https://doi.org/10.1201/b11329-32

Kononenko, M., Khomenko, O., Kosenko, A., Myronova, I., Bash, V., & Pazynich, Yu. (2024). Raises advance using emulsion explosives. *E3S Web of Conferences, 526*, 01010. https://doi.org/10.1051/e3sconf/202452601010

Kononenko, M., Khomenko, O., Kovalenko, I., Kosenko, A., Zahorodnii, R., & Dychkovskyi, R. (2023). Determining the performance of explosives for blasting management. *Rudarsko-Geološko-Naftni Zbornik*, 38(3), 19–28. https://doi.org/10.17794/rgn.2023.3.2

Kononenko, M., Khomenko, O., Sadovenko, I., Sobolev, V., Pazynich, Yu., & Smolinski, A. (2023). Managing the rock mass destruction under the explosion. *Journal of Sustainable Mining, 22*(3), 240–247. https://doi.org/10.46873/2300-3960.1391

Kononenko, M., Khomenko, O., Sudakov, A., Drobot, S., & Lkhagva, T. (2016). Numerical modelling of massif zonal structuring around underground working. *Mining of Mineral Deposits*, 10(3), 101–106. https://doi.org/10.15407/mining10.03.101

Kosenko, A., Khomenko, O., Kononenko, M., Polyanska, A., Buketov, V., Dychkovskyi, R., Polański, J., Howaniec, N., & Smolinski, A. (2025). Sustainable management of iron ore extraction processes using methods of borehole hydro technology. *International Journal of Mining and Mineral Engineering*, 16(1), 92–112. https://doi.org/10.1504/ijmme.2025.145592

Kovalevska, I., Symanovych, H., Jarosz, J., Barabash, M., & Husiev, O. (2020). Geomechanics of overworked mine working support resistance in the laminal massif of soft rocks. *E3S Web of Conferences, 201*, 01003. https://doi.org/10.1051/e3sconf/202020101003

Kumbasaroglu, A. (2010). An experimental study on the effects of anchor rods on infill walled frame systems. *Erzincan Binali Yildirim University*, 211. https://doi.org/10.71008/atauni.thesis.2010.101

Lapshyn. Y., Shevchenko. O., Dybrin S., & Dychkovskyi. R. (2025). Feasibility of Fine Classification in Processing Watered Coal Sludge from Storage: A Case Study of the Dnipro Coke Chemical Plant. *Acta Montanistica Slovaca*, 100. https://doi.org/10.46544/ams.v30i1.07

Lewicka, B., & Lewicka, D. (2019). Environmental risk management in the context of environmental management systems for agriculture based on the ISO 14001:2015 standard. *Acta Innovations*, 33, 63–72. https://doi.org/10.32933/actainnovations.33.6 V

Lewicka, D., & Zakrzewska-Bielawska, A. (2019). Interorganizational Trust in Business Relations: Cooperation and Coopetition. *Contemporary Challenges in Cooperation and Coopetition in the Age of Industry 4.0*, 155–174. https://doi.org/10.1007/978-3-030-30549-9_8

Mackiewicz, M., Krentowski, J. R., Knyziak, P., & Wardach, M. (2022). Consequences of excessive deformation of structural elements in precast buildings. *Engineering Failure Analysis*, 137, 106261. https://doi.org/10.1016/j.engfailanal.2022.106261

Moldabayev, S. K., Sdvyzhkova, O. O., Babets, D. V., Kovrov, O. S., & Adil, T. K. (2021). Numerical simulation of the open pit stability based on probabilistic approach. *Naukovyi Visnyk Natsionalnoho Hirnychoho Universytetu*, (6), 29–34. https://doi.org/10.33271/nvngu/2021-6/029

Myronova, I., Kovrov, O., Dudek, M., Voronkova, Y., & Kononenko, M. (2025). Environmental assessment of the impact of iron ore mine emissions on biological indicators of winter wheat. *IOP Conference Series: Earth and Environmental Science*, 1457(1), 012004. https://doi.org/10.1088/1755-1315/1457/1/012004

Otey, J., Company, P., Contero, M., & Camba, J. (2018). Assessment of Parametric Assembly Models Based on CAD Quality Dimensions. *Computer-Aided Design and Applications*, 16(4), 628–653. https://doi.org/10.14733/cadaps.2019.628-653

Polyanska, A., Pazynich, Y., Petinova, O., Nesterova, O., Mykytiuk, N., & Bodnar, G. (2024). Formation of a Culture of Frugal Energy Consumption in the Context of Social Security. *The Journal of the International Committee for the History of Technology*, 29(2), 60–87. https://doi.org/10.11590/icon.2024.2.03

Psyuk, V., & Polyanska, A. (2024). The usege of artificial intelligence in the activities of mining enterprises. *E3S Web of Conferences*, 526, 01016. https://doi.org/10.1051/e3sconf/202452601016

Rastsvietaiev, V. O., Posunko, L. M., Shyrin, A. L., & Zheglov, S. S. (2015). Estimation of factors limiting efficiency of transport schemes while preparing coal reserves in Western Donbas mines. *Mining of Mineral Deposits*, 9(1), 117–123. https://doi.org/10.15407/mining09.01.117

Ravichandran, G. (2020). Finite Element Analysis. *Finite Element Analysis of Weld Thermal Cycles Using ANSYS*, 25–33. https://doi.org/10.1201/9781003052128-4

Sakurai, S. (2010). Modeling strategy for jointed rock masses reinforced by rock bolts in tunneling practice. Acta Geotechnica, 5(2), 121–126. https://doi.org/10.1007/s11440-010-0117-0

Sala D., & Bieda, B. (2024). Management of the Rare Earth Elements (REE) in the Global Economy: Neodymiun Case Study. Inżynieria Mineralna, 2(2 (52)). https://doi.org/10.29227/im-2023-02-53

Sala, D., & Bieda, B. (2021). Role of Stochastic Approach Applied to Life Cycle Inventory (LCI) of Rare Earth Elements (REEs) from Secondary Sources Case Studies. *Towards a Sustainable Future - Life Cycle Management*, 107–120. https://doi.org/10.1007/978-3-030-77127-0_10

Sobolev, V., Gubenko, S., Khomenko, O., Kononenko, M., Dychkovskyi, R., & Smolinski, A. (2025). Physical and chemical conditions for the diamond formation. *Diamond and Related Materials*, 151, 111792. https://doi.org/10.1016/j.diamond.2024.111792

Sosnowski, P., Dyczko, A., & Kamiński, P. (2024). Quality management in a 3D geological model – reliability of predicted hard coal quality parameters. E3S Web of Conferences, 526, 01003. https://doi.org/10.1051/e3sconf/202452601003

Stöcklein, J., & Kaliske, M. (2022). Thermo-hygro-mechanically coupled modelling of wood including two-phase moisture diffusion for transient simulation of wooden structures at mechanical and climatic loads. *Heat and Mass Transfer*, 59(1), 67–79. https://doi.org/10.1007/s00231-022-03178-2

Sun, X., Cai, F., Yang, J., & Cao, W. (2009). Numerical simulation of the effect of coupling support of bolt-mesh-anchor in deep tunnel. Mining Science and Technology (China), 19(3), 352–357. https://doi.org/10.1016/s1674-5264(09)60066-1

Symanovych, G., Astafiev, D., Vivcharenko, O., & Snigur, V. (2015). Increasing of yielding of frame-anchor support steadiness. *New Developments in Mining Engineering*, 45–48. https://doi.org/10.1201/b19901-9

Tereshchuk, R. M., Khoziaikina, N. V., & Babets, D. V. (2018). Substantiation of rational roof-bolting parameters. *Nauko-*

vyi Visnyk Natsionalnoho Hirnychoho Universytetu, (1), 19–26.

Tokarczyk, J. (2016). Method for Identification of Results of Dynamic Overloads in Assessment of Safety Use of the Mine Auxiliary Transportation System. *Archives of Mining Sciences*, 61(4), 765–777. https://doi.org/10.1515/amsc-2016-0052

Vladyko, O., Maltsev, D., Gliwiński, Ł., Dychkovskyi, R., Stecuła, K., & Dyczko, A. (2025). Enhancing Mining Enterprise Energy Resource Extraction Efficiency Through Technology Synthesis and Performance Indicator Development. *Energies*, 18(7), 1641. https://doi.org/10.3390/en18071641

Vlasov, S., Moldavanov, Y., Dychkovskyi, R., Cabana, E., Howaniec, N., Widera, K., Bąk, A., & Smoliński, A. (2022). A Generalized View of Longwall Emergency Stop Prevention (Ukraine). Processes, 10(5), 878. https://doi.org/10.3390/pr10050878

Vosoughifar, H., Madadi, F., & Rabiefar, A. (2017). Modified dynamic stress concentration factor for twin tunnels using a novel approach of FEM-scattering. Tunnelling and Underground Space Technology, 70, 30–41. https://doi.org/10.1016/j.tust.2017.07.006

Yegorchenko, R.R., Mukha, O.A., & Shirin, L.N. (2022). The methods to calculate expediency of composite degassing pipelines. *Naukovyi Visnyk Natsionalnoho Hirnychoho Universytetu*, (4), 23–27. https://doi.org/10.33271/nvngu/2022-4/023

Zapukhliak, I., Zaiachuk, Y., Polyanska, A., & Kinash, I. (2019). Applying fuzzy logic to assessment of enterprise readiness for changes. *Management Science Letters*, 2277–2290. https://doi.org/10.5267/j.msl.2019.7.026

Zhai, W., He, Q., Bao, Y., & Cai, C. (2025). Suspended monorail system dynamics: fundamental and practice. *Railway Engineering Science*, 1–25. https://doi.org/10.1007/s40534-025-00403-6

Zienkiewicz, O. C., Taylor, R. L., & Zhu, J. Z. (2013). *The finite element method: Its basis and fundamentals*. Butterworth-Heinemann, 756 p.

SAŽETAK

Upravljanje parametrima okvirno-sidrenoga sustava podgrade u pripremnim iskopima za transport teškoga tereta jednotračnim željezničkim sustavom

Članak prikazuje sveobuhvatno istraživanje o upravljanju i optimizaciji okvirno-sidrenoga sustava podgrade u pripremnim jamskim iskopima namijenjenima transportu tereta velike nosivosti pomoću visećega jednotračnog željezničkog sustava. S intenziviranjem podzemne eksploatacije i sve većom primjenom teških transportnih sustava osiguranje stabilnosti i sigurnosti jamskih prostorija pod utjecajem dinamičkih opterećenja postaje jedan od ključnih inženjerskih izazova. U radu je predložena inovativna tehnologija podgrade koja se temelji na kombiniranome učvršćenju jednotračnih željezničkih sustava – spajanjem na tjemena metalnih okvira te izravnim sidrenjem u krovnu stijensku masu pomoću dubokih sidara. Cilj takva pristupa jest smanjenje dinamičkih naprezanja u krovini iskopa i povećanje ukupne pouzdanosti sustava podgrade. Radi procjene učinkovitosti predložene konstrukcije podgrade primijenjena je numerička metoda modeliranja kojom je simulirano međudjelovanje komponenti u dinamičkome sustavu „viseća jednotračna željeznica – podgrada – stijenska masa". Analiza ponašanja stijenske mase pri naprezanju i deformacijama provedena je primjenom softverskoga paketa SolidWorks Simulation. Tijekom simulacija sustavno su mijenjani različiti parametri, uključujući razmake između okvira podgrade, duljinu i dubinu usidrenja sidara te mehanička svojstva stijenske mase. Rezultati analize omogućili su određivanje racionalnih konstrukcijskih parametara koji minimiziraju deformacije i povećavaju nosivost podgrade. Posebno je utvrđeno da optimalna kombinacija razmaka okvira i konfiguracije sidara znatno smanjuje koncentracije naprezanja i poboljšava stabilnost pripremnih prostorija pod djelovanjem dinamičkih opterećenja nastalih kretanjem jednotračnih željezničkih kompozicija. Provedeno istraživanje pokazuje kako učinkovito upravljanje parametrima sustava podgrade može dovesti do povećanja sigurnosti, smanjenja potrošnje materijala i ubrzanja napredovanja jamskih radova. Dobiveni rezultati praktično su primjenjivi u projektiranju podzemnih transportnih ruta te se mogu ugraditi u normativne dokumente koji reguliraju projektiranje i primjenu podgradnih sustava u dinamički opterećenim rudarskim okruženjima.

Ključne riječi:
okvirno-sidrena podgrada, jednotračni željeznički transport, transport teškoga tereta, analiza naprezanja i deformacija, upravljanje rudarskom infrastrukturom, raspodjela dinamičkoga opterećenja

Author's contribution

Herasymenko Andrii (Doctor of Philosophy in Mining Engineering, Assistant Professor) - conceptualization, methodology, formal analysis, original draft; **Shyrin Leonid** (Doctor of Engineering, Professor) - supervision, data validation, review & editing; **Yegorchenko Rostyslav** (Doctor of Philosophy in Mining Engineering, Associate Professor) - data curation, software support, results visualization & investigation; **Iniutkin Ivan** (Candidate of Engineering Sciences, Associate Professor): - mechanical modeling, finite element simulation, technical validation; **Pazynich Yuliya** (Candidate of Political Sciences, Associate Professor) - literature review, environmental assessment, editing and proofreading. All authors have read and agreed to the published version of the manuscript.

RGNZ/MGPB

Improving the efficiency of in-situ uranium leaching via oxygen-enriched lixiviant injection

Rudarsko-geološko-naftni zbornik
(The Mining-Geology-Petroleum Engineering Bulletin)
DOI: 10.17794/rgn.2026.2.13

Preliminary communication

Khalidilla Yussupov[1], Erbolat Aben[1]*, Gulfarizada Abdissattar[1], Saifilmalik Myrzakhmetov[1], Dalelkhan Akhmetkanov[1]
[1] *Satbayev University, Satbayev str.22, Almaty, Kazakhstan.*

Abstract
This paper explores the optimization of in-situ uranium leaching efficiency through the application of oxygen as an oxidizing agent in the lixiviant. With this objective in mind, geological characteristics of the target site were examined, followed by a series of laboratory and pilot-scale experiments. The resulting data were systematically processed and analyzed. The influence of sulfuric acid concentration on the degree of oxygen enrichment in the lixiviant was established. Laboratory tests on core samples from the uranium deposit revealed consistent relationships between uranium concentration in the pregnant solution, the oxidation states of iron (Fe^{2+} and Fe^{3+}) in lixiviant, and the level of oxygen saturation. Comparative results of uranium content in the pregnant solution over time were obtained for both the conventional and oxygen-enriched technologies. Laboratory results demonstrated a 23.0% increase in uranium concentration in the pregnant solution using an oxygen-enriched lixiviant over the control solution, indicating a potential reduction in recovery time and final metal production costs. Pilot-scale tests at a uranium mine confirmed the positive effect of oxygen-enriched lixiviant on iron oxidation and uranium concentration in the pregnant solution. All pumping wells within the test block showed increased or stabilized uranium concentration upon connecting a special injection system for oxidation in injection wells surrounding the pumping wells, and decreased uranium concentration after system disconnection.

Keywords:
in-situ leaching, oxidation, uranium concentration in solution, oxygen enrichment, ferrous and ferric iron

1. Introduction

According to expert forecasts, by 2030 leading uranium producers are expected to extract approximately 1.8 million tonnes of uranium, which would result in the depletion of 37% of the world's explored reserves. In other words, the reserves of primary uranium deposits are projected to decline by more than 1.5 times (**Li & Jia, 2024; Michel et al., 2022**).

With the gradual exhaustion of high-grade uranium ores, many mining enterprises have begun shifting toward the exploitation of low-grade deposits. CRU Group analysts predict that at many active uranium mining sites, the average uranium content is more than 1⁄3 below the global average, and at exploration-stage sites, it is more than 1⁄2. The involvement of such deposits in production requires substantial investment in infrastructure, particularly in remote and hard-to-access regions (**Youssef et al., 2024**). These factors will inevitably increase the production cost of final uranium products.

At present, 439 nuclear reactors are operating worldwide, and this number is expected to increase to 549 in the near future. This growth underscores the strategic importance of the uranium sector for global development and highlights the need to expand uranium resources and reserves. It also requires the efficient and comprehensive use of already explored deposits, considering the strategic importance of uranium as a raw material (**Togizov et al., 2024**). Various technological solutions exist within conventional mining methods to ensure efficient and comprehensive utilization of mineral reserves (**Bitimbayev et al., 2023; Almenov et al., 2025**). Particular attention should be given to the proposed solution, in which all processes at the enterprise are grouped: by degree of exploration, feasibility and economic efficiency. For each of them, certain coefficients were determined on the example of the operation of two specific combined technologies: the extraction of uranium ores and coal (**Dychkovskyi et al., 2018**). However, for low-grade uranium deposits, traditional mining is often economically unviable. In such cases, geotechnological methods particularly in-situ leaching (ISL) have proven to be more effective (**Begalinov et al., 2022; Yusupov et al., 2021b**), which is achieved through determining the change in the volume of miner-

* Corresponding author: Erbolat Aben
e-mail address: y.aben@satbayev.university
Received: 26 June 2025. Accepted: 4 November 2025.
Available online: 13 March 2026

als extracted from the ore body depending on the amount of reagent and the filtration rate, using the laws of physics, chemistry and computer modeling (**Vladyko et al., 2022**). In ISL operations, sulfuric acid is commonly used as the primary lixiviant (**Chen & Li, 2022**).

One of the main limitations in the development of ISL is the low dissolution rate of uranium, which is associated with its occurrence in refractory mineral forms and the low concentration of ferric iron (Fe^{3+}) in both ore and groundwater (**Yussupov et al., 2023; Kenzhetaev et al., 2022**). A typical industrial response to this challenge is to increase the concentration of sulfuric acid in the lixiviant. However, this approach not only raises production costs but is also constrained by the current shortage of sulfuric acid in the Republic of Kazakhstan. This shortage has forced National Atomic Company Kazatomprom JSK to revise production plans and initiate the construction of a new facility with an annual capacity of 800.000 metric tonnes of sulfuric acid.

Accordingly, considerable attention is being directed toward the development of improved in-situ uranium leaching technologies.

Current approaches to intensifying uranium leaching involve physical, physico-chemical and chemical methods (**Yanjing et al., 2023; Rakishev et al., 2022; Pękala, 2017**), as well as the sequential leaching of ore bodies at different depths using boreholes of various diameters and special designs (**Khomenko et al., 2023**). While extensive theoretical, laboratory and pilot-scale tests has been carried out, many of these techniques remain expensive, technically complex for industrial application and often environmentally burdensome (**Chen & Li, 2022; Elmardi Suleiman Khayal & Bashier Elagab, 2022; Oryngozha et al., 2020**).

Both research findings and practical experience indicate that the intensity of uranium leaching is strongly influenced by the concentration of dissolved oxygen in the lixiviant. Oxygen content can be increased either by aeration or by direct injection of liquid oxygen (**Cramer et al., 2023; Banos & Scott, 2020; Zeng et al., 2013**). However, oxygen transitions to a liquid phase only under cryogenic conditions or elevated pressure. Although lower lixiviant temperatures improve oxygen solubility, they negatively affect the leaching kinetics. Conversely, increasing hydraulic pressure fivefold from 60 meters has been shown to raise dissolved oxygen concentrations by 70% and uranium content by a factor of seven. As a result, some uranium producers have experimented with in-situ oxygen dissolution methods. For example, at the Uchkuduk deposit, compressed air was injected into the formation using a compressor system. As the oxygen-enriched lixiviant reached pumping wells, uranium concentrations in the pregnant solution increased from 10.0 mg/L (under baseline conditions) to 35.0 mg/L. In another test block, oxygen saturation was achieved through pressure differentials and vacuum induction, doubling uranium content in the solution.

2. Materials and Methods

To improve oxygen enrichment, this study proposes the use of a specialized injector that intensively mixes air with the lixiviant and enhances oxygen transfer by increasing internal solution pressure (see **Figure 1**). The injector consists of a short pipe with a constriction at the center and an opening for air intake.

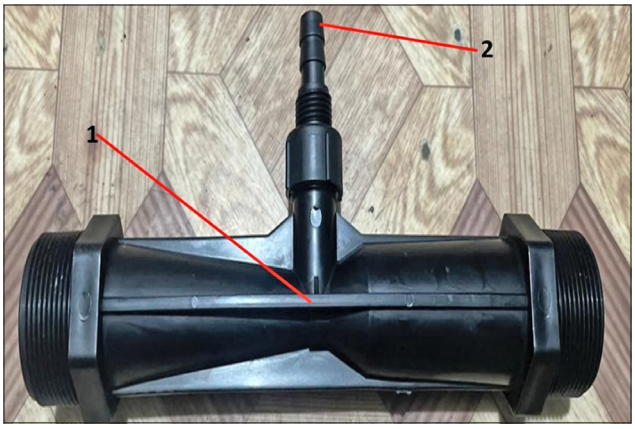


Figure 1. Specialized injector (Venturi tube): 1 –constricted section for pressure drop; 2 – opening for air suction.

As the solution passes through the narrowed section of the injector tube, a pressure drop occurs, causing air to be drawn in. When the solution enters the expanded section, the pressure rises, which promotes the effective dissolution of oxygen from the air into the solution. The advantages of using the specialized injector include low capital and operational expenditures, ease of integration into the lixiviant pipeline, and environmental safety.

To validate the proposed technology, laboratory experiments were conducted using core material from the study site. The Central area of the Mynkuduk deposit was selected as the research object. An analysis of historical leaching data (**Ortalyk Mining Enterprise, 2021**), indicates that, after reaching the maximum uranium concentration in the pregnant solution during the acidification stage with elevated sulfuric acid concentrations of 30.0–50.0 g/L, a distinct and abrupt decline in uranium concentration is observed upon transitioning to the active leaching stage, where the acid concentration decreases to 8.0–10.0 g/L (see **Figure 5**).

The ore body at the study site is predominantly composed of uraninite and coffinite, accounting for approximately 85% and 15%, respectively (**Ortalyk Mining Enterprise, 2021**). It is well known that uranium in uraninite is poorly soluble in sulfuric acid, which necessitates the addition of oxidizing agents to the lixiviant.

Field identification of the core material classified it as gray sand. Data analysis over recent years shows that the average concentration of ferrous iron (Fe^{2+}) in the solution is around 1.3 g/L, while ferric iron (Fe^{3+}) is approximately 0.15 g/L, resulting in a Fe^{3+}/Fe^{2+} ratio of 0.115

(**Ortalyk Mining Enterprise, 2021**). The low concentration of ferric iron also reduces the leaching intensity and similarly necessitates the introduction of oxidants into the lixiviant.

The combined effect of these factors results in a marked decrease in uranium concentration in the pregnant solution.

The research methods consist of analyzing and synthesizing scientific and technical information (**Ortalyk Mining Enterprise, 2021; Vershina LLP, 2010**), as well as practical experience in underground in-situ uranium leaching. They also include laboratory and pilot-scale tests, along with statistical processing and analysis of the results.

Laboratory tests were conducted using a custom-built experimental setup consisting of vessels for the lixiviant, intermediate and pregnant solutions, a core sample from the deposit, and a device for oxygen enrichment of the solution.

The first stage involved determining the influence of sulfuric acid concentration on the degree of oxygen enrichment in the lixiviant. Four vessels were prepared with acid concentrations of 5.0; 8.0; 10.0 and 12.0 g/L. A total of 8 measurements of dissolved oxygen were taken at varying acid concentrations.

Upon determining the optimal concentration of sulfuric acid, subsequent experiments were conducted to examine the relationship between key leaching parameters such as uranium content, the concentrations of ferrous (Fe^{2+}) and ferric (Fe^{3+}) iron, and the degree of oxygen enrichment in the lixiviant. The results obtained using the oxygen-enriched lixiviant were compared with those obtained using the standard (non-enriched) solution.

Oxygen concentration in the lixiviant was measured after passage through the specialized injector. The lixiviant was collected in a sealed vessel designed with a port in the lid for introducing the solution–air mixture, and an electrode was placed at the bottom to measure dissolved oxygen content. Each leaching cycle lasted 7 hours for each core sample. One sample of the initial lixiviant and seven sequential samples of the pregnant solution were taken hourly, totaling eight samples per test. Oxygen concentration was measured using an oximeter, while uranium and iron species were analyzed at the mine's laboratory. The uranium content in the core material used for testing was 0.035%.

For pilot-scale testing, a test block was selected comprising 3 pumping wells and 13 injection wells. Specialized injectors for oxygen enrichment were installed at the injection wells via a bypass line connected to the lixiviant distribution network (see **Figure 2**).

The pilot-scale testing was conducted from late February through November. To obtain comparative data, the operation of the specialized injectors was periodically halted, thereby interrupting the oxygen enrichment of the lixiviant. Uranium concentrations in the pregnant solution were measured in three pumping wells (48-5-04), (48-5-05) and (48-5-06), which were surrounded by injection wells equipped with oxygen injectors. Sampling was carried out in accordance with the operational schedule and supplemented with additional measurements between scheduled dates. It should be noted that, following the installation of oxygen enrichment systems, the average sulfuric acid concentration in the lixiviant was gradually reduced from 12.0 g/L in March to 3.0 g/L by September.



Figure 2. Specialized injectors installed on the lixiviant line via a bypass connection: 1 – main pipeline; 2 – injection well pipeline; 3 – specialized injectors.

3. Results and Discussion

During the laboratory experiments, the initial concentration of dissolved oxygen in the baseline lixiviant was 5.2 mg/L. The results of the laboratory tests assessing the effect of sulfuric acid concentration on the degree of oxygen enrichment in the lixiviant after passage through the specialized injector are illustrated graphically in **Figure 3**.

As shown in **Figure 3**, at a sulfuric acid concentration of 5.0 g/L, the degree of oxygen enrichment in the lixiviant after passing through the specialized injector was 8.4 mg/L in the first test and 8.6 mg/L in the second. Under laboratory conditions, the maximum observed concentration of dissolved oxygen of 9.2 mg/L was achieved when the sulfuric acid concentration was 10.0 g/L. It is important to note that increasing the sulfuric acid concentration from 5 g/L to 10 g/L resulted in an average increase in oxygen enrichment of 8.2%, based on the results of two experimental tests. A further increase in the sulfuric acid concentration to 12 g/L resulted in a decrease of oxygen enrichment of the solution. This finding suggests that sulfuric acid concentration has a significant effect on the degree of oxygen enrichment in the lixiviant, and that its optimal concentration is 10 g/l.

Therefore, further investigations aimed at assessing the effect of oxygen enrichment in the lixiviant on leaching performance were conducted using a sulfuric acid

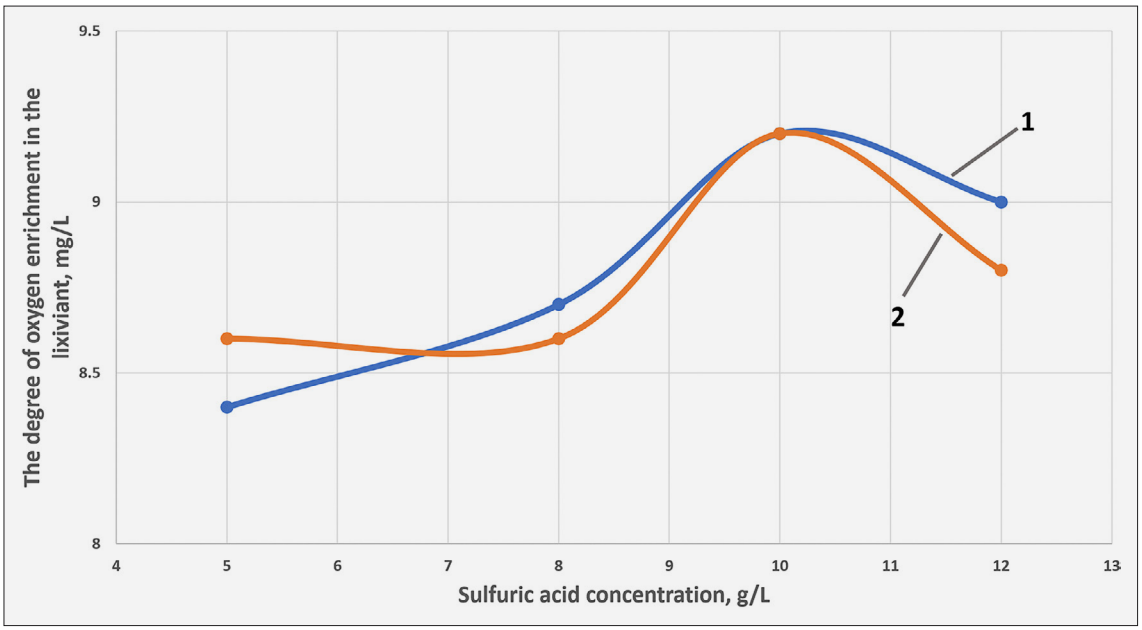


Figure 3. Dependence of oxygen enrichment in the lixiviant on sulfuric acid concentration:
1 – oxygen enrichment, mg/L (Test 1); 2 – oxygen enrichment, mg/L (Test 2).

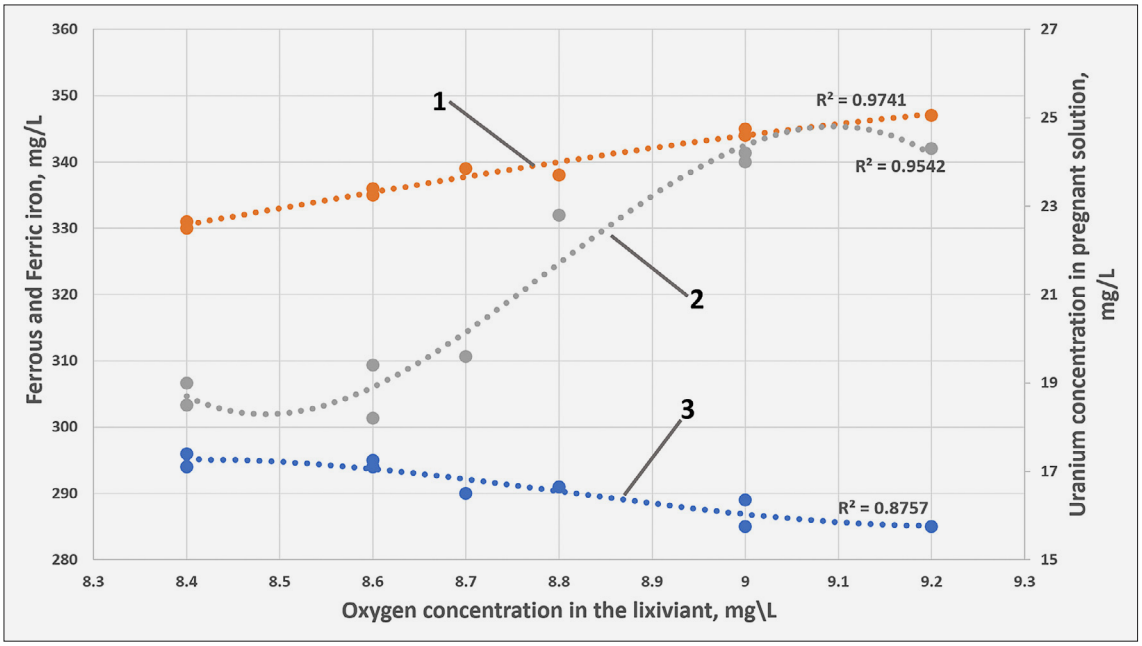


Figure 4. Polynomial regression curves based on dissolved oxygen concentration in the lixiviant:
1 – ferric iron concentration; 2 – uranium concentration; 3 – ferrous iron concentration.

concentration of 10 g/L. The results of this study are illustrated graphically in **Figure 4**.

As shown in **Figure 4**, increasing the degree of oxygen enrichment in the lixiviant from 8.4 mg/L to 9.2 mg/L led to a decrease in ferrous iron concentration from 296 mg/L to 285 mg/L, while the ferric iron concentration increased from 331 mg/L to 347 mg/L. Overall, oxygen enrichment of the lixiviant resulted in an increase in the ferric-to-ferrous iron concentration ratio from 1.12 to 1.22. As the dissolved oxygen concentration in the lixiviant increased from 8.4 mg/L to 9.2 mg/L, and as Fe^{2+} was oxidized to Fe^{3+}, uranium concentration in the pregnant solution increased by 5.8 mg/L.

To compare uranium concentration in the pregnant solution during leaching with and without oxygen enrichment, laboratory experiments were conducted using core material over a period of 7 hours. Comparative plots were generated to illustrate the change in uranium concentration in the pregnant solution during leaching with and without oxygen enrichment (see **Figure 5**).

As shown in **Figure 5**, uranium concentrations in the sixth and seventh samples of the pregnant solution

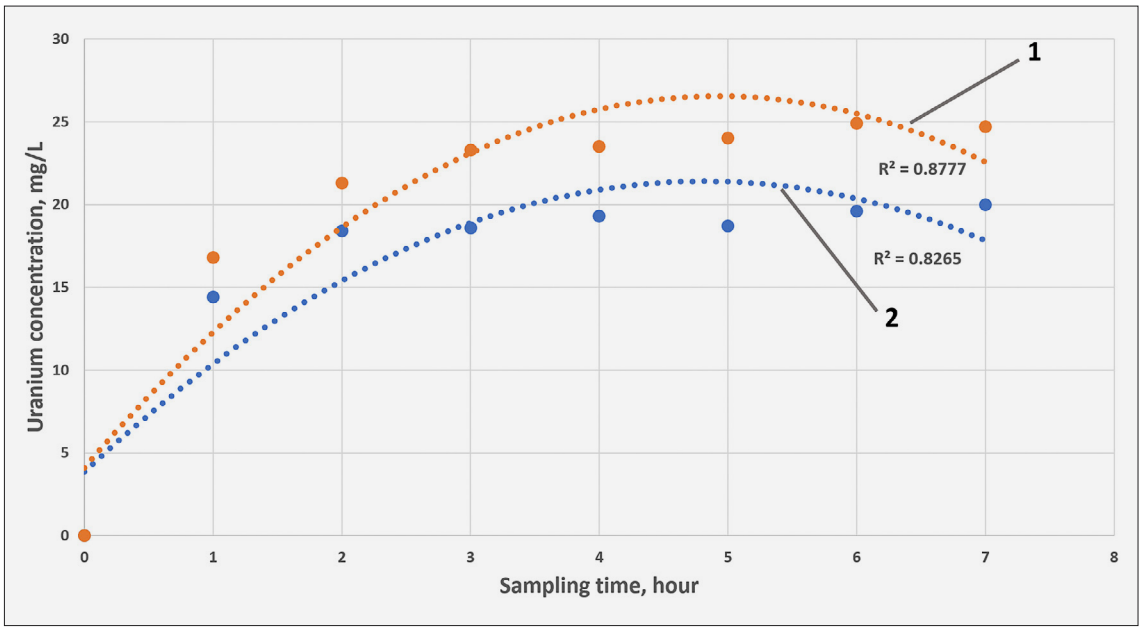


Figure 5. Polynomial regression curves showing uranium concentration in the pregnant solution: 1 – with oxygen-enriched lixiviant, mg/L; 2 – without oxygen enrichment, mg/L.

reached high values under both oxygen-enriched and non-enriched leaching conditions. Laboratory test results demonstrated that leaching with an oxygen-enriched lixiviant yielded uranium concentrations that were, on average of 4.21 mg/L, higher than the concentrations yielded by the baseline (non-enriched lixiviants) technology.

Taking into account the distance between the injection and pumping wells, as well as the filtration coefficient of the formation, positive results from the pilot-scale field trials were observed within 20–30 days after the specialized injector was put into operation. Before solution enrichment with oxygen, the uranium concentration in the productive solution from pumping well 3 (48-5-06) showed a decrease from 113 mg/L to 38 mg/L during the period from February 27, 2024 to March 28, 2024. Following the activation of the injector and the introduction of oxygen-enriched lixiviant, the uranium concentration increased by 10.0 mg/L, or more than 13%. During the course of the pilot operation, a minimal decline in uranium concentration was observed. This was attributed to a reduction in the volume of lixiviant injected into wells 48-4-5, 48-5-10, and 48-5-11, falling below the operational target due to clogging of the well filters. As a result, air intake into the injectors ceased, and oxygen enrichment of the lixiviant was interrupted. After well redevelopment and the restoration of injection flow rates, uranium concentrations in the pregnant solution began to rise again.

In pumping wells 1 and 2, a steady decline in uranium concentration in the pregnant solution was observed over the three months preceding oxygen enrichment of the lixiviant. For example, in pumping well 1, uranium concentration decreased by 10.0 mg/L during the first month, by 20.0 mg/L in the second, and by 30.0 mg/L in the third. After the activation of the specialized injectors and the initiation of oxygen enrichment, uranium concentrations in the pregnant solutions of the experimental wells increased from 108 mg/L to 111 mg/L (well 1), and from 94 mg/L to 98 mg/L (well 2). The difference in uranium content between laboratory and pilot-scale operations can be explained as follows. Laboratory work was carried out using core material over a period of 7 hours, while in pilot industrial operations, the leaching solution passes from the injection well to the pumping well over a period of 15 days. Accordingly, the uranium content in pilot industrial operations will be higher.

As part of the pilot-scale trials, the operation of the specialized injectors was temporarily suspended for comparative analysis. The injectors were turned off between March 20 and May 20, 2024, and again between June 12 and August 1, 2024. It was found that a sharp decline in uranium concentration in the pregnant solution occurred within 20–30 days following the deactivation of the injectors. For example, between May 20 and the end of the month, uranium concentration in the pregnant solution from pumping wells 2 (48-5-05) and 3 (48-5-06) decreased from 97.0 mg/L to 81.0 mg/L and from 86.0 mg/L to 75.0 mg/L, respectively, corresponding to reductions of 16.5% and 12.8%. After reactivating the injectors on June 1, an increase of 3 mg/L was recorded in well 3 (48-5-06), while concentrations in wells 1 and 2 remained stable, indicating no further decline.

As a result, after disconnecting of the special injectors and the termination of oxidation (June 12, 2024 – July 2024), the uranium concentration in the productive solutions exhibited a decline: in well 2 (48-5-05), from 80 mg/L to 62 mg/L (a reduction of 22.5%), and in well 3

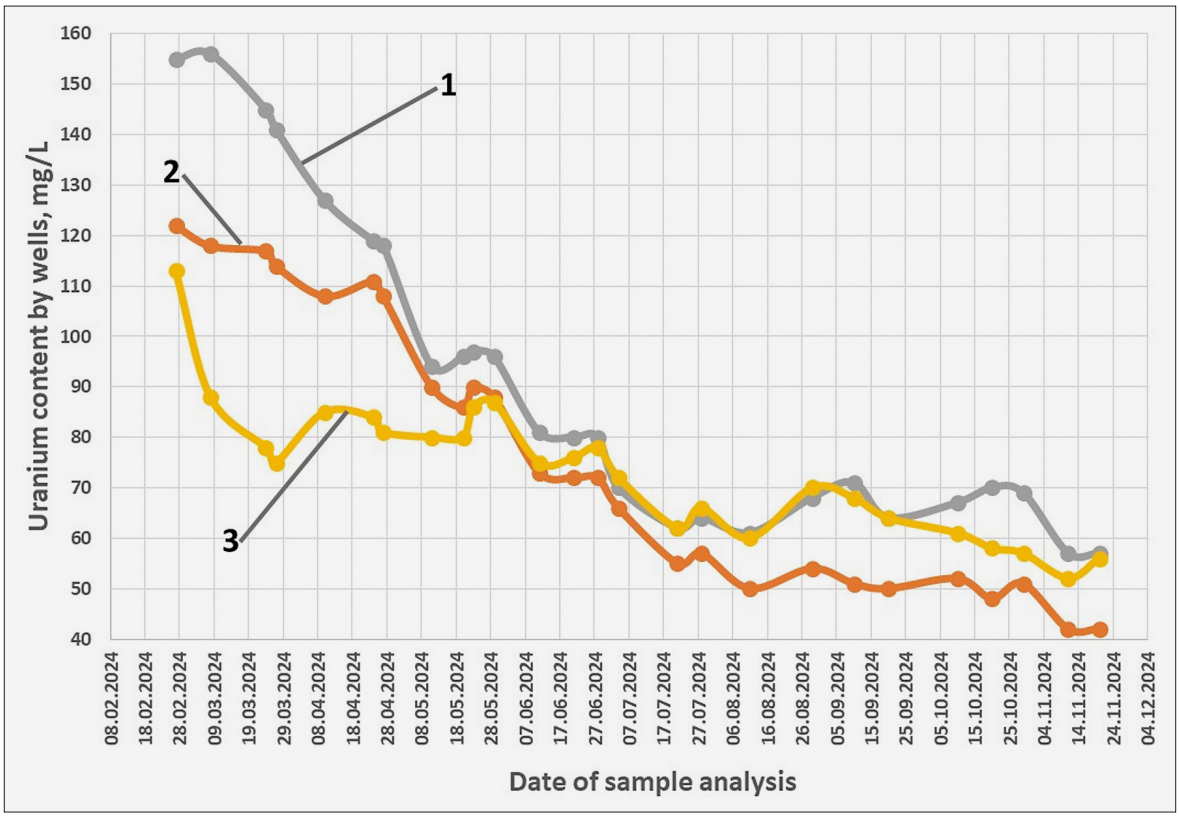


Figure 6. Changes in uranium concentration in the pregnant solution associated with activation and deactivation of the specialized injector at the pilot test block: 1 – uranium concentration in well 48-5-05, mg/L; 2 – uranium concentration in well 48-5-04, mg/L; 3 – uranium concentration in well 48-5-06, mg/L

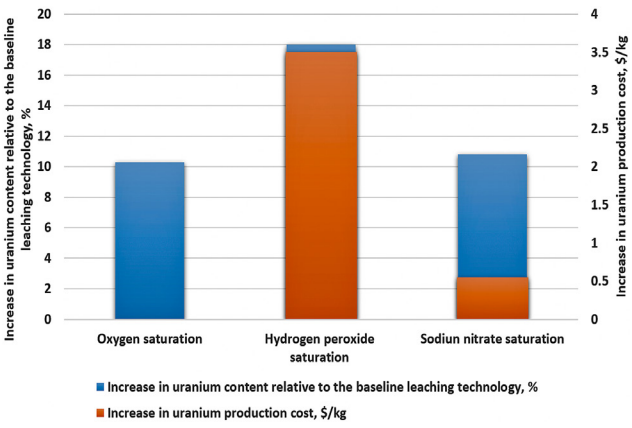


Figure 7. Comparison of selected indicators for different reagents

(48-5-06), from 75 mg/L to 65 mg/L (a reduction of 13.3%). Once the injectors were brought back online between August 1 and August 14, 2024, uranium concentrations in the pregnant solutions of pumping wells 1 (48-5-04), 2 (48-5-05), and 3 (48-5-06) increased from 50.0 mg/L to 54.0 mg/L, from 60.0 mg/L to 68.0 mg/L, and from 60.0 mg/L to 70.0 mg/L, respectively, corresponding to relative increases of 8.0%, 13.3% and 16.7%.

After the subsequent shutdown of the injectors on August 15, a decline in uranium concentrations was again observed: from 54.0 mg/L to 50.0 mg/L in well 1, from 68 mg/L to 64 mg/L in well 2, and from 70 mg/L to 64 mg/L in well 3.

The dynamics of uranium concentration in the pregnant solution associated with the activation and deactivation of the specialized injectors are presented in **Figure 6**.

The evaluation of the proposed technology was performed through a comparative analysis of selected results from previous studies employing various reagents (see **Figure 7**).

The comparative analysis indicates that the use of hydrogen peroxide (**Yusupov et al., 2021a**) and sodium nitrite (**Bashilova & Baibatsha, 2022**) results in an increase in uranium recovery of 7.3% and 0.5%, respectively, relative to atmospheric oxygen. However, this improvement is accompanied by higher production costs: the cost of 1 kg of uranium rises by $3.25 when using hydrogen peroxide and by $0.55 when using sodium nitrite, whereas no additional cost is associated with the use of atmospheric oxygen. It should also be noted that the application of hydrogen peroxide and sodium nitrite necessitates stricter safety measures.

4. Conclusions

Laboratory and pilot-scale studies have demonstrated the positive effect of oxygen-enriched solutions on the

efficiency of in-situ uranium leaching. The increased saturation of the solution with oxygen from air is achieved through the use of a special injector. However, increasing the dissolved oxygen content in the solution promoted the oxidation of ferrous iron (Fe^{2+}) to ferric iron (Fe^{3+}), which in turn enhanced uranium concentration in the pregnant solution.

All three pumping wells in the test block showed either an increase in uranium concentration or a cessation of its decline following the activation of oxygen injectors in the surrounding injection wells. Conversely, uranium concentrations consistently decreased after the injectors were turned off.

On average, the increase in uranium concentration in the pregnant solution amounted to 10.3%, indicating that the implementation of oxygen enrichment technology can reduce the leaching cycle duration and lower operational costs for uranium recovery within the technological block.

A comparison of the results of the proposed technology with previous studies employing various reagents has demonstrated a low production cost of the final product.

As a result of these findings, the oxygen enrichment method using a specialized injector has been adopted by the uranium production enterprise for large-scale implementation.

Funding

This research was funded by the Science Committee of the Ministry of Science and Higher Education of the Republic of Kazakhstan (Grant No. AP26198685).

5. References

Almenov, T., Zhanakova, R., Sarybayev, M. & Shabaz, D.-M. (2025). A Novel Approach to Selecting Rational Supports for Under-ground Mining Workings. *Civil Engineering Journal Iran*, 11(3), 1217–1241. https://doi.org/10.28991/CEJ-2025-011-03-022

Banos, A. & Scott, T. (2020). A review of the reaction rates of uranium corrosion in water. *Journal of Hazardous Materials*, 399, 122763. https://doi.org/10.1016/j.jhazmat.2020.122763

Bashilova, E., & Baibatsha, A. (2022). Geological and Geotechnical Specifics of Uranium Production at Hydrogenetic Deposit Semizbay. *Gornyi Zhurnal*, 7, 61–66. https://doi.org/10.17580/gzh.2022.07.10

Begalinov, A., Shautenov, M., Almenov, T. & Bektur, B. (2022). Leaching process intensification of gold-bearing raw materials. *Mining of Mineral Deposits*, 16, 42-48. https://doi.org/10.33271/mining16.02.042

Bitimbayev, M. Zh., Yusupov, Kh. A., Dzhumabaev, E. I. & Aben, E. (2023). Longline method of underground mining of a deposit (utility model patent). 2023, No.7854. https://gosreestr.kazpatent.kz/Utilitymodel/Details?docNumber=365953

Chen, J. & Li, W. (2022). Analysis on the Current Situation and Trend of Nuclear Energy Development. Proceedings of the 3rd International Conference on Green Energy. *Environment and Sustainable Development*, 277-282. https://doi.org/10.3233/atde220292

Cramer, A., Banos, A., Fung, S., Griffiths, G., Martin, P., Petherbridge, J. & Scott, T. (2023). An investigation of the reaction of metallic uranium with oxygen/nitrogen gas mixtures. *Journal of Nuclear Materials*, 584, 154564. https://doi.org/10.1016/j.jnucmat.2023.154564

Dychkovskyi, R., Vladyko, O., Maltsev, D. & Cabana Cáceres, E. (2018). Some aspects of the compatibility of mineral mining technologies. *Rudarsko-geološko-naftni zbornik*, 33(4), 73-83. https://doi.org/10.17794/rgn.2018.4.7

Elmardi Suleiman Khayal, D. O. M. & Bashier Elagab, D. E. (2022). A Review Study in Mining Industry. *International Journal of Engineering Applied Sciences and Technology*, 7(6), 1–14. https://doi.org/10.33564/ijeast.2022.v07i06.001

Kenzhetaev, Z. S., Kuandykov, T. A., Togizov, K. S., Abdraimova, G. & Nurbekova M. A. (2022). Selection of rational parameters for opening and drilling of technological wells underground uranium leaching. *NEWS of National Academy of Sciences of the Republic of Kazakhstan*, 3, 115–127. https://doi.org/10.32014/2022.2518-170x.184

Khomenko, O., Rudakov, D., Lkhagva, T., Sala, D., Buketov, V. & Dychkovskyi, R. (2023). Managing the Horizon-oriented In-Situ Leaching for the Uranium Deposits of Mongolia. *Rudarsko-geološko-naftni zbornik*, 38(5), 49-60. https://doi.org/10.17794/rgn.2023.5.5

Li, G. & Jia, Y. (2024). A Review of in Situ Leaching (ISL) for Uranium Mining. *Mining*, 4, 120-148. https://doi.org/10.3390/mining4010009

Michel, C., Mercadier, J. & Bonnetti, C. (2022). Classification of Sandstone-Related Uranium Deposits. *Journal of Earth Science*, 33, 236–256. https://doi.org/10.1007/s12583-021-1532-x

Ortalyk Mining Enterprise (2021): Technological Regulations for the Uranium Extraction Process at the Central area of the Mynkuduk Deposit, Shymkent, Republic of Kazakhstan, 136 (not publicly available).

Oryngozha, Ye. Ye., Vorobiev, A. Ye., Zhangalieva, M. & Uteshev, I. Zh. (2020). Study Of Mining-Geological Characteristics Of Uranium Deposits Of Kazakhstan For Development By Underground Well Leaching. *News Of National Academy Of Sciences Of The Republic Of Kazakhstan*, 5(443), 156–164. https://doi.org/10.32014/2020.2518-170x.116

Pękala, A. (2017). Thorium and Uranium in the Rock Raw Materials Used for the Production of Building Materials. Conference: Word Multidisciplinary Civil Engineering – Architecture-Urban Planning Symposium At, Prague, Czech Republic, 12 - 16 June 2017. https://doi.org/10.1088/1757-899X/245/2/022033

Rakishev, B. R., Mataev, M. M., Kenzhetaev, Z. S &. Shampikova, A. Kh. (2022). Innovative methods of intensification in situ leaching of uranium in deposits with low filtration characteristics of ores. *NEWS of National Academy of Sciences of the Republic of Kazakhstan*, 5, 188–206. https://doi.org/10.32014/2518-170x.226

Togizov, K., Kenzhetaev, Zh., Temirkhanova, R., Muzapparova, A., Omirgali, A. & Altaibayev, B. (2024). The Influence of the Physicochemical Characteristics of Ores on the Efficiency of Underground Well Leaching of Uranium Deposits in Kazakhstan. *Minerals*, 14. https://doi.org/10.3390/min14040381

Vershina LLP (2010). Report on the results of detailed exploration of the Central area of the Mynkuduk uranium deposit with uranium reserve estimation, Vershina LLP, Almaty, Republic of Kazakhstan, 131.

Vladyko, O., Maltsev, D., Sala, D., Cichoń, D., Buketov, V. & Dychkovskyi, R. (2022). Simulation of leaching processes of polymetallic ores using the similarity theorem. *Rudarsko-geološko-naftni zbornik*, 37(5), 169-180. https://doi.org/10.17794/rgn.2022.5.14

Yanjing, W., Song, M., Wei, J., You, J., Chen, S., Wang, S. & Wang, Y. (2023). Strengthening Fe(II)/Fe(III) Dynamic Cycling by Surface Sulfation to Achieve Efficient Electrochemical Uranium Extraction at Ultralow Cell Voltage. *Environmental Science & Technology*, 57, 13258–13266. https://doi.org/10.1021/acs.est.3c05133

Youssef, W., El-Maadawy, M., Masoud, A., Alhindawy, I. & Hussein, A. (2024). Uranium capture from aqueous solution using palm-waste based activated carbon: sorption kinetics and equilibrium. *Environmental Monitoring and Assessment*, 196. https://doi.org/10.1007/s10661-024-12560-y

Yussupov, K., Aben, E., Akhmetkanov, D., Aben, K. & Yussupova, S. (2023). Investigation of the solid oxidizer effect on the metal geotechnology efficiency. *Mining of Mineral Deposits*, 17(4), 12–17. https://doi.org/10.33271/mining17.04.012

Yusupov, Kh., Bashilova, E., Tsoy, B. & Aleshin, A. (2021a). Application of Hydrogen Peroxide to Intensify In-Situ Leaching of Uranium. Obogashchenie Rud, 2, 21–26. https://doi.org/10.17580/or.2021.02.04

Yusupov, Kh. A., Rysbekov, K. B., Aben, Kh. Kh. & Bakhmagambetova, G. B. (2021b). Increasing gold leaching efficiency with change of solution rheological properties. *Naukovyi Visnyk Natsionalnoho Hirnychoho Universytetu*, 3, 14–18. https://doi.org/10.33271/nvngu/2021-3/014

Zeng, X-L., Huang, S-Q. & Ju, X-H. (2013). Ab initio study on the reaction of uranium with oxygen. *Journal of Radioanalytical and Nuclear Chemistry*, 298. https://doi.org/10.1007/s10967-013-2442-x

SAŽETAK

Povećanje učinkovitosti terenskoga izluživanja uranija injektiranjem oksidiranoga lužnatog sredstva

U radu se istražuje mogućnost optimizacije učinkovitosti terenskoga izluživanja uranija primjenom kisika kao oksidacijskoga sredstva u lužnatome mediju. S tim ciljem analizirana su geološka obilježja ležišta, nakon čega je provedena serija laboratorijskih i poluindustrijskih istraživanja. Dobiveni podatci sustavno su obrađeni i analizirani. Utvrđen je utjecaj koncentracije sumporne kiseline na stupanj oksidacije lužnatoga sredstva. Laboratorijska istraživanja jezgrinih uzoraka iz ležišta uranija pokazala su konzistentne odnose između koncentracije uranija u bogatoj otopini (*pregnant solution*), oksidacijskih stanja željeza (Fe^{2+} i Fe^{3+}) u lužnatome mediju te razine zasićenosti kisikom. Dobiveni su usporedni rezultati promjene koncentracije uranija u otopini tijekom vremena za konvencionalnu tehnologiju i tehnologiju s oksidiranim lužnatim sredstvom. Laboratorijski rezultati pokazali su povećanje koncentracije uranija za 23,0 % u otopini pri uporabi oksidiranoga lužnatog sredstva u odnosu na kontrolno sredstvo, što upućuje na mogućnost skraćenja vremena izluživanja i smanjenja konačnih troškova proizvodnje metala. Poluindustrijska istraživanja provedena u rudniku uranija potvrdila su pozitivan učinak oksidiranoga lužnatog sredstva na oksidaciju željeza te na povećanje koncentracije uranija u otopini. Sve crpne bušotine unutar istraživanoga bloka pokazale su povećanje ili stabilizaciju koncentracije uranija nakon spajanja posebnoga sustava za oksidaciju u injekcijskim bušotinama koje okružuju crpne bušotine, dok je nakon isključenja sustava koncentracija uranija pala.

Ključne riječi:
terensko izluživanje, oksidacija, koncentracija uranija u otopini, oksidirano lužno sredstvo, dvovalentno i trovalentno željezo

Author's contribution

Khalidilla Yussupov (Doctor of Technical Sciences, Professor): conceptualization, formal analysis, resources, writing – original draft preparation and supervision. **Erbolat Aben** (Candidate of Technical Sciences, Associate Professor): methodology, investigation, writing – review & editing and project administration. **Gulfarizada Abdissatar** (Doctoral student): software and writing – review & editing. **Saifilmalik Myrzakhmetov** (Candidate of Technical Sciences, Associate Professor): validation and visualization. **Dalelkhan Akhmetkanov** (Candidate of Technical Sciences, Associate Professor): validation and visualization.
All authors have read and agreed to the published version of the manuscript.

RGNZ/MGPB

Hydrogeochemical properties of thermal springs for natural therapeutic uses in medical geology at the Ciwidey area, West Java, Indonesia

Rudarsko-geološko-naftni zbornik
(The Mining-Geology-Petroleum Engineering Bulletin)
DOI: 10.17794/rgn.2026.2.14

Original scientific paper

Rizka Maria[1]*, Heri Nurohman[1], Hilda Lestiana[1], Riostantieka Mayandari Shoedarto[1], Eki Naidania Dida[1], Jakah Jakah[1], Ernowo Ernowo[1], Yudi Rahayudin[2]

[1] *Jl. Sangkuriang, Dago, Bandung (Research Center for Geological Resources, National Research and Innovation Agency (BRIN).*
[2] *Jl. Sudirman, Bandung (Polytechnic of Energy and Mining, Ministry of Energy and Mineral Resources, Bandung 40211) Indonesia.*

Abstract

The thermal springs in the Ciwidey region of Indonesia exhibit significant geological heritage and represent significant potential for natural therapeutic applications in medical geology. This study is for assessing hydrogeochemical characteristics of multiple thermal springs in the Ciwidey region and determine their appropriateness for natural therapeutic uses in medical geology. This research examines the hydrogeochemical characteristics of 13 thermal springs in Ciwidey using Atomic Absorption Spectrophotometry (AAS; AA-7000 SHIMADZU), classifying them into three distinct categories based on dominant chemical signatures: Sodium Chloride (Na-Cl), Calcium Sulphate (Ca-SO_4), and Sodium Bicarbonate (Na-HCO_3). Every hydrogeochemical type has unique therapeutic properties linked with their geochemical origin deep geothermal reservoirs, gypsum-rich lithology, or carbonate interactions. The analytical model established from this study identifies specific zones for potential therapeutic use: Na-Cl type waters (e.g. sites P2, P6, P10, P20) promote muscular relaxation and skin relief; Ca–SO_4 type springs (sites P3–P13) improve bone and joint health; and Na-HCO_3 type waters (P9, P14) aid in pH regulation and alleviate digestive and dermatological issues. The present research findings reveal essential insights into the therapeutic potential of Ciwidey's springs and emphasize the significance of site-specific assessments in medical geology.

Keywords:
thermal springs, hydrogeochemical, therapeutic, medical geology, geothermal

1. Introduction

Indonesia is situated along a volcanic pathway known as the Ring of Fire, which spans the islands of Sumatra, Java, the Nusa Tenggara Islands, Sulawesi, and the Maluku Islands. Many of these volcanic paths possess significant potential for geothermal energy (**Waya et al., 2022**). Geothermal sources can arise from three factors: the existence of a heat source, meteoric water, and reservoir rock (**Skopljak et al., 2017; Vlahović & Skopljak, 2019**). Thermal water or light steam ascends to the Earth's surface through faults or joints, which are zones of water passage, manifesting as thermal springs, fumaroles, and solfataras (**Pirajno, 2020**). Thermal springs represent a distinctive geological environment characterized by a high geothermal gradient, ancient volcanism, seismic activity, tectonic conditions, orogeny, and structural features **(Bennett & Walraevens, 2023; Suhail et al., 2024**).

Thermal springs, in addition to being vital natural resources, also signify important geological heritage sites. Thermal spring water, a naturally occurring solution, demonstrates dynamic chemical and physical properties influenced by certain geological conditions (**Li et al., 2024**). Derived from subterranean mineral water, it preserves elevated microbiological cleanliness and demonstrates potential therapeutic properties (**Kekes et al., 2023**), enhanced by diverse chemical composition and health benefits (**Martínez et al., 2017**). Thermal springs are of considerable importance in scientific and medical research, as well as in geotourism and medical geology (**Erfurt-cooper, 2010**). Hydrotherapy utilizing thermal springs water, a type of balneotherapy, originated as an efficacious treatment method for rehabilitation in Europe in the 1800s (**Li et al., 2024**). Thermal springs water hydrotherapy acquired popularity after several decades because of its chemical-physical features, including chemical composition, temperature, and molecular concentration (**Maria et al., 2024**). Thermal springs can be categorized based on their chemical constituents, such as bicarbonate, sulfate, sulfide, and chloride (**Cacciapuoti et al., 2020**).

* Corresponding author: Rizka Maria
e-mail address: rizk002@brin.go.id
Received: 3 August 2025. Accepted: 1 November 2025.
Available online: 13 March 2026

Thermal springs have emerged as a prominent tourist destination. Public interest in thermal springs is observed throughout multiple continents: Europe (42.3%), Asia (26.3%), and Africa (21.7%) (**Valeriani et al., 2018**). In 2017, China accounted for 31.2% of worldwide tourism revenue, attributed to visitors to its thermal springs and mineral resources **(Yeung & Johnston, 2020**). The physicochemical form of thermal waters varies considerably between sources, affected by the rock type and the period of their travel through the rock. This includes a summary of global hydrochemical facies studies, such as those by **Farhat et al. (2021)** in Baltistan, **Rafiq et al. (2024)** in Saudi Arabia, and **Suhail et al. (2024)** in Kullu-Manali, India. These studies highlight the variability in thermal water chemistry due to geological settings, rock types, and subsurface travel time, as emphasized by (**Torres-Ceron et al., 2019**). Certain experts contend that therapeutic thermal water originated decades ago in Asia, where Indians, Japanese, and Chinese initially utilised water extracts from tea and natural thermal springs for medical and spiritual detoxification (**Wangchuk et al., 2021**).

Medical hydrology is a contemporary discipline within medicine; in 1986, thermal springs were recognized as an alternative method for achieving optimal physical and mental health (**Martínez et al., 2017**). Medical hydrology has evolved alongside scientific advancements and is dependent on various disciplines, including Geology, Natural Sciences, Chemistry, Physics, Physiology, and Pharmacy (**Ahaneku & Muogbo, 2024; Li et al., 2023; Finkelman et al., 2018; Buck et al., 2016; Centeno et al., 2016**). Medical hydrology, commonly known as medical water treatment or hydrotherapy, employs water as a therapeutic medium under various physicochemical conditions to prevent and address health issues (**Wangchuk et al., 2021**). Physicochemical techniques are utilized to discover thermal spring water during the earliest stages of hydrothermal resource exploration, particularly in thermally permeable reservoirs (**Farhat et al., 2021; Torres-Ceron et al., 2019**).

Indonesia has adopted the modernisation of thermal spring resorts, especially in urban-proximate regions such as the Patuha volcanic area in South Bandung, West Java (**Rahayudin et al., 2020**). These sites have converted natural thermal springs into leisure wellness destinations, providing accommodations, balneotherapy services, and swimming facilities to entice visitors in pursuit of relaxation and health advantages. The growing wellness trend has prompted enhancements in resort facilities, offering contemporary conveniences while maintaining the therapeutic advantages of mineral-rich waters. The Ciwidey region in West Java, Indonesia, is distinguished due to geothermal activity, which is evident in many thermal springs that have historically been employed for their therapeutic properties. These geothermal features hold significant cultural and economic value while also serving as an intriguing topic for scientific inquiry in medical geology (**Ríos Reyes et al., 2020**). The hydrogeochemical characteristics of thermal springs, including temperature, pH, mineral composition, and trace elements, are essential in assessing their medicinal potential (**Maria et al., 2024**). Minerals, including calcium, magnesium, bicarbonates, and sulfates, prevalent in geothermal fluids, are recognized for their therapeutic benefits in treating musculoskeletal illnesses, dermatological maladies, and circulatory problems (**Cacciapuoti et al., 2020**). Comprehending the geochemical characteristics of these thermal springs elucidates the subsurface processes, water-rock interactions, and geological structures that affect their composition (**Utama et al., 2024**). Furthermore, assessing the therapeutic potential of these waters necessitates a multidisciplinary approach incorporates hydrogeochemistry, and public health considerations.

This study aims to describe the hydrogeochemical properties of various thermal springs with an emphasis on their mineral composition and assess their suitability for natural therapeutic applications in the Ciwidey region of West Java, Indonesia. The uniqueness of this research is that it examines the therapeutic potential of Ciwidey's thermal springs through an analysis of their hydrogeochemical features within the framework of medical geology. This investigation uncovers distinctive water chemistry, geological factors, and public health consequences particular to the Indonesian geothermal region. The study examines the role of several minerals in thermal springs in promoting health advantages, including enhanced circulation, less inflammation, and alleviation of skin disorders. Understanding the geochemical mineralization to comprehend the therapeutic potential of these thermal springs could encourage the advancement of therapeutic and medicinal treatments that leverage natural geothermal resources.

2. Study Area

2.1. Geological Setting

The Indonesian archipelago is located in a very active tectonic zone, where the Eurasian, Indian–Australian, and Pacific plates converge, resulting in frequent earthquakes and volcanic eruptions (**Hamilton, 1973; Katili, 1974**). This severe geological environment created a volcanic belt around Java, encompassing the Ciwidey area in West Java. Ciwidey is situated inside a young volcanic complex, encircled by more ancient volcanoes like Mount Patuha, Puncaklawang, Urug, and Tikukur (**Ashat et al., 2019; Rahayudin et al., 2020; Sriwana et al., 1998, 2000**).

The geological conditions of the Patuha–Ciwidey region are characterized through a range of volcanic and sedimentary rocks that significantly influence the hydrothermal system. The area consists of lava and lahar deposits from Mount Patuha (Qv) and Mount Kendeng

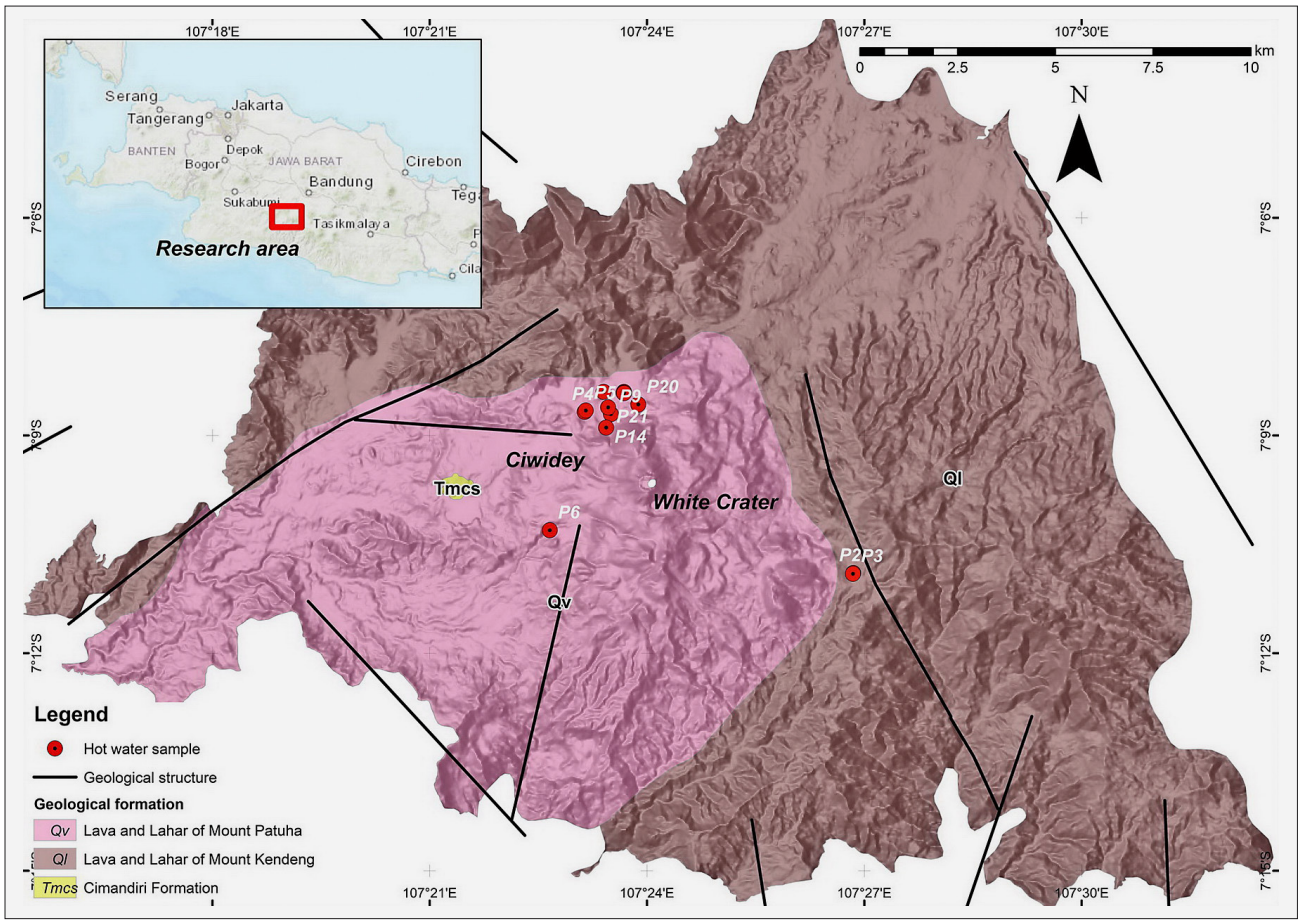


Figure 1. Map of the study area of the Ciwidey region, West Java Province, Indonesia (**Alzwar et al., 1992**)

(Ql), which are Quaternary volcanic materials that improve permeability and promote water–rock interactions. The Cimandiri Formation (Tcms), a Tertiary sedimentary formation consisting of sandstones, shales, and conglomerates, is underlain by significant fault zones (**Alzwar et al., 1992**) (see **Figure 1**). The vertical movement of boiling reservoir steam is responsible for the formation of fumaroles and hot springs in the Ciwidey region. Its ascent to the surface is governed by the Ciwidey normal fault. Ciwidey's sulfuric acid hot water is created when reservoir steam condenses near the surface (steam heating) (**Rahayudin et al., 2020**). The interconnected reservoirs in the Patuha region, located laterally between the White Crater, Cibuni, and Ciwidey. These reservoirs are divided by the Cimanggu Normal Fault, which separates the Cibuni Crater reservoir from the White Crater reservoir, while the Cileulur Normal Fault delineates the White Crater reservoir from the Ciwidey Crater reservoir (**Khasmadin & Harmoko, 2021**). These faults serve as pathways for geothermal fluid movement and define separate reservoirs, enhancing the mineralization and hydrogeochemical variety of the thermal springs. The geothermal system in the Patuha region, especially near White Crater, Kawah Cibuni, and Kawah Ciwidey, indicates surface characteristics like fumaroles and crater lakes that signify an upflow zone, with steam emissions penetrating the surface via permeable geological formations (**Ashat et al., 2019**). This geological context is crucial for comprehending the spatial distribution, recharge processes, and therapeutic potential of Ciwidey's thermal waters.

2.2. Hydrogeological Condition

The heterogeneous geological structure, consisting of lava and lahar deposits from Mount Patuha and Mount Kendeng, along with the Cimandiri Formation, significantly influences the hydrogeochemical properties of the thermal springs in Ciwidey (**Rahayudin et al., 2020**). Volcanic deposits promote vigorous water–rock interaction, leading to increased concentrations of minerals like salt, calcium, and sulphate (**Ashat et al., 2019; Chandra et al., 2022**). The geological features, volcanic structure, fault-controlled permeability, and lithological diversity are essential in determining the hydrogeochemical signatures present in the thermal springs (**Rahayudin et al., 2020; Sumotarto et al., 2021**). Furthermore, the Cimandiri Formation, characterised by its sedimentary strata and fault structures, facilitates groundwater flow and permeability, allowing for deeper circulation of geothermal fluids and stimulating the interaction between magmatic gases and meteoric waters

(**Rahayudin et al., 2020**). Fumaroles, hot springs, and mud pools are examples of geothermal phenomena that are produced by the region's volcanic vents, faults, and precipitous inclines. These geothermal phenomena are particularly prevalent in areas such as Kawah Putih and Kawah Cibuni (**Lazzerini & da Silva, 2020; Rahayudin et al., 2020; Sriwana et al., 2000**).

The thermal springs are direct representations of this dynamic geological environment, significantly influenced by the youthful volcanic complex of Mount Patuha and adjacent peaks, including Mount Urug, Puncaklawang, and Tikukur (**Sriwana et al., 2000; Rahayudin et al., 2020**). The hot springs with moderate temperatures are located on the northern side of the Patuha volcanic area, have a chloride bicarbonate dissolving water type, a neutral pH, and are dominated by Na-Ca-SO_4, indicating a combination of reservoir and meteoric water (**Bujung et al., 2010**). Several of the thermal springs selected here are utilised for bathing and therapeutic purposes (**Maria et al., 2024**). These locations are also situated near prominent trekking paths and tourist destinations. The majority of the chosen locations are situated adjacent to the residential zone. The geological framework not only affects the hydrogeochemistry but also enhances the geothermal potential and therapeutic variety found in the region's thermal waters.

3. Materials and methods

3.1. Sampling and water quality analysis

A total number of 13 thermal springs waters were collected in polyethene screw capped bottles in May 2025. The bottles were washed with tap water followed by rinsing with distilled water before collecting the samples. All precautions were taken during sampling, transportation and storage. The geographical coordinates of each site, including latitude, longitude, and elevation, were documented utilizing the Global Positioning System (Garmin GPS Map 66s). The water temperature, pH, electrical conductivity (EC), total dissolved solids (TDS), oxidation-reduction potential (ORP), and salinity of the thermal springs were assessed in situ using Yieryi New TDS pH/TDS/EC/Temperature meter digital water quality monitor tester meter during sampling. Bicarbonate and chloride concentrations were determined through acidimetric and argentometric titration techniques. In compliance with APHA standard procedures; APHA 2320 B for bicarbonate (alkalinity) using acid titration. APHA 4500-Cl B for chloride measurement applying argentometric titration with silver nitrate (**APHA., 2017**). The sulphate analysis was conducted through a Shimadzu UV VIS 1700 double-beam spectrophotometry. The results were expressed in milligrams per Liter (mg/L), with the exception of pH (measured in units) and electrical conductivity (EC; measured in µS/cm).

3.2. Measurements and Data Analysis

The analysis of sodium, magnesium, calcium, and potassium cations was conducted using an Atomic Absorption Spectrophotometry (AAS) equipment through AA-7000 SHIMADZU, incorporating background correction with Deuterium lamps (D2-lamps) and hollow cathode lamps. Reagent blanks, duplicate samples, and reference standard samples have been created to validate the precision of the analytical methods (**Bisergaeva & Sirieva, 2020**). The analysis of sulphate, chloride, and bicarbonate anions was conducted using UV-Vis spectrophotometry, argentometry (Mohr method), and acidimetry, respectively. The geochemical data were analyzed using Liquid Chemistry Plotting Spreadsheet Version 3, that are was created by Powell Geoscience Ltd (**Powell & Cumming, 2010**). The fluid type was classified using a triangular ternary diagram based on the amounts of chloride (Cl^-), sulfate (SO_4^{2-}), and bicarbonate (HCO_3^-). This graphic facilitates in identifying the origins of geothermal fluids through illustrating the relative concentrations of three major anions, that signify various hydrochemical environments, including volcanic, sedimentary, or meteoric sources.

4. Results

The water physicochemical characteristics are related to its subsurface pathways, the temperature at depth, the mineral composition of the surrounding rocks, and the movement time (**Kieu & Nguyen, 2024; Pham & Nguyen, 2024**). Thermal spring waters have diverse chemical compositions, according to the lithological characteristics (**Mohamedi & Chenakers, 2022**). The Ciwidey region contains abundant groundwater that produces several thermal springs. The current study proposes to identify the physicochemical properties that provide health benefits for natural therapeutic applications in medical geology within the Ciwidey area. A summary of physicochemical characteristics of Ciwidey thermal Springs during the month of April 2025 are shown in **Table 1**. The temperature of thermal springs ranges from 32.6 to 92.6°C. Regarding the context of temperature, mineral waters can be classified as cold (< 20°C at source), hypothermal (20-30°C at source), mesothermal (30-40°C at source), and hyperthermal (> 40°C at source). The thermal spring in Ciwidey is classified as mesothermal – hyperthermal waters. The pH of Ciwidey thermal springs ranges from 1.71 to 7.08. Thermal water is categorised into six types based on pH levels: strong acid ($pH < 2$), acid ($2 \leq pH < 4$), weak acid ($4 \leq pH < 6$), neutral ($6 \leq pH < 7.5$), weak alkaline ($7.5 \leq pH < 9$), and alkaline ($pH \geq 9$) (**Farhat et al., 2021**). The total dissolved solids (TDS) of thermal waters range from 61 to 1170 mg/L. Increased TDS levels may signify extended groundwater residence time and greater flow distance (**Lee et al., 2021**). The hydrogeochemical analysis indi-

Table 1. Physico-chemical parameters of some thermal waters around the Ciwidey region.

Site	Temp	pH	EC	TDS	Na^+	K^+	Ca^{2+}	Mg^{2+}	Cl^-	HCO_3^-	SO_4^{2-}
P2	87.9	2.3	1676	837	0.87	2.09	0.01	0.05	90.85	0.01	596.70
P3	74.8	2.54	108	61	1.54	1.95	0.33	1.86	71.68	0.01	548.78
P4	42.5	6.48	1245	623	89.76	23.22	55.90	60.58	158.11	360.51	186.42
P5	40.2	6.07	1219	624	91.78	24.63	47.38	49.98	116.70	329.40	126.07
P6	92.6	1.71	1176	645	7.36	2.55	0.06	3.54	124.19	0.01	319.11
P9	36.8	6.18	836	409	181.88	22.77	23.30	17.03	48.84	377.59	55.85
P10	52.3	5.66	2370	1170	199.74	83.31	50.35	79.95	345.98	338.55	300.97
P11	57.4	5.86	2300	1120	169.76	76.22	53.48	78.52	344.06	377.59	316.44
P12	47.4	7.08	1664	832	266.82	70.86	47.33	70.91	303.80	330.62	248.24
P13	32.6	6.2	776	387	0.01	17.64	5.82	27.10	89.10	213.50	108.00
P14	70.3	6.13	935	464	429.99	28.93	4.96	20.55	66.10	413.58	56.00
P20	60.8	5.89	2060	1010	293.32	66.79	30.92	61.57	240.54	368.44	285.02
P21	46.3	5.93	1475	706	281.41	54.21	176.73	53.68	250.13	417.85	63.31
min	32.6	1.71	108	61	0.0052	1.94	0.01	0.049	48.84	0.01	55.845
max	92.6	7.08	2370	1170	429.99	83.31	176.73	79.95	345.98	417.85	596.7
average	57.07	5.233	1372	683.69	154.94	36.55	38.198	40.41	173.08	271.36	246.99

Temp: Temperature (°C); EC (µS/cm); All Units mg/L except pH

Table 2. Physico-chemical parameters comparison between Ciwidey thermal springs and other parts of the world.

Parameter	Ciwidey (This study)	Baltistan, Pakistan (Farhat et al., 2021)	Saudi Arabia, (Rafiq et al., 2024)	Manali, India, (Suhail et al., 2024)	Toyam, Japan, (Sasaki et al., 2021)	Fengshun, South China, (Luo et al., 2022)	Gandaki, Nepal, (Chalise et al., 2023)
T	32.6 - 92.6	41	56	49	59.9	80.1	64.3
pH	1.7 - 7.1	7.5	7.9	8.0	7.54	8.0	8.8
EC	108 - 2370	510	3161	-	195	357	16270
TDS	61 - 1170	305	2055	709.9	-	-	6637
Na^+	0.005- 429.9	15	463	231	310	97.7	370
K^+	1.95 - 83.3	3.95	93	45	40	3.9	137
Ca^{2+}	0.01 - 176.7	81	295	37	8.6	3.9	364
Mg^{2+}	0.05 - 79.9	20	2.04	15	0.3	0.1	121
Cl^-	48.8-345.9	10.8	538.52	341	490	12.2	39.64
SO_4^{2-}	55.8 - 596.7	82.5	433.39	70	57	7.7	24.9
HCO_3^-	0.01 - 417.8	271	71.06	296	82	241	490

Units mg/L except pH, EC (µS/cm), Tem. (◦C).

cates that the thermal springs in the Ciwidey region include Na^+ (0.0052–429.99 mg/L), K^+ (1.94–83.31 mg/L), Ca^{2+} (0.01–176.7 mg/L), and Mg^{2+} (0.04–79.9 mg/L). SO_4^{2-} (55.8 - 596.7 mg/L), Cl^- (48.84 - 345.98 mg/L), and HCO_3^- (0.01 - 417.85 mg/L).

The origin of the major ions has been explained as follows (**Hem, 1985**): Na^+ (Sodium): Generally sourced from the weathering of sodium-rich plagioclase feldspars found in andesitic and basaltic volcanic rocks. K^+ (Potassium): released from the transformation of potassium-rich minerals like orthoclase and biotite, usually found in volcanic rocks. Ca^{2+} (Calcium): derives from the dissolution of calcic plagioclase and secondary carbonate minerals such as calcite, which may develop during hydrothermal processes. Mg^{2+} (Magnesium): originates from the decomposition of mafic minerals including pyroxene and

olivine, which are prevalent in basaltic lava flows and lahar deposits. SO_4^{2-} (Sulfate): Generated from the oxidation of sulfide minerals, and the absorption of volcanic gases, which interact with groundwater to yield sulfuric acid. Chloride (Cl^-): Usually injected through magmatic degassing and the leaching of chloride-containing minerals or evaporites within the geothermal reservoir. Bicarbonate (HCO_3^-): Produced by the dissolution of carbonate minerals and the reaction of CO_2 (from magmatic or biogenic origins) with meteoric water. The volcanic deposits of Mount Patuha and Mount Kendeng represent the major lithological sources for these ions, while the faulted sedimentary layers of the Cimandiri Formation enhance fluid circulation and enhance deeper water–rock contact (**Rahayudin et al., 2020**). This comprehensive geological framework elucidates the observed ion concentrations and validates the local geothermal activity and therapeutic water characteristics.

The thermal spring's diverse ion concentrations, including sodium, potassium, calcium, magnesium, sulphate, chloride, and bicarbonate, indicate a complex hydrogeochemical system created from various lithologies and mixed water sources (**Martínez et al., 2017; Kieu & Nguyen, 2024; Pham & Nguyen, 2024**). Elevated sodium chloride, chloride, and sulphate concentrations indicate extended interactions with volcanic rocks and evaporite minerals, potentially involving magmatic contributions, whereas increased calcium and magnesium levels suggest dissolution from carbonates and anhydrites (**Lee et al., 2021**). Bicarbonate enrichment could indicate meteoric water infiltration and CO_2 absorption alongside moving through carbonate deposits (**Kieu & Nguyen, 2024; Pham & Nguyen, 2024**). Collectively, these patterns signify a dynamic system influenced by both profound geothermal processes and surface factors (**Gómez Diaz, 2021**).

The physicochemical form of thermal waters varies considerably between sources, affected by the rock type and the period of their travel through the rock. Thus, the thermal water's ascent to the surface is of crucial significance as it might modify its chemical composition (**Torres-Ceron et al., 2019**). Several studies have also been published on the analysis of hydrochemical facies of hot springs from various regions worldwide (see **Table 2**). The high concentrations of Na^+ and SO_4^{2-} in Ciwidey springs are consistent with the volcanic origin and magmatic gas interactions described in **Torres-Ceron et al. (2019**). **Farhat et al. (2021)** observed elevated Cl^- and HCO_3^- levels in Baltistan springs, which are comparable to our findings, though the geological sources differ. **Rafiq et al. (2024)** identified Na-HCO_3 facies in the Ain Al-Harrah geothermal system, similar to some Ciwidey samples, suggesting analogous water–rock interaction processes. **Suhail et al. (2024)** emphasized the role of lithology and residence time in shaping water chemistry, which aligns with our interpretation of the Ciwidey system's volcanic-sedimentary framework.

5. Discussion

5.1. Hydrogeochemistry Classification of Ciwidey Thermal Spring Waters

The Ciwidey geothermal zone, located within a young volcanic complex and surrounded by older formations, displays numerous geological features that collectively affect the hydrogeochemical qualities of its thermal springs (**Alzwar et al., 1992; Ashat et al., 2019; Rahayudin et al., 2020; Sriwana et al., 1998, 2000**). The interaction between volcanic rocks and geothermal fluids enhances mineral enrichment particularly sodium, calcium, and sulphate while fault-controlled permeability and lithological diversity facilitate deep groundwater circulation and mixing of meteoric water with magmatic gases (**Rahayudin et al., 2020; Sumotarto et al., 2021**). These values holistically support Ciwidey's thermal waters as a promising resource for medicinal and wellness purposes. These strata experience considerable hydrothermal alteration and water–rock contact, leading to the mobilization of various ions into the geothermal fluids (**Hem, 1985; Mahala, 2019**). The water temperature typically fluctuates between 38°C and 45°C, thus being great for improving blood circulation and muscular relaxation (**Mahala, 2019; Yashod, 2025**). The pH values range from 6.8 to 7.5, signifying neutral to slightly alkaline conditions that are friendly on the skin and effective in treating inflammatory diseases (**Mahala, 2019)**. EC levels range from 1,200 to 2,500 µS/cm, indicating a high (**Pham & Nguyen, 2024**) concentration of dissolved ions that boost therapeutic efficacy. Meanwhile, TDS concentrations range from 800 to 1,800 mg/L, providing the water mineral-rich and ideal for balneotherapy, particularly skin and joint treatments (**Mahala, 2019; Yashod, 2025**).

The most significant step in natural hydrogeochemical analysis is to classify the water types for all samples. This study identified water type and source interpretation applying a Piper diagram (**Piper, 1953; Appelo & Postma, 1993**). The Piper diagram is extensively employed to categorize water types based on main cation and anion concentrations, enhancing the analysis of hydrogeochemical processes resulting from the interaction between water and aquifer materials (**Iskandar et al., 2013; Piper, 1953**). The classification of thermal waters can be conducted based on various parameters, including water mineralisation and their physicochemical composition (**Lee et al., 2021; Luo et al., 2022; Malkemus et al., 2021**). The physicochemical composition of thermal waters significantly differs among sources, depending on the duration of transition through rock and the type of rock encountered (**Fikri-Benbrahim et al., 2021**). The hydrogeochemical composition of water samples in the Ciwidey area is summarized in **Table 1**. Major cations and anions were analyzed using the Piper diagram. All water data showed distinction in chemical

characteristics (see **Figure 2a**). The Piper diagram illustrates the chemical composition of the water samples, utilising reaction values derived from the concentrations of their principal constituents (cations and anions). An analysis of the Piper diagram (see **Figure 2a**) reveals that the heat waters distinctly occupy specific regions. The chemical composition of the examined groundwater transitions from fresh to alkaline along the extensive flow course, influenced through by the geological environment characterised between alternating volcanic and carbonate rock formations inside the aquifers.

The thermal water data were classified into Na–Cl, Ca–SO_4, and Na–HCO_3 water types. The relative abundance of specific ions, including Na^+, Cl^-, Ca^{2+}, SO_4^{2-}, and HCO_3^-, in thermal springs is a multifaceted process shaped by diverse geological and hydrological processes s (**Mahala, 2019**). Thermal water dissolve ions from surrounding rocks and transports them to the surface, potentially contributing to the prevalence of the Na-Cl water type identified in the current research. Whenever water traverses the earth's crust, it gets minerals and salts from the rocks it encounters, therefore influencing its chemical composition (**Chalise et al., 2023**). Significantly, Na and Cl are among the most prevalent elements in thermal springs, and their occurrence can be attributed to the dissolution of sodium chloride-bearing rocks, such as halite or rock salt. The thermal water solubilizes these minerals and transports them to the surface. our may be the primary reason for the enrichment of the Na–Cl water type in our study. The Na-HCO_3 characteristics mainly belong to groundwater and water of meteoric origin which are found in locations P9, and P14. The Na-Cl indicates an outflow characteristic of the system, has experienced an intensive dilution process with shallow groundwater in locations P2, P20, and P21.

The concentrations of Ca^{2+} and SO_4^{2-} at sampling points P3, P4, P5, P6, P10, P11, P12, and P13 indicate strong mineralization, consistent with the presence of a Ca–SO_4 water type. The circulation in this case occurs through Patuha mountain with a way through evaporite rocks represented mainly by gypsum, favoring high sulfates content (**Iskandar et al., 2018**). The Ca-SO_4, and Na-HCO_3 types exhibit relatively high concentrations of Ca and Na, along with near-neutral to alkaline conditions, primarily resulting in calcite precipitation (**Rahayudin et al., 2020**), as evidenced by the travertine formations.

The anions elements are also important in signifying a fundamental process of fluids during lateral flow towards the surface (see **Figure 2b**). According to the thermal springs anion Cl–SO_4–HCO_3 ternary diagrams, there are four distinct water anion types in the Ciwidey region, as detailed below:

1. Sulfate–Chloride Waters

The waters-type in volcanic geothermal systems, identified through their position around the SO_4 peak in

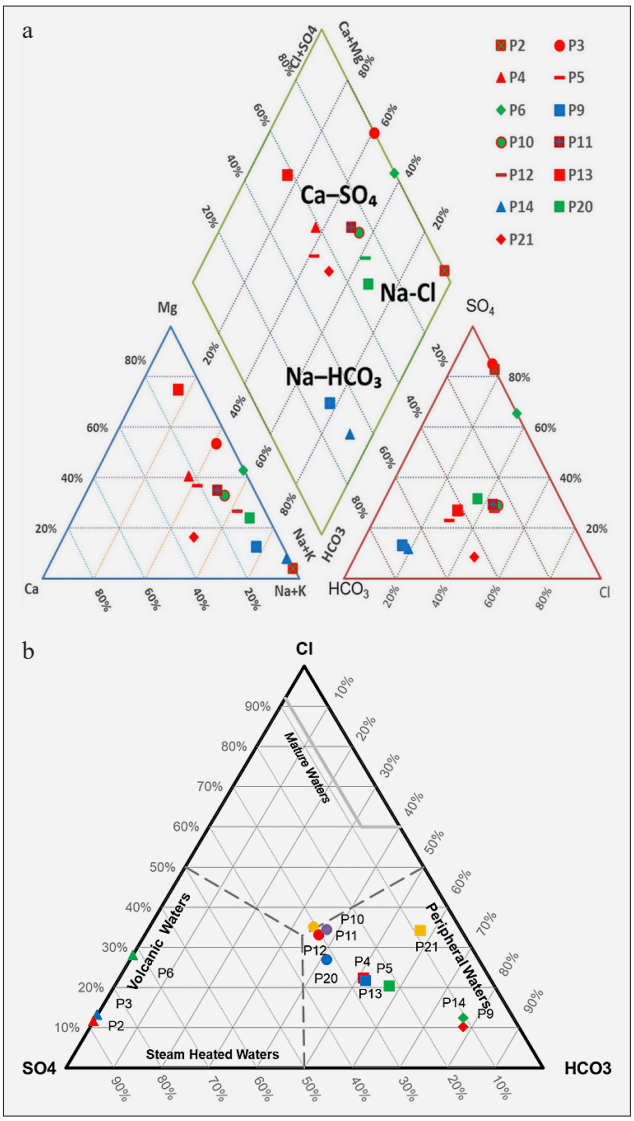


Figure 2. (a) Data plot of thermal springs in a Piper diagram **(b)** Data plot of thermal springs anion Cl–SO_4–HCO_3 ternary diagrams in the Ciwidey region.

Cl–SO_4–HCO_3 ternary diagrams, generally originate from the oxidation of volcanic gases like hydrogen sulfide (H_2S) above the surface or from the oxidation of pyrite (FeS_2) in shallow areas (**Rahayudin et al., 2020**). These processes generate highly acidic fluids composed of sulfate and lacking in chloride and bicarbonate, commonly found around fumaroles, crater lakes, and steam-heated springs (**Sriwana et al., 2000**). In areas like the Patuha Geothermal Field, samples P2, P3, and P6 from the crater lake exhibit this signature, showing interactions between surface gases and acid rock processes that imply magmatic influence and near-surface geothermal activity. The decreased concentrations of calcium and magnesium indicate limited contact with carbonate or silicate formations. Medical Geology for high sulfate levels could trigger gastrointestinal discomfort upon consumption, whereas increased chloride can increase hypertension in susceptible individuals (**Crespo et al.,**

2021). Trace metals such as Fe^{2+} and Mn^{2+} are present in moderate concentrations; although required in minimal quantities, they can become hazardous at higher levels (**Duvert et al., 2019**). These streams could have an acidic pH, enhancing the solubility of toxic metals such as arsenic or lead when these elements exist in the surrounding geology.

2. Bicarbonate-rich waters

Bicarbonate-rich waters have elevated concentrations of bicarbonate and calcium-magnesium, signifying interaction with carbonate rocks like limestone or dolomite (**Quattrini et al., 2016**). The presence of moderate sulfur and chloride indicates potential mixing with deeper geothermal fluids (**Çevikoğlu & Başaran, 2023**). The thermal springs at P9, and P14 presumably derive from shallow meteoric recharge areas that have infiltrated sedimentary formations. Bicarbonate-rich waters are often alkaline, helpful in the neutralization of stomach acid and commonly utilized in therapeutic bathing (**Farhat et al., 2021**). However, increased levels of calcium and magnesium may facilitate the development of kidney stones in people who are at risk (**Sorensen, 2014**). The very low concentrations of trace metals keep these waters suitable for ingestion; nevertheless, monitoring has been necessary (**Moldovan et al., 2022**).

3. Chloride-Bicarbonate Waters

Chloride-Bicarbonate Dilution as Peripheral Water: The majority of thermal springs in Ciwidey are situated between the chloride and bicarbonate elements P4, P5, P13, and P21. The thermal springs exemplify deep geothermal reservoirs that exhibit prolonged residence durations and significant water–rock interaction (**Zhang et al., 2023**). These waters are significantly mineralized and could present hazards when consumed consistently. Increased sodium and chloride levels might impact cardiovascular health, whilst elevated sulfate could cause laxative symptoms (**Fikri-Benbrahim et al., 2021**). The elevated quantities of mineral in this group raise concerns regarding metal toxicity, particularly for susceptible groups such as children and pregnant women. Prolonged exposure might culminate in neurological or renal complications (**Gwenzi et al., 2018**).

4. Mixed Composition Waters

The thermal springs at P9, P10, P11, P12, P20, and P21 situated mixed composition Chloride - Bicarbonate waters. This thermal springs water is generated from the dilution or amalgamation of chloride during lateral flow, facilitated by either groundwater or bicarbonate water (**Joshi et al., 2018**). This water type indicates the boundary of significant upflow and outflow zone structures in elevated terrain systems (**Iskandar et al., 2013**). Elevated chloride concentrations at P10, P11, P12, P20, and P21 signify proximity to the upflow zone. It likely represents a transitional zone where shallow and deep waters mix, possibly influenced by fault zones or fractures that allow vertical fluid movement (**Wang et al., 2018**). Mixed waters can be unpredictable in their health effects. While they may be suitable for balneotherapy, the high trace metal content could pose long-term health risks if used for drinking (**Hamidizadeh et al., 2017**).

5.2. Therapeutic Properties of Ciwidey's Thermal Springs

The therapeutic effects of thermal water are closely linked to its geochemical composition, specifically the concentrations of ions such HCO_3^-, SO_4^{2-}, Na^+, K^+, Ca^{2+}, Mg^{2+}, and Cl^-, these directly affect physiological processes (**Hem, 1985; Mahala, 2019; Pham & Nguyen, 2024; Yashod, 2025**). Calcium and magnesium promote bone strength, muscular function, and nerve signaling, whereas sodium and potassium maintain fluid balance and muscle relaxation. Sulfate and bicarbonate have anti-inflammatory and detoxifying properties, assisting in the treatment of rheumatic and skin disorders. Chloride promotes mineral absorption and hydration. These ions, whose are absorbed through the skin during balneotherapy, have been demonstrated to relieve musculoskeletal pain, enhance circulation, and promote general health, therefore their presence in thermal waters is an important consideration in therapeutic classification (**Hem, 1985; Mahala, 2019; Pham & Nguyen, 2024; Yashod, 2025**).

The mineral composition and temperature fluctuations in Ciwidey's thermal springs indicate unique therapeutic properties: Acidic waters (pH < 4) can facilitate dermatological therapies by promoting exfoliation and microbial regulation (**Cavanah, 2018**). Neutral and bicarbonate-rich springs enhance skin hydration and pH equilibrium, advantageous in spa treatments (**Cavanah, 2018; Fikri-Benbrahim et al., 2021**). The presence of calcium and sulfate suggests a possible benefit for bone and joint health, consistent with treatment methods for rheumatic and musculoskeletal illnesses. Soaking in thermal springs high in calcium and magnesium is essential for stimulating growth and sustaining strong bones. It also aids in alleviating illnesses such as vascular problems, neuritis, arthritis, bronchial infections, and dysmenorrhea. Furthermore, it promotes dermal health and facilitates the conversion of blood glucose into energy **(Torres-Ceron et al., 2019; Cacciapuoti et al., 2020**). Hyperthermal waters with increased ion concentration may improve blood circulation, promote relaxation, and stimulate metabolism (**Cacciapuoti et al., 2020**). Major minerals present in thermal waters can be integrated into society for their nutritional benefits to the human body (**Shoedarto et al., 2016**). Numerous ailments can be addressed via the utilization of various hot springs that include advantageous major minerals often found in thermal water (**Al Dulaymie et al., 2013**).

The hydrogeochemical composition of thermal springs has its own unique advantages for human health. The water derived from these springs has a capacity to

boost digestion, enhance blood circulation, alleviate dermatological illnesses, soothe muscles, speed up the healing process, and detoxify the lymphatic system of the body (**Erfurt, 2011; Martínez et al., 2017; Cavanah, 2018; Lazzerini & da Silva, 2020; Cacciapuoti et al., 2020; Vaidya & Nakarmi, 2020; Zhang et al., 2022**).

5.3. Hydrogeochemistry properties of thermal springs for natural therapeutic uses

The significance to use thermal waters for therapeutic purposes is naturally determined by their thermal and chemical contents. The thermal spring of Ciwidey contains a lot of minerals that affect the human body in different external and internal mechanisms for physical rehabilitation and hydrotherapy. Thermal springs in the Ciwidey region have been divided into three hydrogeochemical types: Sodium Chloride (Na-Cl), Calcium Sulfate (Ca-SO_4), and Sodium Bicarbonate (Na-HCO_3), each offering unique therapeutic advantages (see **Figure 3**). The therapeutic effects correspond with the chemical profiles of each spring type, indicating that their hydrogeochemical compositions are crucial in defining their natural medical applications.

1. Sodium chloride (Na-Cl) thermal springs.

Sodium chloride thermal springs are a significant type of geothermal water, especially found in areas with deep geothermal reservoirs (**Chalise et al., 2023**) . The elevated chloride concentration in these springs signifies that the water derives from deeper subsurface sources and experiences limited interaction with surface water. Na-Cl thermal springs, typically marked by high temperatures, are frequently utilized as markers of advanced geothermal systems (**Çevikoğlu & Başaran, 2023**). Sodium chloride springs, often neutral to slightly alkaline, enhance circulation and skin health owing to their elevated mineral content. In Ciwidey, designate the thermal spring areas as P2, P6, P10, and P20. These springs, rich in salt and chloride ions, may improve skin hydration and aid in maintaining the body's electrolyte balance. Their thermal and chemical properties are considered beneficial for muscle relaxation therapy and for augmenting metabolic activity (**Cacciapuoti et al., 2020**). Consequently, Na-Cl thermal springs are frequently utilized in spa treatments aimed at relieving tension and fatigue (**Martínez et al., 2017**). The Sodium-Chloride thermal water is utilized to address numerous ailments of the musculoskeletal system, encompassing osteoarthritis, rheumatic disorders, arthritis, central nervous system problems, and post-traumatic stress. Sodium chloride is also advised for migraine sufferers (**Mohamedi & Chenaker, 2022**).

2. Calcium sulfate (Ca-SO_4) thermal springs.

Calcium sulfate thermal springs generally arise from the interaction of geothermal water with gypsum or anhydrite-bearing rocks. These springs exhibit high sulfate concentrations, potentially rendering the water slightly acidic. These springs are typically located in hydrothermal areas linked to calcium-rich sedimentary formations (**Zhao et al., 2024**). The $CaSO_4$ thermal springs located at P3, P4, P5, P6, P10, P11, P12, and P13. The presence of calcium and sulfate ions is thought to enhance bone and joint health, rendering these waters advantageous for musculoskeletal therapy. They are commonly utilized in the management of rheumatic diseases and associated disorders (**Vaidya & Nakarmi, 2020**). Moreover, the sulfate concentration in the water may promote skin detoxification and improve peripheral blood circulation (**Cacciapuoti et al., 2020**).

3. Sodium bicarbonate (Na-HCO_3) thermal springs.

Sodium bicarbonate thermal springs generally originate from the interaction of geothermal water with carbonate rocks or from mixing with meteoric water. These springs display high amounts of bicarbonate ions, which enhance their alkalinity. These characteristics are typically linked to shallow geothermal systems or regions where geothermal fluids combine with surface water (**Maria et al., 2024**). The Na-HCO_3 thermal springs are located at P9 and P14. The alkaline properties of Na-HCO_3 rich thermal springs may assist in balancing the pH of the skin and body, potentially benefiting dermatological health (**Vaidya & Nakarmi, 2020**). They are utilized therapeutically to relieve skin irritation, enhance skin elasticity, and are frequently incorporated into treatments for digestive health by alleviating gastrointestinal pain and reducing physiological acidity (**Cacciapuoti et al., 2020**). Clinical studies underscore their advantages for digestive health, such as neutralizing gastric acid, elevating gastric pH, accelerating gastric emptying, and stimulating digestive hormones. (**Capurso et al., 1999**).

The Ciwidey region demonstrates both the complicated geothermal dynamics of the area and its considerable potential for integrative health applications. The unique mineral compositions in each spring type offer a customized basis for therapeutic applications, including dermatology, muscle relaxation, and treatments for joints and metabolism. This association emphasizes the significance of geochemical characterization in optimizing natural resources for wellness interventions, establishing Ciwidey as an appropriate location for sustainable geomedical tourism and therapeutic hydrotherapy development. The therapeutic effectiveness of these springs is intricately linked to their chemical compositions, highlighting the essential importance of hydrogeochemical profiles in determining their natural health uses. The therapeutic application of thermal waters is fundamentally associated with their temperature and mineral composition, that affect diverse physiological reactions. Ciwidey's thermal springs, abundant in important minerals, influence both exterior and internal biological systems, facilitating physical rehabilitation,

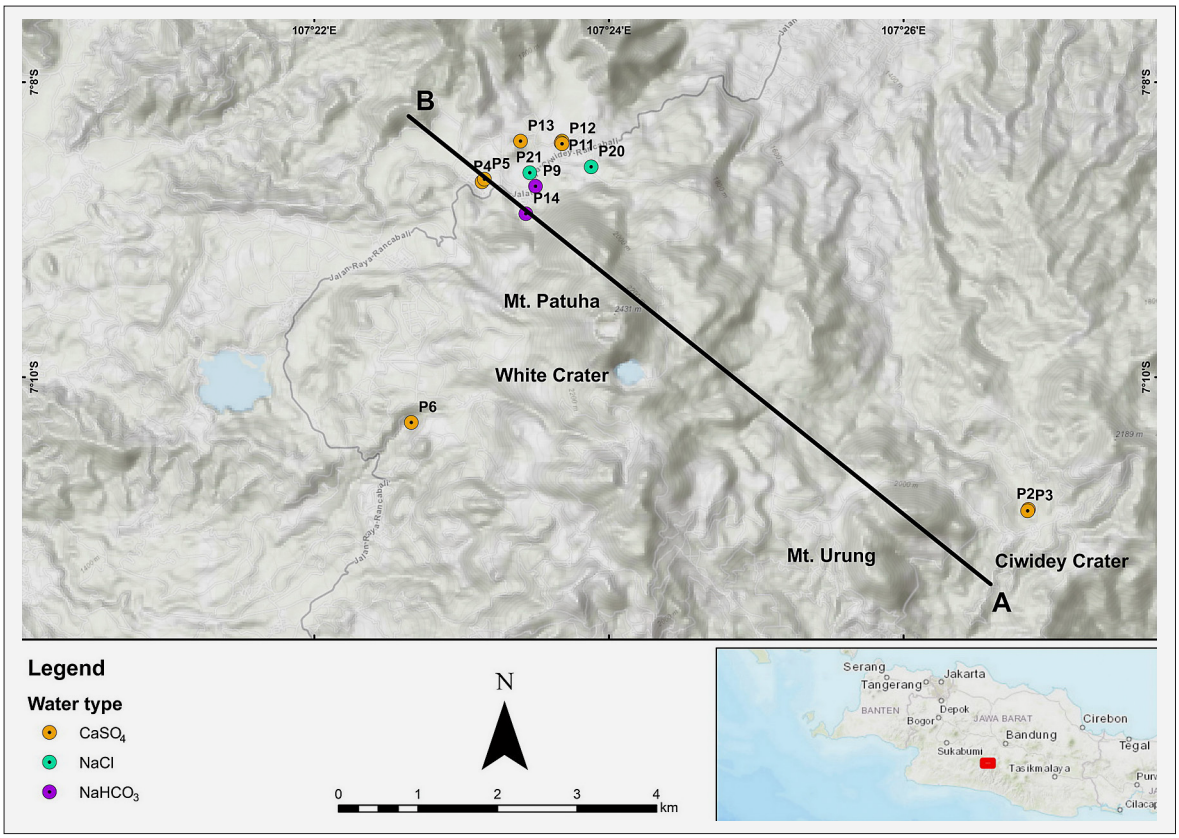


Figure 3. Hydrogeochemical water types in the Ciwidey region

muscular relaxation, cleansing, and enhanced circulation via hydrotherapeutic processes. Their heterogeneous composed renders them great assets for integrative wellness approaches and natural health strategies.

5.4. Conceptual Model of Hydrogeochemistry in Thermal Springs

Thermal springs are natural discharges of groundwater heated by geothermal activity, enriched with various minerals through complex interactions with geological structures (**Shoedarto et al., 2020**). Water traversing the Earth's crust dissolves minerals including halite, gypsum, and carbonates, producing unique hydrochemical fingerprints characterized as sodium chloride (Na-Cl), calcium sulfate (Ca-SO_4), and sodium bicarbonate (Na-HCO_3). These variations are affected by local geology, including evaporite-rich formations near volcanic systems such as Patuha Mountain, and hydrological parameters such as flow naturally, residence time, and dilution through shallow groundwater (**Rahayudin et al., 2020**).

The medical advantages of thermal springs are closely linked to their hydrogeochemical appearance, particularly determines their natural therapeutic properties. The conceptual model of hydrogeochemistry in the Ciwidey thermal springs assists to determine specific therapeutic areas (see **Figure 4**). Thermal springs containing sodium chloride (Na-Cl), commonly found in deep geothermal systems, are distinguished by their high temperatures and increased mineral concentration. Located in Ciwidey at sites including P2, P6, P10, and P20, these springs facilitate skin hydration, improve circulation, encourage muscular relaxation, and assist in alleviating migraines and musculoskeletal ailments. Calcium sulphate (Ca-SO_4) thermal springs arise from the interaction with gypsum-rich rocks and exhibit moderate acidity due to elevated sulphate concentrations. Located at sites P3 to P13, they enhance bone and joint health, facilitate skin cleansing, and promote enhanced peripheral blood circulation. Thermal springs of sodium bicarbonate (Na-HCO_3) at P9 and P14 arise from the interaction of geothermal water with carbonate rocks, yielding alkaline waters recognised for its ability to equilibrate body pH and alleviate digestive and dermatological conditions. This conceptual model illustrates how chemical signatures designate the specific therapeutic potential of each spring type.

Each water variety signifies distinct geochemical origins and therapeutic potentials (**Farhat et al., 2021**). Na-Cl rich springs, located in outflow zones, exhibit reduced mineral content due to interaction with surface aquifers (**Chalise et al., 2023**), whereas Na-HCO_3 dominated springs originate from meteoric and deep groundwater sources, frequently associated with alkaline conditions and calcite precipitation (**Iskandar et al., 2013**). Calcium sulfate waters demonstrate significant mineralization from gypsum-rich formations, promoting sulfate accumulation and observable travertine deposits in areas such

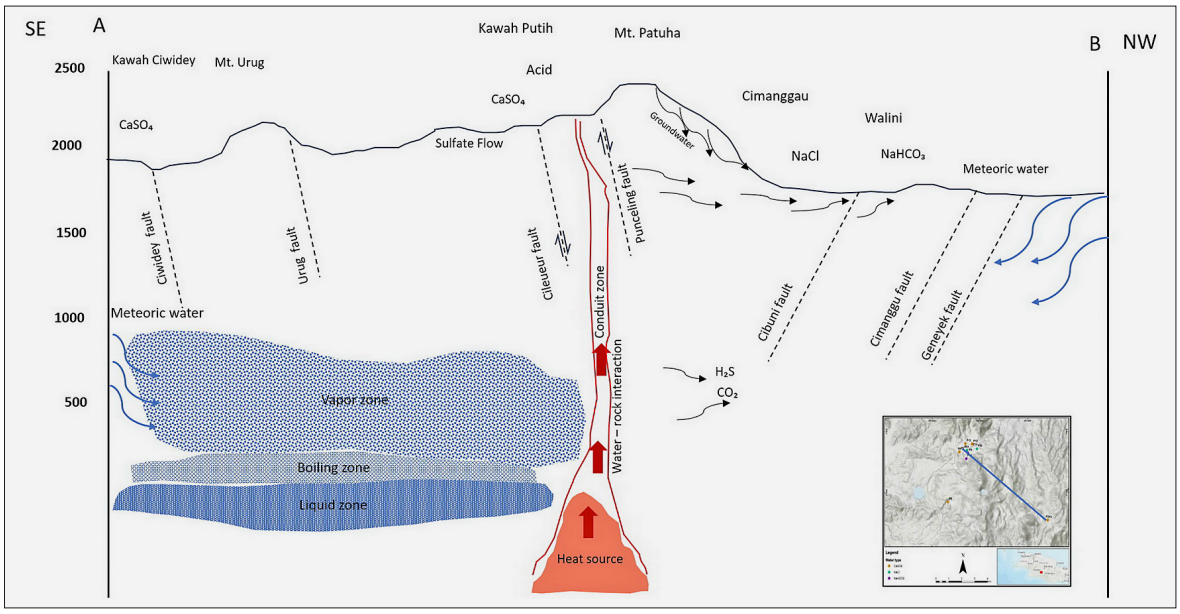


Figure 4. The conceptual model of hydrogeochemistry in the Ciwidey thermal springs, modified after **(Rahayudin et al., 2020)**

as Ciwidey (**Rahayudin et al., 2020**). The physicochemical parameters, including high levels of calcium, salt, chloride, sulfate, and bicarbonate, as well as neutral to alkaline pH, establish optimal environments for balneological uses (**Al Dulaymie et al., 2013**). These mineral waters facilitate treatments for dermatological ailments, musculoskeletal disorders, metabolic regulation, cardiovascular issues, and respiratory health via bathing, ingestion, or inhalation. The hydrogeochemistry of thermal springs provides insight into subsurface geological processes and acts as a resource for natural healing, based on mineral balance and environmental peacefulness.

6. Conclusions

The thermal springs in Ciwidey, Indonesia, represent a unique combination of rock formation and therapeutic properties. This work presents an innovative conceptual zoning approach that associates hydrogeochemical categories with targeted health-related applications. The springs were classified into three primary chemical types: Sodium Chloride (Na-Cl), Calcium Sulphate (Ca-SO_4), and Sodium Bicarbonate (Na-HCO_3), each originating from specific geological settings including deep geothermal fault systems, gypsum-rich formations, and carbonate-influenced lithologies. The algorithm identifies particular spring locations corresponding to specific medical benefits: Na-Cl type springs located at points P2, P6, P10, and P20 facilitate muscular relaxation and support dermatological ailments; Ca-SO_4 type springs situated between sites P3 and P13 are advantageous for skeletal and joint health; and Na-HCO_3 type springs at P9 and P14 contribute to pH balance, enhance digestive functions, and improve skin quality. This integrative methodology, combining geochemistry with medical geology, represents a notable progression in the strategic growth of geomedical hydrotherapy. Incorporating geographic specificity into therapeutic mapping establishes the framework for the sustainable management and maintenance of Ciwidey's geothermal resources, guaranteeing their enduring viability in comprehensive health and wellness applications. Further investigation and frequent monitoring of potential toxic metal elements in thermal spring water are required to assure public health safety. Controlled use is especially important when harmful quantities surpass acceptable limits.

7. Reference

Ahaneku, C. V., & Muogbo, C. D. (2024). Applications Of Geospatial Techniques In Medical Geology : A Applications Of Geospatial Techniques In Medical Geology : A Review. *International Research Journal of Modernization in Engineering, Technology and Science*, *Volume:06/*(August), 2410–2423.

Al Dulaymie, A. S., Hussien, B. M., Gharbi, M. A., & Mekhlif, H. N. (2013). Balneological study based on the hydrogeochemical aspects of the sulfate springs water (Hit-Kubaiysa region), Iraq. *Arabian Journal of Geosciences*, *6*(3), 801–816. https://doi.org/10.1007/s12517-011-0385-5

Alzwar, M., Akbar, N., & Bachri, S. (1992). *Geological Map of the Garut and Pameungpeuk Quadrangle, Java*.

APHA. (2017). Standard Methods for the Examination of Water and Wastewater. In *Washington DC: American Public Health Association* (23rd ed).

Appelo, C. A. J., & Postma, D. (1993). Geochemistry, groundwater and pollution. *Geochemistry, Groundwater and Pollution*.

Ashat, A., Pratama, H. B., & Itoi, R. (2019). Updating conceptual model of Ciwidey-Patuha geothermal using dynamic

numerical model. *IOP Conference Series: Earth and Environmental Science*, *254*(1). https://doi.org/10.1088/1755-1315/254/1/012010

Bennett, G., & Walraevens, K. (2023). Assessment of possibility of finding geothermal energy resources around Mount Meru in northern Tanzania using classical solute geothermometry. *Groundwater for Sustainable Development*, *21*(December 2022). https://doi.org/10.1016/j.gsd.2023.100926

Bisergaeva, R. A., & Sirieva, Y. N. (2020). Determination of calcium and magnesium by atomic absorption spectroscopy and flame photometry. *Journal of Physics: Conference Series*, *1691*(1). https://doi.org/10.1088/1742-6596/1691/1/012055

Buck, B. J., Londono, S. C., McLaurin, B. T., Metcalf, R., Mouri, H., Selinus, O., & Shelembe, R. (2016). The emerging field of medical geology in brief: Some examples. *Environmental Earth Sciences*, *75*(6). https://doi.org/10.1007/s12665-016-5362-6

Bujung, C. A. N., Singarimbun, A., Muslim, D., Hirnawan, F., & Sudradjat, A. (2010). Delineasi Reservoir Panas Bumi Berdasarkan Litologi, Alterasi Hidrotermal Dan Profil Temperatur. *Bulletin of Scientific Contribution*, *8*, 158–165.

Cacciapuoti, S., Luciano, M. A., Megna, M., Annunziata, M. C., Napolitano, M., Patruno, C., Scala, E., Colicchio, R., Pagliuca, C., Salvatore, P., & Fabbrocini, G. (2020). The role of thermal water in chronic skin diseases management: A review of the literature. *Journal of Clinical Medicine*, *9*(9), 1–19. https://doi.org/10.3390/jcm9093047

Capurso, A., Solfrizzi, V., Panza, F., Mastroianni, F., Torres, F., Parigi, A. Del, Colacicco, A. M., Capurso, C., Nicoletti, G., Veneziani, B., Scalabrino, S., & Cellamare. (1999). Increased bile acid excretion and reduction of serum cholesterol after crenotherapy with salt-rich mineral water. *Journal Aging Clinical and Experimental*, *ISSN: 1720*.

Cavanah, C. (2018). Guide To Hydrothermal Spa & Wellness Development. In *Architectural Review* (Third Edit, Issue 1363). Global Wellness Institute.

Centeno, J. A., Finkelman, R. B., & Selinus, O. (2016). Medical geology: Impacts of the natural environment on public health. *Geosciences (Switzerland)*, *6*(1), 6–8. https://doi.org/10.3390/geosciences6010008

Çevikoğlu, T., & Başaran, C. (2023). Hydrogeochemical characteristics and evaluation of the water resources in Tuzlukçu (Konya/Turkey) geothermal area. *Journal of Earth System Science*, *132*(4). https://doi.org/10.1007/s12040-023-02162-6

Chalise, B., Paudyal, P., Kunwar, B. B., Bishwakarma, K., Thapa, B., Pant, R. R., & Neupane, B. B. (2023). Water quality and hydrochemical assessments of thermal springs, Gandaki Province, Nepal. *Heliyon*, *9*(6). https://doi.org/10.1016/j.heliyon.2023.e17353

Chandra, V. R., Ramadhan, Y., Akmala, I., Atmaja, R. W., Sesesega, R. S., & Iskandar, C. (2022). Fault and structure study for field development strategy in Patuha geothermal project. *Proceedings 47th Workshop on Geothermal Reservoir Engineering*, 1. https://pangea.stanford.edu/ERE/db/GeoConf/papers/SGW/2022/Chandra.pdf%0Ahttps://www.researchgate.net/publication/359815140_Fault_and_Structure_Study_for_Field_Development_Strategy_in_Patuha_Geothermal_Project

Crespo, P. V., Campos, F., Leal, M., & Maraver, F. (2021). Effects of sodium chloride-rich mineral water on intestinal epithelium. Experimental study. *International Journal of Environmental Research and Public Health*, *18*(6), 1–12. https://doi.org/10.3390/ijerph18063261

Duvert, C., Priadi, C. R., Rose, A. M., Abdillah, A., Marthanty, D. R., Gibb, K. S., & Kaestli, M. (2019). Sources and drivers of contamination along an urban tropical river (Ciliwung, Indonesia): Insights from microbial DNA, isotopes and water chemistry. *Science of the Total Environment*, *682*, 382–393. https://doi.org/10.1016/j.scitotenv.2019.05.189

Erfurt-Cooper, P. (2010). *The Importance of Natural Geothermal Resources in Tourism*. *April*, 25–29.

Erfurt, P. (2011). *An assessment of the role of natural hot and mineral springs in health, wellness and recreational tourism* [James Cook University]. http://eprints.jcu.edu.au/31110/%0AThe

Farhat, N., Hussain, S., Faisal, F., Batool, I., & Noreen, M. (2021). Physico-chemical characteristics and therapeutic potential of Chutrun thermal springs in Shigar Valley, Gilgit-Baltistan (Pakistan). *Applied Water Science*, *11*(2). https://doi.org/10.1007/s13201-020-01354-5

Fikri-Benbrahim, K., Houti, A., El Ouali Lalami, A., Flouchi, R., El Hachlafi, N., Houti, M., & Rachiq, S. (2021). Main Therapeutic Uses of Some Moroccan Hot Springs' Waters. *Evidence-Based Complementary and Alternative Medicine*, *2021*. https://doi.org/10.1155/2021/5599269

Finkelman, R. B., Orem, W. H., Plumlee, G. S., & Selinus, O. (2018). Applications of Geochemistry to Medical Geology. In *Environmental Geochemistry: Site Characterization, Data Analysis and Case Histories: Second Edition* (Issue January). https://doi.org/10.1016/B978-0-444-63763-5.00018-5

Gomes, C. de S. F. (2013). Naturotherapies Based on Minerals. *Geomaterials*, *03*(01), 1–14. https://doi.org/10.4236/gm.2013.31001

Gómez Diaz, E. (2021). Geochemical Interpretation of Bicarbonate Thermal Springs for the Comprehension of a Geothermal System: A Case Study at Cerro Machin Volcano, Colombia. *Proceedings World Geothermal Congress 2020+1*, *October*, 1–8.

Gwenzi, W., Mangori, L., Danha, C., Chaukura, N., Dunjana, N., & Sanganyado, E. (2018). Sources, behaviour, and environmental and human health risks of high-technology rare earth elements as emerging contaminants. *Science of the Total Environment*, *636*, 299–313. https://doi.org/10.1016/j.scitotenv.2018.04.235

Hamidizadeh, Simaeetabar, Farhad, Sara, Moghadam, & Mohammad Gohari, M. M. P. (2017). Composition of minerals and trace elements at Mamasani thermal source: A possible preventive treatment for some skin diseases. *Journal of Education and Health Promotion*, *6*(Desember), 1–6. https://doi.org/10.4103/jehp.jehp_100_17

Hamilton, W. B. (1973). *Tectonics of the Indonesian Region*. U.S. Geological Survey.

Hem, J. D. (1985). Study and interpretation of the chemical characteristics of natural water. *US Geological Survey Water-Supply Paper*, *2254*.

Holloway, R. (1883). *INDONESIA , GEOLOGY*. 454–460.

Iskandar, I., Dermawan, F. A., Sianipar, J. Y., Suryantini, & Notosiswoyo, S. (2018). Characteristic and mixing mechanisms of thermal fluid at the Tampomas Volcano, west Java, using hydrogeochemistry, stable isotope and222Rn analyses. *Geosciences (Switzerland)*, *8*(4). https://doi.org/10.3390/geosciences8040103

Iskandar, I., Notosiswoyo, S., Purnadi, C., & Pasaribu, T. (2013). Type and Origin of Springs and Hotsprings at Surrounding Ridges of Bandung Basin, Related with its Potential Natural Contamination. *Procedia Earth and Planetary Science*, *6*, 262–268. https://doi.org/10.1016/j.proeps.2013.01.035

Joshi, S. K., Rai, S. P., Sinha, R., Gupta, S., Densmore, A. L., Rawat, Y. S., & Shekhar, S. (2018). Tracing groundwater recharge sources in the northwestern Indian alluvial aquifer using water isotopes (δ18O, δ2H and 3H). *Journal of Hydrology*, *559*, 835–847. https://doi.org/10.1016/j.jhydrol.2018.02.056

Katili, J. A. (1974). *Geological Environment of the Indonesian Mineral Deposits: A Plate Tectonic.* Geological Survey of Indonesia.

Kekes, T., Tzia, C., & Kolliopoulos, G. (2023). Drinking and Natural Mineral Water: Treatment and Quality–Safety Assurance. *Water (Switzerland)*, *15*(13). https://doi.org/10.3390/w15132325

Khasmadin, M. F., & Harmoko, U. (2021). Kajian Potensi dan Pemanfaatan Energi Panas Bumi di Wilayah Kerja Panas Bumi Patuha Ciwidey. *Jurnal Energi Baru Dan Terbarukan*, *2*(2), 101–113. https://doi.org/10.14710/jebt.2021.11187

Kieu, L. D., & Nguyen, P. Q. (2024). Groundwater Quality Assessment in the Middle-Upper Pleistocene Aquifer. *Civil Engineering Journal (Iran)*, *10*(7), 2357–2369. https://doi.org/10.28991/CEJ-2024-010-07-018

Lazzerini, F., & da Silva, P. (2020). Guarani aquifer system (GAS): geothermal spa balneology assessment. *Boletin Sociedad Española Hidrologia Medica*, *35*(1), 33–59. https://doi.org/10.23853/bsehm.2020.0965

Lee, J. M., Koh, D. C., Chae, G. T., Kee, W. S., & Ko, K. S. (2021). Integrated assessment of major element geochemistry and geological setting of traditional natural mineral water sources in South Korea at the national scale. *Journal of Hydrology*, *598*(September 2020). https://doi.org/10.1016/j.jhydrol.2021.126249

Li, F., Yu, T., Huang, Z., Yang, Z., Hou, Q., Tang, Q., Liu, J., & Wang, L. (2023). Linking health to geology-a new assessment and zoning model based on the frame of medical geology. *Environmental Geochemistry and Health*, *45*(10), 7145–7159. https://doi.org/10.1007/s10653-023-01516-9

Li, X., Yang, X., Ou, J., Zhou, Y., Xi, L., Zou, Y., Chen, Z., He, D., Yao, L., & Zhu, W. (2024). Overview and trend analysis of global hot spring research based on bibliometrics and knowledge graph visualization. *Complementary Therapies in Medicine*, *87*(August). https://doi.org/10.1016/j.ctim.2024.103102

Luo, J., Li, Y., Tian, J., Cheng, Y., Pang, Z., & Gong, Y. (2022). Geochemistry of geothermal fluid with implications on circulation and evolution in Fengshun-Tangkeng geothermal field, South China. *Geothermics*, *100*(19). https://doi.org/10.1016/j.geothermics.2021.102323

Mahala, S. C. (2019). Chemistry and Genesis ofThermal Springs ofOdisha, India. *Earth Sciences, SpringerBriefs in Earth Sciences*, 49–73. https://doi.org/10.1007/978-3-319-90002-5_5

Malkemus, D., Perkins, R. B., & Palmer, C. D. (2021). Geochemistry and geothermometry of Breitenbush Hot Springs, Oregon, USA. *Geothermics*, *95*(May). https://doi.org/10.1016/j.geothermics.2021.102134

Maraver, F., & Karagülle, M. Z. (2012). *Medical Hydrology and Balneology: Environmental Aspects*. http://revistas.ucm.es/index.php/ANHM/article/view/39572%5Cnhttp://bioclima.ro/39572-49462-1-PB.pdf

Maria, R., Prasetio, R., Shoedarto, R. M., Nurohman, H., Yuliyanti, A., Lestiana, H., Dida, E. N., Aminuddin, & Rahayudin, Y. (2024). Assessment of Medical Geology from Major Element Trilinear Diagrams Cl- SO4-HCO3 and Na-K-Mg from Geothermal and Non-Geothermal Springs; Case Study the Wayang Windu Geothermal Area, West Java, Indonesia. *IOP Conference Series: Earth and Environmental Science*, *1293*(1). https://doi.org/10.1088/1755-1315/1293/1/012002

Maria, R., Rusydi, A. F., Marganingrum, D., Damayanti, R., Nurohman, H., Lestiana, H., Shoedarto, R. M., Mulyono, A., Rahayudin, Y., Setiawan, T., Iskandarsyah, T. Y. W. M., Suganda, B. R., & Hendarmawan, H. (2024). Use of the Groundwater Quality Index, Multivariate statistics and Hydrogeochemistry for Groundwater Assessment in the Malabar Volcanic Area, Indonesia. *Rudarsko-Geološko-Naftni Zbornik*, *39*(5), 41–62. https://doi.org/10.17794/rgn.2024.5.3

Martínez, J., Ortiz, A., Jaramillo, M., Vera-Romero, I., Reyes, J. M., Soriano, A. O., Jaramillo, M. E., & Romero, I. V. (2017). Physical-Chemical and Therapeutic Properties of Hot Springs and Hydrothermal Waters. *International Journal of Research and Innovations in Earth Science*, *2*(1), 10–12. https://www.researchgate.net/publication/317267668

Mohamedi, M. R., & Chenaker, H. (2022). Hydrogeochemistry and Therapeutic Effects of Thermal waters of Khenchela (North-East Algeria). *Journal of Environmental Science, Computer Science and Engineering & Technology*, *11*(4). https://doi.org/10.24214/jecet.a.11.4.50111

Moldovan, A., Török, A. I., Mirea, I. C., Micle, V., Moldovan, O. T., & Levei, E. A. (2022). Health risk assessment in southern carpathians small rural communities using karst springs as a drinking water source. *International Journal of Environmental Research and Public Health*, *19*(1). https://doi.org/10.3390/ijerph19010234

Pham, N. Q., & Nguyen, G. T. (2024). Evaluating Groundwater Quality Using Multivariate Statistical Analysis and Groundwater Quality Index. *Civil Engineering Journal (Iran)*, *10*(3), 699–713. https://doi.org/10.28991/CEJ-2024-010-03-03

Piper, A.M. (1953). *A graphic procedure in the geochemical interpretation of water analysis*. Washington : U.S. Dept.

of the Interior, Geological Survey, Water Resources Division, Ground Water Branch,.

Pirajno, F. (2020). Subaerial hot springs and near-surface hydrothermal mineral systems past and present, and possible extraterrestrial analogues. *Geoscience Frontiers*, *11*(5), 1549–1569. https://doi.org/10.1016/j.gsf.2020.04.001

Powell, T., & Cumming, W. (2010). *Spreadsheet for Geothermal Water and Gas Geochemistry*. 10. https://earthsciences.stanford.edu/ERE/pdf/IGAstandard/SGW/2010/powell.pdf

Quattrini, S., Pampaloni, B., & Brandi, M. L. (2016). Natural mineral waters: Chemical characteristics and health effects. *Clinical Cases in Mineral and Bone Metabolism*, *13*(3), 173–180. https://doi.org/10.11138/ccmbm/2016.13.3.173

Rafiq, J., Abu-Mahfouz, I. S., Soupios, P., Humphrey, J. D., & Tawabini, B. S. (2024). Hydrochemical Characterization, Geothermometry, and Origin of Ain Al-Harrah Hot Spring and Its Relationship to Al-Lith Geothermal System, Saudi Arabia. *ACS Omega*, *9*(23), 24807–24818. https://doi.org/10.1021/acsomega.4c01343

Rahayudin, Y., Kashiwaya, K., Tada, Y., Iskandar, I., Koike, K., Atmaja, R. W., & Herdianita, N. R. (2020). On the origin and evolution of geothermal fluids in the Patuha Geothermal Field, Indonesia based on geochemical and stable isotope data. *Applied Geochemistry*, *114*(January), 104530. https://doi.org/10.1016/j.apgeochem.2020.104530

Ríos Reyes, C. A., Ríos Gutiéttez, M. P., & Joya Neira, S. (2020). The importance of minerals in medical geology: Impacts of the environment on health. *Archivos de Medicina (Manizales)*, *21*(1), 0–3. https://doi.org/10.30554/archmed.21.1.3589.2021

Sasaki, K., Morita, J., Iwaki, C., & Ueda, A. (2021). Geochemical evaluation of geothermal resources in Toyama Prefecture, Japan, based on the chemical and isotopic characteristics of hot spring waters. *Geothermics*, *93*(March). https://doi.org/10.1016/j.geothermics.2021.102071

Shoedarto, R. M., Aries, F. R., Irawan, D., Perdana, F., Arisbaya, I., & Indrawan, B. (2016). Raising Public Acceptance of Geothermal Utilization Through Direct Application in Indonesia. *Workshop on Geothermal Reservoir Engineering*, *2007*, 9.

Shoedarto, R. M., Tada, Y., Kashiwaya, K., Koike, K., & Iskandar, I. (2020). Specifying recharge zones and mechanisms of the transitional geothermal field through hydrogen and oxygen isotope analyses with consideration of water-rock interaction. *Geothermics*, *86*(January), 101797. https://doi.org/10.1016/j.geothermics.2019.101797

Skopljak, F., Šarić, Ć., & Pobric, V. (2017). Contribution to the genesis of thermal water of the north-east perimeter of the Zenica-Sarajevo Basin, Bosnia and herzegovina. *Rudarsko-Geološko-Naftni Zbornik* (Vol. 32, Issue 4, pp. 17–30). https://doi.org/10.17794/rgn.2017.4.2

Sorensen, M. D. (2014). Calcium intake and urinary stone disease. *Translational Andrology and Urology*, *3*(3), 235–240. https://doi.org/10.3978/j.issn.2223-4683.2014.06.05

Sriwana, T., Van Bergen, M. J., Sumarti, S., De Hoog, J. C. M., Van Os, B. J. H., Wahyuningsih, R., & Dam, M. A. C. (1998). Volcanogenic pollution by acid water discharges along Ciwidey River, West Java (Indonesia). *Journal of Geochemical Exploration*, *62*(1–3), 161–182. https://doi.org/10.1016/S0375-6742(97)00059-9

Sriwana, T., Van Bergen, M. J., Varekamp, J. C., Sumarti, S., Takano, B., Van Os, B. J. H., & Leng, M. J. (2000). Geochemistry of the acid Kawah Putih lake, Patuha Volcano, West Java, Indonesia. *Journal of Volcanology and Geothermal Research*, *97*(1–4), 77–104. https://doi.org/10.1016/S0377-0273(99)00178-X

Suhail, M., Ahmad, I., & Umar, R. (2024). Groundwater for Sustainable Development Hydrochemistry , controlling mechanisms and water quality index in hot springs of the Kullu-Manali region , India. *Groundwater for Sustainable Development*, *24*(December 2023), 101070. https://doi.org/10.1016/j.gsd.2023.101070

Sumotarto, U., Hendrasto, F., & Djajadiningrat, H. S. (2021). Geothermal resource potential of Kawah Putih - Ciwidey area, Bandung, West Java, based on geomorphology, structural geology, and lithology analysis. *AIP Conference Proceedings*, *2363*(November). https://doi.org/10.1063/5.0061150

Torres-Ceron, D. A., Acosta-Medina, C. D., & Restrepo-Parra, E. (2019). Geothermal and mineralogic analysis of hot springs in the Puracé-La Mina Sector in Cauca, Colombia. *Geofluids*, *2019*. https://doi.org/10.1155/2019/3191454

Utama, W., Indriani, R. F., Hermana, M., Anjasmara, I. M., Garini, S. A., & Putra, D. P. N. (2024). Towards Improving Sustainable Water Management in Geothermal Fields: SVM and RF Land Use Monitoring. *Journal of Human, Earth, and Future*, *5*(2), 216–242. https://doi.org/10.28991/HEF-2024-05-02-06

Vaidya, B., & Nakarmi, S. (2020). A Qualitative Study of Patients' Beliefs and Perception on Medicinal Properties of Natural Hot Spring Bath for Musculoskeletal Problems. *Journal of Environmental and Public Health*, *2020*. https://doi.org/10.1155/2020/3694627

Valeriani, F., Margarucci, L. M., & Spica, V. R. (2018). Recreational use of spa thermal waters: Criticisms and perspectives for innovative treatments. *International Journal of Environmental Research and Public Health*, *15*(12). https://doi.org/10.3390/ijerph15122675

Vlahović, T., & Skopljak, F. (2019). Genesis of the thermal-mineral waters of ilidža, Bosnia and Herzegovina. *Rudarsko-Geološko-Naftni Zbornik*, *34*(1), 127–138. https://doi.org/10.17794/rgn.2019.11

Wang, Wang, G. L., Gan, H. N., Liu, Z., & Nan, D. W. (2018). Hydrochemical Characteristics and Evolution of Geothermal Fluids in the Chabu High-Temperature Geothermal System, Southern Tibet. *Geofluids*, *2018*, 1–15. https://doi.org/10.1155/2018/8532840

Wangchuk, P., Yeshi, K., Ugyen, K., Dorji, J., Wangdi, K., Samten, Tshering, P., & Nugraha, A. S. (2021). Water-based therapies of bhutan: Current practices and the recorded clinical evidence of balneotherapy. *Water (Switzerland)*, *13*(1). https://doi.org/10.3390/w13010009

Waya, L., Pritchard, M. E., Wike, L., Reath, K., Gunawan, H., Prambada, O., & Syahbana, D. (2022). Detection of ther-

mal features from space at Indonesian volcanoes from 2000-2020 usingASTER. *Journal of Volcanology and Geothermal Research*, *430*(September 30, 2022). https://www.sciencedirect.com/science/article/pii/S0377027322001585

Yashod, R. Z. (2025). Properties of eco-tourism sites of hot springs in the western. *Journal of East-West Thought*, *15*(1), 762–770.

Yeung, O., & Johnston, K. (2020). Resetting the World with Wellness: A New Vision for a Post COVID-19 Future. *Global Wellness Institute.*

Zhang, Q., O'brien, S., & Grimm, J. (2022). Biomedical applications of lanthanide nanomaterials, for imaging, sensing and therapy. *Nanotheranostics*, *6*(2), 184–194. https://doi.org/10.7150/NTNO.65530

Zhang, T., Wang, P., Wang, M., Liu, J., Gong, L., & Xia, S. (2023). Spatial distribution, source identification, and risk assessment of heavy metals in riparian soils of the Tibetan plateau. *Environmental Research*, *237*(August). https://doi.org/10.1016/j.envres.2023.116977

Zhao, J., Liu, L., Wang, Y., Li, B., Lin, W., & Yao, H. (2024). Hydrogeochemical Characteristics and Genesis of Hot Springs in Da Qaidam Area, Northern Qaidam Margin of the Qaidam Basin. *Water (Switzerland)*, *16*(23). https://doi.org/10.3390/w16233509

SAŽETAK

Hidrogeokemijske značajke termalnih izvora za prirodnu terapijsku upotrebu u medicinskoj geologiji na području Ciwidey, Zapadna Java, Indonezija

Termalni izvori u regiji Ciwidey u Indoneziji odražavaju bogato geološko nasljeđe i pružaju velike mogućnosti za prirodne terapijske primjene u medicinskoj geologiji. Cilj je ovoga istraživanja procijeniti hidrogeokemijske značajke nekoliko termalnih izvora u regiji Ciwidey i odrediti prikladnost za prirodnu terapijsku primjenu u medicinskoj geologiji. U okviru ove studije istražene su hidrogeokemijske značajke 13 termalnih izvora u regiji Ciwidey korištenjem atomske apsorpcijske spektrometrije (AAS; AA-7000 SHIMADZU), klasificirajući ih u tri različita tipa termalnih izvora na temelju dominantnih kemijskih značajki: natrijsko-kloridni (Na-Cl), kalcijsko-sulfatni (Ca-SO_4) i natrijsko-bikarbonatni (Na-HCO_3). Svaki hidrogeokemijski tip ima jedinstvena terapijska svojstva povezana s geokemijskim podrijetlom, dubokim geotermalnim vodonosnicima, litologijom bogatom gipsom ili interakcijama karbonatnih stijena. Analitički model uspostavljen u okviru ove studije identificirao je specifične zone za potencijalnu terapijsku primjenu: vode tipa Na-Cl (npr. lokacije P2, P6, P10, P20) potiču opuštanje mišića i regeneraciju kože; vode tipa Ca-SO_4 (lokacije P3 – P13) poboljšavaju zdravlje kostiju i zglobova; a vode tipa Na-HCO_3 (P9, P14) pomažu u regulaciji pH vrijednosti i ublažavanju probavnih te dermatoloških problema. Rezultati ovoga istraživanja otkrivaju bitne uvide u terapeutski potencijal termalnih izvora u regiji Ciwidey i naglašavaju važnost procjene lokalnih specifičnih značajki u medicinskoj geologiji.

Ključne riječi:
termalni izvori, hidrogeokemija, terapeutski, medicinska geologija, geotermalni

Author's contribution

Rizka Maria (Dr, senior researcher, hydrogeology) performed the field work, provided the geology and hydrogeochemical data, thermal water, and medical geology analysis. **Heri Nurohman** (M.Sc., junior researcher, geological engineering) presented all images and assisted with modelling analysis. **Hilda Lestiana** (M.T., junior researcher, geomatic engineering) provided the geographic modelling analysis. **Riostantieka Mayandari Shoedarto** (PhD., junior researcher, geomatic engineering) provided geological analysis. **Eki Naidania Dida** (M.Il, junior researcher, chemical engineering) provided the chemical data. **Jakah** (MT. junior researcher, geology engineering) provided the XRF data. **Ernowo** (Dr, senior researcher, geology), provided the geology data. **Yudi Rahayudin** (PhD, senior researcher, gological engineering) provided the geological conditions of the research area.
All authors have read and agreed to the published version of the manuscript.

RGNZ/MGPB

The Integrated Analysis of Basement Faults in North Bangka Island, Indonesia, Using Surface Lineament Density and Gravity Anomaly Enhancement

Rudarsko-geološko-naftni zbornik
(The Mining-Geology-Petroleum Engineering Bulletin)
DOI: 10.17794/rgn.2026.2.15

Original scientific paper

Harnanti Yogaputri Hutami[1,2*], Edy Sunardi[1], Iyan Haryanto[1], Sonny Winardhi[3], Nugroho Prasetyo[2], Nur Ayu Anas[4], Erlangga Ibrahim Fattah[2]

[1] *Faculty of Geological Engineering, Universitas Padjajaran, Jln. Raya Bandung-Sumedang Km. 21, Jatinangor, 45363, Indonesia.*

[2] *Department of Geophysical Engineering, Faculty of Industrial Engineering, Institut Teknologi Sumatera (ITERA), Jln. Terusan Ryacudu, Jatiagung, Lampung Selatan, 35365, Indonesia.*

[3] *Department of Geophysical Engineering, Faculty of Mining and Petroleum Engineering, Institut Teknologi Bandung, Jln. Ganesha No. 10, Bandung, West Java, 40132, Indonesia.*

[4] *Geological Engineering Department, Faculty of Engineering, Cendrawasih University, Jln. Kamp Wolker, Papua, 99351, Indonesia.*

Abstract

Bangka Island was formed by the subduction and collision of the Gondwana-derived Sibumasu and East Malaya blocks in the Late Paleozoic. Its northern region comprises Permian metamorphic rocks of the Pemali Complex, Triassic sedimentary units from the Tanjunggenting Formation, and Late Triassic to Early Jurassic granites of the Klabat Formation. Despite multiple tectonic phases shaping Bangka Island, the structural configuration of basement faults and folds in the northern region remains poorly constrained. This uncertainty hampers the assessment of fractured basement reservoirs in the study area. To address this gap, this study integrates surface lineament extraction from DEMNAS with gravity anomaly data from GGMplus to investigate the basement structure of the northern Bangka. Fast Sigmoid Edge Detection (FSED) and Euler Deconvolution were applied to enhance structural interpretation and estimate basement depth. The dominant structural orientations of NW-SE and NE-SW identified at the surface were consistent with the subsurface features; however, FSED and Euler Deconvolution also revealed E-W and N-S trends. Moreover, the findings from the Euler Deconvolution indicated basement depths of 3000-4000 m below sea level. Field fracture measurements from granitic outcrops validate these orientations, confirming a strong correspondence between surface and subsurface structures. These findings offer new insight into the tectonic evolution of the northern region of Bangka Island and highlight fault orientations that may aid in identifying fractured basement reservoir zones in granitic terrains.

Keywords:
lineament density, enhanced edge detection, gravity anomaly, basement fault structures, Bangka Island

1. Introduction

Fractured basement reservoirs have emerged as significant hydrocarbon exploration targets, with important discoveries in Southeast Asia, such as the Bach Ho Field, Vietnam (**Areshev et al., 1992; Cuong & Warren, 2009; Hung et al., 2003; Hung & Le, 2004**) and the Suban gas Field, South Sumatra Basin, Indonesia (**Hennings et al., 2012; Koning et al., 2021; Kurniawan, 2018; Permana et al., 2023; Schultz, 2014**). These fields produce hydrocarbons from fractured granitic basement rock (**Cuong & Warren, 2009; Petford & McCaffrey, 2003**) and the reservoirs are strongly controlled by major fault systems that created interconnected fracture networks, allowing the fluid storage and migration (**Gutmanis, 2009; Guttormsen, 2010; Li et al., 2004**). Unlike conventional clastic and carbonate reservoirs, crystalline basement rocks (e.g. granite) are essentially non-porous and impermeable in their pristine state (**Narr et al., 2006; P'an, 1982**). As a result, their reservoir quality is almost entirely dependent on secondary porosity and permeability by brittle deformation, specifically through faults, shear zones, and fracture networks (**Gillespie et al., 2018; Gillespie et al., 2021; Guttormsen, 2010; Suyoto, 2010; Tjia, 2007**). While carbonates may also function as fracture-controlled reservoirs, they often benefit from additional enhancement through chemical dissolution and karstification, which is absent in crystalline rocks. However, this makes tectonic setting and structural analysis especially critical in assessing the potential of basement reservoirs.

Given the significance of such structurally controlled basement reservoirs in Southeast Asia, attention also turns to Bangka Island, which lies off the east coast of South Sumatra. The island, with a land area of 11,500 km^2,

* Corresponding author: Harnanti Yogaputri Hutami
e-mail address: harnanti.hutami@tg.itera.ac.id
Received: 4 June 2025. Accepted: 1 November 2025.
Available online: 13 March 2026

forms part of the Sundaland continental crust, shaped by long-lived and complex tectonic processes (**Hall et al., 2009; Katili, 1972; Metcalfe, 2017; Van Gorsel, 2018**). Its geology comprises Permo-Carboniferous metamorphic and Triassic sedimentary sequences, intruded by Late Triassic to Jurassic granitic bodies. However, detailed structural studies have been limited by tropical weathering, dense vegetation, and poor outcrop conditions (**Katili, 1967; Ko, 1986**). Earlier surface investigation from **Ko (1986)** provided only a preliminary overview, and despite centuries of tin mining, systematic studies of basement faults remain scarce. Consequently, the structural configuration of Bangka's basement and its implications for fractured reservoir potential remain poorly constrained. To address this gap, this study integrates surface lineament mapping with edge-detected gravity anomalies analysis derived from satellite data to characterise the structural pattern and orientation of Bangka's granitic basement.

Lineaments, expressed as linear features such as faults, folds, or fracture zones, provide a surface manifestation of underlying tectonic structures (**Ahmadi & Pekkan, 2021; Hung et al., 2005**). The term 'lineament' was first introduced by **Hobbs (1904),** who characterised it as a significant linear landscape that exposes the underlying architecture of a distinct rock basement. Their systematic mapping improves understanding of tectonic and structurally controlled reservoirs (**Army & Saepuloh, 2020; Enoh et al., 2021; Florinsky, 2016; Mohammed et al., 2010**). Satellite-derived datasets, such as the National Digital Elevation Model (DEMNAS), allow the systematic extraction of surface lineaments in the observation area (**Han et al., 2018; Prabowo et al., 2021**). To complement surface analysis, gravity anomaly data offered insight into subsurface structures. The enhancement techniques play an essential role in detecting boundaries of geological formations and understanding the structural setting (**Eldosouky et al., 2022; Kumar & Singh, 2021; Kumar et al., 2018; Melouah & Pham, 2021**). In this study, we applied an enhanced edge detection filter, known as Fast Sigmoid Edge Detection Filter (FSED), based on a modified fast sigmoid function and the vertical and horizontal derivatives of the total horizontal gradient of gravity data, as proposed by **Oksum et al. (2021)**. This edge detection filter provides maximum amplitudes on the edges of the anomalous sources and simultaneously balances anomalies from deep and shallow geological sources, as proven by several previous tectonic and structural studies (**Aprina et al., 2024; Liu et al., 2023; Pham et al., 2021; Safani et al., 2023**).

Research into the tectonic and structural geology of Bangka Island has applied diverse approaches, including petrographic, geochemical, and geophysical methods. Petrographic studies revealed granitoids dominated by alkali feldspar-syenogranite, while geochemical data indicated a calc-alkalic magma affinity, consistent with a subduction-collision origin characteristics (**Widana, 2013**). Structural investigations further support this interpretation. **Hendrawan et al. (2024)** documented three main deformation phases, involving folding and faulting, and emphasized the presence of complex metamorphic structures in northern Bangka that related to block collision. Remote sensing had also provided insights into the tectonic framework. Shuttle Radar Topography Mission (SRTM) data highlighted dominant NW-SE and NE-SW lineament orientations, reflecting significant tectonic deformation (**Franto, 2015**). Moreover, major NE-SW trending structures, namely Pemali and Payung faults, exerted a strong influence on the regional radiogenic geothermal system and geological formations in the area (**Siregar et al., 2024**). These studies demonstrated the polyphased tectonic history of Bangka Island. However, the geometry and continuity of basement structures remain poorly understood, underscoring the need for integrated surface and subsurface structural analysis.

The present study provides a comprehensive structural analysis of the Paleozoic-Mesozoic granitic basement in the northern part of Bangka Island by integrating surface lineament mapping with edge-detected gravity anomalies. The objective is to correlate surface and subsurface structures to better constrain the geometry and continuity of basement features and assess their implications for regional tectonic evolution and the potential for fractured reservoirs. Furthermore, natural fracture measurements from granite outcrops were included in the study to validate the integrated analysis, providing important field-based properties to support the structural interpretations.

2. Geological setting

The geology of Bangka Island is characterized by two different settings: (1) northern Bangka (**Mangga & Djamal, 1994**), dominated by the Permian Pemali Complex; and (2) southern Bangka, characterized by the Triassic Tanjung Genting Formation and Jurassic granite (**Margono et al., 1995**). The granite on Bangka Island was formed as a result of the subduction and collision of the East Malaya Block and the Sibumasu Block (**Cobbing et al., 1986; Hutchison, 2014; McCourt et al., 1996; Metcalfe, 2000, 2017**). Field observation through geochemical and petrographic studies (**Widana, 2013**) supported the information. **Figure 1** shows the geology map of the northern Bangka, modified after **Mangga & Djamal (1994)** and **Ko (1986)**. The map illustrates the distribution of the main lithological units, including Permian Pemali Complex (CPp), the Triassic Tanjunggenting Formation (TRt), and the Late Triassic-Jurassic Klabat Granite (TRJkg), along with the Tertiary Ranggam Formation (TQr), Penyabung Diabase (PTrd), and Quaternary alluvium deposits (Qa). This map was complemented by an NW-SE cross-section (line A-A') that

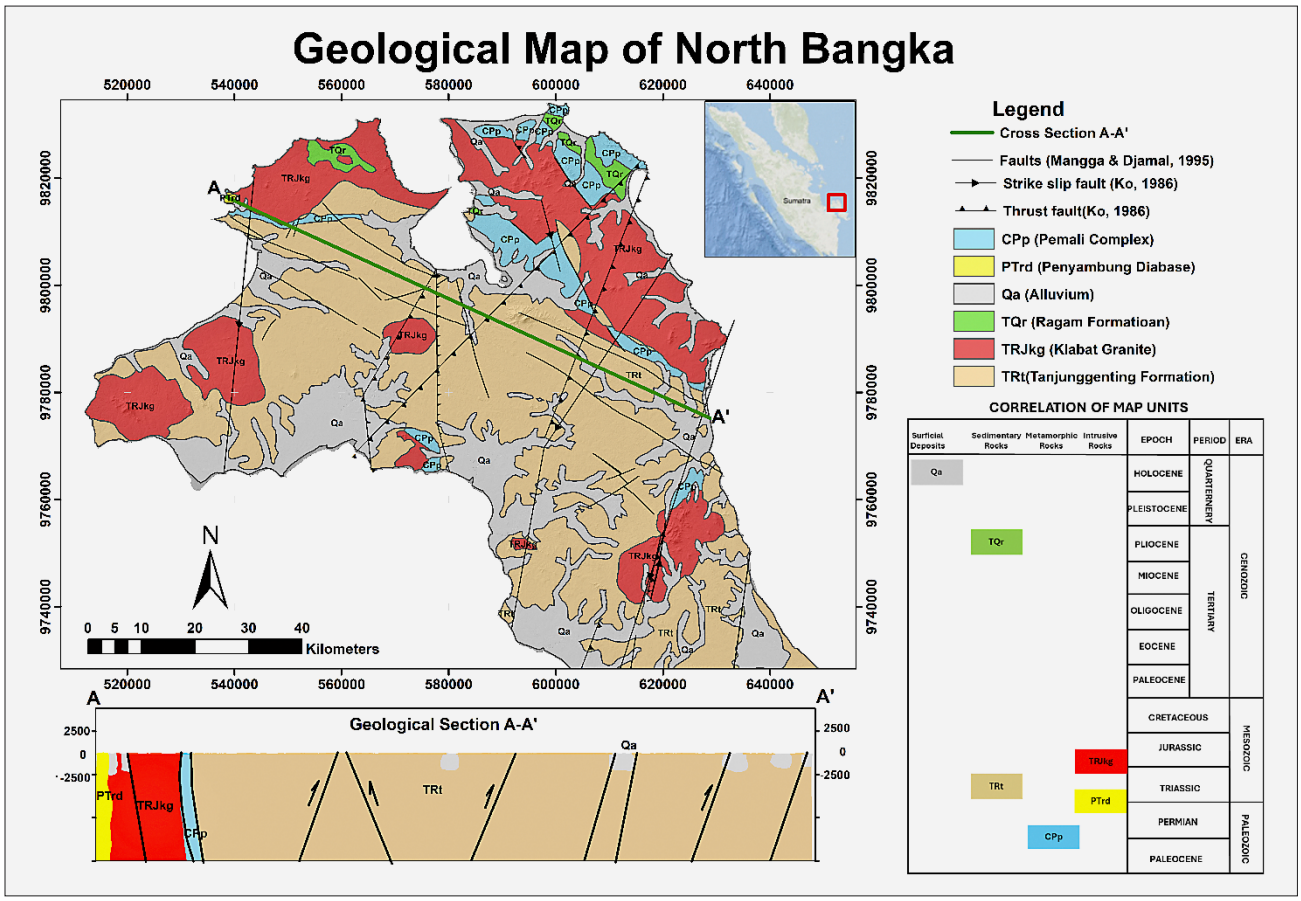


Figure 1. Map of the northern region of Bangka Island with the NW-SE-oriented subsurface model (line A-A'), modified after **Mangga & Djamal (1994)** and **Ko (1986)**.

depicted the stratigraphic relationships between the rock units, the granite intrusions, and associated faults, which represented the block faulting systems in the study area.

The northern region of the island comprised two principal basement sequences: the Pemali Complex consisted of deep marine cherts, black shales, and volcaniclastic sediments deposited in a subsiding continental slope environment, formed on the Paleotethys floor and later incorporated into the accretionary complex during the collision of the Sibumasu Block and the east Malaya Block in the Late Permian (**Barber et al., 2005; Metcalfe, 2013, 2017**). In the Early Triassic, subsidence occurred, and the Tanjung Genting Formation was deposited in the shallow marine environment. This formation unconformably overlies the Pemali Complex and comprises alternating meta-sandstones, sandstones, clayey sandstone, and claystone with oxide limestone. The Tanjung Genting Formation was subsequently folded and locally thrust over the older units, likely linked to Late Triassic tectonism and the granitic intrusion events of the Klabat granite (**Ko, 1986**), which consists of biotite granite, granodiorite, and gneissic granite. These stratigraphic relationships are supported by radiometric data and biostratigraphy, which place the granitoid intrusions near the Norian-Rhaetian boundary (~ 214 – 217 Ma), as confirmed by Sr isotopic studies by **Ng et al. (2017)**.

The tectonic evolution of northern Bangka was marked by at least three deformation phases (**Mangga & Djamal, 1994**): (i) Late Paleozoic NE-SW trending structures, (ii) Triassic-Jurassic NW-SE trending faults and folds, likely linked to the old ocean suture of the Bentong-Raub Line that intersected in the east of Bangka Island (**Ng et al., 2017**), and (iii) Cretaceous N-S faulting (**Franto, 2015**). These multiphase structures strongly influenced the development of fracture systems within the basement rocks. Their identification and validation through surface measurements of natural fractures provide a critical link to understand the study area's tectonic history and assess the fractured basement reservoir potential.

3. Methods

3.1. Data

This study employed a combination of satellite-derived and geophysical datasets to conduct analyses of subsurface structures in the northern region of Bangka Island, Indonesia. The topographic data were sourced from the Digital Elevation Model Nasional (DEMNAS), an official product provided by Indonesia's Badan Informasi Geospasial (BIG). DEMNAS integrates elevation

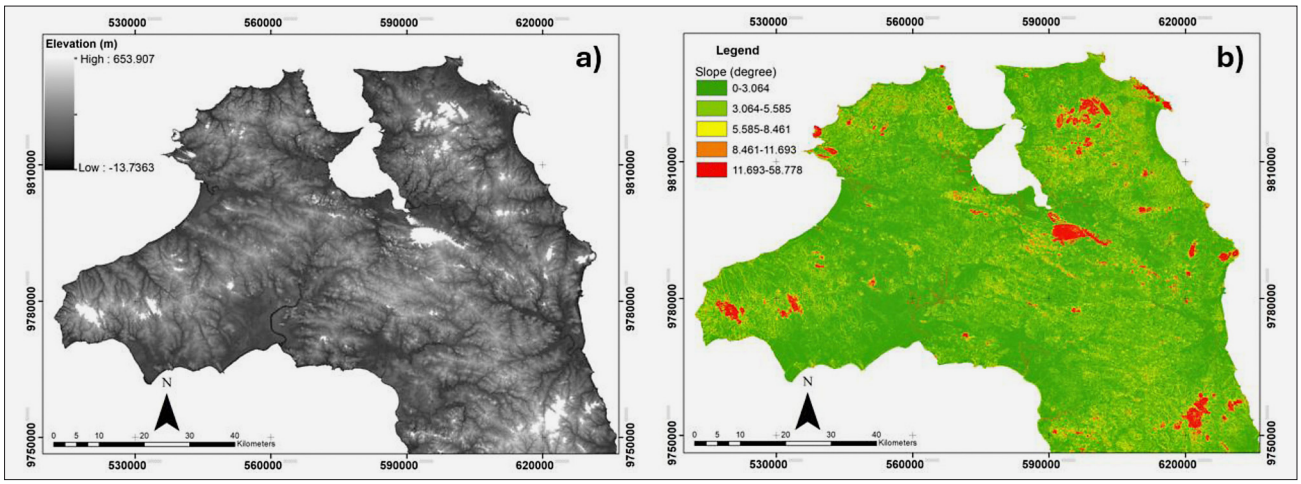


Figure 2. a) DEMNAS input for lineament extraction with a spatial resolution of 8,1 m; b) slope model of the study area

data from multiple sources, including Interferometric Synthetic Aperture Radar (IFSAR) and TerraSAR-X, achieving a high spatial resolution of approximately 8.1 meters (0.27 arc-seconds). This degree of detail is particularly advantageous for detailed geomorphological and structural mapping (see **Figure 2a**). As illustrated in **Figure 2b**, the study area is generally characterized by low-relief morphology, with most of the terrain gently undulating and the highest elevations at 653 meters. Although local hills and ridges are present in association with granitic intrusions and fault-controlled structures, the steepest slope measures approximately 58 degrees. Given these topographic characteristics, the lineaments were semi-automatically digitized from enhanced raster layers, ensuring topographic continuity, alignment with geomorphological features, and geological plausibility.

For subsurface delineation using the FSED technique, we utilized high-resolution satellite gravity data from the Gravity Model Plus 2013 (GGMplus 2013), developed by **Hirt et al. (2013)**, to delineate geological structure patterns and their associated tectonic settings. The GGMPlus model integrates GOCE/GRACE satellite gravity, Earth gravity models (EGM2008), and topographical gravity derived from SRTM topography (**Hirt, 2014; Hirt et al., 2013**). These data provide a spatial resolution of approximately 200 m (~ 7.2 arc-seconds) over both land and marine areas. A gravity anomaly grid covering the Bangka Island region was extracted in GeoTIFF format, projected to WGS 1984 UTM Zone 48S, and resampled to match the spatial resolution of DEMNAS for seamless integration. Free-air gravity anomalies were used to retain structural signals associated with density contrasts in the subsurface granitic basement. Subsequently, several gravity corrections were applied to generate the Complete Bouguer Anomaly (CBA) map covering Bangka Island, which was then utilized as input for residual anomaly analysis and enhanced edge detection techniques.

3.2. Lineament extraction process

The lineament extraction process employed a semi-automated methodology, which required subsequent manual refinements to enhance the accuracy of the extracted lineaments. This approach ensures that the digitized linear features faithfully represent the geological characteristics observed (**Carvalho & Batty, 2005**). This extraction is based on the precise detection of line segments within the imagery (**Azman et al., 2020**). In the preliminary phase, we carefully adjusted various parameters to enhance the accuracy of the extraction results. This optimization process ensured optimal extraction results.

Table 1. List of adjusted parameters utilized in the data input for lineament extraction

No.	Parameter	Value
1	RADI (*Filter Radius*)	10
2	GHTR (*Gradient Threshold*)	100
3	LTHR (*Length Threshold*)	30
4	FTHR (*Line Fitting Error Treshold*)	3
5	ATHR (*Angular Difference Threshold*)	30
6	DTHR (*Linking Distance Threshold*)	20

The raster mosaicking process integrates multiple sections of DEMNAS data from the study area into a cohesive raster format. We produced a hillshade digital elevation model (DEM) image that visually depicts the terrain by simulating the effects of light on the surface. This method effectively emphasizes the area's relief and topographic variations. Our primary objective was to illustrate these variations through light and shadow, tailored to a specified direction of incoming sunlight. By utilizing the shadow effects created by this sunlight, we provided a clear representation of the area's relief and topographic features (**Farmakis-Serebryakova & Hurni, 2020; Rusinkiewicz et al., 2006**). An azimuth angle

and a solar elevation angle of 45 degrees were employed to determine the optimal lighting direction and evaluate the resulting shadow intensity. The results provided a comprehensive and informative representation of the morphological features within the study area, including slopes, ridges, and valleys.

The extracted lineaments were manually corrected in subsequent steps to ensure that the digitized linear features accurately represent the geological characteristics. This extraction relied on detecting linear segments within the imagery (**Ni et al., 2016**). During this process, various parameters were systematically adjusted to enhance the accuracy of the extraction results (refer to **Table 1**). Each parameter utilized in the extraction process was essential for three primary stages: edge detection, threshold determination, and curve extraction (**Bampourda et al., 2017**). These stages involved a series of complex processes that ensured the extracted lineaments were accurate and aligned with the observed geological conditions (**Salui, 2018**).

The initial edge detection stage employs the Canny edge detection algorithm, which generates an edge strength image that underlies the lineament extraction process. This algorithm consists of three systematic steps: (1) *Filtering* - the input image is processed through a Gaussian function (**Bhardwaj et al., 2020**), with the radius determined by the RADI parameter. This step is designed to smooth the image and minimize noise, thereby enhancing the effectiveness of the edge detection process, (2) *Gradient Calculation*–the gradient of the filtered image is computed to detect intensity changes that signify the presence of edges–and (3) *Non-Maximum Suppression* - pixels that do not represent local maxima in the gradient are suppressed by assigning them an edge strength of zero (**Vincent & Folorunso, 2009**). This method ensures the preservation of only the most significant edges for analysis in subsequent stages.

In the second stage of the process, the edge-detected image is further refined by applying a threshold, which produces a binary image. In this binary representation, each ON pixel represents a detected edge element. The thresholding operation is controlled by the GTHR (Edge Gradient Threshold) parameter (**Ng, 2006**), which specifies the minimum edge intensity for inclusion in the extraction. Applyin this threshold ensures that only edge features meeting predefined criteria are retained, while less significant elements are excluded.

In the third stage, the curve extraction process uses the binary edge image generated in the preceding step. This stage encompasses several critical sub-steps to accurately represent the extracted linear features. A thinning algorithm is initially applied to the binary image, transforming the edge elements into one-pixel-wide skeleton curves. Subsequently, each curve is extracted as a series of pixels. To enhance the efficiency of the extraction process, a filtering mechanism is employed to eliminate curves that do not meet the established Curve Length Threshold (LTHR). Curves falling below this threshold are regarded as insignificant for lineament analysis.

Upon completing the curve extraction process, the subsequent step involves converting the pixel curves into vector form by fitting line segments. This process generates a polygonal line that accurately represents the original curve, with the maximum error rate determined by the FTHR (Line Fitting Threshold) parameter. This methodology ensures that the resulting polygonal line closely adheres to the shape of the detected lineament.

In the final stage, the algorithm connects polyline pairs that meet the established criteria. The interconnection of two polylines occurs if the following conditions are met: (1) the terminal segments of each polyline must be oriented toward each other with consistent alignment, with the angle between them being less than the threshold set by the ATHR (Angular Threshold), and (2) the endpoints of the two polylines must be within proximity, with the distance between them being below the DTHR (Distance Threshold) value.

Through this comprehensive process, the system enhances the precision of lineament extraction, ensuring that the detected linear structures accurately represent the geological features at the Earth's surface (**Ahmadi & Pekkan, 2021; Echeverria et al., 2022; Enoh et al., 2021; Salui, 2018**). Finally, a comprehensive analysis of high-density lineament zones was conducted to identify areas of fracturing and rock cutting, as well as regions of greater deformation intensity, which correspond to the deformation phases observed in the study area.

3.3. Fast-Sigmoid Edge Detection (FSED) and Euler Deconvolution Procedures

The Fast-Sigmoid Edge Detection Filter (FSED) was applied to the enhanced gravity anomaly map to delineate structural boundaries and fracture zones (**Oksum et al., 2021; Pham, 2024; Pham et al., 2021**). A recent study using FSED effectively migrates amplitude anomalies arising from causative bodies at varying depths and with distinct properties, enhancing resolution and accuracy in delineating source edges. Notably, this filter avoids generating spurious edges when anomaly sources exhibit opposing density contrasts simultaneously (**Kamto et al., 2023; Oksum et al., 2021; Pham et al., 2021**), and it mitigates noise interference, ensuring superior edge detection quality in potential field data (**Li et al., 2014**). Therefore, edge enhancement techniques have feartly improved the accurate mapping of geological features, including faults, contacts, and dikes, providing critical insights into subsurface structures.

Several preparatory steps are essential before initiating the edge detection procedure using the FSED technique. The first step involves applying an average gravity value of 2.67 g/cm³ to generate a Complete Bouguer Anomaly (CBA) map of the target area. The subsequent

step is to perform a power spectrum analysis to estimate the width and depth of the gravity anomalies within the study area. This analysis also facilitates a comparison of the response spectra of various filtering methods. The power spectrum analysis was conducted utilizing the principles of the Fourier transform applied to horizontal plane gravity anomalies (**Blakely, 1995**).

To effectively separate residual anomalies from regional anomalies and achieve optimal window width estimation, we applied a logarithmic transformation to the amplitude spectrum obtained from the Fourier transform (refer to **Equation 1**). This transformation yielded a straight-line equation, facilitating clearer analysis and interpretation of the data.

$$\ln P = (z_0 - z)|k| \quad (1)$$

The equation illustrates that the component is directly proportional to the amplitude spectrum. Additionally, the linear regression applied to this equation helps to delineate the boundary between the first-order (regional zone) and the second-order (residual zone) zones. The value at this boundary is identified as the determinant of the window width. Moreover, the relationship between wavelength and amplitude is derived from **Equation 2**, which determines the window width (**Blakely, 1995**).

$$k = \frac{2\pi}{\lambda};\ \lambda = n \cdot \Delta x \quad (2)$$

Enhancement techniques play a crucial role in identifying the boundaries of geological formations and understanding their structural settings (**Eldosouky et al., 2022; Kumar et al., 2018; Ma et al., 2014; Melouah & Pham, 2021; Nasuti et al., 2019**). Edge detection methodologies are essential for interpreting potential field data, as they form the foundation for delineating geological structures and identifying subsurface discontinuities (**Liu et al., 2023; Pham, 2024**). Conventional edge detection filters typically rely on the computation of horizontal and vertical derivatives of potential field data or various combinations of these derivatives to accentuate regions of rapid change that signify structural boundaries (**Kamto et al., 2023; Yao et al., 2016**).

This nonlinear transformation function utilizes the sigmoid function to sharpen edge contrasts while suppressing background noise. It offers flexible and robust tools for enhancing subtle gravity gradients. The FSED equation (**Oksum et al., 2021**) is expressed in **Equations 3** and **4** as follows:

$$\mathrm{FSED} = \frac{\mathrm{R} - 1}{1 + |\mathrm{R}|} \quad (3)$$

$$R = \frac{\frac{\partial \mathrm{THG}}{\partial \mathrm{z}}}{\sqrt{\left(\frac{\partial \mathrm{THG}}{\partial \mathrm{x}}\right)^2 + \left(\frac{\partial \mathrm{THG}}{\partial \mathrm{y}}\right)^2}} \quad (4)$$

where ∂THG⁄∂z - vertical derivative of the total horizontal gradient (THG); ∂THG⁄∂x - horizontal derivative of the total horizontal gradient in the X direction, and; ∂THG⁄∂y - horizontal derivative of the total horizontal gradient in the Y direction.

Finally, the basement depth information was acquired through the Euler Deconvolution analysis, as formulated in **Equation 5**.

$$(\mathrm{x} - \mathrm{x}_0)\frac{\partial^2 \mathrm{f}}{\partial \mathrm{x}^2} + (\mathrm{y} - \mathrm{y}_0)\frac{\partial^2 \mathrm{f}}{\partial \mathrm{y}^2} + (\mathrm{z} - \mathrm{z}_0)\frac{\partial^2 \mathrm{f}}{\partial \mathrm{z}^2} = \mathrm{N}\frac{\partial \mathrm{f}}{\partial \mathrm{z}} \quad (5)$$

Although this method was first implemented to determine the positions of lineaments in magnetic data (**Cooper, 2008**). Its employment in the gravity data has been widely acknowledged (**Eldosouky et al., 2022; Ghosh, 2022; Pham et al., 2024; Reid et al., 2003; Safani et al., 2023; Sembiring et al., 2023; Soleha et al., 2019**). The *f* denotes the gravity field at the point of *x,y,z* affected by the anomaly sources at x_0,y_0,z_0 position. The parameter N is defined as the sum of the structural index (SI) and the vertical gradient order of the gravity data (*n*). This value represents the structural index that characterises the geometric parameters of the source (**Cooper, 2008; Melo & Barbosa, 2018; Pham et al., 2024; Reid et al., 2003, 2012**). In the gravity data, SI = -1 represents a lithological contact or fault, 0 is for a thin sheet, 1 is used for a horizontal cylinder, and 2 is the geometric sphere (**Ghosh, 2022; Pham et al., 2024; Safani et al., 2023; Soleha et al., 2019**).

4. Results and Analysis

4.1. Lineament density analysis

The results of the lineament extraction conducted in the study area reveal specific lineaments most closely associated with geological features. A total of 1,266 lineaments were successfully identified, comprising 348 in the granitic Klabat Formation (TRJkg), 287 in the metamorphic Pemali Formation (CPp), 539 in the sedimentary Tanjung Genting Formation (TRt), 79 in the Ranggam Formation (TQr), and 13 in the Diabas Penyabung Formation (PTrd). To facilitate further analysis, the orientation of the lineaments in each formation is illustrated in a rose diagram, as shown in **Figure 3**.

The lineaments observed across the study area predominantly exhibit a northwest-southeast (NW-SE) orientation, which indicates a significant geological structure aligned in this direction. Furthermore, certain formations display additional, less prominent directional trends. For instance, the Quaternary-aged Ranggam Formation (TQr) reveals a north-south (N-S) orientation. At the same time, the Permo-Carboniferous-aged Diabas Penyabung Formation (PTrd) exhibits a northeast-southwest (NE-SW) orientation. A relative east-west (E-W) alignment is also present within the Triassic-Jurassic age formations. Overall, the detected lineament orientations correspond to the structural direction interpreted by **Mangga & Djamal (1994)** on their geological map of North Bangka.

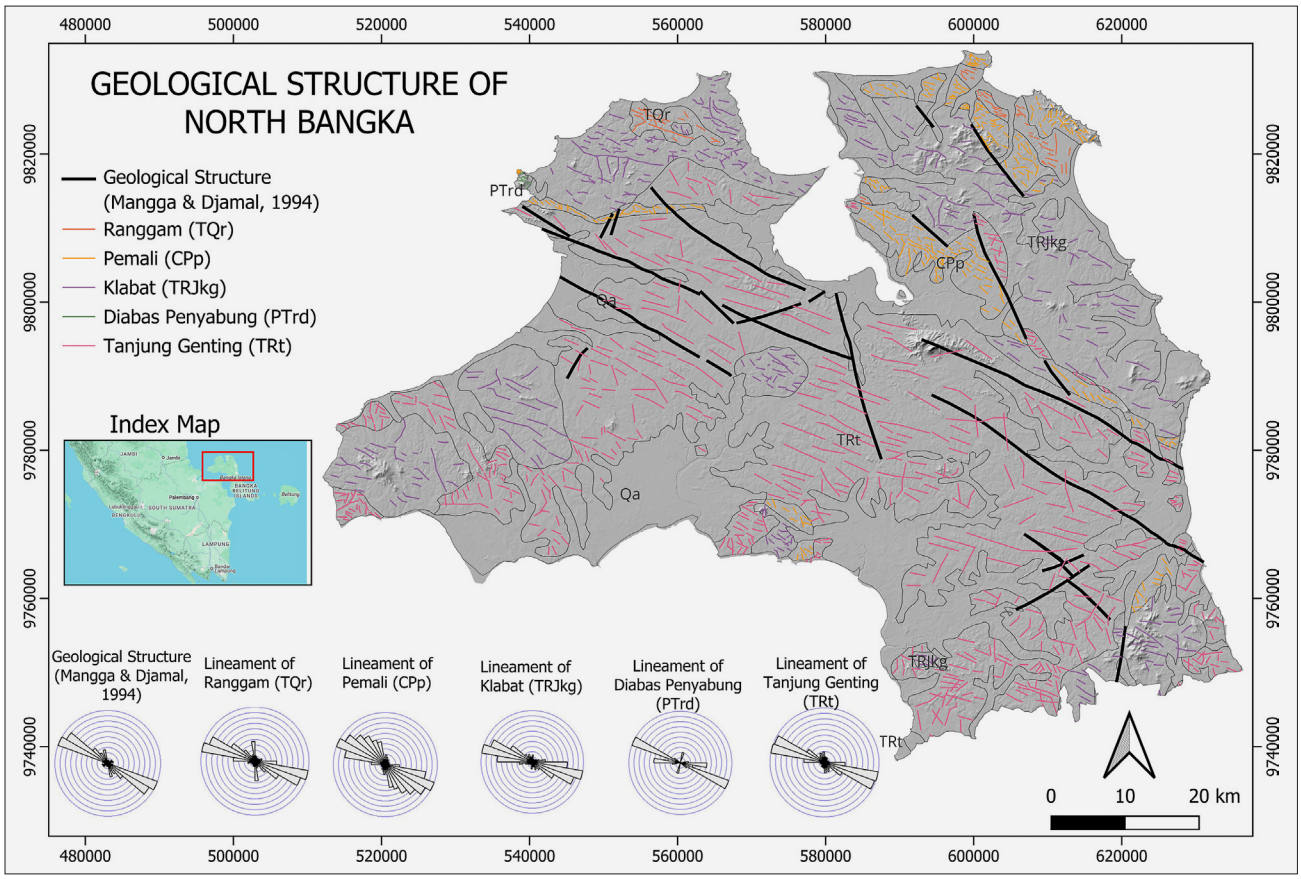


Figure 3. The extracted lineament in northern Bangka Island, Indonesia

Upon analyzing the primary directions of the identified surface lineaments, the next phase involves assessing their density. **Figure 4** illustrates the lineament density map of the study area across various geological formations, highlighting the specific intensity and distribution of structural deformation in relation to lithological characteristics. In this context, lineament length density quantifies the total lineament length per unit area (km/km²), directly indicating the deformation of rocks in response to regional tectonic stress, particularly through the development of fault and fold systems. The spatial distribution of lineament density, as depicted in the figure, shows significant alignment with major geological structures, particularly fault systems oriented in the northwest-southeast (NW-SE) and northeast-southwest (NE-SW) directions. These fault systems are integral to the regional Sumatra Fault pattern and its local branches in northern Bangka. High-density zones frequently coincide with or are parallel to the orientations of these prominent faults, suggesting that the lineaments are manifestations of fracture zones and fold planes resulting from tectonic stress.

A detailed analysis of each rock formation is outlined as follows:

1. **The Pemali Formation (CPp)** comprises Permo-Carboniferous metamorphic rocks, primarily phyllite. Within this formation, high lineament densities, reaching up to 0.70 km/km², are particularly evident in the northern and eastern regions. The phyllite is characterized by its parallel foliation planes, which are prone to fracturing along the foliation or schistosity zones. The dominant lineaments are aligned with fold axes and minor faults that have formed due to regional deformation.
2. **Penyabung Diabase Formation (PTRd)**, an intermediate intrusive body of Permian age, displays the highest lineament density of 10.33 km/km² within a limited geographical area. This elevated lineament occurrence is likely attributable to fault structures at the intrusion's margins. Furthermore, the extremely high density is also influenced by the small spatial extent of the body, which significantly increases the length-to-area ratio.
3. **Ragam Formation (TQr)**, composed of sandstone and clastic sediments from the Late Miocene, exhibits a maximum lineament density of 0.58 km/km², suggesting limited influence of regional structures. The highest density values are found in the northwest, while lower densities are observed in the northeast. Although sandstone can preserve fractures, it is less homogeneous compared to igneous or metamorphic rocks. Local folds and faults may generate minor lineaments within this formation.

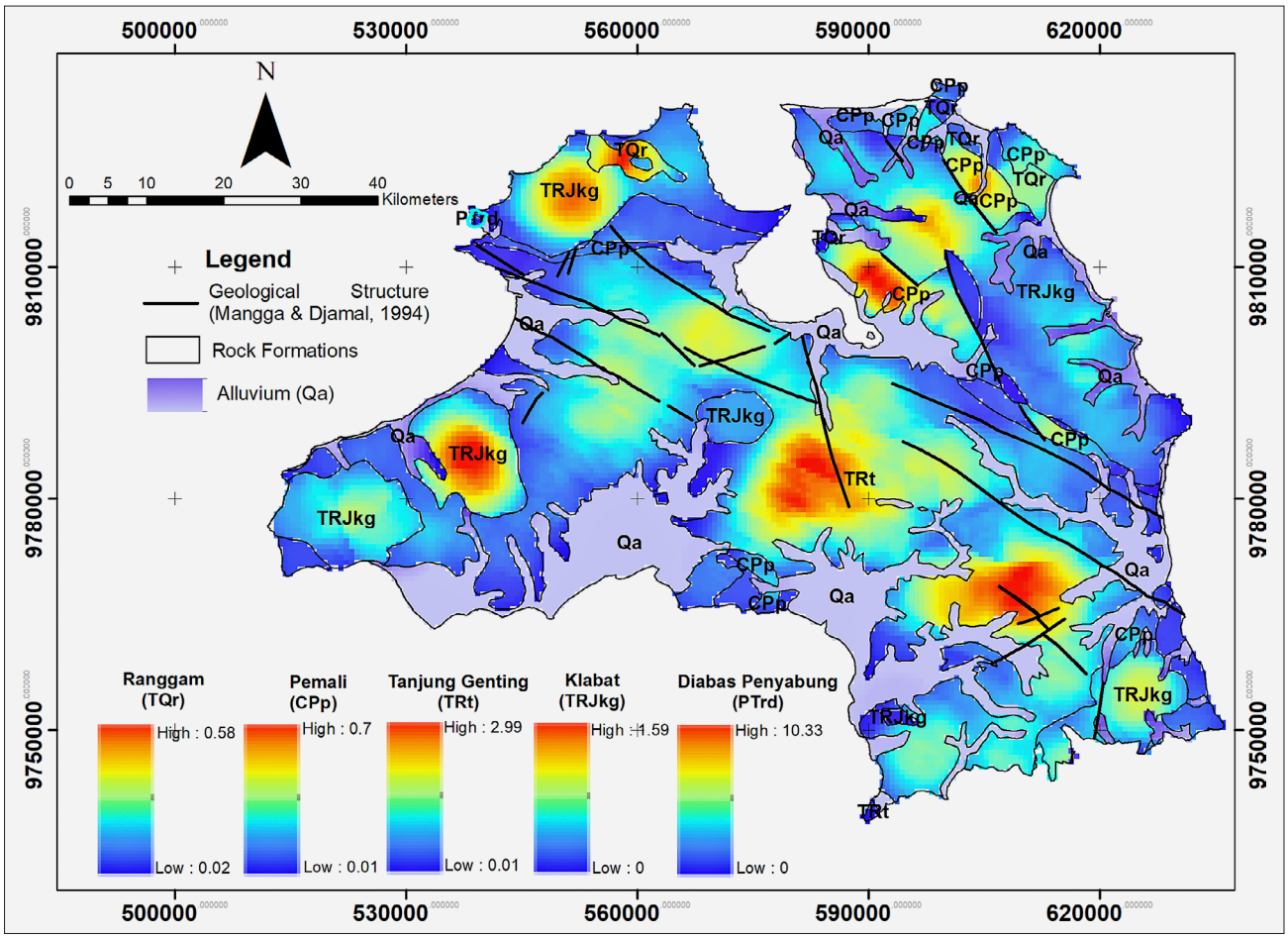


Figure 4. The lineament density map from the formation in the study area

4. **Klabat Granite Formation (TRJkg).** This formation comprises felsic granitoids from the Late Triassic to Jurassic periods. This unit demonstrates relatively high lineament densities, reaching up to 1.59 km/km², particularly in the western and northeastern regions. Due to its hardness, granite is highly susceptible to external stress, resulting in the development of fracture systems and sheet joints. These features manifest as lineaments and are frequently associated with major fault systems.
5. **Tanjung Genting Formation (TRt)**, composed of Triassic sandstones and clastic sediments, exhibits high lineament densities reaching up to 2.99 km/km². This phenomenon can be attributed to the presence of relatively hard rock material within the fault and folding zones of the formation. The alignment of the lineaments predominantly follows a northeast-southwest (NE–SW) direction.

The findings reveal that areas with high lineament density consistently align with major geological structures, indicating that lineaments effectively indicate fault and fold systems in northern Bangka. Variations in density values across different geological formations underscore the importance of conducting lithology-specific lineament analyses rather than relying on broad, regional generalizations, which can lead to interpretive inaccuracies. This formation-based analysis successfully captures the deformation intensity and orientation variability influenced by the region's principal fault and fold systems. Such an approach facilitates the identification of specific deformation zones and provides valuable insights into the mechanical behavior of each lithology under tectonic stress. The strong correlation between lineament density and major geological structures further underscores the utility of lineaments as a crucial tool for structural geological interpretation within the framework of regional tectonics.

4.2. Basement faults interpretation from FSED and Euler Deconvolution

The geological complexities of this region have resulted in a varied distribution of rocks and subsurface structures, significantly impacting the gravity field response. The Complete Bouguer Anomaly (CBA) map, presented in **Figure 5a**, delineates regional variations, with positive gravity anomaly values ranging from 16 to 38 mGal. The areas exhibiting the highest values, depicted in red to violet colours in the western region, reach a maximum of 38 mGal. This phenomenon indicates a greater topographic elevation and the presence of

denser rock types, such as granite intrusions. Conversely, the eastern region displays lower gravity anomaly values, represented by yellow to blue colors, which signify reduced density contrast relative to the surrounding geological structures. These lower gravity anomaly values suggest the presence of rock formations that originated during the Palaeozoic-Mesozoic era, which continue to undergo significant erosion and denudation processes.

The depth estimation of the anomaly source in this study utilizes the Radially Averaged Power Spectrum (RAPS) analysis, adapted from the work of (**Spector & Grant, 1970**). The average power spectrum's slope indicates the depth of discontinuity between two distinct anomalous sources. The segment of the curve with the lowest wavenumber values, ranging from 0 to 0.02 cycles/km, corresponds to deep anomalous sources. In contrast, wavenumbers exceeding 0.2 cycles/km are interpreted as signals from shallow anomalies, which may be classified as noise. Wavenumber values in the intermediate range of 0.02 to 0.2 cycles/km represent anomalies from geological features at intermediate depths. The boundaries of these depth segments for the anomalous sources are illustrated in **Figure 5b**. Following the anomaly separation process, the resulting residual gravity anomaly displays variations between -3 and 2 mGal, indicating the presence of shallower geological features, as shown in **Figure 5c**, specifically referring to the residual anomalies.

The geological characteristics in this study were further enhanced using the FSED technique, which produces values ranging from -1 to 1, as illustrated in **Figure 6a**. Additionally, the estimated depths derived from Euler Deconvolution, as shown in **Figure 6b**, are represented by colored dots distributed across the area, indicating the different depths of geological features that extend up to 3700 meters beneath the surface. The combination of these techniques enables the interpretation of the targeted geological features at the boundary where the value is maximum (**Kamto et al., 2023; Oksum et al., 2021; Pham et al., 2023**), as well as their estimated depths.

The analysis of geological structures utilizing the FSED approach indicates a clear predominance of orientations ranging from northwest-southeast (NW-SE) to north-south (N-S). Furthermore, geological features aligned in the east-west (E-W) direction were also observed as minor orientations. These directional variations are consistent with the geological features identified at the surface through lineament and lineament density analysis. Consequently, the structural features identified using the FSED method applied to gravity anomaly data corroborate the surface observations and suggest vertical continuity of these geological structures.

The analysis of depth estimates through Euler Deconvolution indicates that the identified gravity anomalies, corresponding to structural features, extend to depths of

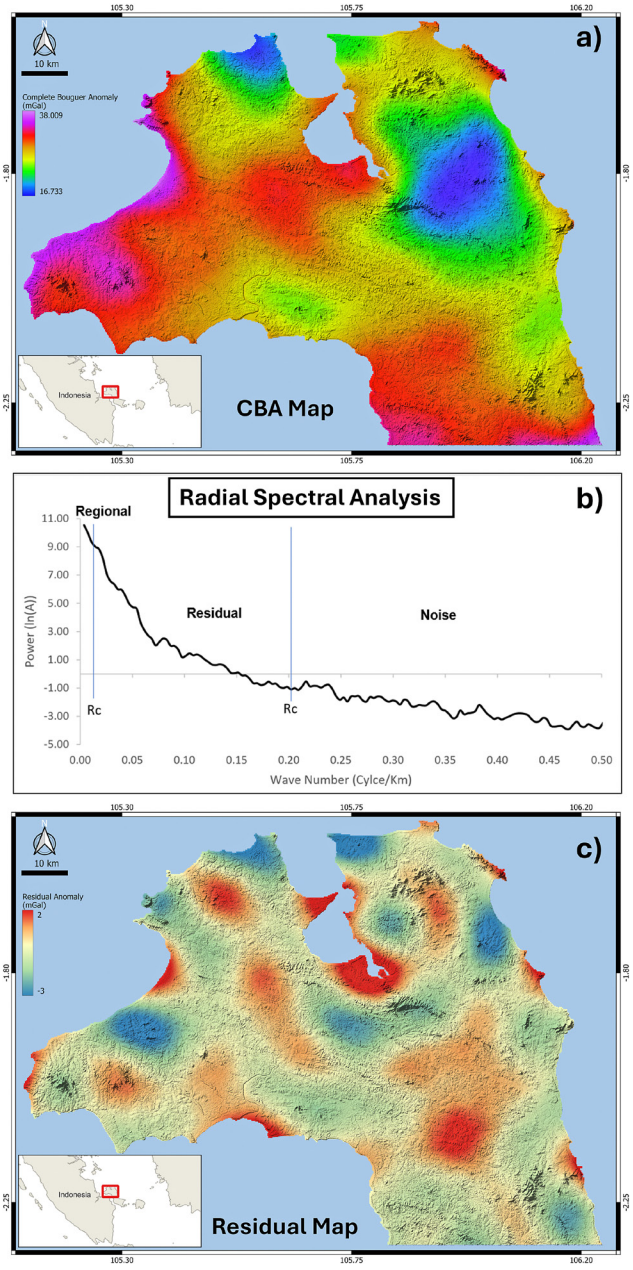


Figure 5. a) Complete Bouguer Anomaly (CBA) map, **b)** radial average power spectrum curve graph CBA data, and **c)** residual map of the study area

3000-4000 meters below sea level. These anomalies exhibit orientations that are consistent with those derived from FSED and surface lineament techniques. The primary structures observed from the Euler Deconvolution analysis are oriented in two predominant directions: northwest-southeast (NW-SE) and east-west (E-W). The NW-SE orientation displays a strong correlation with the second deformation phase associated with the Bentong-Raub thrust line, which extends across the eastern segment of the study area. Conversely, the E-W orientation is linked to thrust faults affecting the Tanjung Genting Formation (TRt) and has played a significant role in the formation of granitic plutons that intruded into the overlying formations in a similar directional pattern.

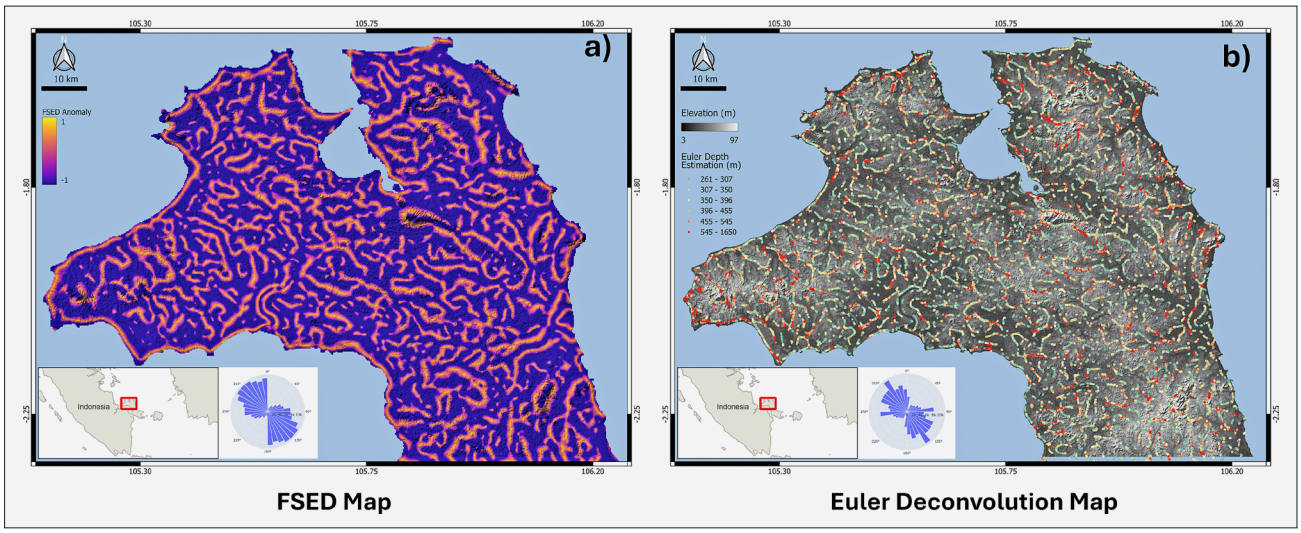


Figure 6. a) Subsurface structural lineaments from FSED and **b)** the estimated depth of structural lineaments from Euler Deconvolution

In addition to these two primary orientations, a minor northeast-southwest (NE-SW) direction, detected through both FSED and Euler Deconvolution, is interpreted as representing the initial deformation phase from the Palaeozoic era. The subduction and collision of the Sibumasu and East Malaya microplates characterise this phase. Furthermore, the north-south (N-S) direction is regarded as the most recently formed minor structure, intersecting older formations in the study area. Its formation is likely influenced by tectonic activity originating from Sumatra that extends to the northern region of Bangka Island and manifests as regional shear faults with similar orientation (**Barber et al., 2005; Franto, 2015**).

The interpretations presented herein are grounded in the findings of prior studies conducted in this area, which employed various surface and subsurface methodologies. The results obtained further substantiate the subsurface structural framework of northern Bangka, using high-resolution data and comprehensive investigative approaches.

5. Discussion

The delineation of subsurface structural settings through the utilization of satellite data, processed with techniques such as surface lineament extraction, enhanced edge detection (FSED), and Euler Deconvolution, produces optimal results that are mutually corroborative. This finding indicates that the lineament traces identified as geological features at the surface are indeed associated with subsurface structures formed during tectonic and deformation events in the northern Bangka Island region, specifically during the Palaeozoic and Mesozoic periods.

This study utilizes natural fracture measurements from granite rock outcrops, estimated to be of Triassic age, located in the Sungailiat area of northern Bangka, to validate the identified geological structures. **Figure 7a** illustrates the sites where these natural fracture measurements were taken. A total of six locations were assessed: Pantai Parai (G1 and G2), Pantai Rambak (G3 and G4), Pantai Batu Ketak (G5), and Pantai Mutiara Tikus (G6). Natural fractures measurements were conducted using the scanline method at each site, following the measurement approach depicted in **Figure 7b**. The measurement results indicate that the natural fractures observed in the granite outcrops exhibit distributions in various orientations, consistent with the regional structural patterns in the area. At locations G1 and G2, the natural fractures are predominantly aligned in the NE-SW and NW-SE directions. Additionally, location G2 exhibits an E-W orientation, which is hypothesized to have formed due to extensional processes.

At sites G3 and G4, in addition to the prevailing NW-SE and NE-SW orientations, a significant N-S direction is also observed, particularly at site G4. Similarly, at locations G5 and G6, the natural fractures primarily display NW-SE and NE-SW orientations. The observed variation in the orientations of natural fractures within the granitic rock outcrops throughout the study area is believed to be closely associated with the orientations of the predominant structural features. These results suggest that the development of natural fractures occurred concurrently with the formation of these regional structures.

Based on the findings from the literature review, as well as observations of natural fractures and the geological map of the study area, several tectonic events are identified that correlate with the formation of the primary structures in this region:

(1) NW-SE Trending Structures - These structures are associated with subduction and collision processes between continental plates (**Barber et al., 2005; Barber & Crow, 2009; Ko, 1986; Widana, 2013**). They correlate with the formation of parallel thrusts between the Pe-

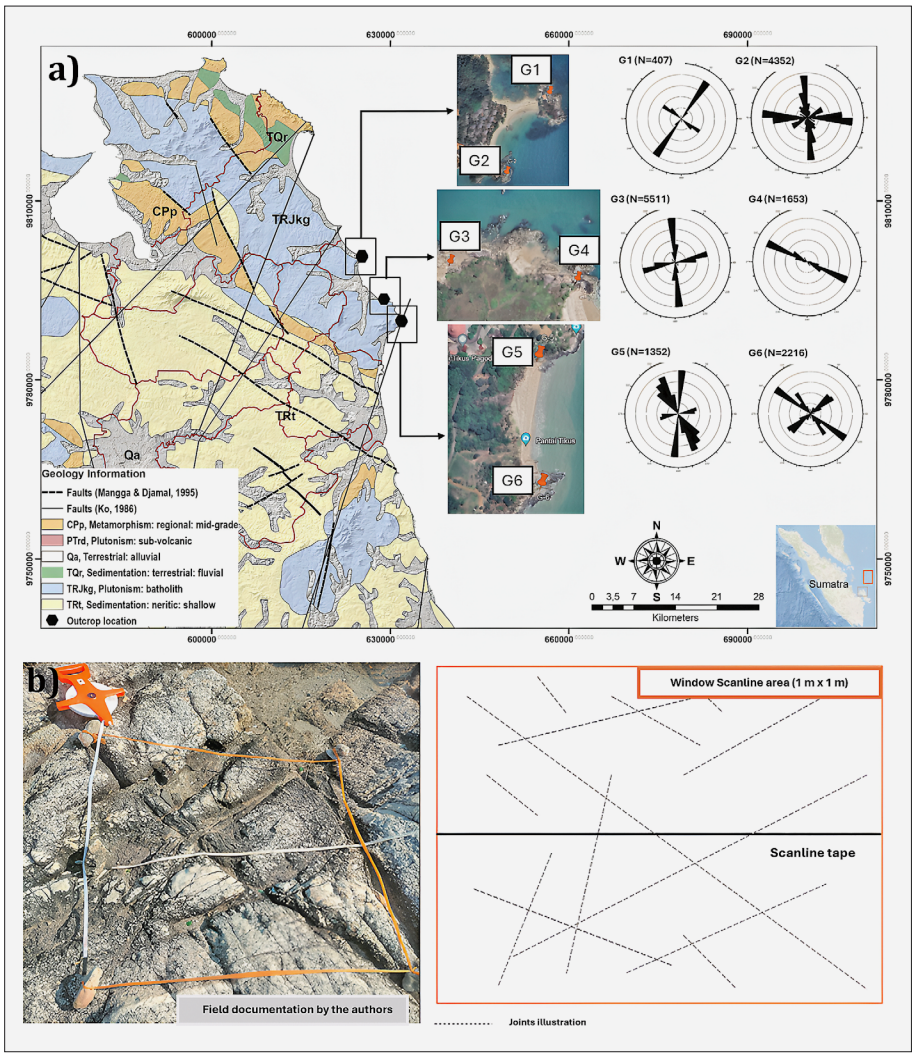


Figure 7. a) location map of measured natural fractures on granitic plutons outcrops; and **b)** the scanline method utilised in the study area

mali Formation and the Tanjung Genting Formation, both of which are aligned in the same NW-SE direction. This tectonic activity also initiated the intrusion of granite along an east-west direction during the Late Permian to Late Triassic period (**Ng et al., 2017; Wang et al., 2021**), mainly detected at location G2. The NW-SE trend is further interpreted to indicate lithological contacts in the northern Bangka region (**Franto, 2015**). Furthermore, the major east-west thrust juxtaposes folded Paleozoic and Triassic sequences, with granite intrusions aligned parallel to these faults, suggesting a genetic relationship (**Siregar et al., 2024**).

(2) the NE-SW trending regional shear faults. These represent tectonic events that have influenced the formation of shear faults, such as the Payung faults and the Pemali faults (**Anggraeni et al., 2023; Katili, 1967**). Subsequently, dextral, north-south-trending strike-slip systems dissected older thrusts and sedimentary packages, corresponding to Tertiary tectonic reactivation and basin subsidence (**Ko, 1986; Susilo et al., 2015**). It is strongly suspected that these faults have influenced the formation of fractures observed at locations G2, G3, and G5.

6. Conclusions

This study provides an in-depth examination of the fault structures beneath the surface of the Paleozoic-Mesozoic granitic basement of Bangka Island. The research utilized a multifaceted approach, incorporating surface lineament extraction, Fast-Sigmoid Edge Detection (FSED), and Euler Deconvolution. The analysis identified significant fault features trending NW-SE to E-W and NE-SW to N-S across various geological formations. These features are consistent with established regional tectonic patterns and indicate multiple phases of deformation.

We successfully identified concealed fault systems by applying FSED and Euler Deconvolution to gravity anomaly data. This methodology effectively delineates distinct rock layers and fractured zones at varying depths. Furthermore, comparing remote sensing data with field measurements of natural fractures within granitic outcrops corroborated the structural trends identified through analyses of satellite and gravity data. The findings of this study underscore the efficacy and cost-effectiveness of integrating high-resolution gravity data

with edge detection filters for analyzing subsurface structures, particularly in regions with limited geological exposure.

The results enhance our understanding of the tectonic framework in northern Bangka and provide a practical approach for identifying fractured basement reservoirs, which are crucial for hydrocarbon exploration in similar granitic environments.

Acknowledgement

The author wishes to express gratitude to several colleagues who contributed valuable insight and engaged in meaningful discussions related to this research. Their contributions have significantly enhanced the comprehensiveness of the interpretations presented in this paper.

Funding

This research is a component of a doctoral study being conducted at the Faculty of Geological Engineering at Padjadjaran University. It is being supported by the Indonesian Education Scholarship (BPI) in partnership with the Centre of Higher Education Financing and Assessment (PPAPT) and the Indonesian Endowment Fund for Education (LPDP) for the period from 2021 to 2025.

7. References

Ahmadi, H., & Pekkan, E. (2021). Fault-Based Geological Lineaments Extraction Using Remote Sensing and GIS – A Review. *Geosciences*, *11*(5), 183. https://doi.org/10.3390/geosciences11050183

Anggraeni, D., Siregar, R. N., & Sismanto, S. (2023). Identification of Subsurface Structures Using Topex Altimetry Satellite Gravity Data: Implications for Preliminary Surveys of Geothermal Existence. *International Journal of Hydrological and Environmental for Sustainability*, *2*(2), 88–96. https://doi.org/10.58524/ijhes.v2i2.261

Aprina, P. U., Santoso, D., Alawiyah, S., Prasetyo, N., & Ibrahim, K. (2024). Delineating geological structure utilizing integration of remote sensing and gravity data: a study from Halmahera, North Molucca, Indonesia. *Vietnam Journal of Earth Sciences*. https://doi.org/10.15625/2615-9783/20010

Areshev, E. G., Dong, T. Le, San, N. T., & Shnip, O. A. (1992). Reservoirs in fractured basement on the continental shelf of southern vietnam. *Journal of Petroleum Geology*, *15*(3), 451–464. https://doi.org/10.1111/j.1747-5457.1992.tb00719.x

Army, E. K., & Saepuloh, A. (2020). Field Verifications of Geological Structures Related to SAR Detected Lineaments. *IOP Conference Series: Earth and Environmental Science*, *417*(1). https://doi.org/10.1088/1755-1315/417/1/012012

Azman, A. I., Talib, J. A., & Sokiman, M. S. (2020). The Integration of Remote Sensing Data for Lineament Mapping in the Semanggol Formation, Northwest Peninsular Malaysia. *IOP Conference Series: Earth and Environmental Science*, *540*(1), 012026. https://doi.org/10.1088/1755-1315/540/1/012026

Barber, A. J., & Crow, M. J. (2009). Structure of Sumatra and its implications for the tectonic assembly of Southeast Asia and the destruction of Paleotethys. *Island Arc*, *18*(1), 3–20. https://doi.org/10.1111/j.1440-1738.2008.00631.x

Barber, A. J., Crow, M. J., & Milsom, J. S. (2005). Sumatra: Geology, Resources, and Tectonic Evolution. In *The Geological Society* (Geological). The Geological Society.

Bhardwaj, A., Jain, K., & Chatterjee, R. S. (2020). Refining IKONOS DEM for Dehradun Region Using Photogrammetry Based DEM Editing Methods, Orthoimage Generation and Quality Assessment of Cartosat-1 DEM. *IECG 2020*, 3. https://doi.org/10.3390/IECG2020-06966

Blakely, R. J. (1995). *Potential Theory in Gravity and Magnetic Applications*. Cambridge University Press.

Carvalho, R., & Batty, M. (2005). Encoding Geometric Information in Road Networks Extracted from Binary Images. *Environment and Planning B: Planning and Design*, *32*(2), 179–190. https://doi.org/10.1068/b31128c

Cobbing, E. J., Pitfield, P. E. J., Darbyshire, P. D. F., & Mallick, D. I. J. (1986). The granites of the Southeast Asian Tin Belt. *Journal of the Geological Society*, *143*, 537–550.

Cooper, G. (2008). Euler Deconvolution with Improved Accuracy and Multiple Different Structural Indices. *Journal of China University of Geosciences*, *19*(1), 72–76. https://doi.org/10.1016/S1002-0705(08)60026-6

Cuong, T. X., & Warren, J. K. (2009). Bach ho field, a fractured granitic basement reservoir, Cuu Long Basin, offshore SE Vietnam: A 'buried-hill' play. *Journal of Petroleum Geology*, *32*(2), pp 129-156. https://doi.org/10.1111/j.1747-5457.2009.00440.x

Echeverria, M. D. P. V., Ortega, A. G. V., Larreta, E., Romero Crespo, P., & Mulas, M. (2022). Lineament Extraction from Digital Terrain Derivate Model: A Case Study in the Girón–Santa Isabel Basin, South Ecuador. *Remote Sensing*, *14*(21), 5400. https://doi.org/10.3390/rs14215400

Eldosouky, A. M., Pham, L. T., Duong, V. H., Kemgang Ghomsi, F. E., & Henaish, A. (2022). Structural interpretation of potential field data using the enhancement techniques: a case study. *Geocarto International*, *37*(27), 16900–16925. https://doi.org/10.1080/10106049.2022.2120548

Enoh, M. A., Okeke, F. I., & Okeke, U. C. (2021). Automatic lineaments mapping and extraction in relationship to natural hydrocarbon seepage in Ugwueme, South-Eastern Nigeria. *Geodesy and Cartography (Vilnius)*, *47*(1), 34–44. https://doi.org/10.3846/gac.2021.12099

Farmakis-Serebryakova, M., & Hurni, L. (2020). Comparison of Relief Shading Techniques Applied to Landforms. *ISPRS International Journal of Geo-Information*, *9*(4), 253. https://doi.org/10.3390/ijgi9040253

Florinsky, I. V. (2016). Lineaments and Faults. *Digital Terrain Analysis in Soil Science and Geology*, 353–376. https://doi.org/10.1016/b978-0-12-804632-6.00014-6

Franto. (2015). Interpretasi Struktur Geologi Regional Pulau Bangka Berdasarkan Citra Shuttle Radar Topography Mis-

sion (SRTM) (Interpretation Structure of Regional Geology on Bangka Island with Shuttle Radar Topography Mission (SRTM)). *Jurnal Promine*, *3*(1), 10–20.

Ghosh, G. K. (2022). Study of gravity signature across the floating basement of Bundelkhand granite using 3D-Euler deconvolution, source edge detection technique and various gravity gradient analyses. *Acta Geophysica*, *70*(4), 1519–1537. https://doi.org/10.1007/s11600-022-00798-4

Gillespie, P. A., Holdsworth, R. E., Long, D., Williams, A., & Gutmanis, J. C. (2021). Introduction: geology of fractured reservoirs. *Journal of the Geological Society*, *178*(2). https://doi.org/10.1144/jgs2020-197

Gillespie, P., Gutmanis, J., Holdsworth, B., Long, D., Mcallister, E., Simon, S., Shell, P., Williams, A., Ameen, M. S., Aramco, S., Di Cuia, R., Laubach, S., & Trice, A. R. (2018, October). *The Geology of Fractured Reservoirs*. www.geolsoc.org.uk/petroleum

Gutmanis, J. (2009). Basement reservoirs - A review of their geological and production characteristics. *Society of Petroleum Engineers - International Petroleum Technology Conference 2009, IPTC 2009*, *1*, 358–364. https://doi.org/10.2523/iptc-13156-ms

Guttormsen, J. (2010). Naturally fractured basement reservoirs: using South Sumatra to characterize the challenges of exploring and exploiting fracture basement reservoirs. *Proc. Indon Petrol. Assoc., 34th Ann. Conv.*, *IPA10-G-18*(May 2010). https://doi.org/10.29118/IPA.742.10.G.183

Hall, R., Clements, B., & Smyth, H. R. (2009). Sundaland: Basement character, structure and plate tectonic development. *Proceedings, Indonesian Petroleum Association Thirty-Third Annual Convention & Exhibition*. https://www.researchgate.net/publication/268358722

Han, L., Liu, Z., Ning, Y., & Zhao, Z. (2018). Extraction and analysis of geological lineaments combining a DEM and remote sensing images from the northern Baoji loess area. *Advances in Space Research*, *62*(9), 2480–2493. https://doi.org/10.1016/j.asr.2018.07.030

Hendrawan, R., Draniswari, W. A., Wahyuni, F. I., Sapiie, B., & Basuki, N. I. (2024). Metamorphic Complex Deformation in North Bangka Island Based on Macrostructures and Microstructures Evidences. *Journal of Geoscience, Engineering, Environment, and Technology*, *9*(2), 134–139. https://doi.org/10.25299/jgeet.2024.9.2.13379

Hennings, P., Allwardt, P., Paul, P., Zahm, C., Reid, R., Alley, H., Kirschner, R., Lee, B., & Hough, E. (2012). Relationship between fractures, fault zones, stress, and reservoir productivity in the Suban gas field, Sumatra, Indonesia. *AAPG Bulletin*, *96*(4), 753–772. https://doi.org/10.1306/08161109084

Hirt, C. (2014). Digital Terrain Models. In *Encyclopedia of Geodesy* (pp. 1–6). Springer International Publishing. https://doi.org/10.1007/978-3-319-02370-0_31-1

Hirt, C., Claessens, S., Fecher, T., Kuhn, M., Pail, R., & Rexer, M. (2013). New ultrahigh-resolution picture of Earth's gravity field. *Geophysical Research Letters*, *40*(16), 4279–4283. https://doi.org/10.1002/grl.50838

Hobbs, W. H. (1904). Lineaments of the Atlantic Border region. *Bulletin of the Geological Society of America*, *15*, 483–506. https://doi.org/10.1130/GSAB-15-483

Hung, N. Du, Le, H. Van, Joc, H. V., & Minh, H. C. (2003). Hydrocarbon Geology of Cuu Long Basin - Offshore Vietnam. *AAPG; Search and Discovery*, *1*(1), 21–24.

Hung, L. Q., Batelaan, O., & De Smedt, F. (2005). Lineament extraction and analysis, comparison of LANDSAT ETM and ASTER imagery. Case study: Suoimuoi tropical karst catchment, Vietnam. In M. Ehlers & U. Michel (Eds.), *Remote Sensing for Environmental Monitoring, GIS Applications, and Geology V* (Vol. 5983, p. 59830T). SPIE. https://doi.org/10.1117/12.627699

Hung, N., & Le, H. (2004). Petroleum Geology of Cuu Long Basin - Offshore Vietnam. *American Association of Petroleum Geologists. Search and Discovery, Article #10062.*

Hutchison, C. S. (2014). Tectonic evolution of Southeast Asia. *Bulletin of the Geological Society of Malaysia*, *60*(December), 1–18. https://doi.org/10.7186/bgsm60201401

Kamto, P. G., Oksum, E., Yap, L., Kande, L. H., & Kamguia, J. (2023). High precision structural mapping using advanced gravity processing methods: a case study from the North region of Cameroon. *Acta Geophysica*. https://doi.org/10.1007/s11600-023-01211-4

Katili, J. A. (1967). Structure and Age of The Indonesian Tin Belt with Special Reference to Bangka. *Tectonophysics*.

Katili, J. A. (1972, June). Plate tectonics of Indonesia with special reference to the Sundaland area. *Proceedings Indonesian Petroleum Association First Annual Convention*.

Ko, U. (1986). Preliminary synthesis of the geology of Bangka Island, Indonesia. In *Bulletin of the Geological Society of Malaysia* (Vol. 1).

Koning, T., Cameron, N., & Clure, J. (2021). Undiscovered Potential in the Basement Exploring in Sumatra for oil and gas in naturally fractured and weathered basement reservoirs. *Berita Sedimentologi*, *47*(2), 67–79. https://doi.org/10.51835/bsed.2021.47.2.320

Kumar, R., & Singh, K. A. (2021). Delineation of subsurface features by gravity technique in parts of Shivpuri District, M.P. *MAUSAM*, *72*(3), 661–668. https://doi.org/10.54302/mausam.v72i3.1316

Kumar, U., Pal, S. K., Sahoo, S. D., Narayan, S., Saurabh, Mondal, S., & Ganguli, S. S. (2018). Lineament Mapping over Sir Creek Offshore and its Surroundings using High Resolution EGM2008 Gravity Data: An Integrated Derivative Approach. *Journal of the Geological Society of India*, *91*(6), 671–678. https://doi.org/10.1007/s12594-018-0922-x

Kurniawan, B. A. (2018). Application of 3D Seismic Volume Curvature for Basement Fracture Delineation, Case Study : Suban Field, South Sumatra Basin. *Proc. Indon Petrol. Assoc., 36th Ann. Conv.*, *C*(May). https://doi.org/10.29118/IPA.0.12.G.170

Li, B., Guttormsen, J., Hoi, T., & Duc, N. (2004). Characterizing Permeability for the Fractured Basement Reservoirs. *Proceedings of SPE Asia Pacific Oil and Gas Conference and Exhibition*, *October 2004*, 271–281. https://doi.org/10.2523/88478-MS

Li, L., Huang, D., Han, L., & Ma, G. (2014). Optimised edge detection filters in the interpretation of potential field data.

Exploration Geophysics, *45*(3), 171–176. https://doi.org/10.1071/EG13059

Liu, J., Li, S., Jiang, S., Wang, X., & Zhang, J. (2023). Tools for Edge Detection of Gravity Data: Comparison and Application to Tectonic Boundary Mapping in the Molucca Sea. *Surveys in Geophysics*, *44*(6), 1781–1810. https://doi.org/10.1007/s10712-023-09784-x

Ma, G., Liu, C., & Li, L. (2014). Balanced horizontal derivative of potential field data to recognize the edges and estimate location parameters of the source. *Journal of Applied Geophysics*, *108*, 12–18. https://doi.org/10.1016/j.jappgeo.2014.06.005

Mangga, A. A., & Djamal, B. (1994). *Peta Geologi Lembar Bangka Utara, Sumatera (Skala 1:250.000)*.

Margono, U., Supandjono, R., & Partoyo, E. (1995). *Geological Map of the South Bangka Sheet, Sumatera*.

McCourt, W. J., Crow, M. J., Cobbing, E. J., & Amin, T. C. (1996). Mesozoic and Cenozoic plutonic evolution of SE Asia: evidence from Sumatra, Indonesia. *Geological Society, London, Special Publications*, *106*(1), 321–335. https://doi.org/10.1144/GSL.SP.1996.106.01.21

Melo, F. F., & Barbosa, V. C. F. (2018). Correct structural index in Euler deconvolution via base-level estimates. *GEOPHYSICS*, *83*(6), J87–J98. https://doi.org/10.1190/geo2017-0774.1

Melouah, O., & Pham, L. T. (2021). An improved ILTHG method for edge enhancement of geological structures: application to gravity data from the Oued Righ valley. *Journal of African Earth Sciences*, *177*, 104162. https://doi.org/10.1016/j.jafrearsci.2021.104162

Metcalfe, I. (2000). The Bentong-Raub Suture Zone. *Journal of Asian Earth Sciences*, *18*(6), 691–712. https://doi.org/10.1016/S1367-9120(00)00043-2

Metcalfe, I. (2013). Tectonic evolution of the Malay Peninsula. *Journal of Asian Earth Sciences*, *76*, 195–213. https://doi.org/10.1016/j.jseaes.2012.12.011

Metcalfe, I. (2017). Tectonic evolution of Sundaland. *Bulletin of the Geological Society of Malaysia*, *63*(November), 27–60. https://doi.org/10.7186/bgsm63201702

Mohammed, A., K, P., Kumanan, C. J., & Ramasamy, SM. (2010). Significance of Surface Lineaments for Gas and Oil Exploration in Part of Sabatayn Basin-Yemen. *Journal of Geography and Geology*, *2*(1), 119–128. https://doi.org/10.5539/jgg.v2n1p119

Narr, W., Schechter, D. S., & Thompson, L. B. (2006). Naturally Fractured Reservoir Characterization. In *Society of Petroleum Engineers*. Society of Petroleum Engineers.

Nasuti, Y., Nasuti, A., & Moghadas, D. (2019). STDR: A Novel Approach for Enhancing and Edge Detection of Potential Field Data. *Pure and Applied Geophysics*, *176*(2), 827–841. https://doi.org/10.1007/s00024-018-2016-5

Ng, H.-F. (2006). Automatic thresholding for defect detection. *Pattern Recognition Letters*, *27*(14), 1644–1649. https://doi.org/10.1016/j.patrec.2006.03.009

Ng, S. W.-P., Whitehouse, M. J., Roselee, M. H., Teschner, C., Murtadha, S., Oliver, G. J. H., Ghani, A. A., & Chang, S.-C. (2017). Late Triassic granites from Bangka, Indonesia: A continuation of the Main Range granite province of the South-East Asian Tin Belt. *Journal of Asian Earth Sciences*, *138*, 548–561. https://doi.org/10.1016/j.jseaes.2017.03.002

Ni, C., Zhang, S., Liu, C., Yan, Y., & Li, Y. (2016). Lineament Length and Density Analyses Based on the Segment Tracing Algorithm: A Case Study of the Gaosong Field in Gejiu Tin Mine, China. *Mathematical Problems in Engineering*, *2016*, 1–7. https://doi.org/10.1155/2016/5392453

Oksum, E., Le, D. V., Vu, M. D., Nguyen, T. H. T., & Pham, L. T. (2021). A novel approach based on the fast sigmoid function for interpretation of potential field data. *Bulletin of Geophysics and Oceanography*, *62*(3), 543–556. https://doi.org/10.4430/bgta0348

P'an, C.-H. (1982). Petroleum in Basement Rocks. *American Association of Petroleum Geologists Bulletin*, *66*(10), 1597–1643. https://doi.org/10.1306/03b5a994-16d1-11d7-8645000102c1865d

Permana, B. R., Yusim, S., Darmadi, Y., & Firdaus, M. (2023). Integration of core analysis, logs, seismic and dynamic data in defining fracture reservoir: case study suban field, south sumatra. *Proceedings, Indonesian Petroleum Association Forty-Seventh Annual Convention & Exhibition*. https://www.researchgate.net/publication/372689625

Petford, N., & McCaffrey, K. (2003). Hydrocarbons in crystalline rocks: An introduction. *Geological Society Special Publication*, *214*(2002), 1–5. https://doi.org/10.1144/GSL.SP.2003.214.01.01

Pham, L. T. (2024). An improved edge detector for interpreting potential field data. *Earth Science Informatics*, *17*(3), 2763–2774. https://doi.org/10.1007/s12145-024-01286-7

Pham, L. T., Eldosouky, A. M., Melouah, O., Abdelrahman, K., Alzahrani, H., Oliveira, S. P., & Andráš, P. (2021). Mapping subsurface structural lineaments using the edge filters of gravity data. *Journal of King Saud University - Science*, *33*(8), 101594. https://doi.org/10.1016/j.jksus.2021.101594

Pham, L. T., Ghomsi, F. E. K., Vu, T. Van, Oksum, E., Steffen, R., & Tenzer, R. (2023). Mapping the structural configuration of the western Gulf of Guinea using advanced gravity interpretation methods. *Physics and Chemistry of the Earth, Parts A/B/C*, *129*, 103341. https://doi.org/10.1016/j.pce.2022.103341

Pham, L. T., Oliveira, S. P., Abdelrahman, K., Gomez-Ortiz, D., Nguyen, D. V., Vo, Q. T., & Eldosouky, A. M. (2024). Selection of Euler deconvolution solutions using the enhanced horizontal gradient and stable vertical differentiation. *Open Geosciences*, *16*(1). https://doi.org/10.1515/geo-2022-0637

Prabowo, I. A., Verdiansyah, O., & Prabowo, R. (2021). *Extraction of Lineament Density Analysis from ASTER DEM for Determine the Vein Direction*. *Figure 1*. https://doi.org/10.4108/eai.30-8-2021.2311530

Reid, A., Geophysics, R., of Leeds, U., FitzGerald, D., & McInerny, P. (2003). Euler deconvolution of gravity data. *SEG Annual Meeting, Dallas, Texas, October 2003*. https://doi.org/http://dx.doi.org/10.13140/2.1.3210.0489

Reid, A., Geophysics, R., & Thurston, J. (2012). The Structural Index in gravity and magnetic interpretation: errors, uses

and abuses. *SEG Technical Program Expanded Abstracts 2012*, 1–6. https://doi.org/10.1190/segam2012-0152.1

Rusinkiewicz, S., Burns, M., & DeCarlo, D. (2006). Exaggerated shading for depicting shape and detail. *ACM Transactions on Graphics*, *25*(3), 1199–1205. https://doi.org/10.1145/1141911.1142015

Safani, J., IBRAHIM, K., DENI, W., RUBAIYN, A., FIRDAUS, F., & HARISMA, H. (2023). Interpreting structural configuration of the Sengkang Basin of Indonesia using edge detection and 3-D Euler deconvolution to satellite gravity data. *Turkish Journal of Earth Sciences*, *32*(7), 894–914. https://doi.org/10.55730/1300-0985.1881

Salui, C. L. (2018). Methodological Validation for Automated Lineament Extraction by LINE Method in PCI Geomatica and MATLAB based Hough Transformation. *Journal of the Geological Society of India*, *92*(3), 321–328. https://doi.org/10.1007/s12594-018-1015-6

Schultz, A. (2014). Satellite Interferometry and the Detection of Active Deformation Associated With Faults in Suban Field, South Sumatra Basin, Indonesia. *Proc. Indonesian Petrol. Assoc., 38th Ann. Conv.*, *May*. https://doi.org/10.29118/IPA.0.14.G.068

Sembiring, D. K., Indriana, R. D., & Yulianto, T. (2023). Subsurface Model Of Mt. Sinabung Using The GGM-Plus Satellite Gravity Data And Deconvolution Euler. *International Journal of Progressive Sciences and Technologies*, *39*(1), 169–176.

Siregar, R. N., Nukman, M., Widana, K. S., Harijoko, A., & Sismanto, S. (2024). Radiogenic geothermal systems of Bangka Island, Indonesia: Implications of high heat production and tectonic framework. *Energy Geoscience*, *5*(4), 100306. https://doi.org/10.1016/j.engeos.2024.100306

Soleha, K. P., Handyarso, A., Fitriani, D., & Supriyana, E. (2019). Modeling of subsurface based on gravity data with second vertical derivative (SVD) and Euler deconvolution optimization. *IOP Conference Series: Earth and Environmental Science*, *311*(1), 012065. https://doi.org/10.1088/1755-1315/311/1/012065

Spector, A., & Grant, F. S. (1970). Statistical models for interpreting aeromagnetic data. *Geophysics*, *35*(2), 293–302. https://doi.org/10.1190/1.1440092

Susilo, Y. S., Anzhar, K., Sastratenaya, S., Godoy, A. R., & Serva, L. (2015). SEISMOTECTONIC CONSIDERATIONS ON BANGKA ISLAND NPP SITING. *Prosiding Seminar Nasional Teknologi Energi Nuklir*.

Suyoto, H. (2010). A fractured pre-tertiary Basement Reservoir Engineering Study. *Proc. Indon Petrol. Assoc., 34th Ann. Conv.*, *May 2010*. https://doi.org/10.29118/IPA.1409.10.E.064

Tjia, H. D. (2007). Fractured Granitic Basement as Reservoir. *Proceedings joint convention bali. The 32th HAGI, the 36th IAGI, and the 29th IATMI Annual Conference and Exhibition*, 1414–1417.

Van Gorsel, J. T. (2018). Bibliography of the geology of Indonesia and surrounding areas - PART II. Sumatra-Sundaland (Sumatra, 'Tin Islands', Sunda Shelf, Natuna). *Bibiliography of Indonesian Geology*, *7.0*, 0–315. http://www.vangorselslist.com/pdf/BIG_I_Regional_7.pdf

Vincent, O., & Folorunso, O. (2009). *A Descriptive Algorithm for Sobel Image Edge Detection*. https://doi.org/10.28945/3351

Wang, Y., Qian, X., Zhang, Y., Gan, C., Zhang, A., Zhang, F., Feng, Q., Cawood, P. A., & Zhang, P. (2021). Southern extension of the Paleotethyan zone in SE Asia: Evidence from the Permo-Triassic granitoids in Malaysia and West Indonesia. *Lithos*, *398–399*. https://doi.org/10.1016/j.lithos.2021.106336

Widana, K. S. (2013). Petrografi dan Geokimia Unsur Utama Granitoid Pulau Bangka: Kajian Awal Tektonomagmatisme. *Eksplorium*, *34*, 1–16. https://www.researchgate.net/publication/318642660

Yao, Y., Huang, D., Yu, X., & Chai, B. (2016). Edge interpretation of potential field data with the normalized enhanced analytic signal. *Acta Geodaetica et Geophysica*, *51*(1), 125–136. https://doi.org/10.1007/s40328-015-0120-x

Bampourda, D., Argialas, D., Nomikou, P., & Tzotsos, A. (2017). An object-based image analysis approach for the extraction of the Kolokthron volcano and associated domes-cones from a digital seabed elevation model. *Bulletin of the Geological Society of Greece*, *50*(3), 1616. https://doi.org/10.12681/bgsg.11881

SAŽETAK

Integrirana analiza rasjeda temeljnoga sloja na otoku Bangka u Indoneziji korištenjem gustoće površinskih lineamenata i pojačanja gravitacijskih anomalija

Otok Bangka nastao je subdukcijom i sudarom blokova Sibumasu i Istočna Malaja, koji su potekli iz Gondvane, u kasnome paleozoiku. Njegovu sjevernu regiju čine permske metamorfne stijene kompleksa Pemali, trijaske sedimentne jedinice formacije Tanjunggenting te graniti formacije Klabat iz kasnoga trijasa do rane jure. Unatoč višestrukim tektonskim fazama koje su oblikovale otok Bangka strukturna konfiguracija rasjeda i nabora u podlozi u sjevernoj regiji ostaje slabo razjašnjena. Ova neizvjesnost otežava procjenu ležišta u rasjednom temeljnom sloju u području istraživanja. Kako bi se popunila ova praznina, ova studija integrira ekstrakciju površinskih lineamenata iz DEMNAS-a s podatcima o gravitacijskim anomalijama iz GGMplus-a kako bi se istražila struktura rasjeda temeljnog sloja sjeverne Bangke. Brza detekcija rubova sigmoidom (FSED) i Eulerova dekonvolucija primijenjene su za poboljšanje strukturne interpretacije i procjenu dubine podloge. Dominantne strukturne orijentacije sjeverozapad-jugoistok i sjeveroistok-jugozapad identificirane na površini bile su u skladu s podzemnim značajkama, dok su FSED i Eulerova dekonvolucija također otkrile trendove istok-zapad i sjever-jug. Štoviše, rezultati Eulerove dekonvolucije uputili su na dubine temeljnoga sloja od 3000 do 4000 m ispod razine mora. Mjerenja pukotina na terenu iz granitnih izdanaka potvrđuju ove orijentacije, naglašavajući snažnu podudarnost između površinskih i podzemnih struktura. Ovi nalazi pružaju nove uvide u tektonsku evoluciju sjeverne regije otoka Bangka i ističu orijentacije rasjeda koje bi mogle poslužiti kao smjernice za identifikaciju zona rasjednih ležišta u granitnim terenima.

Ključne riječi:
gustoća linije, poboljšana detekcija rubova, gravitacijska anomalija, strukture rasjeda temeljnog sloja, otok Bangka

Author's contribution

Harnanti Yogaputri Hutami (Ms.): conceptualisation, investigation, formal analysis, validation, and writing – the original draft. **Erlangga Ibrahim Fattah** and **Nugroho Prasetyo** (Mr.): data curation in FSED and Euler Deconvolution methodologies, visualisation, and formal analysis. **Nur Ayu Anas** (Ms.): data curation in lineament extraction and lineament density methodologies, formal analysis, visualisation, and writing – the original draft. **Edy Sunardi and Iyan Haryanto** (Professor): the supervisor team and validation. **Sonny Winardhi** (PhD): supervisor team, formal analysis, and validation.
All authors have read and agreed to the published version of the manuscript.

RGNZ/*MGPB*

Radovi/*Papers*

1.	Geomechanical Analysis to Determine The Maximum Limit of Water Injection in the Keutapangan Formation, "ZA" Field, North Sumatra Basin *(Zahra Adinda Billqish, Andika Wicaksono, Sismanto Sismanto)*	1-14
2.	Study of the bactericidal-inhibitor properties of new reagents *(Guseyn Gurbanov, Aysel Gasimzade)*	15-30
3.	Optimization of Stope Dimensions in a Geotechnically Complex Mine Using Automated Stability Analysis *(Mohammad Army, Tri Karian, Takashi Sasaoka, Akihiro Hamanaka, Firly Rachmaditya Baskoro, Budi Sulistianto, Hideki Shimada)*	31-46
4.	Feasibility analysis of granitic rocks for use in the dimension stone industry *(Ekin Köken)*	47-57
5.	Facies Architecture and Sedimentary Provenance of the Miocene Ombilin Formation: Interplay of Tectonics and Eustasy in a Neogene Intermontane Basin, Central Sumatra, Indonesia *(Aurio Erdi, Syahreza S. Angkasa, Eko Suwarno, Aswan)*	59-84
6.	The Effect of Calcium and Magnesium Ions on a Crude Oil-Brine-Carbonate Rock System for Enhanced Oil Recovery by Sophorolipid Solution *(Indah Widiyaningsih, Ivan Kurnia, Harry Budiharjo Sulistyarso, Tutuka Ariadji, Taufan Marhaendrajana)*	85-95
7.	Geodynamic and Paragenetic Evolution of the Jbel Houanite Mineralization (Sb-Au; Pb-Zn) Eastern High Atlas of Morocco *(Jaouad Choukrad, Abdelkhiar Ait ali, Mohammed Charroud, Nacir El moutaouakkil, Boubker Boukili, Amine talih)*	97-112
8.	Unveiling Shale Gas Reservoir Structures with Seismic and MT Data: WALDIM-Based Study from East Kalimantan Indonesia *(Suharsono, Yustisio Dianwiyono, Edy Wijanarko, Wahyu Hidayat, Muhammad Fachrul Rozi Kurniawan, Yudha Agung Pratama)*	113-128
9.	Predicting Peak Particle Velocity Induced by Mining Blasting Using Optimized Deep Learning with Coronavirus Herd Immunity Algorithm *(Davood Mohammadi Sargini, Mohammad Ataei, Reza Mikaeil, Akbar Esmaeilzadeh)*	129-146
10.	Hydraulic Connectivity Between the Sava River and Lake Jarun During Drought: A High-Resolution Monitoring and Time Series Approach *(Jelena Parlov, Filip Šegović, Kristijan Posavec, Zoran Kovač)*	147-161
11.	The Effect of Kaolinite on Calcium Carbonate Water-Based Drilling Fluid *(Mohammed Abdalraheem, Basfar S, Elkatatny S)*	163-174
12.	Management of Frame-Anchor Fastening Parameters for Preparatory Excavations in Monorail-Based Heavy Cargo Delivery *(Andrii Herasymenko, Leonid Shyrin, Rostyslav Yegorchenko, Ivan Iniutkin, Yuliya Pazynich)*	175-188
13.	Improving the efficiency of in-situ uranium leaching via oxygen-enriched lixiviant injection *(Khalidilla Yussupov, Erbolat Aben, Gulfarizada Abdissattar, Saifilmalik Myrzakhmetov, Dalelkhan Akhmetkanov)*	189-196
14.	Hydrogeochemical properties of thermal springs for natural therapeutic uses in medical geology at the Ciwidey area, West Java, Indonesia *(Rizka Maria, Heri Nurohman, Hilda Lestiana, Riostantieka Mayandari Shoedarto, Eki Naidania Dida, Jakah Jakah, Ernowo Ernowo, Yudi Rahayudin)*	197-211
15.	The Integrated Analysis of Basement Faults in North Bangka Island, Indonesia, Using Surface Lineament Density and Gravity Anomaly Enhancement *(Harnanti Yogaputri Hutami, Edy Sunardi, Iyan Haryanto, Sonny Winardhi, Nugroho Prasetyo, Nur Ayu Anas, Erlangga Ibrahim Fattah)*	213-228

ISSN 0353-4529

Godište XXXVIII, broj 78 / *Anno XXXVIII, number 78*